Characterisation of Armour Ceramics at the Microstructural Scale for Modelling of Impact



Jiawei Jiang

Corpus Christi College

Department of Materials

University of Oxford

Supervised by:

Professor Richard Todd, Professor Nik Petrinic

Doctor of Philosophy

Trinity Term 2020

Abstract

The present DPhil thesis aims to provide new insights into the deformation and failure mechanisms of armour ceramics by carrying out experimental investigations at the microstructural scale, which can be integrated into numerical modelling to enhance its predictive capability for ceramic armour designs.

Grain size distributions of polycrystalline alumina with varying microstructures were characterised precisely by employing the method of digitising grain contours from SEM images. The experimental results were incorporated to develop an innovative algorithm for generating representative numerical microstructures, and to validate the numerical models via a novel method of virtual cross sectioning.

The effect of shear stresses on brittle failure of grain boundaries was investigated by measuring the strengths of grain boundaries of alumina in combined normal and shear loading. The contribution of the shear component was found to be significant, which overthrew known theories usually adopted in micromechanical modelling that assume otherwise.

Progress towards making reliable toughness measurements of individual microstructural components was made by allowing for, or avoiding the effect of focused ion beam (FIB) damage at notch roots through the following methods.

(a) *Enabling stable crack growth* allowed the stress intensity factor for crack propagation K_p to be measured reliably in Al_2O_3 and SiC. K_p measured in vacuum represented K_c, giving values of 2.8 MPa·m$^{1/2}$ for a-plane sapphire. K_p measured in air was 1.8 MPa·m$^{1/2}$ for both a- and m-plane sapphire, and 2.2 MPa·m$^{1/2}$ for $(\bar{1}100)$ plane SiC. The value was reduced substantially by moisture-assisted subcritical crack growth (SCG) and was close to K_0, with crack velocities on the scale of 10^{-8} m/s. Additionally, cyclic loading tests in vacuum demonstrated the self-healing of interfaces in alumina.

(b) *Clarification of the extent of the effect of the implantation damage*. First, a microstructural investigation of Ga^+- and Xe^+-FIB damage induced in Al_2O_3 and SiC exhibited the formation of amorphous and crystalline damaged layers, which were determined by the combination of ion species, target material and FIB settings. $GaAlO_3$ particles and Xe bubbles were found in Al_2O_3 implanted by Ga^+ and Xe^+, respectively. Second, Ga^+ and Xe^+ implantation stresses (IS) were quantified in Al_2O_3, SiC and Si using a beam-curvature method, and were mostly on the scale of GPa. With increasing ion dose, while the Ga^+ IS in Al_2O_3 and SiC remained compressive, Ga^+ IS in Si and Xe^+ IS in Al_2O_3 and SiC transited from compressive to tensile. For fracture toughness measurement, Ga^+-FIB was recommended for notching all three materials investigated.

Acknowledgements

I would like to thank my supervisors Prof. Richard Todd (Department of Materials) and Prof. Nik Petrinic (Department of Engineering) for their guidance and supervision throughout my studies at Oxford. Richard for his invaluable advice, thoughtful insight and unerring enthusiasm for materials science, and also for his selfless efforts on turning me from an engineer to a scientist through patient mentoring. Nik for his wealth of knowledge on impact engineering and numerical simulations, and for teaching me to be strong. They are the best supervisors I could ever ask for. Thank you both.

Thanks must go to the Defence Science and Technology Laboratory (Dstl, UK Ministry of Defence) for the full sponsorship and for accepting me as a non-UK student, despite the defence nature of the project. It has been a great pleasure working together with the amazing colleagues on the *UNICAM II* project. Heartfelt thanks to Prof. Peter Brown (Dstl) for providing the strong support, guidance and encouragement throughout my DPhil research. Huge thanks to Dr Simone Falco (Oxford) for building the cool models in the project and for providing knowledgeable advice on numerical simulations.

The RIT group members have made DPhil life great fun with lively chats, drinks and pranks. Robin and Alex shared unreservedly their brilliant ideas on ion implantation damage. Gibby and Jesse have made the office a very happy place to do 'scientific work'. It is also a pleasure to share the DPhil journey together with Tom, Mi and the lovely Part II students since my first day in the group.

Thank you to my college advisor, Prof. Peter Nellist, for encouraging and caring my research and university life throughout my DPhil studies. Thanks to everyone in Materials, Engineering, Corpus, and Oxford in general who have been supportive during my DPhil time, including but not limited to Corpus Christi College (especially Prof. Richard Carwardine, Prof. Steven Cowley, Ms. Rachel Clifford, Ms. Sara Watson) for their firm support and warm friendship, IEL (Impact Engineering Laboratory) group for impact tests and tasty coffee, DCCEM staffs for electron microscopy-related training and assistance, A special thank you goes to my good friends Sue, Jin, Myrium and Jinlin for standing by me all the time and for feeding me with a lot of food – the life in Oxford would not have been the same without you.

Various collaborators, although some collaborative work is not mentioned in this thesis, deserve thanks for their help along the way: Jason Foley and Craig Przybyla (AFRL) for in-situ serial-sectioning of alumina, Kristopher Behler and Jerry LaSalvia (ARL) for B_6O work, Ned Thomas and Steven Kooi (Institute for Soldier Nanotechnologies @ MIT) for micro-impact testing, William Smith (Glasgow University) for operating and training me on the Plasma-FIB, Finn Giuliani (ICL) for the access to the in-situ nanoindenter, James Marrow and his group (Oxford) for performing 3D X-ray tomography, Dan Eakin and his group (Oxford) for conducting the in-situ synchrotron impact tests at ESRF.

Thank you to my former colleagues at Airbus in Toulouse, Pete, Milan, Diego, Fred, Patrice, Christel, Ahmadou, Christophe, Kelly, Christiane and so on for their family-like support over these years.

Lastly and above all, I am eternally thankful to my parents and grandmothers, to whom this thesis is dedicated, for their deep love and selfless devotion for all the time.

Preface

This thesis is an account of the work carried out by the author in the Department of Materials, University of Oxford, under the supervision of Prof Richard Todd (Department of Materials) and Prof Nik Petrinic (Department of Engineering Science).

The research work presented is fully funded by the Defence Science and Technology Laboratory (Dstl, UK Ministry of Defence), grant code: DSTL/AGR/00507/01.

No part of this work has been previously submitted for a degree at this or other university. The work of others has been freely drawn upon and is duly acknowledged and referenced in the relevant points in the text.

As listed below, parts of the work described in the thesis are reported in publications, or have been presented at international conferences as posters.

S. Falco, **J. Jiang**, F. De Cola, and N. Petrinic, "Generation of 3D polycrystalline microstructures with a conditioned Laguerre-Voronoi tessellation technique," *Computational Materials Science,* vol. 136, pp. 20-28 (2017).

J. Jiang, R. I. Todd, "Effect of Residual Stress Caused by Gallium-Ion Implantation from FIBing in Alumina," *15th Conference & Exhibition of the European Ceramic Society (ECerS2017)*, Budapest, Hungary (2017).

J. Jiang, R. I. Todd, "Towards Reliable Measurement of Fracture Toughness of Armour Ceramics at the Microstructural Scale," *42nd International Conference on Advanced Ceramics & Composites (ICACC18)*, Daytona Beach, Florida, United States (2018).

The poster was awarded the co-1st place in the 2018 ICACC Best Poster competition by the American Ceramic Society (ACerS).

J. Jiang, R. I. Todd, "Towards Reliable Measurement of Fracture Toughness of Ceramics at the Microstructural Scale," *Symposium on Fine-Scale Mechanical Characterisation and Behaviour, CAMTEC IV*, Cambridge, United Kingdom (2018)

For my grandmother

Contents

Chapter 1. Introduction 9

Chapter 2. Literature Review and Aim of the Research 12

2.1 Ceramic armour 12

2.1.1 Ceramic amour system 12

2.1.2 To defeat what? 13

2.1.3 Projectile impact and penetration mechanisms 13

2.2 Materials 14

2.2.1 Aluminium oxide 15

2.2.1.1 Elastic properties 16

2.2.1.2 Manufacturing and application 17

2.2.2 Silicon carbide 17

2.2.2.1 Elastic properties 19

2.2.2.2 Manufacturing and application 19

2.2.3 Silicon 20

2.2.4 Material properties vs. ballistic performance 21

2.3 Numerical modelling of ceramic armour 23

2.3.1 Generation of microstructure in numerical models 23

2.3.2 Continuum macroscopic constitutive models 26

2.4 Microcantilever beam techniques & strength of grain boundaries 28

2.4.1 Microcantilever techniques 28

2.4.2 Strength of grain boundaries 29

2.5 Reliable fracture toughness measurement 32

2.5.1 Fracture toughness measurement at the microscale 32

2.5.2 Stable crack growth for fracture toughness measurement 34

2.5.3 Subcritical crack growth 36

2.5.4 FIB ion implantation damage at notch tips 39

2.5.4.1 Effects of FIB damage in micro-mechanical tests 39

2.5.4.2 Ion-solid interactions: physical process 41

2.5.4.3 Damage and mechanisms 42

2.5.4.4 Simulation 44

2.5.4.5 Influential factors 45

2.5.4.6 Xe Plasma FIB (PFIB) 50

2.6 Aim of Research 50

Chapter 3. Microstructure – Grain Size Distribution 52
3.1 Experimental 52
3.1.1 Materials manufacturing and density measurement 52
3.1.2 Grain size measurement 54
3.2 Result 56
3.2.1 Microstructural study and density measurement 56
3.2.2 Development of numerical model for representative microstructures 61
3.3 Discussion 67
3.3.1 Effect of ball milling, dopant and sintering temperature 67
3.3.2 Grain size distribution measurement and data calibration 68
3.3.3 Representativeness of the numerical models 69

Chapter 4. Strength of Grain Boundaries 72
4.1 Experimental 72
4.1.1 Methodology 72
4.1.2 Material, sample preparation and testing 74
4.2 Results 77
4.2.1 Strength of grain boundaries 77
4.2.2 Strength of grains 85
4.2.3 Interpretation of experimental results by numerical simulation 86
4.3 Discussion 89
4.3.1 Effect of the cavities and validity of measurement 89
4.3.2 Roles of shear and tensile stresses on grain boundary failure 90
4.3.3 Effect of shear stress under compression 94
4.3.4 Strength of grain boundaries and grains 95

Chapter 5. Reliable Measurement of Fracture Toughness at Microstructural Scale - Stable Crack Growth 97
5.1 Experimental 98
5.1.1 Methodology 98
5.1.2 Sample preparation 102
5.1.3 Testing procedure 104
5.2 Results 105
5.2.1 Development and optimisation of numerical model 105
5.2.2 Fracture toughness of Al_2O_3 measured in air – a-plane 112
5.2.3 Fracture toughness of Al_2O_3 measured in air – m-plane 117
5.2.4 Fracture toughness of Al_2O_3 measured in vacuum – a-plane 120
5.2.5 Fracture toughness of SiC measured in air – (1100) plane 133

5.2.6 Summary of apparent fracture toughness values 137
5.3 Discussion 137
5.3.1 Validation and optimisation of numerical model 137
5.3.2 Subcritical crack growth in alumina and comparison of literature values of K_p 138
5.3.3 Cyclic loading and self-healing 141
5.3.4 Comparison of K_p values for SiC 142

Chapter 6. Reliable Measurement of Fracture Toughness at Microstructural Scale – Understanding the FIB Ion Implantation Damage – Part I. Microstructural Investigation 144
6.1 Experimental 144
6.1.1 Materials and sample preparation 144
6.1.2 FIB conditions 146
6.1.3 SEM and TEM characterisation 148
6.2 Results 149
6.2.1 Ga^+ in Al_2O_3 149
6.2.2 Ga^+ in SiC 156
6.2.3 Xe^+ in Al_2O_3 161
6.3 Discussion 173
6.3.1 SRIM simulation vs. experimental observation 173
6.3.2 Effect of ion species, target materials, and FIB parameters 178
6.3.3 Ga-FIB induced particles 182
6.3.4 Xe-PFIB induced bubbles 185

Chapter 7. Reliable Measurement of Fracture Toughness at Microstructural Scale – Understanding the FIB Ion Implantation Damage – Part II. Quantification of Residual Stress . 188
7.1 Experimental 188
7.1.1 Methodology 188
7.1.2 Materials and sample preparation 190
7.1.3 Annealing 191
7.1.4 Testing procedure 192
7.1.5 Precision of the method 193
7.2 Results 194
7.2.1 Effect of ion dose - low dose regime 196
7.2.1.1 Ga^+ implantation 196
7.2.1.2 Xe^+ implantation 198
7.2.2 Effect of beam current – low current regime 199
7.2.2.1 Ga^+ implantation 199
7.2.2.2 Xe^+ implantation 200
7.2.3 Low to high ion dose regime coupled with low to high beam current 201

7.2.3.1 Ga^+ implantation 201
7.2.3.2 Xe^+ implantation 205
7.2.4 Effect of accelerating voltage 211
7.3 Discussion 212
7.3.1 Mechanisms behind the creation of implantation stresses 212
7.3.2 Development of residual stresses 217
7.3.3 Comparison with literature 225
7.3.4 Residual stresses at notch tips 228
7.3.5 Effect on fracture toughness measurement 229

Chapter 8. Conclusions 232
8.1 Grain size distributions 232
8.2 Strength of grain boundaries 233
8.3 Reliable fracture toughness measurement – stable crack growth 233
8.4 Ion implantation damage – TEM investigation 234
8.5 Ion implantation damage – residual stresses 235

Chapter 9. Future work 237
9.1 Grain size distribution 237
9.2 Strength of grain boundaries 237
9.3 Reliable fracture toughness measurement – stable crack growth 238
9.4 Ion implantation damage – TEM investigation 239
9.5 Ion implantation damage – residual stresses 239

Reference 241

Appendix A Dimensionless compliance and geometrical function 263

Appendix B High resolution SEM images of ion implanted cantilevers 265

Appendix C COMSOL simulation of temperature distribution in FIBed cantilever 284

Chapter 1. Introduction

Ceramic materials have been used in armour systems for personnel and vehicles (ships, tanks, aircraft, land vehicles, space shuttles, space stations) for decades[1-5] [6]. The properties that make ceramics well suited to armour applications include: their high hardness (effective at stopping ballistic projectiles), low density compared to metals (higher mobility, manoeuvrability and cargo capability), as well as high compressive strength (resistant to impact which involves significant compressive loading). Moreover, the possibility to be made transparent makes ceramics a suitable choice for face shields and windows of armoured vehicles.[7]

Despite the extensive application of ceramics in armour systems, the understanding of the failure mechanisms of ceramics upon impact is still limited and non-systematic at present.[6] The *UNICAM* (Understanding and Improving Ceramic Armour Materials) project was therefore initiated by Dstl (Defence Science and Technology Laboratory, UK Ministry of Defence). The first part of the *UNICAM* research program, *UNICAM I*, progressed the development of both experimental[8-10] and modelling[11, 12] methodologies to a certain extent, laying a foundation for the second part of the research project – *UNICAM II*. The overall objective of *UNICAM II* is to better understand ceramic materials for armour applications as well as to enhance predictive modelling capability for ceramic armour designs.

The present DPhil study, an experimental work package of *UNICAM II*, aimed to provide new insights into the deformation and failure mechanisms of armour ceramics by carrying out experimental investigation at the microstructural scale, coupled with a simultaneous and interactive development of informative modelling methodologies.

The planned work included: (i) microstructural characterisation, mechanical and thermal property measurement, and static- and ballistic-indentation behaviour assessment of four materials (Al_2O_3, SiC, B_4C and SiC-B_4C composites) for generating predictive numerical models; (ii) experiments to enable back calculation of quantities relating to microstructure and mechanical properties that could not be

measured directly (e.g. defect distribution, critical resolved shear stress) using the models developed in (i), and (iii) validation of the modelling against suitable experiments.

However, the work did not go as originally planned due to unforeseen circumstances, specifically that the modelling effort in the *UNICAM II* was redirected at the request of the sponsor and was therefore not able to provide extensive interaction in the collaborative work. Additionally, there were unexpected technical difficulties with the numerical homogenisation work package. The back calculation of unobservable parameters and 'validation of the modelling', which were to have been the main areas of scientific novelty, were therefore not possible. As a result, a high percentage of the work planned and, in most of the cases commenced, by the present DPhil candidate was not possible, and alternative scientific work was designed and conducted, which was still connected with the original idea of enabling reliable modelling.

The time-consuming work that had been carried out by the present author near the beginning of the project but was not followed up due to the redirection of the project and the lack of modelling to interact with, included but was not limited to:

- A series of Hertzian indentation tests on Al_2O_3 and SiC armour plates for the measurement of surface pre-existing flaw sizes, linking the impact behaviour of the ceramics with the defect distributions in these materials.
- Rockwell indentation on alumina and extensive characterisation including 3D X-ray tomography, 3D reconstruction of the residual profile using profilometry, SEM examination, testing and characterisation of split-bonded specimens, macroscopic 3D reconstruction of damage zone by serial sectioning at AFRL, for validation of the model and for back calculation of parameters relating to plasticity.
- Design and production of special miniature test specimens which were tested at high strain rate at microscopic scale (i.e. micro-impact tests) at MIT.

With the main objective remaining the same (i.e. understanding and improving armour ceramics), the present DPhil thesis reports research focused on Al_2O_3 and SiC, and adopts the following plan: (i) microstructural investigation of grain size (Chapter 3), (ii) determination of the strength of grain boundaries under combined normal and shear loading and investigation of the effect on failure behaviour (Chapter 4), (iii) measurement of stress intensity values at the microstructural scale during stable crack propagation in air and under vacuum, and investigation of subcritical crack growth (Chapter 5), (iv) investigation of factors involved in the reliable measurement of fracture toughness at microscale through characterisation and quantification of FIB ion implantation damage (Chapter 6 and 7). Only items (i) and (ii) were part of the original project plan.

Before describing this research, the relevant literature is reviewed in Chapter 2. Starting with literature on ceramic armour systems and materials of interest in the present research, microstructural and macroscopic numerical modelling of ceramics is then discussed. Thereafter, the literature on strength of grain boundaries is presented. Finally, fracture toughness measurement at the microstructural scale is discussed, together with previous work on influential factors including moisture-assisted sub-critical crack growth and FIB ion implantation damage.

Chapter 2. Literature Review and Aim of the Research

2.1 Ceramic armour

2.1.1 Ceramic amour system

A typical ceramic armour system consists of two main layers – a ceramic strike face and backing (Fig. 2.1).[13]

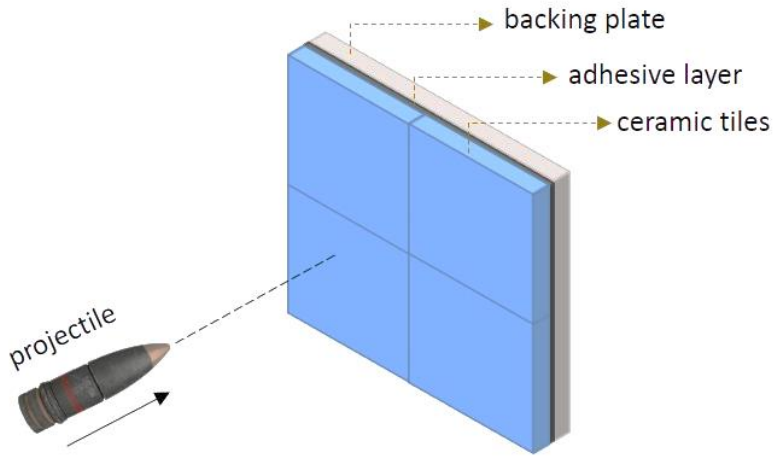


Figure 2.1. Illustration of typical ceramic armour system

The strike face is made of a single monolith or a mosaic-like array of ceramic tiles (Figure 2.2). Having a hardness much higher than that of metals which projectiles are often made of, the ceramics can fracture projectile tips, absorb and dissipate the kinetic energy of projectiles through brittle failure, and improve impact pressure distribution in the following layers.[14]

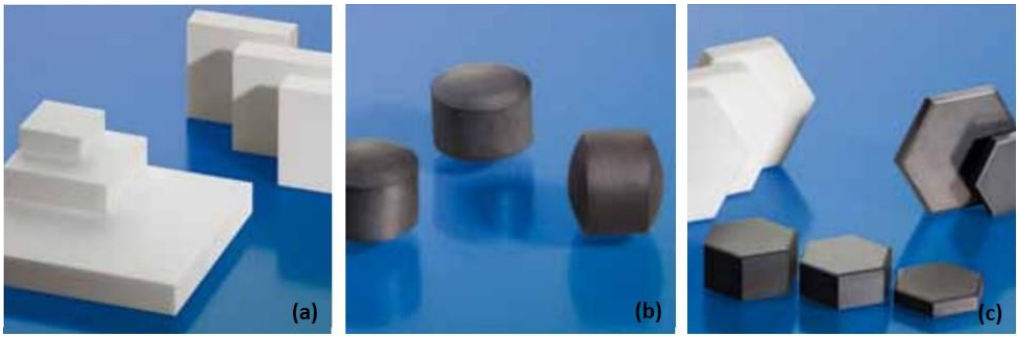


Figure 2.2. Armour ceramics in the shapes of (a) square, (b) cylinder, and (c) hexagon. From reference [15]

Although ceramics have desirable impact-defeating properties (i.e. high bulk and shear moduli, high yield stress to resist deformation, high compressive strength, etc.), they suffer from low tensile

strength. In order to optimise protection capability, ceramics need to be backed by a material with better tensile properties, i.e. a backing plate.

Backing is made of ductile and flexible materials, such as fibre reinforced polymer matrix composites, ultra-high-molecular-weight polyethylene, rubber, or metals.[16] Its function is to physically support the ceramic layer, and more importantly, to stop residual fragments of a projectile and the strike face by absorbing their kinetic energy via plastic deformation.

Ceramic tiles and the backing layer are bonded together by adhesive and interfacial materials[17-19], which will not be further discussed here.

2.1.2 To defeat what?

Ceramic armour is often employed to defeat high-level threats, including arms fire[20, 21], medium to long-rod penetrators and shaped charge jets[14, 22-24].

The dominant ceramic failure mechanism against each type of threat can be different.[25] The shocks generated by arms fire or long penetrators are comparable to the strength of ceramics. However, the shock strength of shaped charges, or orbiting space junk if we think further, are so high that materials strength becomes insignificant and the problem reduces to one of compressive hydrodynamic flow.[14] Shaped charges also bring additional loading from blast and fragments by exploding warheads, which needs to be taken into consideration.[26]

2.1.3 Projectile impact and penetration mechanisms

The process of a ballistic impact against ceramic armour (Figure 2.1) can be described by the following steps: [6, 14, 25, 27, 28]

(i) High-velocity projectile impacts the ceramic strike face and imparts its kinetic energy. Exhibiting a "dwell" [29-32] period, the projectile does not penetrate into the ceramic but is shattered or deformed into a blunt mushroom shape[13, 33] through ductile deformation. The mushrooming effect reduces the local stress in the target and involves more target mass to defeat the projectile. If the impact velocity

does not exceed the so-called "transition velocity"[34, 35], the projectile may be entirely eroded without penetration[29], known as "interface defeat"[28, 31, 36-39].

(ii) A shockwave is launched into the ceramic, followed by a propagation front of fracture.[14] Radial and/or cone cracks are formed ahead of the impactor, with the cracks tending to follow trajectories of maximum tensile stress.[40]

(iii) The projectile advances into the ceramic, being eroded, deformed or shattered as it penetrates. The fragments of the ceramic will likely remain in place and still have high hardness albeit in small size, therefore keeping wearing away the projectile that continues to penetrate.[14]

(iv) The stress in the backing at the central impact zone increases as the projectile advances. The crushed ceramic fragments/powders exert bulking pressure[41] on the surrounding material, which deforms the backing.

(v) If the protection system is successful, fragments of the projectile and ceramic reaching the backing are stopped. The backing may be deformed to a certain extent, with a residual but acceptable momentum transferred to the armoured wearer or equipment.[14]

2.2 Materials

The main criteria considered for the selection of ceramics for armour application include the type of threat to be defeated, level of threat, weight, volume requirement and cost.[6] There is no single 'best' armour material due to the wide range of design criteria. Currently, the most common armour ceramics are alumina, silicon carbide and boron carbide (Table.2.1).[16]

Table 2.1. Fundamental properties of Al_2O_3, SiC and B_4C [5, 6, 42-46]

Material	Theoretical density [g/cm^3]	Elastic modulus [GPa]	Hardness HK2kg [GPa] [6]	K_{IC} [MPam$^{1/2}$]
Al_2O_3	3.99	370 – 390	~1300	4 – 5
SiC	3.21	380 – 430	~1900	3 – 6
B_4C	2.52	420 – 460	~2000	2 – 3

Al_2O_3 and SiC are the main materials of interest in the present research. Si is briefly involved in the studies for referential purpose.

2.2.1 Aluminium oxide

Aluminium oxide (Al_2O_3, or alumina) is a widely used armour ceramic. α-Al_2O_3 is the most common polymorph for general engineering use. Sapphire refers to its single crystal form. The basic crystal structure of α-Al_2O_3 (Fig.2.3) is trigonal in the space group $R\bar{3}c$.[47] Because the oxygen sublattice is arranged in a pseudo-hexagonal close-packed structure with Al occupying 2/3 of the octahedral interstices, a hexagonal cell and four-index Miller-Bravais notation are usually used for describing sapphire's crystal structure.[48] The Al planes have a similar hexagonal close-packed arrangement but with 1/3 of the sites vacant.[49] The lattice parameters of the structure are a=4.758 Å , c=12.991 Å.[50]

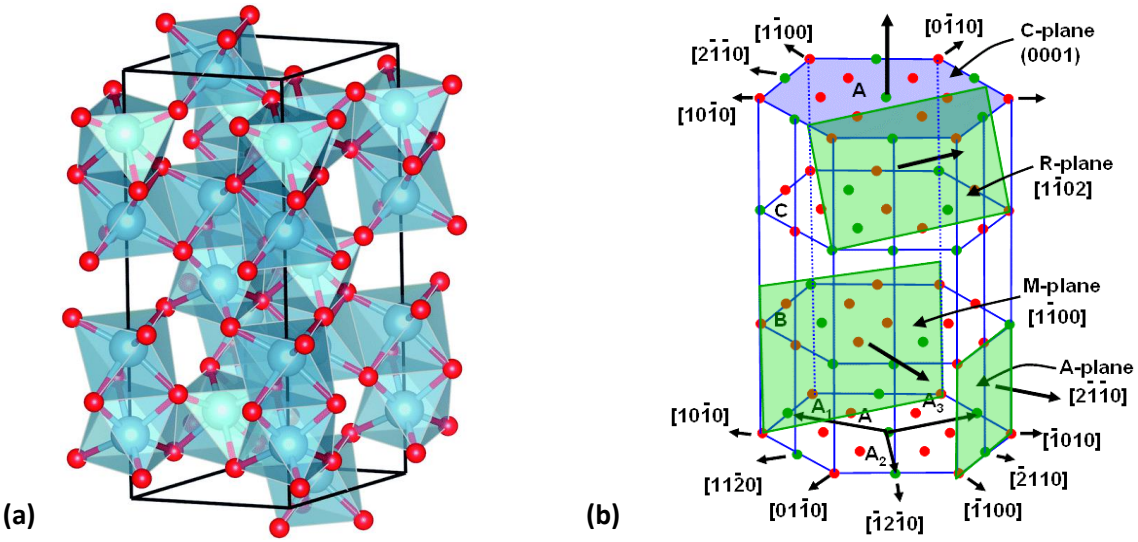


Figure 2.3. (a) The crystal structure of sapphire. The big blue spheres represent Al atoms. The small red spheres represent O atoms. Each Al is octahedrally neighboured by six O while each O is coordinated with four Al. Reprint from[51] (b) The Al sublattice structure of α-Al_2O_3. The red and green dots represent Al cations and Al vacancies respectively. The oxygen planes intercalated with the aluminium planes are not shown in the present figure. Four main crystal planes in its structure are illustrated: a-, c-, m- and r-planes. Reprint from[49].

Strong interatomic bonding provides Al_2O_3 with favourable properties such as chemical and thermal stability, electrical and thermal insulating characteristics and high hardness.[52] The theoretical density of sapphire is 3.99 g/cm^3 at room temperature.[53] The melting point is 2325 K.[54]

2.2.1.1 Elastic properties

There are six independent elastic constants (or compliances) for sapphire.[55] Table.2.2 lists the accepted values of elastic constants c_{ij} and elastic compliance s_{ij} for alumina[56], which are applied thoroughly in the present thesis. 11, 22 and 33 correspond to a-, m- and c-axis respectively, as illustrated in the Fig. 2.4.

Table 2.2. Accepted values of stiffness constants c_{ij} and compliance constants s_{ij} for α-Al2O3. From [56] (The unit of the compliance constants were mistaken in the source paper [56] as 10^{-11} MPa^{-1}, which is corrected to 10^{-12} Pa^{-1} here.)

	10^9 Pa		10^{-12} Pa^{-1}
c_{11}	497	s_{11}	2.35
c_{12}	163	s_{12}	-0.70
c_{13}	116	s_{13}	-0.38
c_{14}	22	s_{14}	-0.48
c_{33}	501	s_{33}	2.16
c_{44}	147	s_{44}	6.93

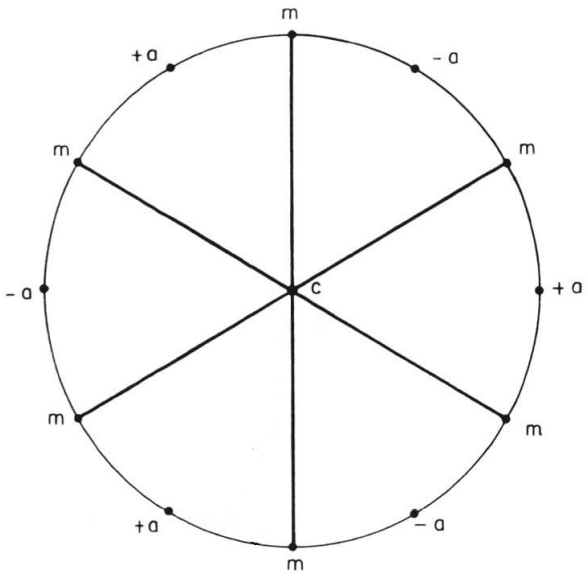


Figure 2.4. The stereographic projection of specimen a-, m- and c-axis in the c-plane. Re-produced from[55]

2.2.1.2 Manufacturing and application

Using alumina power produced via the traditional Bayer process,[57] the alumina armour plates are typically manufactured by solid state sintering,[58] which heats the 'green' compact to the temperature ranging between approximately 1000 °C and 1600 °C[59].

Alumina is widely used for body and vehicle armour due to its low manufacturing cost. However, it is well known that alumina underperforms SiC or B_4C in terms of ballistic performance[60] due to its relatively lower hardness and higher density which is associated with a significant weight penalty.[61] Researchers are working on improving the properties of alumina by means such as introducing zirconia[62, 63] or manufacturing ceramic matrix composites (CMC).[64]

2.2.2 Silicon carbide

Silicon carbide's fundamental structural unit is a tetrahedron consisting of a Si(C) atom surrounded by four C(Si) atoms, as shown in Fig.2.5. The four bonds connected to the neighbour atoms are nearly pure covalent with contribution of ionic bonding estimated to be ~12%.[65]

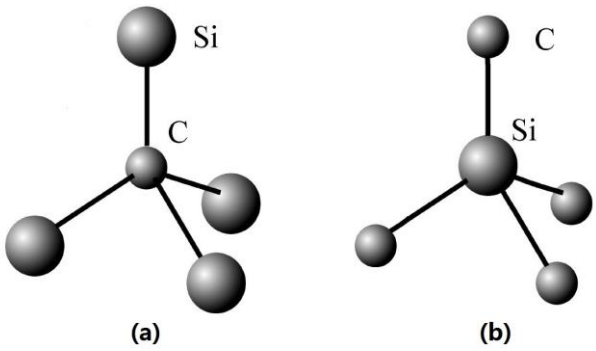


Figure 2.5. Basic elements of SiC crystals: tetrahedron containing (a) one C and four Si; (b) one Si and four C.

The SiC crystal structure exhibits a great variety of stacking sequences of these tetrahedron units, known as polytypism.[65] There are over 250 known polytypes of SiC with each having its own distinct set of properties.[66] The major ones are usually named using the Ramsdell notation[67] (Fig.2.6): the total number of layers contained in a primitive hexagonal unit cell is followed by a letter denoting the overall lattice structure (H – hexagonal, C – cubic, R – rhombohedral). For example, '6H-SiC' indicates

that there are 6 layers stacked in a certain sequence in the primitive lattice stacking. Among all the polytypes, 6H- and 4H- are currently the most common used for armour applications.[66] 6H-SiC has the following lattice parameters at room temperature: a=3.081 Å , c=15.117 Å.[68]

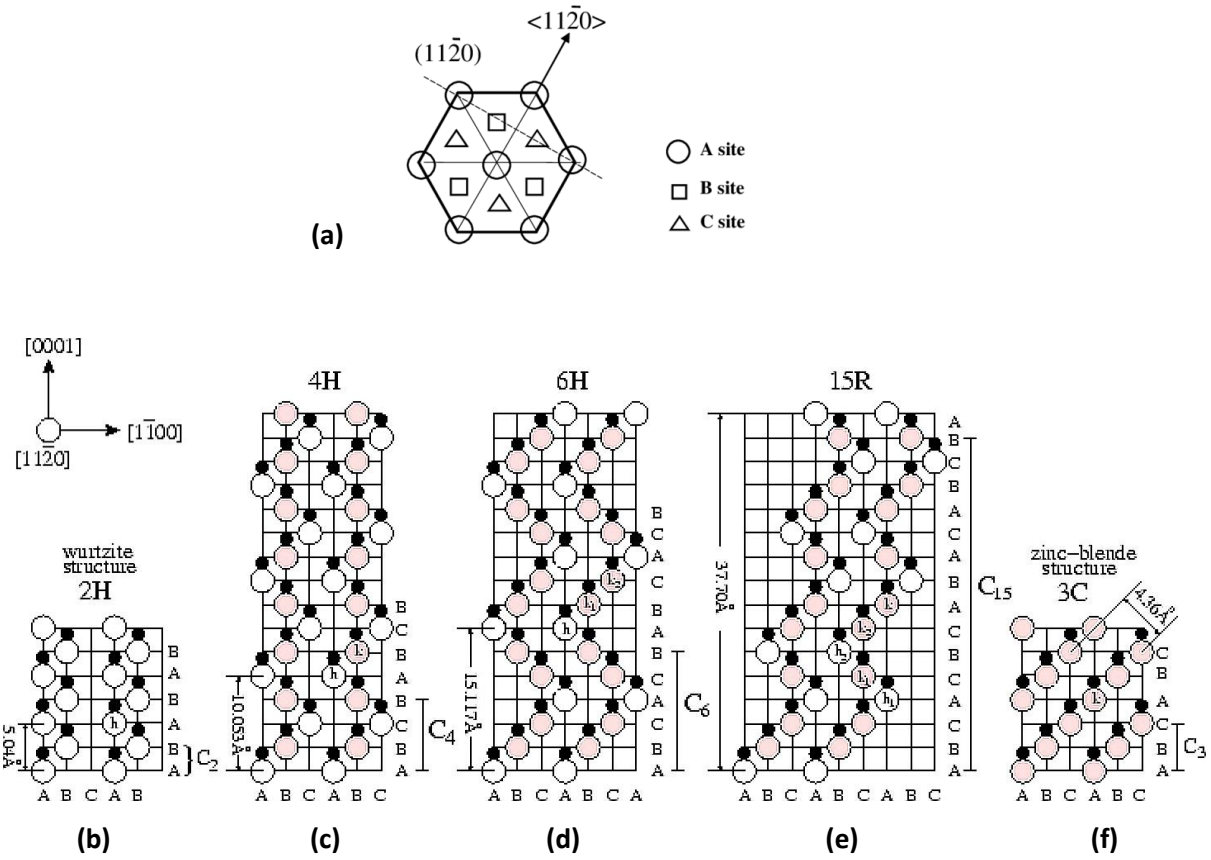


Figure 2.6. (a). Top view along [0001] of the SiC hexagonal structure, showing three possible sites (A, B and C) for Si and C atoms, from[69]. Side view of five major SiC polytypes from [11$\bar{2}$0]: (b) 2H-SiC, hexagonal polytype (wurtzite structure) of SiC with stacking sequences of AB and purely hexagonal bonds. (c) 4H-SiC, hexagonal structure with stacking sequence of ABCB, consisting of 1/2 cubic and 1/2 hexagonal bonds. (d) 6H-SiC, hexagonal polytype stacked in sequence of ABCACB with 2/3 cubic and 1/3 hexagonal bonds. (e) 15R-SiC, rhombohedral crystal structure with stacking sequence of ABCACBCABACABCB, composed of 3/5 cubic bonds and 2/5 hexagonal bonds. (f) 3C-SiC, the only cubic polytype (zinc blende structure) of SiC. The Si atoms labelled 'h' or 'k' denote Si-C bilayers that reside in quasi-hexagonal or quasi-cubic structures with respect to their adjacent above and below bilayers. From reference[66]

2.2.2.1 Elastic properties

For 6H-SiC, c_{14} and s_{14} are both equal to 0. The room temperature elastic constants of 6H-SiC, the polytype that is used in the present project, are listed in Table.2.3.

Table 2.3. Stiffness constants c_{ij} and calculated compliance constants s_{ij} of 6H-SiC at room temperature, based on the measurement from reference[70]

	10^9 Pa		10^{-12} Pa^{-1}
c_{11}	501 (± 4)	s_{11}	2.112
c_{12}	111 (± 5)	s_{12}	-0.452
c_{13}	52 (± 9)	s_{13}	-0.156
c_{33}	553 (± 4)	s_{33}	1.838
c_{44}	163 (± 4)	s_{44}	6.135

2.2.2.2 Manufacturing and application

Different manufacturing methods lead to different microstructures and properties of SiC.[6, 65] (i) SiC made by pressureless solid state sintering (SSS) usually has grain sizes varying significantly from small (3-5 µm) to large (>20 µm), and contains 1-3% porosity.[71-75] It exhibits good high-temperature creep and oxidation resistance[76, 77] but poor fracture toughness (3-4 $MPa \cdot m^{1/2}$) with highly-flaw-sensitive strength[78] at room temperature. (ii) Pressureless liquid-phase sintered (LPS) SiC can exhibit equiaxed fine microstructures (grains of 1-2 µm) and low porosity (1-2%) due to typically low sintering temperatures. A glassy oxide minor phase (5-10%) is often found at triple joints of LPS-SiC grains.[71, 79, 80] (iii) Hot pressed (HP) SiC has low porosity and fine microstructure.[81, 82] (iv) Reaction bonded (RB) SiC[83] has large (10-50 µm) grains, typically no porosity. A silicon minor phase is always present in RB-SiC, which may undergo a pressure-induced phase transformation[84]and adversely affect the ballistic resistance.[6] While hot-pressing results in a harder ceramic, which is optimal for resisting single-hit, reaction-bonding often produces ceramics with better multi-hit performance.[85]

In terms of fracture mode, SSS-SiC is dominated by transgranular fracture, while HP-SiC and LPS-SiC exhibit predominantly intergranular fracture.[6]

Unlike boron carbide, SiC is a line compound and does not undergo amorphisation under high applied dynamic pressures. As a result, SiC is sometimes preferred against B_4C when facing high impact pressures, despite its lower hardness and higher density.[6, 83, 86-92]

2.2.3 Silicon

Silicon is used as a reference material in ion implantation damage investigation in the present thesis. Each atom bonds covalently to four other atoms of the same element (i.e. Si), forming regular tetrahedrons (Fig.2.7), with lattice constant of a_{Si}=5.431 Å.[50]

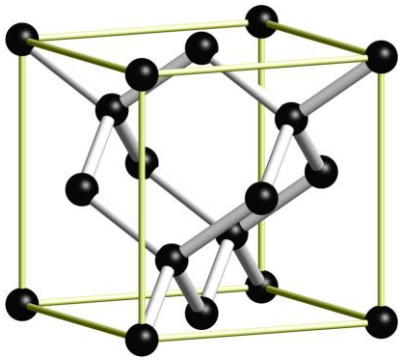


Figure 2.7. The crystal structure of silicon, fcc, with the black balls representing Si atoms.

As cubic crystals, silicon has only 3 independent elastic constants: c_{11}, c_{12} and c_{44}. The room temperature elastic constants of Si are listed in Table. 2.4.

Table 2.4. Stiffness constants c_{ij} and compliance constants s_{ij} of silicon at 25°C. From reference [93]

	10^9 Pa		10^{-12} Pa^{-1}
c_{11}	165.64	s_{11}	7.691
c_{12}	63.94	s_{12}	-2.142
c_{44}	79.51	s_{44}	1.258

2.2.4 Material properties vs. ballistic performance

To date, correlating a single material characteristic with ballistic performance has not been achieved due to the dynamic nature of an event occurring on very short timescales and involving largely varying dynamic loads.[15, 28, 42, 85, 94]

Several representative material properties are listed in Table.2.5 along with their commonly understood roles in ballistic protection and measurement methods.

Table 2.5 Material properties and their roles in ballistic performance

Property	**Role/Effect in ballistic performance**[6]	**Measurement method**
Microstructure (grain size, porosity, minor phase, stress-induced phase transformation or amorphisation)	Affects the other properties listed in the present table.	SEM, TEM, XRD, etc.
Density	Weight of the armour system	Archimedes method
Hardness[95]	Damage to the projectile, penetration resistance	Knoop hardness test[96] Vickers hardness test[97]
Elastic modulus	Stress wave propagation, projectile damage during dwell	Resonance method[98-100]
Strength	Multi hit resistance, fracture type	Four-point bending[101]
Fracture toughness (K_{IC})	Multi hit resistance, field durability	Bending specimens with pre-developed cracks[102] Indentation tests at micro- or macro-scale
Fracture mode (inter- vs. trans-granular)	Energy absorption	Quasi- or high-speed indentation, bending test
Defect distribution	Source of cracking	Hertzian indentation

Some of the properties are further discussed as follows.

- Microstructure

Microstructure has a notable influence on ceramic ballistic performance by affecting the following mechanical properties and behaviour.[103] (i) Grain size affects numerous mechanical properties of ceramics[104], such as hardness[105], strength[16, 105-108], and fracture toughness[109]. (ii) Less porosity[110] leads to higher hardness of bulk materials. (iii) Tougher grain boundaries can potentially improve overall mechanical properties. (iv) Microstructure also dominates the mode of fragmentation, which governs both the duration of the dwell period and the abrasive efficiency of ceramic debris in the subsequent penetration phase.[103] For instance, single crystal alumina has a higher hardness and elastic modulus than polycrystalline alumina, but it shows a weaker ballistic efficiency due to its finer fragmentation accompanied by high crack density.[103]. In an armour system, larger and coarser fragments are desirable since it is harder to move them out of the way and thus provides a higher penetration resistance while more severely abrading the penetrator.[85, 103, 111, 112]

- Hardness

It is widely accepted[36, 113, 114] that the hardness of a target ceramic dominates the level at which the projectile is fragmented or eroded.[115-117] However, the relationship can be altered by the backing material.[118, 119] For instance, a steel backing enhance the positive influence of an increasing hardness of alumina whereas the opposite is true using aluminium backing[120], which could be explained by the low dynamic stiffness of Al alloy[103].

- Elastic modulus

High elastic modulus results in high ballistic resistance by extending dwell interaction and by forming a beneficial fragmentation mode with less cracks.[103] It is because a higher elastic modulus gives a faster speed of stress wave propagation, which actives a larger area. Young's modulus may not remain constant during the impact[103] due to the alterations in lattice structures[121-125].

- Fracture toughness

A high fracture toughness can minimise the shattering of the ceramic upon impact and therefore be useful in resisting multiple hits.[6, 126] However, optimising fracture toughness does not necessarily result in a better armour ceramic[16, 85] as a higher toughness usually comes at the cost of lower hardness.[71]

- Strength

If shock pressure of the impact is at the lower or quasi-equal level of the material strength, the target ceramic will respond by forming a typical cone which spreads the load over a larger area. Contrarily, the ceramic will fail in the form of a hole, similar to the impact behaviour of metals.[14] Failure strength is highly linked to the critical flaw size[127, 128] and the inherent toughness of ceramics.[129]

2.3 Numerical modelling of ceramic armour

Reliable modelling at both micro- and macro-scale is crucial in ensuring the predictive capability of the numerical models for the ballistic response of ceramic armours.

2.3.1 Generation of microstructure in numerical models

For the simulation of polycrystalline materials, reproducing microstructural features accurately in the numerical models is fundamental for ensuring the reliable prediction of materials' mechanical behaviour. This is particularly important for brittle materials, such as ceramics, due to the fact that their failure is dominated by crack propagation mechanisms that depend strongly on the local microstructural features.[130, 131]

Voronoi tessellation is a commonly applied method for the generation of polycrystalline microstructural models, providing an analytical formulation that is able to reproduce the non-regularity of polycrystalline morphologies.[132] Among the several variations of the Voronoi tessellation algorithm, the classic Voronoi is the most widely used one due to the excellent compromise that it offers between representativeness and simplicity of formulation.[133]

As the first step of Voronoi tessellation, a finite set of *N* nuclei are positioned arbitrarily in the three-dimensional space R^3. Secondly, the Voronoi tessellation decomposes the space R^3 into one cell per nucleus, which consists of all the points closer to the master nucleus than to any other nucleus. A boundary plane is then formed between two neighbouring nuclei, which is located at the middle of and also perpendicular to the line connecting them (called 'Delaunay triangulation'). An illustration of the tessellation is shown in Figure 2.8.

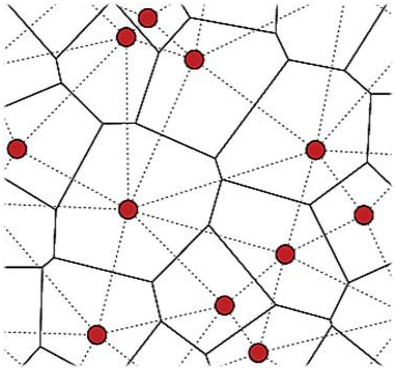


Figure 2.8. 2D Illustration of Voronoi tessellation. The red circles represent the arbitrarily-positioned nuclei. The dashed lines show the Delaunay triangulation and the solid lines are the associated boundary planes. Reproduced from reference[134]

Mathematically, the classic Voronoi can be expressed as in Eq.2.1.

$$\{R_{P_i}\} = \{x \in \mathrm{R}^3 : \|P_i - x\| \leq \|P_j - x\|\} \qquad (2.1)$$
$$j = 1, 2, \ldots, N : j \neq i$$

where P_i and P_j are the positions of the *i*-th and *j*-th nucleus respectively, R_{P_i} is the cell associated to the nucleus P_i, and x is the position of a generic point in the space R^3.

Eq.2.1 shows that the classic Voronoi tessellation generates intersections of exactly-half spaces, which therefore cannot represent the wide range of real grain sizes nor the presence of large grains within the microstructure.

In order to overcome the limit of the classic Voronoi, the methodology has been further developed based on the Laguerre-Voronoi technique to enable the control over the size and shape of the cells, allowing for a more accurate simulation of polycrystalline microstructures.

The main modification from classic- to Laguerre-Voronoi is the definition of 'distance': in place of the Euclidean distance used in the classic Voronoi formulation, the Laguerre-Voronoi tessellation introduces the so-called *power distance*, which is defined in the following formulation.

$$pow\big(x,(P_i,w_i)\big) = \|P_i - x\|^2 - w_i \tag{2.2}$$

where w_i is the weight associated to the *i*-th nucleus.

The weights (*w*) are interpreted as the square of the sphere radius (*r*) (i.e. $w_i = r_i^2$), which allows the formulation of the Laguerre-Voronoi tessellation to be written as in Eq.2.3.

$$\begin{gathered}\{R_{P_i}\} = \{x \in \mathrm{R}^3 : \|P_i - x\|^2 - r_i^2 \ \leq \|P_i - x\|^2 - r_j^2\} \\ j = 1, 2, \ldots, N : j \neq i\end{gathered} \tag{2.3}$$

where *x* is the position of a generic point in R_3; w_i is the weight of the generic *i*-th nucleus located at P_i, and w_j is the weight of the generic *j*-th nucleus located at P_j. Please note that, if all the weights are equal, the Laguerre Voronoi tessellation becomes equivalent to the classic Voronoi tessellation.

While Laguerre-Voronoi modification improves the control over the outcome of the tessellation, additional degrees of freedom are added to the system, leading to the loss of biunivocal relation between final tessellation and nuclei seeding. As a consequence, the following degenerated conditions may occur (visual examples are illustrated in Fig.2.9).

- Cells do not necessarily contain their corresponding nuclei (e.g. cell *i* does not contain the nuclei P_i).
- Cells may contain multiple (or zero) nuclei (e.g. cell *j* contains nuclei *i*, *j* and *k*).
- Not every nucleus necessarily generates a cell (e.g. nucleus P_k does not generate any cell).

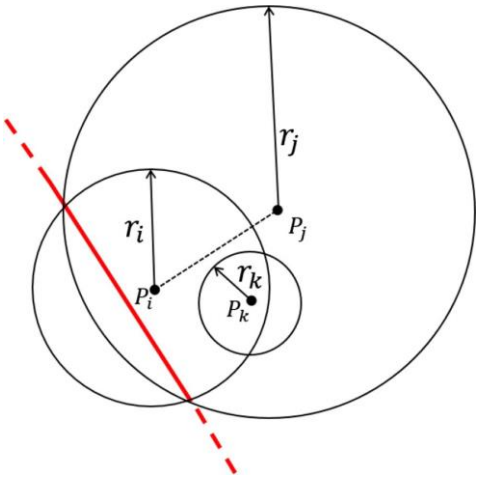


Figure 2.9: Illustration of a grain boundary (red line) between cell i (left) and cell j (right) generated by the nuclei P_i and P_j.

These undesired conditions may affect the quality of the final tessellation and hinder the further discretisation procedure required to generate finite elements models of microstructures.

In order to assure that every nucleus generates a cell and lies within it, an innovative method for efficiently generating dense packing of spheres is developed by imposing a non-overlapping condition on the spheres representing the weights of the nuclei, as presented in Chapter 3.

2.3.2 Continuum macroscopic constitutive models

Significant progress has been made on modelling capabilities over the past two decades[135], in terms of both material constitutive behaviour in its initial undamaged condition[136, 137] and evolution of damage[138-143]. They provide a useful and previously unavailable test-bed for refining theoretical notions on dynamic damage and for interpreting experimental data. However, the current computational capability is not yet reliably predictive, with further development required.

Considering that most of the parameters in the existing macroscopic constitutive models for ballistic impact are essentially empirical, the *UNICAM II* project therefore aimed to incorporate the mechanical properties of microstructural components and real microstructures obtained from reliable tests and characterisations to enhance the predictive capability of the models for ceramic armour applications. The present experimental work thus took the responsibility of identifying the dominant features,

properties, physical processes and mechanisms for the models to capture, conducting and analysing the relevant tests to provide the models with empirical data.

The continuum models can be categorised into the following two groups.[12]

(i) Isotropic models

The models developed by Johnson and Holmquist (commonly known as JH1[144], JH2[145] and JHB[146]) are widely used in the simulation of ceramics behaviour, including their extensive application in ceramic armour design[147, 148]. Among these, JH2 is the one that is commercially favoured and is also the only JH model that takes into account the gradual decay of material strength caused by the increasing severity of damage.[146] The input of parameters in the JH models relies on empirical metrics, often coupled with polynomial fits of results.

As another well-known isotropic model for ceramics, the model developed by Simha[149] predicts the damage propagation by an explicit function of time and effective stress, with the coefficients of the function calibrated with empirical quantities.

Additionally, a micro-mechanics based 3D constitutive model featuring inelastic deformation and fracture of ceramics was developed by Deshpande and Evans[141]. For the purpose of simplification, cracks are considered to be identical, independent and uniformly distributed. The propagation of cracks from initial defects depends on the stress state, fracture toughness and characteristics of the defects. The combined effects of micro-crack growth and plastic slip are taken into account.

The assumption of isotropic evolution of damage, which offers great simplicity in computing, is usually justified by proving that upon high-speed test where the target ceramic is deformed rapidly to a comminuted state, the effect of the anisotropy is negligible[150].

(ii) Anisotropic models

An orthotropic evolution of damage was first presented in the model developed by Denoual and Hild[151]. The degree of anisotropy increases to a higher level in Espinosa's model[152, 153], in which the damage can propagate in a theoretically-indefinite number of arbitrary directions. This multi-plane

microcracking model is capable of demonstrating shear dominated failure which appears in almost all dynamic confined compression experiments.[154] Later on, a fully anisotropic model was developed by Riou[155] based on the experimental observation of damage evolution and characterisation of stress fields, which is capable of evaluating the maximum damage direction.

Anisotropic models comes at a price of higher computational cost due to the increased complexity of formulations and parameter extrapolations. However, the implementation of the anisotropic failure mechanism is of great importance if the realistic crack initiation and propagation, or if the physical properties of the ceramic are highly linked to the constitutive model for exploration and/or validation.

2.4 Microcantilever beam techniques & strength of grain boundaries

Mechanical property measurements of individual microstructural components (i.e. grains, grain boundaries) of armour ceramics are indispensable to a full understanding of properties and impact behaviour of the bulk materials, and to enabling the predictability of numerical models.

2.4.1 Microcantilever techniques

The microcantilever technique can measure a range of mechanical properties of chosen microstructural features in both bulk and thin film samples, including elastic modulus[156-158], plastic flow stresses[159], fracture toughness[160], strength[161] and stress corrosion crack growth rate[162].

The method consists of the milling of microscale cantilever beams using Focused Ion Beams (FIB) followed by measurement of the dimensions using Scanning Electron Microscope (SEM) imaging before loading to failure near the free end using a nanoindenter. For fracture toughness measurement, a FIBed notch is included at a chosen microstructural feature. Selective microetching[163-166] is an alternative method to manufacture microcantilevers in certain materials, but could not be applied to most ceramics and therefore is not used for these materials.

The testing of FIBed miniatures can be in a variety of configurations for different micro-mechanical measurements,[167, 168] such as three-point bending beams[164, 166], clamped beam bending[169], double

cantilever bending[170], pillar splitting[171], etc. The microcantilever[167, 168] is the main configuration used in the present research.

Cross-sections of microcantilevers can be chosen over a wide range. The most common ones are triangular[172], pentagonal[160] and rectangular[173]. There are different types of notch as well, for example, some notches are formed by milling successively deeper rectangles in the beam followed by milling a line in the centre of the notch[160], some are a straight through notch[161], controlled flaws[157, 161], side-grooves[174] or chevron notch[175], etc. Notches can be at or away from grain boundaries depending on the purpose of study.

2.4.2 Strength of grain boundaries

Understanding the contribution of normal and shear strength in the failure of grain boundaries is important in investigating the failure mechanisms of polycrystalline ceramics as well as in enabling the accurate modelling of intergranular crack propagation within polycrystalline microstructures.

According to the classical linear elastic fracture mechanics theory[127], the equivalence between the mechanical energy release rate G and the stress intensity factor K is expressed as below (with mode III excluded),

$$G = \frac{K_I^2}{E'} + \frac{K_{II}^2}{E'} \tag{2.4}$$

where K_I and K_{II} are the mode I and mode II stress intensity factor respectively, $E'=E$ in plane stress and $E'=E/(1-\nu^2)$ in plane strain.

The stress intensity factors are in turn dependent on the relevant mode of the stress state (σ_I and σ_{II} are uniform applied stresses in Mode I and Mode II respectively), the geometry (with Y being the dimensionless geometry term) and the size of initiation defects (c represents the crack length), according to Equation.2.5[127].

$$K_I = Y\sigma_I c^{\frac{1}{2}}$$
$$K_{II} = Y\sigma_{II} c^{\frac{1}{2}} \tag{2.5}$$

The combination of Equation.2.4 and 2.5 leads to the formulation of the failure criterion expressed in Eq.2.6, suggesting that the normal and shear components of the stress have equivalent contributions to the intergranular failure of brittle interfaces.

$$\left(\frac{\sigma_I}{S}\right)^2 + \left(\frac{\sigma_{II}}{S}\right)^2 \geq 1 \tag{2.6}$$

where S represents intrinsic strength of grain boundary.

Nevertheless, the existing literature is not necessarily consistent with Eq.2.6.

Terms S_N and S_T, representing the normal and shear strength of the grain boundary respectively, are introduced to give a little extra freedom by allowing S_N and S_T to be different, as shown in Eq.2.7, which is often applied in numerical modelling failure conditions (e.g. TIEBREAK_CONTACT[176] and MAT_COHESIVE_TH (185)[177] in LS-Dyna).

$$\left(\frac{\sigma_I}{S_N}\right)^2 + \left(\frac{\sigma_{II}}{S_T}\right)^2 \geq 1 \tag{2.7}$$

The well-known paper by Zavattieri et al.[178] states that both normal and shear components of grain boundary strength need to be taken into account as properties of numerical cohesive interface elements, and proposes the cohesive-law model (which describes the evolution of the tensile and shear tractions in terms of both normal and tangential displacement jumps), with the non-dimensional effective displacement jump defined as in Eq.2.8.

$$\lambda = \sqrt{\left(\frac{u_n}{\delta_n}\right)^2 + \beta^2 \left(\frac{u_t}{\delta_t}\right)^2} \tag{2.8}$$

where u_n and u_t are the actual normal and tangential displacement jumps at the interface estimated by the finite element analysis, δ_n and δ_t are critical values at which interface failure takes place, and $\beta = \sqrt{\frac{G_{IIc}}{G_{Ic}}}$ is the factor that governs the contribution of the shear component.

Simonovski and Cizelj[179] explore numerically the effect of shear components by comparing the fracture behaviour of grain boundaries between β = 0 and = 1, which concludes that the 'shear

separation impact is far from negligible'. Although the main mechanism for failure in their work is plasticity, which is different from that for brittle fracture of weak interface, it is a good starting point to demonstrate the importance of the shear component on the assumption that Equation 2.8 is correct.

However, despite all the theoretical evidence showing the importance of the shear component [127, 178, 179], the numerical models of polycrystalline materials often either neglect interfacial properties between grains[180-182], or overlook the effect of shear stress in intergranular failure[183-185] due to the lack of experimental information on the exact contribution of shear component in interface failure. Some researchers[185] ignore the effect of shear stress right from the beginning, while some[183, 184] firstly acknowledge that both the tensile opening and shear sliding dominate the intergranular failure, but then move forward to build numerical models assuming that the crack is initiated exclusively by excessive strains in the normal direction and ignoring the shear component. Others[186] do take the shear component into consideration, but set β to be 1 just for simplicity without any justification.

Since, to the author's best knowledge, no experimental literature exists to verify the relative importance of normal and shear stress components to the brittle failure of intergranular interfaces, the present study aims to fill the gap by evaluating experimentally the contribution of shear strength to the failure of grain boundaries. As the microcantilever technique is an ideal method to measure the inherent strength of grain boundaries in ceramics[187] and diffusion bonded bi-crystals are useful to provide artificial grain boundaries[188, 189], the strengths of differently oriented grain boundaries have been investigated here by testing differently orientated grain boundaries in bi-crystal cantilever beams in the present study. The results are presented in Chapter 4.

2.5 Reliable fracture toughness measurement

2.5.1 Fracture toughness measurement at the microscale

Despite the extensive investigations of fracture behaviour of ceramics at the macroscopic scale[127], the characterisation and understanding of ceramic fracture properties on the microscopic scale has been relatively limited. The microscale investigation is of great importance and has unique capability to evaluate directly the fracture response of individual microstructural components, such as grains and grain boundaries, which determine the global fracture behaviour but cannot be measured in isolation by performing macroscopic tests. Moreover, testing at the microstructural scale can also provide useful information about subcritical crack growth which involves very slow crack velocities which are very difficult to measure at the macroscale on a laboratory timescale.

Fracture toughness measurements using the FIB-milled microcantilever technique was first introduced by Di Maio and Roberts[160], with a straight through notch FIBed on pentagonal cross-sectional silicon and WC beams. The fracture toughness K_{IC} can be calculated using Eq.2.9.

$$K_{IC} = \sigma_f \sqrt{\pi\alpha} F(\frac{\alpha}{h}) \qquad (2.9)$$

where α is the notch depth, h the height of the beam, $F(\frac{\alpha}{h})$ is a dimensionless factor determined by FEM simulation, σ_f the stress at failure.

Since then, the technique has been further developed and has been widely employed to measure the fracture toughness at the microscale for a variety of materials, such as silicon[157], copper[172, 190], alumina[187], fused quartz[173], Si_3N_4[191], tungsten[192], SiC, etc.

The simplicity of Eq.2.9 means that it only represents the idealistic case where the notch tip is atomically sharp and free of stress prior to the test, and the crack nucleation is not affected by the test environment. In reality, however, the following factors are thought to affect the accuracy of fracture toughness measurement. (a) Internal damage, such as surface contamination, ion

implantation[187], residual stresses[161], vacancies and redeposited materials[161] along the periphery of the FIB beam trajectory. (b) Imperfection of artificial features like bluntness of the notch[193, 194], nature and morphology of the notch surface[161]. (c) Environmental effects[161] like water, oil, etc. The mixture of these factors leads to highly scattered values of measured K_{IC} at the microscale - some agree with the accepted macroscopic values[157, 167, 195-197], some range to higher values[160, 198-202], while others result in underestimation[203, 204].

Among the factors listed above, the following three are thought to be the most influential: notch bluntness, ion implantation residual stresses around the notch tip, and subcritical crack growth. It has been commonly observed that FIB-milled notches are blunt rather than sharp,[157, 205] which results in overestimated apparent stress intensity factors obtained at failure in certain ceramics.[187] With extensive investigation, calibration methods are provided by Norton et al.[187] for correcting for the effect of notch bluntness.

FIB induced residual stress has been found to have a significant effect on crack initiation at notch tips in certain ceramics, especially that the stress intensity factor is overestimated if the residual stress is compressive.[187] Details of this will be further discussed in Chapter 7 (FIB ion implantation damage). The effect of subcritical crack growth on crack initiation and propagation in brittle materials has long been investigated using macroscopic specimens[206, 207] and has later on been extended to microscale tests[187, 208], suggesting that the environmental stress corrosion at the crack tip results in underestimation of fracture toughness. More details will be discussed in Section 2.5.3.

The strategy of the present study therefore focuses on eliminating the effect of FIB ion implantation damage to achieve the reliable fracture toughness measurement, via the following two ways. (a) Enable stable crack growth. (b) Quantify residual stresses induced by FIB ion implantation damage and hence correct the results for their effect. The effect of subcritical crack growth will be investigated by measuring the apparent stress intensity at fracture in air and vacuum.

2.5.2 Stable crack growth for fracture toughness measurement

Stable crack growth (i.e. crack propagates in a stable manner rather than fast brittle fracture) allows the fracture toughness to be measured as the crack evolves, from the zone beyond the notch tip where the crack front is atomically sharp and free from the effects induced by FIBing (such as FIB ion implantation[187] and residual stresses[161] at the notch tip, notch bluntness[193, 194], nature and morphology of the notch surface[161]).

The chevron notch geometry[209, 210] (Figure 2.10) was first applied in microscale fracture toughness measurements by Mueller et al.[173] as a promising approach to enable stable crack growth beyond the FIB damaged region. Loaded by a load-controlled nanoindenter, alumina and fused quartz, both of which are inherently brittle materials, exhibited stable crack growth. The design of chevron notch cantilever was later on extended to enable toughness measurement with stably propagating crack length in silicon[211], tungsten[192], etc.

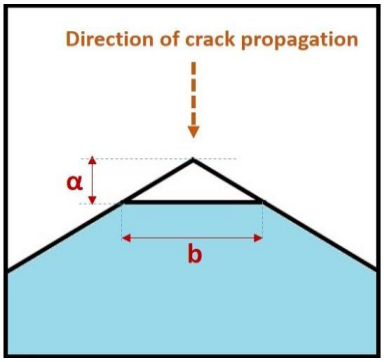


Figure 2.10. Chevron notch is a triangular ligament. α is the crack length, b is the width of the crack front.

A chevron notch was also incorporated into bowtie shape clamped micro-beams by Cui and Vinci[212] for toughness measurement of fused quartz and glass. A major advantage of having an up-side-down chevron notch beneath the beam, is that its notch apex is thinner than that of the classic chevron notch because of the collimation effect of FIB ion beam (i.e. Gaussian ion beam spot profile)[213], which facilitates the nucleation of the crack from the notch tip.

Chevron notches cannot, however, ensure 100% success rate of enabling stable crack growth due to the complex nature of cracking in brittle materials as well as the difficulties in sample preparation (e.g.

milling perfectly-shaped chevron notches in ceramics is difficult because of the slow milling rate and redeposited material. A sufficiently thin chevron notch is crucial in nucleating cracks at low load but is difficult to achieve from the practical point of view). For instance, the chevron-notched silicon microcantilevers prepared by Li et al.[192] exhibit purely fast brittle fracture, without a sign of stable crack growth as shown by the sudden load drop to zero after the elastic region in the load-displacement curves. Moreover, the explanation for the 'slightly curved crack front' on the fracture surface is probably because the crack goes ahead so quickly (i.e. fast fracture) that it goes into the compressive part of the beam so the crack path deviates (known as 'cantilever curl' or 'compression curl')[214], rather than transition from stable to unstable. The failure to achieve stable crack growth, despite the use of a chevron notch, is likely attributed to the inevitable bluntness of the starter notch and to the load-controlled nature of the nanoindenter used in their research.

In addition to the chevron notch, a double cantilever beam (DCB) geometry, coupled with in-situ SEM nanoindentation, is proposed by Sernicola et al.[215] to enable the measurement of the evolution of fracture energy with stably-propagated crack length at the microscale. This loading geometry is applied on single crystal SiC, with the fracture toughness of 6H-SiC (0001) plane measured to be 1.80 ± 0.26 MPa·$m^{1/2}$, while density functional theory (DFT) calculations performed by the same group of researchers suggest K_{IC} to be only slightly higher (i.e. 2.01 to 2.18 MPa·$m^{1/2}$ depending on the applied DFT theory). Like the chevron notch design, this DCB geometry provides the advantage of reducing the effect of notch bluntness and FIB ion damage at notch tips on the toughness measurement. However, unlike the chevron notched microcantilever test which can be operated in a conventional ex-situ nanoindenter, an in-situ SEM nanoindenter is required by the DCB method to measure the crack length and opening. Another key limit of the DCB method is the geometrical requirement: the symmetry of the DCB is important and the crack propagation needs to be oriented parallel to the indentation direction. In practice, this needs the fracture to happen in a preferred crystal orientation or through an artificial weak interface.

Although stable crack growth can be achieved in general via chevron notch or DCB geometries as mentioned above, the techniques do not suit the purpose of measuring fracture toughness of natural individual grain boundaries. This is because the direction of crack propagation, which follows the plane of the target grain boundary, is required to be parallel to or aligned with the nanoindenter tip's central axis, while it is very difficult to find an ideally-located grain boundary with the required direction and dimensions.

2.5.3 Subcritical crack growth

Moisture-assisted subcritical crack growth (SCG) is a well-known issue involved in fracture toughness measurement of ceramics.[216] The moisture in the testing environment interacts with the atomic bonds at the crack tip to assist in its propagation, which potentially results in a stress intensity factor K measured at failure below the critical value K_{IC}, with the crack advancing at a slow rate in the material.[127, 217] The phenomenon has been extensively investigated using macroscopic specimens[218-222] back to the 1980s, and was later on extended to the microscopic scale[187, 208] in recent years.

The crack behaviour affected by SCG can generally be categorised into the following three regions[206, 207, 223-225] (Figure 2.11). In *Region I*, the crack begins to propagate once the stress intensity factor reaches a threshold value for subcritical crack growth K_0, while no propagation occurs when K is below K_0. The crack growth velocity strongly depends on the stress intensity factor due to the limit imposed by the moisture-assisted chemical reaction at the crack tip. The relationship between the crack velocity (v) and stress intensity factor (K) is generally assumed to obey a power law, $v = AK^n$, where A and n are constants depending on the material and specific testing environment.[216] In *Region II* at higher K, as the crack propagates, the transport rate of the moisture diffusing from the environment to the crack tip via the atmosphere gets close to the maximal value, hence limiting the velocity of crack growth. This results in a quasi-plateau in Region II, where the crack advances at an almost constant rate with increasing stress intensity factor. In *Region III*, as K reaches the critical stress intensity K_C, the

chemical 'attack' of the moisture is no longer dominant at the crack tip and the crack growth velocity increases significantly, leading to unstable rapid fracture.

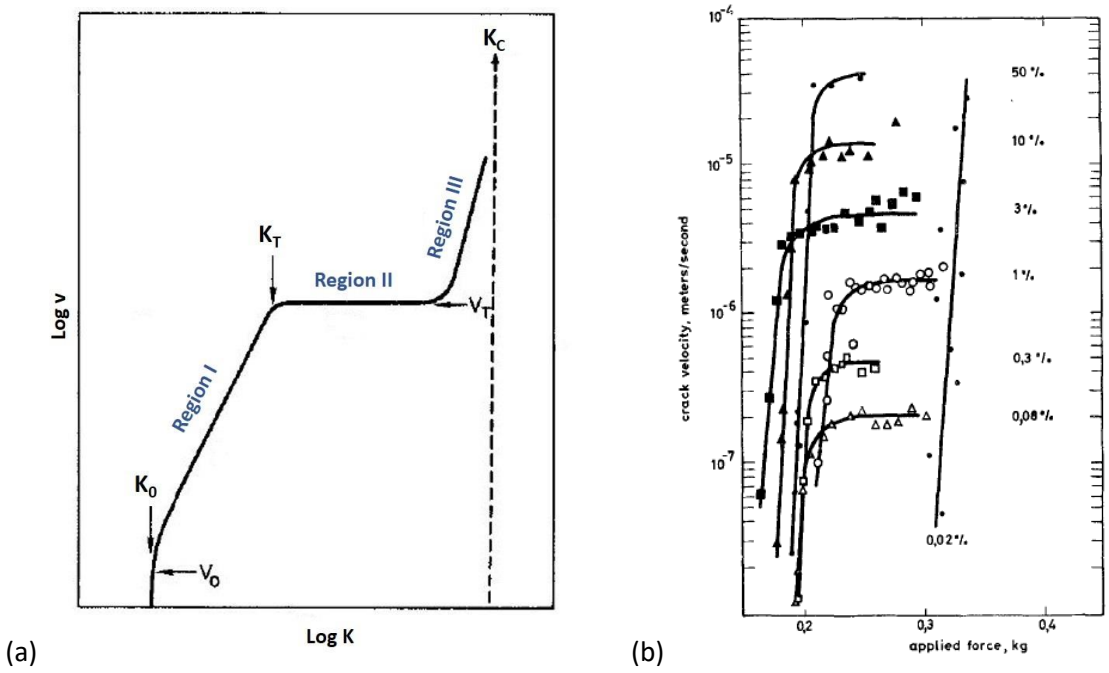


Figure 2.11. (a) Schematic of crack velocity (v) as a function of stress intensity factor (K) in SCG. Reprinted from reference[216]. (b) Crack velocity against applied force (linked to stress intensity factor) for sapphire fracturing on the rhombohedral plane in different relative humidity (from Wiederhorn[206]).

In order to minimise the influence of SCG in fracture toughness measurements, the testing environment can be adjusted to exclude moisture, such as by using silicone oil[187, 226], inert, dry gas[227, 228] or by testing in vacuum. Tests can also be conducted in water[187] or a highly-moisturised environment[206] to investigate the extent of the effect of moisture in underestimated fracture toughness values.

In the 1960s, a series of fracture test were conducted by Wiederhorn[206, 227, 229] to reveal the effect of SCG on ceramics in a systematic manner (e.g. Figure 2.11b), which lays the groundwork for future research in the construction of $v - K$ curves.[127] Later on, further investigation on SCG was carried out by many other researchers using macroscopic specimens, with some of the results compared by Salem[228]. The SCG data is highly scattered, which is considered as common in sapphire, due to difficulties of measuring very low crack growth rates with macroscopic specimens on the laboratory time scale. Salem[228]'s own experiment on single-edge notched beams suggests a fracture toughness

value of 2.31 ± 0.12 MPa·$m^{1/2}$ for a-plane sapphire based on measurements conducted in dry nitrogen, while the threshold stress intensity factor at crack propagation is significantly lower (1.95 ± 0.03 MPa·$m^{1/2}$ for a-plane), with the data collected on the m-plane being close to that from the a-plane.

The investigation of the effect of SCG on brittle fracture has been extended to microscopic specimens in the recent decade as micromechanical testing methods have developed. Norton et al.[187] test sapphire microcantilevers with straight-through notches in air, water and silicon oil. With corrections for notch bluntness and FIB implantation residual stresses at notch tips, the K_p values on m-plane sapphire are reported to be much lower for tests conducted in air (1.5 ± 0.2 MPa·$m^{1/2}$) than in oil (3.5 ± 0.2 MPa·$m^{1/2}$), with even lower K_p values from specimens tested in water (0.9 ± 0.2 MPa·$m^{1/2}$), concluding that the effect of SCG on microscopic specimens is significant so that K_p measured in air should be close to K_0, while that measured in oil should be close to K_C.

As the chevron notch configuration is applied successfully on microcantilevers, K_p is measured in nanocrystalline alumina with stably propagated cracks in air by Mueller et al.[175]. Despite the fact that the measurement is conducted in air, it is reported that the effect of SCG is absent in their tests[208] and the measured K_p (2.34 ± 0.15 MPa·$m^{1/2}$) is concluded to represent the fracture toughness K_C on the basis that their K_p values are similar to what people have measured for K_C for similar materials.[175] Moreover, the crack velocities, which are not reported, are claimed to be big enough for the measured K_p to be K_C.[208] However, it is difficult to see how the crack velocity in such stable test (i.e. on the scale of 10^{-7} m/s as estimated based on the experimental information provided in the reference[175]) can be sufficient to see K_C (for which the crack velocity is on the scale of 10^{-5} m/s according to Figure 2.11b). Therefore further investigation seems to be required to check the validation of the justification for excluding the effect of SCG in their tests[175].

In the present study, in order to further investigate the effect of SCG on sapphire at the microscale, chevron-notched microcantilevers are employed to measure stress intensity values as well as the crack velocities during crack propagation in air and in vacuum.

2.5.4 FIB ion implantation damage at notch tips

2.5.4.1 Effects of FIB damage in micro-mechanical tests

The high energy FIB ions have the potential to cause amorphisation[230], phase transformation[231] or chemical changes in target materials[232]. Damage from FIB Ga^+ has been well documented in the use of TEM (Transmission Electron Microscopy), APT (Atom Probe Tomography) and EBSD (Electron Backscatter Diffraction) techniques.[233-235]. Additionally, FIB ion damage has been found to alter mechanical properties, such as strength[236], crack initiation[237], hardness[236, 238-240], etc.

Above all, residual stresses induced in ion damaged layers at the tips of FIBed notches (Fig. 2.12) are what the present research is most concerned with due to their effects on fracture toughness measurement[187]. Norton et al.[187] notice that the fracture toughness measured in sapphire is increased substantially by the compressive implantation residual stress at the notch tip.

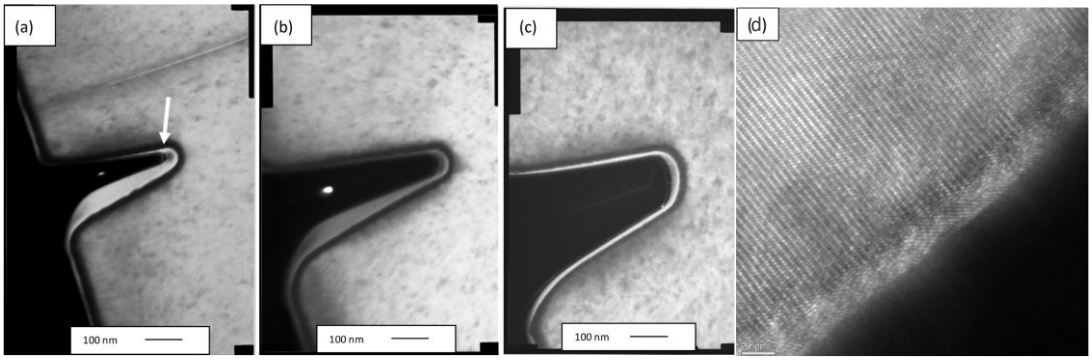


Figure 2.12. TEM of FIB milled notches, filled with platinum from the specimen preparation, at the surface of sapphire using FIB beam currents of: a) 10 pA, b) 100 pA, and c) 1000 pA. (d) HRTEM of implanted surface showing lattice fringes and thin layer (~2 nm) of redeposited material. From reference[187]

Annealing treatment is found to be helpful in removing implantation residual stresses.[187] However, it is not suitable for many ceramics, e.g. non-oxide ceramics can easily get oxidised and diamond graphitises during high temperature annealing. Therefore, calibrating the effect of implantation stress becomes a more promising way to solve the problem.

For microcantilever tests, Eq.2.10 is proposed[187] for correcting the effect of residual stress and notch radius in ceramics based on the method of Fett and Munz[241, 242]:

$$K = K_{app} \tanh\left(2\psi\sqrt{\frac{d\alpha}{\rho}}\right) + \sigma_{res}\psi\sqrt{\pi d\alpha} \quad (2.10)$$

where K_{app}=applied stress intensity factor, ψ=appropriate geometrical factor for a short crack in uniform loading, $d\alpha$ = flaw size, ρ=notch radius, σ_{res}=residual stress in the implanted region.

Due to the limit of length scale and available techniques, the understanding of implantation stresses remains highly elusive. FIB induced lattice strain in gold nano-crystal[243] is resolved using the Bragg Coherent X-ray Diffraction Imaging (BCDI) technique, with the residual stresses induced by large ion fluences found to be far beyond the bulk tensile strength of gold. As BCDI requires the specimens to be perfect nanocrystals and FIB-milling is not allowed in the preparation process, it is only applicable to a handful of materials.

30 keV Ga^+ FIB is found to induce -16 ± 6 GPa compressive residual stress in sapphire over a depth of ~20 nm, based on the variation in R1 Cr^{3+} fluorescence peak position measured from FIB implanted TEM samples.[187] This method requires a sufficient amount of Cr^{3+} in the assessed materials to ensure good quality of signals, which therefore limits the type of materials that can be examined.

Molecular Dynamics (MD) simulation indicates that FIB induced residual stresses in silicon vary from superficial tension to sub-surface compression[244, 245], while the residual stress in silicon is observed empirically to be tensile from the bending of a FIBed silicon AFM arm.[269] The AFM arm bending method is limited to silicon, but it inspires the development of the cantilever technique in the present project.

The effect of ion implantation on fracture toughness measurement is material-dependent – FIB ion damage is found to have no perceivable effect in fracture toughness measurement of silicon[167, 191], in contrast to what is observed in alumina[187]. Moreover, FIB conditions and ion species also have effective influence on the magnitude of residual stresses. To better understand the implantation stresses, it becomes essential to look into the physical mechanisms behind the FIB technique.

2.5.4.2 Ion-solid interactions: physical process

Ion-solid interaction has been extensively investigated for decades and the fundamentals are well explained in several elementary and advanced textbooks, e.g. those of Nastasi[246], Carter and Grant[247] and Chadderton[248]. Fig. 2.13 illustrates the interactive events between the incident ions and target atoms. Essentially there are two types of collisions: elastic and inelastic, depending on whether the momentum of the incident ion is transferred to the atom as a whole or only to the electron cloud of the atom. The former leaves the electron configuration of the atom unchanged and potentially displaces the atom from its original position, which can lead to a cascade of atomic collisions[249] and disrupt the lattice structure (Fig. 2.14). The latter changes the electron configuration of the atom and results in phenomena such as emission of secondary electrons, secondary ions and X-rays.[250]

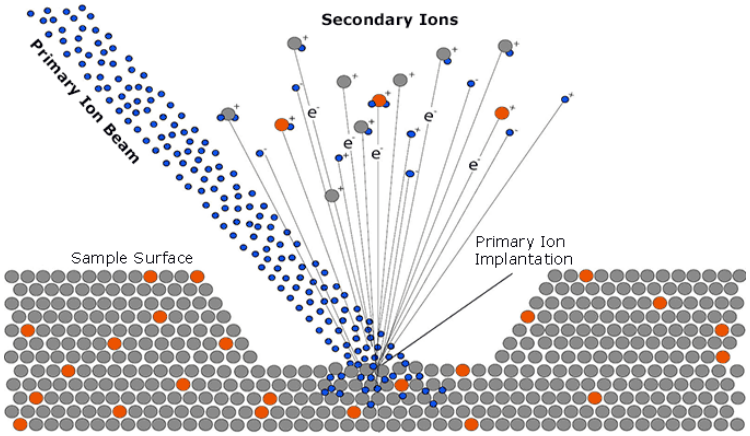


Figure 2.13. Schematic of the interactions between incident ions and the target solid. The blue balls represent the incident ions, grey balls are the matrix atoms, and the orange balls are the impurity atoms. From[251]

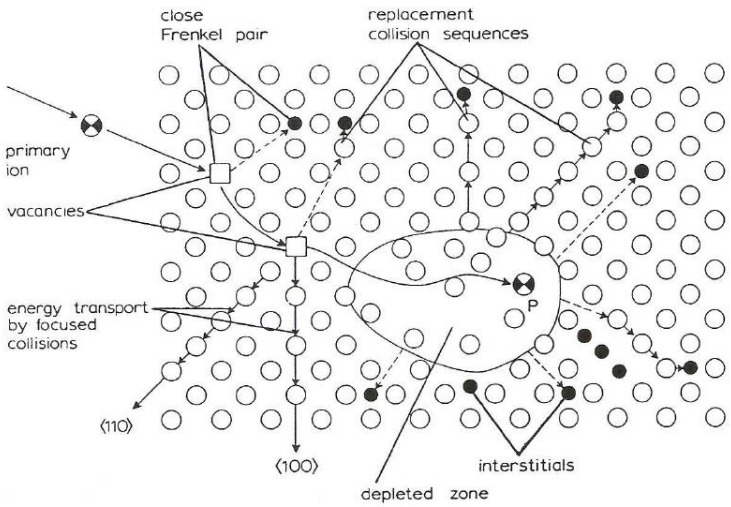


Figure 2.14. Schematic of the collision cascade process and the damage at atomic scale. Reprint from [252]

At the early stage of ion bombardment, the kinetic energy that ions possess is at the peak, the elastic core interaction is thus likely to be the dominant stopping mechanism. With the ions losing more energy as they penetrate further, the dominant physical interaction becomes inelastic.[253] A part of the kinetic energy that is not used in either nuclear or electronic stopping is released in the form of thermal energy and increases the local temperature, commonly described as *thermal spike*.[253]

The following two terms are often used to describe the level of ion-solid interactions[253]: *Stopping power* represents the ability of the target material to stop incident ions from further penetration, which is governed by the incident ion energy, the atomic mass and number of the ion and target atoms.[253] *Longitudinal projected range*, R_p, is the depth that the majority of ions are stopped at, which links to the highest ion concentration.[246, 250, 253, 254]

2.5.4.3 Damage and mechanisms

- Amorphisation or/and crystal defects

The energetic ion bombardment is a dynamic process of breaking atomic bonds and generating defects. Isolated point defects gather and turn into defect clusters as ion dose increases. When the thresholds of energy level and ion dose are achieved, the crystalline target loses the long-range order of its crystalline structure, indicating the occurrence of amorphous transformation.[255, 256] FIB induced amorphisation has been observed in many materials, such as diamond[257], Si[256, 258, 259], InP[260], CdTe[260], etc. Fig.2.15a exhibits ion-amorphised Si as an example. When the bombarding energy is high enough to displace atoms, but the incoming ion dose does not reach the critical value to move sufficient atoms, the target remains crystalline but with defects, as shown in Fig. 2.15b.[256]

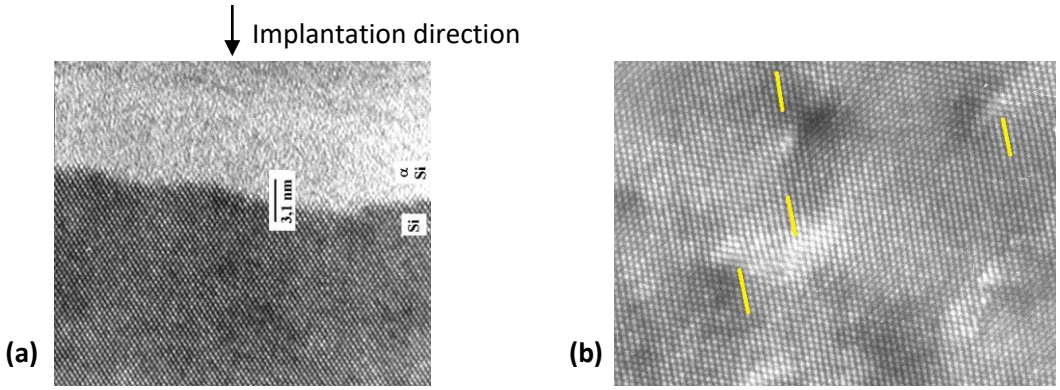


Figure 2.15. The HR-TEM images of ion implanted silicon. (a) The top implanted layer has been amorphised while the material beneath it remains crystalline. A clear boundary can be seen. (b) Lattice defects are observed in the crystalline area (lower part in (a)). The yellow lines indicate ending dislocation planes. Reprint from [256]

Ion irradiation is essentially a simultaneous competition between damage recovery and accumulation. A large amount of external energy is required to 'heal' the damage, which could be supplied by the thermal energy partially converted from the incident energy[257] or external thermal treatment[261]. MD simulation[262] suggest that the cascade effects in NiAl are affected significantly by thermal spikes and the local melting generated by 10 keV implantation. However, the local thermal spikes are believed to have little chance to overcome the rate of damage formation in most irradiations.

- Ion implantation

Most incident ions end up resting in the target material, known as 'ion implantation'.[263, 264] The distribution of 30 keV Ga implantation in Si probed using Atom Probe Tomography (APT)[234] (Fig. 2.16) exhibits an implantation depth of about 30-35 nm on the sidewalls which are almost parallel to the incident ion beam. The implantation depth increases at the apex of the specimen as the ion beam incidence angle decreases.

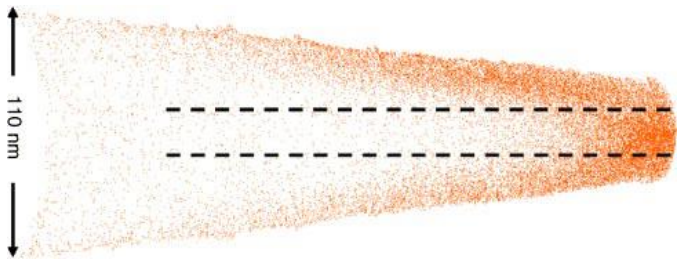


Figure 2.16. Atomic map of Ga-implanted Si, under FIB voltage of 30 keV. Orange dots = Ga atoms. Reprint from reference[234]

The concentration of implanted ion dose (Fig. 2.17a)[234] does not follow a continuously decreasing trend along the depth – the peak concentration is found at ~18 nm depth beneath the surface at 30 keV. The mass spectrum (Fig. 2.17b) estimates the amount of implanted Ga ions, indicating that a higher beam voltage will result in a higher quantity of implanted ions.[234]

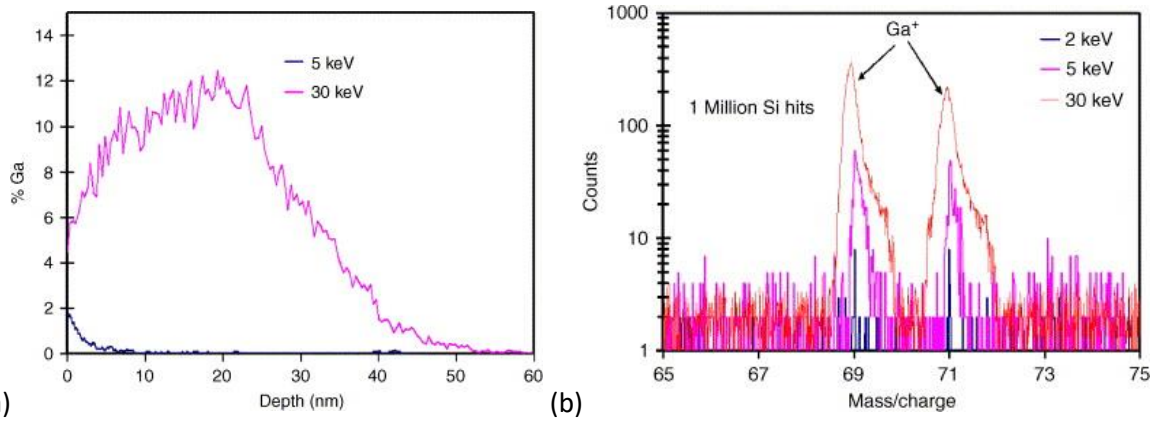


Figure 2.17. (a) 1-D Ga+ implantation profile in Si with FIB acceleration voltages of 5 and 30 keV at the normal incident angle., measured using APT. (b) The mass spectrum of Ga implanted region with FIB acceleration voltages of 2, 5 and 30 keV. Reprint from reference [234]

2.5.4.4 Simulation

SRIM (The Stopping and Range of Ions in Matter)[250], is a binary collision approximation (BCA) simulation software that has been widely used to predict the ion implantation process. It applies a static method based on Monte Carlo algorithms, which gives quantitative information of atomic and ion collision activities, such as ion range, concentration of vacancies, sputtering rate, etc. Despite the lack of consideration of crystal structure (all targets are assumed to be amorphous in SRIM) and dynamic changes in material composition and structure[250], SRIM is believed to be reliable with the accuracy of predicted sputtering rate claimed to be within ~10%.[253] The ion implantation depth simulated by SRIM also shows a close agreement to the empirical observation from the APT result (Fig.2.16 and 2.17) in the studies of Ga-FIB implanted Si.[234]

Dynamic BCA models, such as TRIDYN[265], take into account the dynamic alterations of substrate composition and properties caused by ion deposition, implantation, atomic relocation and sputter erosion, therefore providing more realistic results than SRIM.[266, 267]

Molecular dynamics (MD) simulation can simulate the formation of atomic defects, amorphisation mechanisms at atomic level, thermal spike, and so on.[257] As an example, MD simulation of Ga^+ implantation in single crystal diamond[257] shows the local temperature generated by high energy ion collisions to be 1454.6 K with a voltage of 16 keV.

In this thesis, only SRIM will be used due to the limit in time and computational capability.

2.5.4.5 Influential factors

A careful selection of milling conditions with a logical choice of ion species can be helpful in minimising the ion damage.

- *FIB acceleration voltage*

It has been demonstrated empirically that the implantation ion range increases with beam voltage (e.g. Fig.2.18, Fig.2.19).[234, 257, 260, 268]

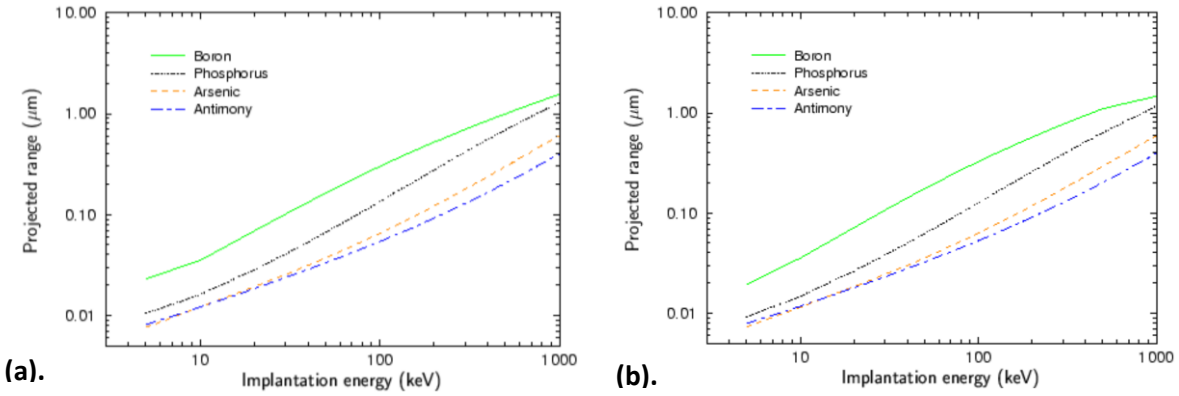


Figure 2.18. Projected ranges of various ion species as a function of the implantation energy in two materials: (a). Si, (b). SiO_2. Reprint from reference[268]

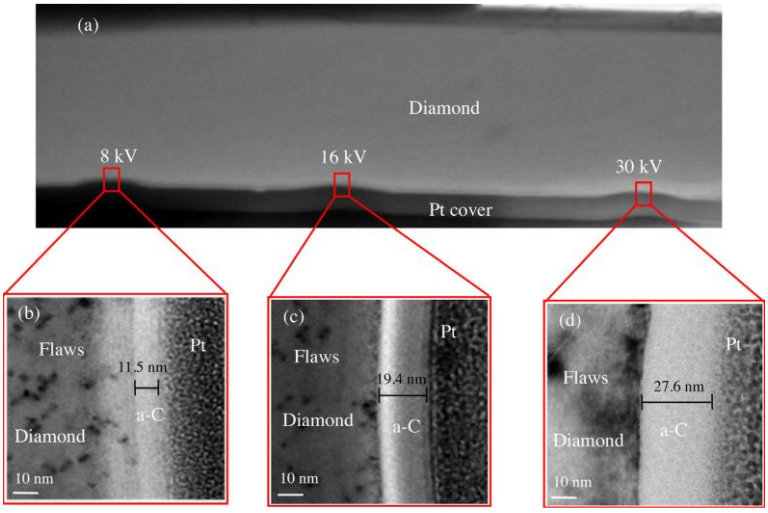


Figure 2.19. EFTEM images of Ga-FIB induced damage in single crystal diamond. (a) An overview of the TEM sample; (b – d) The EFTEM images of the ion-induced damage layers formed under beam voltages of 8 keV, 16 keV, and 30 keV, exhibiting thickness of~11.5 nm, ~19.4 nm and ~27.6 nm, respectively. From reference [257]

As another example, thicknesses of Ga amorphised Si layers measured under different FIB voltages[233, 261, 269] are found to increase apparently with ion acceleration voltage (Fig.2.20).

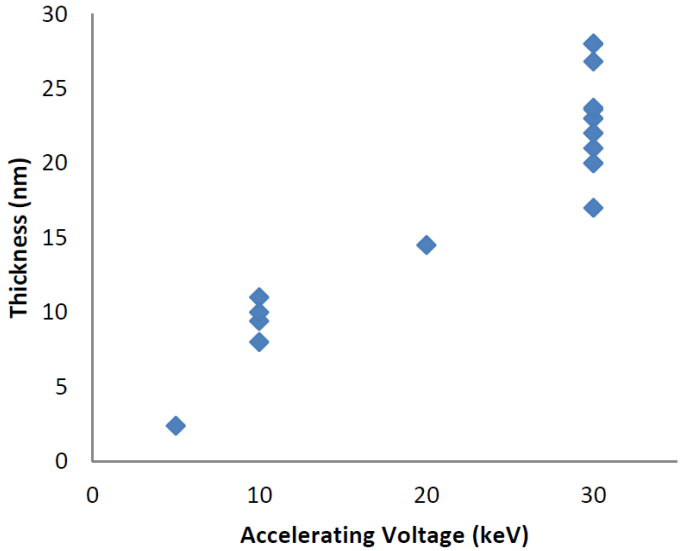


Figure 2.20. Thicknesses of amorphous layers caused by Ga-FIB implantation in Si. Please note that the other FIB conditions (i.e. current, dose, etc.) and the Si substrates were not exactly the same in these studies. Reprint from [270]

- *FIB beam current*

The higher the beam current is, the more ions are transported per unit time, thus a higher sputtering rate. The influence of beam current on amorphisation is not very well defined yet. Some[271] claim that the thickness of amorphous layer is independent of the beam current, while others[272] disagree.

- *FIB beam incidence angle*

Increasing the incidence angle (i.e. the angle between the normal incidence of target surface and the incoming ion beam) not only increase volume of interaction[253] and facilitates the escape of the sputtered material, but also reduces the thickness of the amorphous layer.[260, 272]

SRIM simulation (Fig. 2.21)[253] suggests that 80° (± 5°) is the incidence angle at which the materials exhibit the highest sputtering yield (*Y*, indicating the average number of target atoms ejected from the sample per incident ion), which leads to the best milling efficiency, although being associated with an enhanced level of redeposition.

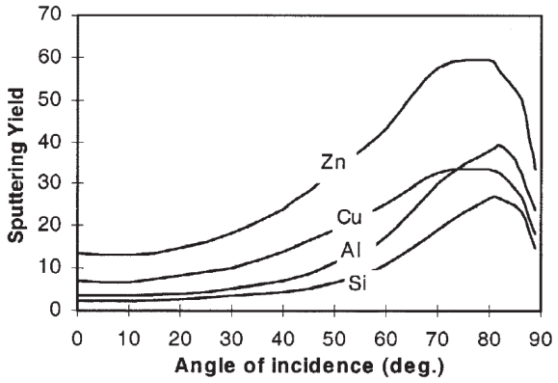


Figure 2.21. The TRIM simulated results showing the relations between the sputtering yield and the incident angle. Reprint from reference[253]

- *Ion dose*

Damage accumulates with more implanted ions[269] until a saturation ion dose is reached, with amorphisation occurring at a threshold ion dose. The ion dose threshold for amorphising Si under 30kV is found to be 1E+14 ions/cm^2, with the saturation dose being around 2E+16 ions/cm^2.[273] Rubanov[273] also suggests that the maximum ion dose accumulated by the sample can be calculated by $D_{max}=0.5\times R_p\times Y^{-1}$ (where R_p is the projected range of implanted ion and Y is the sputtering yield), which is derived as the balance between the damage formation and sputtering.

- *Ion species*

Ion species with higher atomic mass are claimed to result in a shorter ion range in the target solid[260], which has been demonstrated by implanting ions of different species into Si[268] as shown in Fig. 2.18.

Different impinging ions may also behave differently in the same target materials. For example, high densities of dislocation loops are observed in CdTe that is implanted by Ar^+, however, these dislocation loops are never present with I^+ milling.[260]

Moreover, milling is more efficient when the ion species have similar atomic mass to constituent elements in target materials due to optimum momentum transfer during bombardment.[260]

- *Target material*

Each material has its unique atomic composition, crystal structure and chemical bonds, which define their interatomic potentials that govern the materials' physical characteristics.[253] For example, ion irradiation tends to generate dislocations in metals but form amorphisation in ceramics, which can be explained by the high defect mobility in metals.

Fig.2.22a illustrates the strong material dependency of sputtering behaviour, showing the non-linear connection between the sputtering yield and the atomic number of the target atom.[253]

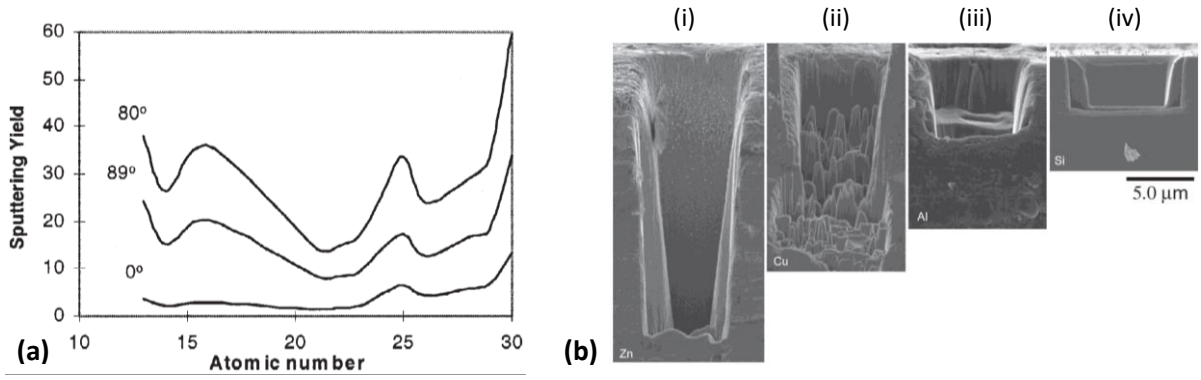


Figure 2.22. (a) SRIM simulation showing the relation between the sputtering yield and atomic number of target materials, at different incident angles. Reprint from[253] (b) Trenches of same target surface dimensions (10 µm x 5 µm) milled in different materials with same FIB conditions (25 kV, 1000 pA, 0° incident angle, ~7.5x1012 Ga^+ dose): (i). polycrystalline Zn, (ii). single crystal (100) Cu, (iii). polycrystalline Al, (iv). single crystal (100) Si. Reprint from [253]

Fig. 2.22b demonstrates empirically that the volume of removed material varies with atomic number under the same FIB condition, which is in agreement with the simulation results in Fig.2.22a and Table.2.6. Moreover, roughness of the finished surface and sloping angle of sidewalls also show significant differences.

Table 2.6. Predicted sputtering yield vs. atomic number

Target material	Zn	Cu	Al	Si
Sputtering yield predicted by modelling (atoms/Ga^+ ion)[253]	12.9	7.0	3.5	2.1
Atomic number	30	29	13	14

Comparing SRIM simulation results with empirical data (Fig.2.23), Prenitzer et al.[253] find that the peak positions of stopping powers correlate strongly with the density of the target material. Melting temperature (T_m), which is a direct indicator of bonding strength, shows an inverse correlation with *Y* (Fig.2.23c), because stronger bonding forces make atoms more difficult to be knocked off.

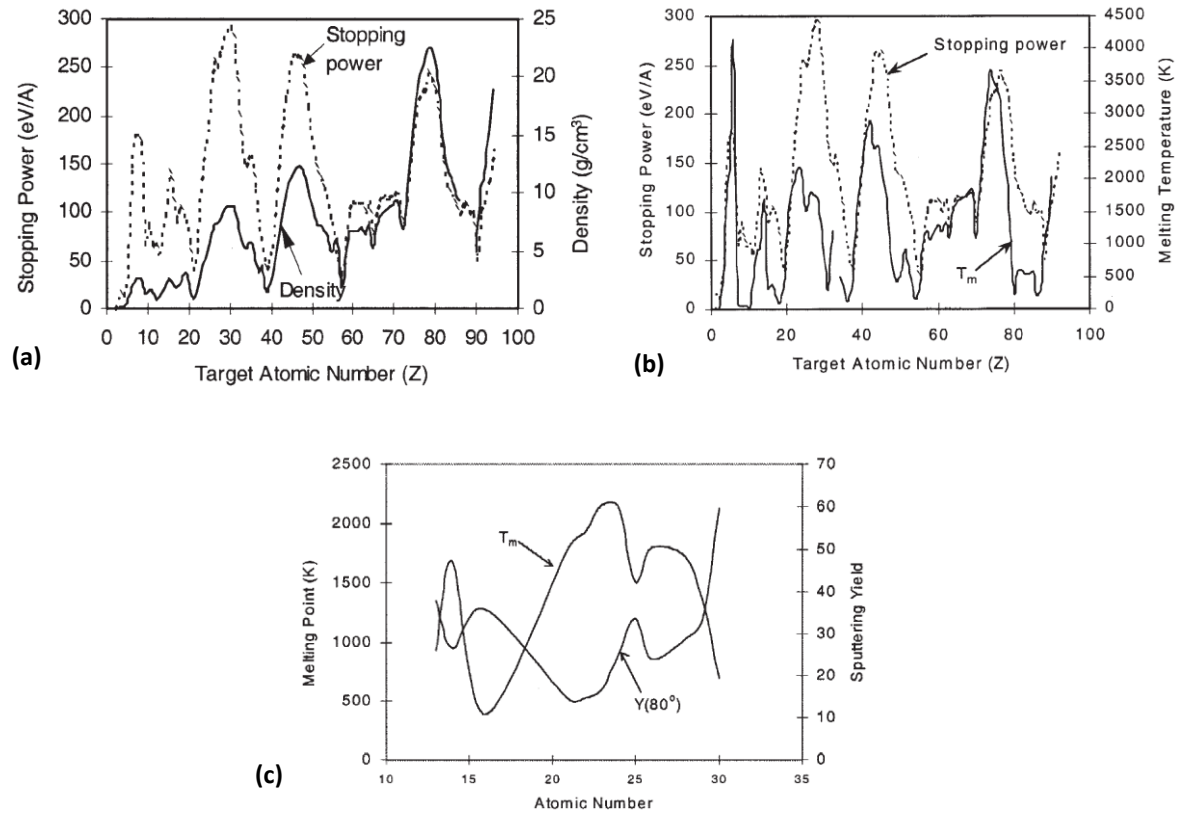


Figure 2.23. Simulated stopping power compared with (a). density, (b). melting temperature, and (c) simulated sputtering yield compared with melting point, all associated with atomic numbers. Reprint from [253]

In addition to the influential factors listed above, channelling effect[270] and temperature/heat treatment[261] also have effects on the ion implantation behaviour, which will not be discussed here.

2.5.4.6 Xe Plasma FIB (PFIB)

Xenon Plasma FIB (PFIB) is an emerging technique offering an interesting alternative to the conventional gallium FIB (Ga-FIB), replacing the liquid metal ion source (LMIS) with an inductively coupled plasma (ICP) Xe source[274]. The technique offers fast material removal rates by allowing for high beam currents without overly compromising the resolution offered by Ga-FIB.[275]. Xe ions are heavier than Ga ions, therefore offering an increased sputter yield and a reduced penetration depth.

PFIB is of interest to the present project because it is claimed by the manufacturers that PFIB induces less damage than Ga-FIB does in target materials. It has been reported[230] that the depth of amorphous damage introduced in Si by XPFIB is smaller than Ga-FIB by 20-40% at glancing angle incidence. The higher quality of EBSD patterns indicates that there is less damage on sample surfaces that are produced by PFIB.[232, 276] Burnett *et al*.[232] consider that the noble nature of Xe source reduces its possibility of chemical interactions with target materials.

Due to the fact that PFIB has only been commercialised very recently, the existing investigation of the PFIB damage is very limited, in particular there is no literature available concerning the PFIB damage in ceramics. As a trending technique for sample preparations for micromechanical testing, the damage introduced by PFIB needs further examination to compare with that generated by Ga-FIB.

2.6 Aim of Research

Despite the extensive use of ceramics in armour systems, the understanding of deformation and failure mechanisms in ceramics is non-systematic at present. The predictive capability of numerical simulation of ceramic impact behaviour is also limited. The present DPhil research was therefore undertaken with the following key objectives.

(a) Enable the reliable characterisation of mechanical properties of individual microstructural features. The current lack of understanding and consideration of FIB ion damage in ceramics result in inaccurate measurement of fracture toughness using the widely-used microcantilever technique. This can be overcome by either calibrating FIB ion damage or enabling stable crack

growth. Moreover, the validity of the constant disregard in models of the effect of shear stress on the failure of grain boundaries also needs to be investigated.

(b) Enhance the predictability of modelling of impact by integrating the experimental investigation into numerical development, including realistic microstructures (i.e. distributions of grain sizes) and correct mechanical properties of microstructural features (e.g. strength and toughness of grains and grain boundaries).

The corresponding results and discussion are presented in the following chapters:

Chapter 3 characterises the microstructure of armour ceramics. The empirically-assessed grain size distribution is incorporated into an innovative algorithm for generating representative microstructures numerically, and into the validation of the models by virtual sectioning.

Chapter 4 measures the strength of grain boundaries in combined normal and shear loading and demonstrates the importance of the shear stresses on the failure behaviour of grain boundaries.

Chapter 5 enables the reliable measurement of fracture toughness and crack velocities at the microscale by producing stable crack growth using chevron-notched cantilevers. Testing in air and under vacuum allows for the investigation of the effect of moisture-assisted subcritical crack growth. Cyclic loading demonstrates the self-healing capability of alumina.

Chapter 6 investigates the FIB ion damage induced by different ions (Ga^+, Xe^+) in Al_2O_3 and SiC at the microstructural scale, in order to advance the understanding of fracture toughness measurement at the microscale which inevitably receives FIB ion damage at notch tips.

Chapter 7 quantifies the residual stresses caused by FIB ion damage in materials of interest (Al_2O_3, SiC and Si), in order to calibrate the fracture toughness measured using the microcantilever bending test where the FIB residual stresses at notch tips play an important role in the accuracy of the results.

Chapter 8 outlines the key conclusions drawn from the present research.

Chapter 9 suggests future work to be undertaken.

Chapter 3. Microstructure – Grain Size Distribution

Microstructure dominates the bulk behaviour of ceramics and therefore needs to be fully understood. Moreover, consisting of realistic microstructure is essential for the numerical model to ensure the predictive capability for ceramic armour impact behaviour.

This chapter presents precise measurements of grain size distributions of alumina sintered at different temperatures, coupled with the development of a numerical method for the generation of 3D microstructure models with high representativeness. The innovative method of comparing the virtual and empirical serial sectioning outcome also enables the calibration of grain size results. The study has been published in reference[277] and contributed to the creation of a new routine in the simulation software LS-DYNA.

3.1 Experimental

3.1.1 Materials manufacturing and density measurement

Highly-dense alumina samples were manufactured using TM-DAR alumina powder (⩾ 99% purity, mean particle size 150 nm, Taimei Chemicals Co., Ltd, Tokyo, Japan). MgO powder (UBE, Japan, mean particle size 120 nm) was used as a dopant. The balls used for ball milling were polycrystalline alumina.

In order to obtain different microstructures, the following two compositions and powder processing routes were applied.

- Two material compositions
  - (i) Raw TM-DAR powder.
  - (ii) Raw TM-DAR powder + 0.2 wt% MgO.
- Two powder processing methods
  - (i) With ball milling (Fig.3.1): the powder was processed with 24h wet ball milling in ethanol → rotary evaporating → 24h dry ball milling with alumina balls → sieving (100 mesh) → calcining (600 °C, 1h).

(ii) As-received powder without ball milling.

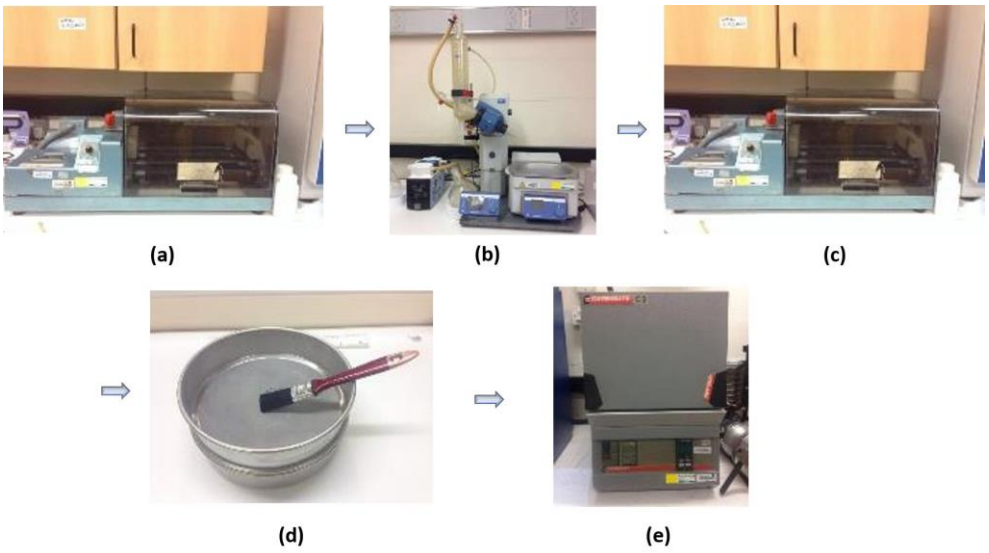


Figure 3.1. (a) wet balling, (b) rotary evaporating, (c) dry ball milling, (d) sieving, (e) calcining in a box furnace

The prepared powder then went through the following sintering process: uni-axial press (50 MPa, held for 5 minutes) to form green bodies (Fig.3.2a) → green bodies sealed in plastic bags → cold isostatic press (200 MPa for 4 minutes) (Fig.3.2b) → sintering in a tube furnace (Fig.3.2c,d).

Five sintering temperatures were applied to generate the difference in microstructures: 1350˚C, 1400˚C, 1450˚C, 1500˚C and 1550˚C (all held for 1h, 5˚C/min heating/cooling rate from/to room temperature, in air).

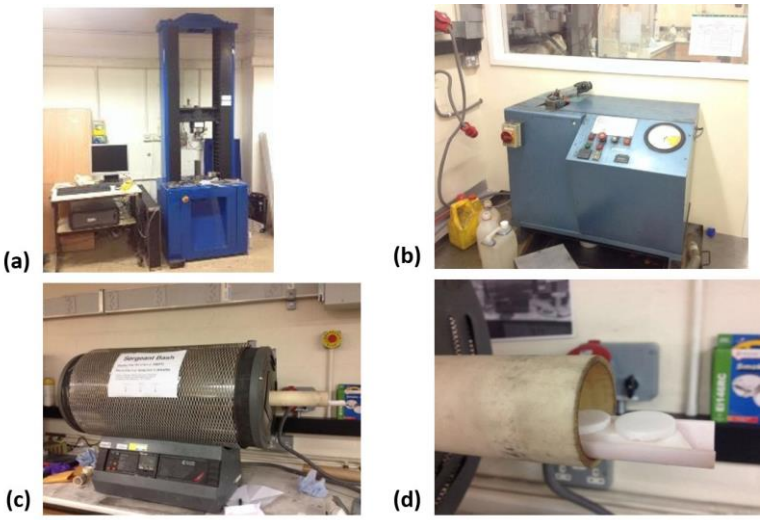


Figure 3.2. Images of the equipment used for sequent manufacturing steps. (a) Iso-static press, (b) cold isostatic press, (c) tube furnace for sintering, (d) as-sintered samples

The densities of the sintered specimens were measured using the Archimedes method. Firstly, the mass of the dry sample was measured in air using a high-accuracy balance for five times and the average was taken. The sample was then weighed in distilled water to have the mass averaged from five measurements. Lastly, the sample was set in boiling water for ten minutes to saturate the surface defects saturated with water, followed by having the mass of the damped sample averaged from five times measurement in air. The density could then be calculated using Eq.3.1.

$$\rho_{rel} = \frac{\rho_{liquid}}{\rho_{theoretical}} \times \frac{m_{dry}}{m_{damp} - m_{wet}} \times 100 \qquad (3.1)$$

where

ρ_{rel} = relative density, ratio between the density of alumina sample in respect to the theoretical fully-dense alumina density, expressed in %

$\rho_{liquid} = \rho_{water}$ = 0.998 g/m^3 when water temperature is 20°C

$\rho_{theoretical}$ =3.98 g/m^3

m_{dry} = mass of the dried sample

m_{wet} = apparent mass of the saturated sample weighed in distilled water

m_{damp} = mass of the saturated sample weighed in air

3.1.2 Grain size measurement

Sintered specimens were cut using a high-speed diamond blade to expose the cross sections. The cross sections were polished using a Buehler EcoMet 3000 automatic polisher sequentially with diamond slurry (Kemet) of different grades from 55µm down to 1µm. The polished samples were then thermally etched in an air furnace (all the samples were sintered and etched in the same furnace) at 50°C lower than their sintering temperature for 18 minutes to reveal grain boundaries. Samples were mounted on SEM pin stubs using electro-conductive silver dag to gain conductivity, followed by being sputter coated with platinum of 3 nm thickness to enhance the conductivity. SEM micrographs of the microstructures were then taken using a low voltage field emission gun SEM (JEOL 6500F, Japan).

For each sample, at least five images at random places were taken on the polished surfaces in order to provide a statistical average. One dimensional average grain sizes were firstly evaluated using the linear intercept method[278] through Eq.3.2.

$$G = 1.56\left(\frac{L}{MN}\right) \tag{3.2}$$

where G is the average grain size. L is total length of the intercepting lines. M is the magnification of the micrograph. N is the count number of grain boundary intersections. The number 1.56 is a geometrical factor to convert two-dimensional linear intercepts to equivalent 3D diameters derived by Mendelson[279].

Secondly, in order to enable a more precise measurement of the grain size, two-dimensional areas of grains were evaluated using the following elaborate method. Four samples sintered from as-received TM-DAR powder without ball milling, at four temperatures 1400 °C, 1450 °C, 1500 °C and 1550 °C, were selected for the analysis. At least 6 SEM images were taken for each specimen at random positions on the treated cross-sectional surfaces. Given the low contrast in the SEM images, the grain boundaries were highlighted manually using tracing paper, followed by digitisation. The 2D area of each grain on the images were measured using *ImageJ* software, with all the grains on the edges of the images excluded. The collected data were analysed using *OriginPro* software to plot the grain size distribution.

Additionally, for each considered grain, *ImageJ* software provides the values of shape descriptors – circularity (*C*), roundness (*R*), and aspect ratio (*AR*) – defined respectively as in Eq.3.3.

$$C = \frac{4\pi A}{P^2}\ ,\quad R = \frac{4A}{\pi d_{max}^2}\ ,\quad AR = \frac{d_{min}}{d_{max}} \tag{3.3}$$

where *A* and *P* are the area and perimeter of the particle, and d_{max} and d_{min} are the values of the length of the major and minor axis of the fitting ellipse.

3.2 Result

3.2.1 Microstructural study and density measurement

An SEM image of a cold-isostatic-pressed green body (Fig.3.3) was taken to have a first estimation of particle size before sintering. The individual particle size varied from 100 nm to 200 nm.

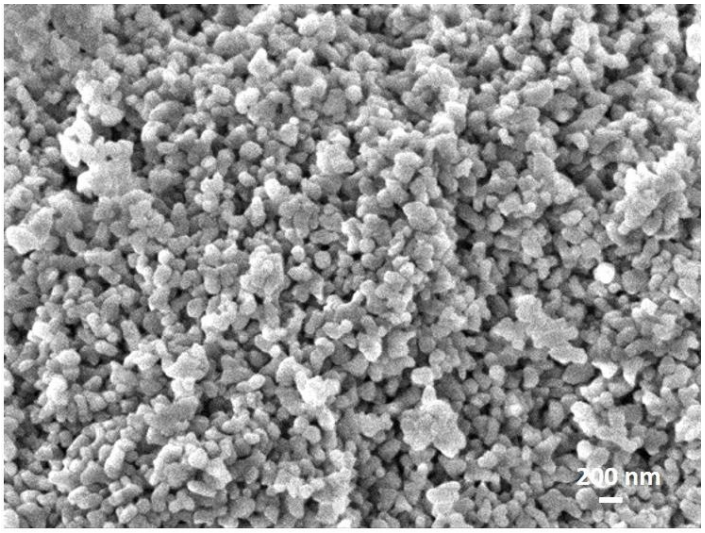


Figure 3.3. SEM images of a green body produced from pure TM-DAR powder without ball milling.

The SEM images of the alumina produced with the following different preparation processes are shown in Fig.3.4. Both (a) and (b) were ball milled and sintered at 1350°C but (a) was sintered from pure TM-DAR powder and (b) was from TM-DAR powder + 0.2% MgO. (c-f) were not ball milled and all sintered from pure TM-DAR powder, but at different temperatures - (c) 1350°C, (d) 1400°C, (e) 1450°C and (f) 1500°C.

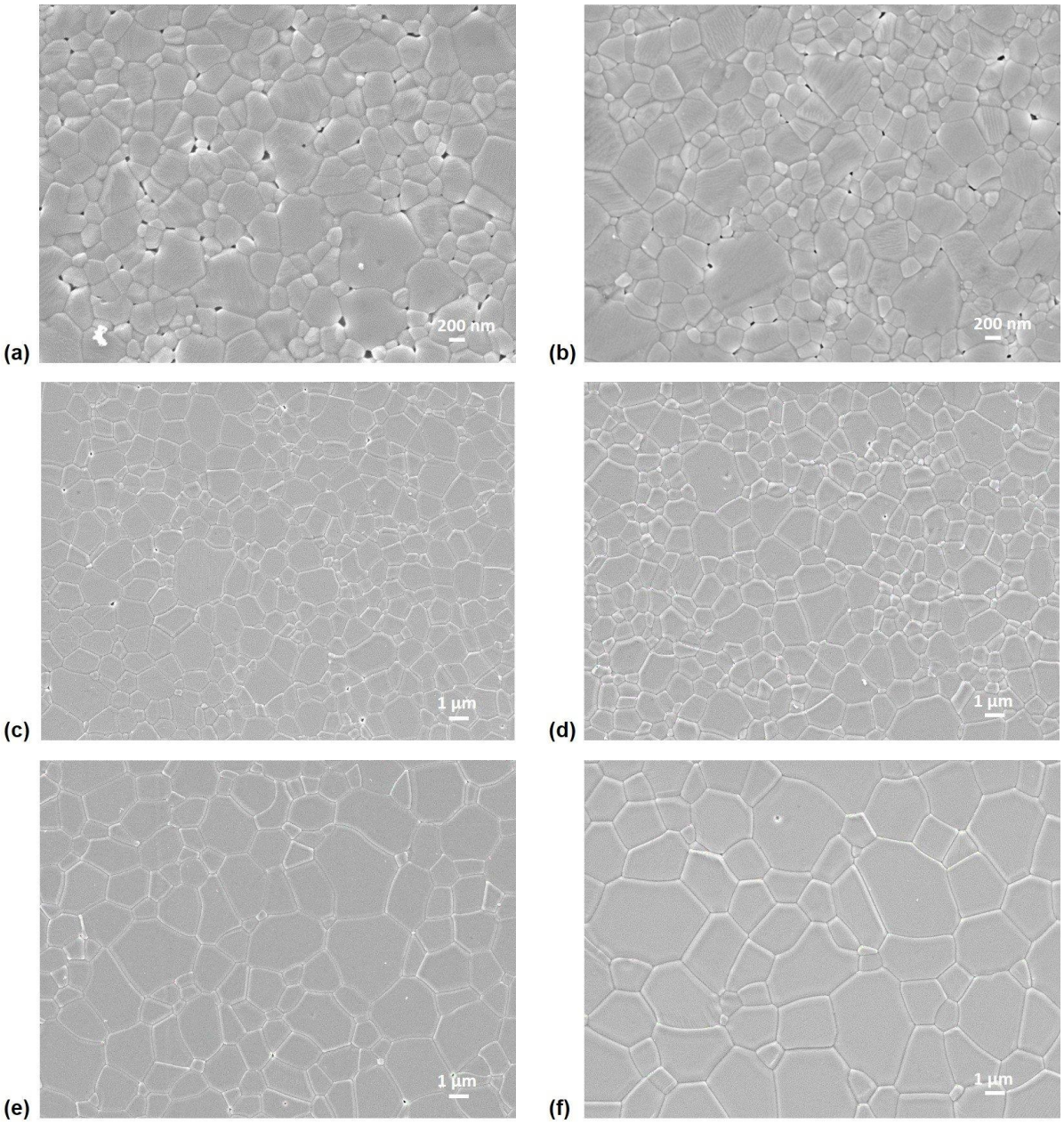


Figure 3.4. SEM images of Al_2O_3 samples produced with different preparation process. (a) pure TM-DAR powder, ball milled, sintering T = 1350°C, (b) TM-DAR powder + 0.2% MgO, ball milled, sintering T = 1350°C. (c-f) were produced from pure TM-DAR powder without ball milling, sintered at (c) 1350°C, (d) 1400°C, (e) 1450°C and (f) 1500°C. Please note that the scale bar of (a)-(b) is different from that of (c)-(f) to optimise the visualisation of grains.

The densities measured using the Archimedes method (Eq.3.1) and the 1D grain sizes evaluated using the linear intercept method (Eq.3.2) are listed in Table 3.1. Coupled with the SEM images presented in Fig.3.4, the results showed that both ball milling and the inclusion of MgO were effective in reducing the grain size. However, a relatively high percentage of porosity was observed in alumina samples processed with ball milling, while the samples sintered at the same temperature and without ball milling were almost fully-dense. The grain size was found to increase slowly when the temperature

went up from 1350 °C to 1400 °C. However, grains grew significantly when temperature went up to 1450 °C and higher.

Table 3.1. Density and mean grain size of alumina manufactured with different preparation process

Sintering temperature [°C]	Material source + preparation method	Etch temperature [°C]	Relative density *	Mean grain size [nm]
1350	Pure TM-DAR powder with 24h wet ball milling + 24h dry ball milling	1300	90.3%	510 ± 19
1350	TM-DAR powder + 0.2% MgO with 24h wet ball milling + 24h dry ball milling	1300	90.3%	468 ± 17
1350	Pure TM-DAR powder without ball milling	1300	99.4%	1503 ± 35
1400	Pure TM-DAR powder without ball milling	1350	99.9%	1551 ± 29
1450	Pure TM-DAR powder without ball milling	1400	100.4%	2518 ± 104
1500	Pure TM-DAR powder without ball milling	1450	99.8%	3296 ± 96

** Theoretical density of alumina = 3.99 g/cm³*

2D grain areas were evaluated using the digital method presented in the current study. Figure 3.5 exhibits examples showing the original SEM images and the corresponding digitalised images for 2D grain area measurements.

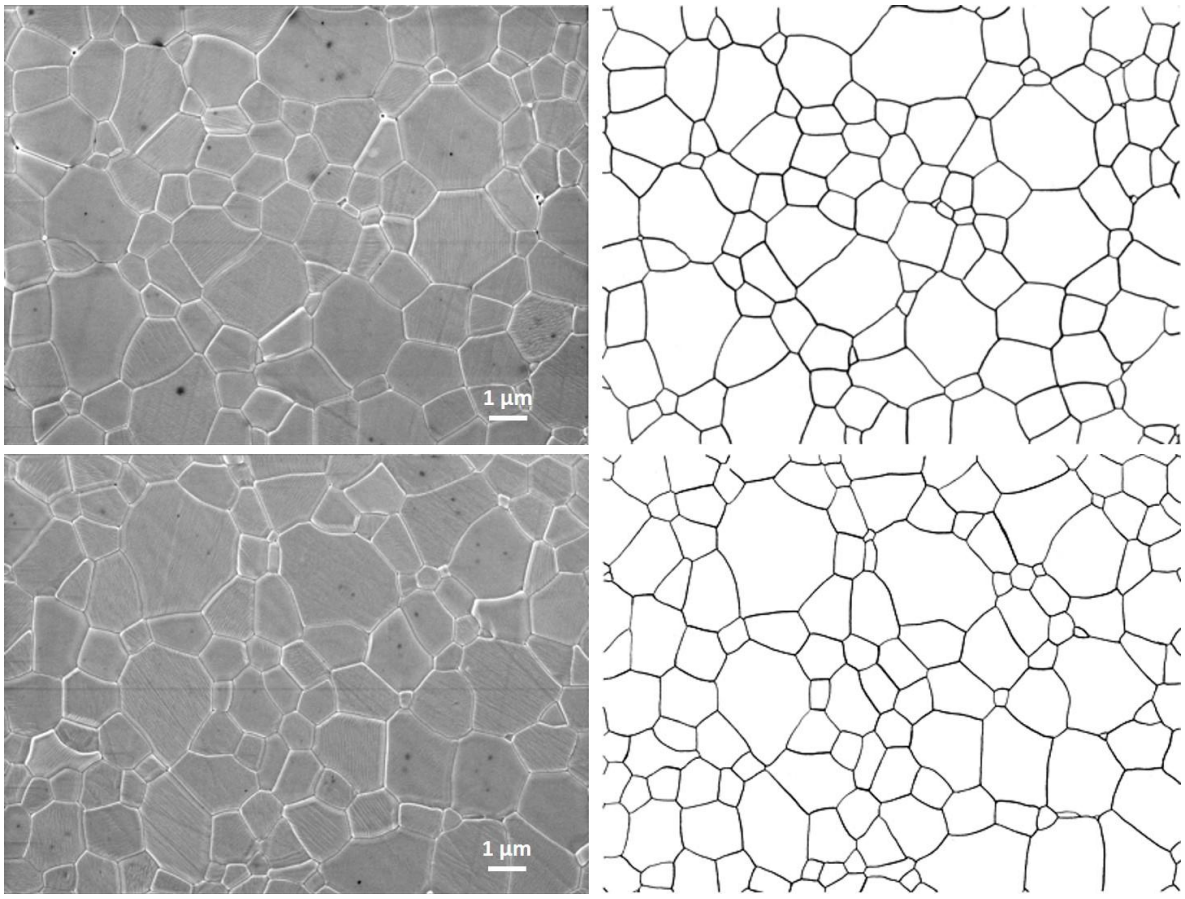


Figure 3.5. SEM image of the 1400 °C sintered alumina (left) and digitisation of the grain boundaries (right)

The details of the analysis and the average 2D grain area are summarised in Table.3.2. The number of grains analysed was more than 500 for each sample. With only 50 °C difference in sintering temperature, the average grain area of alumina sintered at 1450 °C was more than two times of that sintered at 1400 °C. With the temperature increased to 1500 °C, the grain area was almost doubled again compared with that sintered at 50 °C lower. The grain growth slowed down with the temperature rising further to 1550 °C.

*Table 3.2. Average 2D grain size of alumina. G*rains on the edges of the images were excluded

Sample Ref.	Sintering Temperature [°C]	Number of SEM image	Number of grains*	Average grain area [µm^2]
A1010	1400	6	519	1.32
A1001	1450	6	722	2.78
A1004	1500	9	635	5.01
A1015	1550	7	501	6.52

The distributions of individual grain areas and their cumulative probabilities are illustrated in Fig.3.6 and Fig.3.7, respectively. A few grains with abnormally large area had been observed in each sample, but none of the distributions was binomial.

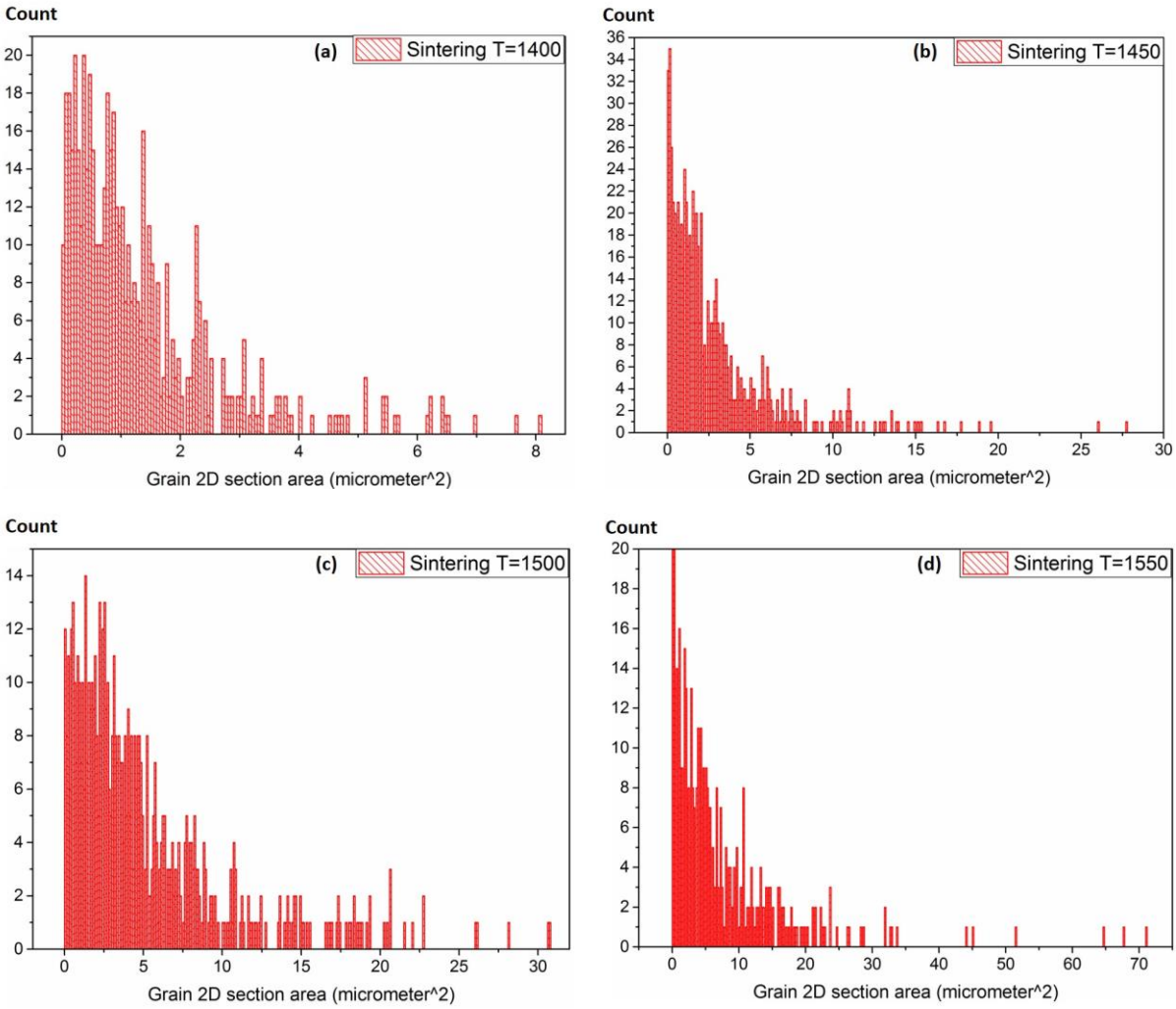


Figure 3.6. Grain area distributions of alumina samples sintered at 1400 °C, 1450 °C, 1500 °C and 1550 °C.

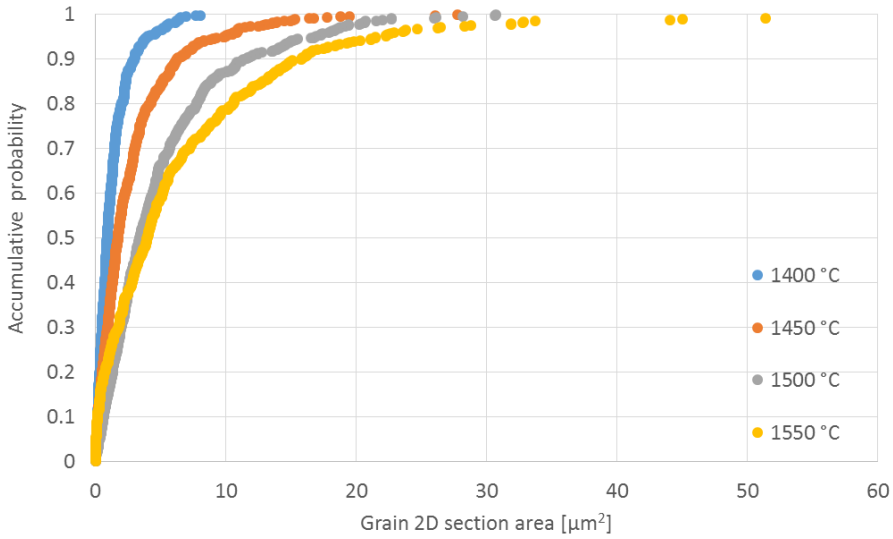


Figure 3.7. Cumulative probability of 2D grain area of alumina sintered at 1400°C, 1450°C, 1500°C and 1550°C

In order to eliminate the dependence of the distribution on the sampling exhibited by the histogram representation, the results of three sintering temperatures (1400 °C, 1450 °C and 1500 °C) in Fig.3.6 were converted to the probability distribution function (PDF) of the grain areas (*A*), based on Gamma Distribution (ϒ-distribution)[280]. Results are shown in Fig.3.8. The red lines are the ϒ-PDF, which provides a good description of the size distribution by defining only two parameters k and θ, as expressed in Eq.3.4.

$$\Upsilon - PDF(A; k, \theta) = \frac{A^{k-1} e^{A/\theta}}{\theta^k \Gamma(k)} \tag{3.4}$$

where k is the shape parameter, θ is the scale parameter, and $\Gamma(k)$ is the Gamma function defined as below.

$$\Gamma(k) = \int_0^\infty x^{k-1} e^{-x} dx \tag{3.5}$$

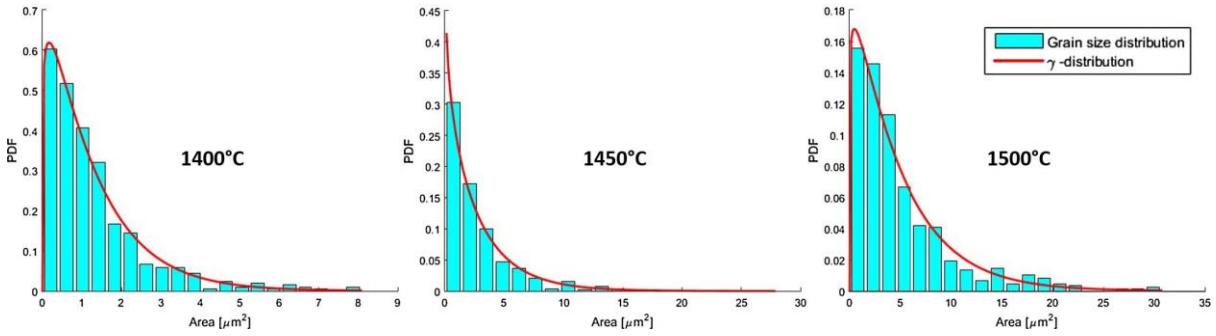


Figure 3.8. Histogram and ϒ-distribution of experimentally measured grain areas from alumina sintered at 1400 °C, 1450 °C and 1500 °C.

The obtained ϒ-PDF, representing the distribution of grain areas, was applied as input distribution of weights for generating the numerical model, as described below.

3.2.2 Development of numerical model for representative microstructures

The grain size distributions analysed from 2D SEM images, as described above, were used both as input data for the generation of the numerical model and as comparison data for the validation of the generated numerical models. The numerical model was mainly developed by Dr. Simone Falco, as collaboration.

- Laguerre-Voronoi tessellation coupled with a conditioning method for the nuclei seeding

In the present study where the representativeness of real microstructure is highly desired for ensuring the predictive capability of the ultimate numerical model, the Laguerre-Voronoi modification is applied to overcome the limit of the classic Voronoi, as discussed in Section 2.2.2. The preliminary input values of the weights for the tessellation are estimated based on the empirical values of the equivalent grain size distributions obtained in the present study, with the weights (*w*) equal to the square of the grain radius (*r*) (i.e. $w_i = r_i^2$).

Though the Laguerre-Voronoi tessellation offers an increased modelling capability, it comes at the cost of a non-bijective relation between the nuclei and the cells. In order to solve the issue (i.e. assuring that every nucleus generates a cell and lies within it), a conditioning method is developed to generate efficiently dense three-dimensional packing of spheres with an arbitrary radius distribution, based exclusively on tangency conditions and the *3D-clew* packing algorithm developed by De Cola et al.[281]

In this method, the spheres (with radii $r_i = \sqrt{w_i}$) are generated following a three-dimensional spiral pattern. First, the origin of the local coordinate system is defined as the centre of the first sphere (i.e. *central*). Second, the x-axis is defined by the position of the centre of the second sphere, which is tangent to the central one. With repeating the first two steps, each subsequent sphere is added by imposing its tangency both to the central sphere and to the one that was previously inserted.

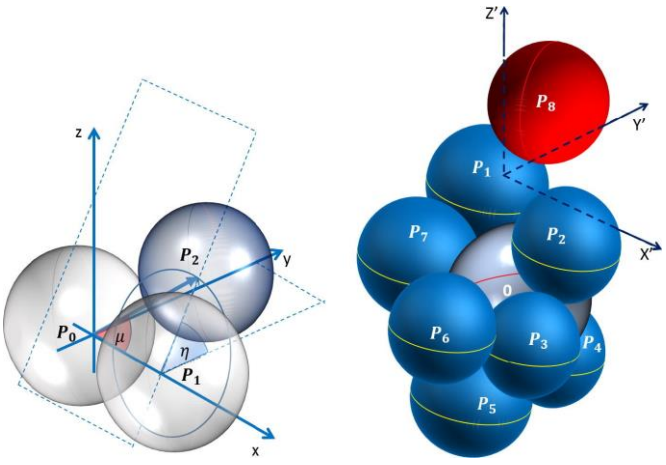


Figure 3.9. Illustration of (a) the tangency condition and (b) the positioning of a sphere (red) around a new central one.

The angle μ_j (Fig.3.9) is defined based on the tangency condition, as mathematically expressed in Eq.3.6, while the angle η is assigned with a random value.

$$\mu_j = \cos^{-1}\left[\frac{r_0^2 + r_0 \cdot r_i + r_0 \cdot r_j - r_i \cdot r_j}{(r_0 + r_i) \cdot (r_0 \cdot r_j)}\right] \tag{3.6}$$

where r_0, r_i, and r_j are, respectively, the radius of the central, the previous, and the current sphere (P_0, P_1, and P_2 in Fig. 3.9a, respectively).

The newly added sphere may appear to have overlap with the previously added ones, which was checked by evaluating the distance between their centres. If any overlap is detected, the newly added sphere would be translated incrementally along the blue circle (Fig.3.9a) by varying η whilst keeping μ constant. If no value of η is found to generate a sphere that does not overlap with any of the previous ones, the central sphere would be considered as saturated, and the second sphere would be imposed as the new central, as illustrated in Fig.3.9b.

The method described above is capable of generating random geometrical packing of non-overlapping spheres with arbitrary radii distribution. The position of the centres of the spheres in the obtained assembly and the relative radii were then used as coordinates and weights of the nuclei for the Laguerre-Voronoi tessellation. An example of the conditioning spheres and the relative tessellation is illustrated in Fig.3.10.

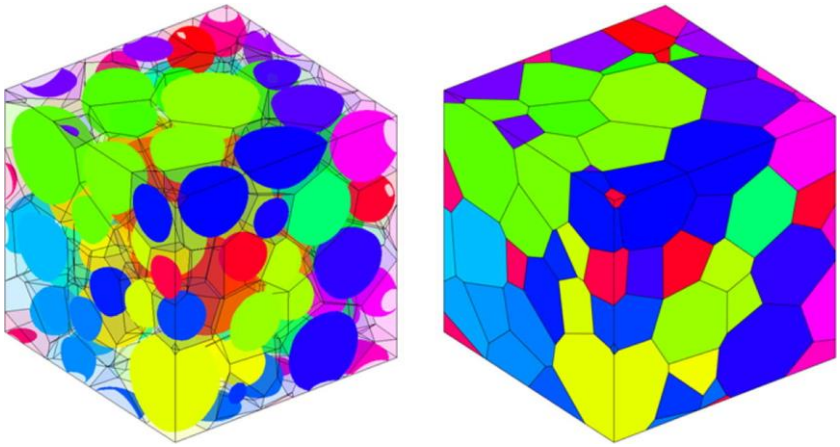


Figure 3.10. Packing of conditioning spheres (left) and relative Laguerre-Voronoi tessellation (right).

- Serial sectioning and comparison

To calibrate the empirical data of 2D grain areas, as well as to assess the quality of the generated models, the comparison of the 3D numerical model and the 2D microstructural images was performed by a virtual serial-sectioning of the cells in the model. In brief, the numerical structure was sectioned along parallel planes, producing 2D models directly comparable against the experimental SEM images, as illustrated in Fig.3.11.

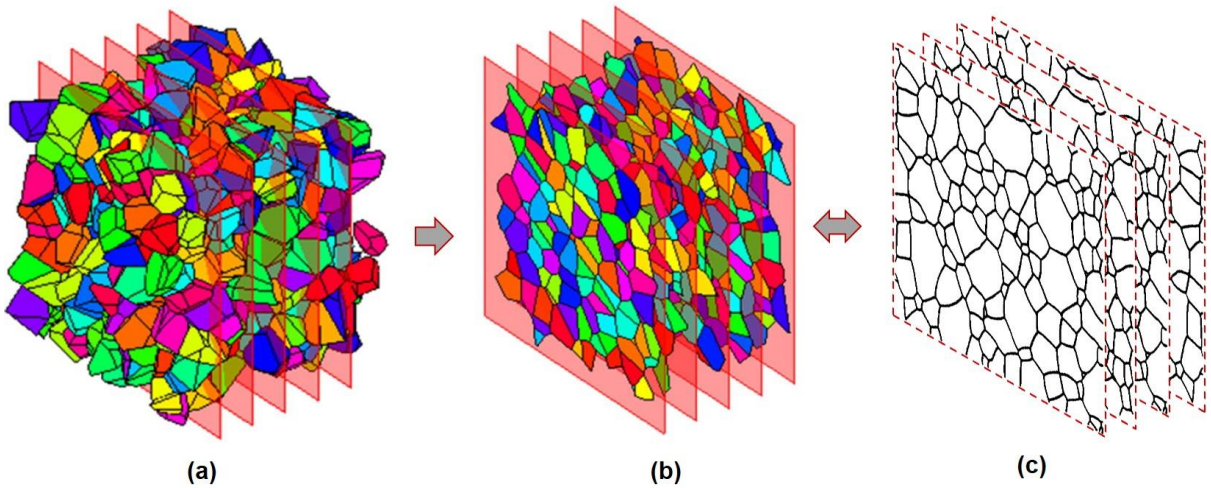


Figure 3.11. The process of validation of the numerical model. (a) Serial-sectioning of the 3D numerical model. (b) The generated 2D cross sections of the model. (c) Experimental 2D images for the validation against the numerical results in (b).

The numerical method used for virtually sectioning the structure[11], mimics the real cutting procedures by cropping the cells along arbitrarily oriented planes. It is achieved by the following procedure: (i) Detect the nodes beyond the cropping plane (Fig.3.12a). (ii) Find the intersection of the cropping plane with the cell edges connected to the external nodes (Fig.3.12b). (iii) Create the new face with the nodes lying on the cropping plane (Fig.3.12c). The procedure is repeated to all the cells to generate the 2D cross section of the structure.

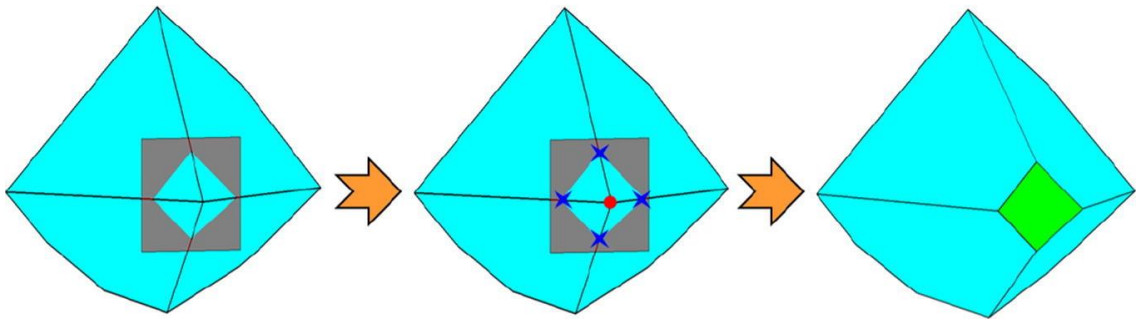


Figure 3.12. Cropping of a cell (blue) along a plane: The external node (red circle) is replaced by the intersections of the cell edges with the plane (blue crosses), and a new face (green) is created.

The weights were divided in discrete bins of values, expressed as fractions of the maximum equivalent size measured for the specific material considered. The effect of the number of bins used (hereinafter referred to as N_w) was explored using 3, 4, 5, and 6 unevenly spaced values of the weight.

In Fig.3.13, the ϒ-PDF of the results of 5 tessellations (consisting of ~100 grains each), obtained using the experimental equivalent radius distributions, are reported. The effect of N_w was illustrated by comparing four different unevenly spaced sets of bins for the weights (w_i), expressed as fractions of the maximum equivalent radius measured experimentally.

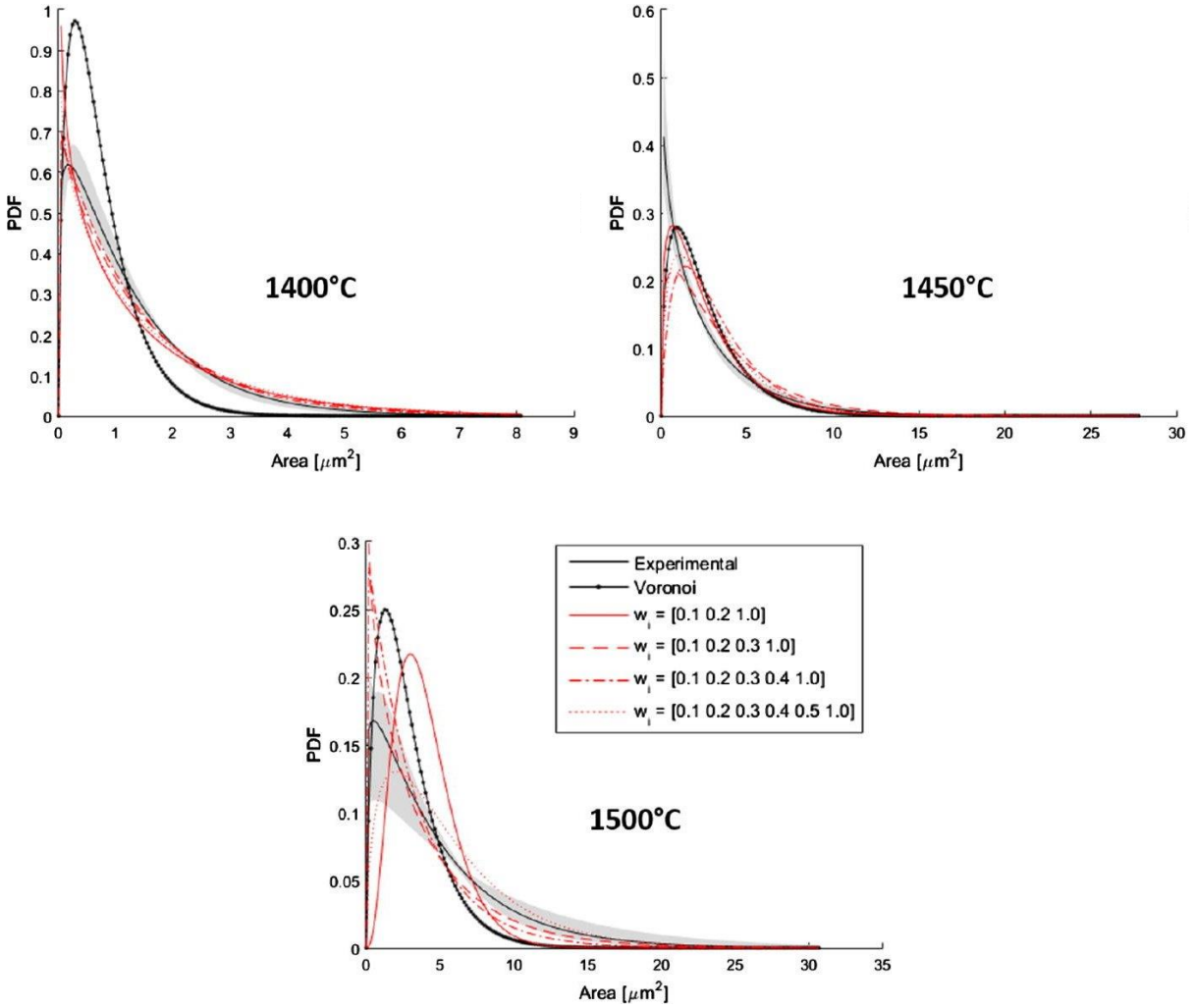


Figure 3.13. Comparison of grain area distributions of experimental measures and numerical models generated with classic Voronoi and Laguerre-Voronoi with different N_w. As examples, the weights are divided into three bins (w_i = [0.1, 0.2, 1.0]) when N_w is 3, the weights are divided into six bins (w_i = [0.1, 0.2, 0.3, 0.4, 0.5, 1.0]) when N_w is 6. From reference[277]

The increase of N_w appeared qualitatively to reduce the difference between the numerical and the experimental distribution of 2D grain areas, thus improving the representativeness of the

microstructural models generated, which for some configurations fall mostly within the experimental scatter represented by the grey area. Moreover, the comparison against the classic Voronoi tessellation exhibited the improvement of the Laguerre formulation in reproducing the presence of large grains in the structure.

- Optimisation

Further improvement in the representativeness of the numerical model, in terms of grain size distribution, was achieved by optimising the value and the distribution of the weights assigned.

Given the good quality of the initial estimation of weight values determined from the empirical data, the following *brute-force* type method is adopted for the optimisation. With the number and values of the weights remaining constant, a finite number of variations ($2n_i+1$) to the fraction of each assigned weight ($F_{w_i}^0$) are imposed. All the possible combinations are tested and the one that has the best fit to experiment is selected.

In particular, given an arbitrarily assigned quantity δ, the vector of all the variations of the generic weight fraction F_{w_i} can be expressed as:

$$F_{w_i} = F_{w_i}^0 + (k - n_i - 1)(-1)^k \delta \qquad \forall k = 1,2,\dots,(n_i + 1) \tag{3.7}$$

The total number of numerical models generated during the optimisation process is given by the permutation of the F_{w_i} for all the weights examined, which can be expressed mathematically as:

$$C_w = \prod_{i=1}^{N_w} (2n_i + 1) \tag{3.8}$$

If the number of variations is equal to n for all the $F_{w_i}^0$, the number of models becomes $C_w = (2n + 1)^{N_w}$. In particular, the optimisations presented in the present study use input $n = 1$ and δ equal to 2.5 times the minimum initial proportion of weights.

The comparison of the result of the optimisation against the experimental results is presented in Fig.3.14.

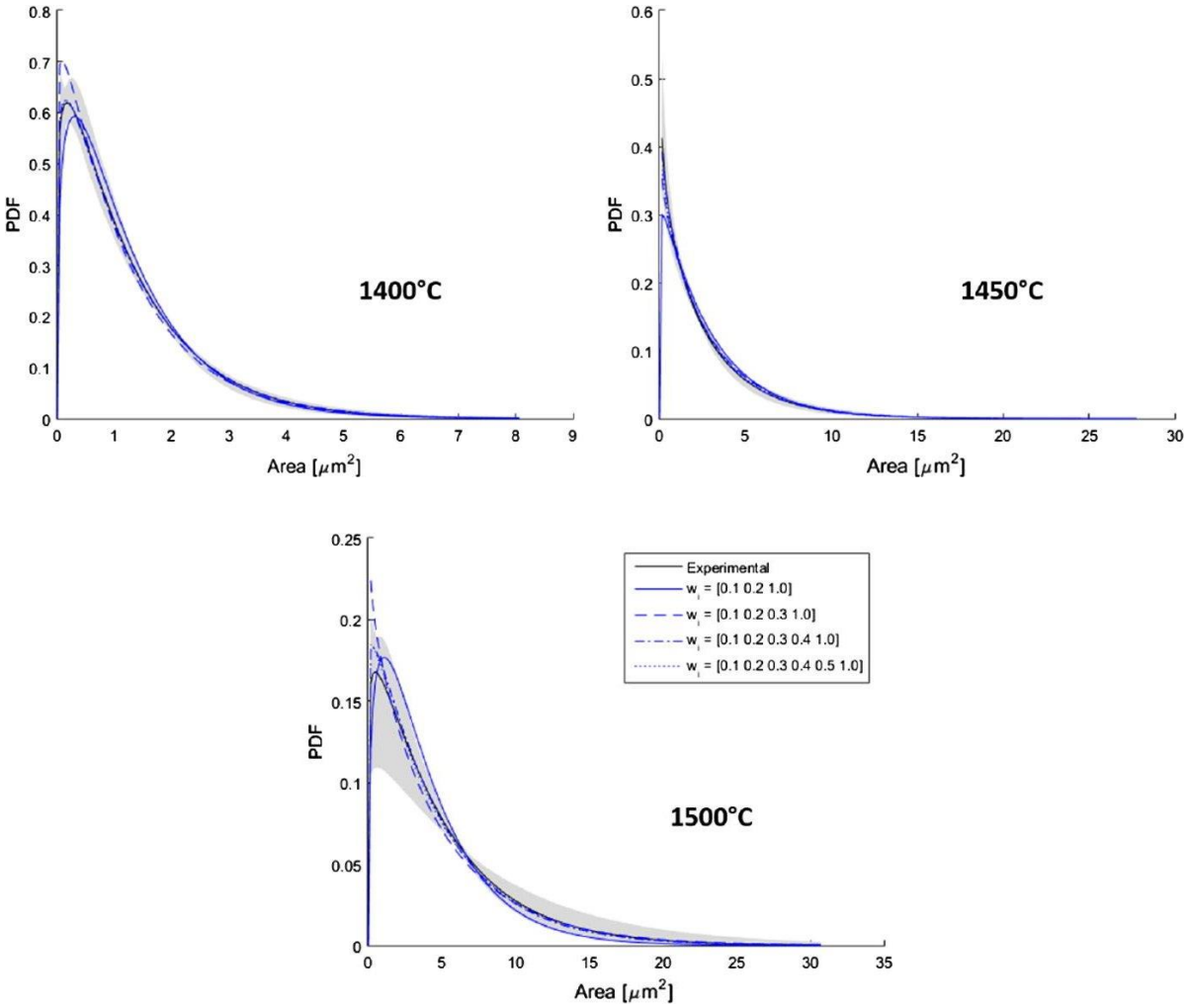


Figure 3.14. Comparison of ϒ-distributions of experimental data and optimised numerical models with different N_w. From reference[277]

For all the combinations explored, the result shows that the optimisation process improves the quality of the distributions by improving their level of agreement with the statistical variation of the experimental values.

3.3 Discussion

3.3.1 Effect of ball milling, dopant and sintering temperature

Ball milling has shown to reduce the average grain size in a significant manner (Table 3.1). Such effect could be explained by the following two possibilities. (i) Ball milling breaks up agglomerates in the raw powder which leads directly to small grains.[282] (ii) The pores in the sintered alumina, caused by impurities introduced into the raw powder during the ball milling process[283], limit the growth of grains.

Despite the reduced average grain sizes, the defects caused by the milling process were not desired features in sintered ceramics. Consequently, it was decided to produce all further alumina samples in the present project without ball milling, considering that controlling the sintering temperature would be sufficient to achieve the variations in grain sizes.

Adding MgO as dopant has also restricted grain growth to a certain extent, according to the result presented in Table 3.1. The positive role that MgO plays in controlling grain growth could be explained by the following two mechanisms. (i) MgO reduces the grain boundary mobility in alumina.[284] (ii) MgO is effective in roughening the alumina faces that are originally atomically smooth, which makes the grain growth controlled by diffusion rather than interface reaction, therefore leading to finer grains.[285] However, due to the fact adding dopants requires ball milling process, coupled with the disadvantage of ball milling explained in the paragraph above, MgO dopant is not further used in manufacturing alumina samples for the present research.

The grain sizes measured from alumina sintered at different temperatures (Table 3.1 and Table.3.2) showed clearly that increasing the sintering temperature would lead to grain growth in ceramics. It is because sintering is basically a thermally activated process of densification of compacts, and increasing temperature would provide higher thermal energy which leads to grain growth by exhibiting Ostwald ripening (i.e. larger grains grow bigger at the expense of smaller grains).[48] Knowing that grain size has a direct effect on the macroscopic properties, the systematic configuration of the grain size distribution against processing routes in the present study becomes useful in designing the manufacturing process for intended microstructures and properties.

3.3.2 Grain size distribution measurement and data calibration

Compared to alternative grain size measurement techniques (e.g. the conventional mean linear intercept method[279] estimates only 2D grain width; EBSD[286] requires high quality of surface finish and conductivity, as well as being highly time-consuming), the digitalised grain area measurement method presented in the current study provides an ideal balance between accuracy and cost of time.

Due to the nature of intersections (i.e. two-dimensional and arbitrarily-located), the grain area measured using the present method is always ≤ the area of the largest cross section of the grain. An example is illustrated in Figure 3.15. The issue has been overcome by the special calibration method developed in the present study - the specifically-designed virtual cross sectioning technique, followed by the comparison between the empirical and numerical data.

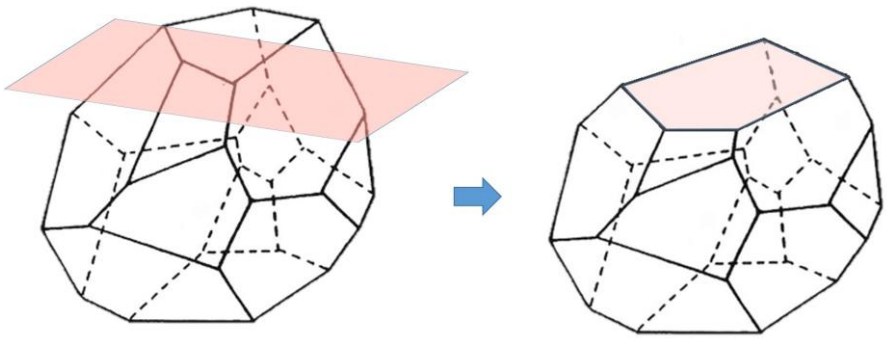


Figure 3.15. Illustration of the cross sectioning process of a grain

The process is as following: (1) Generate a numerical model with empirical data input as the initial estimation of weight values. (2) Serial cross section the 3D microstructures generated in the numerical model to obtain the 2D grain size distribution, which is afterwards compared with the empirical data. (3) Keep adjusting the weight values input in the numerical model (which is achieved using a computational algorithm developed in the present study) and repeating the step (2) until the 2D grain size distribution from the virtual cross sectioning agrees with the empirical results. The adjusted weights obtained in the end could then represent the actual grain sizes.

3.3.3 Representativeness of the numerical models

To evaluate the representativeness of the numerical models, an error parameter ($\eth$) is defined in Eq.3.9, based on the quadratic deviation of the numerical PDF_n from the experimental PDF_e, as a function of grain area (A).

$$\eth = \int_0^\infty \frac{[PDF_n(A) - PDF_e(A)]^2}{PDF_e(A)} dA \tag{3.9}$$

- Before optimisation

Without optimisation, the error δ for the classic Voronoi tessellation and for the Laguerre-Voronoi tessellations with different N_w are presented in Table 3.3.

Table 3.3. Values of error for the different tessellation for the three materials analysed

Material [°C]	ð (classic Voronoi)	ð (Laguerre-Voronoi)			
		ð(N_w=3)	ð(N_w=4)	ð(N_w=5)	ð(N_w=6)
1400	0.2802	0.0845	0.0391	0.0162	0.0935
1450	0.2264	0.0528	0.0820	0.1583	0.0943
1500	0.3275	0.0676	0.0279	0.0931	0.0054

Exhibiting smaller error values, the Laguerre-Voronoi tessellation has proved to improve the representativeness of the numerical models noticeably with respect to the classic Voronoi tessellation.

The effect N_w on the error has shown not to be linear. For the 1400 °C data set, as an example, increasing N_w from 3 to 5 reduces the error to a certain extend until N_w is further increased to 6 which leads to a jump in error.

- After optimisation

After optimisation, the error δ for the Laguerre-Voronoi tessellations with different N_w is reported in Table 3.4.

Table 3.4. Values of error of the optimised tessellations for the three materials analysed.

Material [°C]	ð(N_w=3)	ð(N_w=4)	ð(N_w=5)	ð(N_w=6)
1400	0.0073	0.0087	2.51×10^{-4}	1.98×10^{-5}
1450	0.0111	0.0043	8.59×10^{-4}	0.0019
1500	0.0401	0.0093	0.0028	0.0015

Comparing Table 3.3 and 3.4, the optimisation process has shown to reduce the error δ significantly for each tested N_w. The small errors demonstrate that the excellent agreement has been achieved between the optimised tessellation and empirical data.

It worth noting that the choice of the number of values for the input of the weights is a trade-off between the quality of the initial guess and the computational cost of the optimisation algorithm.

The current chapter has shown how to connect experimental measurement of grain size distributions with numerical modelling of representative microstructures, by incorporating empirical data to the development of an innovative algorithm for the numerical generation of microstructures and validating the numerical models via a novel method of virtual cross sectioning.

The next chapter deals with one of the major assumptions that is required in numerical modelling – the contribution of normal and shear stresses on the brittle fracture of grain boundaries.

Chapter 4. Strength of Grain Boundaries

Intergranular fracture is the governing failure mode of polycrystalline alumina subjected to low strain rate loads. Understanding the failure mechanism of grain boundaries is therefore crucial in investigating the material's failure behaviour as well as in enabling the predictive capability of numerical modelling. However, the shear component is often overlooked in the existing microscale measurements of grain boundary strength[183]. It is thus important to initiate the experimental investigation on the effect of shear stress on the grain boundary failure.

In the present chapter, bi-crystal alumina containing an artificial grain boundary was formed by diffusion bonding two pieces of sapphire. The failure stresses were measured by testing microcantilevers made across the grain boundary with selected inclinations with respect to the longitudinal axis of the cantilever. The comparison of the corresponding normal and shear stresses at failure between different grain boundary inclination angles is analysed, allowing the respective importance of the two loading modes on the failure of grain boundaries to be understood.

4.1 Experimental

4.1.1 Methodology

The cantilevers in the present study have triangular cross sections of width W and height H, with a total beam length of S (Fig.4.1). The angle between the grain boundary and the cross sections of the cantilever is θ. L_f the distance between the loading point and the intersection of the grain boundary and the top tension surface. The cantilever bends under the increasing load of F applied by nanoindenter near the free end and breaks at the load of failure F_f.

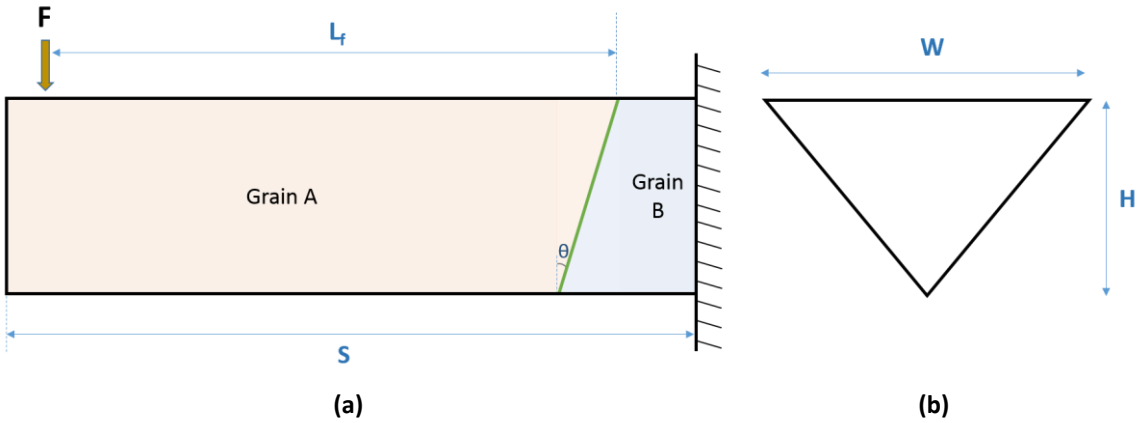


Figure 4.1. Schematic of the cantilever. (a) The side view, showing the grain boundary (indicated in a green line) and the grains on the two sides. (b) The cross section of the cantilever.

Based on the Euler-Bernoulli theory for elastic beams, the failure stress of the grain boundary σ_f can be calculated from Eq. 4.1.

$$\sigma_f = \frac{F_f L_f y}{I} = \frac{12 F_f L_f}{W H^2} \tag{4.1}$$

where *y* is the distance through the beam thickness from the tensile surface to the neutral axis of the cross section, *I* the second moment of area of cross section.

Euler-Bernoulli beam theory is used rather than Timoshenko beam theory because of the sufficiently high slenderness ratio of $L{:}\,H$. The shear stress at the grain boundary originated by the applied load F, $\tau_F = \frac{F}{A}$ (where A is the cross sectional area of the beam with $A = WH/2$), is negligible compared to the tensile stress σ_F (The ratio $\tau_F{:}\,\sigma_F$ is 2.1% ± 0.2% in the present study).

In the case where θ = 0° (Fig.4.2a), the bending stress on the grain boundary is purely tensile. If 0° < θ < 90° (Fig. 4.2b), the bending stress on the grain boundary has both tensile and shear components.

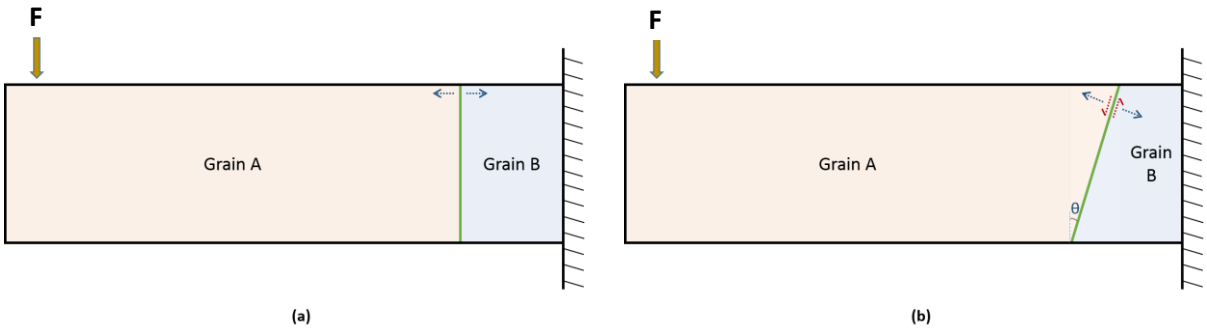
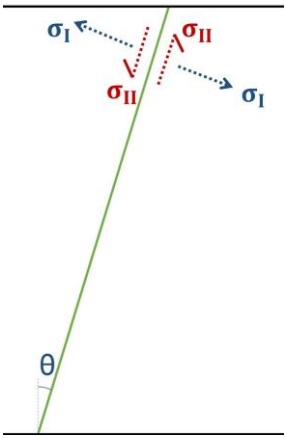


Figure 4.2. Sketch of the microcantilever used to measure the failure strength of grain boundaries. The blue dashed arrows represent the tensile stresses, while the red dashed arrows represent the shear stress. (a) The angle between the grain boundary and the longitudinal axis of the cantilever is 90°, therefore there is no shear component. (b) The angle between the two is θ (0° < θ < 90°), therefore there are both normal and shear components.

The normal stress σ_I and shear stress σ_{II} at the top of the grain boundary can be calculated from the stress transformation equations, Eq. 4.2 and Eq. 4.3 respectively.



$$\sigma_I = \frac{F_f \cdot cos\theta}{A/cos\theta} = \sigma_f \cdot \cos^2\theta \qquad (4.2)$$

$$\sigma_{II} = \frac{F_f \cdot sin\theta}{A/cos\theta} = \sigma_f \cdot sin\theta \cdot cos\theta \qquad (4.3)$$

4.1.2 Material, sample preparation and testing

Two pieces of the C-plane (0001) sapphire substrates (PI-KEM, UK. Diameter = 20 mm, thickness = 2 mm, both sides polished to fine finish by the manufacturer) were cleaned in the UV Ozone cleaner for 30 minutes to remove organic residues on the surface. They were diffusion bonded together with a general twist angle using the spark plasma sintering (SPS) technique (Dr. Fritsch DSP507, Germany). Sintering was carried out under vacuum with a maximum temperature of 1550 °C, 50 °C/min heating rate and 15 minutes dwell time. A uniform pressure of 82.5 MPa was applied constantly on the sample (20.75 MPa on the SPS punch) from the beginning of the heating until the end of the dwell. The sample was left cooling naturally in the graphite die. The misorientation angle was checked using EBSD (Fig.4.3)

on the polished cross sectional surface of the bi-crystal, showing a twist grain boundary of ≈22 degrees.

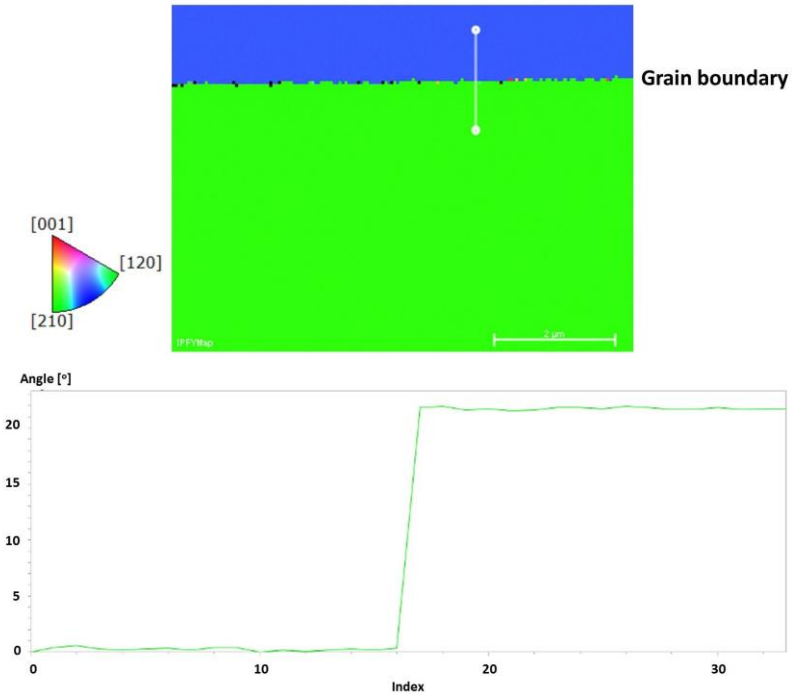


Figure 4.3. Misorientation angles in reference to the original point

The sintered bi-crystal was cross sectioned with parallel cuts using a diamond blade (Fig. 4.4a). The slice was sectioned again with the parallel cuts at a chosen inclined angle (0°, 15° and 45°) to the sample top surface (Fig. 4.4b). The surface sectioned from the last parallel cuts were polished down to 1 µm diamond slurry and finished by colloidal silica. The crystal orientations of each polished surface were measured using EBSD and applied in the numerical models for anisotropic properties.

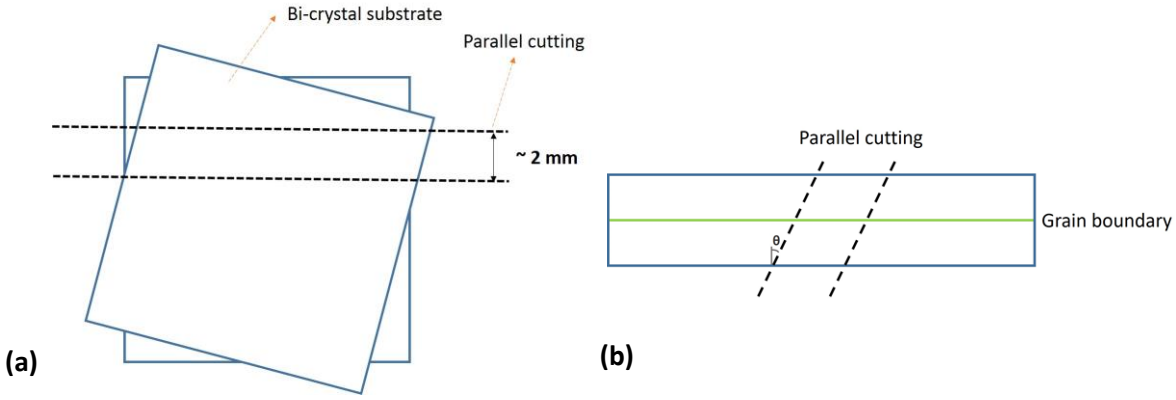


Figure 4.4. The schematic showing the cutting procedure for preparing the bulk specimen.

The bulk samples were mounted onto pin stubs using silver dag and sputter-coated with Pt to gain conductivity. Thermal etching was not used to reveal grain boundaries because the grooves created by the etching at the grain boundaries have significant effect on strength measurement.[161] The grain boundary was identified in the FIB based on the contrast difference between grains and grain boundary. Microcantilevers with triangular cross sections were manufactured across the grain boundary using the FIB by following standard microcantilever FIBing procedures[187], with the fixed end of the cantilevers located a few hundred nanometres behind the grain boundary.

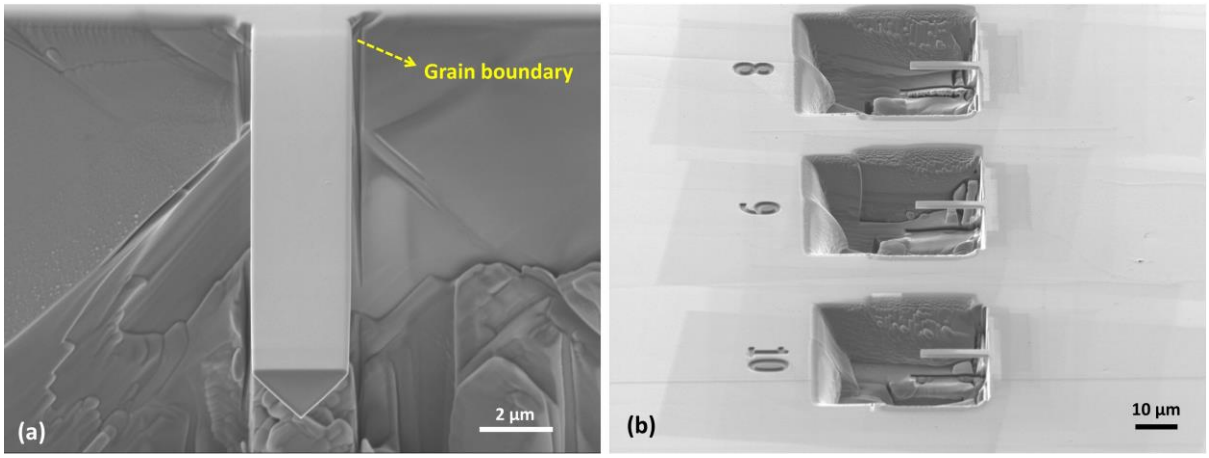


Figure 4.5. SEM images of (a) a typical microcantilever that has triangular cross section and contains a grain boundary near the fixed end, (b) an array of the microcantilevers made along the 45° grain boundary.

Prior to the cantilever bending test, the specimens were thermally annealed (1100°C, 1h dwell, 3 °C/min heating and cooling rate) to remove the FIB implantation residual stresses deriving from the cantilever manufacturing process. The cantilever bending test was carried out in a G200 nanoindenter (Keysight Technologies, USA) coupled with a diamond Berkovich nanoindenter tip (Synton-MDP, Switzerland) with the following procedure: a scanning load of 0.5 µN was applied to scan the top surface of the cantilever and the area around it under the AFM scanning mode, which enables the visualisation of the shape and location of the cantilever. An indentation point was marked in the scanned map informing the nanoindenter tip of where to load the cantilever. The cantilever was bent under a displacement-controlled testing mode with a displacement rate of 3 nm/s until failure.

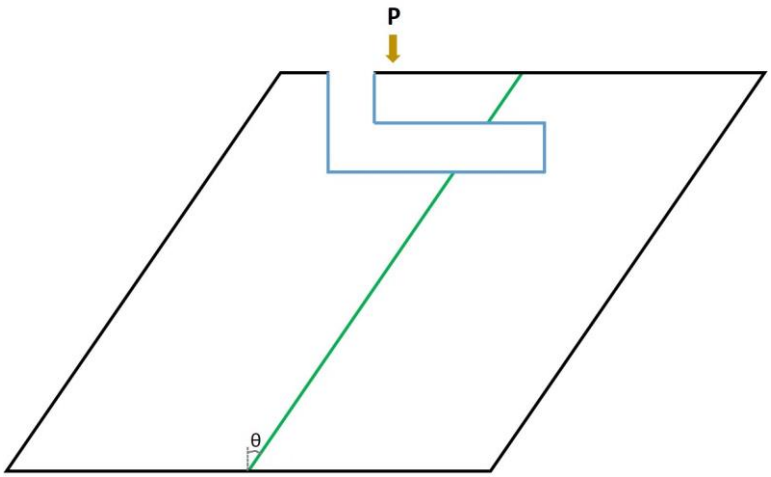


Figure 4.6. Schematic showing the side view of a microcantilever made along the inclined grain boundary and loaded under a load P. The grain boundary is indicated in the grain line and has an angle of θ to the loaded surface of the cantilever.

4.2 Results

4.2.1 Strength of grain boundaries

- 0° grain boundary

Ten cantilevers were manufactured on the 0° grain boundary specimen. However, four of the cantilevers were broken during the AFM scanning process, which disabled the bending test. Therefore, the test was completed on six cantilevers, with the relevant data listed in Table.4.1.

Table 4.2. Dimensions (S, L_f, W, H), fracture load (F_f), failure displacement (D), elastic modulus (E) and grain boundary strength (σ_f) of cantilevers with 0° grain boundary

#	S [µm]	L_f [µm]	W [µm]	H [µm]	F_f [µN]	D [nm]	E [GPa]	σ_f [GPa]
1	15.0	12.8	2.9	1.7	283.1	1288.9	395.9	5.3
2	19.1	15.1	2.9	1.8	230.0	1885.5	304.4	4.3
3	18.6	14.9	2.9	1.9	309.2	2434.0	312.3	5.4
4	18.9	14.9	3.0	1.9	329.7	2509.2	296.3	5.6
5	19.2	15.9	3.1	1.9	247.5	2094.5	306.4	4.4
6	19.0	13.6	2.7	1.6	243.3	1690.1	425.8	5.6

Figure 4.7a indicates the crystal orientations for the group of cantilevers No.1 and No.6, while Figure 4.7b is for the cantilevers No.2-5. There was no clear difference in strength between the two groups of specimens.

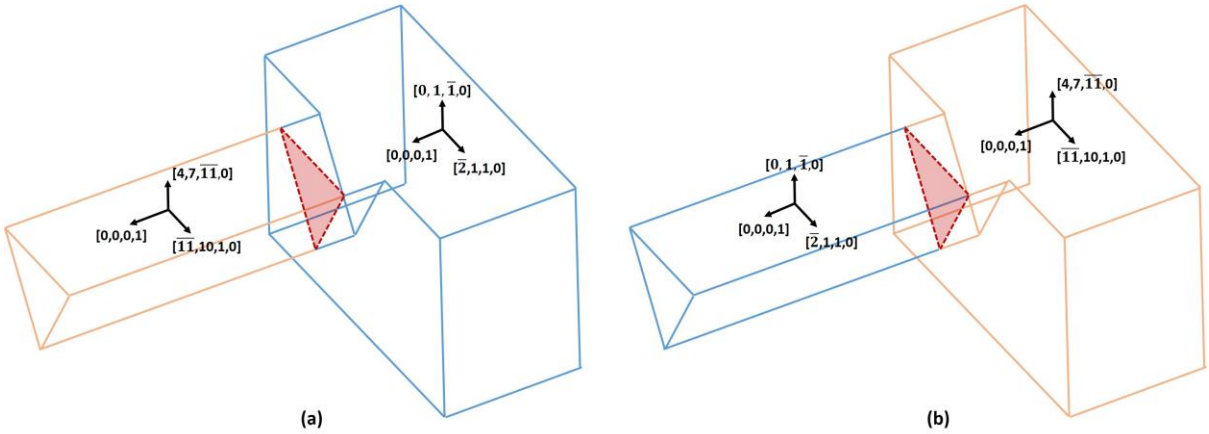
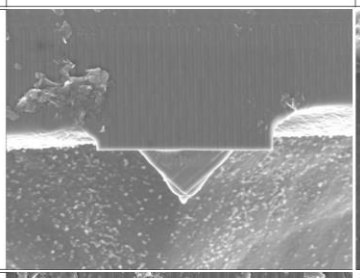
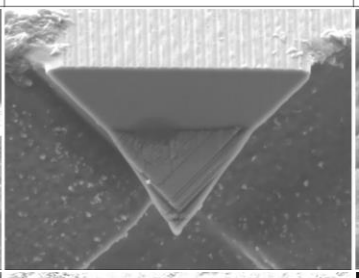
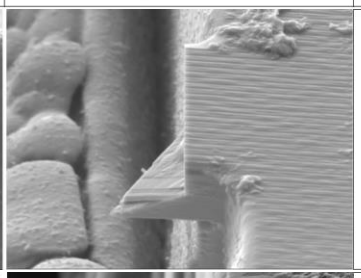
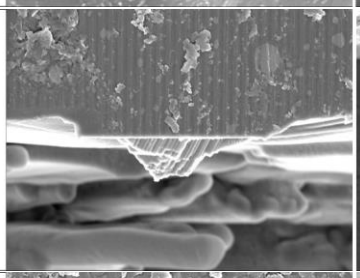
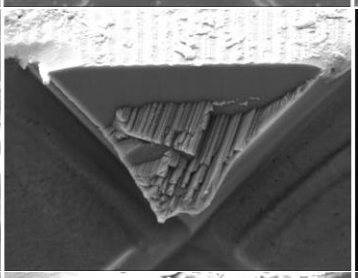
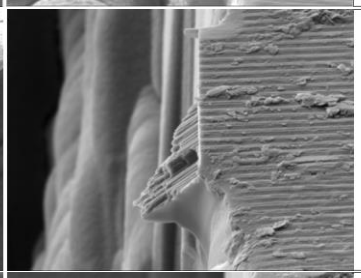
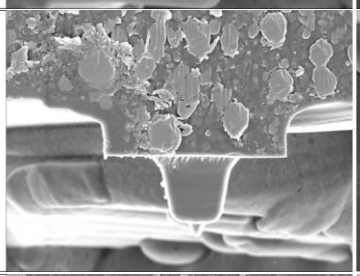
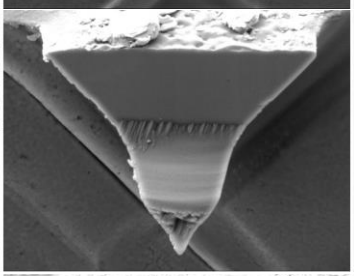
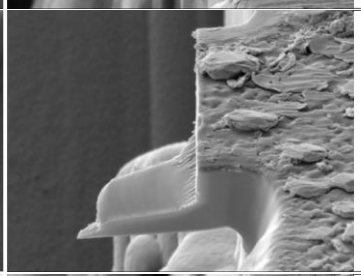
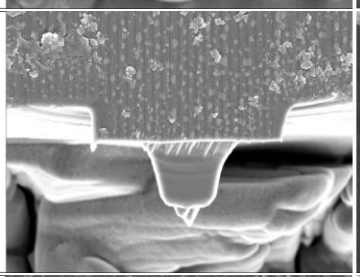
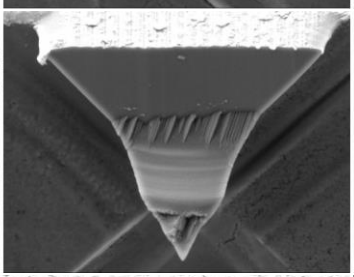
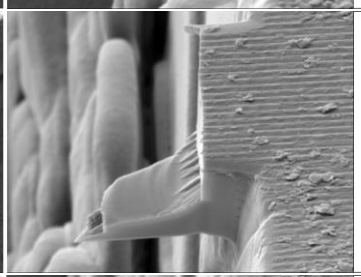
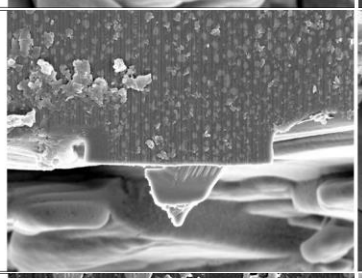
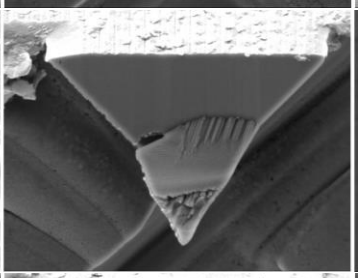
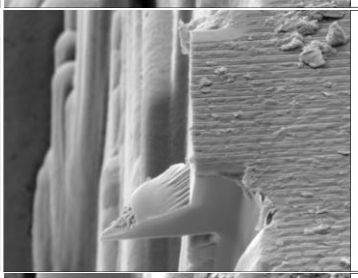
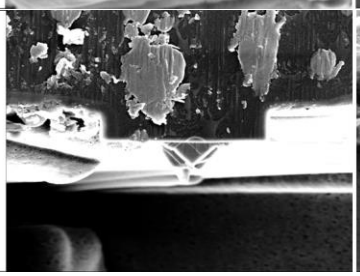
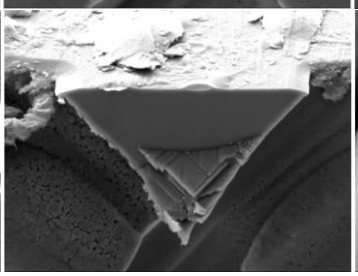
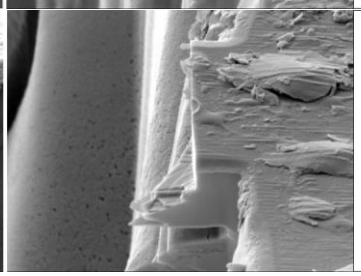


Figure 4.7. Crystal orientations of 0° cantilevers. (a) Cantilevers No.1 and No.6. (b) Cantilevers No.2-5.

SEM images of the fracture surfaces and the corresponding grain boundary strengths (evaluated using Eq. 4.1) are summarised in Table 4.3. The fractures all initiated at the grain boundary, with the upper part of the fracture surface being smooth and flat. The crack path deviated from the straight-through direction in the lower part of the fracture surfaces and formed 'cantilever curl'[287]. The average values of the grain boundary strength and standard error are 5.1 ± 0.3 GPa, and the corresponding tensile and shear stresses at failure (evaluated using Eq. 4.2 and 4.3) were therefore $\sigma_{I.0^\circ} = \sigma_{f.0^\circ} = 5.1 \pm 0.3$ GPa, $\sigma_{II.0^\circ} = 0$ GPa, respectively.

Table 4.3. Fracture surfaces of the cantilevers tested with the 0° grain boundary and the corresponding fracture strengths

No.	Top view 1 µm	Front view* 1 µm	Side view* 1 µm	σ [GPa]
1				5.3
2				4.3
3				5.4
4				5.6
5				4.4
6				5.6

* The angle between the specimen top surface and the electron beam was 30°.

- 15° grain boundary

Six cantilevers were tested on the 15° grain boundary specimen. Cantilever No.1 broke during the AFM scanning in the nanoindenter, thus not providing any useful data. Cantilevers No.4 and 6 exhibited cavities at the top of their fracture surfaces. The results from these specimens are consequently discarded. The dimensions of each cantilever, alongside the measured Young's moduli and strengths, are listed in Table 4.4.

Table 4.4 Dimensions (S, L_f, W, H), fracture load (F_f), failure displacement (D), elastic modulus (E) and grain boundary strength (σ_f) of cantilevers with 15° grain boundary

#	S [µm]	L_f [µm]	W [µm]	H [µm]	F_f [µN]	D [nm]	E [GPa]	σ_f [GPa]
2	19.7	16.1	3.5	2.0	245.3	1809.4	290.9	3.3
3	19.8	16.3	3.5	2.1	356.3	2384.3	269.6	4.4
4	19.8	16.1	3.2	2.0	166.2	1394.2	285.3	~~2.3~~
5	19.8	16.7	3.3	1.9	248.8	2505.0	291.7	4.1
6	19.8	16.5	3.8	2.3	265.6	1083.5	289.5	~~2.6~~

All cantilevers had the same crystallographic orientation in this case (Figure 4.8).

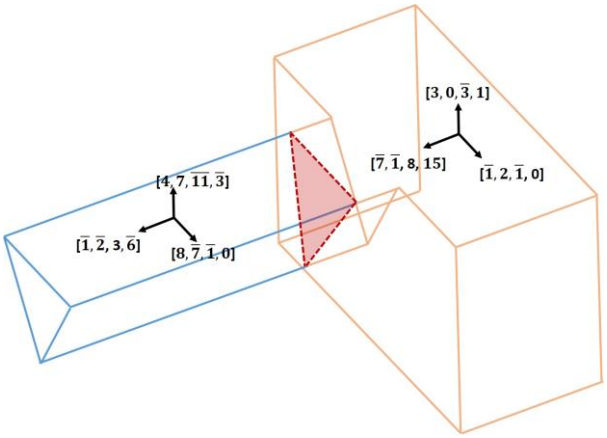
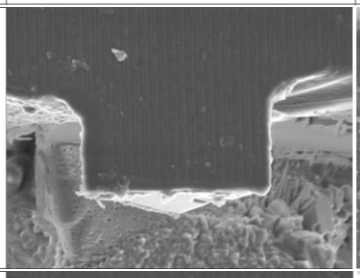
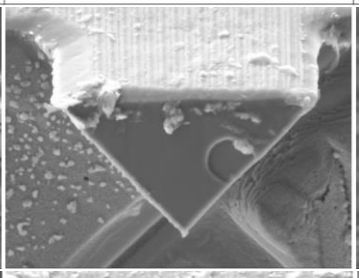
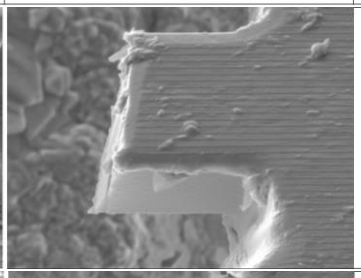
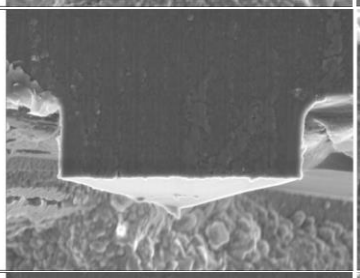
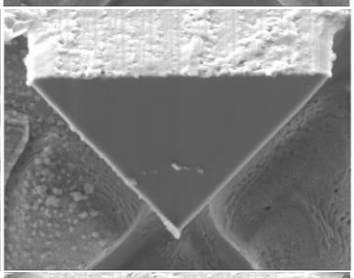
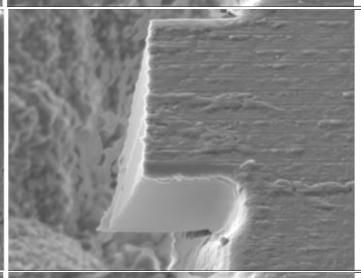
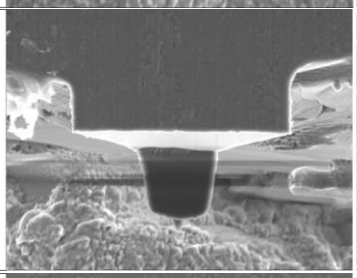
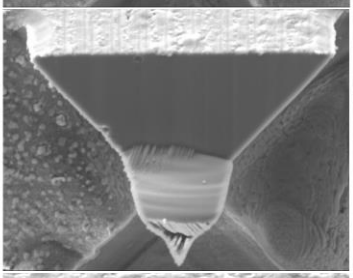
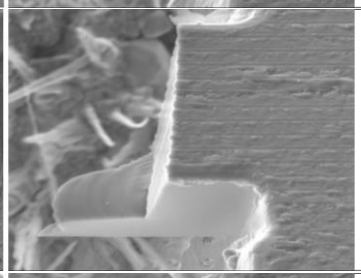
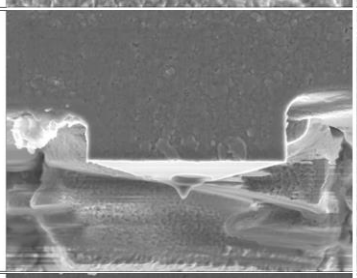
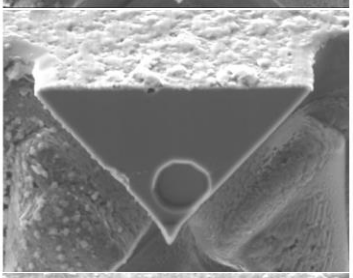
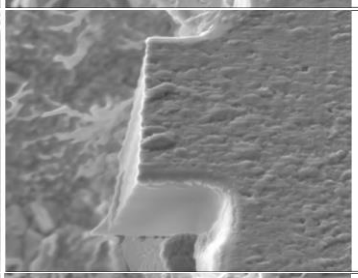
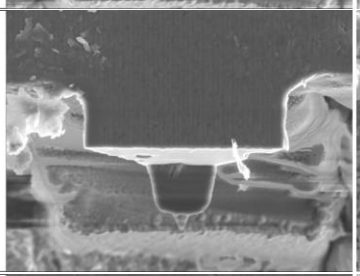
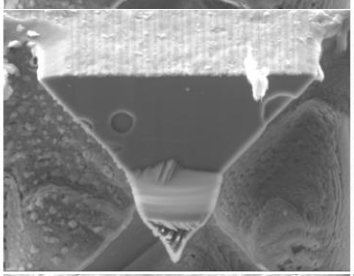
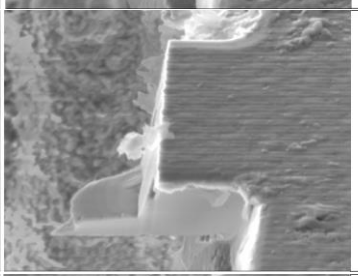
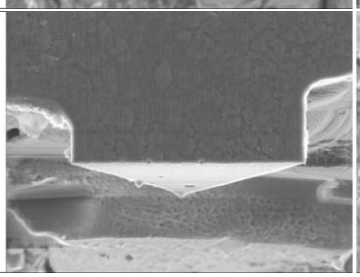
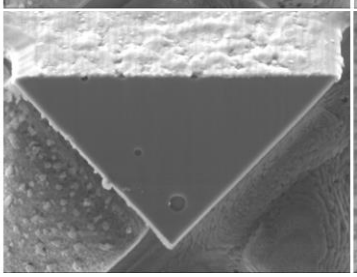
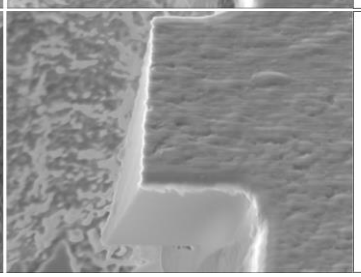


Figure 4.8. Crystal orientations of the 15° cantilevers.

The fractured grain boundaries and their measured strengths are summarised in Table 4.5. The average values of the grain boundary strength and standard error obtained from the usable cantilevers (i.e. No.2, 3 and 5) was 4.0 ± 0.3 GPa. The corresponding tensile and shear stresses at failure are $\sigma_{I.15^\circ} = = 3.7 \pm 0.3$ GPa, $\sigma_{II.15^\circ} = = 1.0 \pm 0.1$ GPa, respectively.

Table 4.5. Fracture surfaces of the cantilevers tested with the 15° grain boundary and the corresponding fracture strengths

No.	Top view 1 µm	Front view* 1 µm	Side view* 1 µm	σ [Gpa]
1				~~N/A~~
2				3.3
3				4.4
4				~~2.3~~
5				4.1
6				~~2.6~~

* The angle between the specimen top surface and the electron beam was 30°

- 45° grain boundary

Ten cantilevers were tested on the 45° grain boundary specimen, with the dimensions, measured Young's modulus and strength listed in Table 4.6. As shown in Table 4.7, all the cantilevers fractured at the grain boundary apart from No.3 and 7. No. 3 broke through an alternative path and exhibited hackle. No. 7 showed partial fracture in the grain. It is not clear from the fracture surface where the fracture initiated but it may have been at the left hand corner. The calculations of strength were therefore not performed for these cantilevers. The cantilevers in which cavities were found at the top of the fracture surfaces, i.e. No.1, 2 and 9, are discarded in the final result.

Table 4.6. Dimensions (S, L_f, W, H), fracture load (F_f), failure displacement (D), elastic modulus (E) and strength (σ_f) of each cantilever with 45° grain boundary

#	S [μm]	L_f [μm]	W [μm]	H [μm]	F_f [μN]	D [nm]	E [GPa]	σ_f [GPa]
1	17.1	10.6	2.7	1.6	274.6	1492.3	299.5	~~5.3~~
2	15.9	13.2	2.3	1.5	126.1	1698	275.8	~~3.7~~
3	17.2	12.1	2.8	3.2	332.1	1456.8	424.5	~~6.2~~
4	15.5	10.5	2.4	1.5	281.0	1676.9	392.4	6.9
5	16.7	13.5	2.9	1.8	217.9	1437.1	288.1	3.7
6	16.6	14	2.9	1.7	238.1	1242.5	440.9	4.5
7	16.4	12.9	2.9	1.7	273.5	1493	326.6	~~4.8~~
8	16.4	9.9	2.6	1.6	297.7	973.4	345.5	5.1
9	16.4	13.2	2.5	1.5	151.5	1459.6	360.8	~~4.1~~
10	16.5	12.9	2.8	1.7	229.0	1651.3	321.0	4.7

All cantilevers had the same crystallographic orientation in this case (Figure 4.9).

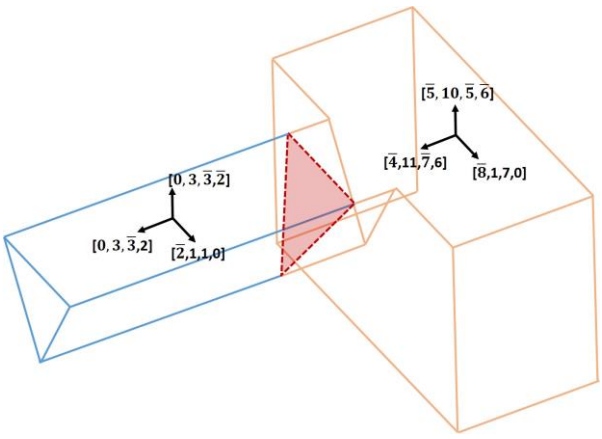
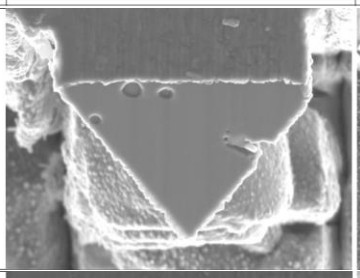
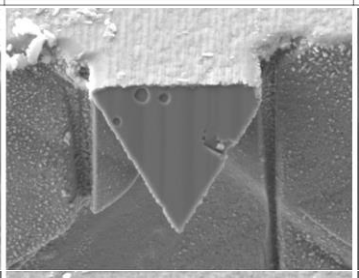
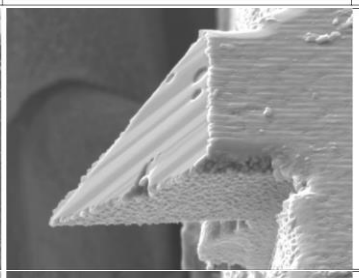
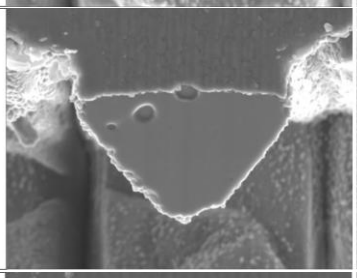
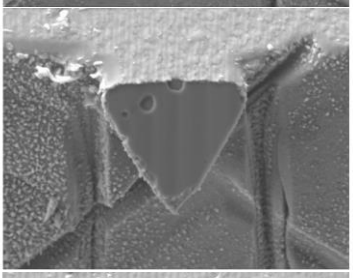
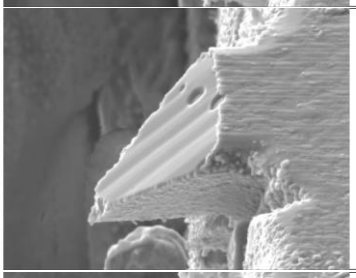
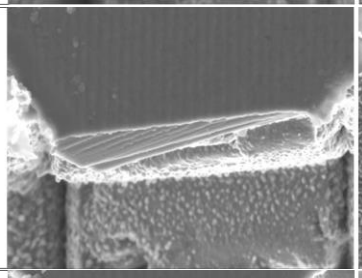
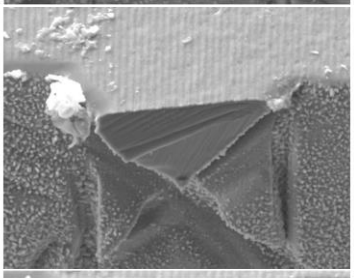
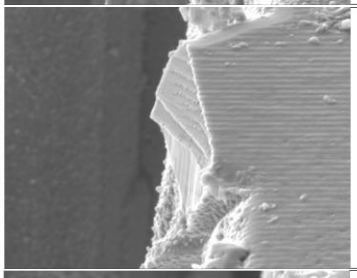
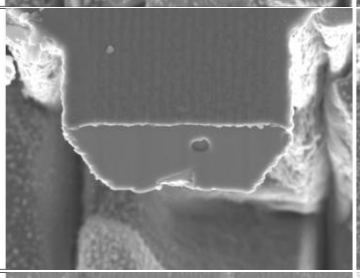
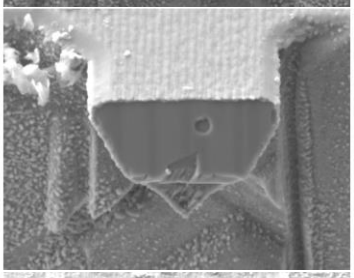
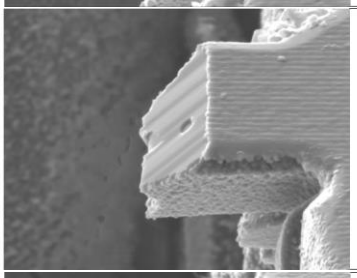
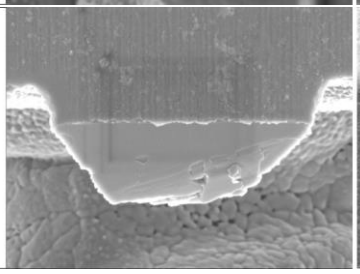
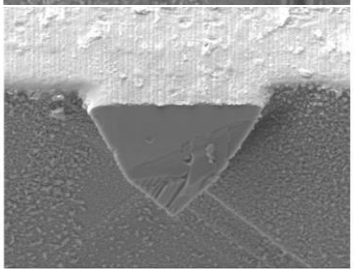
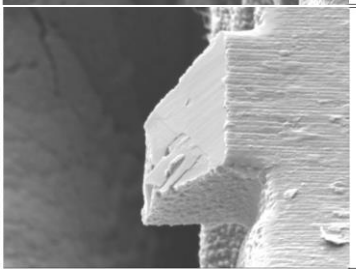
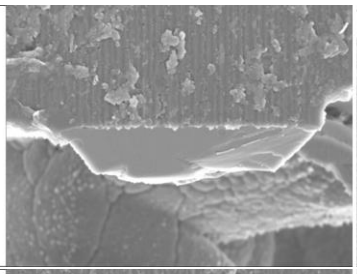
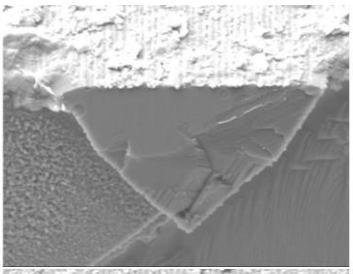
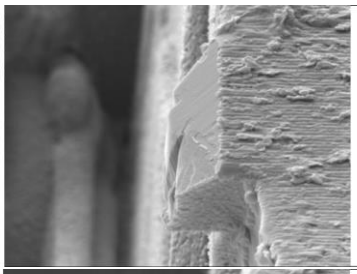
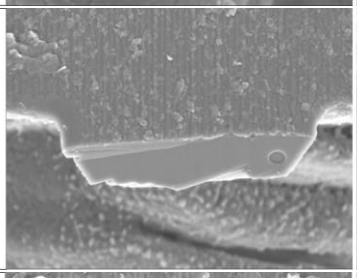
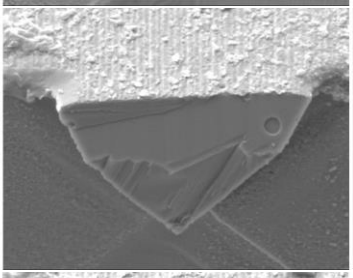
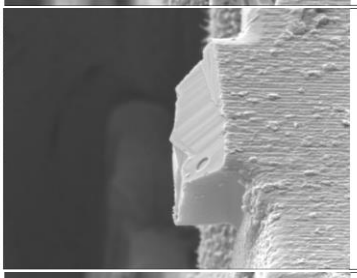
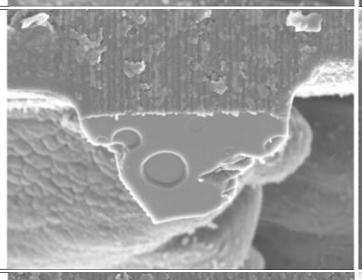
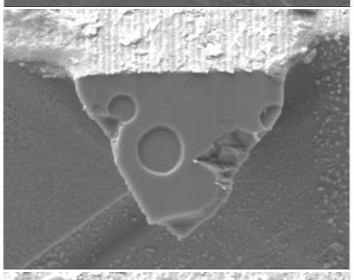
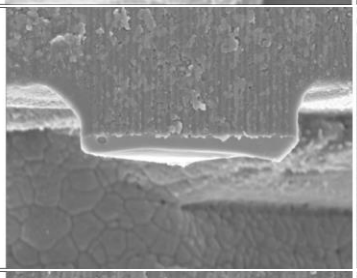
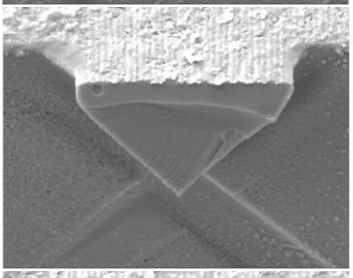
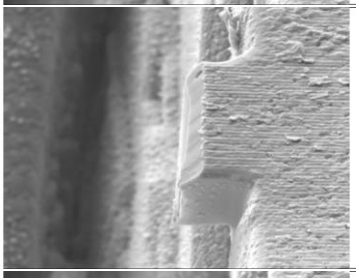
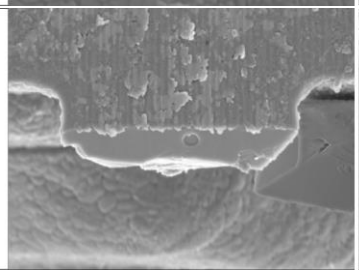
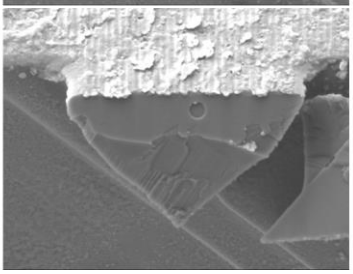
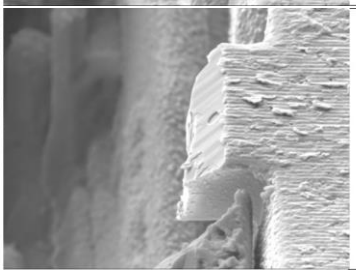


Figure 4.9. Crystal orientations of the 45° cantilevers.

The SEM images of the fracture surfaces and the corresponding grain boundary strengths are summarised in Table 4.7. The usable data (from cantilevers No. 4, 5, 6, 8 and 10) gave an average grain boundary strength and standard error of $\sigma_{f.45^\circ} = 5.0 \pm 0.5$ GPa. The corresponding tensile and shear stresses at failure were $\sigma_{I.45^\circ} == \sigma_{II.45^\circ} == 2.5 \pm 0.3$ GPa.

Table 4.7. Fracture surfaces of the cantilevers tested with the 45° grain boundary and the corresponding fracture strengths. Please note that the table is separated into 2 pages due to the excessive length.

No.	Top view 1 µm	Front view* 1 µm	Side view** 1 µm	σ [Gpa]
1				~~5.3~~
2				~~3.8~~
3				~~6.2~~
4				6.9
5				3.7

6				4.5
7				~~4.8~~
8				5.1
9				~~4.1~~
10				4.7

* The angle between the specimen top surface and the electron beam was 45°

** The angle between the specimen top surface and the electron beam was 30°

4.2.2 Strength of grains

Five cantilevers were tested within grains instead of at grain boundaries, with relevant data listed in Table 4.8.

Table 4.8. Dimensions (S, L_f, W, H), fracture load (F_f), failure displacement (D), elastic modulus (E) and strength (σ_f) of cantilevers fractured in a grain

#	S [µm]	L_f [µm]	W [µm]	H [µm]	F_f [µN]	D [nm]	E [GPa]	σ_f [GPa]
1	15	13.3	3.1	1.8	479.2	1783.7	455.3	8.1
2	15.1	13.4	2.8	1.7	403.9	2004.5	424.0	8.1
3	15.3	13.2	2.6	1.6	301.1	2280.9	369.5	7.6
4	15.1	13.3	2.7	1.6	302.0	1863.8	371.8	6.5
5	14.1	11.3	2.4	1.6	359.8	2047.3	323.8	8.1

All the cantilevers on the single grain had the same crystallographic orientation (Figure 4.10).

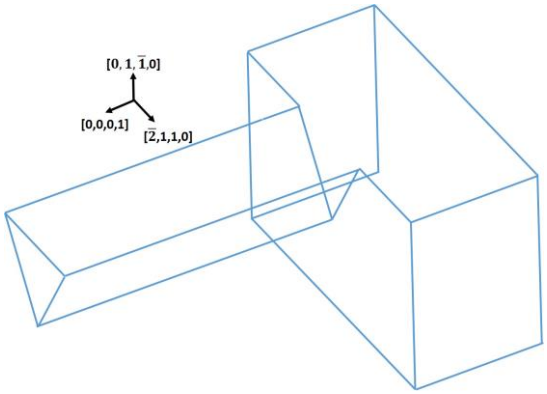
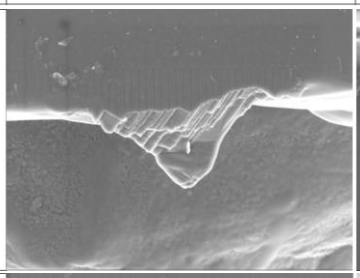
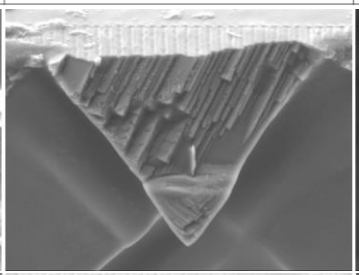
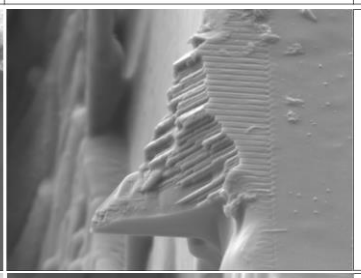
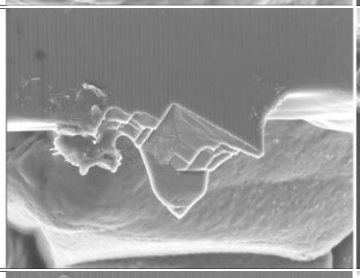
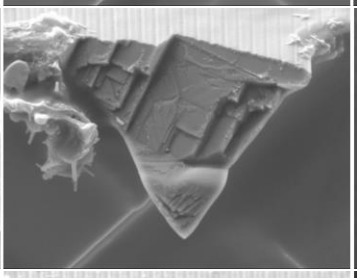
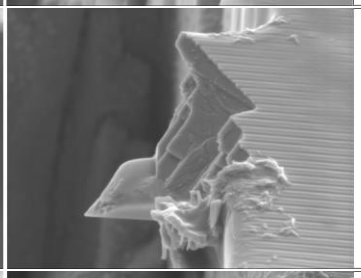
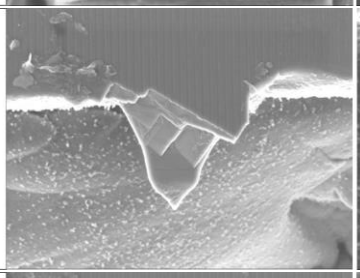
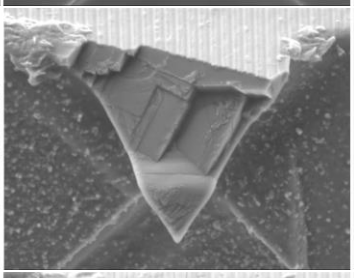
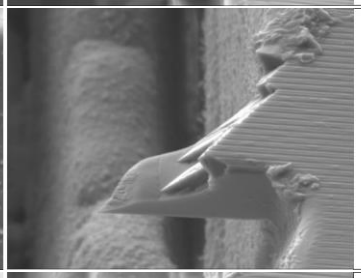
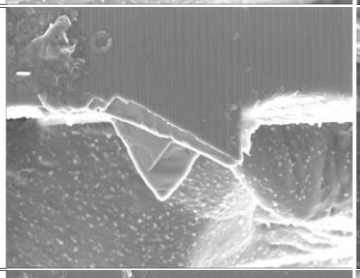
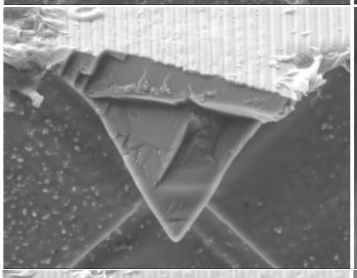
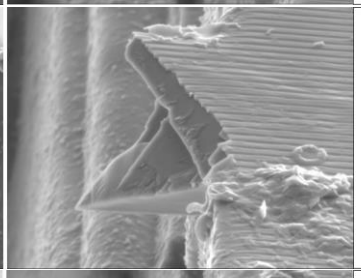
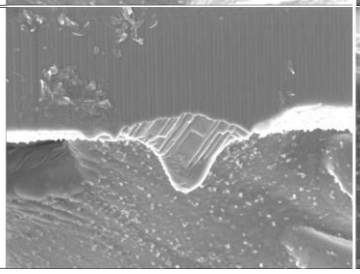
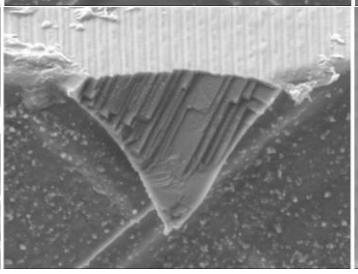
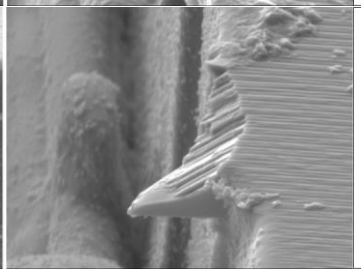


Figure 4.10. Crystal orientations of the cantilevers in the single grain

As shown in Table 4.9, all these cantilevers exhibited heavily facetted fracture surfaces. This is because the cross section of the cantilever was aligned with the basal plan of sapphire (Figure 4.10), which had extremely high toughness[229, 288] and was therefore not favoured for fracture. The orientations of most of the facets appeared consistently on the same preferred fracture plane (likely to be r-plane according to crystallography) that had a lower toughness. These cantilevers also exhibited the 'cantilever curl' at the bottom of the fracture surface. The average values of the grain strength and standard error is 7.7 ± 0.3 GPa.

Table 4.9. Fracture surfaces of the cantilevers tested within grains with the corresponding fracture strengths

No.	Top view 1 µm	Front view* 1 µm	Side view* 1 µm	σ [Gpa]
1				8.1
2				8.1
3				7.6
4				6.5
5				8.1

* The angle between the specimen top surface and the electron beam was 30°.

4.2.3 Interpretation of experimental results by numerical simulation

Numerical models of the bi-crystal cantilever beams have been generated to interpret the experimental data, taking into account the deformation of the support, which has been proven to have a significant effect on the overall deformation of the beam (i.e. around 10%)[12].

Additionally, the analytical formulation presented, based on Euler-Bernoulli theory, considers the beam to be isotropic. Neglecting the actual anisotropic nature of the single crystal and the effect of the crystallographic misorientation across the grain boundary on the stress-state of the interface, would result in inaccurate results.

The 3D linear elastic models were built up by Dr Simone Falco using LS-Dyna (Livermore Software Technology Corporation, USA). Each beam was modelled using the empirically measured dimensions. The crystallographic orientation of each crystal were defined using the EBSD measurement as reported in Figure 4.7, Figure 4.8 and Figure 4.9, coupled with the elastic constants listed in Table 2.2. With hexahedron mesh, gradient mesh size was applied to balance the accuracy of results and computational time, with the mesh size set to be 0.05 near the grain boundaries and doubled to 0.1 away from the grain boundaries. Finally, zero-thickness cohesive elements were added between the two crystals in the FEM model, to evaluate the stress state of the material at the failure state. A side-view image is presented for one cantilever at each inclination angle in Figure 4.11.

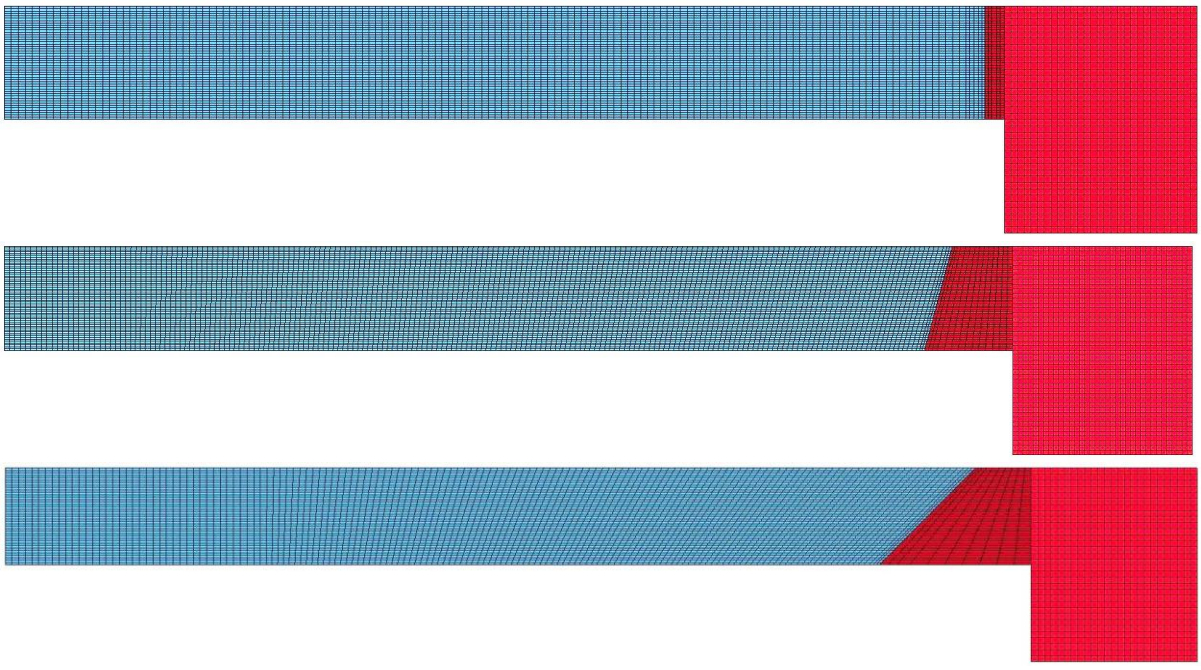


Figure 4.11. Side view of the cantilever numerical models. Top to bottom: 0°, 15° and 45° inclination angle of grain boundaries.

The load increases linearly at quasi-static rate until it reaches the load at failure as indicated in the empirical loading curve (i.e. using fracture load as failure criterion). The stress along the longitudinal

direction of the beam measured in the elements on the top surface across the grain boundary provided the numerical evaluation of the failure strength$\sigma_{f\ (numerical)}$.

The compliance of the cantilever indicated in the numerical model was verified against the empirical value, the difference between which was potentially caused by errors in the measurement of sample dimensional characteristics, especially the height.[12] Therefore, the value of height was adjusted in the model until the numerical compliance matched with the empirical one, providing the accordingly-updated value of stress at failure $\sigma_{f\ (numerical-adjusted)}$. These values did not differ much from $\sigma_{f\ (numerical)}$, thus are not presented here for the reason of simplicity.

For each usable cantilever, $\sigma_{f\ (analytical)}$ and $\sigma_{f\ (numerical)}$ are plotted in Figure 4.12. The numerical evaluations are systematically lower than the corresponding analytical one, which is presumed to be because of the compliance of the bulk support connected to the fixed end of cantilever.[12] The failure stresses at different interface angles were at similar values – spreading around ~5 GPa, while the fracture stress measured at 15° was slightly lower.

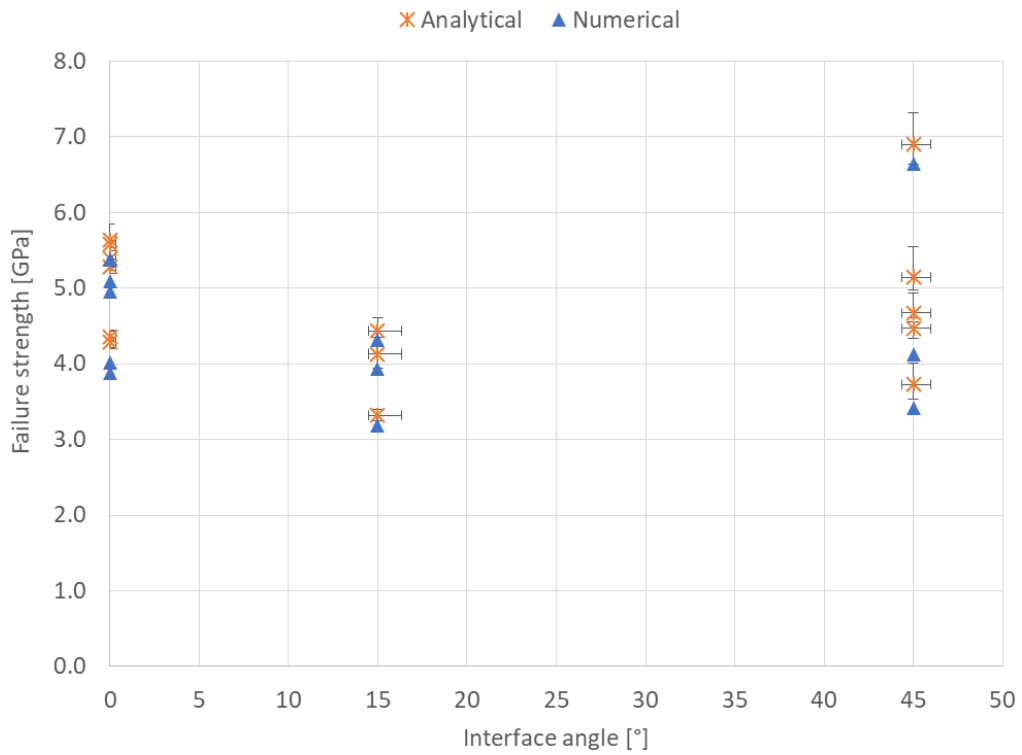


Figure 4.12. Tensile stress at failure along top surface of cantilevers, measured from grain boundaries with different interface angles, from analytical calculation and numerical calibration. For 45°, only 3 cantilevers out of 5 are calibrated numerically due to the shortage of the time.

The analytical values of normal and shear components of the failure stresses were calculated using Eq.4.2 and Eq.4.3, whilst the numerical values were measured directly in the cohesive elements inserted between the crystals in the FEM models. Both analytical and numerical results summarised in Figure 4.13. Normal stresses decreased with the interface angle, while shear stresses did the opposite. At 45°, the normal and shear stresses reached same values, averaging at 2.4 GPa.

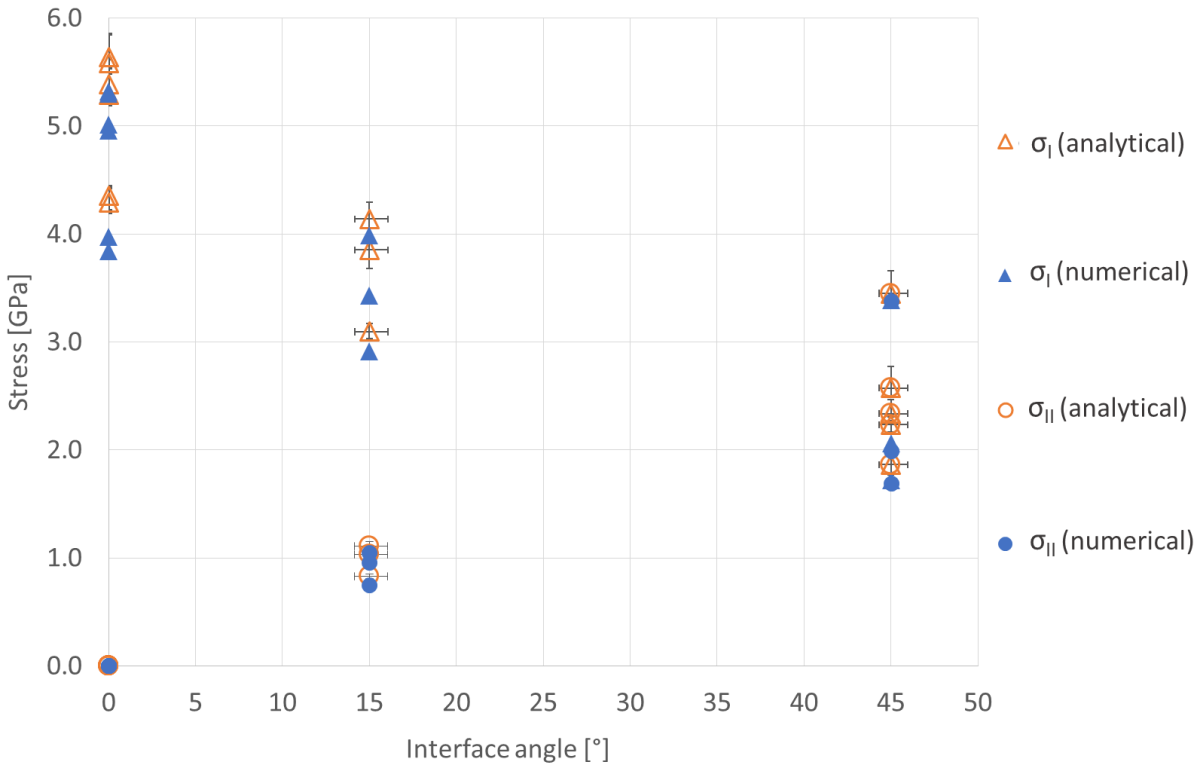


Figure 4.13. Normal and shear components of grain boundary strength measured from microcantilevers containing grain boundaries of three different interface angles: 0°, 15° and 45°.

The numerical values $\sigma_{f\ (numerical)}$ will be used for analysis in the rest of the chapter.

4.3 Discussion

4.3.1 Effect of the cavities and validity of measurement

In the present study, cavities were formed on the grain boundary, possibly because the quick sintering speed employed during the SPS process did not allow enough time for full diffusion bonding. Since the fracture initiated at the intersection of the grain boundary and cantilever top surface, in

correspondence of the maximum bending stress, the cavities found at the intersection are thought to affect the validity of the measured strength and therefore the relevant results were discarded.

Based on Equation.2.5, with K_{IC} assumed to be 2 MPa·m$^{1/2}$, Y=2.24/$\sqrt{\pi}$ for a thumbnail crack and σ_C=4.8 GPa, the critical flaw size is estimated to be $c = \left(\frac{K_{IC}}{Y \cdot \sigma_C}\right)^2 \approx$ 109 nm, which is smaller than the cavities formed on the grain boundaries as can be seen from the SEM images. The cavities located away from the intersection are therefore thought to have negligible influence on the initiation of the grain boundary failure so the results presented are considered to be valid.

The intergranular strength of diffusion-bonded sapphire has been measured by Norton et al.[161, 187], with the grain boundary perpendicular to the longitudinal axis of the microcantilevers and therefore assumed to fail under a purely tensile stress state. The results show that the un-notched bi-crystal microcantilevers have a mean fracture strength of 5.1 ± 0.1 GPa, which is very close to that measured in the present research (4.8 ± 0.3 GPa) with the cantilevers that also have longitudinal axis perpendicular to the grain boundary. Such a close match suggests that the different sintering methods for producing the bi-crystals (SPS was used in the present study while hot press was used by Norton[161]) and the cavities away from the top surface in the present work (Norton's grain boundaries had no cavities) do not have a considerable influence on the measurement of grain boundary strength.

Although the cavities did not contribute directly to the initiation of the cracks, they might still have had a certain influence on the stress distribution on the interfaces. The 15° and 45° grain boundaries exhibited higher densities of cavities than the 0° grain boundary, which had the potential of resulting in underestimated $\sigma_{f.15^\circ}$ and $\sigma_{f.45^\circ}$ values in the present study.

4.3.2 Roles of shear and tensile stresses on grain boundary failure

Combining Equation 2.7 and 2.8, the failure condition of brittle interface can be written as follows.

$$\left(\frac{\sigma_I}{S}\right)^2 + \beta^2 \cdot \left(\frac{\sigma_{II}}{S}\right)^2 \geq 1 \qquad (4.4)$$

In the case where the contribution of shear and normal components on interface failure is considered to be equal[127] (β^2 is 1), by combining with Equation.2.5, 4.2 and 4.3, Equation.2.4 can be rearranged to the following expression.

$$G_C = \frac{Y^2 \cdot c}{E'} \cdot \sigma_f^2 \cdot (\cos^4\theta + \cos^2\theta \cdot \sin^2\theta) = \frac{Y^2 \cdot c}{E'} \cdot \sigma_f^2 \cdot \cos^2\theta \qquad (4.5)$$

which leads to Equation 4.6

$$\beta^2 = 1: \qquad \sigma_f = \sqrt{\frac{G_C \cdot E'}{Y^2 \cdot c}} \cdot \frac{1}{cos\theta} = \sigma_{f.0^\circ} \cdot \frac{1}{cos\theta} \qquad (4.6)$$

In another well-known assumption, the contribution of shear stress in interface failure is considered to be negligible[183-185] (β^2 is 0), the factor defining the relationship between σ_f and $\sigma_{f.0^\circ}$ thus becomes $\frac{1}{\cos^2\theta}$ as expressed in Equation 4.7.

$$\beta^2 = 0: \qquad \sigma_f = \sqrt{\frac{G_C \cdot E'}{Y^2 \cdot c}} \cdot \frac{1}{\cos^2\theta} = \sigma_{f.0^\circ} \cdot \frac{1}{\cos^2\theta} \qquad (4.7)$$

To test the possibility that the shear component contributes more than the normal component in the failure of interface, β^2 is set (arbitrarily) to be 2, which leads to Equation 4.8.

$$\beta^2 = 2: \qquad \sigma_f = \sqrt{\frac{G_C \cdot E'}{Y^2 \cdot c}} \cdot \frac{1}{cos\theta \cdot \sqrt{1+\sin^2\theta}} = \sigma_{f.0^\circ} \cdot \frac{1}{cos\theta \cdot \sqrt{1+\sin^2\theta}} \qquad (4.8)$$

In order to find out which 'theory' explains better the empirical results, Figure 4.14 plots σ_f as a function of $\frac{1}{\cos^2\theta}$, $\frac{1}{cos\theta}$, and $\frac{1}{cos\theta \cdot \sqrt{1+\sin^2\theta}}$, corresponding to β^2=0, 1 and 2, respectively. The straight lines representing β^2=1 and β^2=2 exhibit a better fitting than β^2=0, suggesting that the effect of normal stress may be similar to or even subordinate than that of the shear stress. However, the small amount of sample tested for each inclination angle, and the consequent large scatter in the measured

data, may not be statistically sufficient to determine which theory tested can be firmly valid against the others.

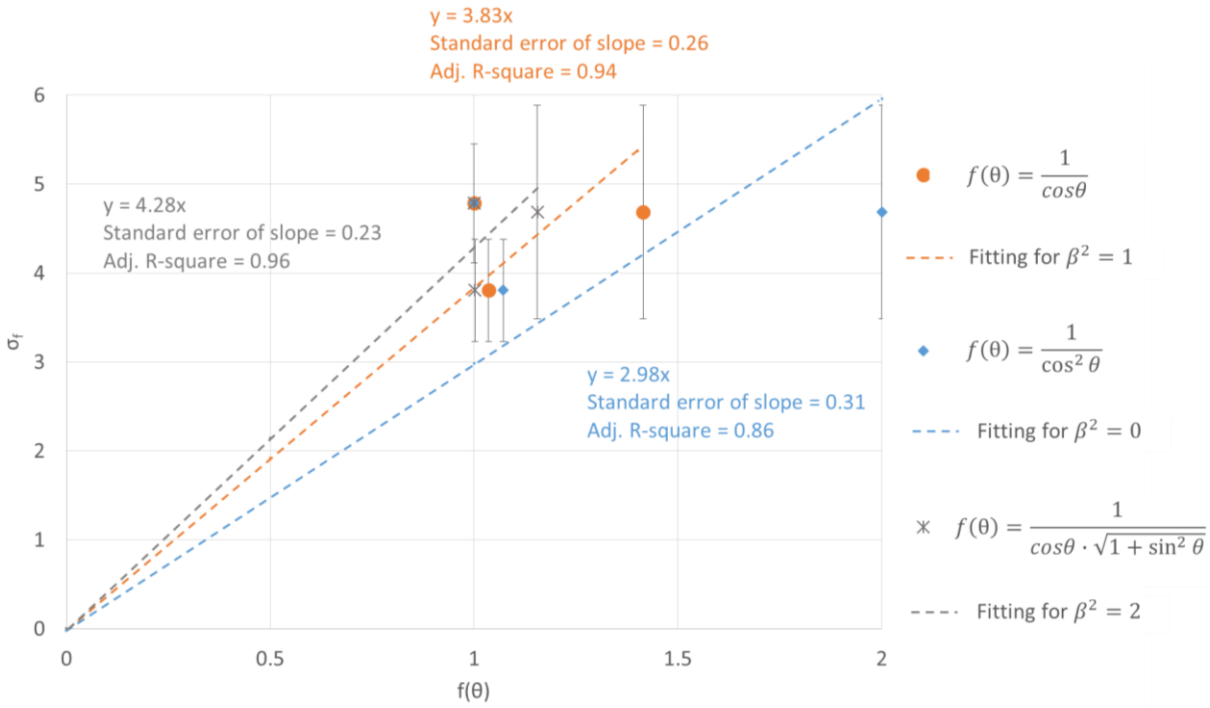


Figure 4.14. σ_f as function of $\frac{1}{cos^2\theta}$, $\frac{1}{cos\theta}$, and $\frac{1}{cos\theta\cdot\sqrt{1+sin^2\theta}}$ for testing the theories which consider β^2 to be 0, 1 and 2 respectively. Each set of data points is fitted with linear function (dashed lines) going through the interception at (0, 0).

In Figure 4.15, the normal and shear components of empirical failure stresses are compared with their theoretical expressions $\sigma_I = \sigma_f \cdot \cos^2\theta = \sigma_{f.0^\circ} \cdot \cos\theta$ (Eq. 4.2) and $\sigma_{II} = \sigma_f \cdot sin\theta \cdot cos\theta = \sigma_{f.0^\circ} \cdot sin\theta$ (Eq. 4.3) with $\sigma_{f_0^\circ}$ set to be 3.8 GPa (i.e. the best fit value indicated in Figure 4.14 with β^2=1). The close match suggests β^2=1 to be reasonable and therefore the contribution of shear stress in failure is not only non-negligible, but in fact seems to be comparable to the contribution of normal stress in tension.

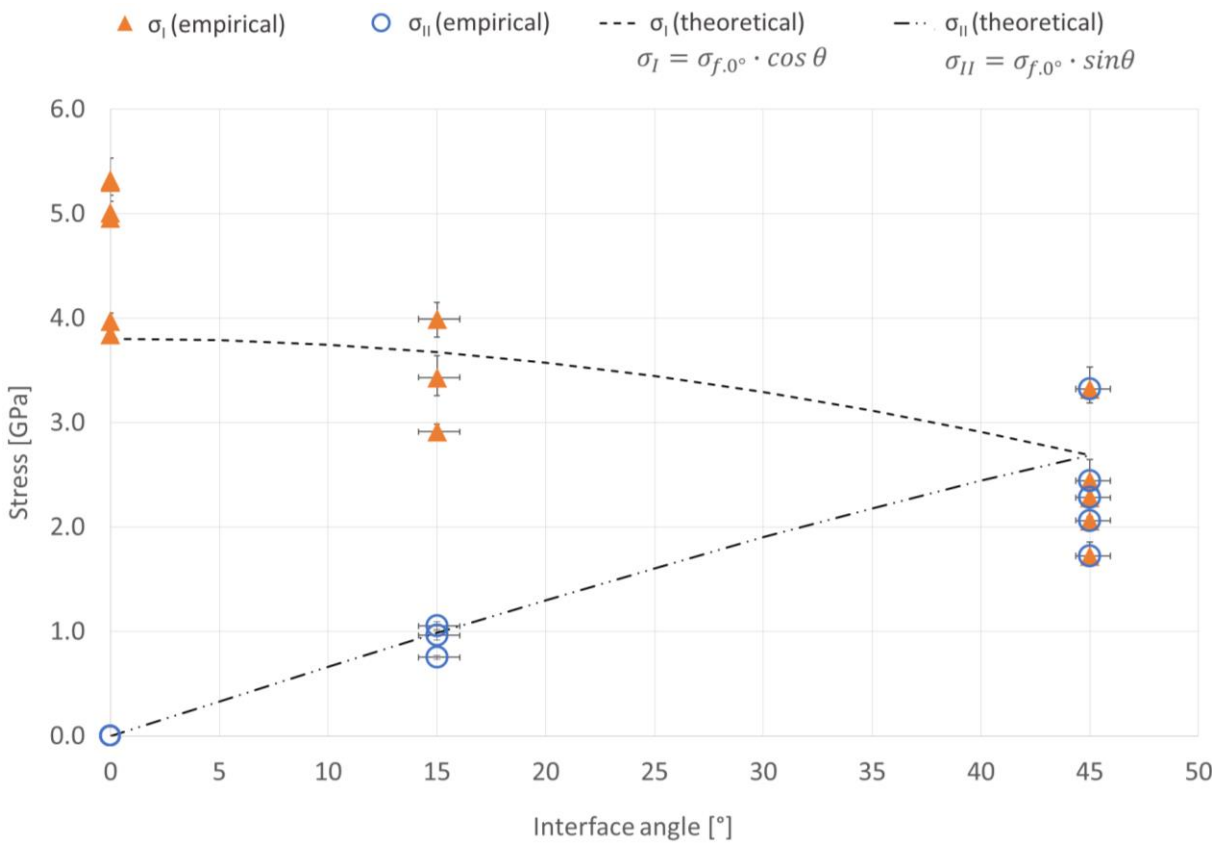


Figure 4.15. Normal and shear components at failure

The limited statistical fit of the data with any known theory may be possibly due to different sizes of crack formed on grain boundaries of different angles during mechanical polishing. The fact that the critical flaw of tens of nanometres cannot be seen on the fracture surface suggests that the failure initiated from a crack on the grain boundary rather than a pore. As the crack was possibly produced by mechanical polishing during sample preparation, and samples with different inclination angles were polished separately, cracks of different sizes might have been produced, introducing a systematic bias in the results.

The potential effect from the crystal orientation is overthrown based on the fact that the two groups of opposite bi-crystal crystal orientations in the 0° data set did not provide systematically different measures of the strength. Additionally, the full anisotropic elastic behaviour of the crystals was reproduced in the FEM models, and did not show significant influence on the numerical results.

Finally, the similarity of the results from the adjustment of height in models for $\sigma_{f\ (numerical-adjusted)}$ also suggests that inaccuracy in dimensions is not the source of lack of fit of the data to any known theory.

4.3.3 Effect of shear stress under compression

The magnitude of the compressive stress at the bottom of a triangular cross section cantilever is twice as large as the tensile stress on the top surface. For example, if the overall tensile stress at failure at the top surface of the cantilever is, say 4.8 GPa, then the shear stress on a 45° boundary at the bottom surface is 2 x 0.5 x 4.8 = 4.8 GPa while the normal stress on this 45° boundary at the top surface is only 0.5 x 4.8 = 2.4 GPa. However, despite the relatively large amount of tested polycrystalline microcantilevers[161, 187], no grain pull-out or other sign of cracking has ever been observed from the compressed volume of the beam. The cantilevers containing the 45° inclination grain boundary showed no sign of grain boundary sliding at the bottom of the cantilevers, even though brittle failure under compression is favoured at 45° based on the maximum shear stress criterion[127].

This suggests that the failure criterion expressed in Equation 4.4 is only valid when σ_I is tensile (i.e. $\sigma_I > 0$). In the case where σ_I is compressive, it does not apply any more.

This is attributed to the following two reasons. (a) The compressive normal stress does not contribute to initiate the crack as tensile stress does. Simonovski and Cizelj[179] indicate that a compressive deformation does not initiate damage and suggest to use the Macaulay bracket ⟨ ⟩ on the normal term, as shown in Equation 4.9, so that when δ_n is tensile, $\langle\delta_n\rangle = \delta_n$; when δ_n is compressive, $\langle\delta_n\rangle = 0$.

$$\delta_m = \sqrt{\langle\delta_n\rangle^2 + \delta_s^2 + \delta_t^2} \tag{4.9}$$

where indices *n*, *s* and *t* denote the normal and two orthogonal shear directions.

(b) The confined compressive loading enhances the shear resistance of the interface by increasing the friction between particles,[186, 289] therefore preventing the grain boundary from sliding as an *interlocking* effect.

As a combination of the two factors above, the failure criteria can be rewritten as below.

$$\left(\frac{\langle\sigma_I\rangle}{S}\right)^2 + \beta^2 \cdot \left(\frac{\sigma_{II}}{\alpha \cdot S}\right)^2 \geq 1 \qquad (4.10)$$

where ⟨⟩ is the Macaulay bracket (=1 if the normal stress is tensile, =0 if compressive), α is the factor of shear resistance (=1 if the normal stress is tensile, >1 if compressive).

4.3.4 Strength of grain boundaries and grains

The strength of grain boundaries is compared to the strength of grains which are also measured in the present study. The former (≈5 GPa) is lower than the latter (≈8 GPa), which explains why polycrystalline alumina favours intergranular fracture against transgranular. It is well known that grains are theoretically stronger than grain boundaries because the former are at thermodynamic equilibrium while the latter have excess free energy[290].

Table 4.10 compares the strength of alumina measured on single crystals and poly-crystals, at different scales (micro-/macro-scale). At the same scale, the strength measured from single crystals is higher than that from polycrystalline alumina, because the latter contains defects as well as grain boundaries that are weaker than grains. The strength measured at the microscale is higher than that measured from macroscopic tests due to the vast difference in the size of the fracture origin – macroscopic samples usually fail from polishing or sintering defects, while the microscopic ones often fail from a chosen microstructural feature, such as a grain boundary or an artificial flaw[161]. Moreover, the 'size effect'[291], which is described conventionally through Weibull statistics, also contributes to the discrepancies in strength measured at microscopic and macroscopic scales.

Table 4.10. Strength of alumina measured at macroscopic test (macroscopic 4-point bending flexural strength) and microscopic test (microcantilever bending test), on single crystals and poly crystals. All measurements are at ambient temperature.

Source	Method & scale	Crystallography	Strength [GPa]
Schmid and Harris[292]	Macroscopic 4-point bending	single crystal	0.9 ± 0.1
Norton[161]	Macroscopic 4-point bending	polycrystalline	0.3 ± 0.0
Norton[161]	Microcantilever test	polycrystalline	3.8 ± 0.2
Present study	Microcantilever test	bi-crystal	4.5 ± 0.3
Present study	Microcantilever test	single crystal	7.7 ± 0.3

The current chapter shows that in contrast to the assumptions in many studies, it is important to take the shear component into account when modelling the failure stress of grain boundaries. Fundamentally, to understand this, the toughness needs to be understood, which is dealt with in the next chapter.

Chapter 5. Reliable Measurement of Fracture Toughness at Microstructural Scale - Stable Crack Growth

Toughness measurements of individual microstructural components of armour ceramics, especially grain boundaries, are indispensable to fully understand the mechanical properties and impact behaviour of the bulk materials, as well as to enable the improvement of these properties via mechanistically informed grain boundary engineering. Moreover, accurate measures of fracture toughness are essential to provide correct input for the numerical modelling of the behaviour of polycrystalline ceramics (like the one presented in Fig.5.1), especially in terms of crack initiation and propagation mechanisms.

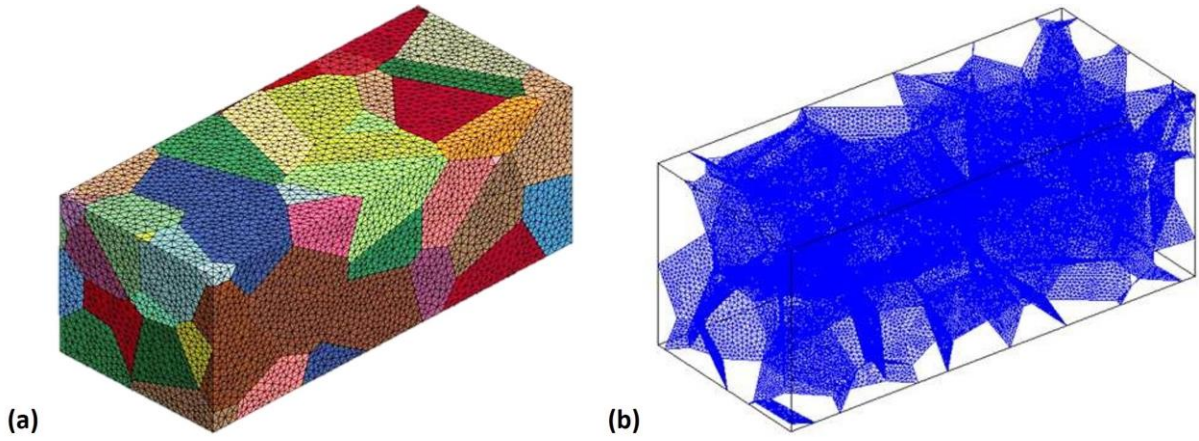


Figure 5.1. (a) Numerical model of polycrystalline ceramics at the micro-scale, showing the grains (presented in different colours) and the numerical meshing of the model. (b) The relative grain boundary elements in the model, shown in blue. The model was developed by Dr. Simone Falco.

Testing microcantilevers machined using FIB is one of the potential methods for making such measurements (Figure 5.2). However, the bluntness of FIBed notches and residual stresses caused by FIB-ion implantation at the notch root are thought to influence the results[1]. Enabling stable crack growth could allow the fracture toughness values to be measured from the material away from the FIB-affected zone, thereby providing reliable measurements of fracture toughness.

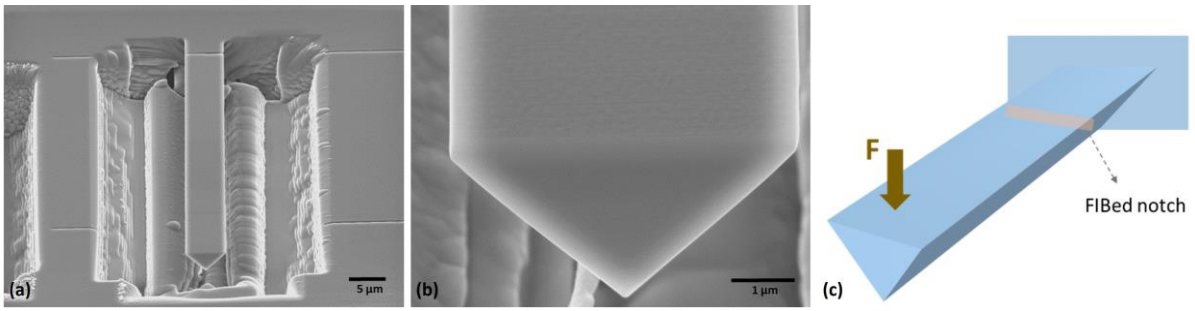


Figure 5.2. (a) Microcantilever with triangular cross section, machined using FIB. (b) The free end of the microcantilever. (c). Schematic of the microcantilever bending test, with a notch FIBed near the fixed end and the load F applied near the free end.

In the present chapter, the fracture toughness of Al_2O_3 and SiC have been measured using chevron-notched microcantilevers which enable stable crack growth. The tests were performed in air and in vacuum to investigate the effect of subcritical stable growth.

5.1 Experimental

5.1.1 Methodology

The cantilevers in the present study were manufactured with pentagonal cross sections, as illustrated alongside the relevant dimensions indicated in Fig.5.3. The thin notch is in the shape of a chevron. Both the bottom point of the pentagonal cross section and the apex of the chevron notch are nominally central. All the tested cantilevers in the present study have $a_1 \leq H$, with the largest width of the ligament equal to W.

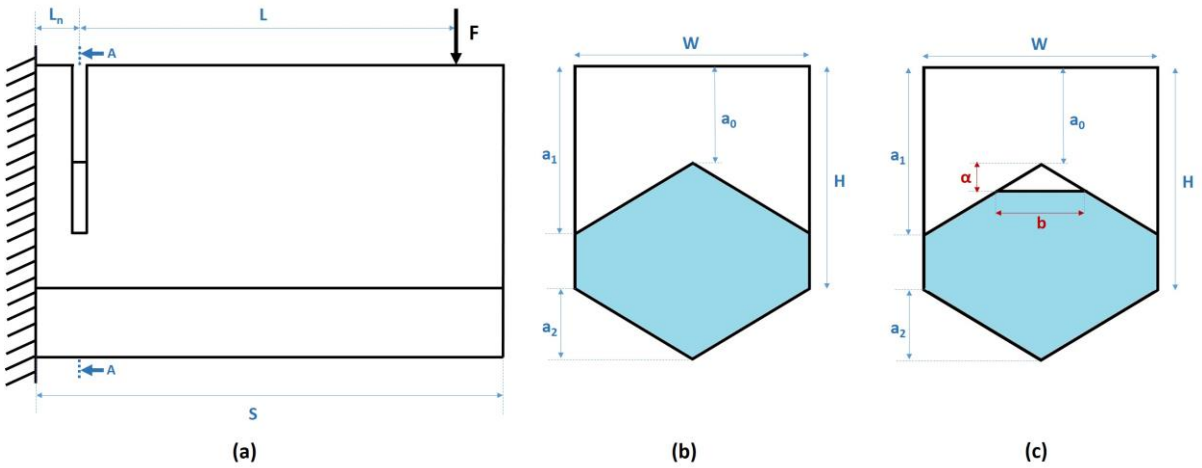


Figure 5.3. Schematic of the chevron-notched cantilevers. (a). The side view of the cantilever. (b). Cross section of the notch as manufactured, prior to cracking. (c). Cross section of the notch while the crack nucleates and propagates. The blue area is the ligament connecting the parts of the system on either side of the notch.

The beam bends under the load *F*, initiating a Mode I crack from the apex of the ligament, which is a distance a_0 from the beam top surface. While the crack propagates, it grows to a length α and width $b = W \cdot \alpha/(a_1 - a_0)$.

Under an applied load *F*, the deflection (δ) of the beam that has a compliance *C*, can be calculated using the following equation.

$$\delta = FC \tag{5.1}$$

where *C* is the compliance.

The stored elastic energy can be expressed as:

$$U_E = \frac{1}{2}\delta F = \frac{1}{2}F^2 C = \frac{1}{2}\frac{\delta^2}{C} \tag{5.2}$$

Assuming that α increases by an increment $d\alpha$ (i.e. crack grows) but δ remains constant (i.e. the loading system does no work), the change in the mechanical energy, U_M, is:

$$dU_M = dU_E = \frac{\partial}{\partial C}\left(\frac{\delta^2}{2C}\right)dC = -\frac{\delta^2}{2C^2}dC = -\frac{1}{2}F^2 dC \tag{5.3}$$

It can be shown that this is also true when δ is not constant for incremental crack extension.

The mechanical energy release rate, *G*, is given by:

$$G = -\frac{dU_M}{dA} \tag{5.4}$$

where *A* is the cracked area and $dA = b \cdot d\alpha$.

Therefore,

$$G = -\frac{dU_M}{dA} = \frac{\frac{F^2 dC}{2}}{bd\alpha} = \frac{F^2}{2b}\frac{dC}{d\alpha} \tag{5.5}$$

This is used to determine the value of *G* for a given notch depth. In order to perform this calculation, dimensionless values of the compliance and the crack length are defined as:

$$\alpha' = \frac{\alpha}{H} \tag{5.6}$$

$$C' = CEH \tag{5.7}$$

E shall be the effective modulus accounting for anisotropy[293], which is taken to be the Young's modulus in the basal plane = $1/s_{11}$ in the present study.

Therefore,

$$G = \frac{F^2}{2b}\frac{1}{EH^2}\frac{dC'}{d\alpha'} = \frac{F^2}{2H^2bE}\frac{dC'}{d\alpha'} \tag{5.8}$$

The stress intensity factor, *K*, can then be calculated:

$$K = \sqrt{GE} = \frac{F}{H\sqrt{b}}\left(\frac{1}{2}\frac{dC'}{d\alpha'}\right)^{\frac{1}{2}} = \frac{F}{H\sqrt{W}}\left(\frac{1}{2}\,\frac{a_1 - a_0}{\alpha}\,\frac{dC'}{d\alpha'}\right)^{\frac{1}{2}} \tag{5.9}$$

The factor $\left(\frac{1}{2}\frac{a_1-a_0}{\alpha}\frac{dC'}{d\alpha'}\right)^{\frac{1}{2}}$ is a dimensionless factor $Y(\alpha')$. The equation can then be rewritten as:

$$K = \frac{F}{H\sqrt{W}}Y(\alpha') \tag{5.10}$$

The compliances of particular cantilevers at different crack lengths were calculated using numerical simulation, which gave a set of data points of C' vs. α' for each beam. The data were fitted by a fifth-order polynomial.

$$C' = B_0 + B_1\alpha' + B_2\alpha'^2 + B_3\alpha'^3 + B_4\alpha'^4 + B_5\alpha'^5 \tag{5.11}$$

C increases with increasing *α*, therefore so does *C'*.

The component of dC'/dα' in Y(α') can be derived.

$$\frac{dC'}{d\alpha'} = B_1 + 2B_2\alpha' + 3B_3\alpha'^2 + 4B_4\alpha'^3 + 5B_5\alpha'^4 \tag{5.12}$$

Y(α') could then be calculated as shown in Equation 5.13.

$$\begin{aligned} Y(\alpha') &= \left(\frac{1}{2}\frac{a_1 - a_0}{\alpha}\frac{dC'}{d\alpha'}\right)^{\frac{1}{2}} \\ &= \left[\frac{1}{2}\frac{a_1 - a_0}{\alpha}(B_1 + 2B_2\alpha' + 3B_3\alpha'^2 + 4B_4\alpha'^3 + 5B_5\alpha'^4)\right]^{\frac{1}{2}} \end{aligned} \tag{5.13}$$

Substituting a crack length α' during the stable crack growth, coupled with the instantaneous applied load, the stress intensity factor can be calculated using Equation 5.10.

The derived Y(α') points were fitted with a fifth-order polynomial.

$$\mathrm{Y}(\alpha') = N_0 + N_1\alpha' + N_2\alpha'^2 + N_3\alpha'^3 + N_4\alpha'^4 + N_5\alpha'^5 \tag{5.14}$$

Y(α') exhibits a minimum value at a specific crack length α_c which also gives a minimum value to K_I for a given *F*. The values of α'_c and $\mathrm{Y}(\alpha'_c)$ could be obtained via the stationary point of the *Y(α')* curve when the following equation is satisfied.

$$\mathrm{Y}'(\alpha_c') = N_1 + 2N_2\alpha'_c + 3N_3\alpha_c'^2 + 4N_4\alpha_c'^3 + 5N_5\alpha_c'^4 = 0 \tag{5.15}$$

Crack growth is therefore stable under load-controlled conditions for $\alpha < \alpha_c$, and α_c is the crack length at which the crack growth transited from stable to unstable. Coupled with the load applied at this moment, F_C, the stress intensity factor K_p (with p denoting 'propagation') at the crack length α_c can be calculated using the equation below.

$$K_{p\,(\alpha_C)} = \frac{F_C}{H\sqrt{W}} Y(\alpha'_c) \tag{5.16}$$

During the stable crack period ($\alpha < \alpha_c$), the instantaneous stress intensity factor to propagate the crack, K_p, could be back calculated via the following process. The compliance *C(α)* at each measure condition is derived by $C(\alpha)=\delta(\alpha)/F(\alpha)$. The corresponding *C'(α)* could be calculated using Equation 5.7. Deploying Equation 5.11, α' could be back calculated, which enables the calculation of *dC'/dα'*, *Y(α')* and therefore $K_p(\alpha')$.

Now knowing the instantaneous crack length α ($=\alpha' \cdot H$), coupled with the corresponding time at measurement, the crack velocity, *v*, can then be calculated from the following equation.

$$v = \frac{d\alpha}{dt} \tag{5.17}$$

5.1.2 Sample preparation

The following two materials were chosen for the investigation: c-plane (0001) sapphire (5 × 5 × 0.5 mm^3 substrate, from AdValue Technology), and single crystal (0001) 6H-SiC (5 × 5 × 0.33 mm^3 substrate, from MTI Corporation). The samples were supplied with the surface chemically polished by silica slurry with a fine finish. The substrate was mounted to a SEM pin stub using silver paint which was followed by carbon coating (Edwards E306, Sweden) to gain conductivity.

The crystal orientations were identified using EBSD (Zeiss Merlin). The a- and m-axes were marked on the sapphire surface using FIB, while $[11\bar{2}0]$ and $[\bar{1}100]$ axes were marked on the SiC surface (Fig.5.4).

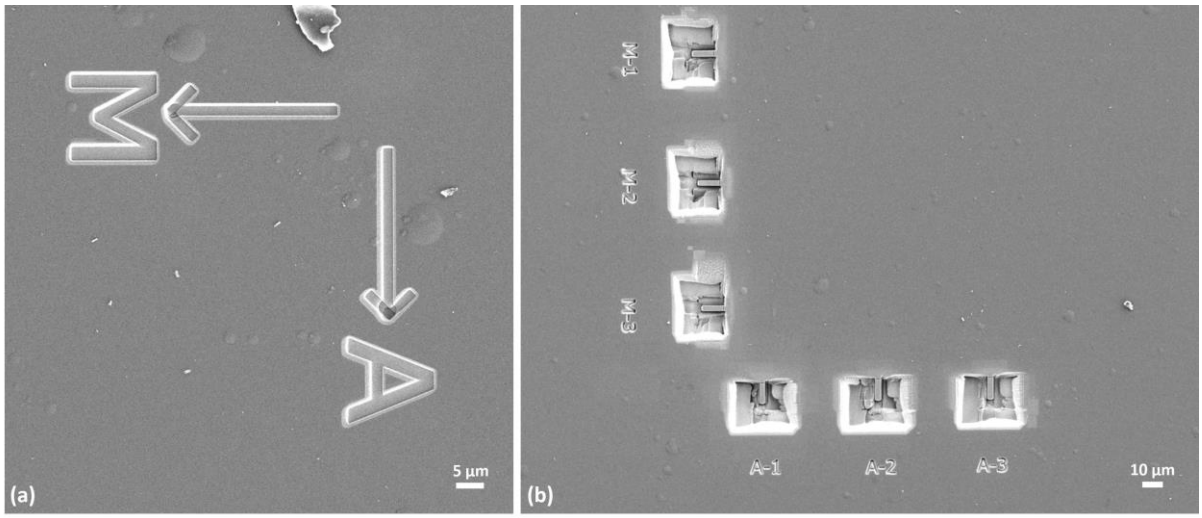


Figure 5.4. (a) Marks on the sapphire sample surface indicating the m- and a- axes. (b) Microcantilevers manufactured along the m- or a- axis.

Microcantilevers were manufactured using FIB (Zeiss Auriga FIB-SEM, Germany) by following the standard microcantilever FIBing procedures[187] (Figure 5.5). For sapphire, the longitudinal directions of the beams were aligned along either the a- or the m- axis so that the notches were in the m- or a-plane respectively. For SiC, the notch was aligned on the $(\bar{1}100)$ plane.

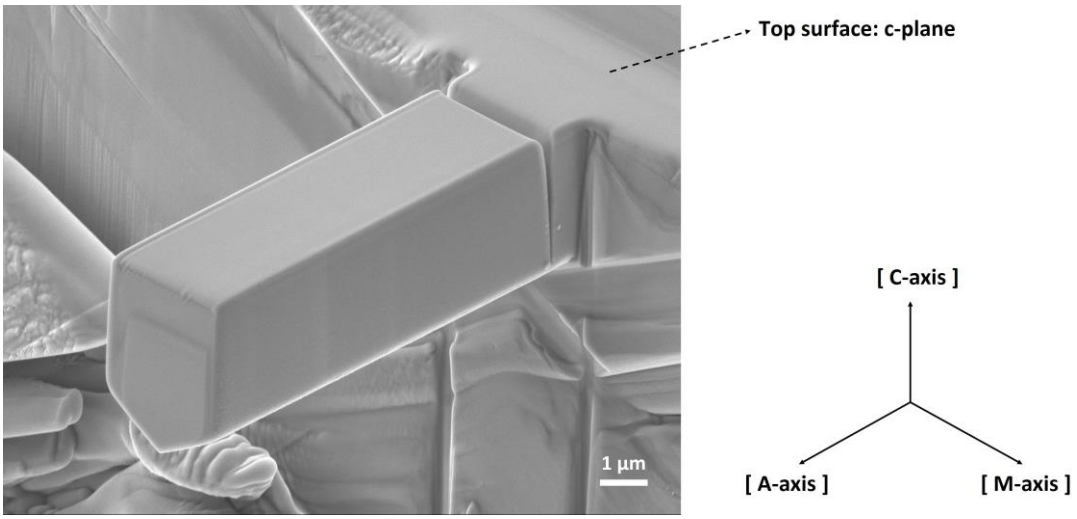


Figure 5.5. A sapphire cantilever aligned longitudinally along the a-axis and notched along the m-axis with a chevron shape notch.

The final and the most crucial step was to mill the chevron notch. A 50 pA beam current was applied, with the notch shaped to have the apex angled at about 90°. In order to minimise the effect of a Gaussian ion beam spot profile[213], which could blunt the notch tip, the apex of the notch was located well below the top surface of the beam, ensuring $a_0/H \geq 0.4$ as suggested by Mueller et al.[175] High-resolution SEM images were taken of the cantilevers for measuring the beam dimensions (Fig.5.6).

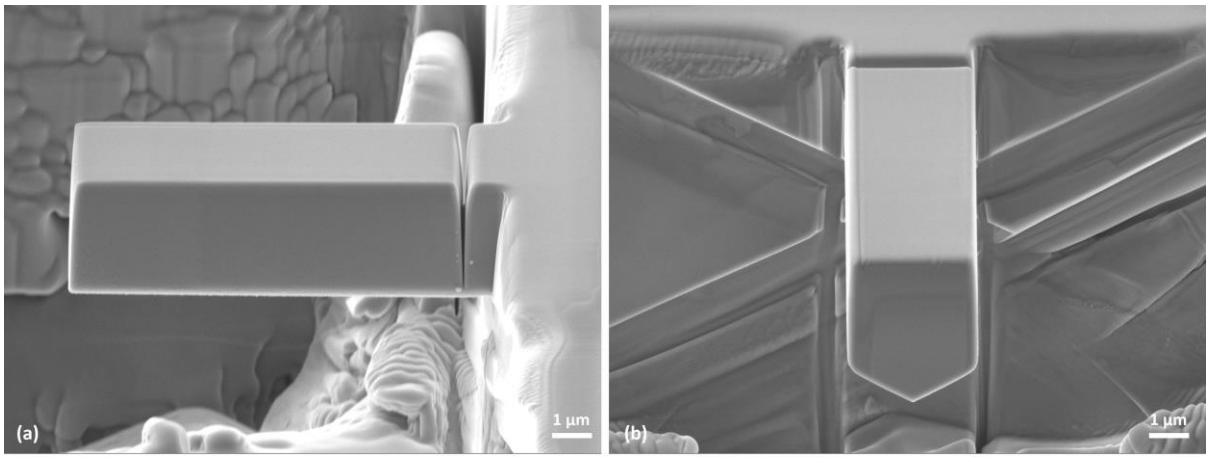


Figure 5.6. SEM images of a chevron notch cantilever. View from its (a) side and (b) front.

The sapphire and SiC specimens were annealed in an argon gas tube furnace (Carbolite STF 16/60/180) at 1100 °C and 1200 °C, respectively, for 1h, with 3 °C/min heating and cooling rate. This step was for removing the residual stresses introduced by FIB in the cantilevers, especially at the notch.

5.1.3 Testing procedure

For the tests in air, the microcantilevers were tested using a G200 nanoindenter (Keysight Technologies, USA) coupled with a diamond Berkovich nanoindenter tip (Synton-MDP, Switzerland). A scanning load of 0.5 µN was applied to scan the top surface of the cantilever and the area around it in order to visualise the shape of the cantilever as well as to locate its position. An indentation point was defined in the scanned map informing the nanoindenter tip of where to load the cantilever (Figure 5.1b). The cantilever was bent under a displacement-controlled testing mode with a displacement rate of 2 nm/s until failure, with the data recording time interval of 0.2 s. The relative humidity of the testing environment in air was 53.6 ± 6.8% (measured at room temperature using OMEGAETTE HH311, OMEGA).

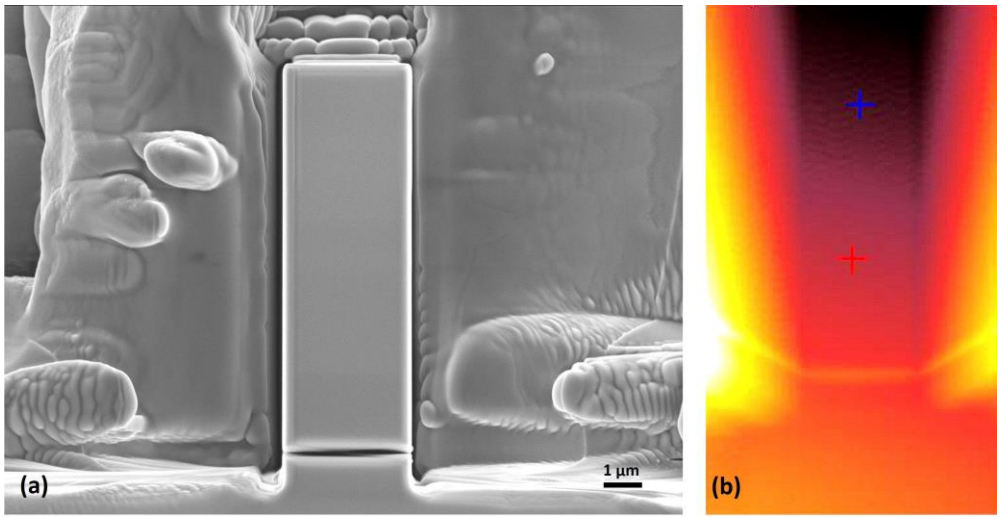


Figure 5.7. (a) SEM image of a chevron-notched cantilever. (b). The AFM map scanned in the nanoindenter of the cantilever, showing the shape of the cantilever as well as the location of the notch by contrast differences. The blue cross indicates the indentation point.

For the tests in vacuum, the cantilevers were tested using an intrinsically displacement-controlled in-situ SEM nanoindenter (Alemnis, Switzerland) placed in a FEI Quanta 650 SEM. The indenter stage was 20° pre-tilted in order to enable the visibility of the sides of cantilevers. A cube corner diamond nanoindenter tip (Synton-MDP, Switzerland) was used to load the cantilevers, as shown in Figure 5.8. The tests were performed under the displacement-controlled mode, enabled by the piezoelectric transducer in the Alemnis nanoindenter. A displacement rate of 2 nm/s was applied to ensure a low

crack propagation speed. A series of SEM images was taken every 2 seconds during the cantilever bending process, with a SEM frame scan time of 1.6 seconds. The machine was operated by Siyang Wang from Dr Finn Giuliani's group at Imperial College London.

The load drift rate was evaluated by $(F_f - F_0)/t_f$, where F_f is the raw load at failure reported by the nanoindenter when the cantilever is separated from the indenter tip (i.e. point f in Figure 5.29), F_0 is the load before loading and is therefore equal to 0, t_f is the total loading time.

For the monotonic loading tests, the displacement drift rate was evaluated by correcting the compliance of the cantilever during elastic bending to the compliance calculated from the corresponding numerical model at 0 crack length. For the cyclic loading tests, the displacement drift rate was evaluated based on the recorded timeline and the displacement drift between the starting point (i.e. $F = 0$) of each two adjacent loading cycles, giving a close value to that evaluated based on the compliance of the cantilever from numerical models and therefore validating the above.

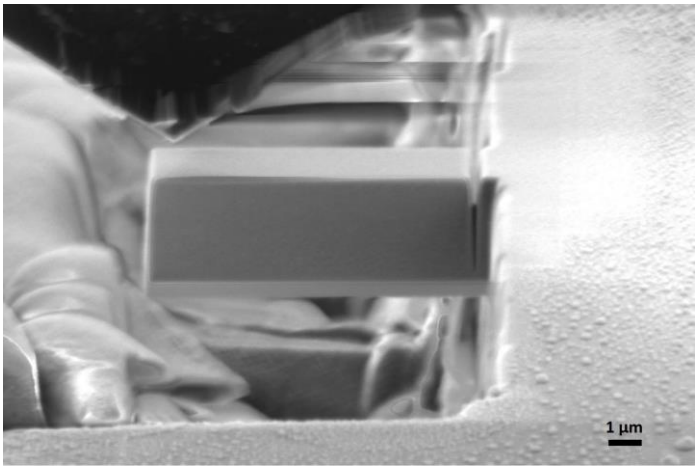


Figure 5.8. SEM image of in-situ microcantilever test in vacuum. The cube corner indenter tip is placed on top and near the free end of the chevron notched microcantilever, prior to the bending test.

5.2 Results

5.2.1 Development and optimisation of numerical model

Knowing the compliance development of each cantilever during the crack propagation is essential in calculating their fracture toughness. However, due to the difficulties in analytical calculation of

compliances of cantilevers with chevron-notched pentagonal cross section, numerical modelling was required to interpret the compliance.

3D linear elastic models were developed by Dr Simone Falco, using the commercial software LS-Dyna (Livermore Software Technology Corporation, USA). The numerical models were built with pentagonal cross section and chevron notch (Figure 5.9), with dimensions defined to that measured empirically from SEM images. The cross section was discretised mostly with quad elements, with the cross-sectional mesh extruded to form 3D mesh consisting predominantly of hexahedral elements with a small percentage (<1%) of pentahedron elements. The material properties were modelled as anisotropic using the values from Table 2.2.

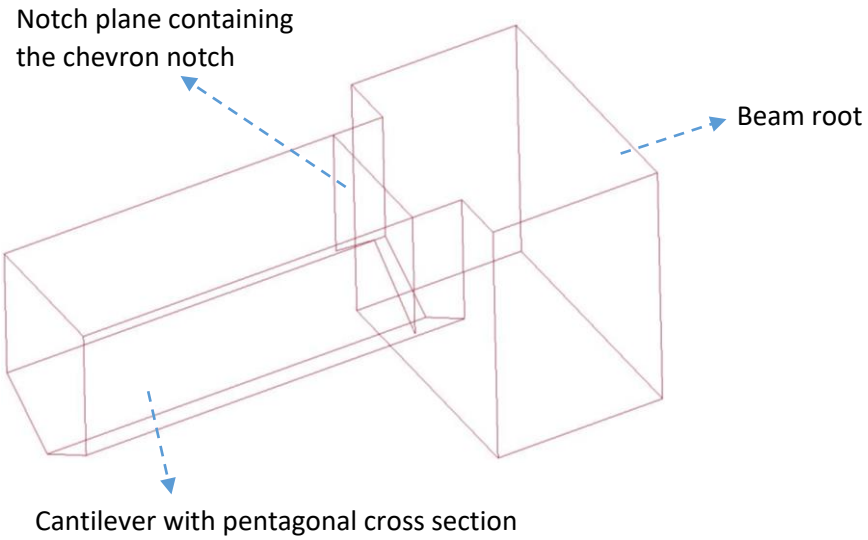


Figure 5.9. The numerical model of the pentagonal cantilevers with chevron notch and built-in beam root.

A model was individually constructed for each cantilever at a specifically-defined crack length using the dimensions from experimental measurements. The 2D notch plane was generated based on the coordinates of 9 points defining the cross sectional dimensions (Fig. 5.10) followed extrusion into a 3D beam to an experimentally-measured length, with the notch plane situated at the distance to the fixed end which was also measured from the experiment. A support was added to the fixed end of the cantilever, which has all its faces constrained with fixed displacement apart from the top surface and the surface to which the cantilever is attached. In order to mimic the real nanoindenter tip and to

avoid local deformation caused by stress concentration in the model, a pressure load was applied on a square area of 0.8 µm side length, centred at the experimentally measured loading point.

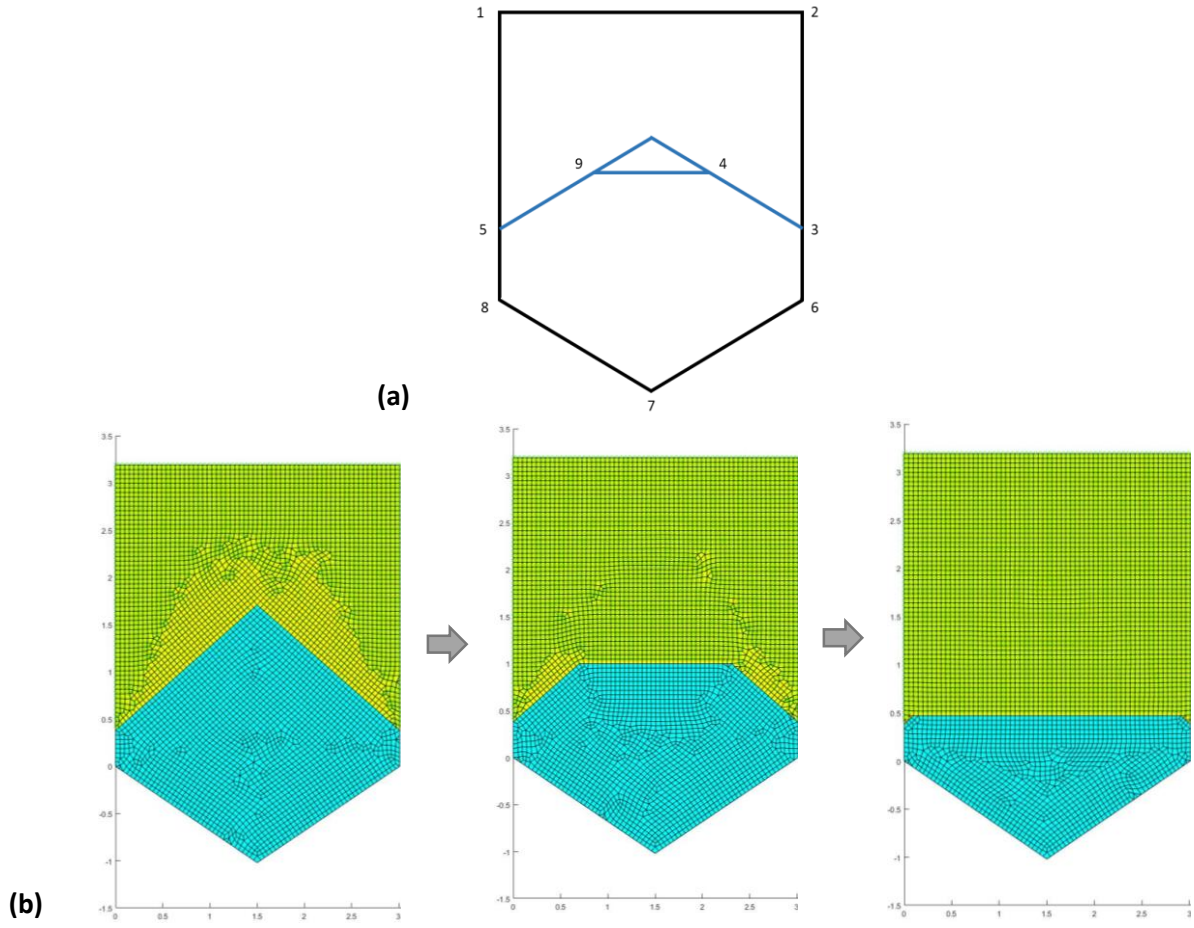


Figure 5.10. Cross section of the notch plane in the numerical model. (a) The schematic showing the 9 points used to define the notch plane. When there is no crack, the point No.4 and No.9 have the same coordinates. During the crack propagation, (b) The illustration of the meshed notch plane for 3 example crack lengths.

In order to ensure the ideal balance between the accuracy of the simulation results and the length of computation time, the FE models were optimised in terms of the size of meshes (graded mesh size with the ≤ 0.05 µm mesh size at the notch and ≤ 0.4 µm away from the notch) and the compliant built-in root (which had width = height = length = 6 µm). The optimisation was based on the results from the following investigation.

- Mesh size sensitivity

The effect of the mesh size on the accuracy of compliance results was first investigated by constructing numerical models of a rectangular beam without the root. The beams had dimensions of width 3 µm,

height 3 µm and effective length 8 µm. The following uniform mesh sizes were tested and compared to analytical analysis: 0.75, 0.6, 0.4, 0.25, 0.2 and 0.1 µm. Example models are shown in Figure 5.11.

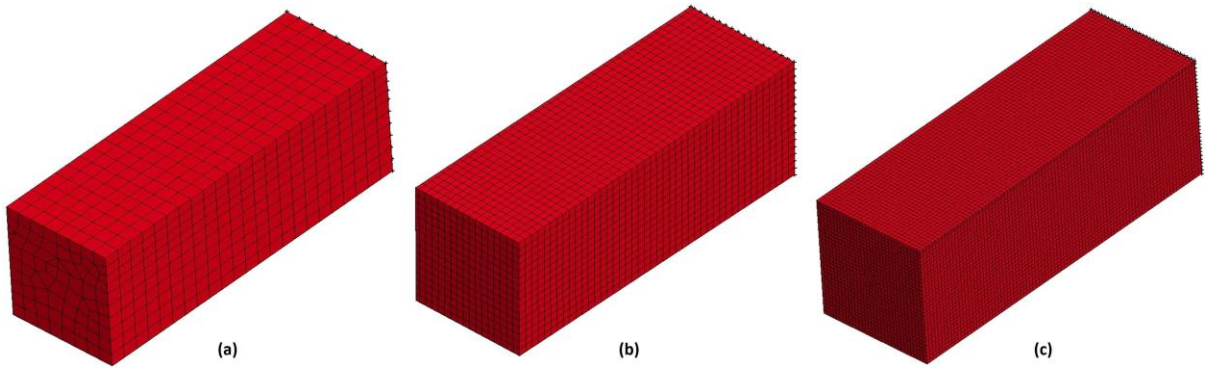


Figure 5.11. Numerical models of rectangular cross-sectional cantilevers with mesh sizes of (a) 0.4, (b) 0.2, and (c) 0.1.

The compliance results from different mesh sizes are shown in Figure 5.12, comparing the results to the analytical values based on Euler-Bernoulli and Timoshenko theories and showing the convergence of the compliance a mesh size of 0.4 µm.

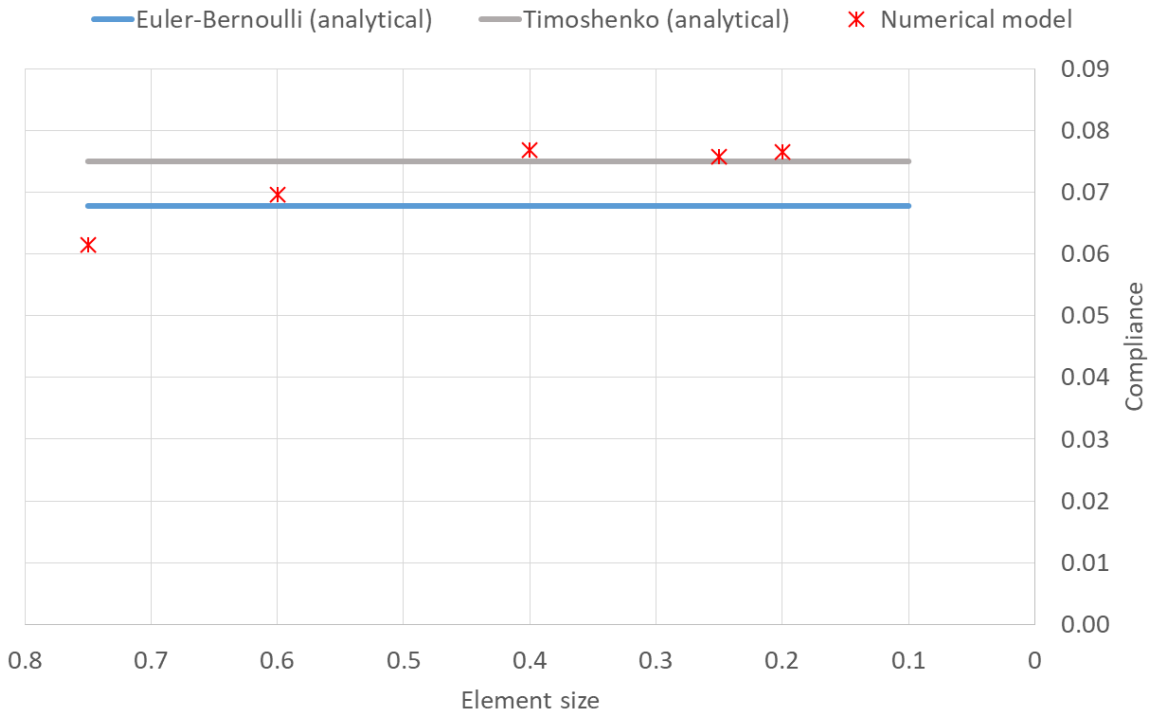


Figure 5.12. Compliance from numerical beam model (W3, H3, L8, no root) uniformly meshed with element sizes of 0.75, 0.6, 0.4, 0.25, 0.2 and 0.1. The results are compared to the analytical values based on Euler-Bernoulli and Timoshenko theories.

- Effect of beam root

It is known that the local deformation of the bulk material connected to the cantilever contributes to the compliance measurement.[156] The effect of the beam root was therefore evaluated using un-notched rectangular-cross sectional cantilevers with typical dimensions of width 3, height 3 and effective length 8. The compliance was numerically calculated using the models with mesh size 0.1, featuring a range of root sizes: no root, $W_r6_H_r4_L_r4$, $W_r6_H_r6_L_r4$, $W_r6_H_r6_L_r6$, $W_r9_H_r6_L_r6$ and $W_r9_H_r9_L_r9$ (W_r, H_r, L_r represent the width, height and length of the root, respectively). Example models are shown in Figure 5.13.

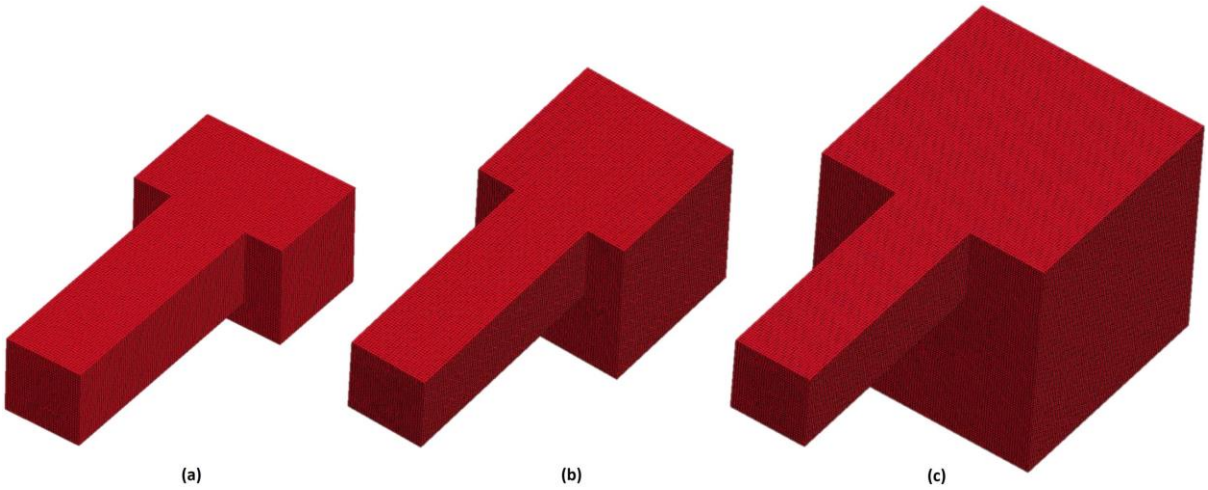


Figure 5.13. Numerical models of rectangular cross-sectional cantilevers with root sizes of (a) $W_r6_H_r4_L_r4$, (b) $W_r6_H_r6_L_r6$, and (c) $W_r9_H_r9_L_r9$.

The compliances simulated from the numerical models were compared with the analytical results based on the Euler-Bernoulli beam and Timoshenko beam theories, where the beam root was not taken into consideration, as shown in Figure 5.14. Compared to the $W_r9_H_r9_L_r9$ model result, the Euler-Bernoulli theory, the Timoshenko theory and the numerical model of the beam without root all underestimated the compliance by significant amounts. The compliance values from the models with roots were convergent from $W_r6_H_r6_L_r4$, with the difference to $W_r9_H_r9_L_r9$ being only 2.0%.

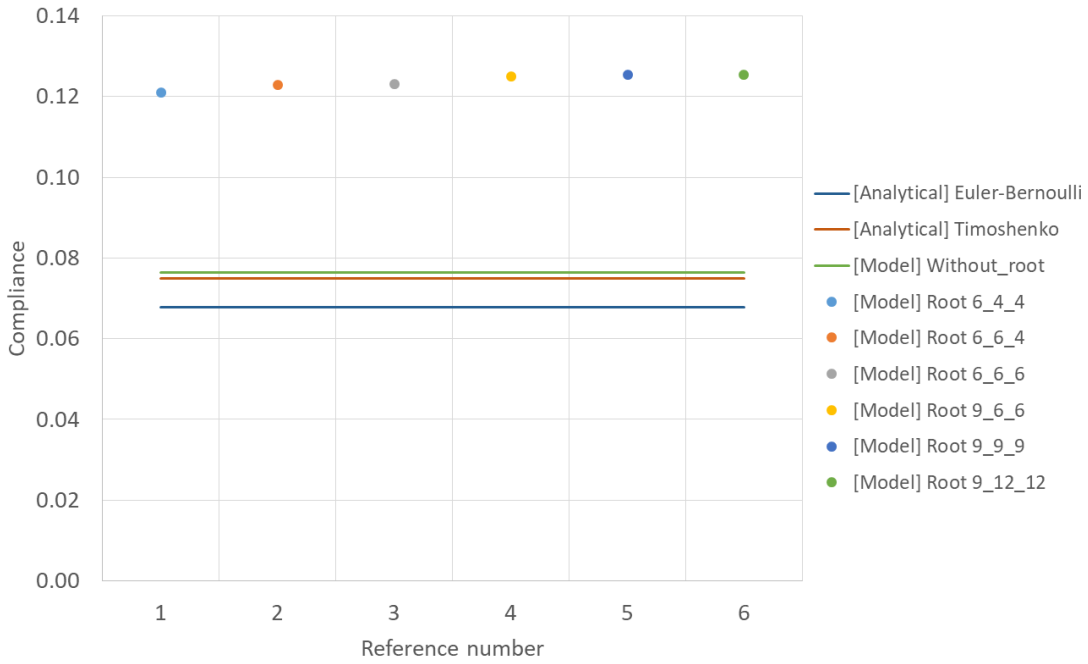


Figure 5.14. The compliances calculated by analytical and numerical solutions, for evaluating the effect of the beam root. The annotation for the beam models is in the form of Root_W_r_H_r_L_r.

- Graded mesh size

In order to optimise the computation time while ensuring the accuracy of the compliance calculation, a graded element size was applied to the models. The mesh size was finest at and near the plane of the notch, and increased gradually towards the free and fixed ends of the beam with a maximum value of 0.4, as shown in Figure 5.15.

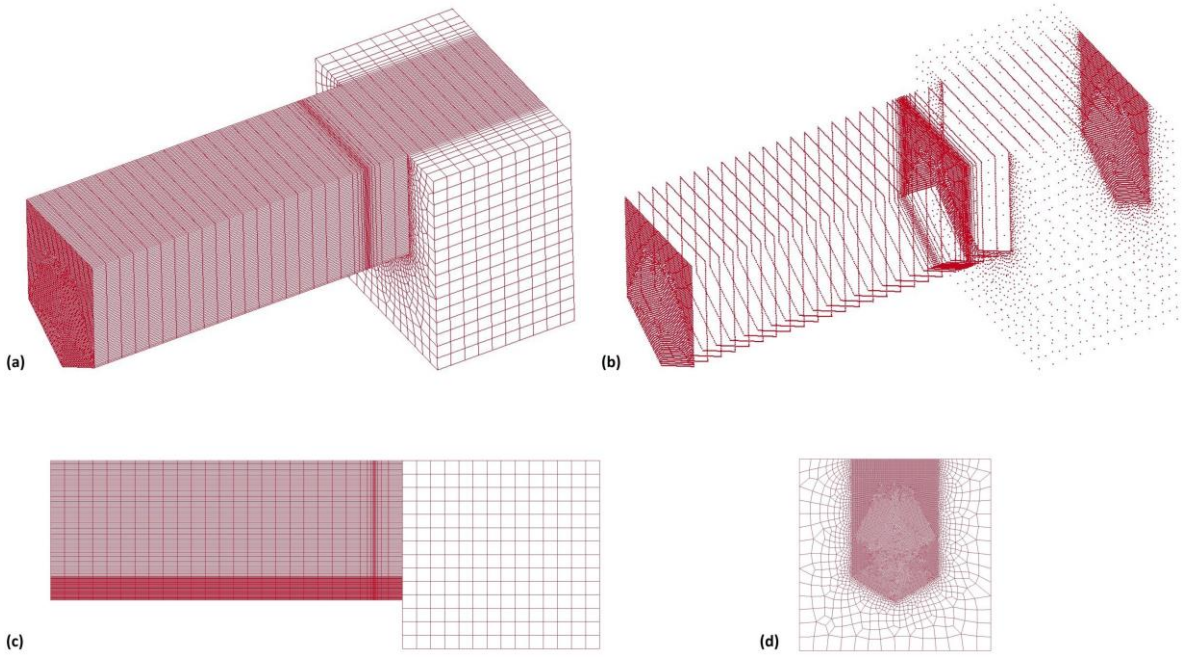


Figure 5.15. The FE model meshed with graded mesh size, under the views of (a) View under the HidEle mode to exhibit the graded mesh size along the beam. (b) View under the WirEle mode to highlight the chevron notch. (c) Side view showing the fine mesh around the notch plane. (d) Front view showing the fine mesh in the cross sectional planes.

The effect of mesh size was further investigated with an advanced model: with the root of the chosen size (W_r6, H_r6, L_r4) and graded mesh size. For the finest meshing part in the graded mesh system, three different sizes were tested: 0.03, 0.04 and 0.05. In Fig. 5.16 which shows the compliance values for a series of crack lengths, no notable difference could be seen among the compliances simulated from the three tested mesh sizes. Therefore, 0.05 was imposed as the maximum element size at the chevron notch in all the FE models used in the present study.

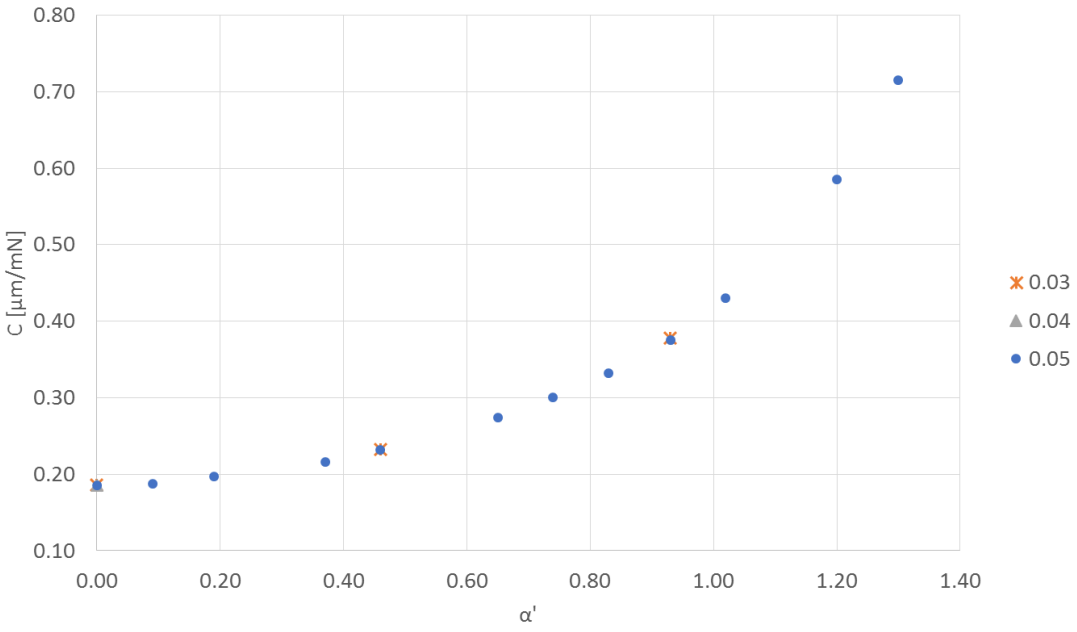


Figure 5.16. Compliance simulation of chevron-notch pentagonal beams with graded mesh size at a sequence of crack lengths, for comparing different fine mesh sizes.

Under the optimised balance between accuracy of simulation results and computation time, in practice, it takes around 50 hours to complete the simulation of each model even having 5 CPU cores work in parallel. Considering that 13 to 15 models need to be run for one cantilever, about 650 to 750 hours processing time is required for obtaining the compliance curve of each cantilever. With the majority of the empirically tested cantilevers analysed with the assistance of numerical simulation, there were 3 cantilevers that could not be simulated due to the shortage of time in the present study.

5.2.2 Fracture toughness of Al_2O_3 measured in air – a-plane

A total of 8 chevron-notched a-axis sapphire cantilevers were tested. 5 of them exhibited stable crack growth and 3 showed fast brittle fracture during the bending test. The results from the ones that fractured without stable crack growth were discarded. SEM images of the five cantilevers that succeeded in stable crack growth are shown in Figure 5.17.

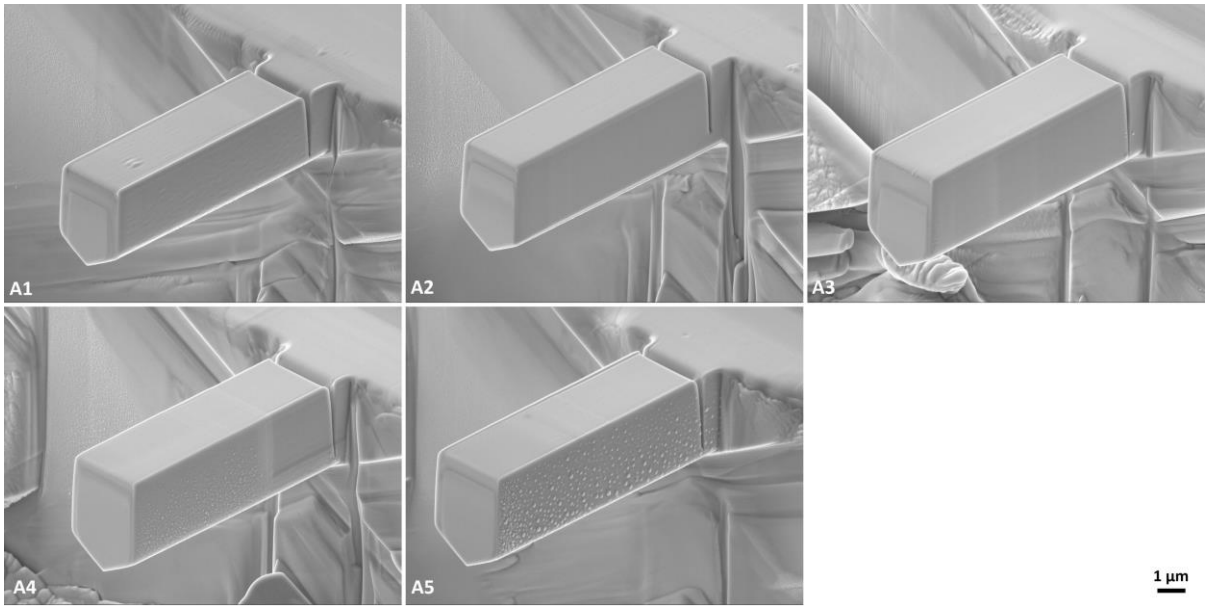


Figure 5.17. SEM images of the a-axis sapphire chevron-notched cantilevers that exhibited stable crack growth during bending test, numbered from A1 to A5.

The dimensions of each cantilever are retrieved from the high-resolution SEM images (Table 5.1).

Table 5.1. Cantilever reference number (#), loading rate ($\dot{y}$), and sample dimensions (W to L_n as defined in Figure 5.3) for a-plane chevron-notched sapphire cantilevers tested in air.

#	$\dot{y}$ [nm/s]	W [µm]	H [µm]	a_0 [µm]	a_1 [µm]	a_2 [µm]	L [µm]	L_n [µm]
A1	2	2.90	2.71	1.37	2.50	0.97	7.15	0.92
A2	2	2.87	3.14	1.48	2.78	0.83	7.01	1.13
A3	2	3.36	3.16	1.69	3.08	1.06	7.04	1.02
A4	2	3.26	3.29	1.61	3.06	0.96	7.04	0.83
A5	2	3.28	3.16	1.46	2.95	1.02	7.12	0.87

The fracture surfaces of A1 - A5 are shown in Figure 5.18. All fractures occurred neatly at the chevron notch, with the fracture surfaces being almost perfectly smooth and flat. No regions of stable or unstable crack growth, nor the transition moment from one to the other, could be distinguished from the fractography.

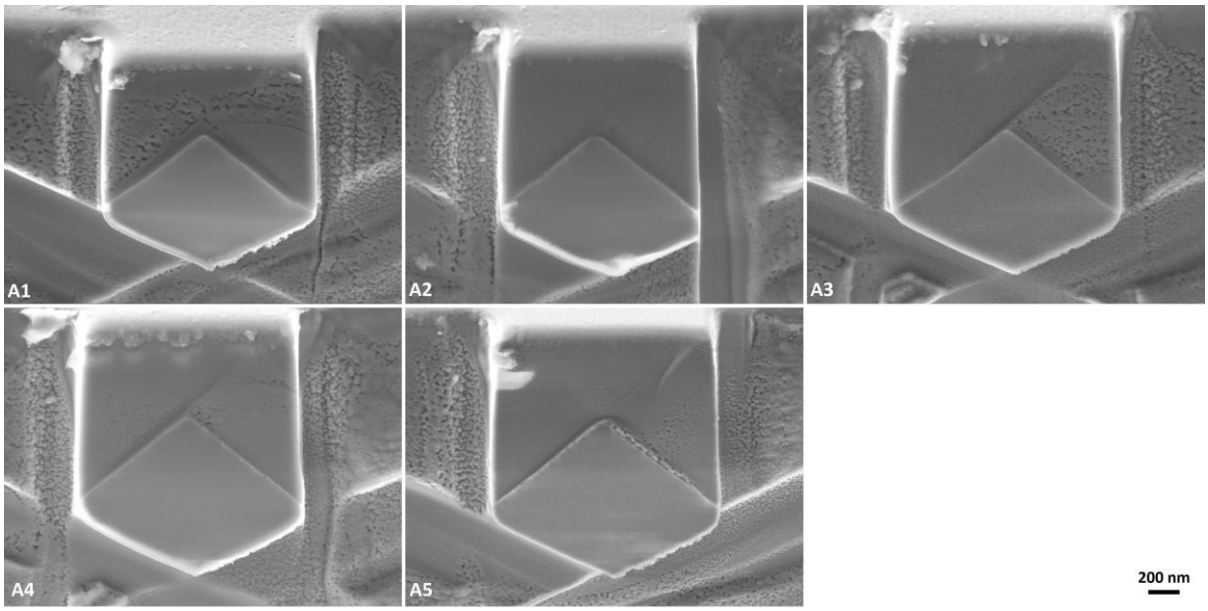


Figure 5.18. Fracture surface of A1 to A5, exhibiting the chevron notches. Imaging stage tilt = 60°.

Load-displacement curves for the beams A1 to A5 are shown in Figure 5.19. All the curves are linear during the elastic bending. The crack nucleation is presented by the onset of nonlinear extension shown in the curves, which is followed by stable crack growth. For the beams A1, A2 and A3, the stable crack propagation manifests as extensive plateaus, accompanied with a few stepwise increases in load. A3 showed a pop-in when the crack started to grow (i.e. the points were further apart). The points were not evenly spaced in the rest of the curve, suggesting that the crack growth was not occurring at a uniform speed. For the beams A4 and A5, knowing that the points are equally spaced in time in Figure 5.19, the wide spacing of the data points after the purely elastic region indicated that the instability of the crack growth. Once the fast brittle fracture occurred, the nanoindenter tip followed the broken cantilever to fall down quickly in depth.

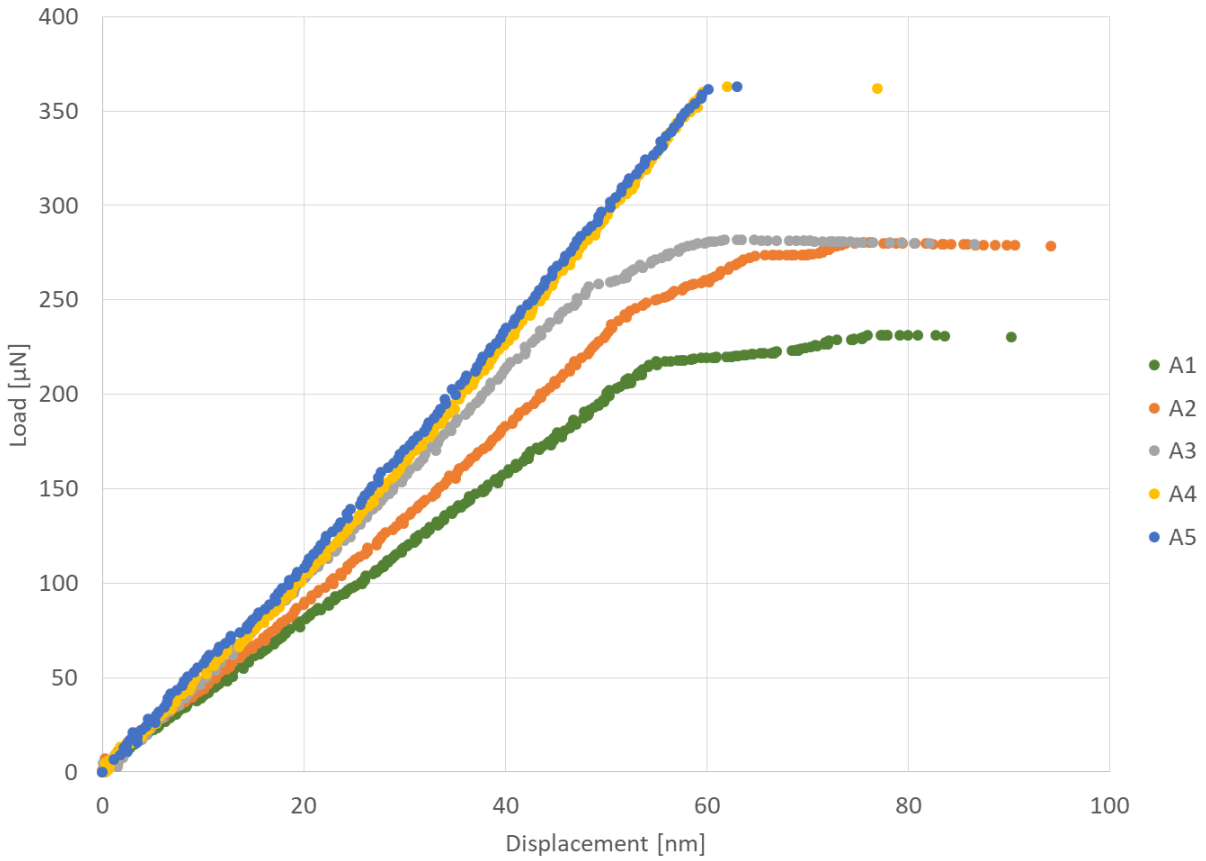


Figure 5.19. Load-displacement curves of five a-axis chevron cantilevers tested in air

Each cantilever was coupled with a specifically-built FE model to calculate the beam compliance during crack propagation, based on the dimensions measured from SEM images (Table 5.1). The compliances from 12 ~ 15 crack lengths were interpreted numerically for each cantilever, with an individual sub-model created and run for each crack length to obtain the load-displacement responses. The numerical compliance was compared to that measured from the empirical load-displacement curves, exhibiting close values to each other, with less than 10% difference for all the cantilevers tested in the present study.

The dimensionless compliance of each beam at each crack length is plotted in Figure 5.20 as a function of the normalised crack length. The compliance calibration curve was generated by fitting the collected data points with a fifth-order polynomial.

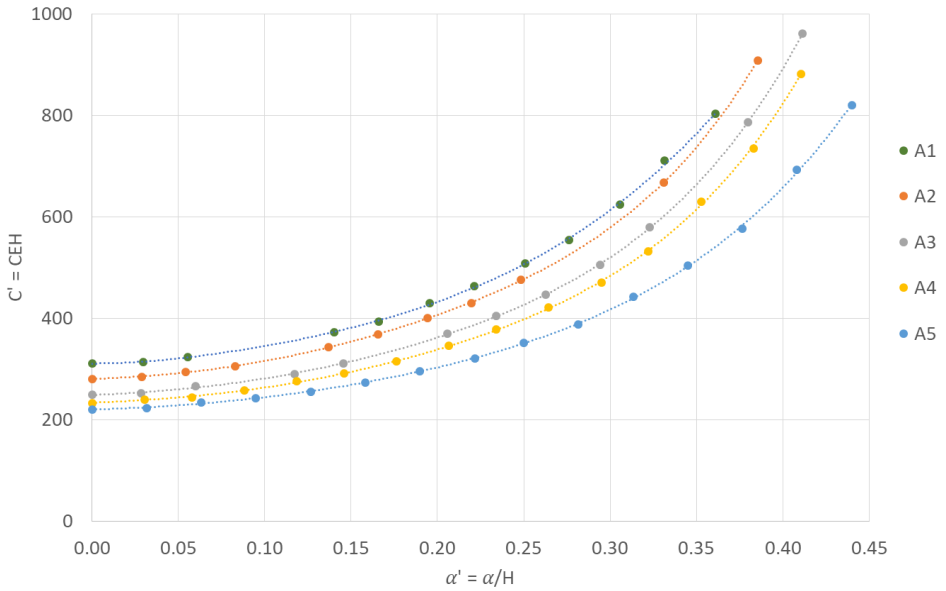


Figure 5.20. Dimensionless compliance C' as a function of normalised crack length α' for the five a-axis chevron beams

The polynomial exponents of *C'(α')* were then used to calculate the geometrical parameter *Y(α')* = $\left(\frac{1}{2}\frac{a_1-a_0}{\alpha}\frac{dC'}{d\alpha'}\right)^{\frac{1}{2}}$ at each crack length. Each data point was plotted in Figure 5.21 as a function of the normalised crack length α' and again fitted with a fifth-order polynomial. The *Y(α')* curve for A2 exhibited some slightly flat distribution of points at the bottom, which could be explained by the fact that the numerical models and the polynomial fit of the data points in Figure 5.20 cannot be perfect.

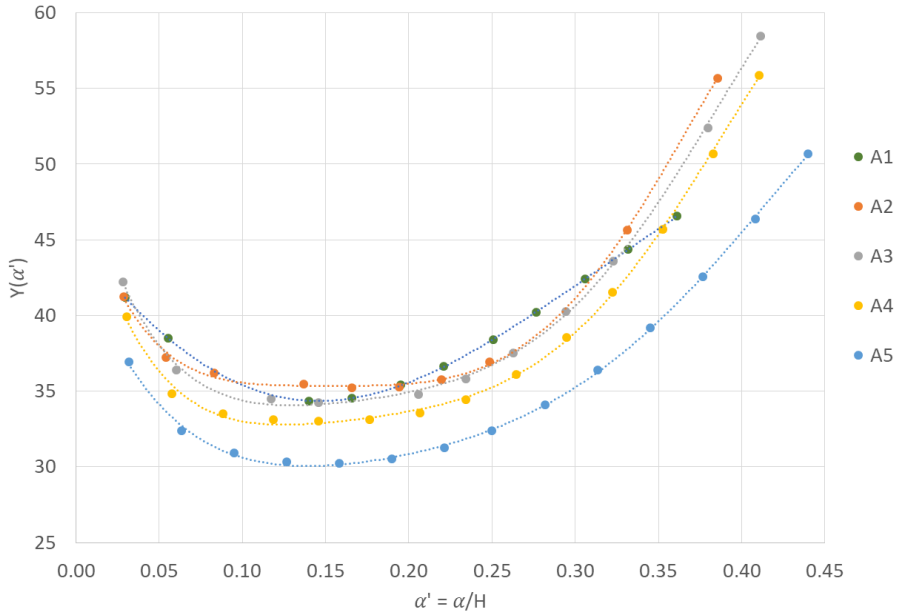


Figure 5.21. Geometrical function Y(α') as a function of normalised crack length

Based on the deduced polynomial equations, the critical crack length (α'_c), and the corresponding minima of the geometrical parameter Y (α_c') were calculated for each cantilever, as summarised in

Table 5.2. Knowing the peak load measured in the test, the apparent stress intensity factor K_p at the critical crack length α'_c can be deduced using the method described in Section 5.1.1. The results for A4 and A5 are discarded because the crack growth was unstable, as indicated in Figure 5.19.

Table 5.2. The critical load (P_c), critical crack length (α_c'), minima of the geometrical parameter ($Y(\alpha_c')$) and $K_p(\alpha_c')$ measured on the a-plane of sapphire, with the average value expressed with standard error.

#	P_c [μN]	α'_c	$Y(\alpha_c')$	$K_p(\alpha_c')$ [MPa·m$^{1/2}$]	Average $K_p(\alpha_c')$ [MPa·m$^{1/2}$]
A1	231.4	0.15	34.3	1.72	
A2	276.1	0.16	35.4	1.84	1.76 ± 0.04
A3	285.2	0.13	34.7	1.71	

The K_p values of A1, A2 and A3, measured at each data point during the stable crack propagation was also evaluated using the back-calculation method described in Section 5.1.1, with the results presented in Figure 5.22. The stable crack growth did not start at α'=0 but at a slightly larger value due to the 'pop-in' event. K_p remained almost constant at values around 1.6 to 1.9 MPa·m$^{1/2}$ during the crack growth.

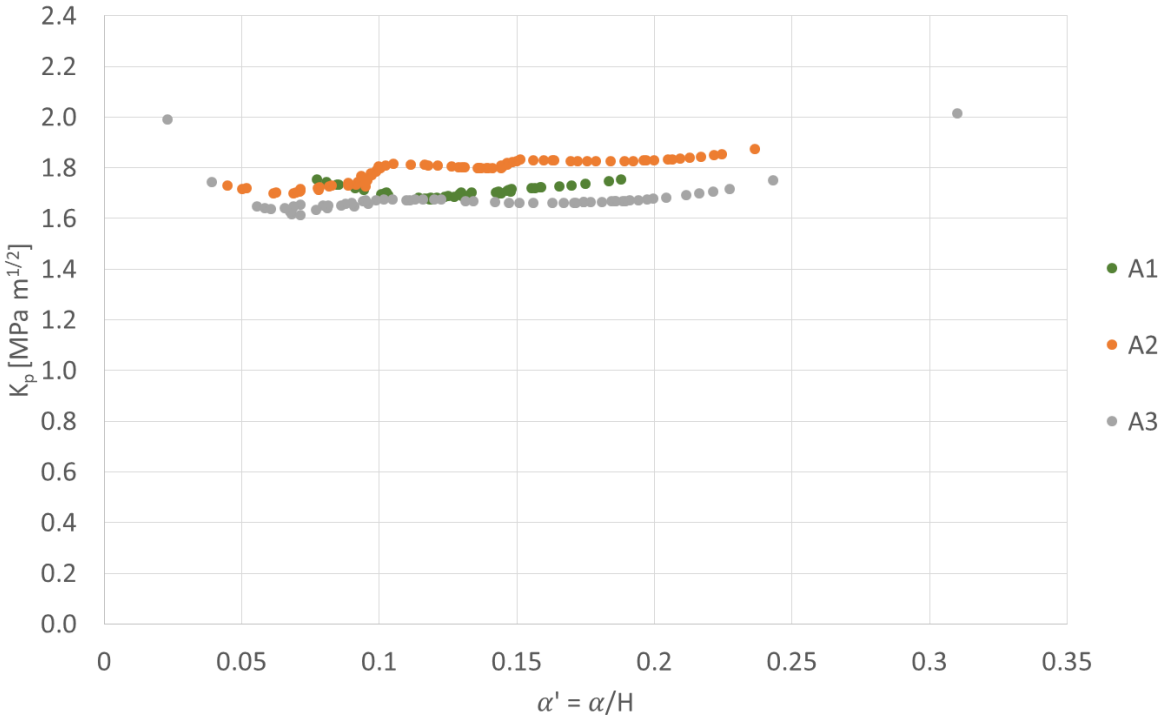


Figure 5.22. Fracture toughness measured during stable crack propagation

The crack propagation is demonstrated in Figure 5.23 by plotting the crack length as a function of time, starting from the moment when the crack initiated. Each crack propagated at average velocities on the scale of 10^{-8} m/s (i.e. A1: ~2.8×10^{-8} m/s, A2: ~2.9×10^{-8} m/s, A3: ~3.6×10^{-8} m/s) all the way through the cracking process, until the last moment prior to the fast brittle fracture when the crack velocity increased significantly.

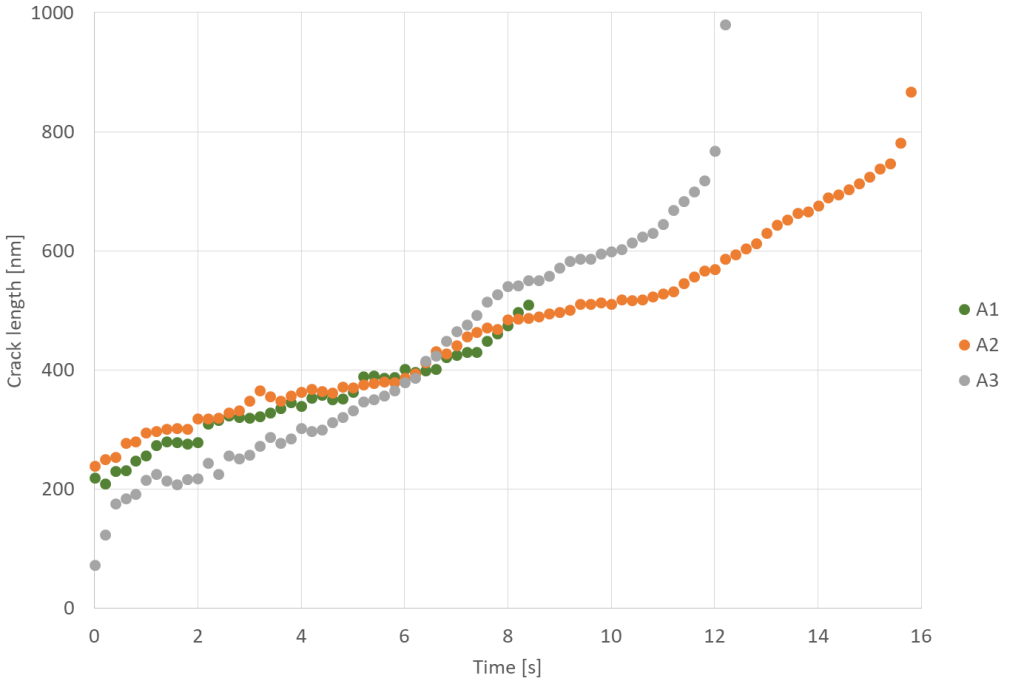


Figure 5.23. Crack length as a function of time during stable crack growth process, for sapphire cantilevers tested in air.

5.2.3 Fracture toughness of Al_2O_3 measured in air – m-plane

Three chevron-notched cantilevers aligned in the m-axis were tested, with their dimensions listed in Table 5.3.

Table 5.3. Cantilever reference number (#), loading rate (ẏ), sample dimensions (W to L_n, as defined in Figure 5.3) for m-plane chevron-notched sapphire cantilevers tested in air.

#	ẏ [nm/s]	W [µm]	H [µm]	a_0 [µm]	a_1 [µm]	a_2 [µm]	L [µm]	L_n [µm]
M1	2	2.71	2.79	1.35	2.51	0.73	7.31	1.05
M2	2	2.48	3.00	1.07	2.62	0.78	7.00	0.66
M3	2	2.61	2.93	1.45	2.54	0.74	7.13	0.91

The load-displacement curves (Figure 5.24) show that stable crack growth occurred in all the three cantilevers, exhibiting similar behaviour to that observed in a-axis sapphire cantilevers. The data point was recorded every 0.9 s during the test of M1 and M2 due to a faulty equipment setting, which was longer than the standard data recording interval 0.2s, thus the big gaps between each data point. In M2, the crack grew stably only until not long after the crack initiation, followed by fast brittle fracture. The dimensionless compliance C' and geometrical parameter Y(α') at a specifically-defined crack length were interpreted numerically using the FE models for M1 and M3, with details shown in the Appendix A (M2 was not analysed in the present thesis due to the lack of time for numerical simulation.)

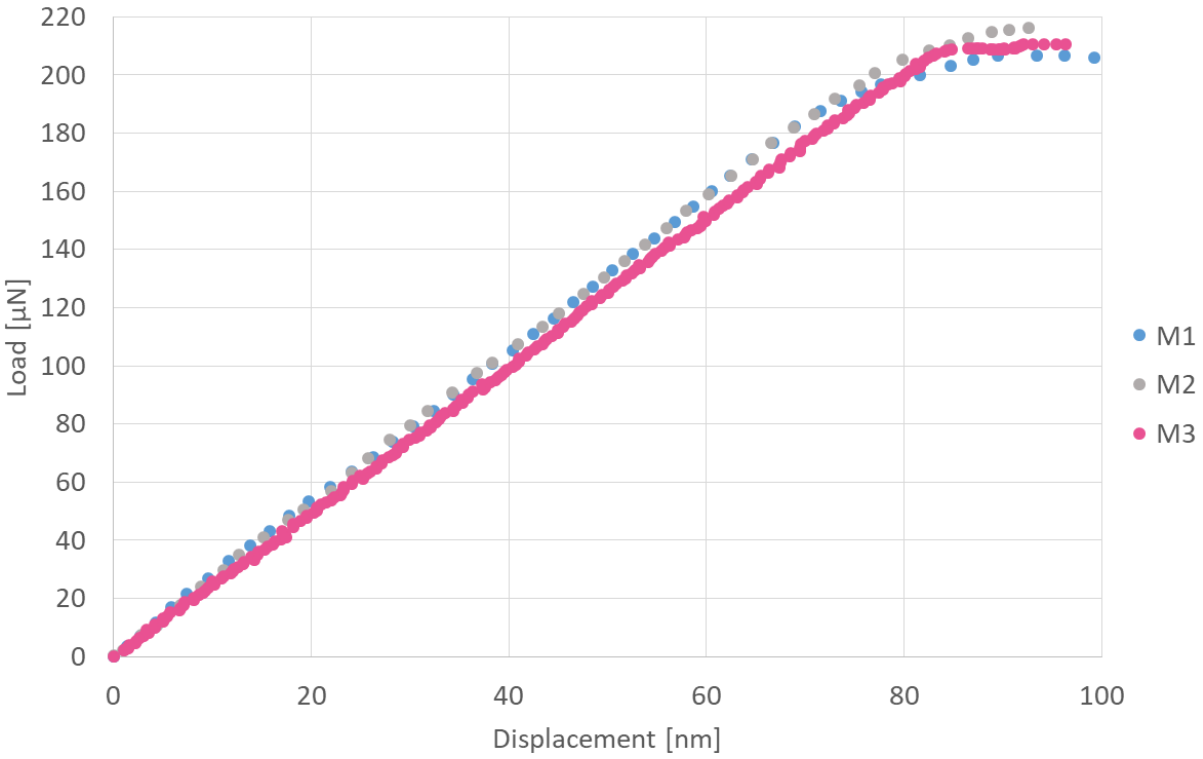


Figure 5.24. Load-displacement curves of three m-axis chevron cantilevers tested in air

The apparent stress intensity factor K_p at the critical crack length α'_c was calculated for M1 and M3 based on their peak load and minima of Y (α_c'), showing values averaged at 1.98 ± 0.08 MPa·m$^{1/2}$ (Table 5.4), which is close to that measured on a-plane in air.

Table 5.4. The critical load (P_c), critical crack length (α_c'), minima of the geometrical parameter ($Y(\alpha_c')$) and $K_p(\alpha_c')$ measured on m-plane of sapphire in air, with the average value expressed with standard error.

#	P_c [μN]	α'_c	$Y(\alpha_c')$	$K_p(\alpha_c')$ [MPa·m$^{1/2}$]	Average $K_p(\alpha_c')$ [MPa·m$^{1/2}$]
M1	206.8	0.16	42.3	1.91	1.84 ± 0.08
M3	210.7	0.13	39.6	1.76	

The K_p values measured during the stable crack propagation is shown in Figure 5.25. Due to the 'pop-in' event, the crack growth became stable at a length of around α' = 0.1. The apparent K_p values were almost constant during crack propagation, showing values between 1.7 to 1.9 MPa·m$^{1/2}$.

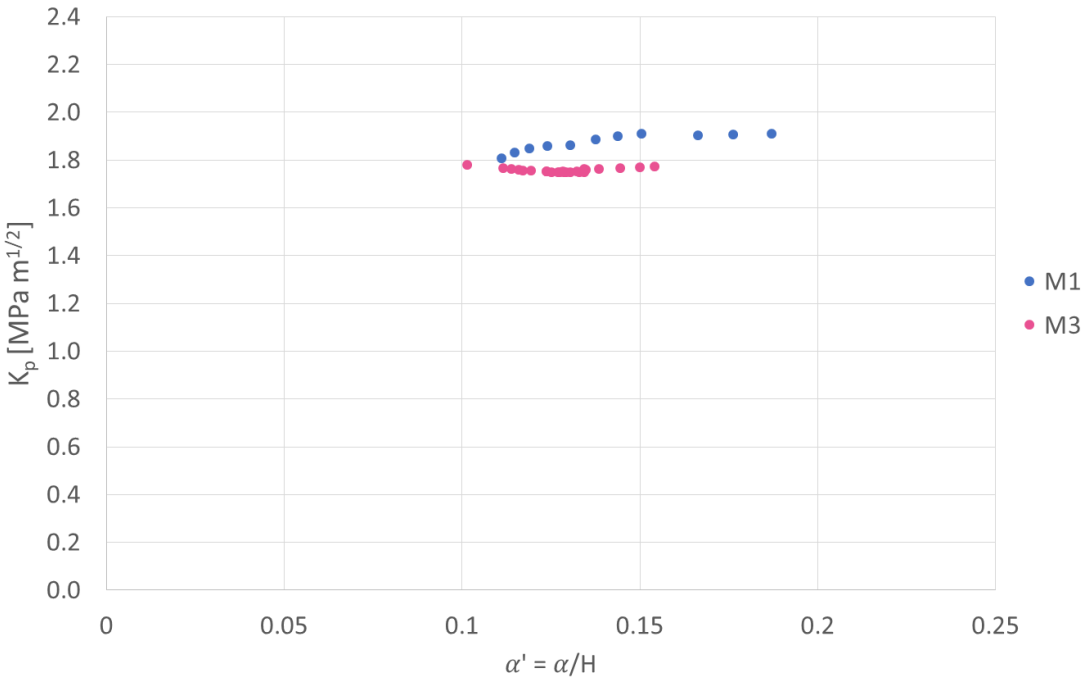


Figure 5.25. Fracture toughness measured during stable crack propagation in m-axis sapphire tested in air.

During the stable crack growth (Figure 5.26), the crack propagated at a velocity of 10^{-8} m/s (i.e. M1: ~2.6×10^{-8} m/s, M3: ~2.1×10^{-8} m/s) as was reported previously for a-plane sapphire cantilevers (i.e. A1, A2 and A3).

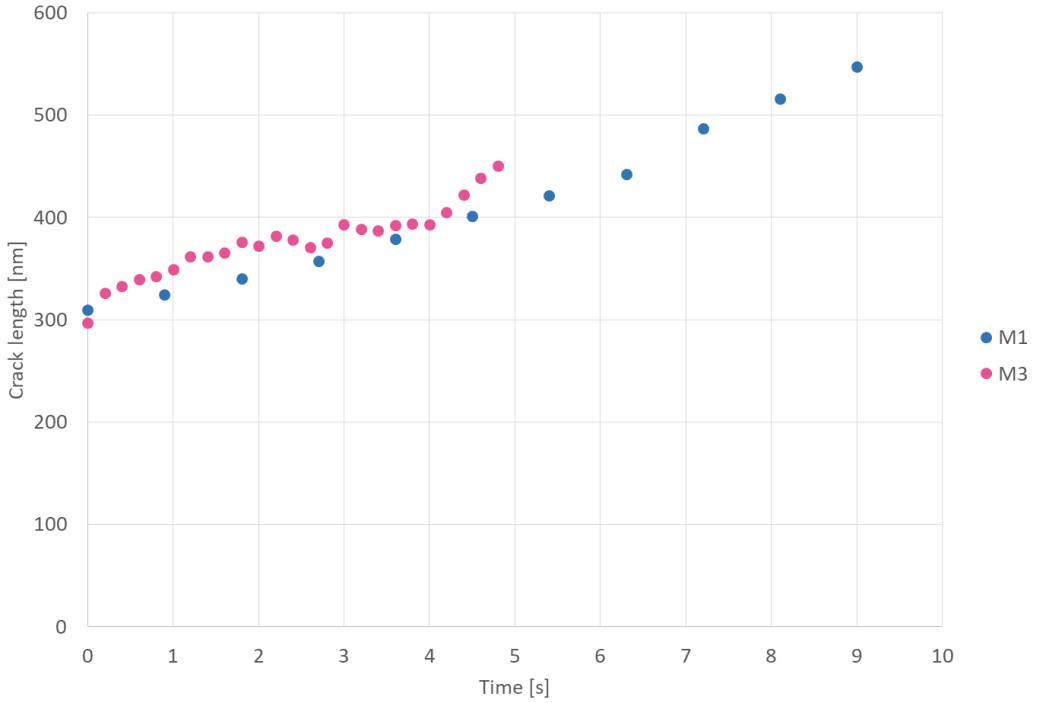


Figure 5.26. Crack length as a function of time during stable crack growth process, for sapphire cantilevers tested in air.

5.2.4 Fracture toughness of Al_2O_3 measured in vacuum – a-plane

A total of six chevron-notched a-axis sapphire cantilevers were tested in vacuum, using the intrinsically displacement-controlled in-situ SEM nanoindenter. The dimensions of the cantilevers are listed in Table 5.5, with the SEM images shown in Figure 5.27.

Table 5.5. Cantilever reference number (#), loading rate ($\dot{y}$), sample dimensions (W to L_n, as defined in Figure 5.3) for a-axis chevron-notched cantilevers tested in vacuum using the in-situ SEM nanoindenter.

#	$\dot{y}$ [nm/s]	W [µm]	H [µm]	a_0 [µm]	a_1 [µm]	a_2 [µm]	L [µm]	L_n [µm]
AV1	2	3.22	3.41	1.65	3.13	1.07	8.57	0.48
AV2	2	3.22	3.31	1.54	3.07	0.99	9.20	0.64
AV3	2	3.11	3.43	1.54	3.00	0.97	9.01	0.59
AV4	2	3.20	3.57	1.62	3.23	0.95	9.34	0.54
AV5	2	2.56	3.45	1.33	2.56	0.76	8.82	0.70
AV6	2	3.00	3.44	1.52	3.01	0.91	9.07	0.48

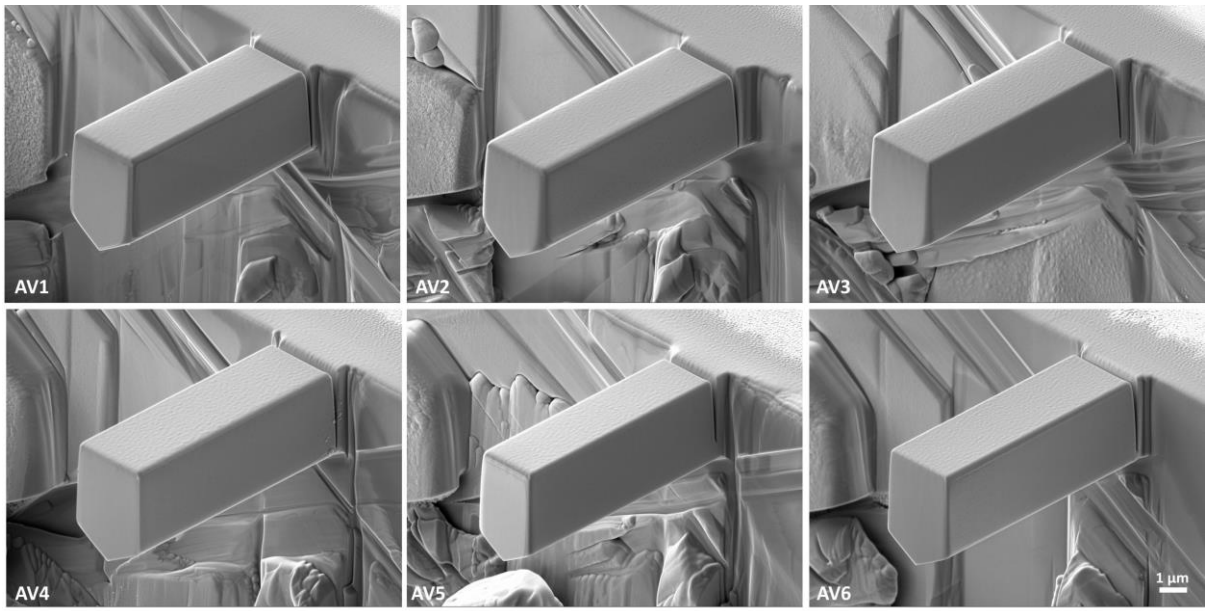


Figure 5.27. SEM images of the chevron notched cantilevers for the bending test in vacuum

Cantilevers AV1, AV2, AV3 and AV5 were loaded continuously until complete failure at one go, while AV4 and AV6 were tested under cyclic loading. Details are given below.

As AV1 was tested as a trial cantilever, the load-displacement data was not usable and therefore not presented here. The loading curves of AV2, AV3 and AV5 are shown in Figure 5.28. The load increased proportionally to the displacement as the cantilever bent elastically. Once cracks initiated at the apex of the chevron notch, as the experiment is performed under intrinsic displacement control mode, cracking is inherently stable throughout the fracture process, with the load eventually decreasing stably to very small values.

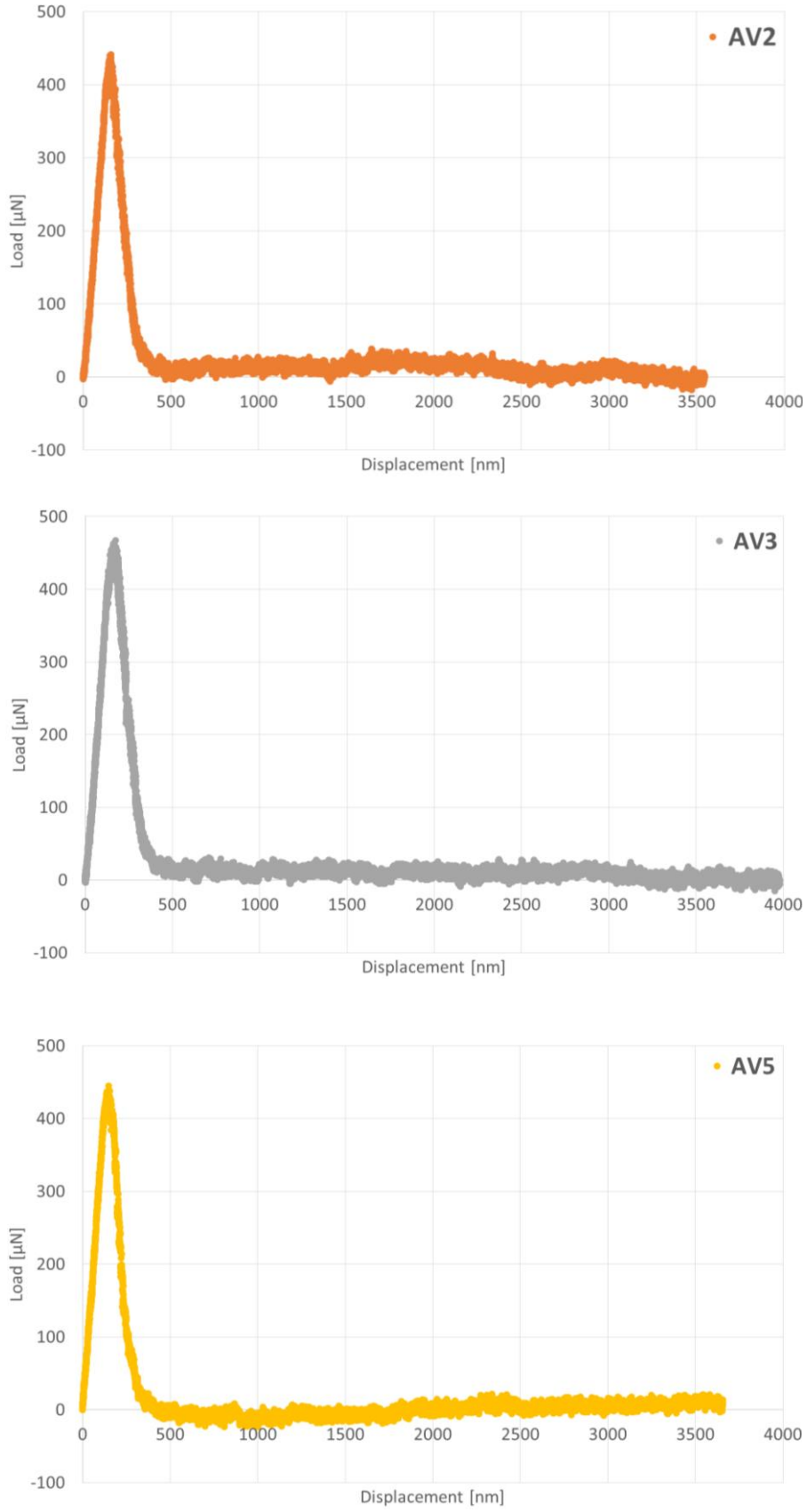


Figure 5.28. Load-displacement curves of AV2, AV3 and AV5 (with load drift corrected). Tests were performed under the displacement-control mode with a displacement rate of 2 nm/s.

SEM images were taken every 2 seconds to record the loading behaviour of the cantilevers. Videos integrated from the SEM image frames are available but could not be displayed here due to the limit of format. Six SEM frames from the loading process of cantilever CV3 are selected to demonstrate the loading process, and are correlated with the loading curve as shown in Figure 5.29. The loading process can be summarised into 3 segments: (I) Points *a* to *b*: load increases linearly from zero during elastic bending, followed by stable crack growth with the crack advancing to the critical point *b*. The propagation of the crack cannot be observed clearly from the side of the notch due to small opening. (II) Points *b* to *c*: load decreases gradually to only a few μN. Crack continues to propagate stably thanks to the intrinsic stability of displacement control enabled by sufficiently high stiffness of the nanoindenter, exhibiting further gradual opening of the notch. (III) Points *c* to *f*: the load remains at around a few μN until the failure of cantilever. The growth of the crack remains stable through the entire fracture surface.

The loading behaviour of all the tested cantilevers is highly repeatable, in terms of both loading curves and the stable crack propagation recorded by SEM imaging.

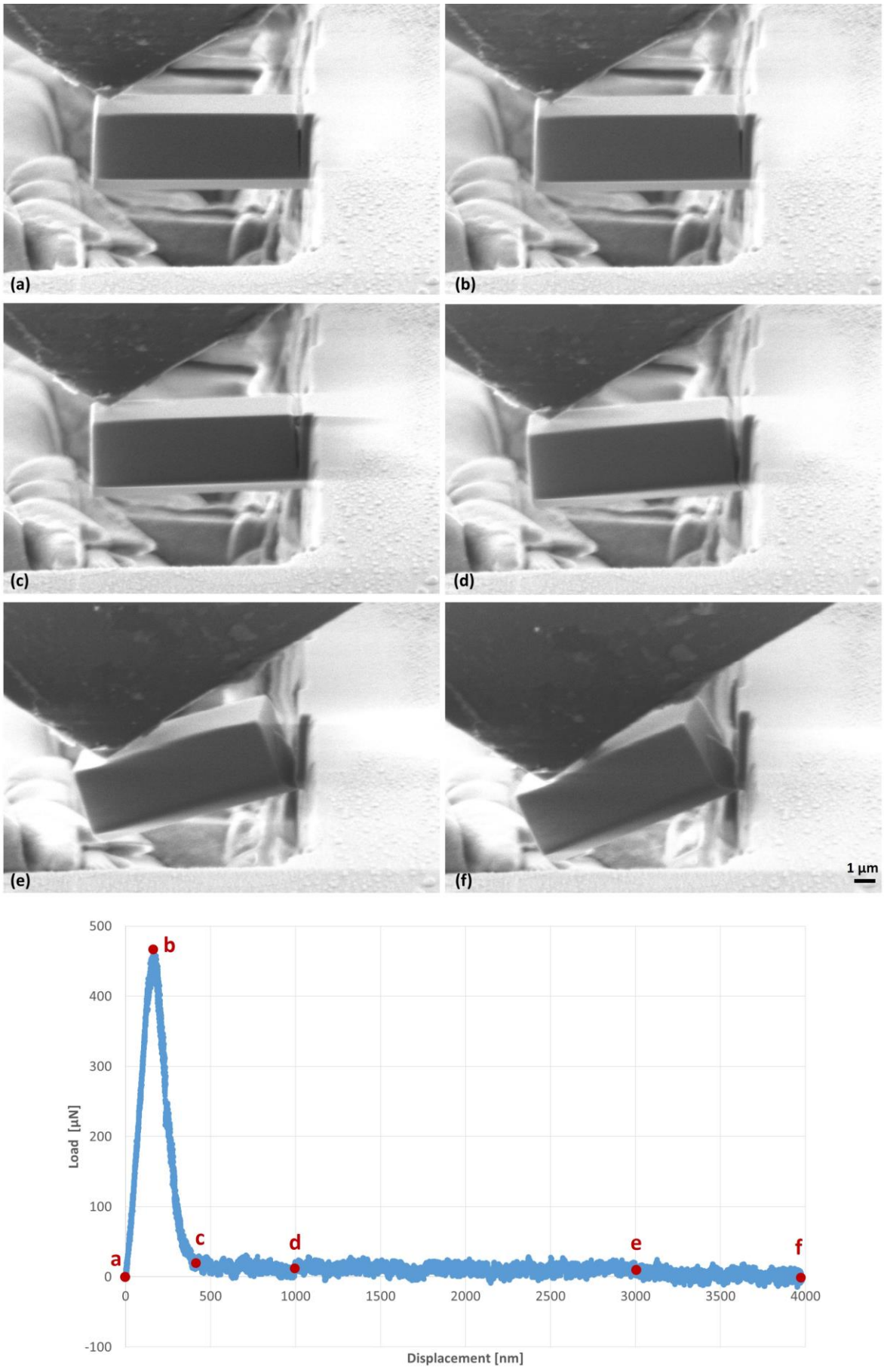


Figure 5.29. SEM images and loading curve of AV3. The red dots correspond with the numbering of the SEM images.

The fracture surfaces of the four tested cantilevers are shown in Figure 5.30, with all exhibiting perfectly smooth surfaces.

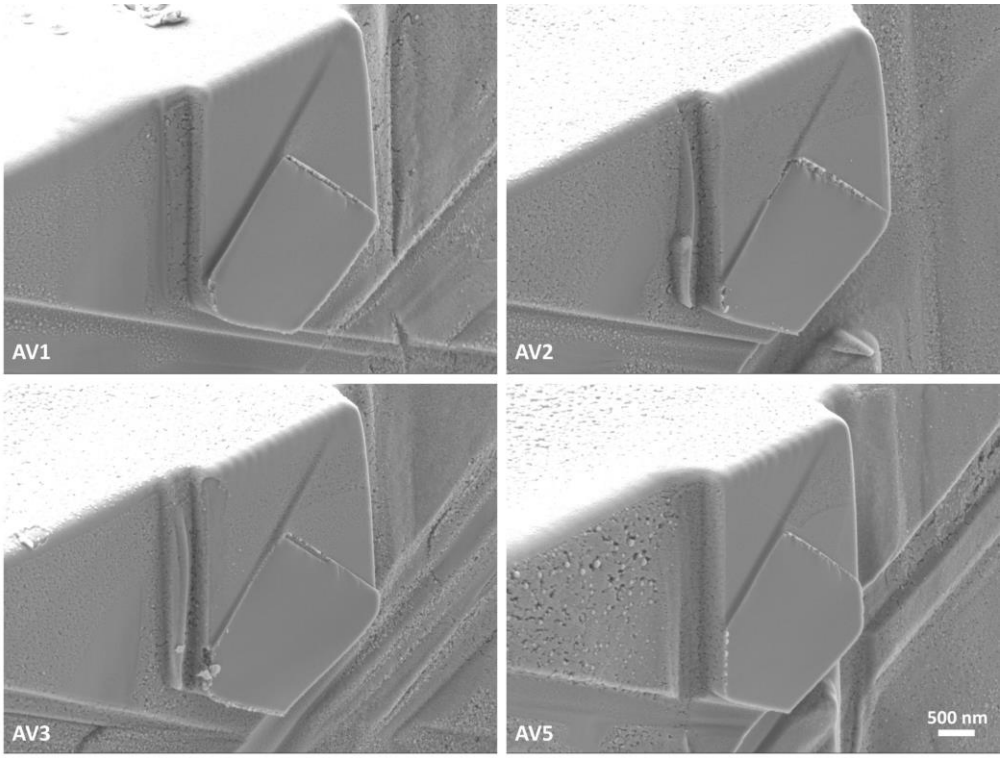


Figure 5.30. SEM images of the fracture surfaces of AV1, AV2, AV3 and AV5, from side view.

Due to the shortage of time, only AV3 has been interpreted using numerical simulation in the present thesis, with the dimensionless compliance C' and geometrical parameter Y(α') shown in Figure A.2 in the Appendix A.

The load-displacement curve featuring the elastic bending and the early stage of stable crack growth is displayed in Figure 5.31, to enable the visualisation of the loading process during the main stage of stable crack growth.

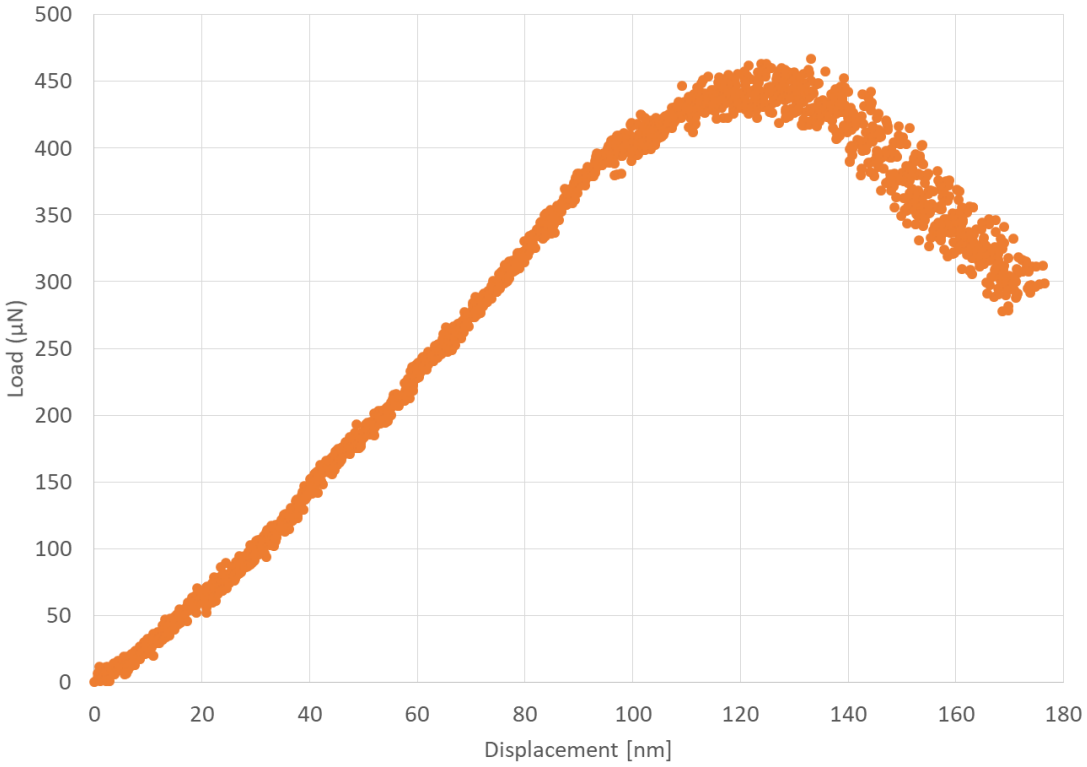


Figure 5.31. Load-displacement curve for AV3

The K_p value at the critical crack length α'_c was calculated based on the peak load and minima of Y (α_c'), giving a value of 2.84 MPa·m$^{1/2}$, which is higher than that measured from the sapphire cantilevers in air. K_p measured during the stable crack propagation (Figure 5.32) indicates that the crack growth became stable at around α' = 0.1 after the 'pop-in' event, with the measured K_p remaining at around 2.5 - 2.8 MPa·m$^{1/2}$. The analysis was performed up to $\alpha' \approx 0.37$ corresponding to the end of the notch (points 3 and 5 in Figure 5.10), beyond which the compliance of the cantilever was not evaluated using numerical models.

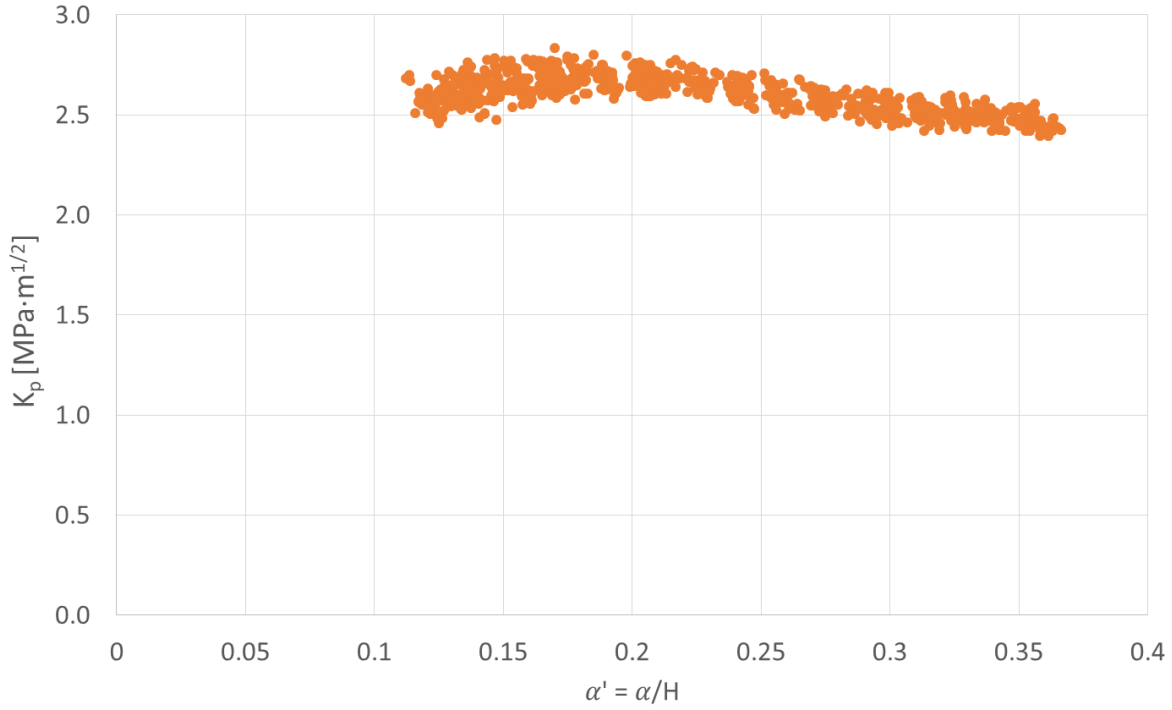


Figure 5.32. Fracture toughness measured during stable crack propagation in a-axis sapphire cantilever tested in vacuum.

The average rate of crack propagation was around ~2.0×10^{-8} m/s, as shown in Figure 5.33.

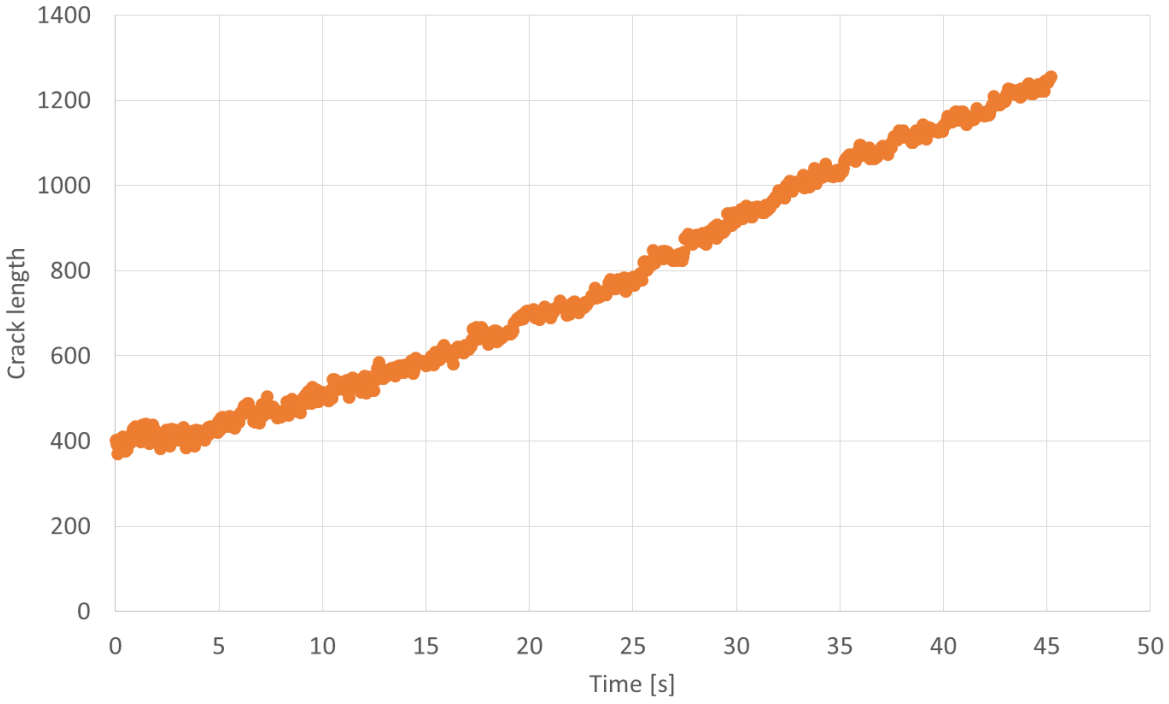


Figure 5.33. Crack length as a function of time during stable crack growth process, for the sapphire cantilever AV3 tested in vacuum.

Cantilever AV4 and AV6 were tested under cyclic loading – loading was retracted completely after the crack propagated for a measurable length, followed by re-loading to advance the crack length to a

further extent, and repeated a few times until the cantilever was loaded to a complete failure in the final loading cycle.

For AV4, five cycles of loading were applied, as shown in Figure 5.34. For the 1st loading cycle, the load response behaved in the same way as reported in monotonic-loaded cantilevers (i.e. AV2, AV3, AV5), with the unloading process taking place at a crack length of ~60 nm. For the loading curves of the sequential loading cycles (i.e. cycle 2 to 5), the load first increased linearly with the same slope as of the cycle 1 loading, showing that the crack had healed up, but popped in at a lower load, eventually re-joining and continuing from the previous curve at the point at which unloading had commenced. In the last loading cycle (i.e. cycle 5), the load is applied until the very end of the complete failure.

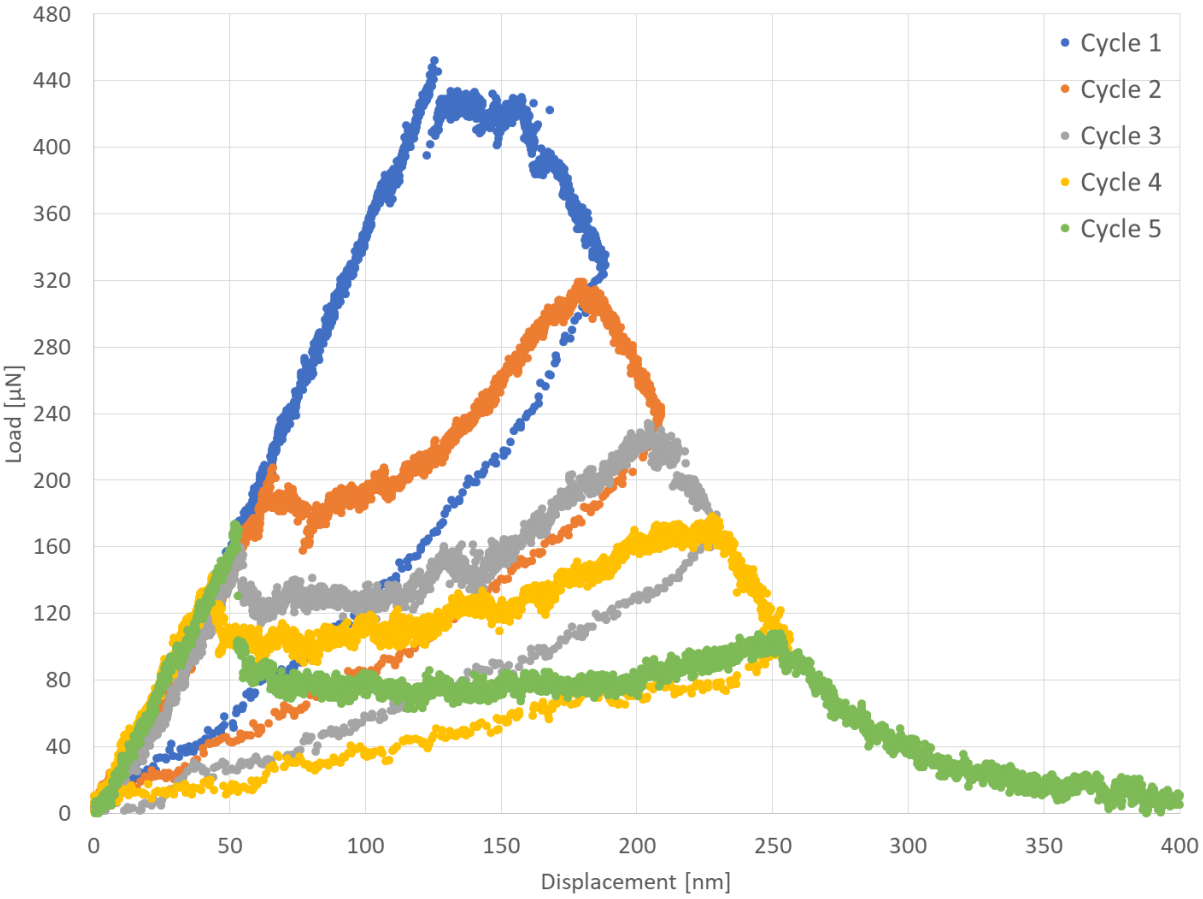


Figure 5.34. Load-displacement curve of cantilever AV4 with cyclic loading in vacuum.

Two SEM images are selected for each loading cycle (Figure 5.35) – one is for the moment when the displacement of the indenter was at 0, and the other for the moment right before the unloading. The notch opened up during each loading cycle and closed back to its original status after unloading.

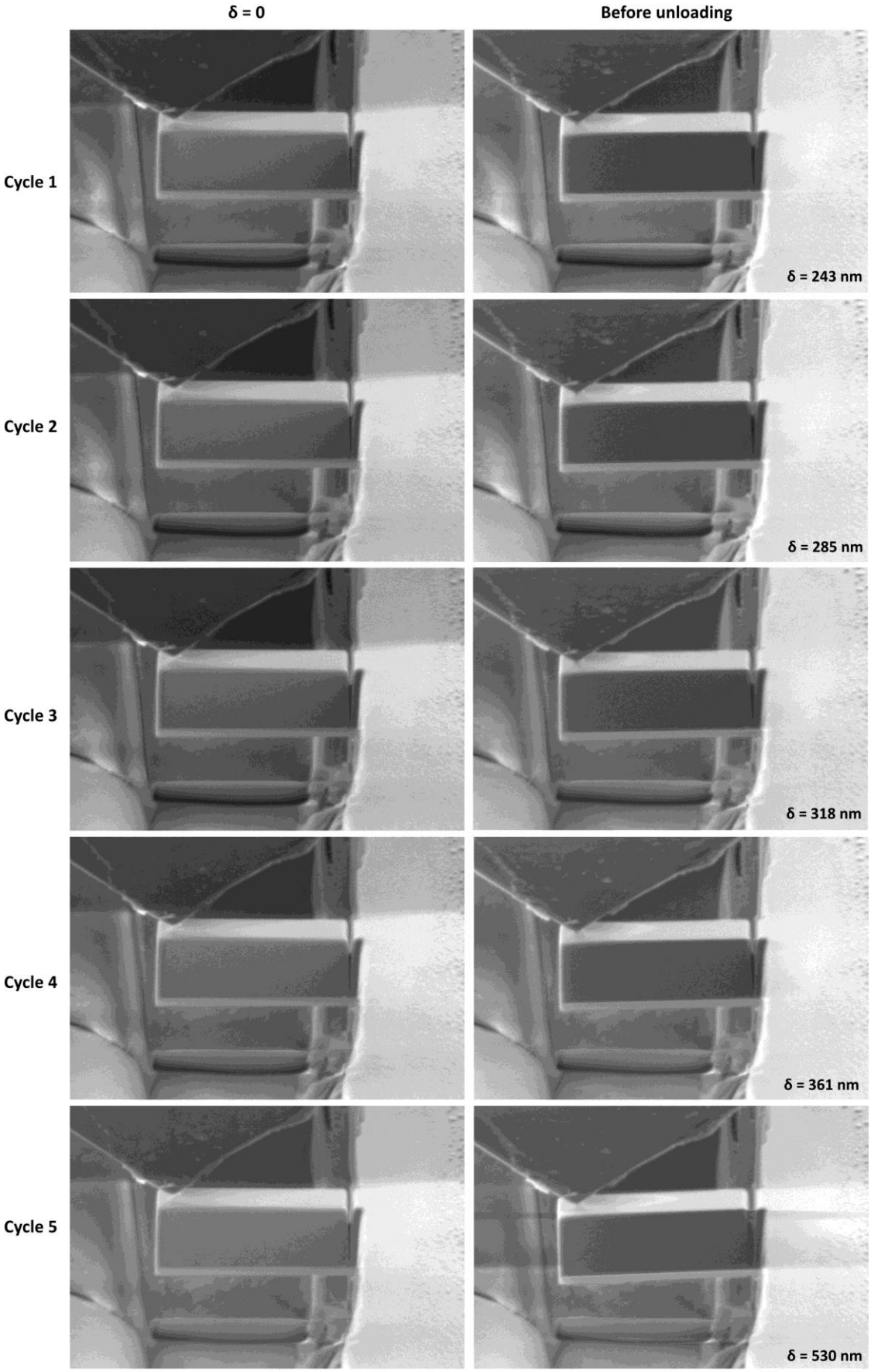


Figure 5.35. SEM Images of the five loading cycles for the cantilever AV4. For cycle 5, the image shown in the 'Before unloading' column corresponds to point c *on the loading curve (Figure 5.29).*

Due to the shortage of time for performing numerical simulations, the compliance of AV4 during crack growth could not be obtained from numerical interpretation, therefore the analysis could not proceed further.

Cantilever AV6 also underwent cyclic loading, with the number of cycles increased to six. After applying a correction for displacement drift of +0.11 nm/s, the loading curves are shown in Figure 5.36. The loading behaves similarly to that in AV4.

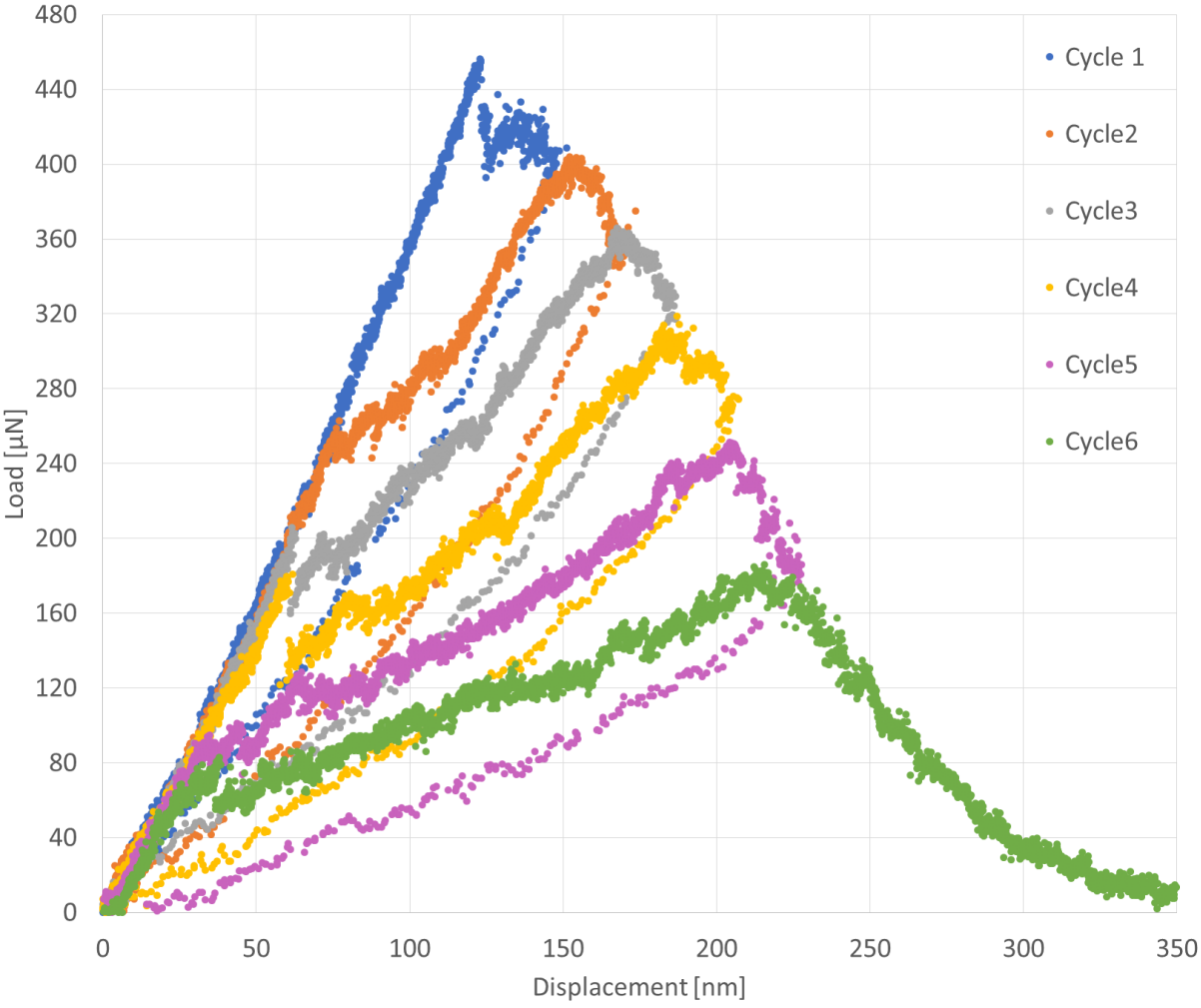


Figure 5.36. Load-displacement curve of cantilever AV6, with cyclic loading.

Two SEM images are selected for each loading cycle (Figure 5.37) as for AV4. For the final cycle (i.e. the cycle 6), the image shown in the 'Before unloading' column corresponds the point f on the loading curve (i.e. the moment before the complete failure of the cantilever).

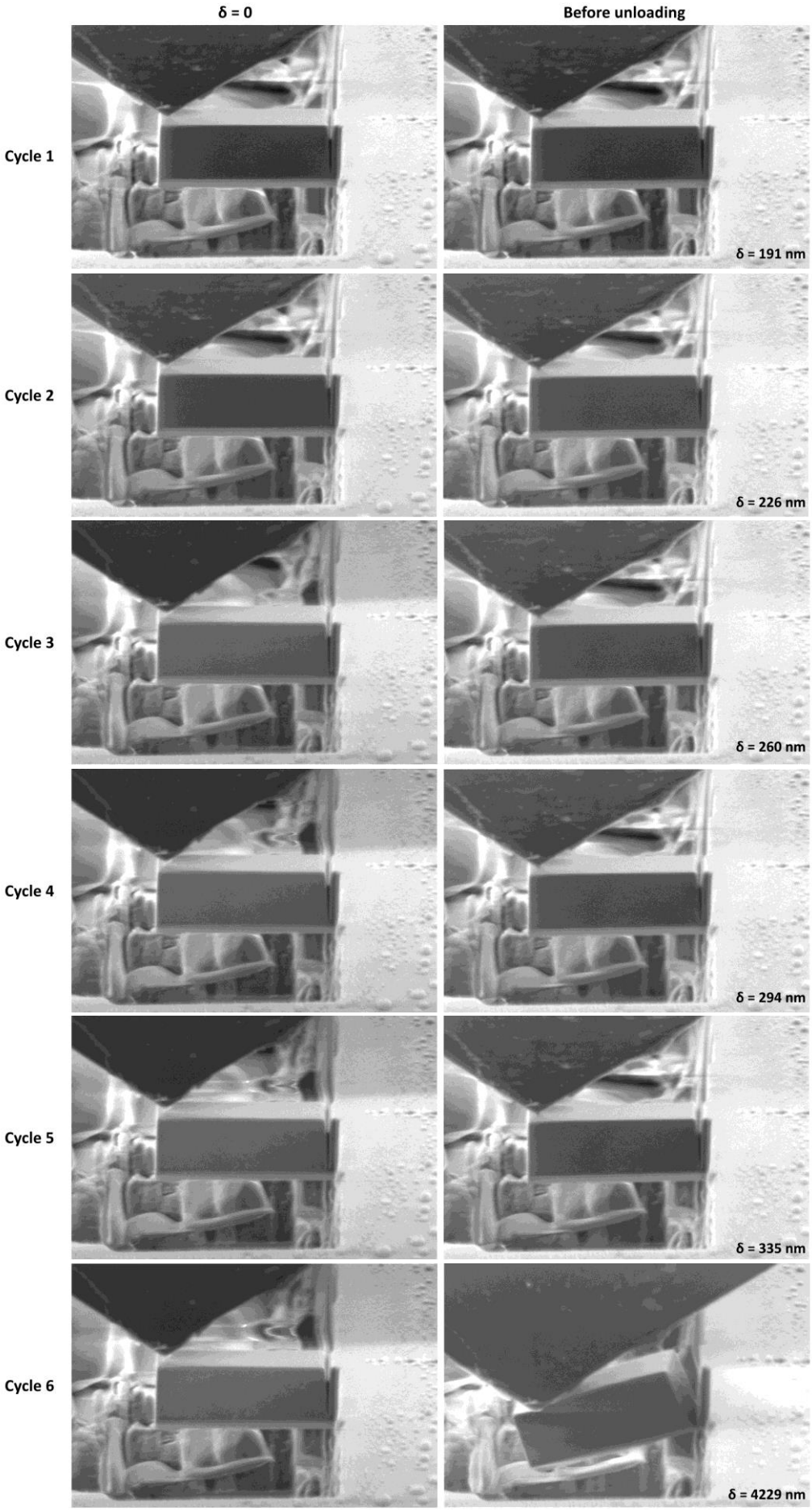


Figure 5.37. SEM images of the cantilever AV6, tested with cyclic loading.

With the dimensionless compliance C' and geometrical parameter Y(α') shown in Figure A.3, K_p at the critical crack length α'_c was calculated for the cycle 1 loading, giving a value of 2.84 MPa·m$^{1/2}$.

K_p values measured during crack propagation during loading cycles 1-4 are shown in Figure 5.38 (Loading cycles 5 and 6 were not analysed here because the crack has propagated beyond the extent of the notch [i.e. points 6 and 8 in Figure 5.10], and the compliance curve therefore did not apply anymore). For loading cycles 2-4, the crack re-initiated at a low $K_{p\ (healed)}$ in the healed-up material, and arrested at the crack length reached during the previous cycle, followed by further crack extension at a higher $K_{p\ (intrinsic)}$. $K_{p\ (healed)}$ decreased from one loading cycle to next (from ≈1.6 MPa·m$^{1/2}$ in Cycle 2, to ≈1.2 MPa·m$^{1/2}$ in Cycle 3, then ≈1.0 MPa·m$^{1/2}$ in Cycle 4), while $K_{p\ (intrinsic)}$ exhibited highly consistent values around 2.6 to 2.8 MPa·m$^{1/2}$, similar to the value observed in the monotonic tests.

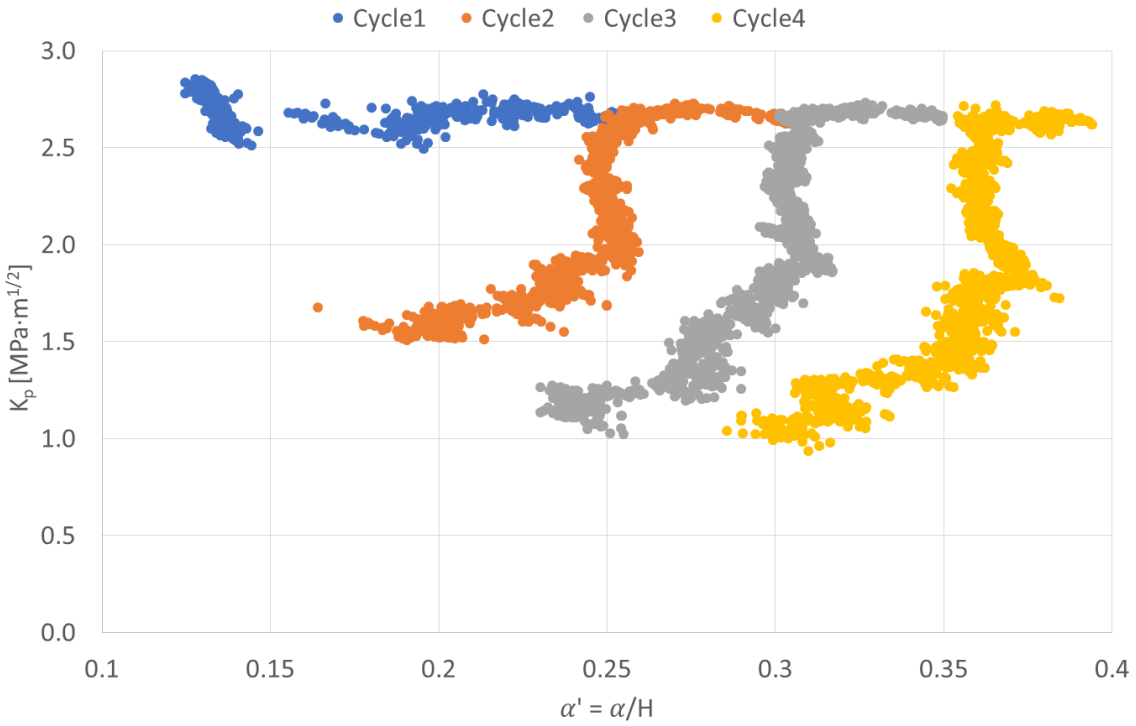


Figure 5.38. Fracture toughness measured during stable crack propagation in a-axis sapphire cantilever tested in vacuum.

The crack length is plotted in Figure 5.39 as a function of time. Regardless of crack propagation in healed or intrinsic material, the crack velocities exhibited similar values between 1.9 × 10^{-8} and 2.2 × 10^{-8} m/s when propagating.

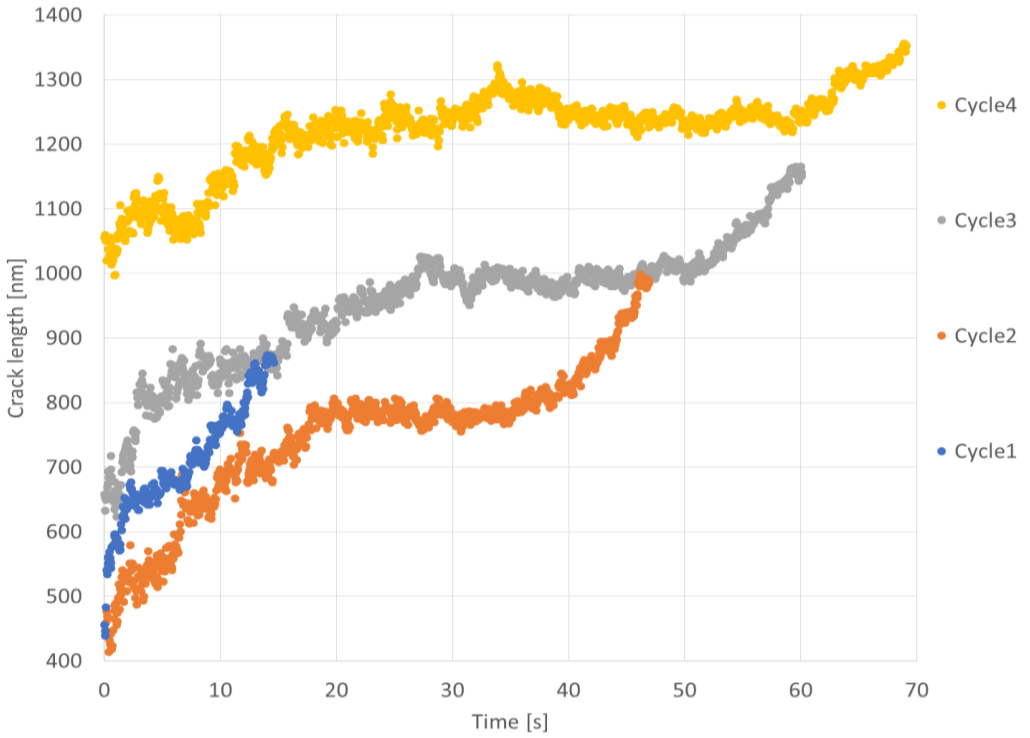


Figure 5.39. Crack length as a function of time during crack propagation at each loading cycle, for sapphire cantilevers AV6 tested in vacuum. Time is reset to 0 from the point at which the crack first extends during loading for each cycle.

5.2.5 Fracture toughness of SiC measured in air – $(\bar{1}100)$ plane

Six SiC chevron-notched cantilevers were tested in total, with two of them (S1 and S2) not annealed prior to the test. The dimensions of the cantilevers are listed in Table 5.6, with the SEM images shown in Figure 5.40.

Table 5.6. Cantilever reference number (#), loading rate ($\dot{y}$), sample dimensions (W to L_n, as defined in Figure 5.3) for $(\bar{1}100)$-plane chevron-notched SiC cantilevers tested in air.

#	$\dot{y}$ [nm/s]	W [µm]	H [µm]	a_0 [µm]	a_1 [µm]	a_2 [µm]	L [µm]	L_n [µm]
S1	2	3.18	4.05	/	/	/	12.26	0.73
S2	2	3.04	4.07	1.42	2.67	0.86	11.85	0.32
S3	2	2.93	3.95	1.66	2.86	0.93	11.3	0.61
S4	2	2.50	3.82	1.26	2.36	0.73	11.48	0.80
S5	2	2.79	3.93	1.42	2.66	0.83	12.02	1.02
S6	2	3.28	4.10	1.82	3.26	0.95	11.91	1.17

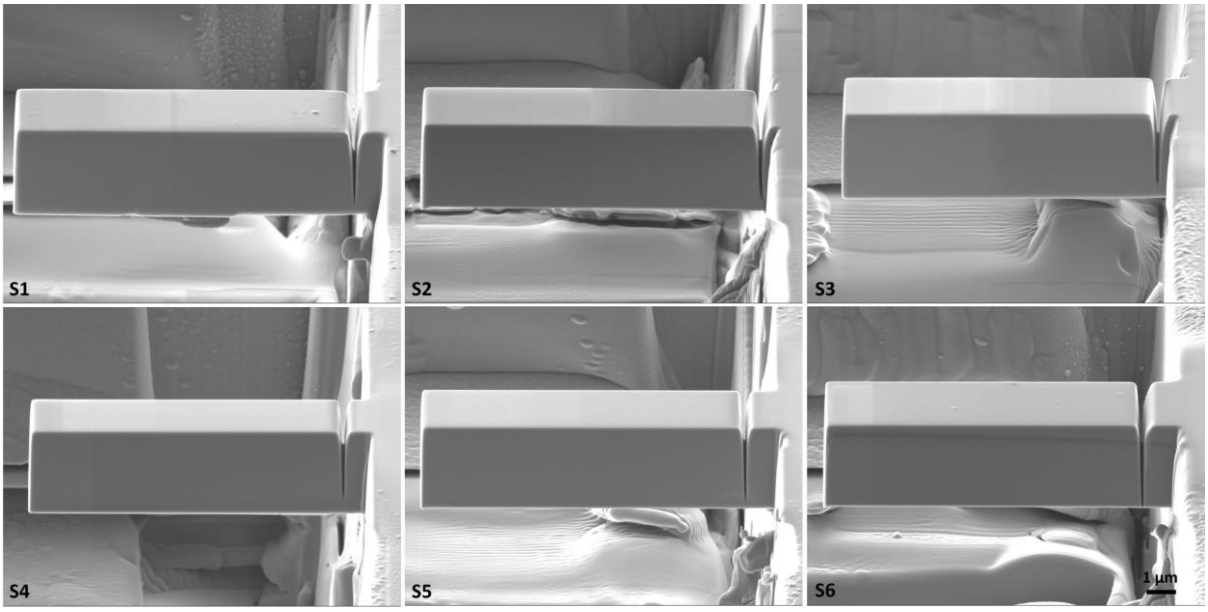


Figure 5.40. SEM images of the chevron notched SiC cantilevers, from side view.

SEM images of the fracture surfaces are shown in Figure 5.41. S1 still has the cantilever attached to the bulk sample after the test (likely due to charging), so the fracture surface cannot be seen and the dimensions of the chevron notch are therefore not measured. Wrinkles could be seen on all the fracture surfaces, lining up in the vertical directions (i.e. [0001] direction).

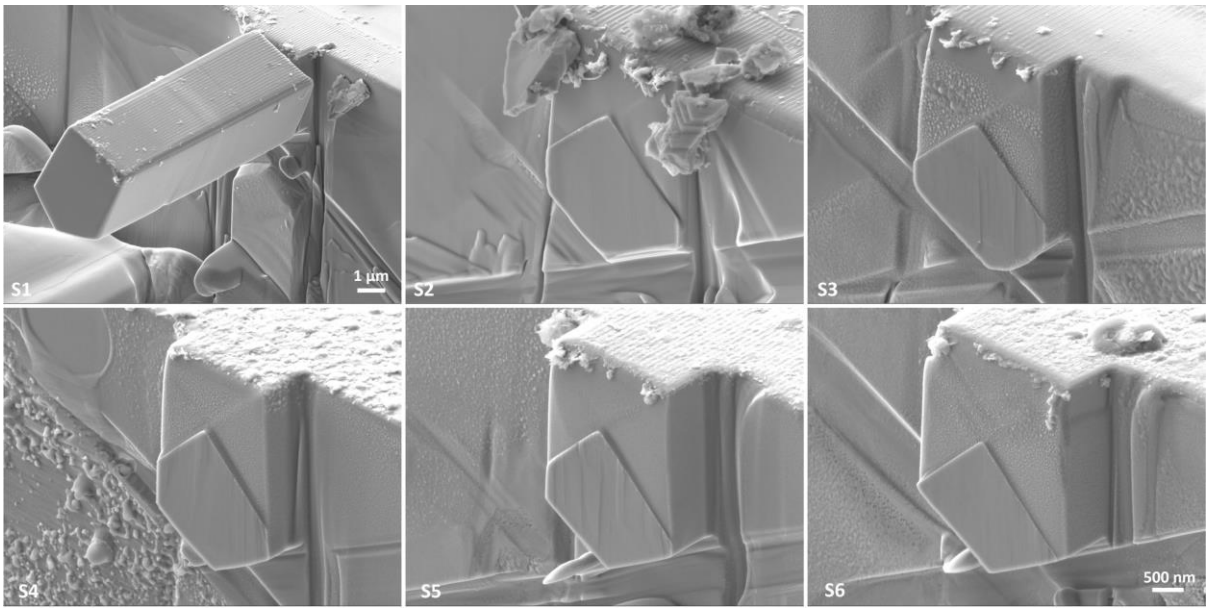


Figure 5.41. Fracture surface of the chevron notched cantilevers. The scale bar for S1 is different from the rest of the images.

Among all the six tested cantilevers, only S5 showed stable crack growth, with the rest of the cantilevers all exhibiting fast, unstable brittle fracture. The load-displacement curve of the cantilever S5 is shown in Figure 5.42. The stable crack propagation manifests as extensive plateaus, accompanied with a few stepwise increases in load, similar to that was seen in some of the Al_2O_3 cantilevers (Figure 5.19).

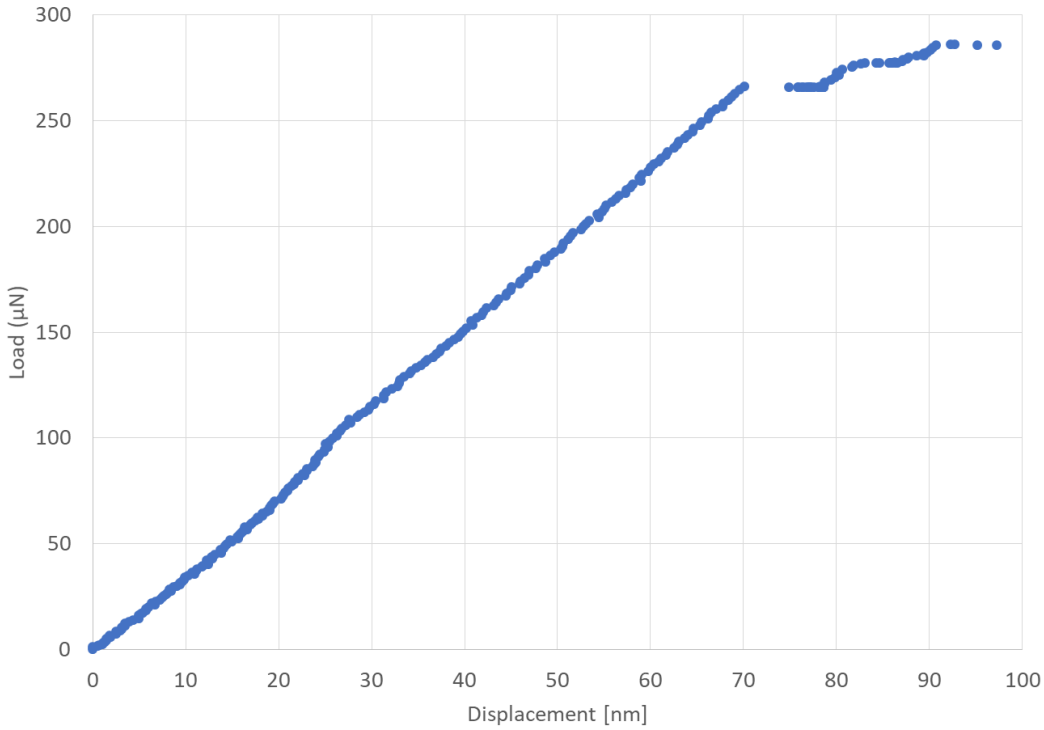


Figure 5.42. Load-displacement curve of cantilever S5

The dimensionless compliance C' and geometrical parameter Y(α') of S5 at multiple crack lengths interpreted numerically using FE models are shown in Figure A.4.

The apparent stress intensity factor K_p at the critical crack length α'_c calculated based on the peak load and minima of Y (α_c'), gives a value of 2.22 MPa·$m^{1/2}$, which is slightly higher than that measured in sapphire. The K_p values measured during the stable crack propagation is shown in Figure 5.43, showing values around 2.0 to 2.3 MPa·$m^{1/2}$.

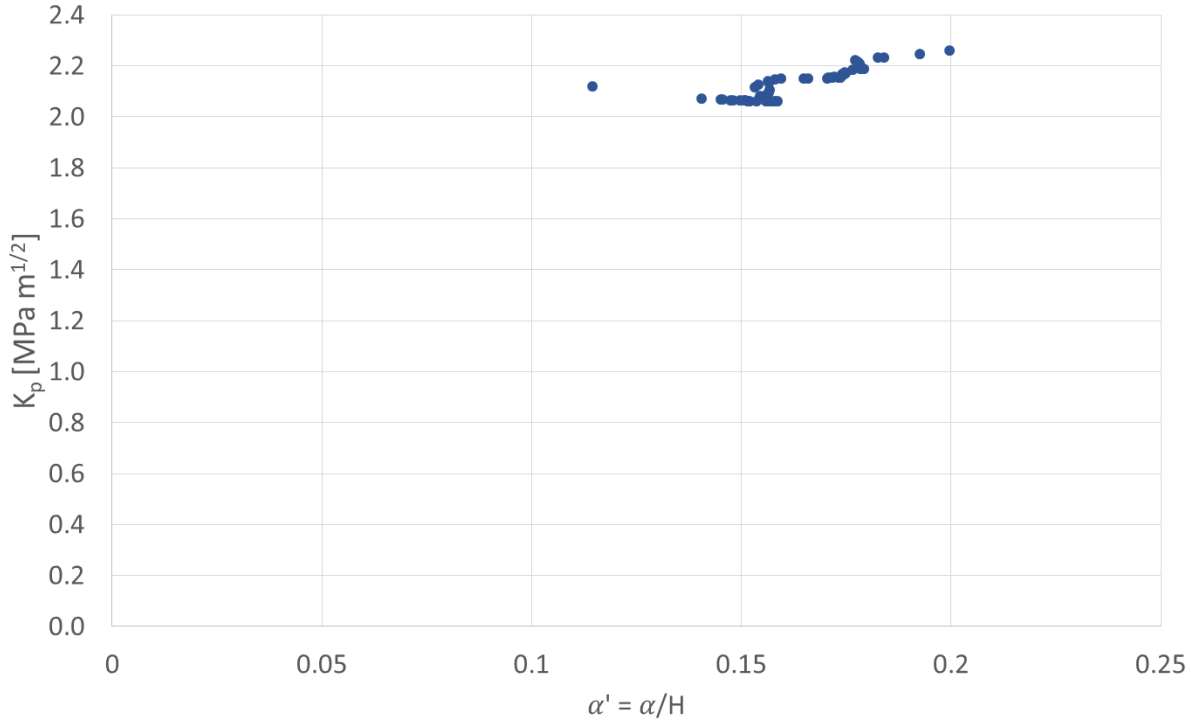


Figure 5.43. Fracture toughness measured during stable crack propagation in SiC cantilever tested in air.

The crack propagation curve in Figure 5.44 shows an average value of ~1.1×10^{-8} m/s during the stable crack growth.

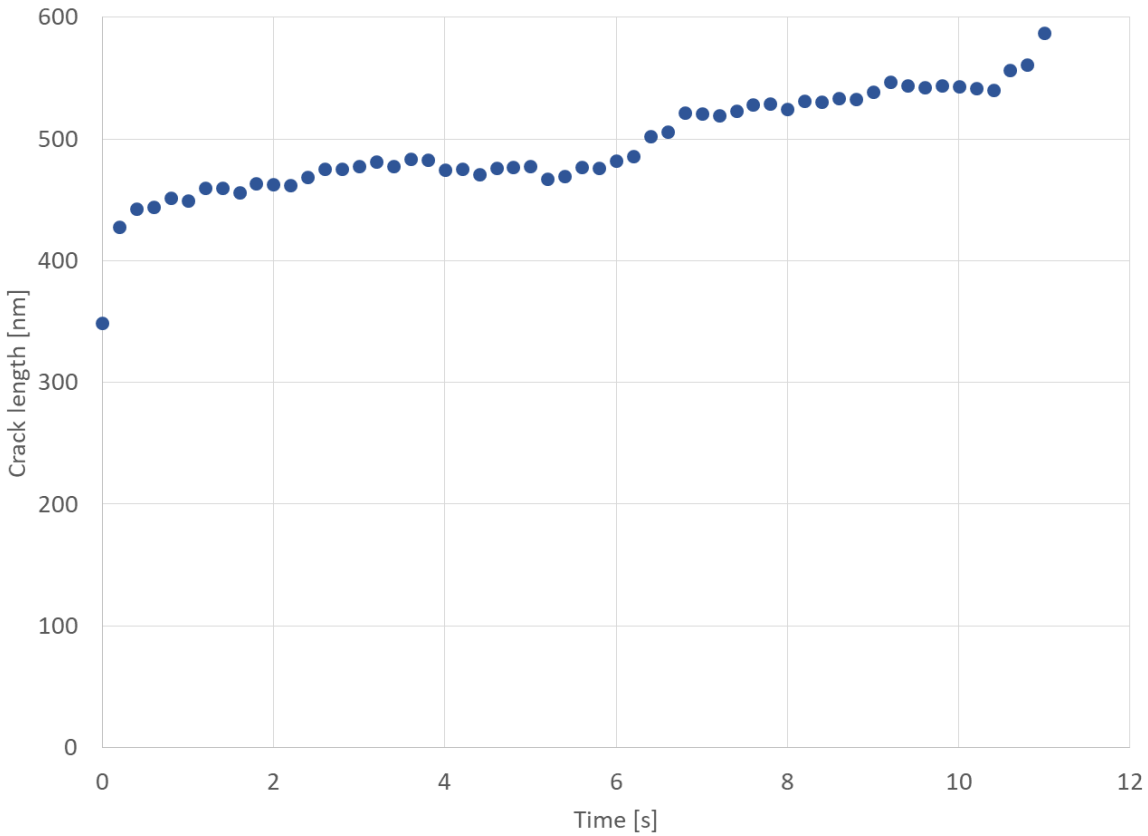


Figure 5.44. Crack length as a function of time during stable crack growth process, for SiC cantilevers S5 tested in air.

5.2.6 Summary of apparent fracture toughness values

The results from the toughness measurements in the present study are summarised in Table 5.7. For sapphire, K_p values of a-plane and m-plane measured in air are close to each other, exhibiting no crystallographic effect. K_c measured in vacuum is much higher than that measured in air. Obtained from test in air, K_p value of SiC is higher than that of Al_2O_3. The average crack velocities are all on the scale of 10^{-8} m/s, regardless of testing environment, target material or fracture location.

Table 5.7. Summary of the fracture toughness measurement in the present study using chevron-notched microcantilevers

Material	Fracture location	Environ-ment	Loading method	K_p at α'_c [MPa·m$^{1/2}$]	K_p measured during stable crack growth [MPa·m$^{1/2}$]	Crack velocity [m/s]
Al_2O_3	a-plane	air	monotonic	1.76	1.6 – 1.9	$2.8 \times 10^{-8} – 3.7 \times 10^{-8}$
	m-plane	air	monotonic	1.84	1.7 – 1.9	$2.1 \times 10^{-8} – 2.6 \times 10^{-8}$
	a-plane	vacuum	monotonic	2.84	2.5 – 2.8	$\sim 2.0 \times 10^{-8}$
	a-plane	vacuum	cyclic	2.84	2.6 – 2.8	$1.9 \times 10^{-8} – 2.2 \times 10^{-8}$
SiC	$(\bar{1}100)$	air	monotonic	2.22	2.0 – 2.3	$\sim 1.1 \times 10^{-8}$

5.3 Discussion

5.3.1 Validation and optimisation of numerical model

Both the analytical theories (i.e. Euler-Bernoulli and Timoshenko beam theories, which do not take the beam root into account), as well as the numerical model that did not contain a beam root, underestimated the beam compliance by a significant amount (Fig. 5.14). It is because the deformation of the beam root contributes to the deflection of the cantilever.[156] The importance of including the beam root in the numerical models to get the correct compliance values therefore becomes very clear, especially for the case where the drift correction is enabled by the compliance evaluated in numerical models as for monotonic test of sapphire in vacuum in the present study.

The investigation of the mesh size effect (Fig. 5.12) suggested that large mesh sizes led to underestimated values of compliance. Therefore, mesh size needs to be smaller than a threshold value to ensure the accuracy of modelling. The use of a graded mesh size system, as shown in the present study (Figure 5.15), is recommended to optimise the balance between the computational cost and the reliability of models.

Although the importance of validating the reliability of numerical models is generally recognised in the field of numerical simulations[12], it barely receives sufficient attention in experimental literature despite the wide application of numerical models for assisting empirical analysis. The present study shows the necessity of ensuring the reliability of numerical models as it affects directly the accuracy of fracture toughness values.

5.3.2 Subcritical crack growth in alumina and comparison of literature values of K_p

Table 5.7 shows that the stress intensity for crack propagation K_p for a-plane sapphire in vacuum was 2.8 MPa·m$^{1/2}$, while that for both a- and m-plane sapphire in air was much lower at 1.8 MPa·m$^{1/2}$, showing unequivocally that K_p measured in air was significantly affected by the moisture-assisted subcritical crack growth (SCG). Moreover, the crack velocities measured in the present study in air (i.e. on the scale of 10^{-8} m/s) were in the region where SCG would be expected to have a big effect (i.e. Region I) according to Figure 2.11b. Therefore, K_p values obtained in air were supposed to be close to the threshold stress intensity for SCG K_0, while K_p measured in vacuum which was much less affected by SCG represented K_C.

SCG data from published literature and the present study are summarised in Table 5.8, exhibiting wide variations, which is presumed to be mainly due to the difficulty of investigating low crack growth rates (especially with macroscopic specimens), the use of different test methods and procedures (e.g. testing rate and humidity). Nevertheless, the overall trend agrees with the fracture behaviour affected by moisture-assisted SCG – the exclusion of moisture by testing in oil/vacuum/inert gas significantly

increases apparent K_p values compared with the values measured in air and conversely testing under water reduces it.

Table 5.8. Reported K_p values for Al_2O_3

Environment	Fracture location	Testing scale	Crack rate [++]	K_p [MPa·m$^{1/2}$]	Source
vacuum	a-plane	micro	10^{-8} m/s	2.84 ± 0.05	Present study
oil	a-plane	macro	/	3.14 ± 0.30	Iwasa and Bradt[288]
	m-plane	micro	F	3.5 ± 0.2	Norton et al.[187]
dry nitrogen	a-plane	macro	S	2.31 ± 0.12	Salem[228]
	m-plane	macro	10^{-4} m/s	2.59 ± 0.29*	Wiederhorn[229]
air	a-plane	micro	10^{-8} m/s	1.84 ± 0.03	Present study
	a-plane	macro	S	2.06 ± 0.21	Salem[228]
	a-plane	micro	F	1.4 ± 0.2	Norton et al.[187]
	m-plane	micro	10^{-8} m/s	1.84 ± 0.08	Present study
	m-plane	macro	F	2.33 ± 0.07	Mitamura and Wang[294]
	Nano-crystalline	micro	S	2.34 ± 0.15	Mueller et al.[175]
water	m-plane	micro	F	0.9 ± 0.2	Norton et al.[187]
	m-plane	macro	S	1.94 ± 0.07	Salem[228]
	a-plane	macro	S	1.95 ± 0.03	Salem[228]

[++] 'F' denotes fast fracture. For stable fracture, if the crack velocity is reported, it is noted as the scale on which the crack velocity is, in the unit of m/s. If the crack velocity is not reported, 'S' is applied to denote slow/stable fracture.

*The value is converted from the m-plane fracture energy 7.3 J/m^2 as reported in the reference and based on the assumption of isotropy and E=430 GPa.

When a test is conducted in an environment where moisture is completed excluded, like oil, perfect vacuum or 100% inert gas, K_p is expected to be in Region III of the SCG curve (Figure 2.11a) and represents K_C.[127, 206] K_p measured in vacuum in the present study (2.8 MPa·m$^{1/2}$) lay between the values of those measured in oil (3.1 MPa·m$^{1/2}$ by Iwasa and Bradt[288] using macroscopic specimens and 3.5 MPa·m$^{1/2}$ by Norton et al.[187] using a microcantilever technique) and those measured in dry nitrogen, suggesting that a good vacuum level was achieved in the SEM chamber and therefore the measured K_p value is close to the intrinsic K_C of the material. The K_p values measured in dry nitrogen are generally lower than those measured in vacuum and oil, which is likely due to the inclusion of a certain amount of humidity in the commercial inert gas used in the experiments.

For the test conducted in air in the present study, due to the large amount of moisture in the testing environment (i.e. 53.6 ± 6.8% relative humidity), the effect of SCG is expected to be significant, therefore suggesting that the K_p values measured in air ($\approx$1.8 MPa·m$^{1/2}$ for both a- and m-planes) were close to the threshold value for SCG, K_0[206, 216], considering the very low crack velocity recorded. K_0 measured in the present study agreed to within experimental error with that reported by Salem[228] on a-plane using macroscopic specimens (2.06 ± 0.21 MPa·m$^{1/2}$). The K_0 value is likely overestimated by Mitamura and Wang[294] due to the relatively blunt saw notch (tip radius = 0.1 mm) employed in their measurements, therefore not comparable. The K_0 values reported by Norton et al.[187] (1.4 ± 0.2 MPa·m$^{1/2}$) involves big corrections for FIB implantation stresses and notch bluntness, which might have resulted in significant underestimation of K_0 values due to the potential over-correction of the implantation residual stresses according to the conclusion in Chapter 7 in the present DPhil thesis.

Although using the same chevron-notched microcantilever technique, the K_p values measured for nanocrystalline alumina by Mueller et al.[175] in air (2.34 ± 0.15 MPa·m$^{1/2}$) are higher than that measured in the present study in a similar environment. It is unlikely because that the effect of SCG is absent in their test as claimed by Žagar et al.[208], considering the moisturised testing environment and the slow crack velocity (which is not reported in their papers but should be close to that measured in the present study). The higher K_0 value reported by Mueller et al.[175] is potentially linked to the effect

of polycrystalline structure on the fracture toughness measurement, such as grain bridging toughening in polycrystalline alumina[295]. Moreover, it is possible that the K_p values are overestimated in Mueller et al.'s study[175] due to the imperfection of the numerical models, with the combined contribution of the following factors based on the discussion in Section 5.3.1. (i) The element size applied for meshing the models is not sufficiently fine (e.g. the elements at the free end of the beam are half size of the beam length), which makes the cantilever too stiff to deform correctly and therefore results in the underestimation of cantilever compliance. (ii) The indentation point is simulated as one single node, which causes load concentration and therefore unrealistic local deformation. (iii) The notch is placed at the interface between the beam and the support, which might result in an incorrect stress field around the notch area.

No test was carried out in water in the present study due to the unavailability of equipment capable of performing such a test and shortage of time, so literature values from tests in water become important for understanding the effect of SCG in toughness measurement. However, the results from the existing literature are highly scattered, with the $K_{0\,(water)}$ values reported by Salem[228] (1.94 ± 0.07 MPa·m$^{1/2}$) being much higher than that reported by Norton et al.[187] (0.9 ± 0.2 MPa·m$^{1/2}$). Such a significant difference may be attributed to the difficulties in performing the test in liquid environments, notably for tests conducted at microscopic scale. Moreover, as mentioned above, it is possible that Norton et al.[187] overcorrects the K_p values for implantation residual stresses given the results in Chapter 7 in the present study, therefore might have resulted in underestimation of $K_{0\,(water)}$ values.

5.3.3 Cyclic loading and self-healing

The intrinsic displacement control coupled with the chevron notch and sufficiently high stiffness of the nanoindenter, enabled multiple rounds of fracture toughness measurement using only one single cantilever through cyclic loading, with each aiming at a measurable and stable increase in crack length.

As the crack propagated further by the end of each cyclic loading, the longer crack length resulted in an increase of cantilever compliance. However, the slope of the first linear part of each cyclic loading

curves exhibited a good match with that from the 1st cycle (as shown in Figure 5.34 and Figure 5.36), indicating that the compliance remained the same during the elastic bending at the beginning of each loading cycle. This shows that the fracture surface retreated and healed itself upon withdrawal of the external load, which was enabled by the self-healing capability of alumina[296-298].

Although the crack reversibility in alumina has long been observed via TEM examination[298], with cracks initiated by indentation exhibiting spontaneous closure and healing, this is the first time that a quantitative measurement of the extent of the healing has been made. Figure 5.38 indicates that re-opening of the healed interface required a lower K_p ($\leq$ 1.6 MPa·m$^{1/2}$) than that was needed to propagate the crack in the pristine material ($\approx$2.6 MPa·m$^{1/2}$), demonstrating that the healed fracture surface did not fully recover its strength during the self-healing process. This strength degradation is potentially attributed to an incomplete restoration of the lattice across the separation interface. The 'lattice mismatch' caused by cleavage steps[299] is suggested to be the predominant source of obstruction to lattice restoration across the fracture interface.[298, 300] Additionally, intruding chemical species[297] (such as gas molecules, carbon contamination, etc.) from the SEM chamber might have been accommodated at the crack walls while they were closing up, which prevents the lattice from complete restoration.

It is also noted that $K_{p\ (healed)}$ decreased with the number of times the interface had healed, suggesting the accumulation of the effects preventing complete healing at the fracture interface during successive cycles.

5.3.4 Comparison of K_p values for SiC

The K_p value measured on the $(\bar{1}100)$ plane of 6H-SiC in the present study (2.2 MPa·m$^{1/2}$) agrees well with that measured using the nanoindentation technique[301] on the same fracture plane, as well as with the 'theoretical' value estimated using the density functional theory (DFT) calculations[215] (2.0 to 2.2 MPa·m$^{1/2}$, depending on the applied DFT theory). The K_p value from the present study is higher than that obtained on the (0001) plane using the double cantilever beam technique[215] (1.8 MPa·m$^{1/2}$),

which is potentially attributed to the anisotropic properties of the material – toughness values vary with crystal planes. As listed in Table 5.9, the variation of most of the reported K_p values seems to be within a conceivable range, taking into the consideration of the quoted errors, different measurement methods, variation in sample preparation, etc.

Table 5.9. Reported K_p values for 6H-SiC, measured using microscopic specimens

Fracture location	Environment	K_p [MPa·m$^{1/2}$]	Method	Source
$(\bar{1}100)$	air	2.22 ± 0.08	Chevron-notched microcantilever	Present study
(0001)	vacuum	1.80 ± 0.26	Double cantilever beam	Sernicola et al.[215]
(0001)	vacuum	2.01 – 2.18	DFT	Sernicola et al.[215]
$(\bar{1}100)$	air	2.4 ± 0.18	Nanoindentation	Kitahara et al.[301]
/	air	2.26 ± 0.07	Micropillar splitting	Liu et al.[302]
/	air	2.4 – 3.5	Straight-notched microcantilever	Frazer et al.[303]

Chapter 6. Reliable Measurement of Fracture Toughness at Microstructural Scale – Understanding the FIB Ion Implantation Damage – Part I. Microstructural Investigation

The ion implantation damage induced by FIB, the tool used for notching microscale specimens, affects the accuracy of fracture toughness measurement in certain materials. For microscopic features that are difficult to have fracture toughness measured reliably by enabling stable crack growth (e.g. natural grain boundaries), understanding the FIB ion damage therefore becomes crucial.

To clarify the extent of this effect, the present chapter presents a systematic TEM-based study at microstructural scale to reveal more details of the core nature of FIB ion damage from both conventional gallium FIB (Ga-FIB) and xenon plasma FIB (PFIB), in single crystal Al_2O_3 and SiC. FIBed notches were chosen as the investigated feature to match the actual geometry and ion damage status that are included in the microscale fracture toughness measurement.

6.1 Experimental

6.1.1 Materials and sample preparation

Two materials were chosen for the microstructural investigation: c-plane (0001) sapphire and single crystal (0001) 6H-SiC.

Ga^+ and Xe^+ implantations were carried out in a Zeiss Auriga dual-beam FIB with Ga source (Ga-FIB) and a FEI Helios Plasma dual-beam FIB with Xe source (PFIB), respectively. Each specimen was prepared with the following procedure (Fig.6.1). (1) The substrate was sputter coated with platinum (Cressington 208HR platinum coater) to induce conductivity. (2) In the FIB, a notch of 3 µm length was milled on the sample surface with defined FIB parameters (Section 6.1.2). Line milling was chosen as the milling pattern to mimic notching microcantilevers. (3) A strip of platinum was deposited on top to cover the exposed notch to protect the surface from additional ion damage during lamella preparation. The electron beam was employed for Pt deposition[304] rather than the ion beam to avoid

potential ion damage and contamination[305]. (4) Another notch was milled next to the previous notch with a gap of ~1.5 µm in between, again followed by being covered up with e-beam deposited Pt layer. (5) Repeat the previous step until the last notch was milled and covered with Pt. (6) An extra layer of Pt was then deposited on the top covering all the notches in a row to provide further protection to the sample for TEM lamella manufacturing.

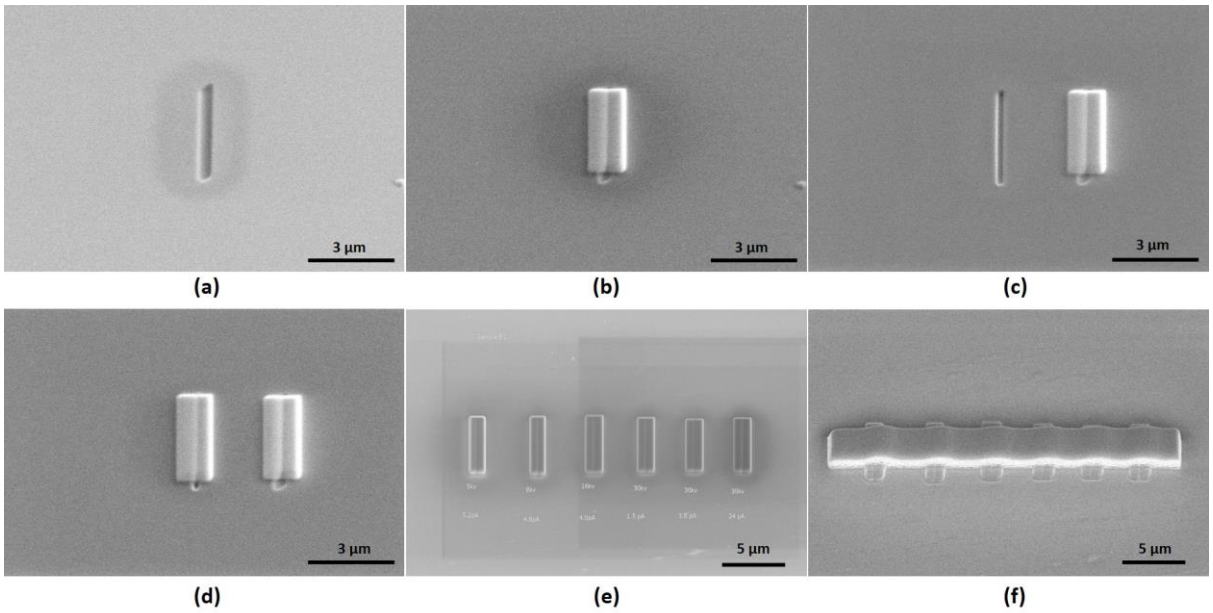


Figure 6.1. The preparation process for ion implantation samples. (a) Step 2. (b) Step 3. (c-d) Step 4. (e) Step 5. (f) Step 6.

Cross sectional TEM lamellas were produced, perpendicular to the longitudinal axis of the notches using a gallium-source dual-beam FIB (Zeiss NVision 40 FIB-SEM), with assistance from Dr. Ian Griffith, by following the following standard procedure (Fig.6.2). Trenches were dug on both sides until the standing lamella containing features of interest was thinned down to ~1 µm. The lamella was lifted out in-situ in the FIB-SEM and mounted to a copper grid. It was then thinned down further to less than 100 nm so that the electron transparency was achieved (Figure 6.3). As the last step, low voltage (2 keV) cleaning was applied to minimise any ion induced damage at the sample surface.

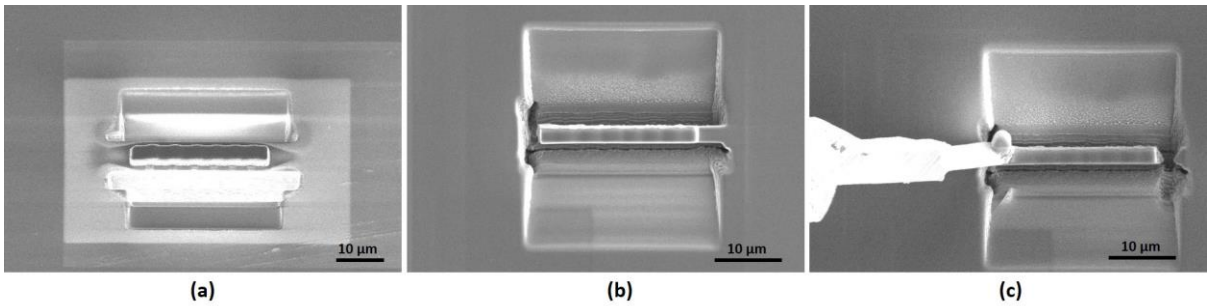


Figure 6.2. The process of TEM sample preparation. (a) Dig trenches on both sides. (b) Thin down the lamella to ~1 µm. (c) In-situ lift out of lamella.

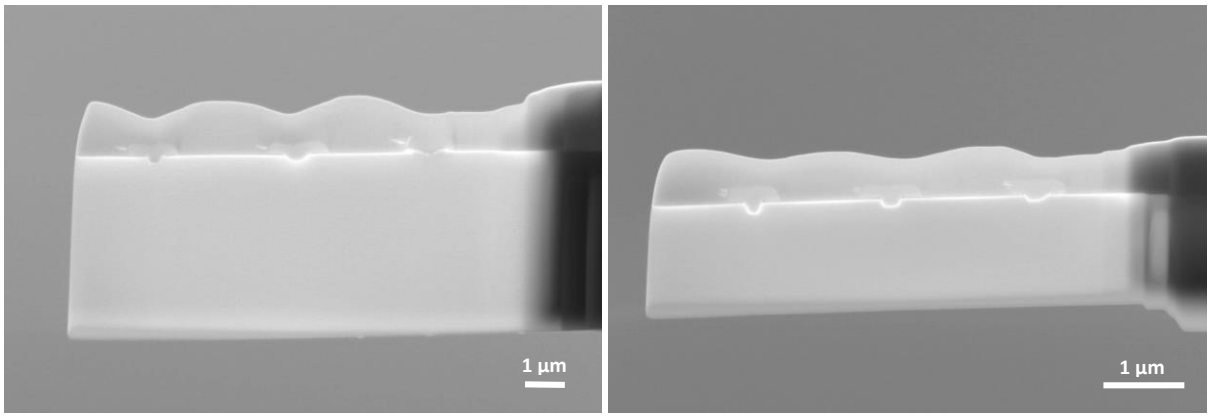


Figure 6.3. Two pieces of Al_2O_3 TEM specimens, with each containing three notches milled by PFIB under different FIB conditions. Thicknesses of the specimens were measured to be ~70 nm, with electron transparency fully achieved under 5 keV.

6.1.2 FIB conditions

As listed in Table.6.1, five variables were taken into consideration for investigating their respective influences over the ion damage.

- Target material
- Ion species
- Ion dose
- Beam acceleration voltage
- Beam current

Other than these five variables, the other parameters were held constant, e.g. the normal incidence angle.

Table 6.1. The summary of the FIB ion damage experiment, with a range of target materials, ion species and FIB parameters. The ones coloured in grey were in the original plan but failed during TEM sample preparations. These failed experiments were not repeated due to lack of time, therefore no result was available for them.

Ion species	Target Material	Voltage [keV]	Current [pA]	Dose [x10^9 ion/µm]	Ion species	Target Material	Voltage [keV]	Current [pA]	Dose [x10^9 ion/µm]
Ga^+	Al_2O_3	15	250	3.1	Xe^+	Al_2O_3	5	5.2	2.9
		15	250	15.6			8	4.8	2.9
		30	240	3.0			16	4.0	2.9
		30	5	3.0			30	1.5	2.9
		30	20	3.0			30	3.8	2.9
		30	1000	4.2			30	24	2.8
Ga^+	SiC	15	250	3.1	Xe^+	SiC	5	5.2	2.9
		15	250	15.6			8	4.8	2.9
		30	240	3.0			16	4.0	2.9
		30	5	3.0			30	1.5	2.9
		30	20	3.0			30	3.8	2.9
		30	1000	4.2			30	24	2.8

Acceleration voltage. Two voltages (15 and 30 keV) were chosen in the Ga-FIB and four voltages (5, 8, 16 and 30 keV) in the PFIB, based on the existing settings and conditions of the machines. Despite having a wider range of available voltages (i.e. 1, 2, 5, 15 and 30 kV), the Ga-FIB only had 15 and 30 kV usable for the present research purpose due to the unsatisfactory status of the other voltages.

Beam current. The currents applied in the Ga-FIB ranged from 5 pA to 1000 pA. Big gaps were set to enhance any difference in implantation behaviour. The currents used in the PFIB were kept within the low range (up to 24 pA) due to its high milling speed. The currents were not in continuous values in the equipment and only a selection of defined currents were available in the existing built-in programs. Therefore, 5 pA (Ga-FIB) and 3.8 pA (PFIB) were the closest values to each other within the range of interest and the difference was considered as negligible, as it was for 20 pA (Ga-FIB) vs. 24 pA (PFIB).

Ion dose. Two highly different ion doses were applied under 15 keV 250 pA with Ga-FIB. For the rest of the combinations, the dose was kept constant: ~ 3.0 x 10^9 ion/µm (the values were not exactly the same due to the differences in currents and equipment settings).

By grouping the listed experiments in a systematic fashion, the influence of each variable could be analysed separately. For instance, the combination of (Ga^+_Al_2O_3_30keV_5pA) vs. (Xe^+_Al_2O_3_30keV_3.8pA), or (Ga^+_Al_2O_3_30keV_20pA) vs. (Xe^+_Al_2O_3_30keV_24pA) can be compared to study the effect of implanted ion species.

6.1.3 SEM and TEM characterisation

A Zeiss Merlin SEM coupled with EDX detector was employed at 5-10 keV 500 pA for the Energy-Dispersive X-ray Spectroscopy (EDX) examinations in SEM. A JEOL-2100 TEM and a JEOL-300F TEM were used at 200 keV and 300 keV, respectively, for High-Resolution TEM (HR-TEM) imaging and EDX examination in TEM.

A JEOL-ARM200F STEM was used at 200 keV accelerating voltage for studying the Xe^+ implanted Al_2O_3. The 0.03 nA beam current (Probe 8C 30 µm aperture) was applied for STEM imaging. EDX and Electron Energy Loss Spectroscopy (EELS) coupled in the STEM were applied to examine the chemical composition of features of interests, with beam currents of 0.14 nA and 0.04 nA (Probe 5C 30 µm aperture) respectively.

EELS was also used to measure the thickness of the selected sample area. The thickness was derived by Poisson statistics of inelastic scattering[306]:

$$t = \lambda \ln(\frac{I_t}{I_0})$$

where I_0 is the integral of zero-loss peak counts, I_t is the integral of total spectrum counts (zero-loss peak + extrapolated loss part). The mean free path of the scattering λ was estimated to be 115.1 nm for Al_2O_3 (40 atom% Al (13) + 60 atom% O (8)) at 200 keV, using the method developed by Malis *et al.*[306]. The intensities of the spectra were analysed using Gatan DigitalMicrograph software.

TEMs were operated by Dr. Ian Griffith and Dr. Neil Young, from the David Cockayne Centre for Electron Microscopy (University of Oxford). All the rest of the work (i.e. SEM operation, data processing and analysis, etc.) were carried out by the present author.

6.2 Results

6.2.1 Ga^+ in Al_2O_3

Table.6.2 summarises the milling conditions for the six notches milled in Al_2O_3 using the Ga-FIB. Notches No.⑤ and ⑥ were damaged and destroyed, respectively, during the TEM lamella preparation (Fig.6.4). No relevant data was therefore available for analysis in the following studies.

Table 6.2. The overview of the Ga^+ implantation damage in Al_2O_3

Ion specie & Target Material	No.	Voltage [keV]	Current [pA]	Dose [x10^9 ion/µm]	Notch depth [nm]	Thickness of amorphous layer [nm]	Thickness of crystalline damaged layer [nm]	Total thickness of damaged layers [nm]
Ga^+ in Al_2O_3	①	15	250	3.1	95	25	~20	~45
	②	15	250	15.6	416	25	~56	~81
	③	30	240	3.0	179	40	~46	~86
	④	30	20	3.0	232	41	~42	~83
	⑤	30	5	3.0	/	/	/	/
	⑥	30	1000	4.2	/	/	/	/

Fig.6.4 gives an overview of TEM microstructure of the six notches, showing their shapes and depths. The comparison of notches No.③, ④ and ⑤ showed that under a constant voltage, a lower beam current delivered a sharper notch with smaller mouth width due to the smaller size of aperture. The notch was consequently deeper with the same ion dose. Comparing notches No.① and ③ (similar beam current and ion dose), higher voltage led to deeper notch. It is because either the 30 keV beam sputtered off more materials than the 15 keV beam, or the 15 keV beam was not well aligned, which provided a broader beam and thus a larger irradiated area.

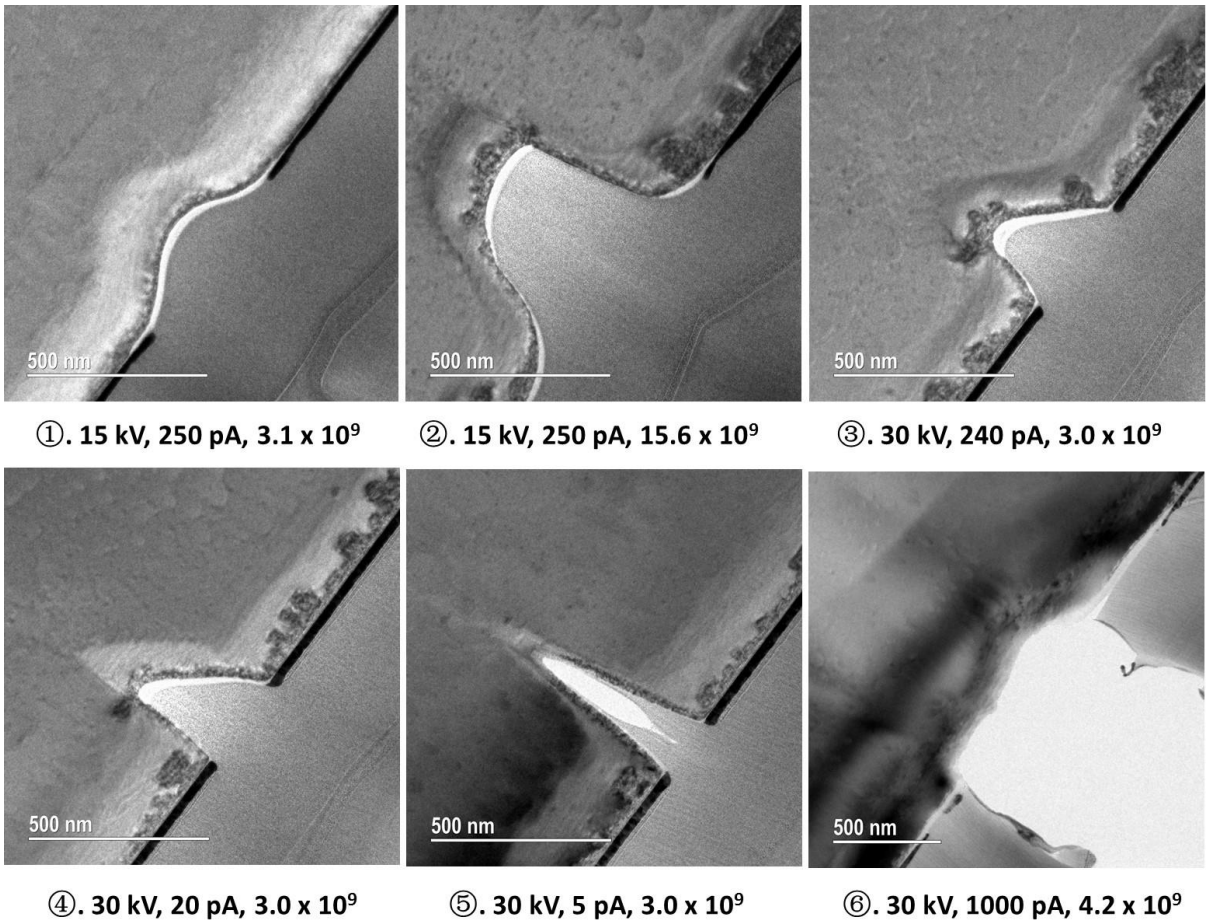


Figure 6.4. Low magnification TEM images of the notches FIBed under different conditions (voltage, current, ion dose [ion/μm]). Target material: Al_2O_3. Ion species: gallium. The notches ⑤⑥ were damaged during sample preparation so they were not usable.

Fig. 6.5 shows bright-field images for each usable notch (No.①-④). The main features can be categorised into the following four layers. ***(Layer No.I)*** This layer on top of the target material was *the platinum protection layer*. ***(Layer No.II)*** *L*ocated at the top surface in the target material along the notch profile and was therefore in direct contact with the incident ions, this layer was amorphised by the energetic ion bombardment and was thus also named as the '*amorphous layer*'. (***Layer No.III***) *Crystalline damaged layer*. This layer was the second damaged layer of the target materials, right beneath *layer No.II*. The crystallinity in this layer was partially preserved, because the dose and energy of the ions it received did not reach the threshold values to cause the loss of the long-range order in the lattice structure despite the existence of damage. (***Layer No.IV***) The material beneath the *layer No.III* was beyond the reach of ion damage and thus remained undamaged. This denotation system of different layers will be applied throughout the rest of the thesis.

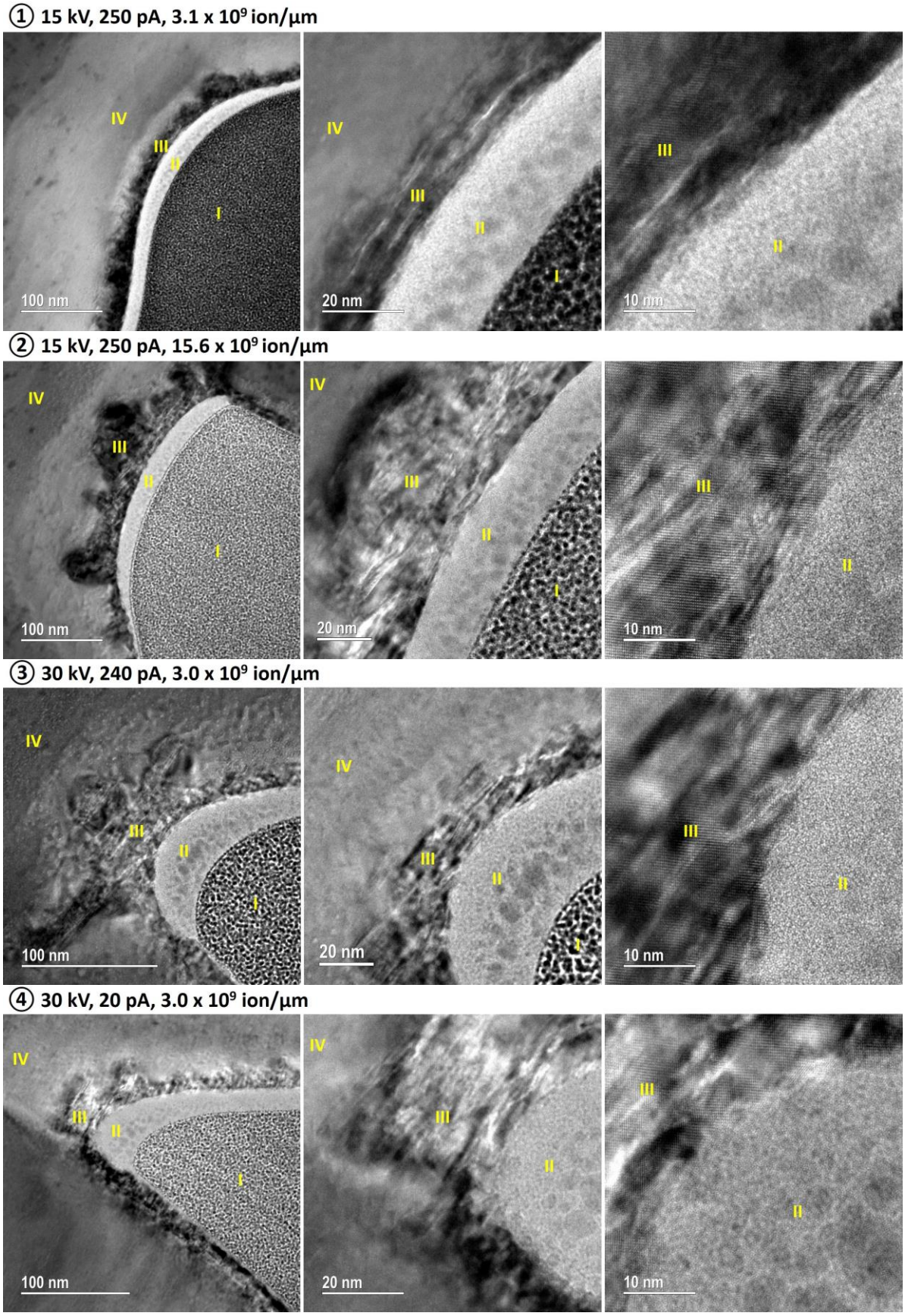


Figure 6.5. TEM bright-field images showing four notches of Al_2O_3 Ga-FIBed under different FIB conditions. (a) Notch tips. (b) A closer look at the notch tips. (c) Displayed at an even higher magnification, revealing more details such as lattice arrays. Layers I – II are indicated in the images. In Layer IV, the top part around the notch tip exhibits brighter contrast than the rest of the layer due to special FIB milling behaviour around features during TEM sample preparation.

Despite the variety in FIB conditions, all the four notches exhibited *Layers No.I - IV*. The largest amorphisation thickness was always found at the bottom of each notch, where the ion beam incident angle was 0°. Particles were observed embedded within all the amorphous layers, appearing darker than the surrounding material.

Comparing notches No.①, ②, ③ and ④, the thickness of the amorphous layer thickness (Table 6.2) was found to remain the same with the same voltage, or was thicker with a higher voltage, regardless of applied current and dose.

Notch ③ was selected for a series of EDX investigations to examine the chemical compositions. The mapping of element distribution (Fig.6.6) in a SEM showed a high concentration of Ga in the amorphous layer, while the high Ga density did not seem to extend to the crystalline damaged layer.

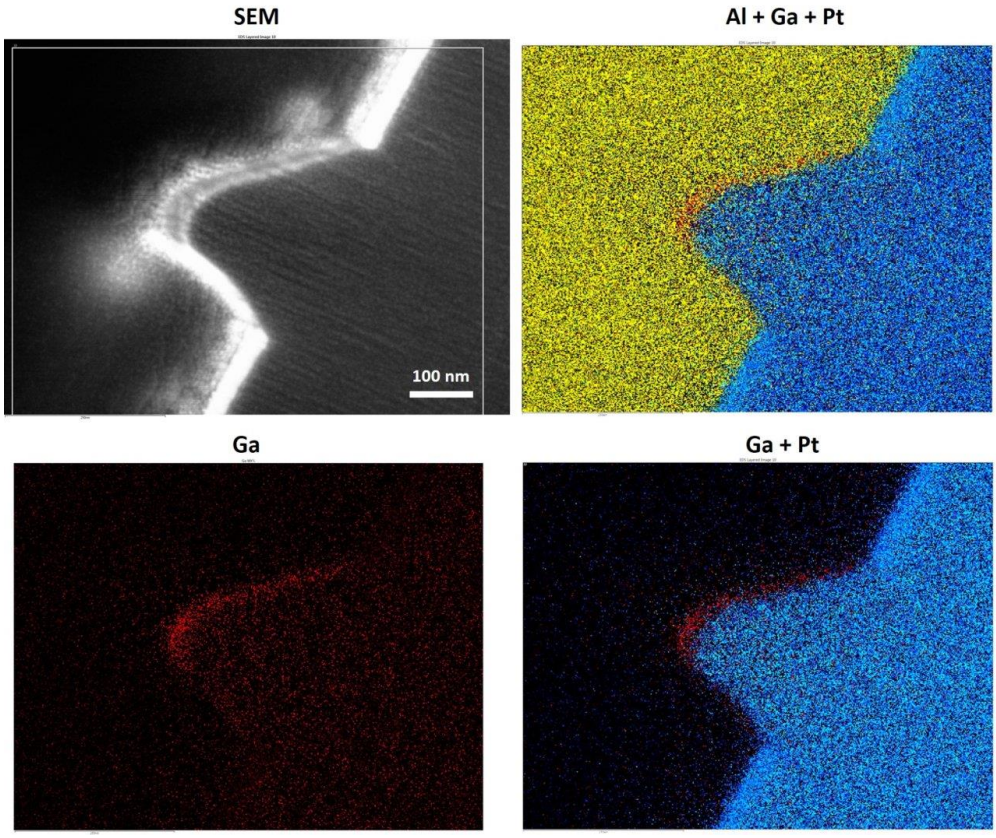


Figure 6.6. SEM-EDX mapping of the notch No.③. The mapped area is framed in the white box in the SEM image. Yellow, red and blue mark the distribution of Al, Ga and Pt elements respectively.

EDX coupled with HAADF was employed to reveal further information at a smaller scale, focusing at the amorphous layer in order to find out the chemical compositions of the embedded particles. As shown in Fig.6.7, four points within the particles (points No. 1, 2, 3 and 6) and two points within the background material of the amorphous layer (points No. 4 and 5) were selected for examination. The result (Table 6.2 and Fig. 6.8) showed that the particles and the surrounding background materials had notable differences in their chemical compositions, with the average atomic ratio of Ga:Al:O rounded to 1:1:3 in the former while being 1:5:10 in the latter.

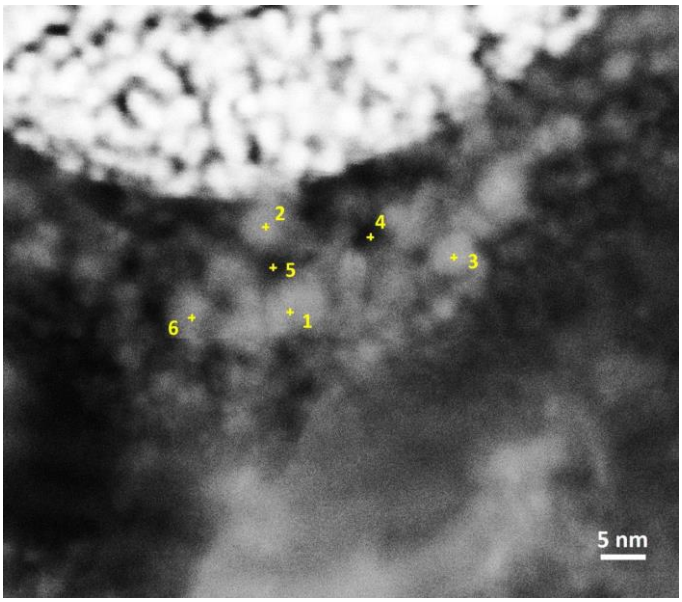


Figure 6.7. HAADF-STEM image of the notch tip of Ga^+ implanted Al_2O_3 with six points within the amorphous layer selected for EDX examination

Table 6.3. The atomic percentage of the detected elements in the indexed points

	Within particle feature					Within background		
	1	**2**	**3**	**6**	**average**	**4**	**5**	**average**
O	47.5	58.4	54.4	56.1	54 ± 2	61.4	59.3	60 ± 1
Al	23.0	24.3	28.3	26.1	25 ± 1	31.8	31.9	32 ± 0
Ga	26.8	11.5	16.4	17.8	18 ± 3	5.3	7.1	6 ± 1

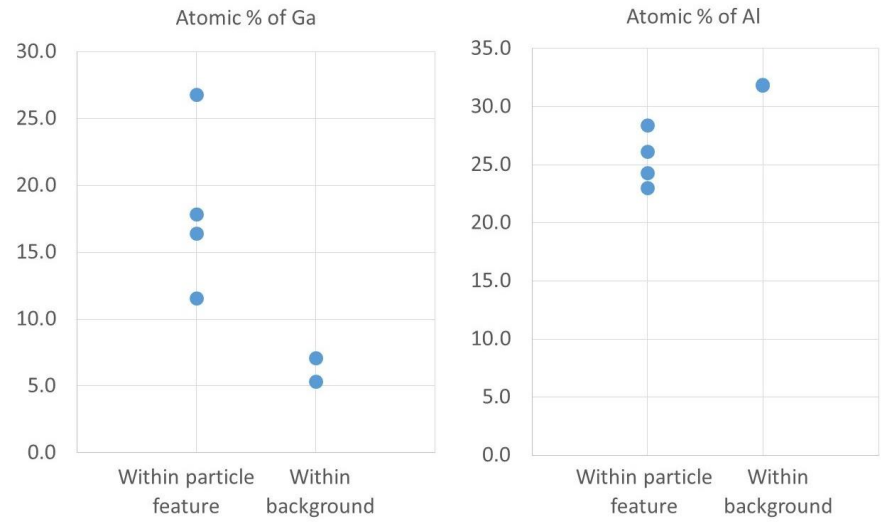


Figure 6.8. Atomic % of Ga and Al detected in the indexed 6 points, showing the difference between the particles and the surrounding materials.

An EDX line scan (Fig.6.9) shows the variation of elemental concentrations along the implantation depth. The atomic concentration of Ga peaked clearly at the places where the particles were located. The densities of Al and O dropped down slightly at the places where there were rises in atomic% of Ga, and vice versa, which agreed with the result from the EDX point scan in Fig.6.7.

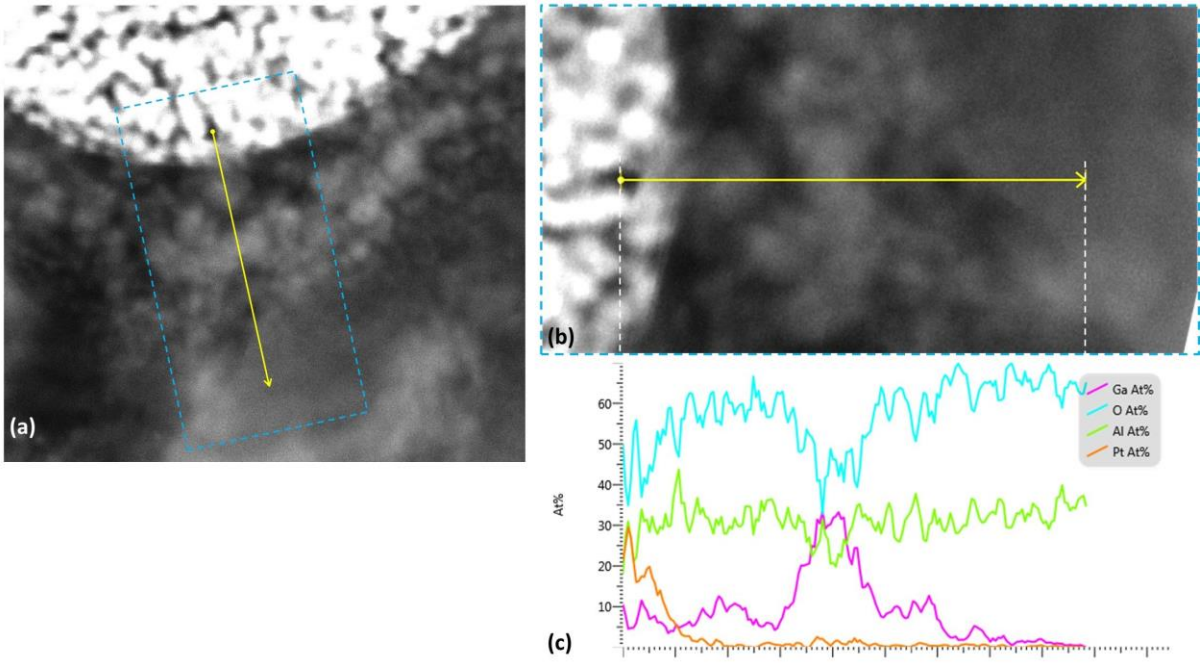


Figure 6.9. STEM-EDX line scan across the amorphous layer, starting from the platinum layer and extending to the crystalline damaged layer. (a) TEM image of the notch No.③. The yellow line indicates the scanning path with the arrow pointing towards the scanning direction. (b) The zoomed-in TEM image of the blue-dash framed area in (a), showing details of the scanned area at a high resolution. (c) The atomic percentages of the detected elements along the line scan.

A HAADF-EDX mapping (Fig.6.10 and Fig.6.11), providing an overview of the element distribution at the nanoscale, confirmed once again that the concentration of Ga followed the shape of the particles in the amorphous layer.

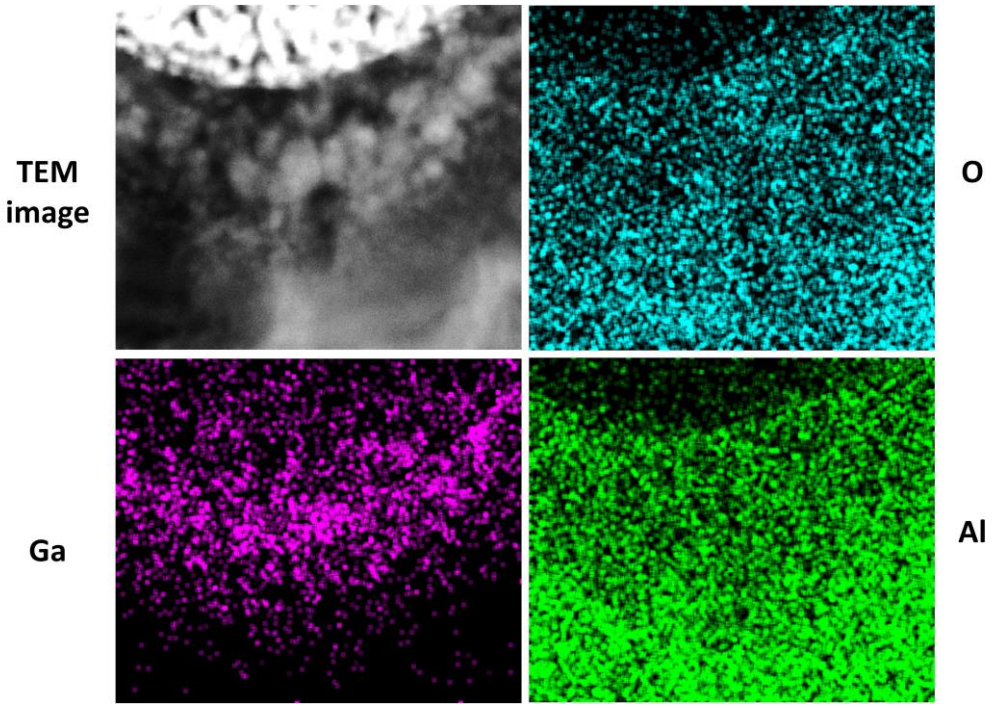


Figure 6.10. HAADF-EDX mapping showing the distribution of Ga, Al and O.

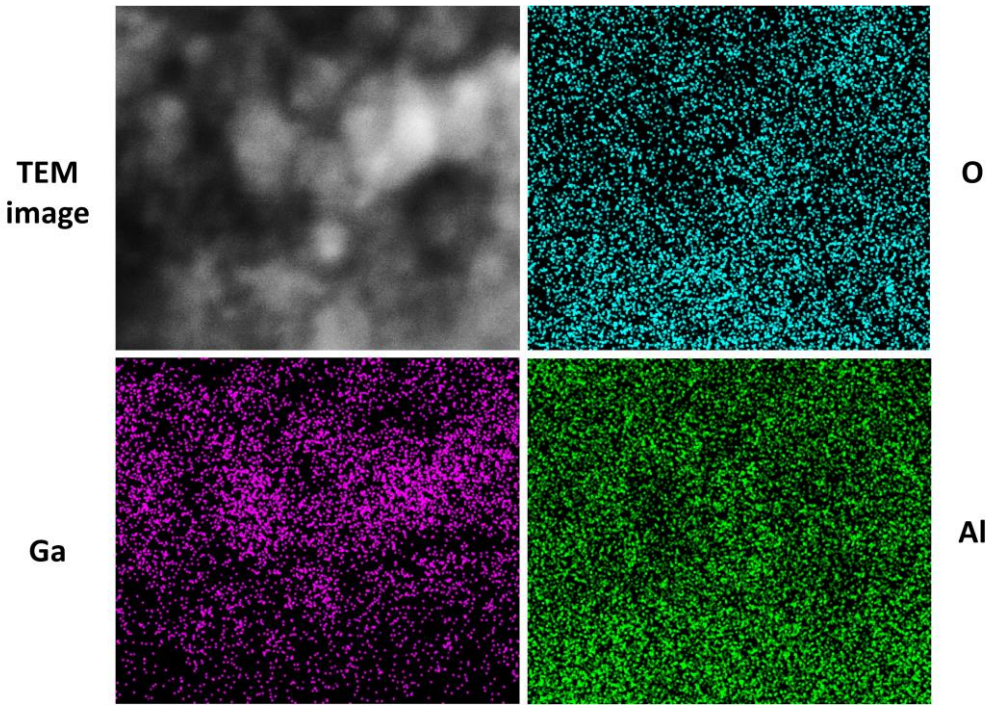


Figure 6.11. HAADF-EDX mapping within the amorphous layer

6.2.2 Ga^+ in SiC

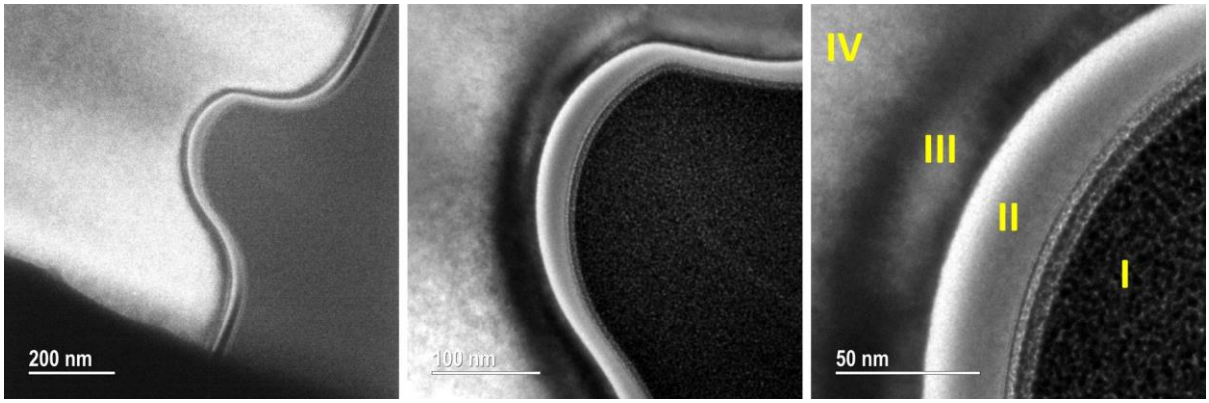
Seven notches were prepared in SiC using the Ga-FIB (Table.6.4).

Table 6.4. The overview of the Ga^+ implantation damage in Al_2O_3

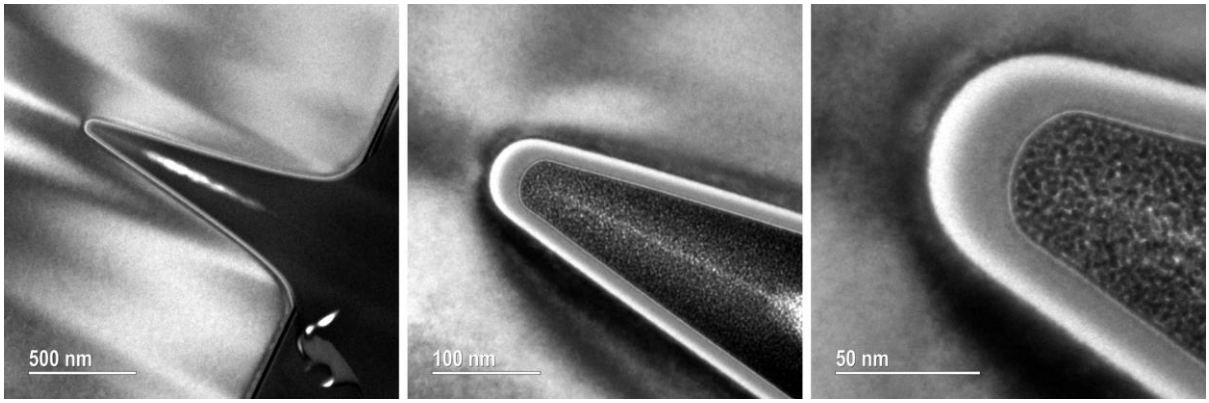
Ion specie & Target Material	No.	Voltage [keV]	Current [pA]	Dose [x10^9 ion/µm]	Notch depth [nm]	Thickness of amorphous layer [nm]	Thickness of crystalline damaged layer [nm]	Total thickness of damaged layers [nm]
	①	15	250	3.1	238	30	6	36
	②	15	250	15.6	595	30	5	34
	③	30	240	3.0	497	50	8	58
Ga^+ in SiC	④	30	20	3.0	595	50	5	55
	⑤	30	5	3.0	512	50	7	57
	⑥	30	1000	4.2	127	50	3	53
	⑦	30	1000	12.5	403	50	4	54

Same as observed in Ga-FIBed Al_2O_3, SiC also exhibited layers *No.I – IV* (Fig.6.12). However, compared with its counterpart in Ga-FIBed Al_2O_3 where particles were observed, the amorphous layer in Ga-FIBed SiC showed no particle or similar feature. Moreover, the amorphous layer was composed of two parts - the top sub-layer exhibited a darker contrast than the lower sub-layer, with both sub-layers appearing to be uniform. *Layer No. III* appeared thinner with less severe damage in SiC than that in Al_2O_3 (Fig.6.5) with the same FIB conditions.

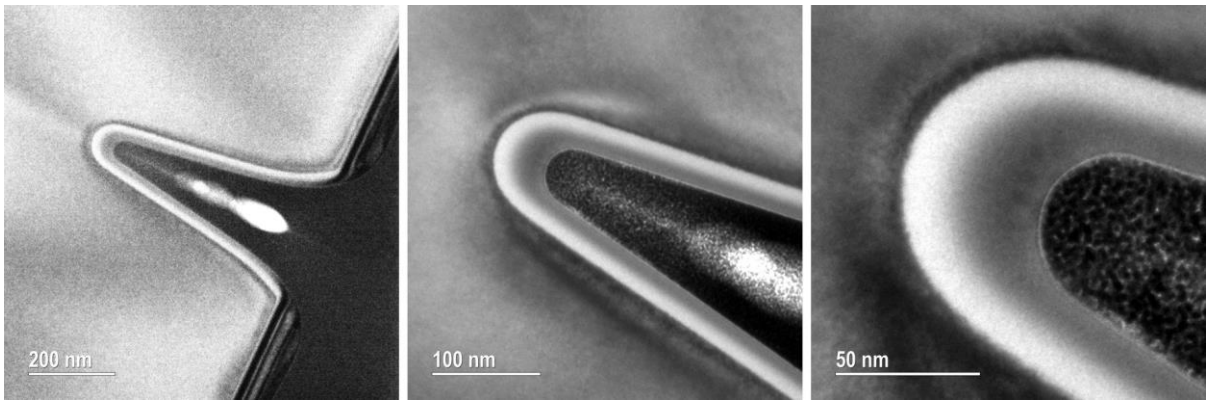
① 15 kV, 250 pA, 3.1 x 10^9



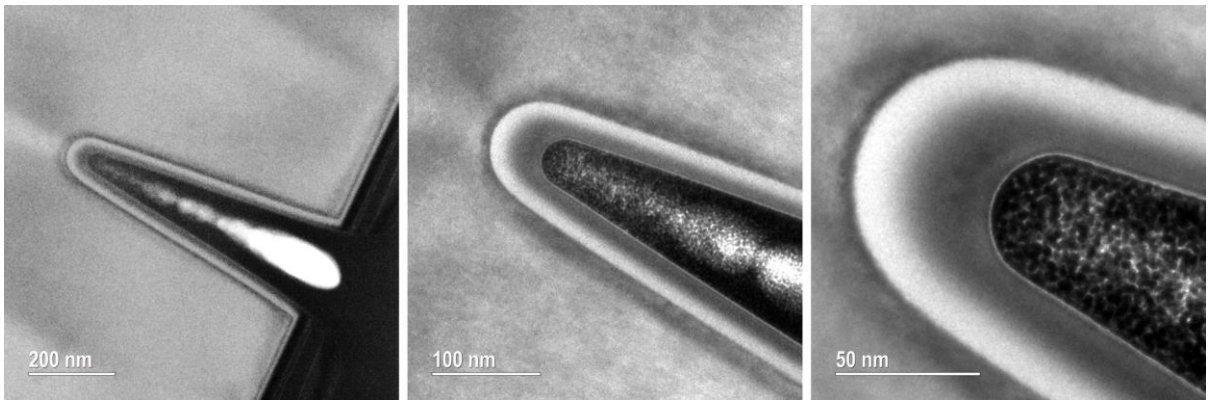
② 15 kV, 250 pA, 15.6 x 10^9



③ 30 kV, 240 pA, 3.0 x 10^9



④ 30 kV, 5 pA, 3.0 x 10^9



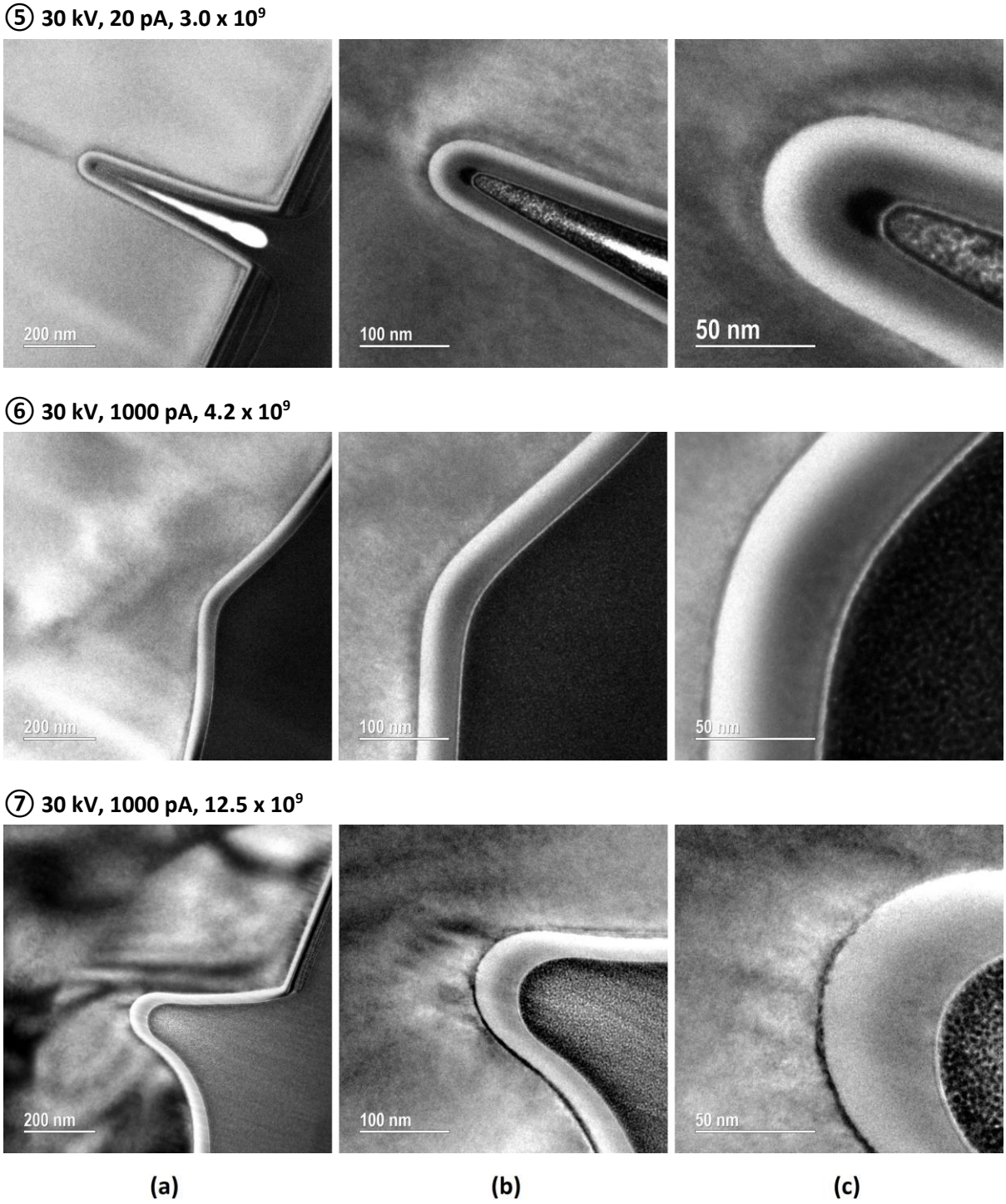


Figure 6.12. STEM-BF images showing seven notches of SiC Ga-FIBed under different FIB conditions. (a) The overview of the notches showing the shapes and milling depths. (b) Focusing at notch tips at higher magnifications. (c) A closer look at the notch tips, revealing more details of the Ga-FIB damage in SiC. Please note the differences in some of the scale bars. The images are separated into two pages.

According to the distribution of the elements detected by SEM-EDX (Fig.6.13), Ga concentrated in the amorphous layer along the profile of the notch. Due to the limit of resolution in the SEM image, it was hard to tell if Ga had extended to the crystalline damaged layer. Si was also detected in the damaged material but the quantity was lower than that in the undamaged material.

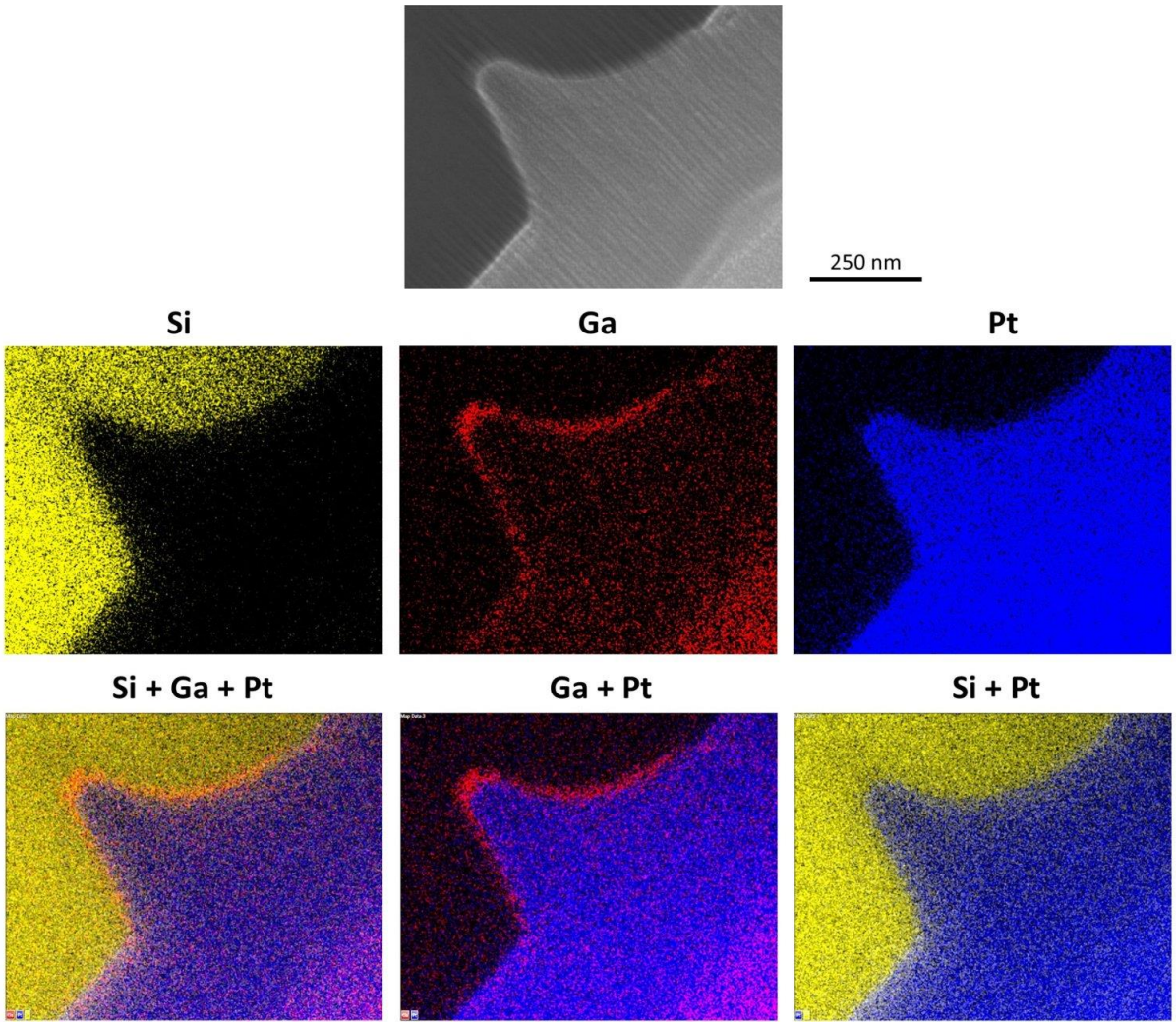


Figure 6.13. SEM-EDX mapping of Si, Ga and Pt elements in Ga-FIBed SiC (Notch No.⑦)

The mapping was followed by EDX line scans on the same specimen (Fig.6.14). The concentration of Ga was found to peak at the damaged layers. The quantity of Si increased gradually along the depth of the damaged material, until a constant value was achieved when reaching the undamaged material. The concentration of C is not displayed in Line 1 scan because the carbon contamination on the surface of the TEM foil exceeded the amount of C detected in SiC.

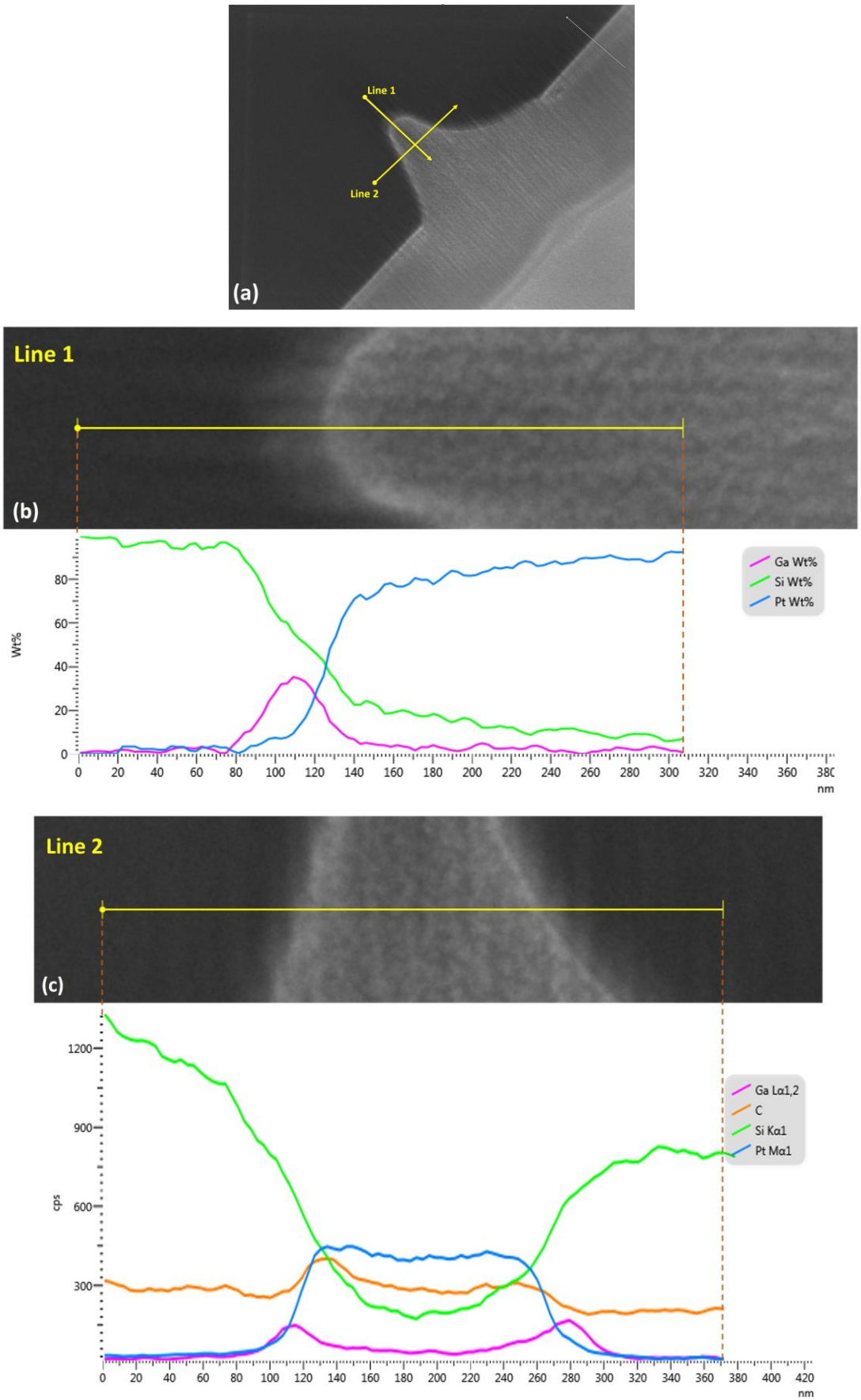


Figure 6.14. SEM-EDX line scan across the tip of notch ⑦. (a) Overview of the two line scans across the examined notch. (b) Line scan No.1, originated from the undamaged material, crossed the damaged layers and extended to the Pt protection layer. (c) Line scan No. 2, across the notch tip from undamaged material on one side of the notch to that on the other side.

HAADF-EDX examination (Fig.6.15) confirmed the observation from the SEM-EDX examination (Fig.6.13, 6.14): the damaged material contained both Si and Ga, while the amount of Si in the damaged material was lower than that in the undamaged area.

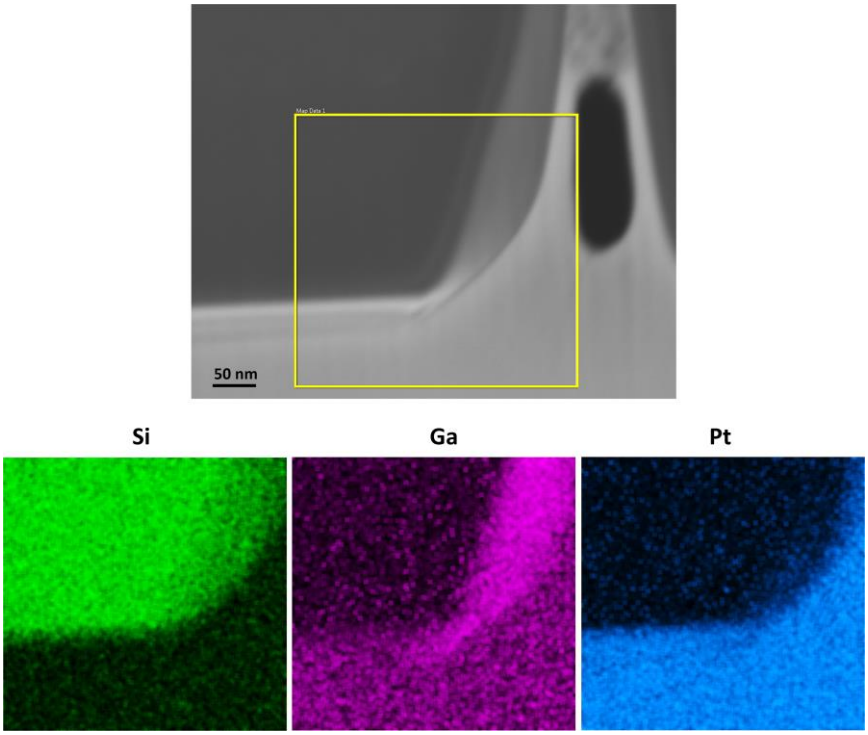


Figure 6.15. HAADF-EDX maps exhibiting atomic% of detected elements (Si, Ga and Pt).

6.2.3 Xe^+ in Al_2O_3

Six notches were prepared in Al_2O_3 using the Xe source PFIB (Table.6.5).

Table 6.5. The overview of the Xe implantation damage in Al_2O_3

Ion specie & Target Material	No.	Voltage [keV]	Current [pA]	Dose [x10^9 ion/µm]	Notch depth [nm]	Thickness of amorphous layer [nm]	Thickness of crystalline damaged layer [nm]	Total thickness of damaged layers [nm]
	①	5	5.2	2.9	120	9	~11	~20
	②	8	4.8	2.9	205	11	~10	~21
Xe^+ in Al_2O_3	③	16	4.0	2.9	214	17	~8	~25
	④	30	1.5	2.9	125	27	~14	~41
	⑤	30	3.8	2.9	222	30	~14	~44
	⑥	30	240	2.8	309	28	~14	~42

Notches milled using the PFIB (Fig.6.16) were blunter than that milled using the Ga-FIB (Fig.6.4). Note that in notches ① and ③, the e-beam deposited Pt protection layer was not directly attached to the target material and was separated by a layer of vacuum trapped in place during the Pt deposition.

As observed previously with Ga^+ implantation, both the thickness of the amorphous layers and the total thickness of damaged layers here increased with FIB voltage. With the same voltage (i.e. 30 keV), the thicknesses of amorphous layer, crystalline damaged layer and the entire damaged layer remained almost constant, regardless of milling current or dose.

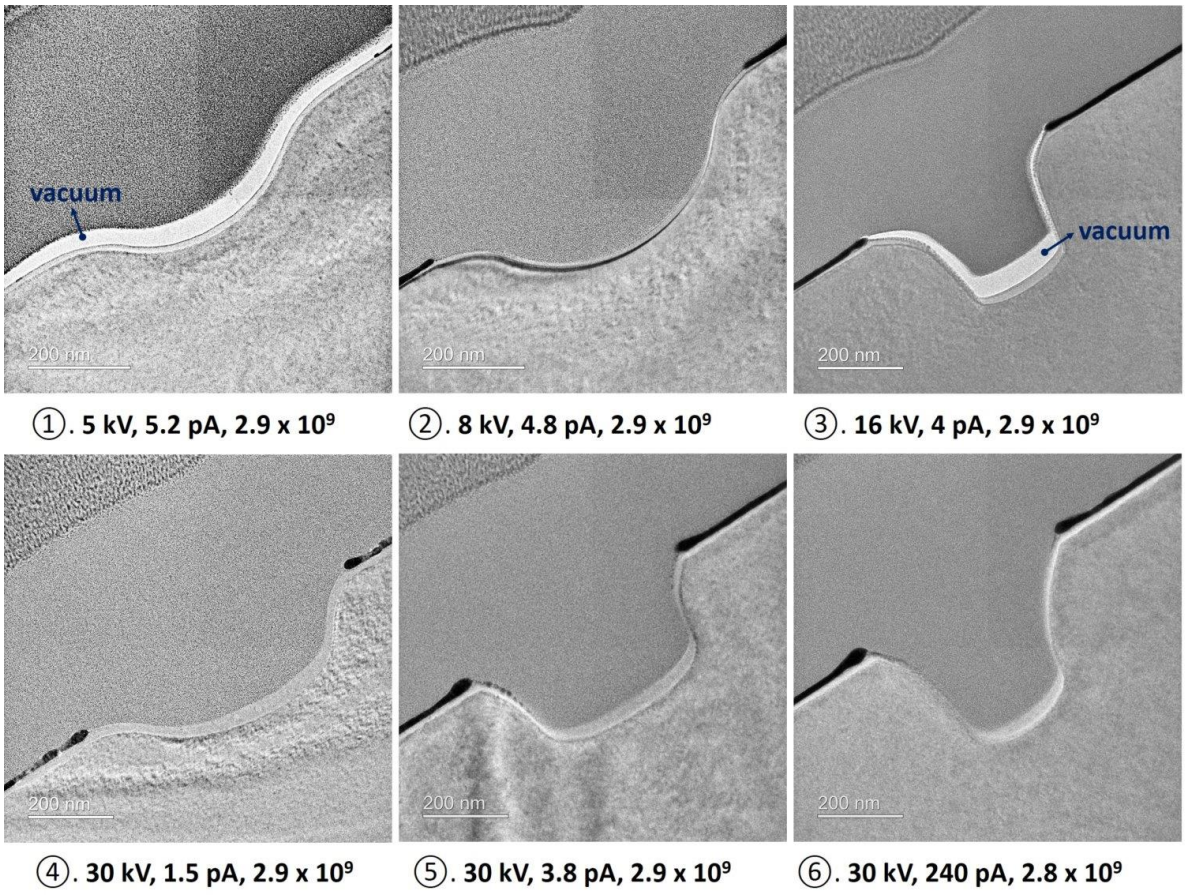
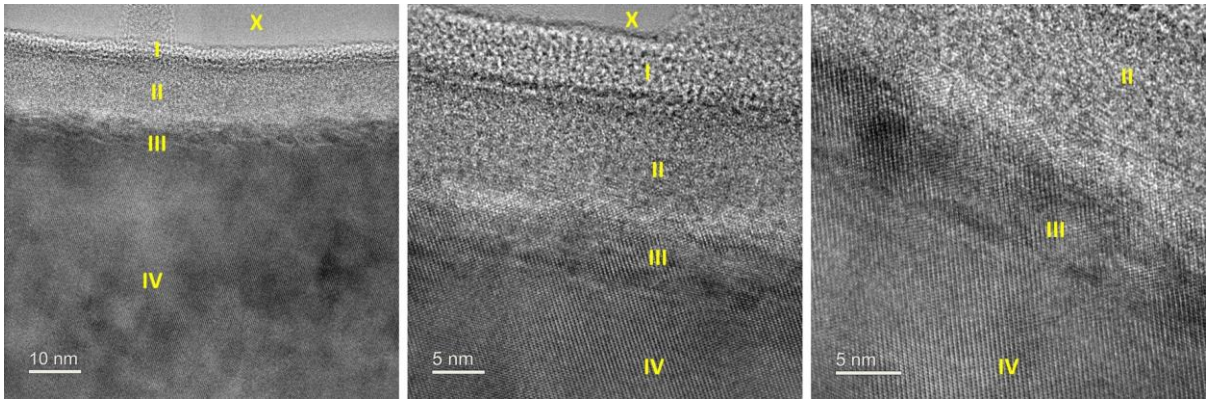


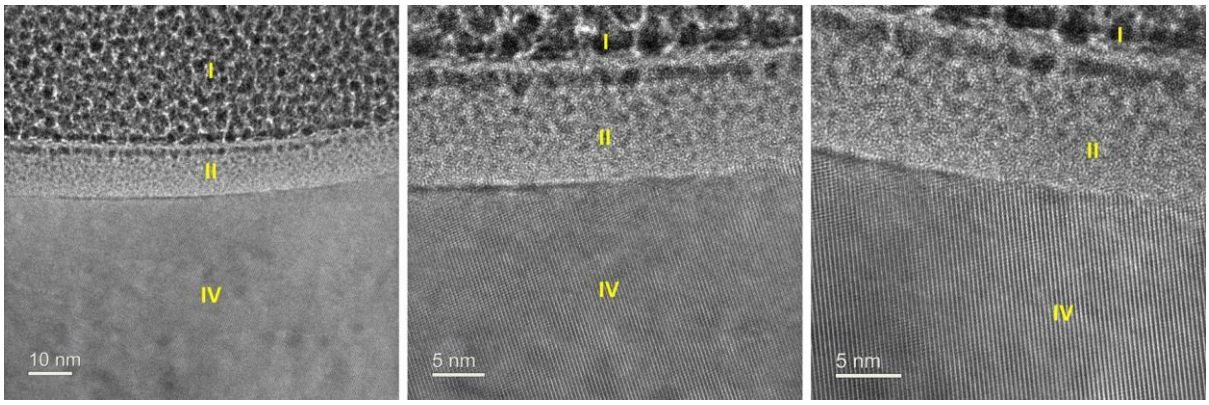
Figure 6.16. Bright-field TEM images of the six notches PFIBed in Al_2O_3 using a range of FIB conditions.

Each notch was investigated with HR-TEM to reveal information of the ion damage at the lattice scale (Fig.6.17). Different layers were annotated using the same naming system as defined previously (i.e. *layer No.I - No.IV*) as the response was similar to that was observed earlier. Additionally, *Layer No.X* in the micrographs is the vacuum trapped accidently between the Pt protection layer and the protected target. Under the similar FIB conditions, the damaged layers developed here by Xe^+ implantation appeared to be thinner than that created by Ga^+.

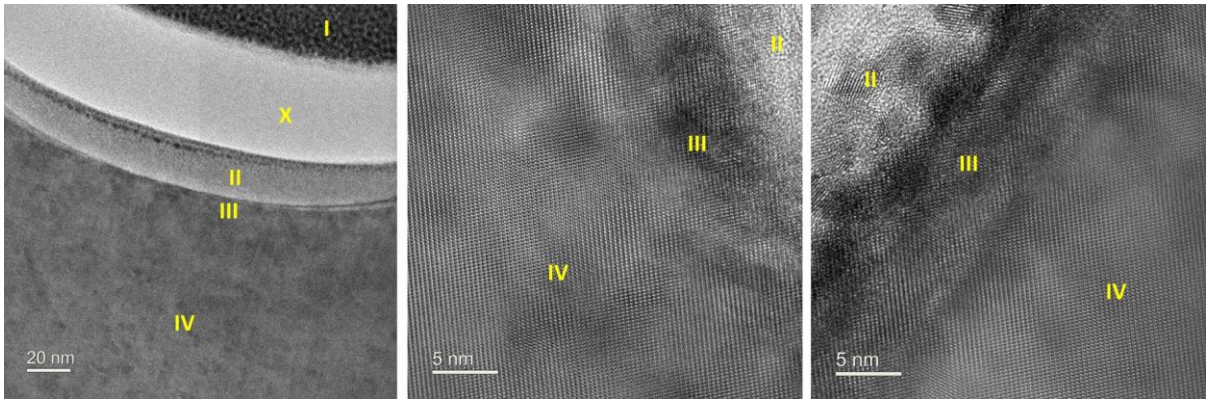
① 5 kV, 5.2 pA, 2.9×10^9



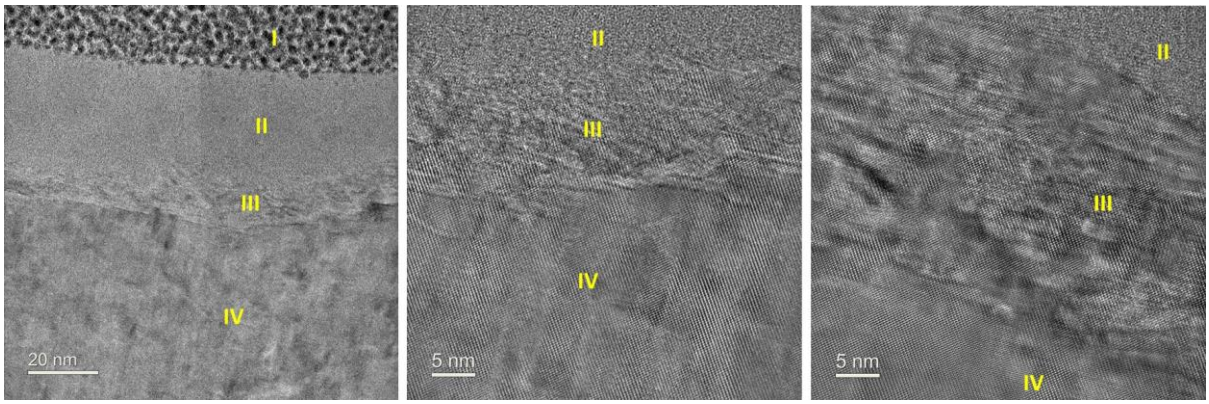
②. 8 kV, 4.8 pA, 2.9×10^9



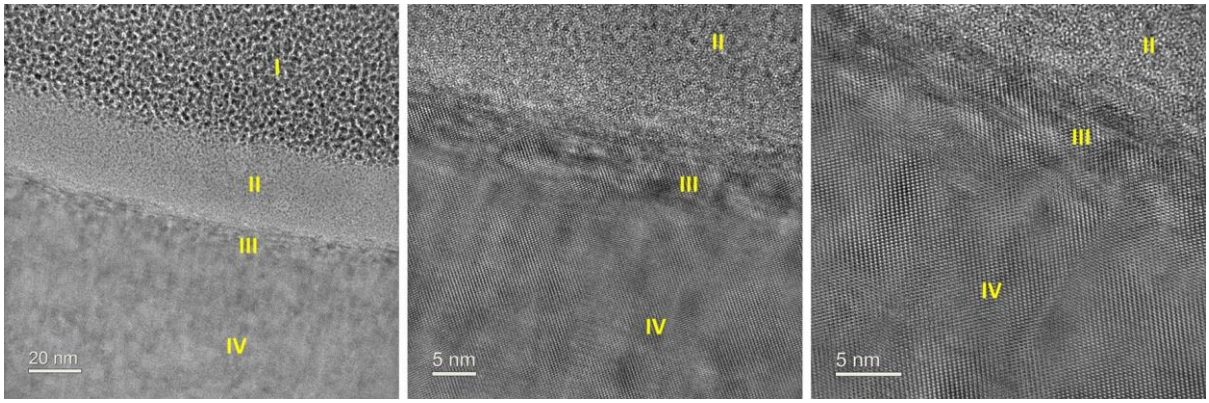
③. 16 kV, 4 pA, 2.9×10^9



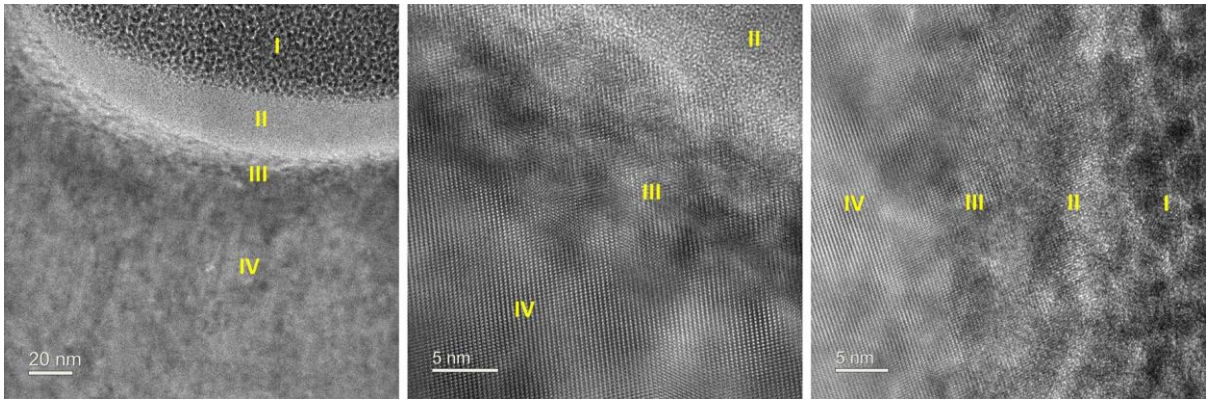
④. 30 kV, 1.5 pA, 2.9×10^9



⑤. 30 kV, 3.8 pA, 2.9×10^9



⑥. 30 kV, 240 pA, 2.8×10^9



(a) **(b)** **(c)**

Figure 6.17. On-axis HR-TEM bright-field images of the six PFIBed notches in Al_2O_3, showing the lattice damage. Layer I – Pt protection layer, II – amorphous layer, III – crystalline damaged layer, IV – undamaged material, and X – vacuum layer. (a) overview of notch tip. (b)(c) imaging at higher magnifications exhibiting the details of crystal lattice. Please note that the images are separated into two pages.

Fast Fourier Transform (FFT) patterns were generated for the following six selected areas in Notch ④ for the examination of the crystallinity quality (Fig.6.18). (*a*) A big bubble was found in the middle of the amorphous layer. (*b*) A few small bubbles at the bottom of the amorphous layer. Only diffuse rings were seen in the FFT patterns (*a)* and (*b).* In the amorphous layer, since the electrons were absorbed and scattered in arbitrary directions due to lattice disruption, the intensity of TEM background noise increased and the contrast was reduced significantly.[257] (*c*) The top crystalline damaged layer which was adjacent to the amorphous layer. Due to the disordered structure, the atoms were no longer perfectly aligned in columns compared to the undamaged region, which led to the reduction of the quality and uniformity of lattice fringe contrast. The reciprocal lattice started to appear in the FFT pattern from this layer on. (*d*) The bottom crystalline damaged layer which was further away from the

amorphous layer. There was a much reduced amount of damage in this area compared to the top crystalline damaged layer, exhibiting clearer crystal lattice. (*e*) An area of severer damage within the bottom crystalline damaged layer. It showed that the damage left by ion bombardment in the bottom of the crystalline damaged layer was not uniformly distributed but was in the form of damage clusters. The furthest point that the ion damage reached was at depth of ~65nm. (*f*) Undamaged material which showed a clear crystalline structure.

A gradual transition from amorphous to crystalline was observed across the damaged layers.

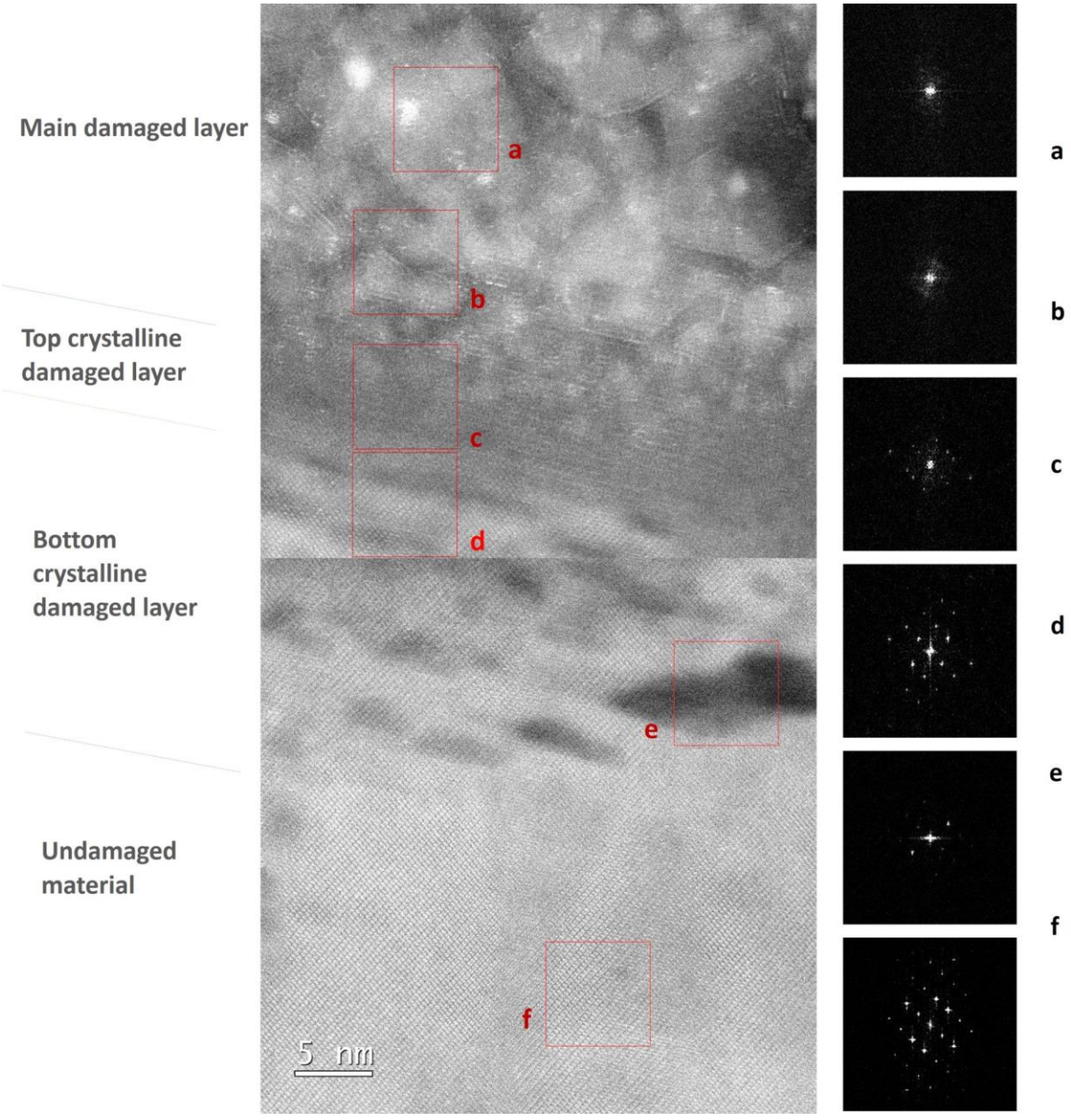


Figure 6.18. HR-TEM images of the structure across the damaged and undamaged area, with FFT of selected domains.

Compared to Fig.6.16 where the notches were imaged under TEM mode, the HAADF images (Fig.6.19) exhibited enhanced contrast differences and thus revealed more compositional information in the amorphous layers.

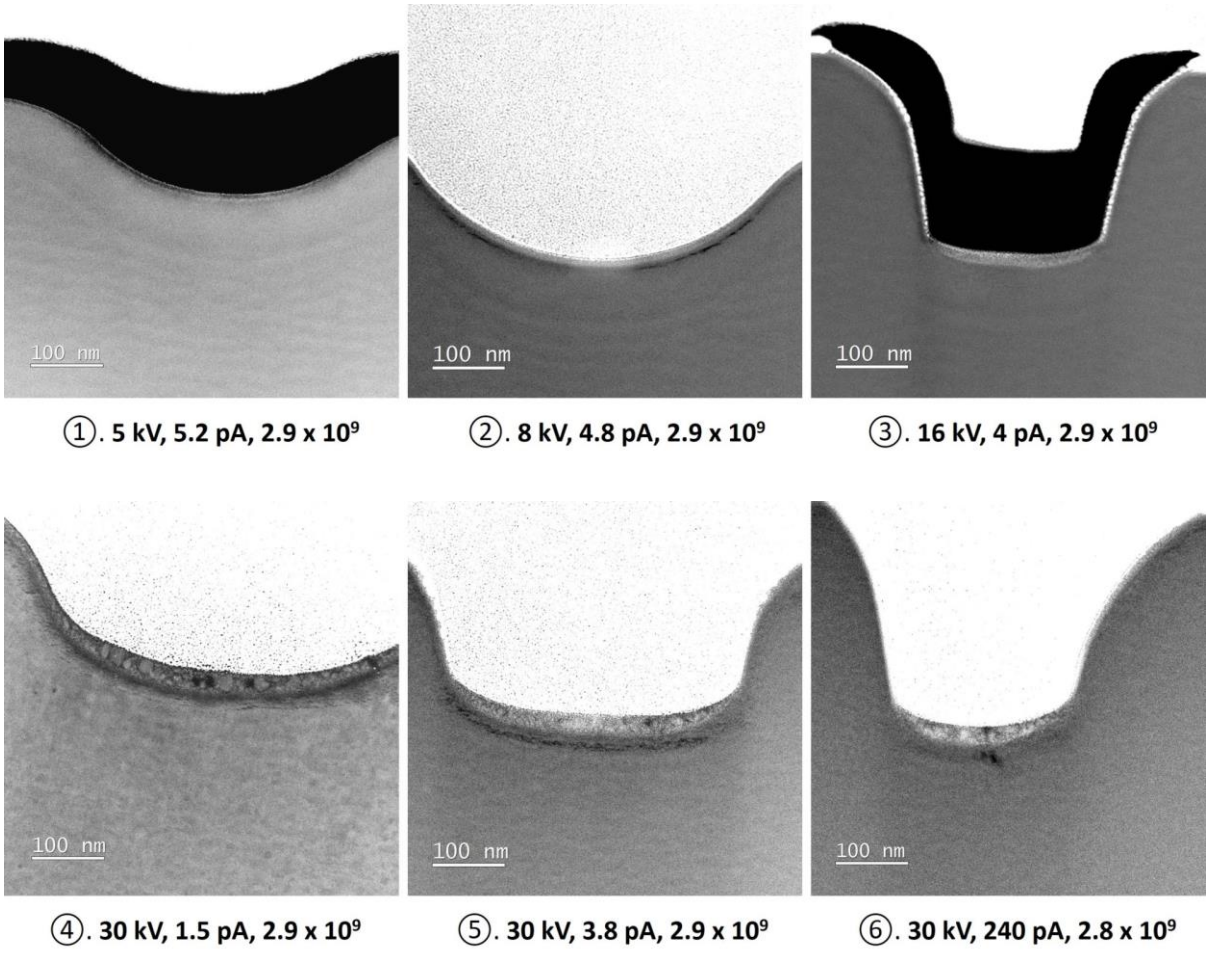
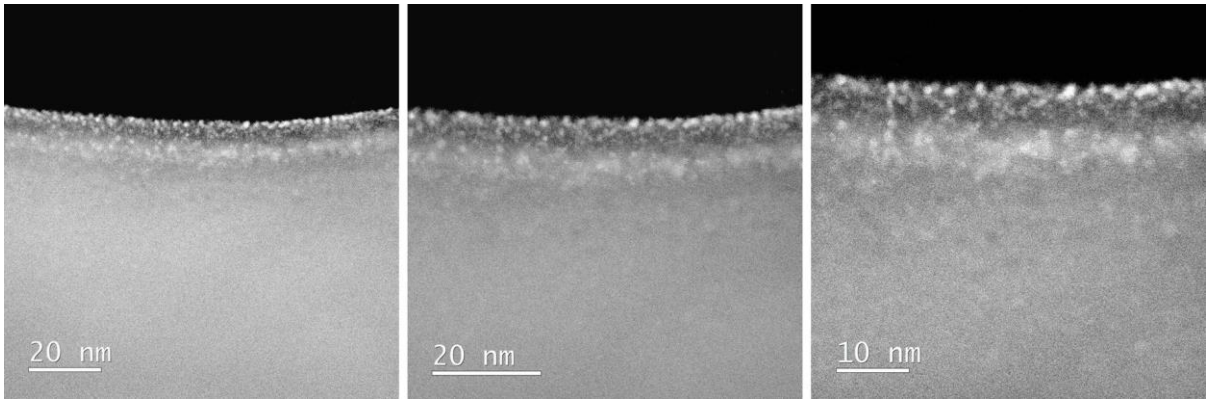


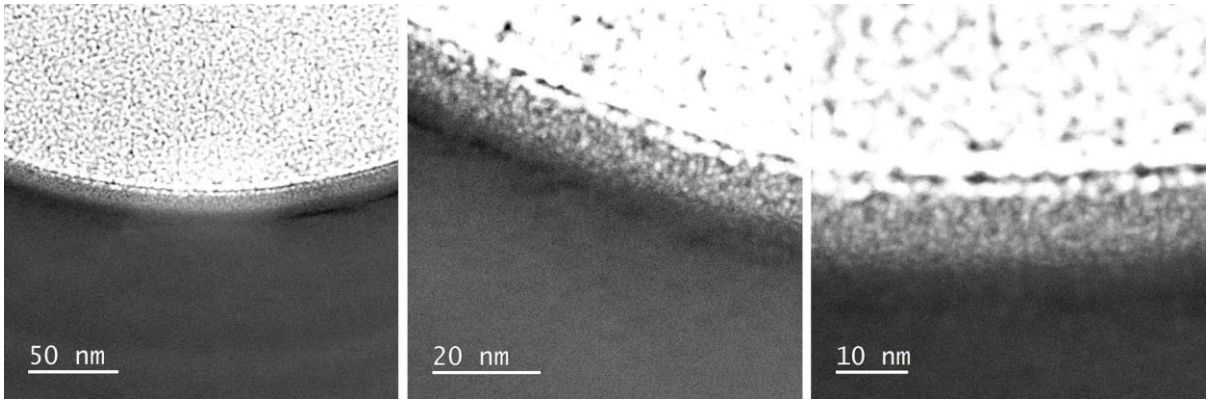
Figure 6.19. HAADF images of the six notches PFIBed in Al_2O_3 using the defined range of FIB parameters. Magnification = 400K

At higher magnifications (Fig.6.20), high densities of bright features were observed in the amorphous layers – it will be shown later that these features are high concentrations of Xe, which are referred to as bubbles in this thesis. In notches ④, ⑤ and ⑥, these bubbles appeared to be particularly large, which were less clear in notches ⑤ and ⑥ than that in notch ④.

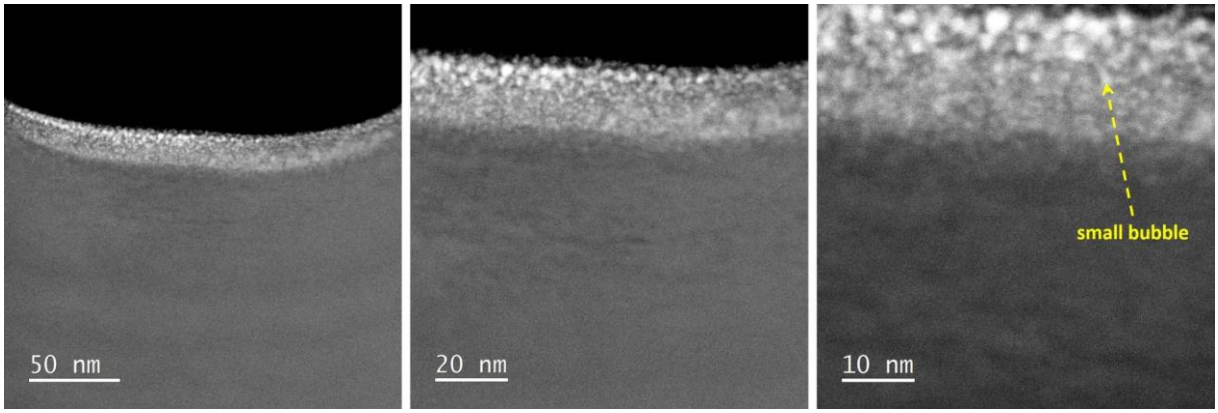
① 5 kV, 5.2 pA, 264 s, 2.9 × 10^9



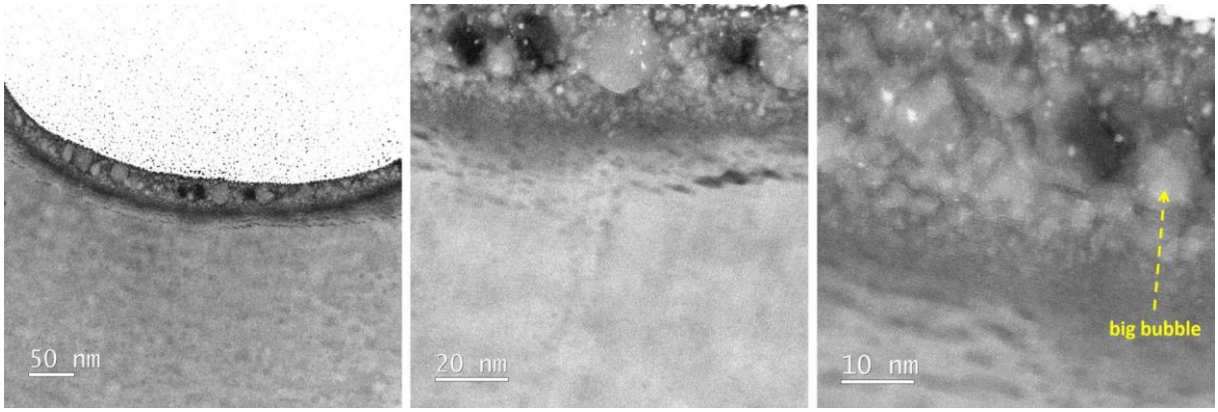
②. 8 kV, 4.8 pA, 286 s, 2.9 × 10^9



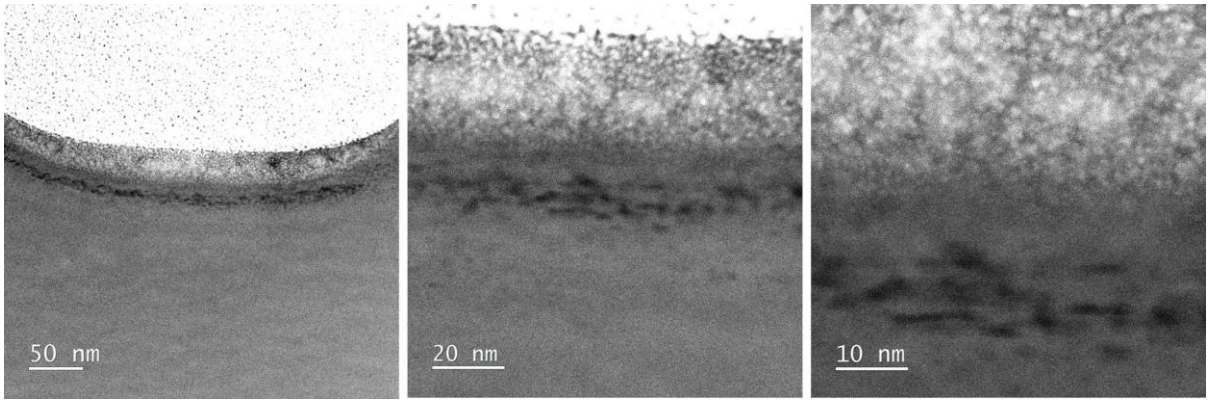
③. 16 kV, 4 pA, 342 s, 2.9 × 10^9



④. 30 kV, 1.5 pA, 912 s, 2.9 × 10^9



⑤. 30 kV, 3.8 pA, 360 s, 2.9×10^9



⑥. 30 kV, 240 pA, 56 s, 2.8×10^9

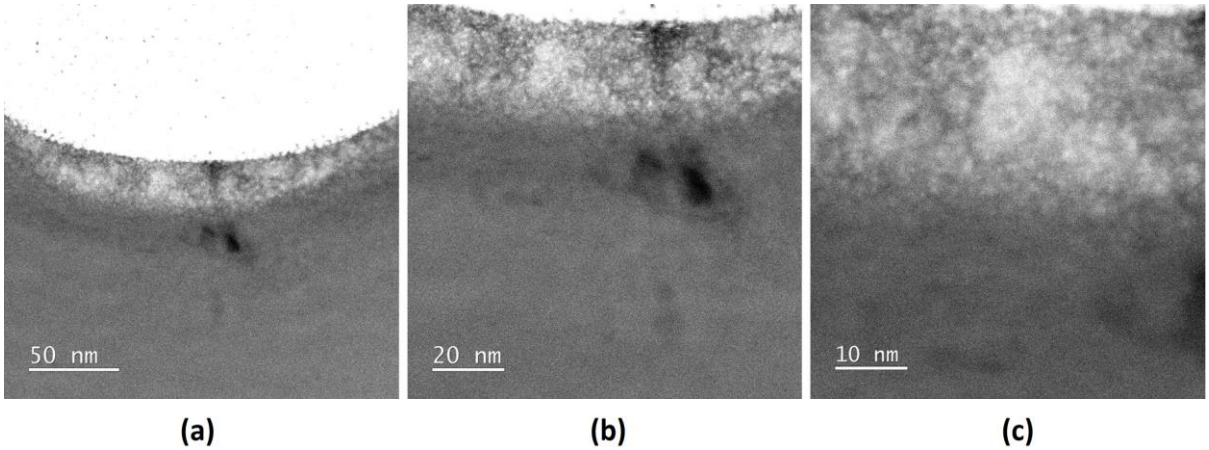


Figure 6.20. HAADF images of the six PFIBed notches in Al_2O_3, taken in the JEOL-ARM200F, show the ion implantation damage. Images are separated into two pages.

Notch ④ was, again, selected for further investigation due to its special appearance. The bubbles in its amorphous layer were highly visible in Fig.6.21, exhibiting a range of different sizes.

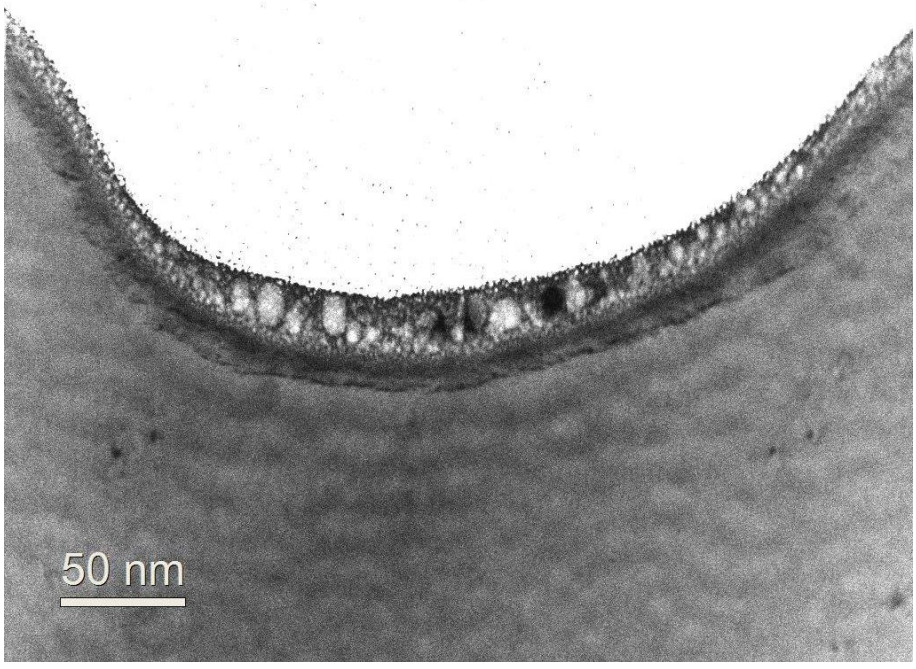


Figure 6.21. HADAAD image of the notch ④. Image taken in the JEOL TEM-3000F

As shown in Fig.6.22. The diameters of the bubbles varied over a range of ~2nm to ~24nm, with most of the large ones sitting in the upper area and the small ones lying in the lower part. Below the layer of bubbles, the crystalline damaged layer drew a clear boundary between itself and the undamaged material.

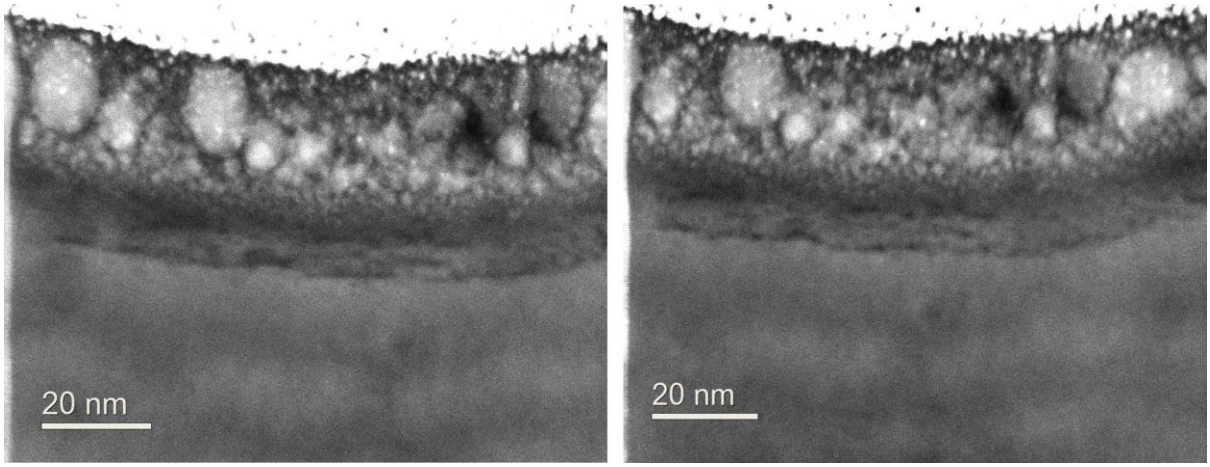


Figure 6.22. HAADF images showing the bubbles in the amorphous layer in the notch ④.

According to EDX examination (Figure 6.23), Xe was detected in the amorphous layer, the amount of which peaked at the amorphous layer and decreased along the depth beneath it. The amount of Al and O appeared to be almost constant in the amorphous layer, but was less than that in the undamaged material.

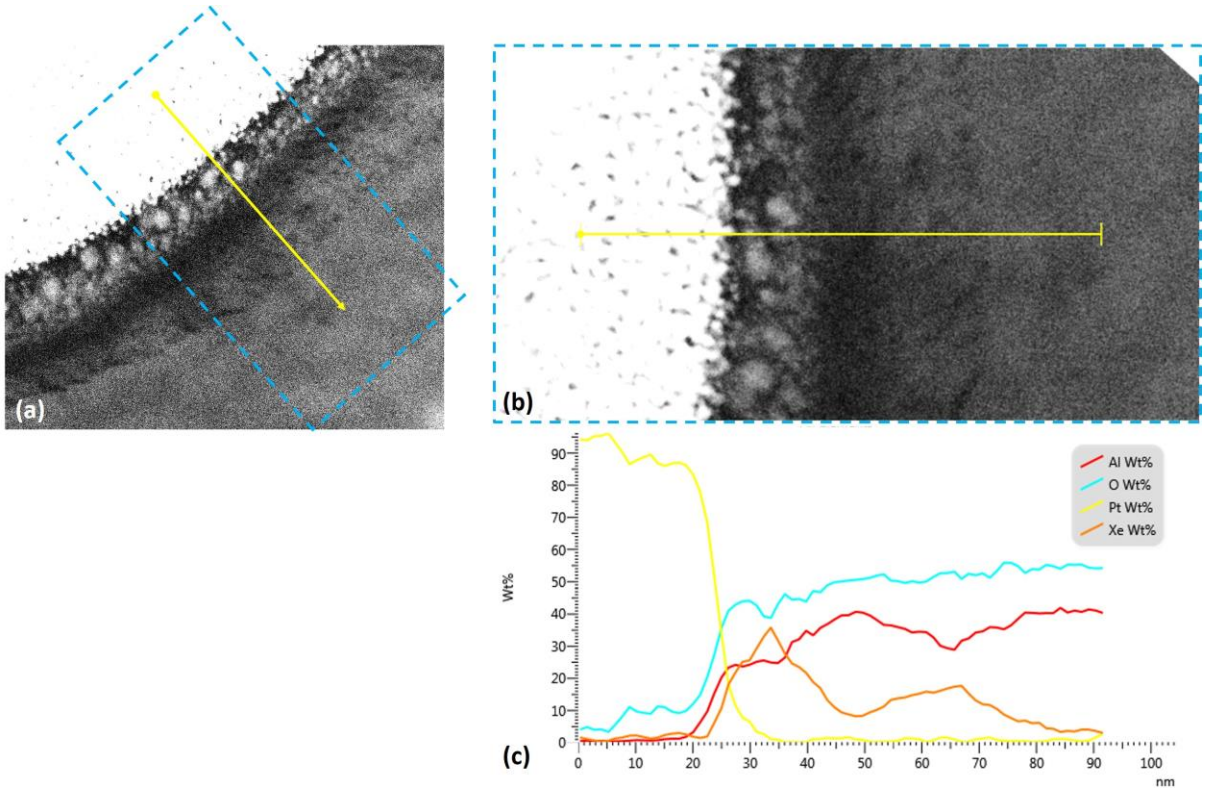


Figure 6.23. TEM-EDX line scan across the amorphous layer, originating from the Pt protection layer and ending in the undamaged material. (a) HAADF image of the notch No.④. The yellow line indicates the EDX scanning path with the arrow pointing towards the scanning direction. (b) The zoomed-in TEM image of the blue-dash framed area in (a). (c) The weight percentages of the detected elements along the scanning line. Examination performed in the JEOL TEM-3000F.

The specimen was further investigated using JEOL-ARM200F which was capable of providing higher resolutions and was coupled with EELS. EDX analytics was performed with the probe current increased to ~5 times of that applied for standard STEM imaging. As shown in Fig.6.24, the background material surrounding the bubbles was rich in Al and O. The large scanned bubbles were, however, broken down by the EDX examination and therefore no element was detected within them. At the bottom area of the amorphous layer where small bubbles gathered, a high density of Xe was detected alongside Al and O.

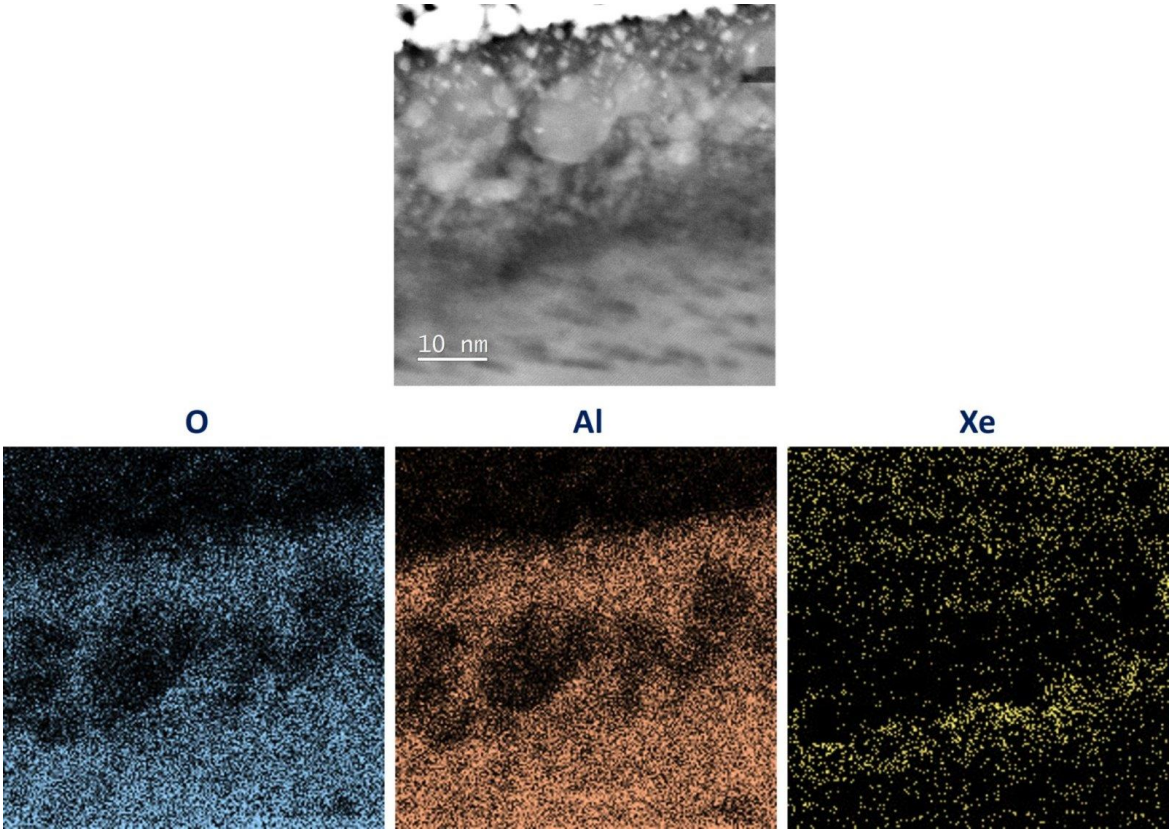


Figure 6.24. The HAADF image on the top shows an area across the amorphous layer that was selected for EDX mapping. The coloured pictures below are the distribution maps of Al, O and Xe elements. There was a slight drift during the mapping.

An EDX line scan was performed across bubbles of different sizes (Fig.6.25*).* At the time when the big bubble was selected as the scanning target, it showed the normal bright contrast in the HAADF image, the same as the other bubbles. However, after the beam alignment and a quick trial scan, the bubble turned 'dark' as shown in Fig.6.25*a*, suggesting that the bubble was damaged once in contact with the electron beam. The scan was carried out nevertheless. Only Al and O were detected – the signals were stronger at the background material surrounding the bubbles than within them (Fig. 6.25*b*). Although

the electron beam was highly focused along the scanning line profile, the big bubbles next to the one that was scanned, which had no direct contact with the electron beam, also broke down (Fig. 6.25*c*).

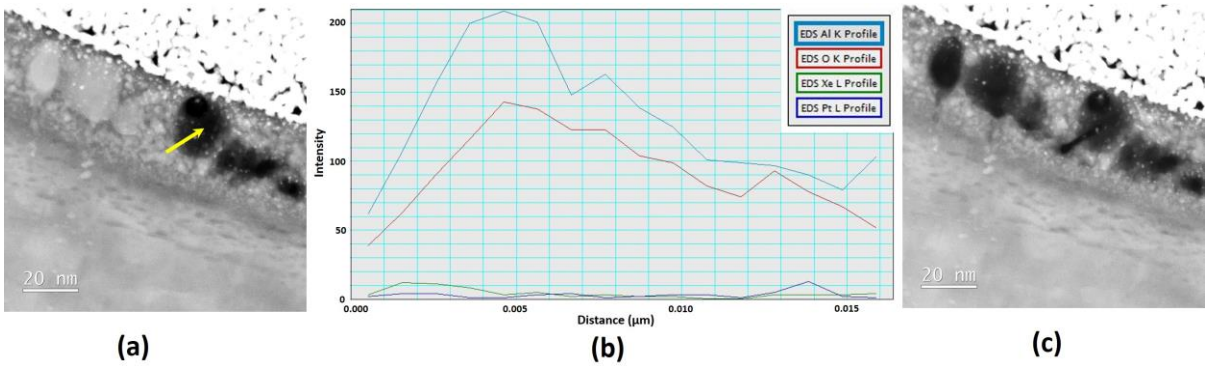


Figure 6.25. (a) A dark-field image prior to the line scan. The yellow line shows the line scan path with the arrow indicating the direction of scan. (b) EDX line profiles of Al, O, Xe and Pt. (c) A DF image of the same area as in (b) but after the line scan.

Fig.6.26a and 6.26b feature the same notch before and after, respectively, going through the high-current STEM imaging and EDX scanning. Many large bubbles were found to have broken down (Fig. 6.26b, 6.26d) during the EDX examination process.

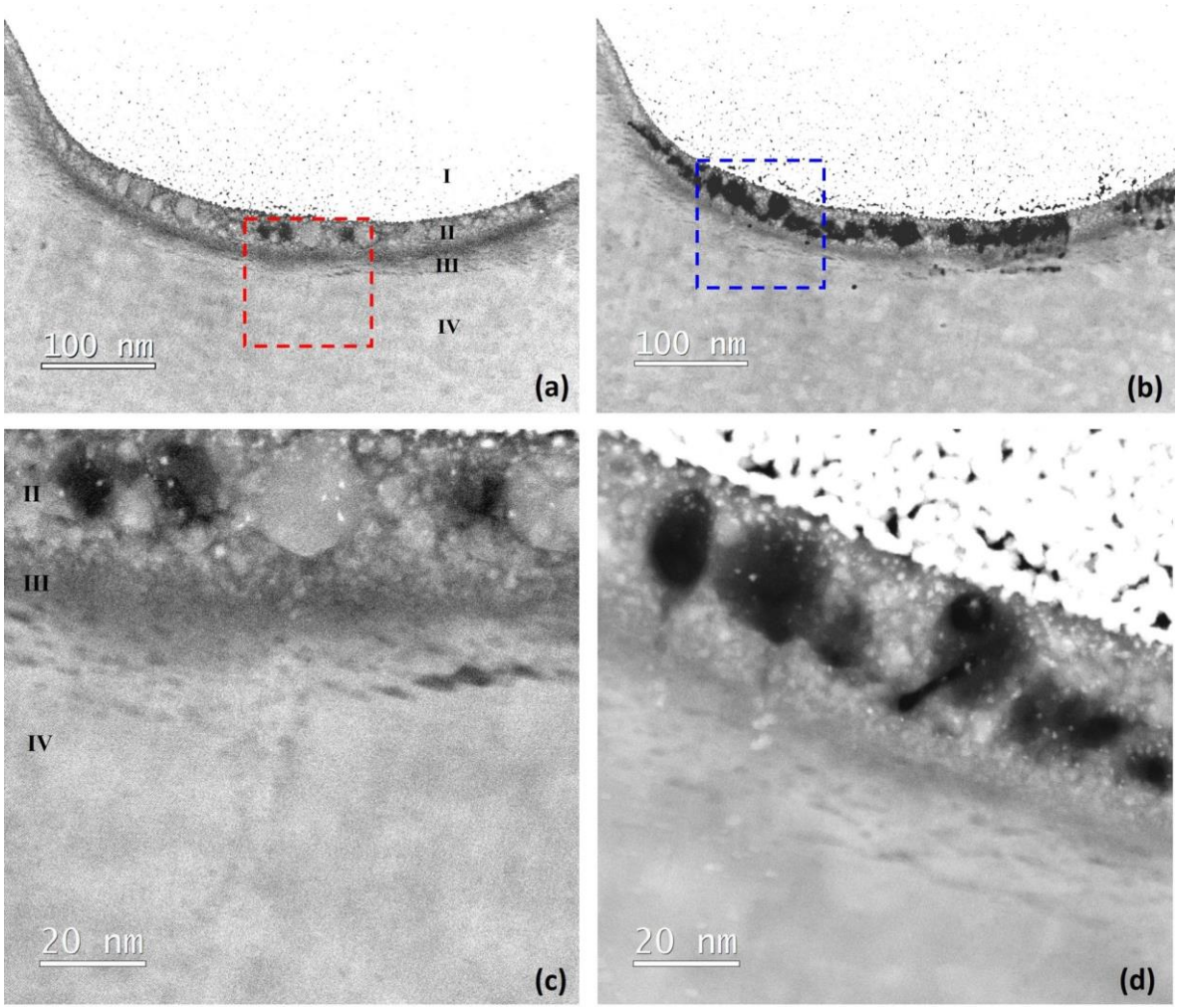


Figure 6.26. HAADF images of the notch milled by XPFIB. (a) and (c) Before any high-current STEM imaging or EDX scanning had taken place. (c) and (d) HAADF images of the red- and blue-framed area in (a) and (b) respectively, after the EDX and EELS characterisation process. They show that some rounded features in the amorphous layer appear dark.

EELS was employed to perform further investigation on the chemical composition of the bubble fillings, making use of its relatively lower beam current (Fig.6.27a). The energy loss spectrum was acquired across intact bubbles that had not been scanned by EDX beforehand. The intensity of the core-loss peaks was not strong due to the limited number of atoms interacting with the incident electrons. However, the core level ionisation edges could be clearly identified in the spectrum and had an excellent match with the nominal EELS spectrum of Xe from the EELS dataset by Gatan[307] peaked at ~688 eV. This suggested that the bubbles were filled with Xe.

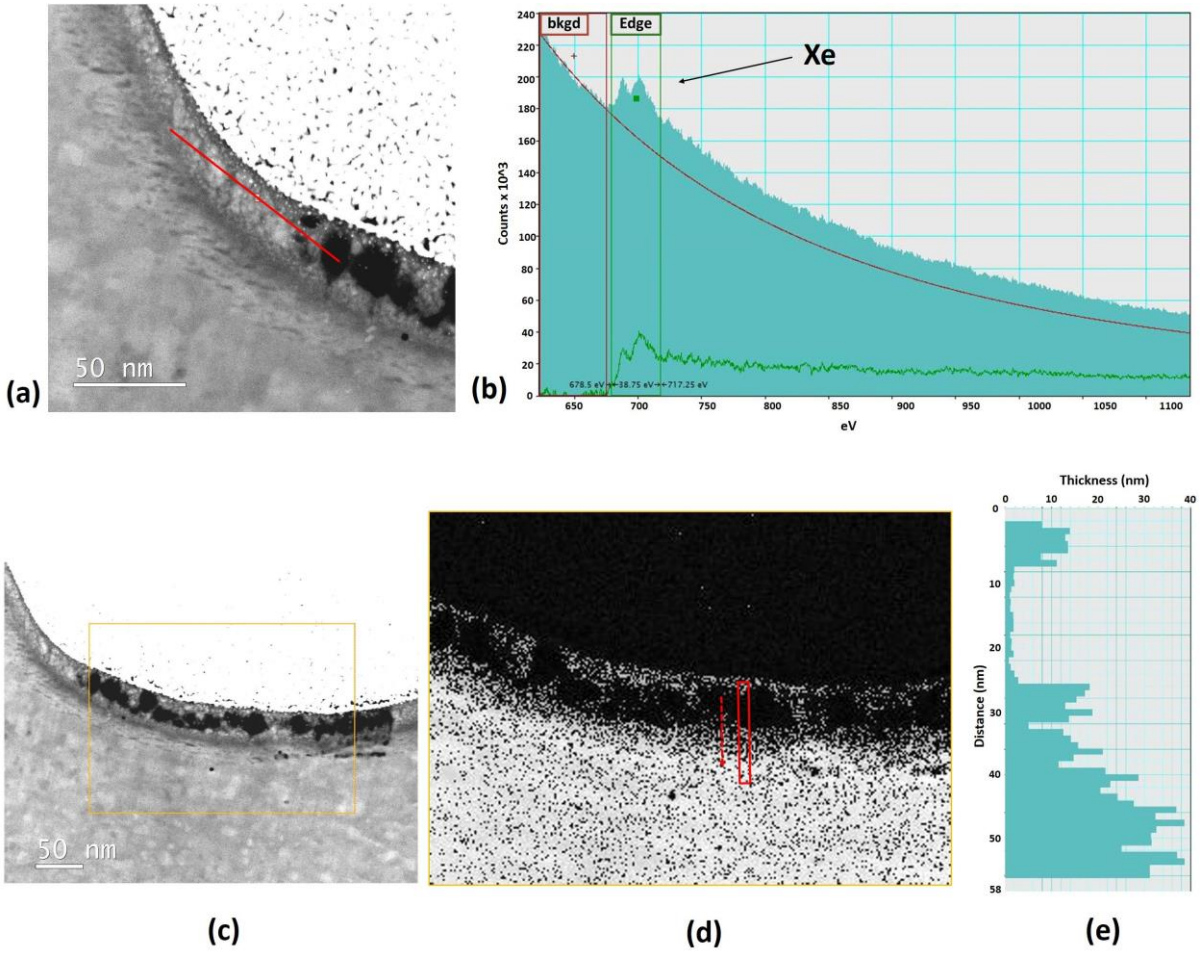


Figure 6.27. (a) The red line across the bubbles in the HAADF image was the selected area for an EELS line scan. (b) EELS spectrum detected by the EELS line scan. 'bkgd' is the background removal, 'edge' is the resultant spectrum after the background removal. (c) HAADF image shows that the area in the orange frame was selected for EELS mapping. (d) Relative thickness map of the selected area, generated using Gatan DitigalMicrograph software. Brighter contrast indicates larger thickness and vice versa. (e) Thickness values extracted along the red line in the thickness map in (d).

6.3 Discussion

6.3.1 SRIM simulation vs. experimental observation

The ion implantation was simulated using the Stopping and Range of Ions in Matter (SRIM) code[250] under the 'monolayer collision – surface sputtering' mode, with the input parameters applied in the simulations listed in Table 6.6. Si and diamond are also analysed here for comparison purpose. For each simulation, the statistic was gathered at 10000 ions.

Table 6.6. Material parameters applied in the SRIM simulation[250] The compound data for Al_2O_3 and Si were from the SRIM Compound Dictionary. The displacement energy data for SiC and diamond were extracted from the studies of Lucas et al.[308] and Guthoff et al.[309], respectively.

Target	Element	Displacement energy[1] [eV]	Surface Binding energy[2] [eV]	Lattice binding energy[3] [eV]	Atomic number	Weight [amu]	Density [g/cm^3]
Al_2O_3	Al	25	3.36	3.0	13	26.98	3.98
	O	28	2.00	3.0	8	15.99	
SiC	Si	38	4.70	2.0	14	28.08	3.21
	C	19	7.41	3.0	6	12.01	
Si	Si	15	2.00	4.7	14	28.08	2.32
Diamond	C	43	7.41	3.0	6	12.01	3.51

Figure 6.28 compares the thicknesses of the amorphous layers measured from the TEM images and the maximum ion ranges simulated using SRIM, showing close agreement. The ion penetration depth increases with the acceleration voltage, and the damage depth follows an order of Ga^+-Si > Ga^+-SiC > Ga^+-Al_2O_3 > Ga^+-diamond > Xe^+-Al_2O_3 for implantation at 30 kV.

[1] Displacement energy: the energy that a recoil needs to overcome the lattice forces and to move at least one atomic spacing away from its original site.
[2] Surface binding energy: the energy that target atoms must overcome to leave the surface of the target.
[3] Lattice binding energy: the energy that every recoiling target atoms loses when it leaves its lattice site and recoils in the target.

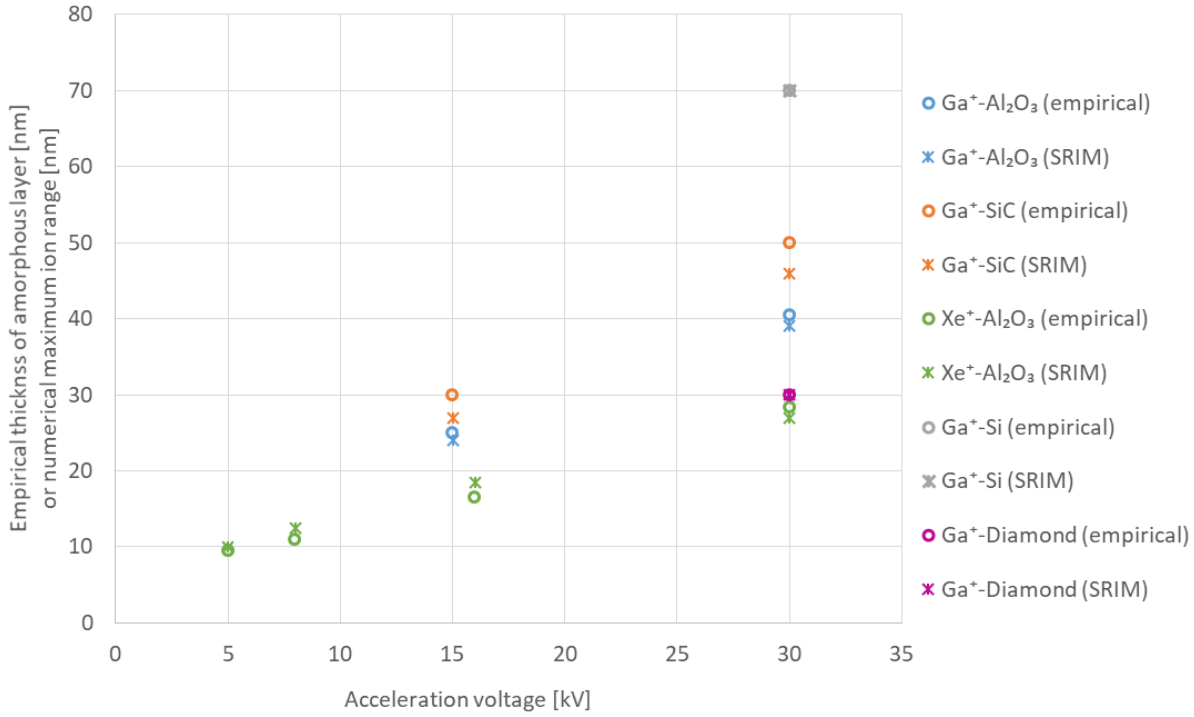


Figure 6.28. Comparison of amorphous layer thickness empirically measured from TEM observation and maximum ion range from SRIM simulation. The empirical data for Si and diamond is from Rubanov[273] and Tong and Luo[257], respectively.

The good agreement between the empirical observation and SRIM simulation is also shown in Figure 6.31, Figure 6.32 and Figure 6.33. Such consistent agreement proves the reliability of SRIM's estimation, suggesting that the input parameters for SRIM simulation (i.e. displacement energy, surface binding energy, lattice binding energy, atomic weight, density of substrate) can be the core of discussion for explaining the differences in implantation behaviour of various ion species and target materials.

Despite the highly reliable prediction of amorphous layer thickness, SRIM underestimates the total damage depth which includes both amorphous and crystalline damaged layers. This may be attributed to (a) SRIM's lack of consideration of crystal structure, and (b) SRIM's lack of consideration of dynamic changes in material composition and structure during the collision cascades[250]. For example, the damage in the amorphous layer, such as the formation of particles or bubbles, facilitates the further travel of incident ions in the target material due to the change of densities or lattice arrangement. The underestimation of implantation depth has also been demonstrated in the study of 30 keV Ga^+

implantation in Si[234], where a maximum ion range estimated by SRIM (~42nm) was smaller than the maximum implantation depth analysed using the Atom Probe Technique (~52nm)[234].

Figure 6.29 compares the distribution profiles of ion and vacancies in the four different materials under 30 keV Ga^+ implantation. As the total amount of implanted ions was constant for each ion specie, the deeper it penetrated, the lower the peak concentration of implanted ions was. Si had the largest total amount of vacancies, highest vacancy peak concentration, as well as the longest vacancy range. Both the orders of maximum ion range and vacancy range are as follows: Si > SiC > Al_2O_3 > diamond. Similar trend was seen with Xe^+.

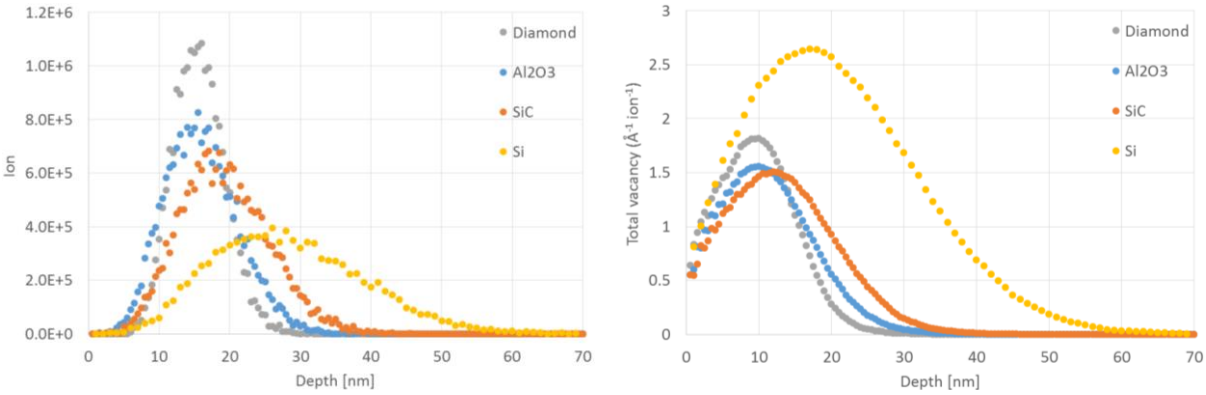


Figure 6.29. Distribution of ions and vacancies from 30 keV Ga^+ implantation

Fig. 6.30 shows the SRIM-simulated average amount of vacancies that every incident ion generated in the target materials, which increased almost-linearly with voltage. The numbers of vacancies that Ga^+ and Xe^+ generated in the same material were almost the same when the voltage was ≤ 10 keV. With the voltage increasing to >10 keV, Xe^+ generated slightly more vacancies than Ga did. The amount of vacancies that each Ga^+ generated in different target materials followed a consistent order: Si > Al_2O_3 > SiC > diamond.

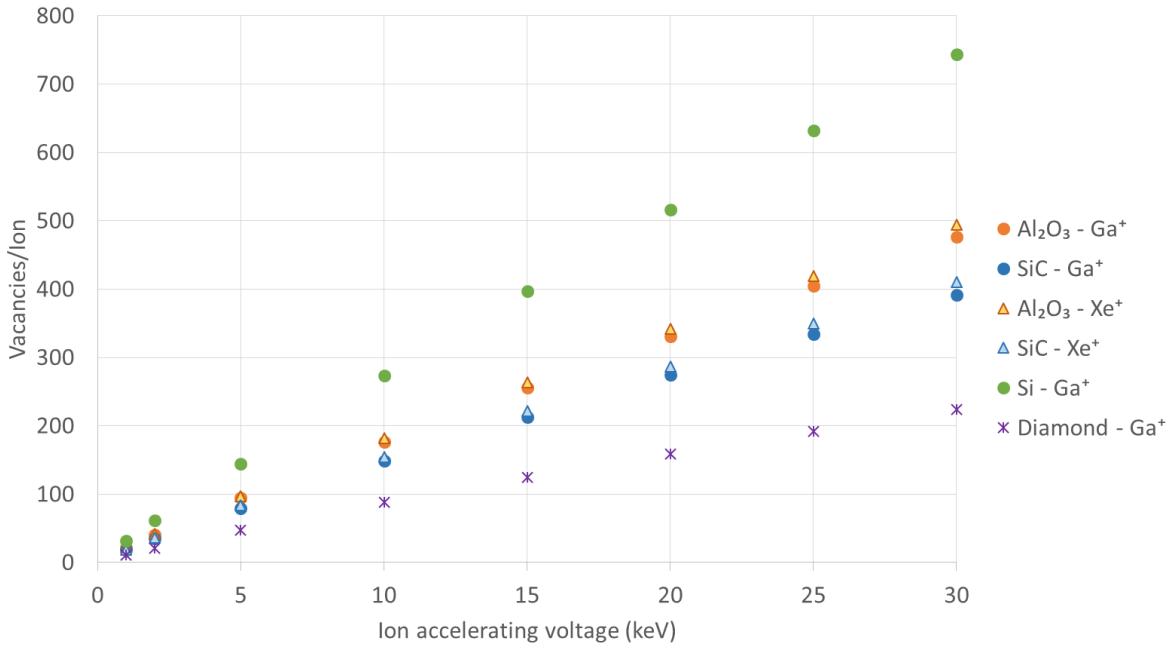


Figure 6.30. Average number of vacancies per incident ion estimated using SRIM in different target materials (Al_2O_3, SiC, Si and diamond) by different ion species (Ga^+ and Xe^+).

Table 6.7 shows that the efficiency of generating vacancies and interstitials is much higher than sputtering. Moreover, interstitials/vacancies are more easily created in Si than Al_2O_3, followed by SiC and diamond.

Table 6.7. Sputtering yield, interstitial and vacancy created per ion under 30 keV, simulated using SRIM

Ion species	Target material	Sputtering yield/ion	Interstitial/ion	Vacancy/ion
Ga^+	Al_2O_3	Al - 1.9, O - 4.0	484	477
	SiC	Si - 1.4, C - 0.8	403	392
	Si	Si - 2.3	805	744
	Diamond	C - 1.7	231	224
Xe^+	Al_2O_3	Al - 2.5, O - 5.3	500	494
	SiC	Si - 1.8, C - 1.1	420	410

SRIM-simulated distributions of implanted ions and vacancies at 30 kV are plotted against the damage depth, coupled with relevant TEM images. In all the following cases investigated, the maximum ion range obtained from SRIM simulation matched well with the thickness of the amorphous layer.

For Ga^+-implanted Al_2O_3 (Figure 6.31), the sizes of the particles formed correlated well with the Ga concentration – large particles were formed at high Ga concentration while the small ones were formed at relatively low Ga concentration.

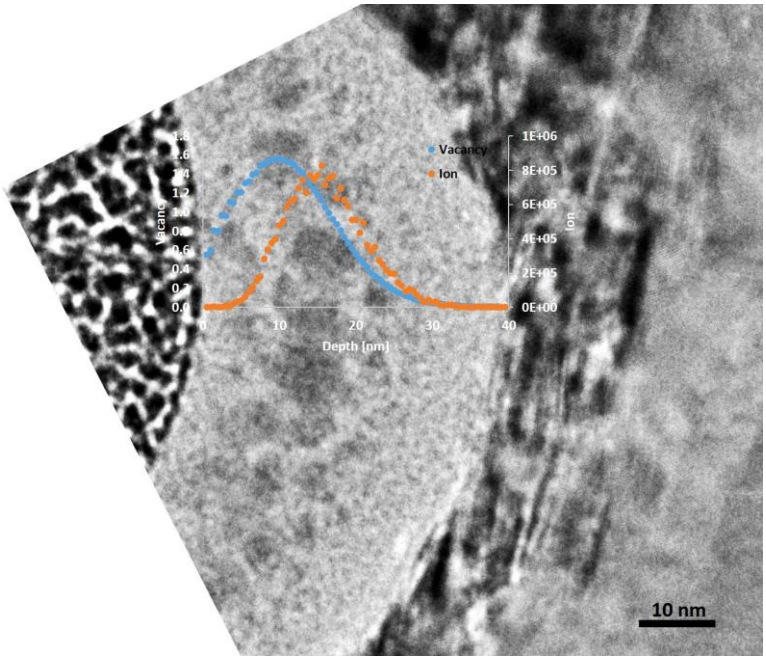


Figure 6.31. TEM bright-field image of Ga-FIB notched Al_2O_3 notch tips, coupled with vacancy and Ga concentration profiles simulated using SRIM. Implantation at 30kV, 240 pA. The TEM image and the graph have the same scale bar.

For Ga^+-implanted SiC (Figure 6.32), the transition from the top sub-layer (which exhibited a darker contrast) to the lower sub-layer follows the concentration of Ga – the contrast becomes brighter with the decreasing concentration of implanted ions.

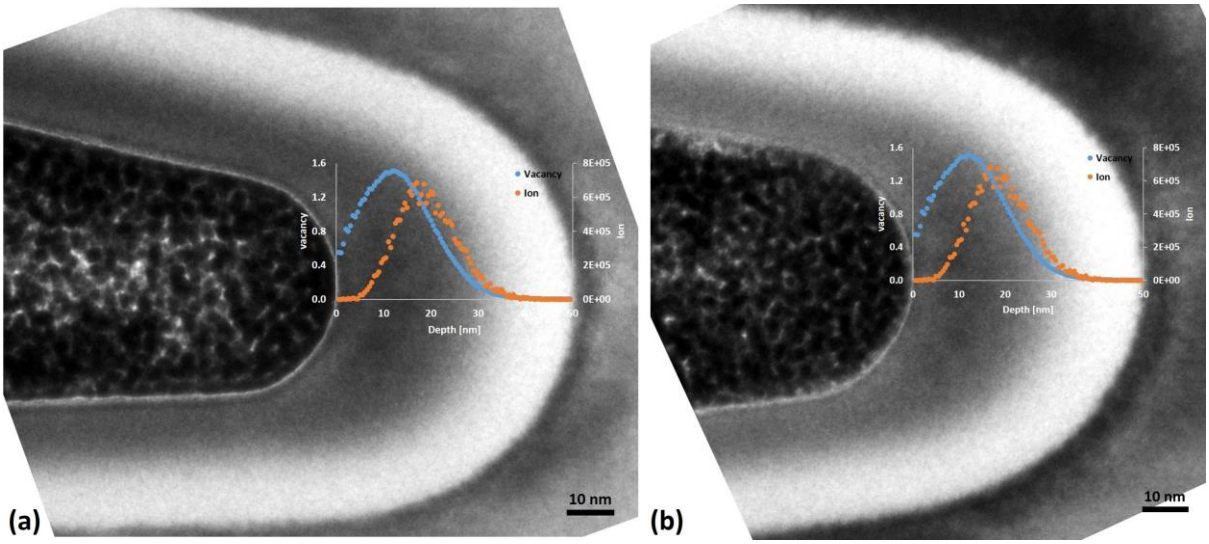


Figure 6.32. STEM bright-field images of Ga-FIB notched SiC notch tip, coupled with vacancy and Ga concentration profiles simulated using SRIM. Implantation at 30kV, (a) 5pA, (b) 240pA. The TEM images and the graphs have the same scale bar.

For Xe^+-implanted Al_2O_3 (Figure 6.33), the bubbles formed at places where there were high concentrations of vacancies and implanted Xe, with the large bubbles found close to the surface where there were more vacancies.

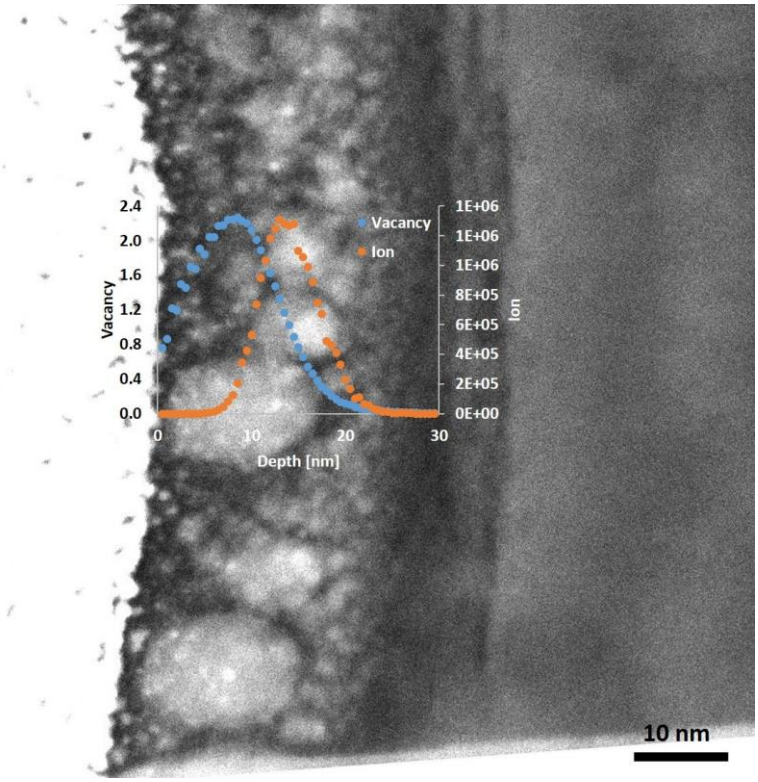


Figure 6.33. HAADF image of PFIB notched Al_2O_3 notch tip, coupled with vacancy and Xe concentration profiles simulated using SRIM. Implantation at 30kV, 1.5 pA. The TEM image and the graph have the same scale bar.

6.3.2 Effect of ion species, target materials, and FIB parameters

Amorphous layer and crystalline damaged layer were observed in all the specimens investigated in the present study. The lack of reciprocal lattice in Fig.6.18 *a*-b confirmed the amorphous status of *Layer II*, where the energetic ion bombardment broke the atomic bonds and destroyed the long-range order.[249] Fig.6.18 *c-e* indicated that the crystal structure in the crystalline damaged layer had been partially preserved despite receiving ion damage. This was because the dose and energy of ions had not reached the threshold values to cause the entire loss of the long-range order in the lattice structure.[249] The contrast differences in the TEM images of the crystalline damaged layer may be attributed to differences in levels of damage or chemical composition which led to different local densities (e.g. implantation of gallium[257]) or thickness, or strain around defects[310], etc. The increasing

level of crystallinity in *Layer III* through the depth meant that the severity of ion damage decreased with the distance that ions travelled into the target material, linked to the reduced concentration of vacancies at further depth as shown in Figure 6.29.

The effects of incident ion species, target materials and FIB parameters on the damage behaviour are discussed as follows.

- Ion species

Damage behaviour of Al_2O_3 implanted by Ga^+ and Xe^+ appeared to be different in terms of both crystallographic and compositional modifications. Knowing that SRIM only takes into account the atomic number and mass of incident ions, the following discussion focuses on the atomic mass and electron configurations (Table 6.8).

Table 6.8. Properties of the incident ions[48, 311]

	Atomic number	Electrons per shell	Atomic mass [g/mol]	Atom radius*[Å]	First ionisation energy [kJ/mol]	Melting point [°C]
Ga	31	2,8,18,3	69.72	13.6	578.8	29.76
Xe	54	2,8,18,18,8	131.29	10.8	1170.4	-111.8

First, the depth of damage decreases with heavier ion mass.[312] Knowing that a target atom receives less energy from a heavier incident ion,[250, 260] if emitted under the same acceleration voltage, Ga^+ transferred more energy to a particular target atom than Xe^+ did, resulting in a longer range of collision cascade. This is confirmed by thicker damaged layers in Ga^+-implanted Al_2O_3 than in Xe^+-implanted Al_2O_3 as observed in the present study, as well as by the larger depth of recoil-induced vacancies created by Ga^+ than Xe^+ (Figure 6.34).

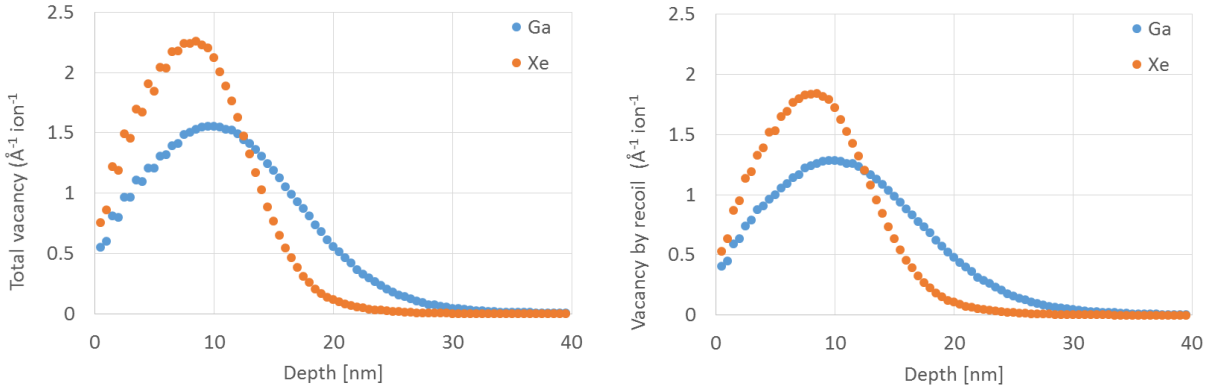


Figure 6.34. SRIM simulation of Ga and Xe implantation in Al_2O_3, showing concentrations of total vacancies and vacancies created by recoil.

Second, the formation of special features (i.e. particles in Ga^+-implanted Al_2O_3 and bubbles in Xe^+-implanted Al_2O_3) demonstrated the chemical effect[313] of ion species on implantation damage. The electron configurations determines that the level of difficulty in forming compounds with target atoms is much higher for Xe than Ga. Moreover, the low melting temperatures indicate that Xe has a high diffusion coefficient[314], which facilitates Xe's movement in the host matrix. The details will be further discussed in Section 6.3.3 and 6.3.4.

- Target materials

Among all the SRIM input parameters listed in Table 6.6, displacement energy, atomic weight and density are the major influences on the damage behaviour of target materials.

Displacement energy is the threshold that determines whether an atom could be displaced from its original positon[250], which means that a lower displacement energy would allow for the atoms to be displaced more easily and for more vacancies to be created. For example, the C atoms in SiC could be displaced more easily than C atoms in diamond if receiving same amount of energy, therefore creating more vacancies.

Based on the mass ratio of the incident ion to that of the target atom, a target atom with a heavier weight would receive more energy from the incident ions/atoms, and therefore have a higher chance to be displaced.[250] For example, Al and O have similar displacement energy in Al_2O_3, since Al has a heavier weight than O, there are more Al vacancies than O vacancies.

A higher atomic density means more atoms involved in the interaction within a fixed volume, thus the incident energy is consumed within a shorter distance.[253] This agrees well with the empirical observations in the present study and literature (Figure 6.28) that the thickness of amorphous layers followed an order of Si > SiC > Al_2O_3 upon similar implantation conditions. As a test, if changing the density of Al_2O_3 from 3.98 g/cm^3 to 3.21 g/cm^3 in the SRIM simulation, with the rest of the parameters remaining the same, the vacancy distribution in Figure 6.35 also confirms that a lower density results in a longer damage range.

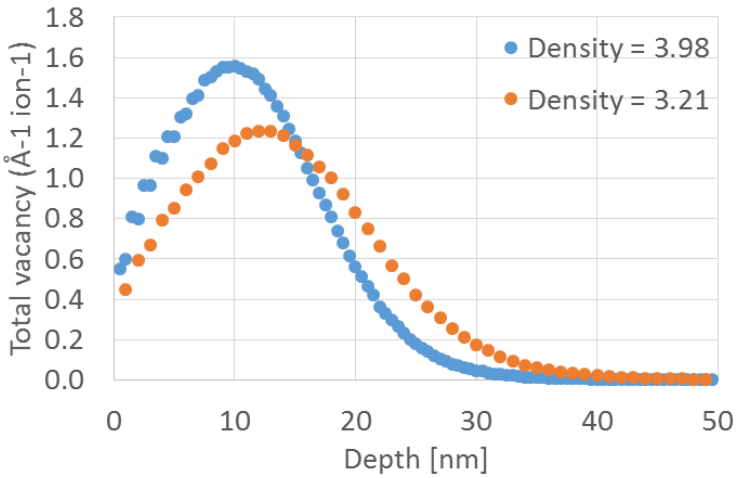


Figure 6.35. Distribution of total vacancies

- FIB parameters

During the defect accumulation process, amorphisation occurs when a critical dose threshold is achieved, and the thickness of the amorphous layer increases until the dose reaches the saturated dose threshold.[315] In the present study, both the critical and saturated dose thresholds have been achieved in all the cases investigated as amorphous layers were observed in each case and the thicknesses of these layers had obviously reached a steady state. According to the literature (Table 6.9), the critical dose thresholds for 6H-SiC, Si and diamond are all in the order of 10^6, with saturated dose thresholds in the order 10^8. Although no literature is found for Ga^+ irradiated Al_2O_3, on the basis of small variations from Table 6.9, its critical and saturated dose thresholds may also be on the order of 10^6 and 10^8 respectively. The ion doses applied in the present study are all in the order of 10^9 - 10^{10} which are beyond the saturated dose threshold, thus steady state is reached in each implantation case.

Table 6.9. Critical and saturated dose thresholds for amorphisation

Target material	Ion specie	Critical dose threshold [ion/µm^2]	Saturated dose threshold [ion/µm^2]	Resource
6H-SiC	Ga^+	3.3×10^6	~5.3×10^8	He et al.[315]
Si	Ga^+	1.0×10^6	~2.0×10^8	Rubanov[273]
Diamond	Ga^+	2.9×10^6 *	~3.0×10^8	Rubanov and Suvorova[316]

** converted by dividing the reference result (5.2×10^{10} vacancies/µm^3) by peak vacancy per ion simulated using SRIM (1.82×10^4 vacancies/ion/µm).*

Beam voltage determines the energy that the incident ion brings to the interaction with the target solid – increasing the voltage will directly increase the range of collision cascade and thus generates thicker amorphous layers. Both the TEM observation and SRIM simulation agreed with this theory – the amorphous layers were thicker with higher beam voltages or remained almost-constant with the same beam voltage, based on the fact that the steady state has been achieved as discussed above. The positive correlation between the beam voltage and damage depth has also been extensively demonstrated by studies in Si[234, 270] and diamond[257].

Beam current, i.e. ion flux, is usually thought not to have a direct effect on implantation damage and is not considered in the SRIM code either. In the present study, changing FIB current under the same beam voltage did not result in difference in thickness of amorphous layer. However, in the case of 30 keV Xe implantation in Al_2O_3, the formation of large bubbles was favoured in the low current (i.e. 1.5 pA) implantation against the higher ones (i.e. 3.8 pA, 240 pA). The explanation for this phenomenon will be further discussed in Section 6.3.4 by coupling with the bubble formation mechanism.

6.3.3 Ga-FIB induced particles

In Ga-FIBed Al_2O_3, particles containing high concentrations of Ga, Al and O were found in the amorphous layers (Fig.6.6 - 6.11). The Al_2O_3-Ga_2O_3 equilibrium diagram[317] (Figure 6.36), exhibiting the extensive solid solubility of $GaAlO_3$ in the alumina-gallia system at room temperature, suggests

the possibility of chemical reactions happening during Ga implantation in Al_2O_3. Taking the average of the atomic percentages of Ga (18.1%), Al (25.5%) and O (54.1%) detected in the particles using EDX (Table 6.3), the ratio of Ga:Al:O is 1.0 : 1.4 : 3.0, which is not far from the atom ratio of $GaAlO_3$ and is well within the range of solid solution at room temperature shown in Figure 6.36. It therefore suggests that the particles were formed as a new compound $GaAlO_3$ during Ga implantation and embedded in the Al_2O_3 matrix.

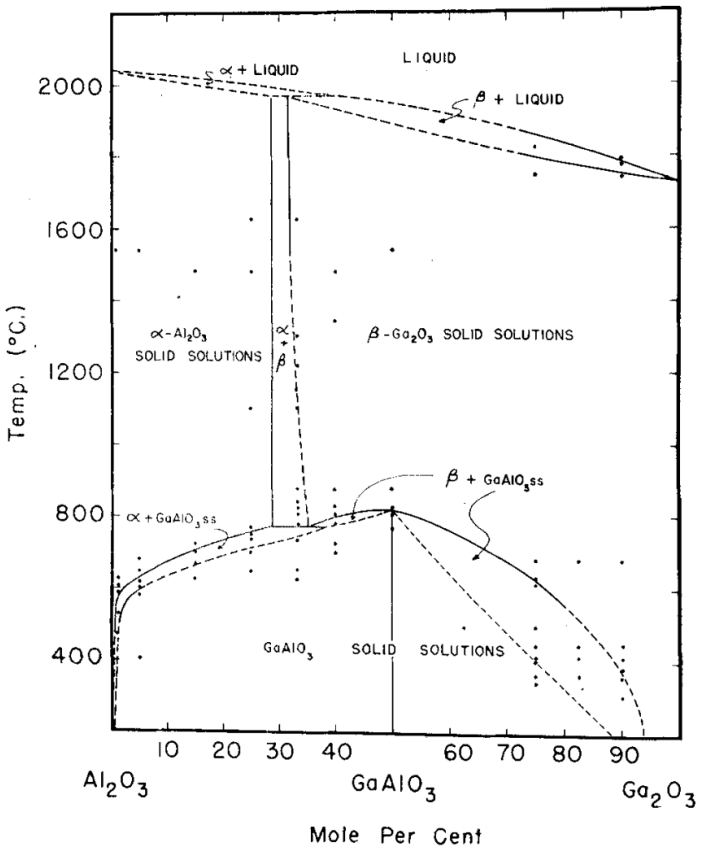


Figure 6.36. Equilibrium diagram for the system Al_2O_3-Ga_2O_3. Reprint from reference[317]

The difference in the FIB settings assessed (i.e. 15/30 keV beam voltage, 20/240/250 pA beam current, $3 \times 10^9/16 \times 10^9$ ion/µm ion dose) did not make visible differences in the appearance of particles in the amorphous layers, as shown in Figure 6.5, which suggests a steady state was reached in these settings. Figure 6.31 shows that the formation of big particles was driven by high concentration of implanted ions rather than vacancies, with the size of the particles decreasing with ion concentration. This indicates that the implanted Ga ions tended to rest in position where they used up their kinetic energy

by forming compounds with the host atoms, rather than diffusing to places where there were higher concentrations of vacancies.

In fact, ion implantation has been long developed as a method to produce a wide range of nanocrystal precipitates in irradiated materials, as reviewed by Meldrum[318]. It was therefore not overly surprising to observe these features in the present study. However, despite the fact that the generation of nanoparticles by ion implantation is well established, its extension to the FIB damage studies has barely been mentioned or considered. One reason is that the voltage employed in the industrial ion implantation technique (usually at the scale of 10^2 - 10^3 keV) is much higher than that used in FIB (usually 2 ~ 30 keV). Additionally, Ga is not a key element of interest in the ion implantation industry.

In the case of Ga-FIBed SiC, Ga, Si and C were detected in the amorphous layers (Fig.6.13 - 6.15). However, no particle was found in these layers, which is different to what was observed in Ga-implanted Al_2O_3. Figure 6.32 shows that the implantation of Ga darkens the TEM image contrast due to the change of density and chemical composition. At the depth after the peak of ion concentration, the gradient of contrast change followed the profile of ion concentration. However, the less contrast difference was observed at depths before the peak of ion concentration, suggesting that there were more ions at the shallow depth than that was predicted by SRIM. The almost-uniform distribution of the implanted ions in the upper sub-layer could be attributed to the low mobility of implanted ions in SiC due to the strong covalent bonds.[319]

Figure 6.14a suggests an atomic ratio of (Si:Ga) $\approx$ (7:5) at the peak concentration of Ga (i.e. converted from weight% data). Knowing that the solid solubility of Ga is weak in Si[320] and the formation of gallium carbide is not favoured at room temperature, it is unlikely that a new phase consisting of Ga, Si and C has been formed during the implantation. Further investigation is required to make decisive conclusions on the compositional change in the damaged areas.

6.3.4 Xe-PFIB induced bubbles

The formation of inert gas bubbles in solids, mostly metals and alloys, in high-energy radiation environments has been extensively discussed at a NATO Advanced Research Workshop[321] and by Was[322]. The process of Xe bubble formation in the present study can be summarised as the following four steps based on Gao and Ghoniem's model[323]. (i) Ion implantation. The energetic ion bombardment created vacancies, interstitials and Frenkel Pairs in the target lattice. The incident Xe ions used up their energy during the electronic and atomic collisions, and rest in the interstitial or substitutional positions in the matrix as neutral Xe atoms. (ii) Bubble nucleation. The implanted Xe atoms diffused to join each other to form clusters of Xe, becoming the nuclei of bubbles. The number of the atoms to form a nucleus could be as low as 3 according to the study of helium implantation in tungsten[323]. (iii) Bubble growth. As implantation carries on, some of the newly-implanted Xe atoms and vacancies were attracted towards the already-nucleated Xe bubbles, leading to the growth of the bubbles. The present and the previous steps took place simultaneously, which means that the nucleation and growth of bubbles were in competition with each other. (iv) Bubble coalescence. The bubbles move in the matrix, either driven by the stress and temperature gradients in the matrix, or buffered by xenon and vacancy fluxes. Coalescence then happened when one bubble met another, growing the bubbles to larger sizes rapidly.

Unlike Ga that can easily generate new bonding with the target anions, Xe is unlikely to activate chemical reactions to bond with matrix atoms due to its noble gas nature.[232, 324] This allows the implanted Xe ions to diffuse into clusters of vacancies instead of bonding with the adjacent matrix atoms, as confirmed by the correlation between TEM observation and SRIM simulation in Figure 6.33.

At low PFIB voltages (i.e. 5, 8 and 16 keV), small Xe bubbles were found to spread over the amorphous layers in Al_2O_3 (Fig. 6.20 ①②③), while big Xe bubbles formed when the PFIB milling voltage increased to 30 keV (Fig. 6.20 ④⑤⑥). This suggests that the energy was playing an important role in the evolution of bubble size. In order to understand the relationship between the beam voltage and bubble formation, the vacancies and ions generated by Xe implantation in Al_2O_3 were estimated using

SRIM by applying the same ion dose (10000 Xe ions) under different beam voltages (6, 16, 30 keV). The concentration profiles (Figure 6.37) show that whilst a higher beam energy generated a lower ion peak concentration, it created a higher vacancy peak concentration as well as a higher total amount of vacancies. Coupled with Figure 6.33 which demonstrates that the formation of big bubbles occurred near the peak concentration of vacancies rather than ion dose, the above suggests that the formation of big Xe bubbles was enabled by the high concentrations of vacancies created by a high beam voltage.

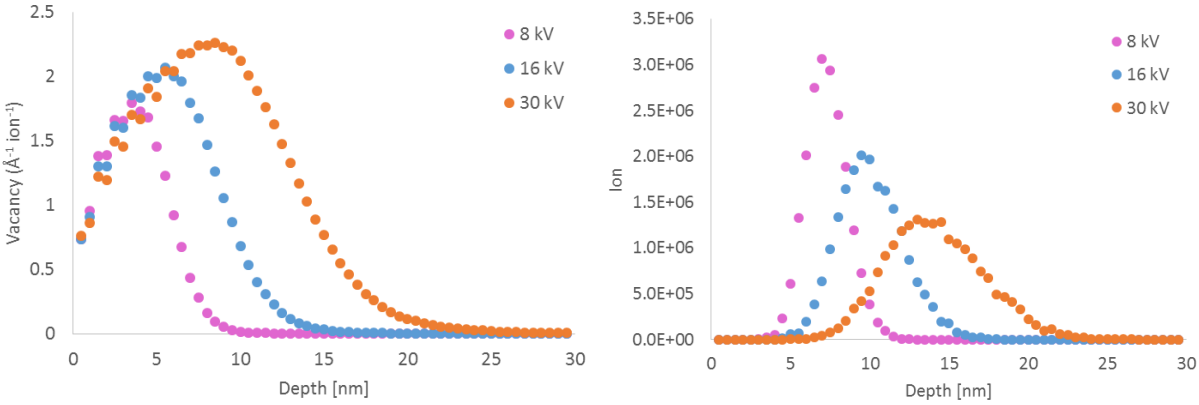


Figure 6.37. Concentrations of vacancy and implanted ion against the implantation depth at voltages of 8, 16 and 30 keV.

As mentioned in Section 6.3.2, the formation of large bubbles was found to be favoured by low beam current. This is mainly because the coalescence rate of bubbles is highly time dependent.[323] A lower current means a longer implantation time for the same amount of ion dose, the Xe atoms have more time to diffuse to have bubbles grow towards one another and therefore result in larger sizes.

The significant reduction in specimen thickness after the bubbles were damaged by the EDX examination indicated that they were burst by the high current electron beams. No detection of Xe within these burst bubbles meant that the internal gas was released into the TEM chamber. The bursting of bubbles was likely attributed to the localised temperature rise induced by the TEM electron beam.[325] The e-beam heating increased the internal pressure of the bubbles and led them to break down. Under the HR-TEM mode, the electron beam was coming in parallel which would not generate significant localised heating, therefore no bubble bursting happened during the HR-TEM imaging. On the contrary, the electron beam was highly focused under the STEM mode, where the local heating

was inevitable. The e-beam-induced damage in bubbles was less severe under the HAADF imaging (0.03 nA beam current) and EELS modes (0.04 nA) than the EDX mode (also 0.14 nA), suggesting that the high electron beam current contributed significantly to the localised temperature rise.

The bubbles with smaller sizes demonstrated a higher chance of survival from electron beam damage (Fig.6.26). This has two possible explanations: (1) The bubbles with small radii were under the equilibrium condition of internal pressure where the stability criterion of the bubbles was satisfied, while the big bubbles were over-pressured due to their large radii.[322] (2) The material left between the big bubbles and the free surface of the TEM foil was thinner than that for small bubbles.

As mentioned in Chapter 2, the main factors assuring the fast milling speed of XPFIB were generally summarised to be the high probe current that Xe^+ plasma ion source can have plus its high sputtering efficiency (as shown in Table 6.7). The present study demonstrates the possibility that the formation and bursting of bubbles might be another factor contributing to PFIB's fast milling rate. In addition to sputtering away target atoms with high energy bombardment, Xe 'injects' itself into the target material by forming gas bubbles which were then burst by the ion beam. The material that was 'intruded and occupied' by the bubbles were then removed at the same time. This preliminary analysis needs further confirmation for bulk surfaces.

The formation of a high density of subsurface bubbles often results in modifications of material properties (e.g. hardening[326], embrittlement[327], and reduction of thermal conductivity[328] in metals). In the present study, the lattice stress that is induced by the formation and bursting of the bubbles and all the other observations seen in this chapter is more of interest and will be further linked to the development of implantation residual stresses in the next chapter.

Chapter 7. Reliable Measurement of Fracture Toughness at Microstructural Scale –Understanding the FIB Ion Implantation Damage – Part II. Quantification of Residual Stress

In this chapter, the Ga-FIB and Xe-PFIB ion implantation-induced residual stresses are quantitatively characterised in alumina, silicon carbide and silicon, using a beam-curvature method. Such quantification potentially allows correction of the microscale fracture toughness measurement that uses FIB-notched microcantilevers for the effects of the residual stresses. The effects of ion dose, FIB parameters, crystal orientations and ion species on the development of residual stresses are investigated in order to obtain a thorough understanding of the FIB implantation damage.

7.1 Experimental

7.1.1 Methodology

The thin cantilevers in the present study had rectangular cross sections of W (width) × d (thickness) and length L. The upper layer of the cantilever was subjected to ion damage with a thickness t_f. The residual stresses induced by the ion implantation in the upper layer bent the cantilever to a curvature of ρ (=1/R, where R is the radius of the curvature). The substrate layer that was free of residual stress had therefore a thickness of $t_s = d\text{-}t_f$. The schematic is illustrated in Fig.7.1.

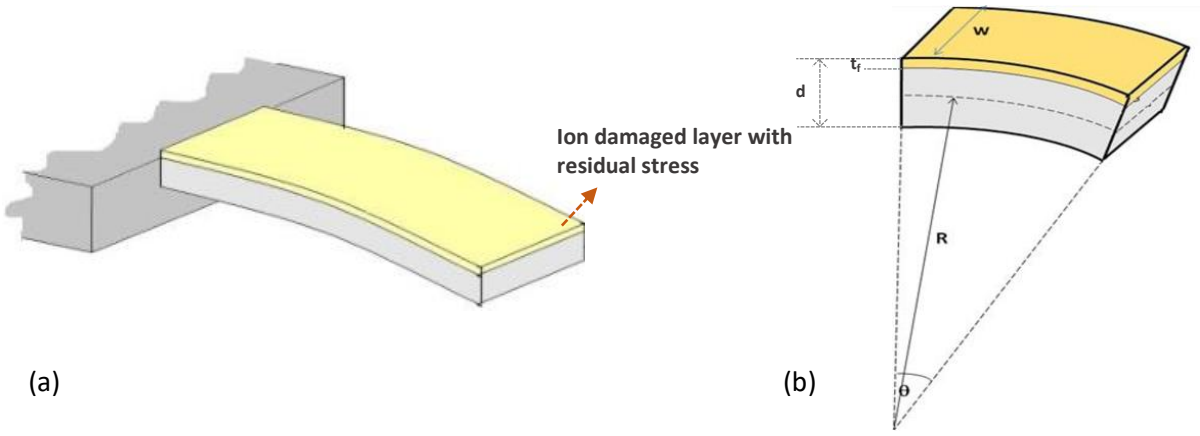


Figure 7.1. (a) The thin cantilever bent by the ion implantation residual stress in the upper damaged layer. (b) One section of the bent cantilever indicating the bending curvature and the beam dimensions. Reprint from[329].

Considering that the conventional Stoney equation[330, 331] requires the ratio t_f/d to be small and the removal of the material during implantation in the present study can be significant, Equation 7.1[332], which is developed based on the same basis as the conventional Stoney equation and is applicable even when the condition *t<<d* is no longer satisfied, is applied to evaluate the magnitude of the residual stresses to ensure accuracy.

$$\sigma_{res} = \frac{t_s^3}{6t_f(t_s + t_f)} \cdot E' \cdot \frac{1}{R} \tag{7.1}$$

where σ_{res} is the magnitude of residual stress in the implanted layer. *E'* is the biaxial elastic modulus. *R* is the radius of curvature of cantilever that is measured from high-resolution SEM images.

The values of the applied biaxial elastic moduli (Table.7.1) are evaluated using the elastic constants summarised in Chapter 2.

Table 7.1. Biaxial elastic moduli of c-, a-plane sapphire, (0001) 6H-SiC and (100) Si, applied for calculating residual stresses

	E' [GPa]	**Note**
c-plane sapphire	606	$1/(s_{11} + s_{12})$
a-plane sapphire*	553	$(s_{11}-s_{13})/(s_{11}\cdot s_{33}-s_{13}^2)$
(0001) 6H-SiC	602	$1/(s_{11} + s_{12})$
(100) Si	180	$1/(s_{11} + s_{12})$

**The longitudinal direction of the beam in the a-plane sapphire is along the c-axis.*

The thickness of the implantation layer, t_f (Table.7.2), used the maximum ion range simulated using the Stopping Range of Ions in Matter (SRIM) code[250] under the "monolayer collision - surface sputtering" mode.

Table 7.2. Thickness of implanted layer in single crystals Al_2O_3, SiC and Si, simulated using SRIM. Unit: nm

	Ga^+				Xe^+
	1 keV	**2 keV**	**5 keV**	**30 keV**	**30 keV**
Al_2O_3	4.8	7.2	12.0	39.0	27.0
SiC	5.6	8.2	14.1	45.5	34.3
Si	10.0	13.8	22.5	70.0	

For the implantations of high ion dose, sputtering of the target material cannot be neglected. Therefore the thickness of the cantilever, *d*, was measured after each implantation and updated in the residual stress calculation.

7.1.2 Materials and sample preparation

The following four materials were investigated. (i) c-plane (0001) sapphire and (ii) a-plane $(11\bar{2}0)$ sapphire, 5 x 5 x 0.5 mm^3, from AdValue Technology. (iii) single crystal 6H-SiC (0001), 5 x 5 x 0.33 mm^3, from MTI Corporation. (iv) un-doped single crystal Si (100), 5 x 5 x 1 mm^3, from Pi-KEM Ltd.

Each substrate was mounted to a 45° pre-tilted SEM stub and was then sputter coated with platinum to gain or enhance conductivities.

Thin cantilevers were manufactured using FIB milling (Ga-source FEI FIB200 or Zeiss Auriga FIB-SEM) under 30 keV. They were prepared along the edge of the substrate material with the top surface and long edge being parallel to, respectively, the top surface and edge of the bulk substrate (Fig.7.2a). The manufacturing procedure was as follows: (i) rough trenches were dug using high beam current (e.g. 16 nA) to clear out space around the cantilever. (ii) 2nA beam current was used to thin down the cantilever to ~2 µm thick and ~5 µm wide. (iii) 1 nA beam current was applied to remove re-deposited material around the cantilever from the previous two steps. (iv) The cantilever was then thinned down to about 1 µm thick using a beam current of 600 pA. In order to ensure the beam cross section was neatly rectangular, an additional 2.5° tilt was applied to compensate for the shape of the ion beam

tail. The angle between the ion beam and the cantilever surfaces in the last step was close to parallel so that the ion damage was minimised.

The beam dimensions were then measured using HR-SEM images. Typical dimensions of the cantilevers were: length ~50 µm, width 3-5 µm, thickness 0.5-1.2 µm. Each as-made cantilever had highly uniform thickness along the beam, with > 99% uniformity. An example of a cantilever is shown in Fig.7.2b.

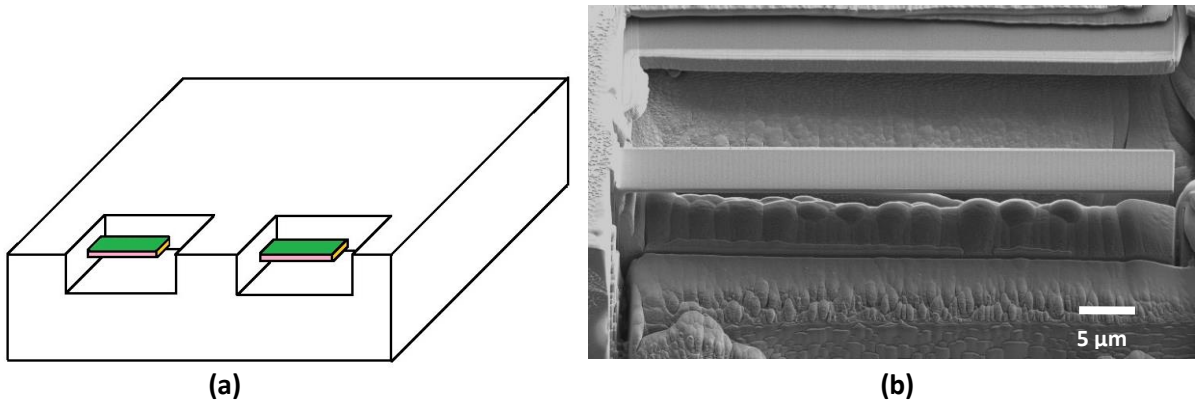


Figure 7.2. (a) Schematic of the thin cantilevers manufactured along the right-angle edge of a bulk sample. (b) A thin cantilever made on c-plane sapphire, imaged at an inclined angle in SEM.

7.1.3 Annealing

An annealing treatment[333, 334] was carried out to remove the residual stresses induced by ion damage during the cantilever manufacturing process. Sapphire, SiC and Si were annealed in an argon gas tube furnace (Carbolite STF 16/60/180) at temperatures of 1100 °C[187], 1200 °C and 900 °C[335] respectively, with a dwell time of 1 hour, and heating and cooling rates of 3 °C/min. Argon kept flowing through the furnace tube from two hours prior to the heating until the furnace cooled down to room temperature. A piece of titanium rod and a crucible of graphite powders sat in the tube alongside the samples to consume the residual oxygen.

By comparing SEM images of the cantilevers before and after annealing, no change in curvature was observed.

7.1.4 Testing procedure

The Ga^+ implantation test was performed in a dual-beam Ga-FIB (Zeiss Auriga FIB-SEM, University of Oxford). The investigations of Xe^+ implantation stress were carried out using a Plasma Xenon FIB (FEI Helio dual beam PFIB, University of Glasgow).

The testing procedure was as follows. (i) The cantilever was positioned so that its top surface was parallel with the electron beam and its lateral surface was thus perpendicular to the electron beam (Fig.7.3a). High resolution SEM images of the lateral edge were taken for measuring the curvature. (ii) The cantilever was then positioned to have its top surface perpendicular to the ion beam (Fig.7.3b). Ions of a controlled dose were implanted over the entire cantilever top surface with defined FIB parameters, using the 'serpentine' raster mode. (iii) The previous two steps were repeated in the following order until the end of the experiment: SEM images taken of the lateral edge to measure the beam bending caused by the previous ion implantation damage → implant the beam top surface to further induce ion damage under systematic conditions.

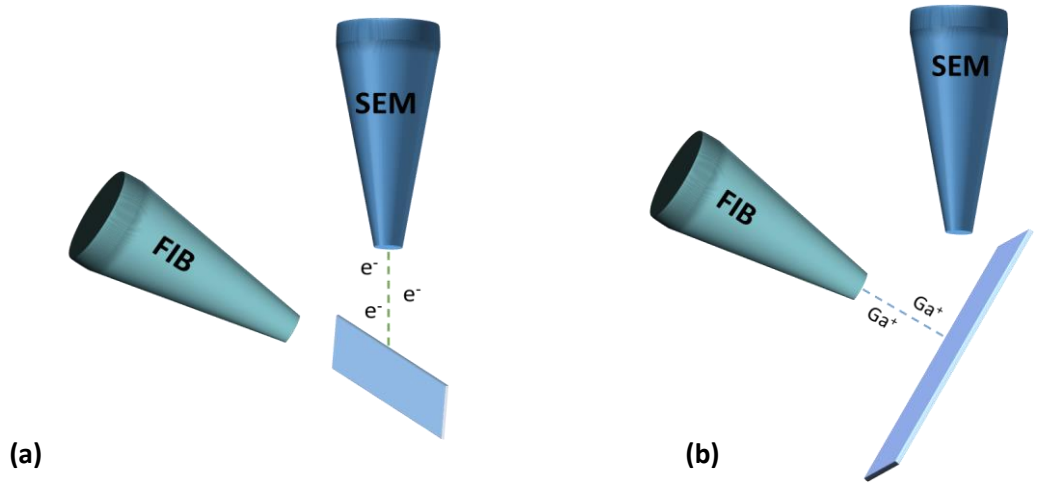


Figure 7.3. Schematic of the two positions during the test. (a) The cantilever is positioned at the place where its lateral edge is perpendicular to the electron beam. The beam curvature can be measured by taking HR-SEM images of the lateral edge. (b) The top surface of the cantilever is perpendicular to the ion beam so that it can receive ion implantation from the ion beam.

For the measurement of bending curvature, 50 points along the edge of the cantilever were captured in the high resolution SEM images. The bending radius was calculated by fitting the coordinates of these 50 captured point to circles, with the standard error of the fitting being typically <1 nm. Figure 7.4 shows an example of the curve fitting.

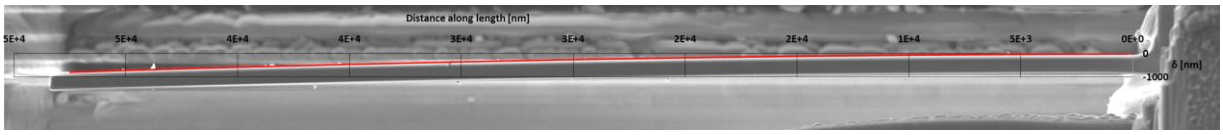


Figure 7.4. Demonstration of curve fitting - a Ga^+ implanted c-plane cantilever (Ref. Cantilever.1.1. Ga-c.Al_2O_3, implantation step No.10) is shown as an example. The circle curve coloured in red is generated based on the 50 points captured along the top edge of the cantilever.

The following five factors were considered in the test. (i) ion species, (ii) target material, (iii) ion dose, (iv) FIB accelerating voltage, (v) FIB beam current. The applied parameters were chosen subject to the availability of the equipment and the testing procedures were adjusted accordingly. All the implantations were carried out at 0° incident angle – the ion beam was perpendicular to a target surface. More details are described in Section.7.2.

7.1.5 Precision of the method

The main source of error in calculating the residual stress via Equation 7.1 originates from the measurements of cantilever thickness and curvature from SEM images, and thicknesses of implantation layer estimated using the SRIM simulation. The error propagation can be calculated using Eq.7.2[336], which shows that the substrate thickness gives the heaviest weight to the error.

$$\delta\sigma_{res} = |\sigma_{res}| * \sqrt{(\frac{\delta t}{t})^2 + (\frac{\delta R}{R})^2 + 4(\frac{\delta d}{d})^2} \qquad (7.2)$$

where $\delta\sigma_{res}$ is the calculated error in the residual stress. δt, δR and δd are the upper limits for errors in implantation layer thickness, radius of curvature and substrate thickness, respectively.

The error is generalised for each cantilever and shown as an error bar in each result graph.

7.2 Results

Each sample, which is tested under a specific set of FIB settings (i.e. ion dose, beam current and voltage), is numbered in the format as 'Cantilever.(reference number of the cantilever).(ion species).(target material) ((Main use of the cantilever))'. For example, 'Cantilever.1.1. Ga-c.Al_2O_3 (Effect of ion dose)' represents a c-plane Al_2O_3 cantilever implanted with Ga^+ for investigating the effect of ion dose, numbered as 'Cantilever.1.1'.

A summary of the experiments is provided in Table 7.3. For the high dose implantation tests, highlighted as '**H** (xxx pA, xxx ion/nm^2)' in Table 7.3, not all the implantation steps are listed in the summary but only the step that had the highest implantation dose during the entire process. The residual stress (RS) noted for each test is the RS calculated at the end of each test, rather than showing the development of the stresses through each implantation step. Whether a steady state has been reached within the applied ion dose range is also shown in the table.

The relevant SEM images for all cantilevers not shown in the main part of the thesis are in the Appendix B.

Table 7.3. Summary of the tests carried out in the present study, listing the reference number of each test, the FIB settings applied in each test (voltage, ion dose, current), the sign of residual stress at the end of each test ('C' denotes 'compressive', 'T' denotes 'tensile, 'C→T' means the transition from compressive to tensile), the magnitude of the residual stress measured at the end of each test, and whether the test achieved a steady state in the end ('Y' means 'yes', 'N' means 'no', 'NS' means 'not sure')

Ion	Target	Exp. No.	Voltage [kV]	Dose [ion/nm^2]	Current [pA]	Sign of RS	RS [GPa]	Steady state?
Ga	c-plane Al_2O_3	1.1	30	10x0.1+2x0.5+ 2x1	1	C	-0.8	Y
		1.2	30	4	1→2→5→10→20→50	C	-0.8	Y
		1.3	2→5→30	4	20	C	-0.9	Y
	a-plane Al_2O_3	2.1	30	10x0.1+2x0.5+ 2x1	1	C	-1.6	Y
		2.2	30	4	1→2→5→10→20→50	C	-1.8	Y
		2.2.x	30	**H** (1000pA, 7000 ion/nm^2]		C	-0.3	Y
		2.3	2→5→30	4	20	C	-1.9	NS
	SiC	3.1	30	10x0.1+2x0.5+ 2x1	1	C	-1.0	Y
		3.1.x	30	**H** (4000pA, 5000 ion/nm^2]		C	-0.9	Y
		3.2	30	4	1→2→5→10→20→50	C	-1.0	Y
		3.2.x	30	**H** (2000pA, 4000 ion/nm^2]		C	-0.9	Y
		3.3	2→5→30	4	20	C	-1.1	NS
	Si	4.1	30	10x0.1+2x0.5+ 2x1	1	C	-0.04	NS
		4.1	30	5	1→2→5→10→20→50→120	C	-0.14	Y
		4.1.x	30	**H** (2000pA, 2000 ion/nm^2]		C→T	0.4	N
Xe	c-plane Al_2O_3	5.1	30	7x0.6+3	1.5	C	-0.6	NS
		5.2	5→8→16→30	4	1.5	C→T	0.4	N
		5.2.x	30	**H** (1800pA, 6000 ion/nm^2]		C→T	22.2	Brittle fracture
	a-plane Al_2O_3	6.1	30	6x0.06+2x0.6+6	1.5	C	-0.7	N
		6.1.x	30	**H** (1800pA, 6000 ion/nm^2]		C→T	1.1	Brittle fracture
		6.2.x	30	**H** (6700pA, 6000 ion/nm^2]		T	24.4	N
	SiC	7.1	30	8x0.6	1.5	C	-1.2	NS
		7.1.2	30	5	1.5→2.8→24→230	C	-1.0	NS
		7.1.x	30	**H** (6700pA, 7800 ion/nm^2]		C→T	1.1	NS
		7.2.x	30	**H** (6700pA, 12000 ion/nm^2]		C→T	0.5	N

The material removal rates are summarised in Table 7.4.

Table 7.4. Materials removal rate measured in the present study at 30 kV.

Ion specie	Target material	Removed thickness [per 1 ion/nm^2]
Ga^+	Al_2O_3	0.01 nm
	SiC	0.02 nm
	Si	0.03 nm
Xe^+	Al_2O_3	0.03 nm
	SiC	0.03 nm

7.2.1 Effect of ion dose - low dose regime

7.2.1.1 Ga^+ implantation

Ga^+ implantation stresses measured with gradually increasing ion doses at the early stage of implantation (i.e. low dose regime) are summarised in Fig.7.5. For all the target materials tested, the compressive residual stress increased progressively with the ion dose until a quasi-steady state was reached within the low dose regime (although it did seem to reach a plateau at this stage, it will be seen later in the thesis that this was not actually a steady sate, therefore named 'quasi-steady state'). The residual stress was the highest in a-plane sapphire (≈ -1.6 GPa), followed by SiC (≈ -1.0 GPa), then c-plane sapphire (≈ -0.8 GPa), and was the lowest in Si (≈-0.05 GPa).

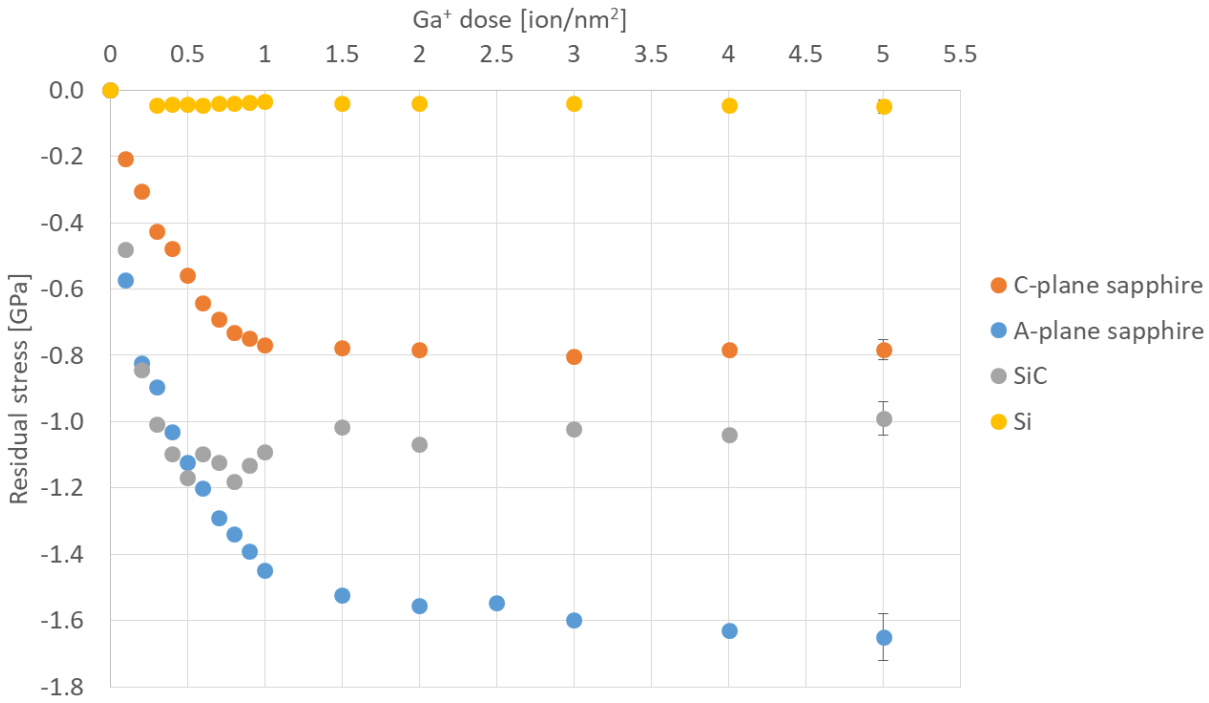


Figure 7.5. Residual stresses induced by FIB Ga^+ implantation with increasing ion dose, in c-plane sapphire, a-plane sapphire, SiC and Si. FIB condition: 30 keV, 1 pA. The relevant SEM images for a-plane sapphire, SiC and Si are shown in Figure B.3, Figure B.6 and Figure B.10 in the Appendix B, respectively.

SEM images for the c-plane sapphire specimen (i.e. cantilever.1.1.Ga-c.Al_2O_3) are shown in Figure 7.6, as an example, exhibiting progressive downwards bending with increasing ion dose until the quasi-steady state.

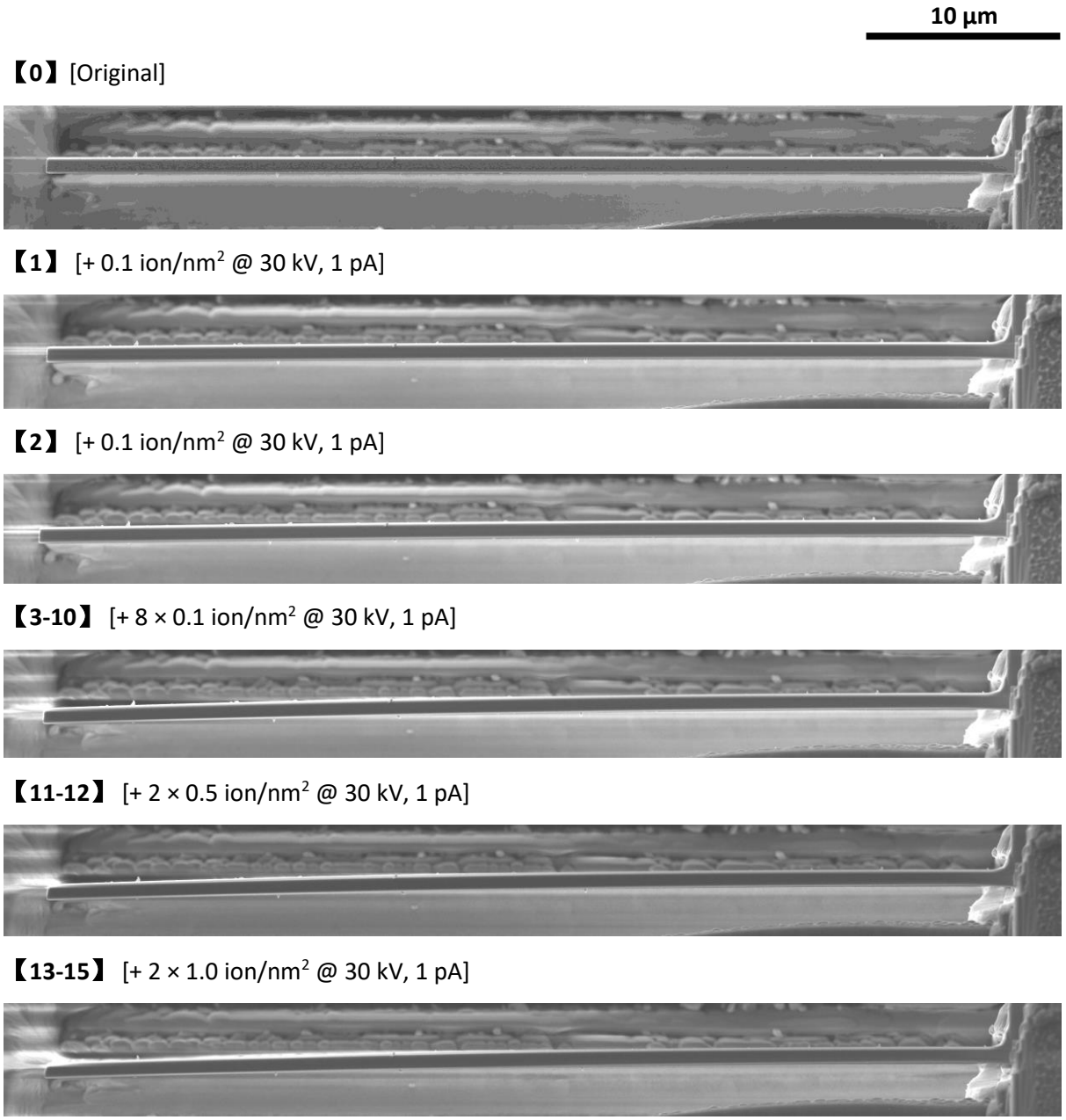


Figure 7.6. SEM images of the c-plane cantilever from the side view showing the curvatures. The ion dose was given under 30 keV, 1pA, following sequential steps 10 × 0.1 ion/nm² → +2 × 0.5 ion/nm² → +2 × 1.0 ion/nm2, inducing compressive residual stresses on the top surface of the cantilever which led to the progressive downwards bending.

The measured curvatures from steps [0]–[10] are illustrated as individual curves in Fig.7.7 to enhance visibility of the progressive increase in the curvature of the cantilever.

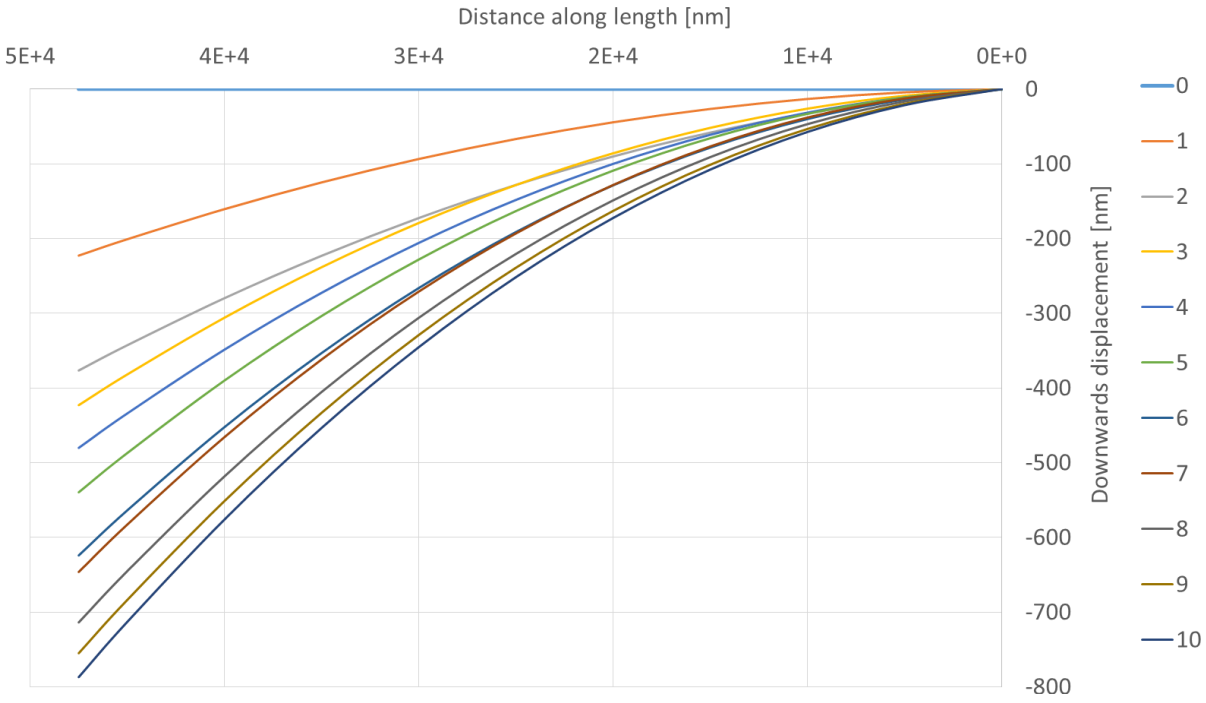


Figure 7.7. The curvatures of the cantilever from ion implantation steps No.[0]-[10], illustrated in the form of digital curves to amplify the visibility of the bending.

7.2.1.2 Xe^+ implantation

Tests with gradually increasing ion dose were also conducted with Xe^+, under 30 kV, 1.5pA. Xe^+ implantation also developed compressive residual stresses within the low dose regime in the materials tested, with the measured values summarised in Fig.7.8. For the same target material, the peak compressive residual stress induced by Xe^+ (-1.0, -1.4 and -1.3 GPa for c-, a-plane sapphire and SiC, respectively) was lower than that induced by Ga^+. The materials ranked in the same order as for Ga^+: c-plane sapphire < SiC < a-plane sapphire.

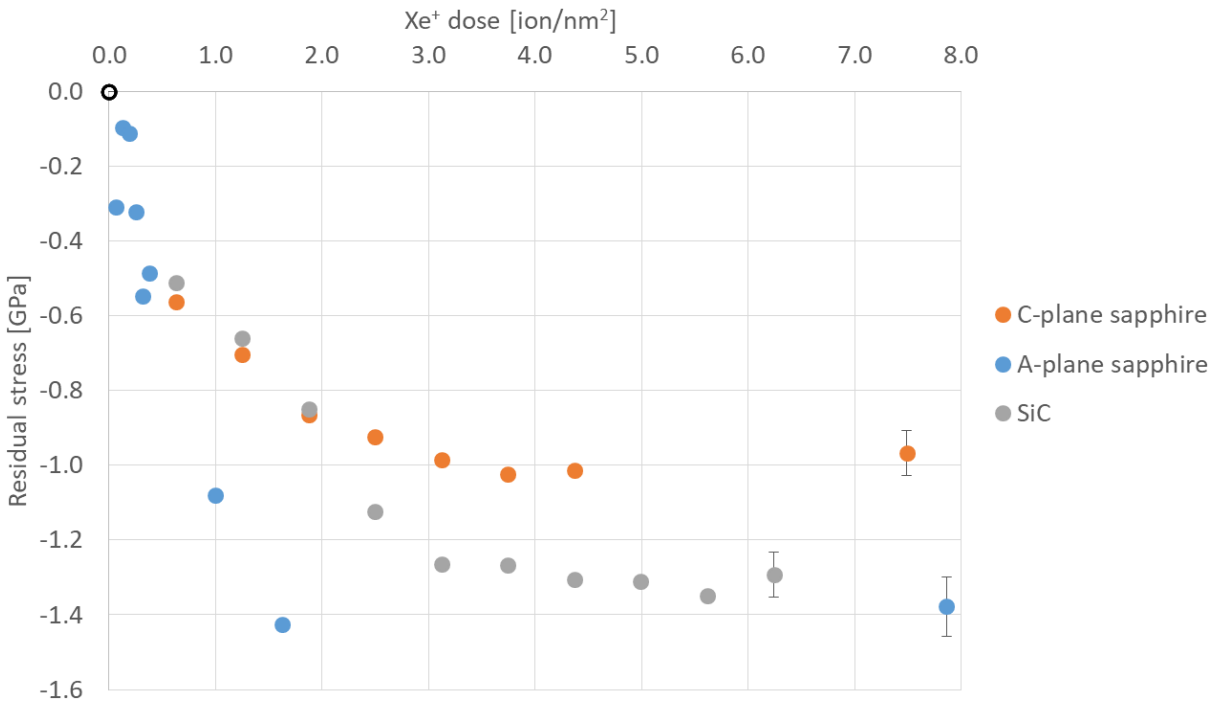


Figure 7.8. Residual stresses induced by PFIB Xe^+ implantation with increasing ion dose, in c-plane sapphire, a-plane sapphire and SiC. FIB condition: 30 keV, 1.5 pA. The corresponding SEM images can be found in Figure B.13, Figure B.16 and Figure B.18 in the Appendix B.

7.2.2 Effect of beam current – low current regime

7.2.2.1 Ga^+ implantation

With Ga-FIB at 30 keV, the beam current was increased gradually from 1 to 50 pA, with 4 ion/nm^2 (i.e. a dose at which the stresses reached a quasi-steady state according to Figure 7.5) given at each current. The residual stresses measured for c-, a-plane sapphire, SiC and Si are summarised in Fig.7.9. In each target material, the magnitude of the compressive residual stress increased to a peak value at low current, followed by a slight drop and then remained at an almost constant value (about -0.8, -1.9, -1.0 and -0.1 GPa for c-, a-plane sapphire, SiC and Si, respectively).

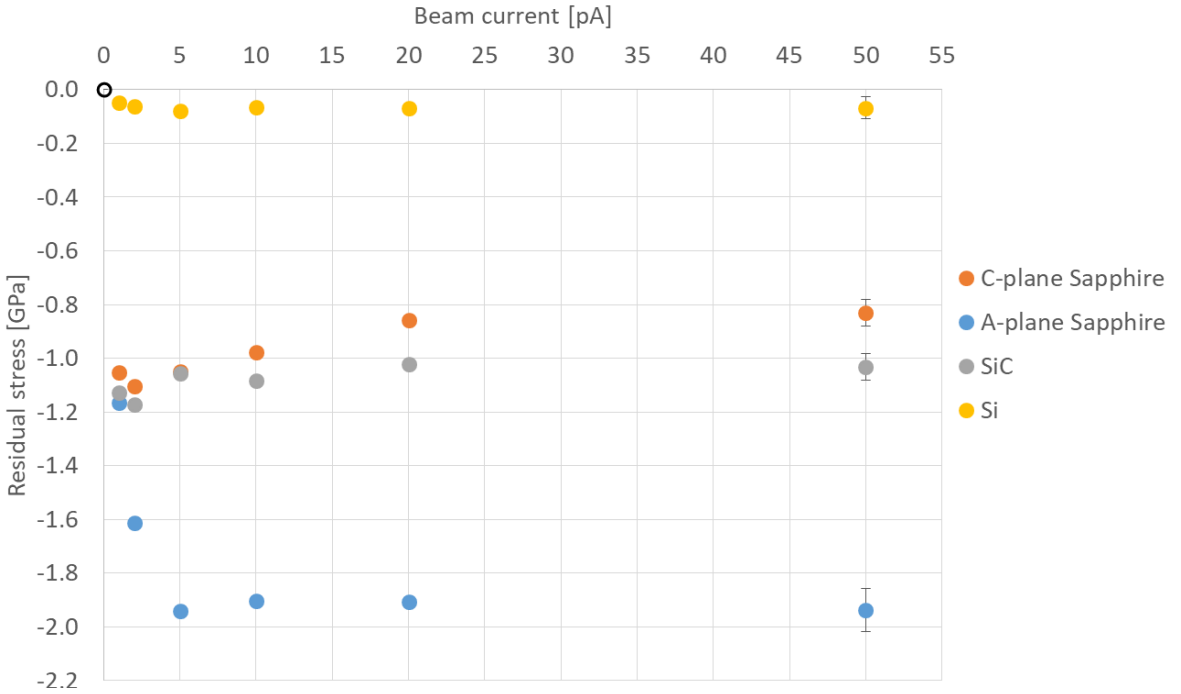


Figure 7.9. Residual stresses induced by FIB Ga^+ implantation with increasing beam current (1 pA → 2 pA → 5 pA → 10 pA → 20 pA → 50 pA) in c-plane sapphire, a-plane sapphire, SiC and Si. FIB condition: 30 keV, 4 ion/nm^2 at each implantation. The corresponding SEM images can be found in Fig.B.1, Figure B.4, Figure B.7 and Figure B.11 in the Appendix B.

7.2.2.2 Xe^+ implantation

A similar test was conducted with Xe^+ on SiC with the current ranging from 1.5 pA to 230 pA, voltage remaining at 30 kV and ion dose being 4 ion/nm^2 for each current. The residual stress (Figure 7.10) decreased slightly while the current increased from 2.8 pA to 24 pA and 230 pA, ending up at-1.1 GPa.

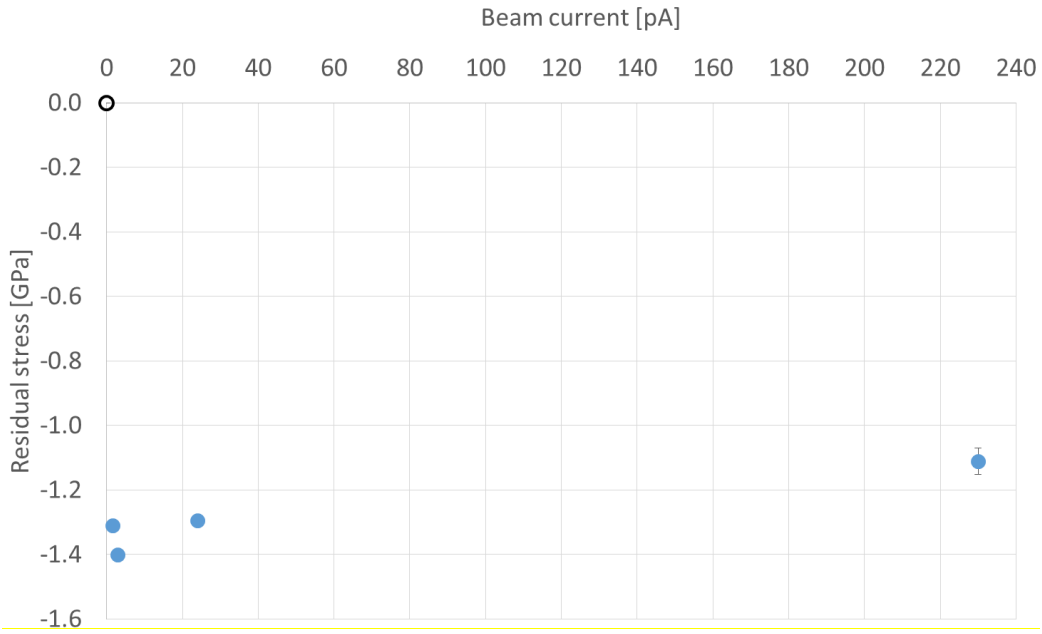


Figure 7.10. The compressive residual stresses introduced by FIB Xe^+ implantation in SiC with increasing beam current. The relevant SEM images can be found in Figure B.19 in the Appendix B.

7.2.3 Low to high ion dose regime coupled with low to high beam current

The development of residual stresses at 30 kV within the complete ion dose range (including both low and high dose regimes) is presented in Figure 7.11 and Figure 7.17 for Ga^+ and Xe^+ implantation, respectively.

The stress development of different materials and ion species exhibits the same trend: (Stage I) Within the low dose regime, compressive residual stress developed gradually until reaching a quasi-steady state which lasts for only a limited ion dose range (the zoomed-in graphs are shown in Figure 7.5 and Figure 7.8). (Stage II) With further increasing ion dose, the compressive residual stresses decreased, with some remaining compressive in the end (i.e. Ga^+ in sapphire and SiC) and the others transiting to tensile (i.e. Ga^+ in Si, Xe^+ in sapphire and SiC).

7.2.3.1 Ga^+ implantation

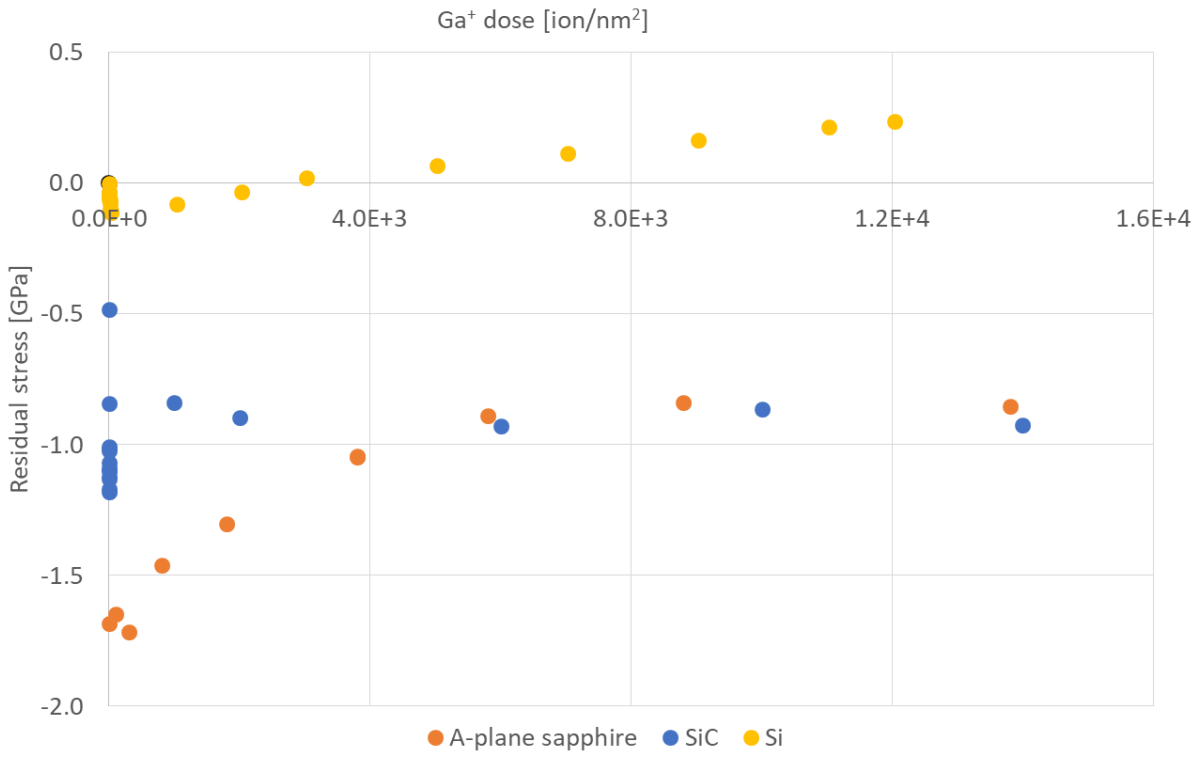


Figure 7.11. Ga^+ implantation in three different materials with complete ion dose range. For the currents applied at each implantation, please refer to the graphs for individual cantilevers presented in the section below.

Details of the ion dose and beam current employed for each test are presented in Figure 7.12 – Figure 7.15 below. Although both ion dose and beam current increased during the implantation procedures, increasing beam current did not seem to have a strong influence on the development of residual stress, suggesting that the factor dominating the development of residual stress is ion dose.

Table 7.5. Ga^+ implantation with high ion doses and beam currents

Cantilever Ref.	RS results	RS in the end	Removed thickness [nm]	Remaining thickness [nm]
2.2. Ga-a.Al_2O_3	Figure 7.12	-0.8 GPa	635	528
3.1. Ga-SiC	Figure 7.13	-0.9 GPa	233	702
3.2. Ga-SiC	Figure 7.14	-1.0 GPa	478	725
4.1. Ga-Si	Figure 7.15	+0.2 GPa	416	407

- **Cantilever. 2.2. Ga-a.Al_2O_3**

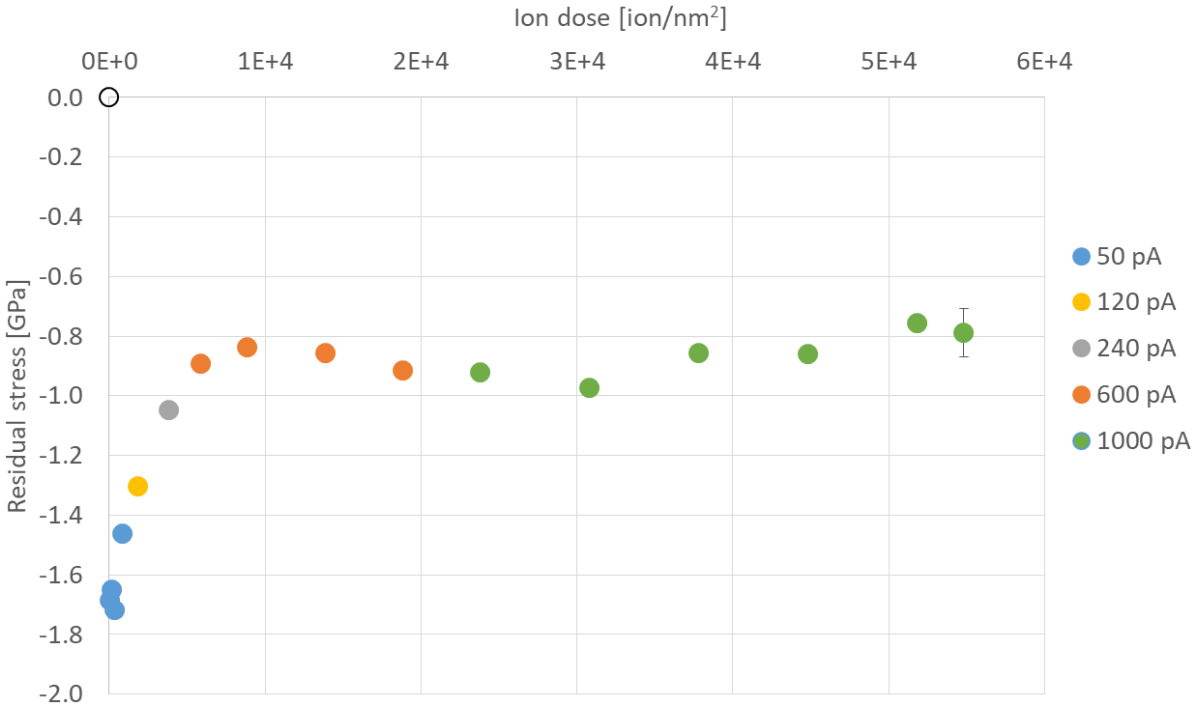


Figure 7.12. The compressive residual stresses introduced by FIB Ga^+ implantation in a-plane sapphire under 30 keV, with increasing ion dose and beam current.

➢ **Cantilever. 3.1. Ga-SiC**

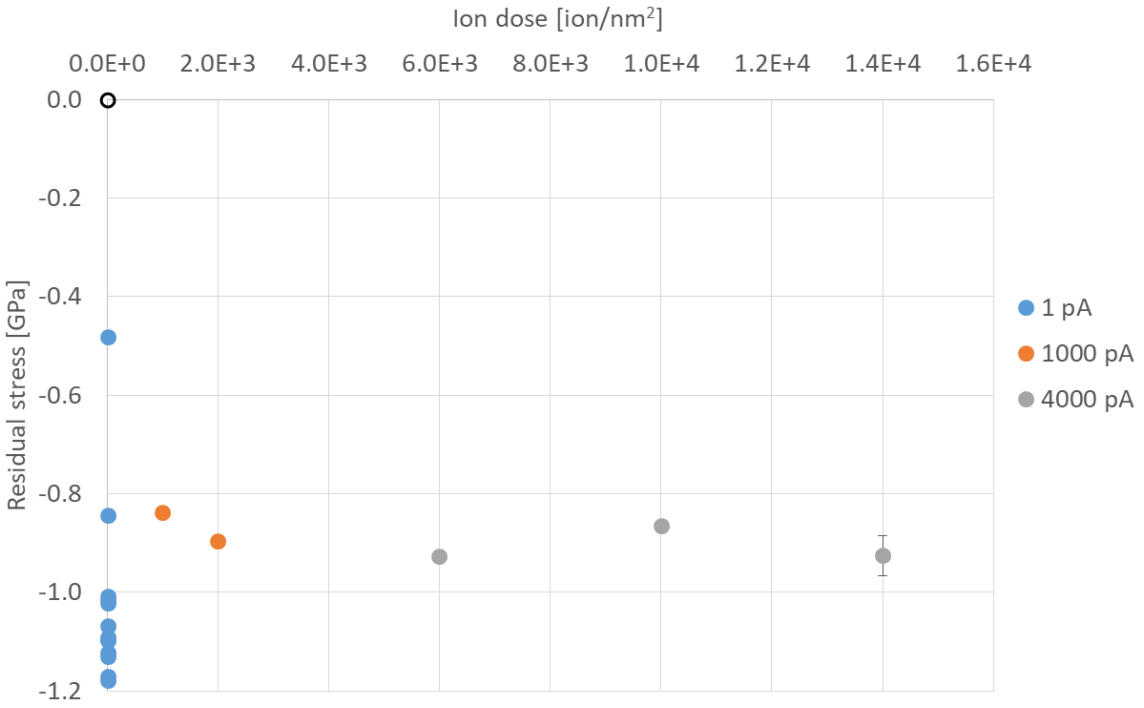


Figure 7.13. Residual stresses induced by FIB Ga⁺ implantation in SiC at 30 keV with increasing ion dose and beam current. The corresponding SEM images are shown in Figure B.7 (Appendix B).

➢ **Cantilever. 3.2. Ga-SiC**

A similar test was performed on SiC with a higher dose and more beam currents, exhibiting similar behaviour to Figure 7.13.

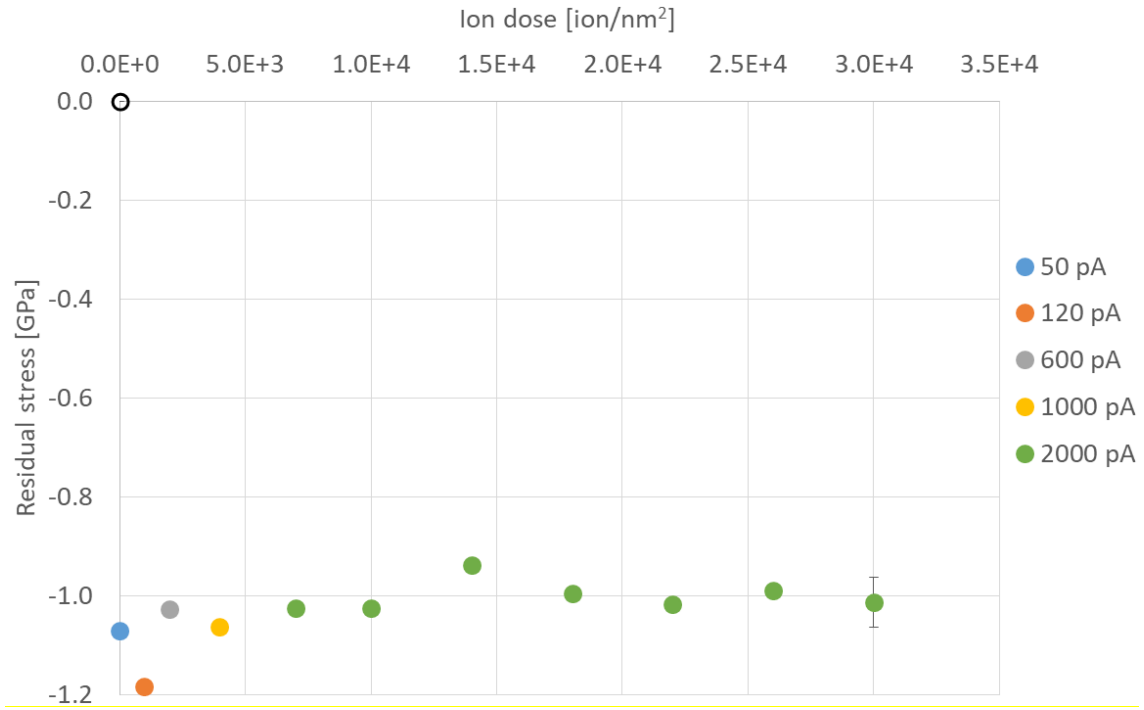


Figure 7.14. Residual stresses induced by FIB Ga⁺ implantation in SiC at 30 keV with increasing ion dose and beam current. The corresponding SEM images are shown in Figure B.8 (Appendix B).

➢ **Cantilever. 4.1. Ga-Si**

The residual stress transited from compressive to tensile, exhibiting an almost linear relationship versus ion dose. As one of the thinnest cantilever after implantation, the curvature was significant despite the low residual stress. Changing beam current did not seem to have affected the trend of the residual stress development.

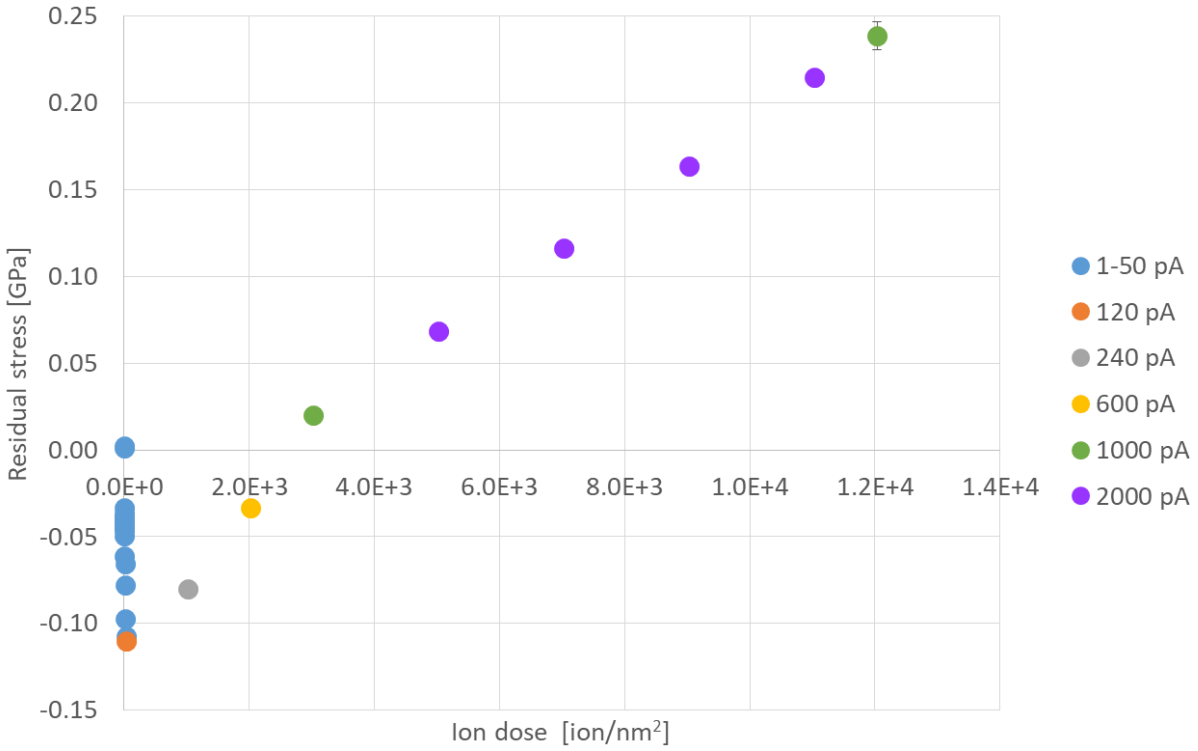


Figure 7.15. The residual stresses introduced by FIB Ga^+ implantation in Si with increasing ion dose and different beam currents, including Process #1, #2 and #3. The corresponding SEM images are shown in Figure B.12 (Appendix B).

The cantilever ended up with a significant upwards bending, as shown in Figure 7.16.

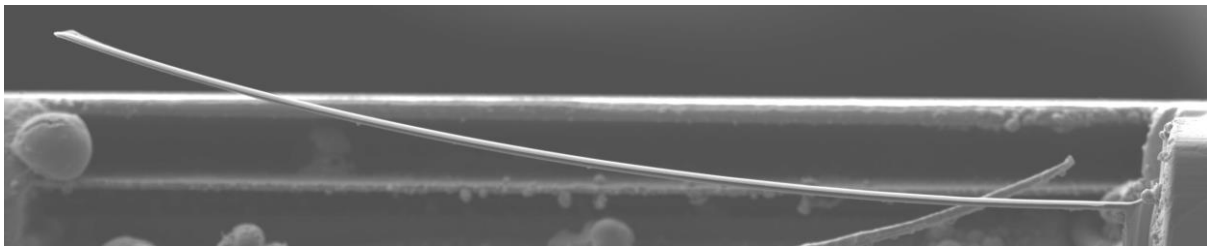


Figure 7.16. SEM images of the Si cantilever from the side view after the last step of implantation.

7.2.3.2 Xe^+ implantation

For Xe^+ implantation, the results are more complicated. Therefore, only two examples for a-plane sapphire and SiC are summarised in Figure 7.17, followed by details for each individual test in Figure 7.18 – Figure 7.27.

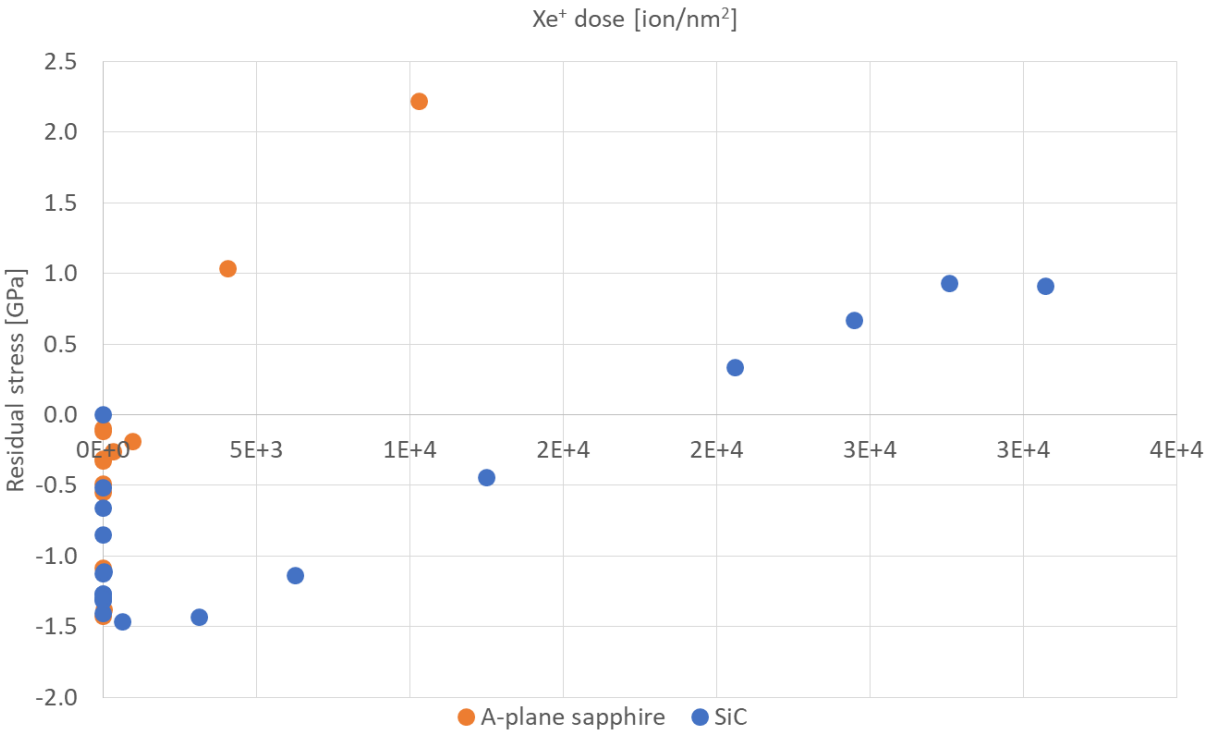


Figure 7.17. Xe^+ implantation in a-plane sapphire and SiC with complete ion dose range.

Table 7.6. Ga^+ implantation with high ion doses and beam currents

Cantilever Ref.	Results	RS in the end	Removed thickness [nm]	Remaining thickness [nm]
5.2. Xe-c.Al_2O_3	/	22.2 GPa	406	692
6.1. Xe-a.Al_2O_3	Figure 7.20	+2.2 GPa	146	977
6.2. Xe-a.Al_2O_3	Figure 7.23	+24.5 GPa	415	507
7.1. Xe-SiC	Figure 7.25	+0.8 GPa	1059	258
7.2. Xe-SiC	Figure 7.27	+0.6 GPa	918	315

- **Cantilever. 5.2. Xe-c.Al_2O_3**

Although the previous implantation step of 3000 ion/ nm^2 at 1800 pA developed the residual stress stably to -0.5 GPa, after being given another high dose implantation (6000 ion/ nm^2) at the same current, the cantilever exhibited a significant curvature and fractured at the root of the cantilever (Figure 7.18), indicating an apparent tensile residual stress of 22.2 GPa.

The cantilever curved more near the fixed end than the free end, possibly because the incident angle of ion beam increased along the length towards the free end due to the bending of the cantilever, which resulted in more damage near the fixed end. Therefore, the residual stress was calculated based on the curvature of the half cantilever near the fixed end, which exhibits clear circularity.

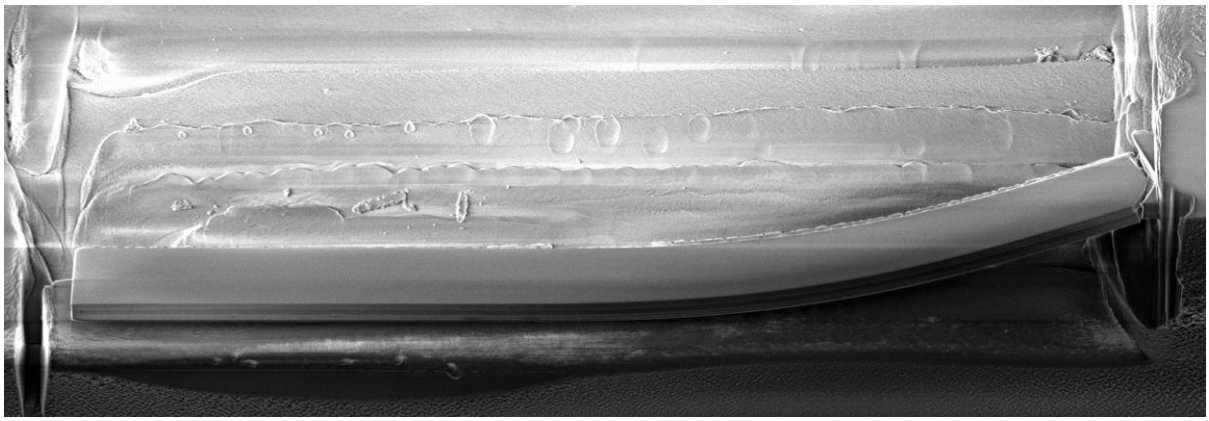


Figure 7.18. SEM images of the c-plane Al_2O_3 cantilever implanted by Xe^+. The rest of the SEM images can be found in Figure B.15 (Appendix B).

The fractured root (Figure 7.19) exhibited a chevron shape (possibly be explained by the fracture along preferred cleavage planes) and faceted fracture surface with twist hackle[214] on its top part.

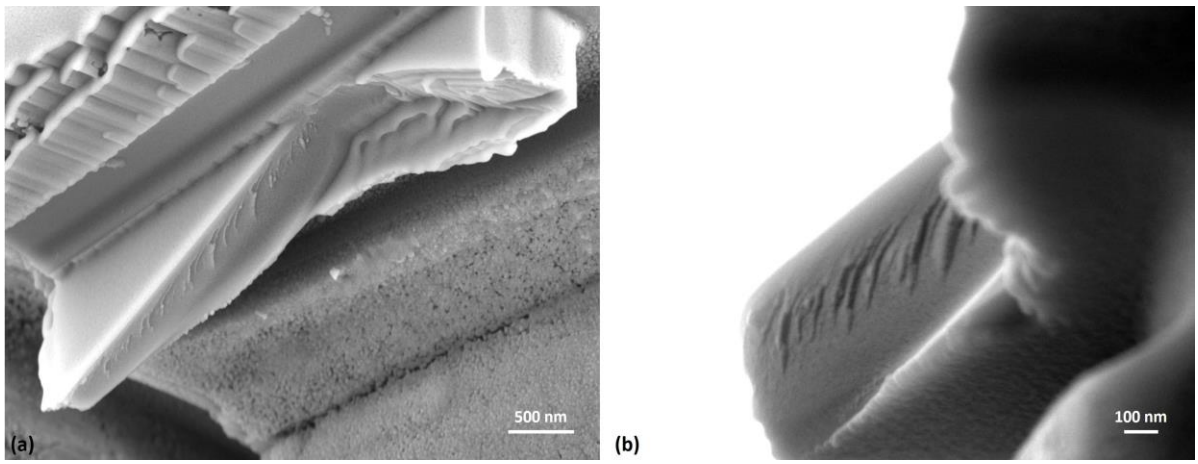


Figure 7.19. Fracture surface of Cantilever. 5.2. Xe-C.Al_2O_3 after high dose implantation. (a) Inclined view to enable optimal visualisation of the fracture surface. (b) View from bottom surface of the cantilever towards the fracture surface.

➢ **Cantilever. 6.1. Xe-a.Al_2O_3**

With the current remaining at 1.5 pA, a significant decrease of the residual stress occurred with the total ion dose increased from 8 ion/ nm^2 to 320 ion/ nm^2. The compressive stress decreased further and transited to tensile with further increase in ion dose. Once the stress became tensile, it increased almost proportionally to the ion dose. In the last step of implantation (not shown in Figure 7.20 due to small amount of ion dose), the cantilever was broken just after a dose of ~ 54 ion/nm^2 (Fig.7.21), indicating that the cantilever fractured at a residual stress around 2.2 GPa.

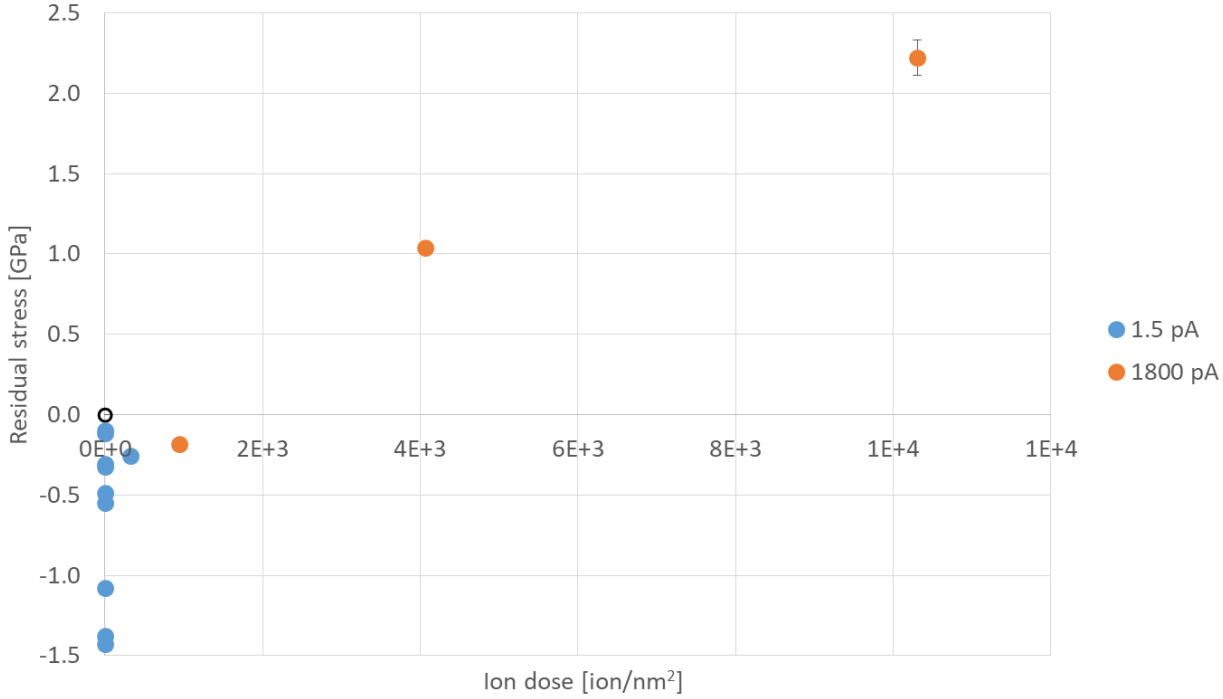


Figure 7.20. The residual stresses introduced by FIB Xe^+ implantation in Si with increasing ion dose and beam current. The corresponding SEM images are shown in Figure B.17 (Appendix B).

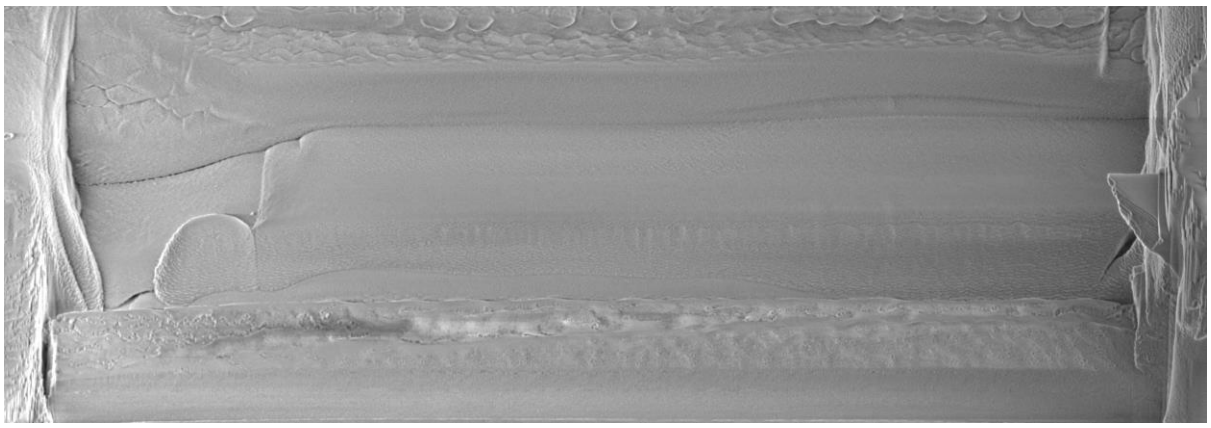


Figure 7.21. SEM image showing that the a-plane Al_2O_3 cantilever fractured during the last step of Xe^+ implantation.

The fracture surface of the cantilever was heavily faceted as shown in Figure 7.22, because the cross sectional plane of the cantilever was the most unfavoured cracking path of sapphire, i.e. c-plane.

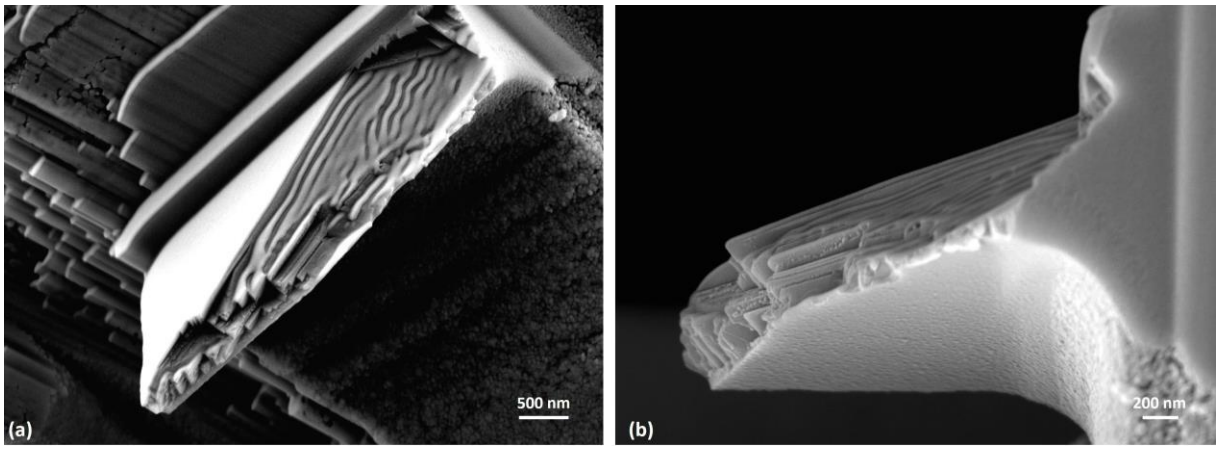


Figure 7.22. The fracture surface of a-plane sapphire cantilever implanted by Xe^+.

- **Cantilever. 6.2. Xe-a.Al_2O_3**

The cantilever exhibited an extreme bending after a high dose and high current implantation (Figure 7.24), indicating an apparent residual stress of 24.5 GPa. No visible cracks were found on the cantilever from SEM microstructural investigation.

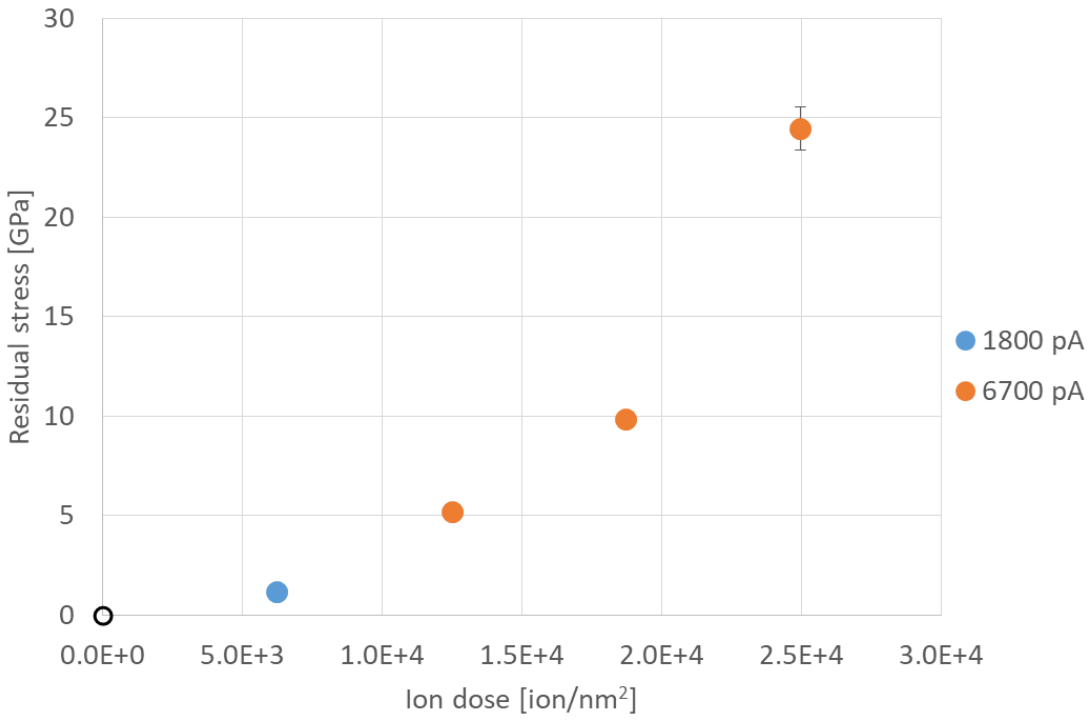


Figure 7.23. The residual stress by FIB Xe^+ implantation in a-plane Al_2O_3 with high doses and currents at 30 kV. For the implantation steps [2-4], the cantilever curved more at the root than near the free end due to the change of ion beam incident angle along the length. The residual stress was therefore calculated based on the curvature of the section near the root where the ion beam incident angle was about 0°.

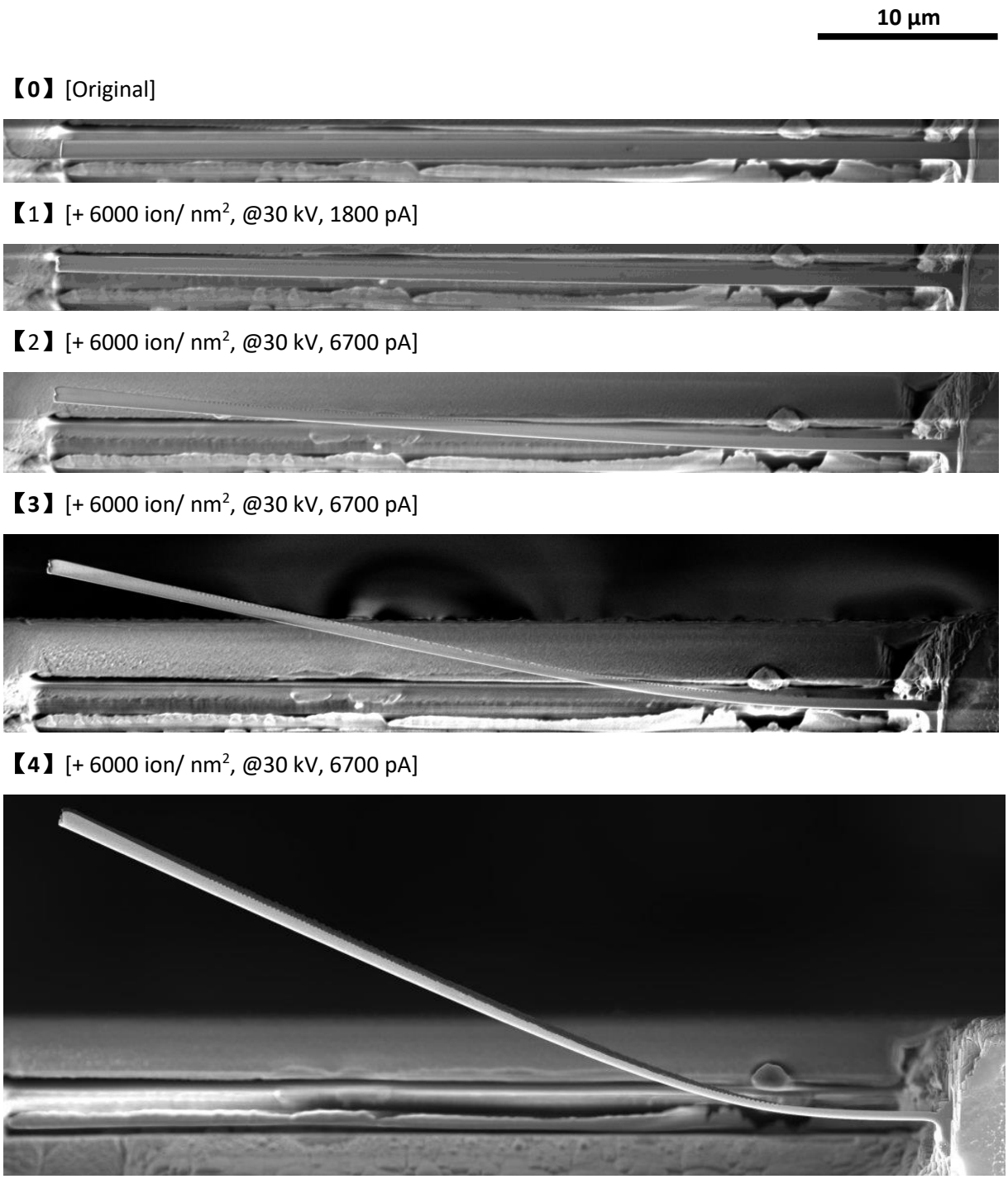


Figure 7.24. SEM images of the side view of the a-plane Al_2O_3 cantilever implanted by Xe^+ with high doses at high currents

➢ **Cantilever.7.1. Xe-SiC**

The residual stress transited from compressive to tensile, and increased in an almost linear manner with the ion dose, ending up at around +0.8 GPa.

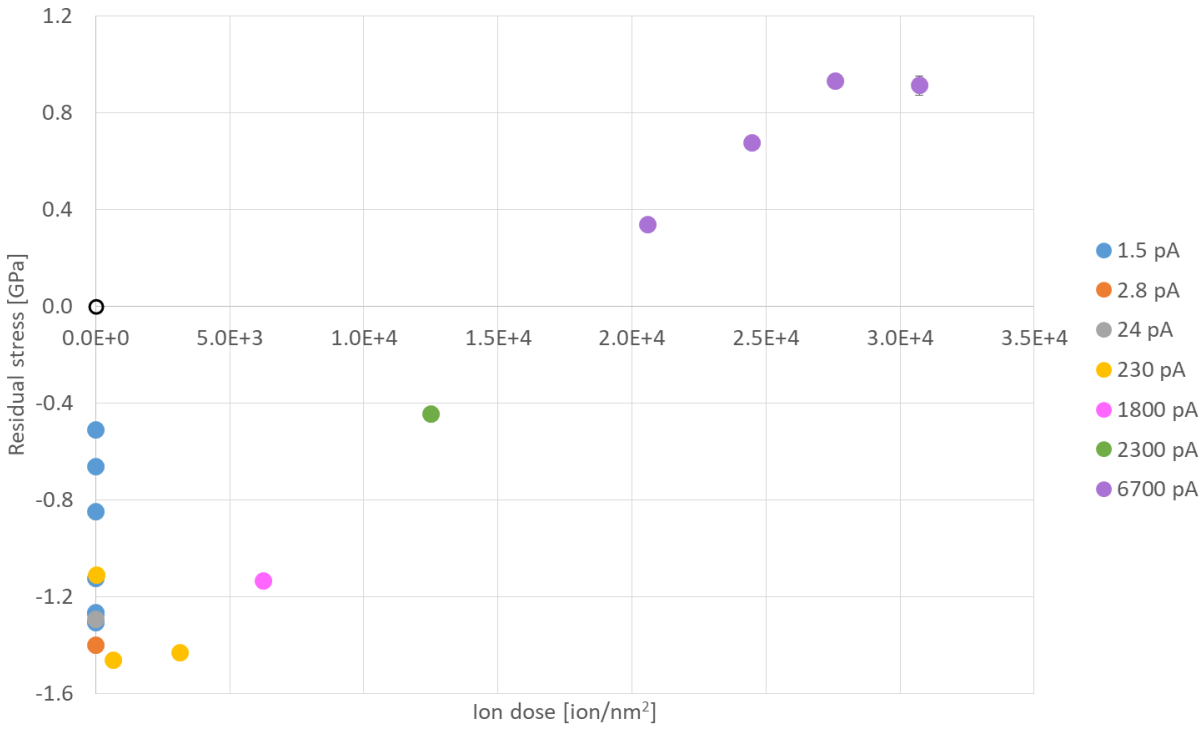


Figure 7.25. The residual stress stresses introduced by FIB Xe^+ implantation in SiC with high ion doses and beam current.

Figure 7.26 shows the significant upwards bending after the last step of implantation.

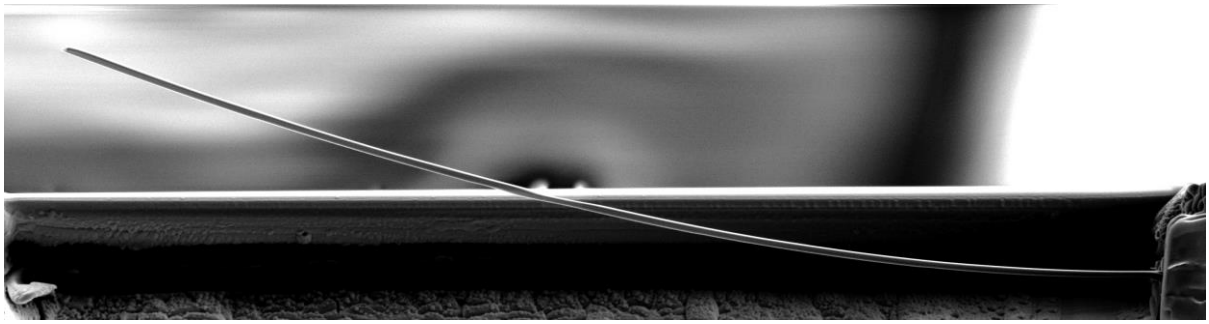


Figure 7.26. SEM images of the side view of the SiC cantilever implanted by Xe^+ with high doses and high currents.

➢ **Cantilever. 7.2. Xe-SiC**

The implantation started with a high current straight away, at 230 pA, with the dose remaining small (0.6 ion/nm^2). As shown in Figure 7.27, the implantation developed compressive residual stress at low

ion dose range, followed by transiting progressively to tensile with increasing ion dose. Changing beam current did not affect the magnitude of the residual stress, again suggesting that ion dose was the main factor on the development of residual stress.

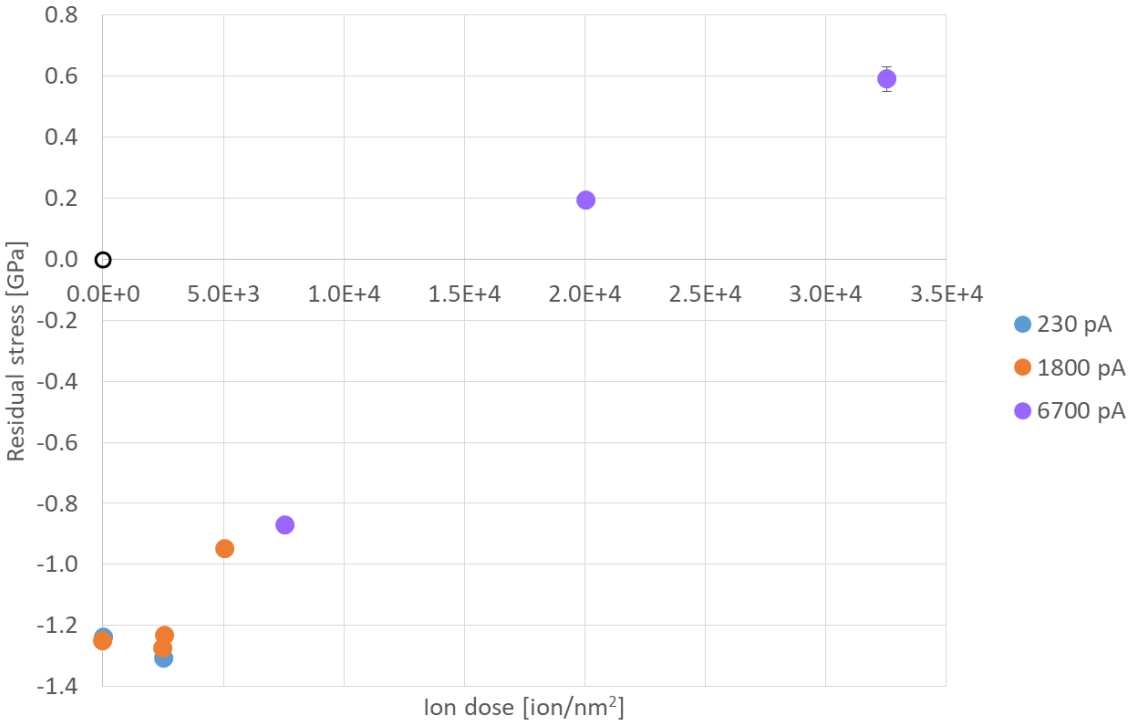


Figure 7.27. The residual stress stresses induced by FIB Xe^+ implantation in SiC with high ion doses and high currents. The residual stress transited from compressive to tensile. The corresponding SEM images are shown in Figure B.21 (Appendix B).

7.2.4 Effect of accelerating voltage

For c-, a-plane sapphire and SiC, the residual stresses measured with increasing Ga-FIB acceleration voltages are summarised in Fig.7.28, with the same current (20 pA) and ion dose (4 ion/nm^2 per implantation) applied throughout the tests (i.e. conditions chosen based on the results from Figure 7.5 and Figure 7.9 which exhibited a quasi-steady state at 4 ion/nm^2 and 20 pA within the low dose regime). In all three materials investigated, the residual stresses increased with FIB beam voltages in a non-linear manner, exhibiting values of around -0.9, -2.0 and -1.1 GPa for c-, a-plane sapphire and SiC respectively, which are similar to those reported for the tests of effect of ion dose within low dose regime (Figure 7.5).

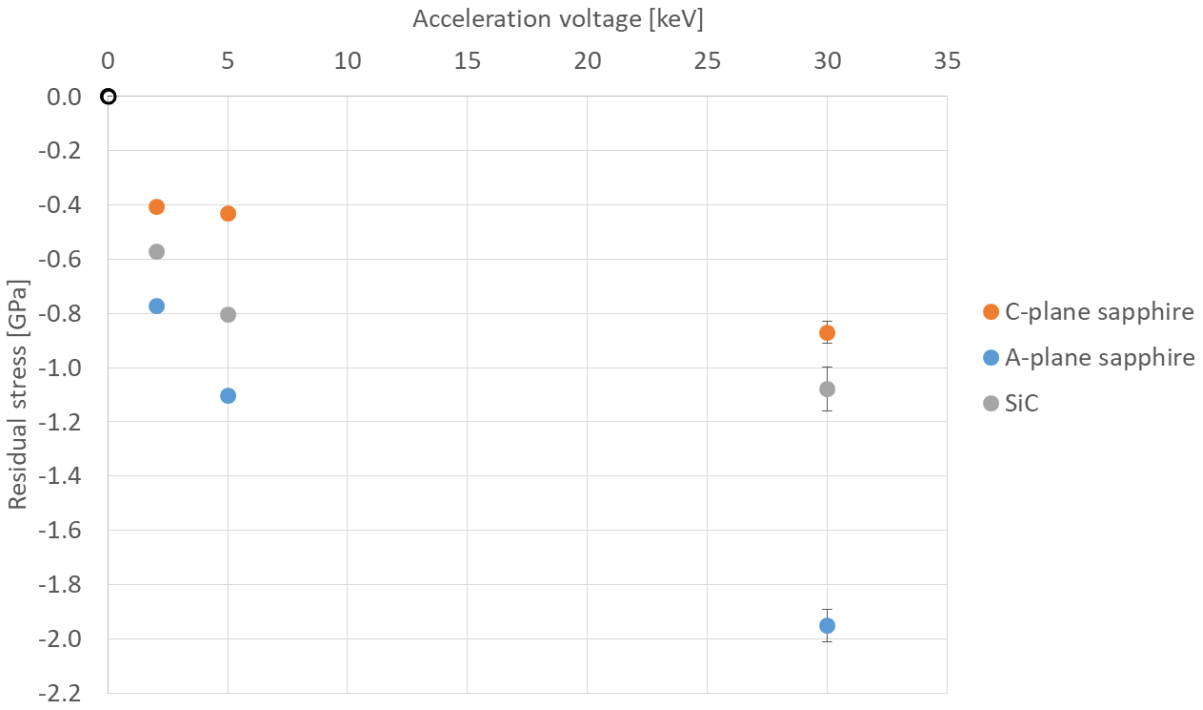


Figure 7.28. Residual stresses induced by FIB Ga^+ implantation with increasing beam acceleration voltage (1 keV → 2 keV → 5 keV → 30 keV), in c-plane sapphire, a-plane sapphire and SiC. FIB condition: 20 pA, 4 ion/nm^2 for each implantation step. The corresponding SEM images are shown in Figure B.2, Figure B.5 and Figure B.9 in the Appendix B, respectively.

7.3 Discussion

7.3.1 Mechanisms behind the creation of implantation stresses

Before interpreting the stress evolution in each implantation case, the five main mechanisms involved in the implantation process (i.e. vacancy-induced swelling, implanted-ion-induced swelling, thermal spike, densification and plasticity mechanisms) are discussed separately. In the case of Xe^+ implantation, an additional mechanism (i.e. bubble mechanism) also contributes to the stress formation.

(1) Vacancy-swelling mechanism (*Compressive RS*)

The collision cascade driven by the incident ion creates vacancies and interstitials in the target crystal lattice until complete amorphisation. For these Frenkel pair defects, the vacancies remain well localised, while interstitials are highly mobile and are absorbed in the matrix as dislocation loops, contributing to plastic flow[337]. The excess volume of vacancies therefore dominates the volumetric

swelling of the lattice[338], known as the 'swelling effect'. This vacancy-induced swelling is a well-known mechanism in the field of radiation damage - it has been widely demonstrated in irradiated Al_2O_3[339, 340], SiC[315, 341-346], Si[347], and others[337, 340], using a variety of techniques such as XRD measurement, AFM scanning, TEM characterisation and MD simulation.

In the present study where the top damaged layer is constrained by the undamaged substrate, the volumetric swelling of the ion implanted layer results in lateral compressive residual stress in the damaged layer.

The vacancy-swelling mechanism is the primary swelling mechanism, compared to the implanted-ion-swelling mechanism which will be explained in the following section, because the number of vacancies created per implanted ion in a perfect crystal is typically of the order of 10^2 to 10^3 as predicted by SRIM simulation for the conditions used in this study.

(2) Implanted-ion-swelling mechanism (*Compressive RS*)

The implanted atoms with bigger size than the matrix atoms (i.e. the ionic crystal radii are 0.054 nm for Al^{3+} and 0.062 nm for Ga^{3+})[348] rest in the target matrix as substitutional or interstitial defects,[349] which add additional volume to the structure and therefore lead to volumetric swelling. Acting as the secondary swelling mechanism (relative to the vacancy-swelling mechanism), the constrained swelling induced by the implanted ions also contributes to the generation of compressive residual stress in the damaged layer.

The implanted-ion-swelling mechanism becomes ineffective when a steady state is achieved at the threshold implantation dose, which means that the number of implanted atoms is equal to the number that get sputtered away.

(3) Thermal spike mechanism (*Tensile RS*)

The thermal spike is a well-known phenomenon during ion implantation, which has been widely investigated by modelling the displacement cascades at the atomic scale. Upon the impact of each incident ion, the temperature in the target area increases significantly within ~2 picoseconds.[350] The

relaxation time that it takes the thermal spike to cool down to room temperature is typically within about 3 to 30 picoseconds[257, 351, 352] depending on the thermal conductivity of the material. As an example, the MD simulation of Ga^+ implantation in single crystal diamond[257] demonstrates that the local temperature rise from a single ion collision can reach as high as 1454.6 K (= 1181.5 °C) with a beam energy of 16 keV, which afterwards drops to the ambient temperature within 3 ps.

The high temperature of the thermal spike causes local melting[344] or severe lattice disorder, and leads to instant volumetric expansion of the implantation affected region. However, the high temperature core is constrained by the surrounding lattice in the lateral direction, which leads to the biased swelling and relaxation of the structure in different directions due to the in-plane stress. The compressive strain induced by the surrounding lattice on the expanded core yields plastic deformation.

Upon rapid cooling (also known as 'quenching'), the plastically-deformed core shrinks, which results in a smaller lateral dimension than its original size. As a quick calculation based on gross assumptions, knowing that the linear thermal coefficient of alumina increases with temperature (e.g. the thermal expansion coefficient of alumina is about 7.2×10^{-6} K^{-1} at 300K, ~9.0×10^{-6} K^{-1} at 1000K, ~1.0×10^{-5} K^{-1} at 1500K)[353], taking the thermal expansion coefficient at 1500K and the biaxial elastic modulus of alumina as 600 GPa, portioning the stress within rigid surroundings of 0.5 as approximation, when the temperature increases by 1000K, the thermal expansion stress is ~3.0 GPa. Knowing that the yield strength of alumina drops significantly with increasing temperature (e.g. the yield strength of polycrystalline alumina drops from ~4 GPa to ~1.5 GPa when the temperature increases from 300K to 1000K[354]), this indicates that the yield strength of the microscopic high-temperature core is likely to drop below the constraining stress and therefore yields plastically. Plasticity can happen via either dislocation motion or diffusion. For the latter, the atoms are driven to flow onto the surface by the high lateral pressure created by the thermal expansion.[355] Upon rapid cooling, recrystallisation[352] occurs and the expanded volume tends to shrink back to its original size. With the atoms that have flowed on the surface remaining on the surface and becoming 'adatoms'[356] to increase the thickness,

which has been demonstrated numerically[357] and experimentally[358], the lateral dimension will become smaller than its original size to compensate for the increased thickness.

The microscopic constrained thermal expansion results in localised plastic lateral shrinking, which extends to the macroscopic lateral shrinking during the ion beam rastering process. Since the lateral shrinking is constrained by the undamaged layer, tensile residual stress is generated in the damaged layer.

(4) Densification mechanism (*Tensile RS*)

If chemical changes occur during ion-solid interaction, leading to formation of a second phase that has a more densely packed structure than the original one, densification (i.e. density increases) occurs. In the present study, Ga^+ implantation in Al_2O_3 forms denser second phase particles ($GaAlO_3$[359], hexagonal unit cell with lattice constants of a = 5.70 Å, c = 8.92 Å, atom density [~99.3 atom/nm^3] which is higher than that of amorphous Al_2O_3 [~93.8 atom/nm^3]) when the ion dose reaches a threshold value, as indicated by the TEM microstructural investigation in Chapter 4.

Equivalent to shrinking, the densification results in tensile residual stress in the damaged layer which is constrained by an undamaged substrate.

(5) Bubble mechanism (*Compressive RS → Relaxation of compressive stress*)

It is widely recognised that inert gas implantation can enable the formation of bubbles in irradiated materials due to the limited solubility of the gas in a ceramic matrix.[322] The work done in Chapter 4 has demonstrated well the formation of Xe bubbles in Plasma-FIBed Al_2O_3. In addition to that, the bubbles induced by implanted inert gas ions are observed in materials like SiC[319, 360-363], Al_2O_3[364-369], Si[370, 371] and others[319, 369, 372]. An extensive summary is provided by Zinkle[319] in terms of dose threshold for the formation of visible bubbles.

The bubble-induced swelling[371, 372] that is constrained by the undamaged substrate results in a compressive residual stress in the damaged layer.

However, blistering of the formed bubbles is a well-known phenomenon in many materials that are exposed to keV to MeV ion beams.[319, 373-375] It happens when the internal pressure increases to a sufficiently high value that yield strength[376] is exceeded, via either localised heating or increasing gas atom concentration, which leads to progressive cracking at the ligatures between highly pressurised gas bubbles.[319] The results in Chapter 4 show that the Xe bubbles formed in Al_2O_3 can easily be burst by the local heating induced by the focused high-energy electron beam. It has also been widely observed that blistering occurs when the implantation dose reaches a threshold value.[319] For instance, the threshold blistering for He implantation in Al_2O_3 at room temperature is ~3×10^{21} ion/nm^2, corresponding to a peak implanted He concentration of ~20 at.%, while it is slightly higher for SiC – threshold dose of >5×10^{21} ion/nm^2, corresponding to a peak concentration of >30 at.%.[319] Moreover, the threshold dose of blistering decreases with increasing temperature.[319]

When a bubble bursts and leaves an empty void behind, the deformed lattice around the void relaxes and expands into the void, therefore reduces the overall swelling of the damaged layer and decreases the swelling-induced compressive residual stress.

(6) Plasticity mechanism (*Relieving RS*)

Radiation-enhanced plasticity[377, 378] is known to occur due to the radiation-induced stresses[379] and thermal spikes. Si amorphised by the irradiation of high-energy heavy ions is found to deform plastically in the ion damaged region in the same way as conventional glasses.[380] In crystalline materials, dense interstitial dislocation loops are found in irradiated Al_2O_3[340, 366, 368], SiC[360, 363], and other materials[319], which are formed by atomic clustering of the highly mobile[337] interstitial atoms.[319]

As well as being involved in the generation of residual stress in some of the above mechanisms, plasticity can also relieve the stresses in the damaged region. [377, 378]

7.3.2 Development of residual stresses

Dynamic interaction between different mechanisms leads to different integrated stress status, which separates the development of implantation stress into the following two stages.

- **Stage I. Low dose at low current**

With ions impacting the pristine crystalline target, the number of vacancies created during the collision cascade of a single incident ion impact is typically at the order of 10^2 to 10^3 as predicted by SRIM simulation for the conditions used in this study. The vacancies therefore play the dominant role in the generation of stresses at the early stage of implantation[381, 382] and the dominating mechanism at Stage I is thus the vacancy-swelling mechanism.

This applies to all the implantation cases presented in the present study, because the original status of all the employed target materials was pristine crystal. The constrained swelling results in the lateral compressive residual stress in the damaged layer, which matches with the observations in the present study (Figure 7.5, Figure 7.8).

The parameters that influence the magnitude of residual stress developed at Stage I are discussed below.

Ion dose. At Stage I, the strain development process can be categorised into the following three regimes based on ion dose.[334] (Regime I) At low ion dose, isolated vacancies are generated. The consequent strain is almost proportional to the vacancy density, which is directly determined by the ion dose. (Regime II) The vacancy density keeps increasing with the augmenting ion dose. However, the efficiency of the damage accumulation drops due to the decreasing crystallinity of the target solid, leading to the deceleration of lattice swelling. In this regime, isolated defects also start to cluster into larger defects.[383] (Regime III) The amorphisation threshold (i.e. defect density = relative lattice disorder = 100%) is reached and the damaged layer is completely amorphised, which means that the vacancy density mechanism saturates. At this point, the vacancy-induced swelling mechanism becomes ineffective, Stage I thus ends.[347]

The residual stresses measured during Stage I of implantation in the present study with increasing ion dose, as summarised in Figure 7.5 and Figure 7.8, can be well linked to this three-regime theory. Figure 7.29 takes Ga implantation in sapphire as examples to demonstrate these three regimes (which also applies to SiC).

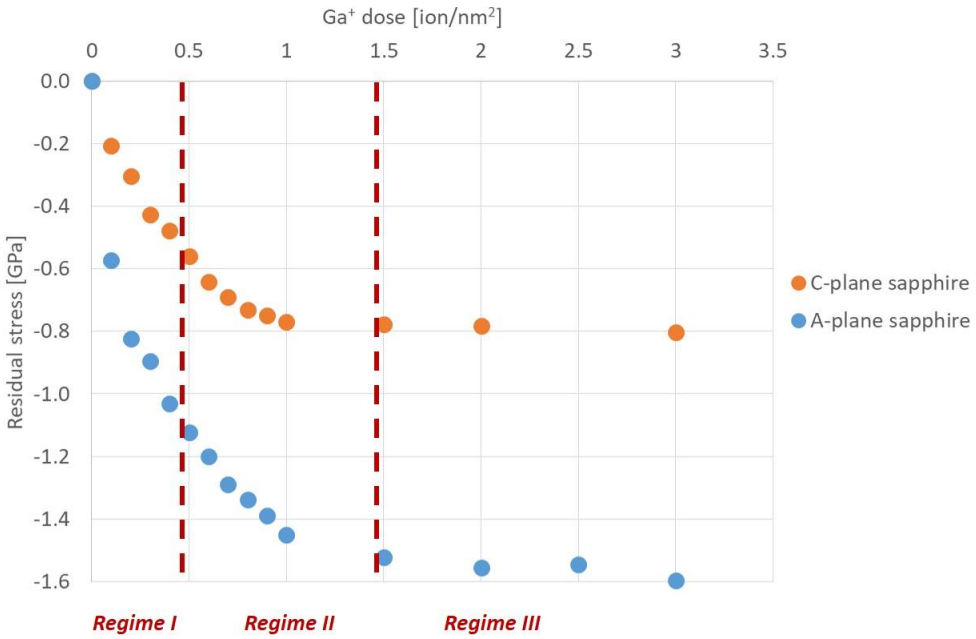


Figure 7.29. Three regimes of stress development as a function of ion dose in sapphire

Beam voltage. The results (Figure 7.28) show that the magnitude of the residual stress increases with beam voltage, which is attributed to the fact that a higher energy not only results in more vacancies in total but also a higher concentration of vacancies per unit length[384] as demonstrated in Figure 7.30.

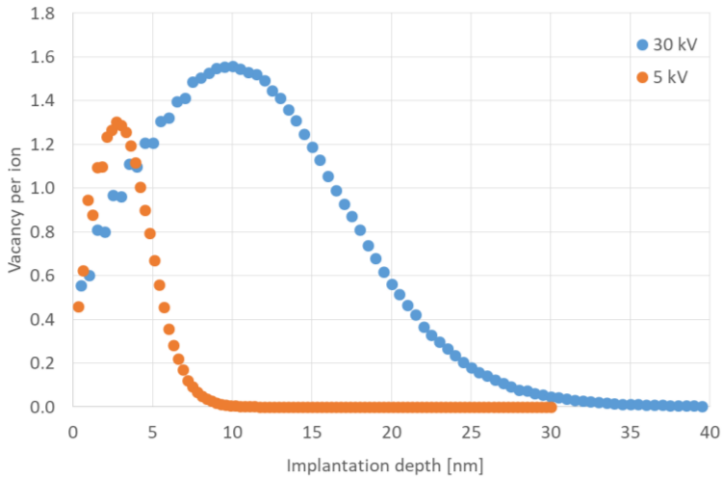


Figure 7.30. Concentration of vacancies along the implantation depth for Ga implantation in sapphire, with beam voltage of 30 kV and 5 kV, simulated using SRIM.

Beam current. The results (Figure 7.9) show that the residual stress remains almost constant with increasing beam current, apart from a slight drop within the low beam current range (< 10 pA). Beam current is thought not to have a direct effect on the implantation stress for the following two reasons. (1) Changing beam current does not affect the total amount of vacancies created nor the concentration of defects. (2) Within the range of beam currents investigated in the low current regime, the thermal spike induced by each incident ion has been relieved before the arrival of the next incident ion, so there is no overlap. Assuming that the incident beam targets at one point (rather than rastering), the time interval between the arrival of each incident ion is 1.6×10^5 ps for a 1 pA beam current (=6.25×10^6 ion/s), and 3.2×10^3 ps for 50 pA beam current (=3.13×10^8 ion/s). The time is much longer than the relaxation time for the thermal spike to cool down to room temperature. The reason for the slight drop in residual stress within the low beam current range therefore remains unexplained with the existing information and needs further investigation.

Type of target material. The results show that the steady state compressive residual stress developed in Stage I is much higher in Al_2O_3 and SiC, than in Si. This significant difference is attributed to the anti-site defects that exist in the chemical compounds (Al_2O_3, SiC)[338] but not in the simple substance (Si)[385], which are bigger on average than the perfect lattice and therefore enhance vacancy-swelling mechanism.

Additionally, the densities of the target crystals before and after amorphisation are compared in Table 7.7, suggesting that the swelling effect from amorphisation (i.e. phase transformation) is more significant in Al_2O_3 and SiC than in Si, which explains why the compressive residual stress is in the order Al_2O_3 > SiC > Si.

Table 7.7. Densities of the investigated materials in the crystalline and amorphous states, measured at 300 K. Unit: g/cm³

	$\rho_{crystalline}$	$\rho_{amorphous}$	Difference $(\rho_{crystalline} - \rho_{amorphous})/ \rho_{crystalline}$
Al_2O_3[386, 387]	3.98	3.18	20.1%
SiC[388]	3.21	2.75	14.3%
Si[389]	2.33	2.29	1.7%

Crystal orientation of target material. With the same FIB conditions and ion doses, the residual stresses developed in a-plane sapphire turned out to be higher than those in c-plane sapphire, which is attributed to the following two reasons. (1) The anisotropic elastic properties of sapphire result in different magnitudes of elastic swelling[344] along different crystal orientations – it is stiffer along the c-axis (Young's Modulus in this direction is 463 GPa) than the a-axis (425.5 GPa), therefore the swelling stress is higher in damaged a-plane sapphire than that in the c-plane sapphire. (2) The channelling effect might result in a higher concentration of vacancies and/or a longer ion range in a-plane sapphire than that in c-plane sapphire.

- **Stage II. High dose with high current**

Since the vacancy-swelling mechanism is no longer effective at the end of Stage I, the rest of the mechanisms (thermal spike, densification and/or bubble mechanisms) take over at Stage II, which reduces the compressive residual stress in the damaged layer and has the potential to turn the residual stress tensile.

The beam currents applied in Stage II are higher than that in Stage I, within the range of 120 to 6700 pA. Assuming that the incident beam targets at one point (rather than rastering), the time interval between the arrival of each incident ion is 24 ps for a 6700 pA beam current (=4.19×10^{10} ion/s), which is close to the relaxation time for the thermal spike to cool down to room temperature. The overlap between the thermal spikes induced by the incident ions might therefore exist, which means that the effect of high beam current can no longer be ruled out and might be contributing to the development of residual stresses. However, it also needs to be noted that it is unlikely for the ions to arrive at exactly the same point on the target surface due to large FIB aperture size and wide distribution of incident ions, which reduces the risk of the thermal spike overlapping to a certain extent.

For currents within the range of 120 to 4000 pA, the effect of high beam current has been shown to be minimal. In some cases, increasing current did not make any changes on the stresses (e.g. Figure 7.12, Figure 7.13, Figure 7.14, Figure 7.27). In the cases where stresses changed proportionally with

ion dose, changing currents did not affect the trend of the stress developments (e.g. Figure 7.15, Figure 7.25). The only exceptional case was when the current was 6700 pA. Then, the stress increased in an exponential manner instead of being proportional with ion dose, which indicates that above a certain current threshold, the effect of beam current can no longer be ignored.

Nevertheless, ion dose is still the dominant factor in the development of residual stresses in Stage II. While in Stage I, materials behave similarly, in Stage II, materials perform in very different ways to each other due to different combinations of effective mechanisms. Therefore, the discussion of Stage II is categorised by ion species and target materials.

Ga^+ in Al_2O_3

During Stage II implantation, the compressive residual stress decreases gradually until reaching a steady state (Figure 7.12). The significant reduction of compressive stress is attributed to the combination of the thermal spike mechanism and the densification mechanism (i.e. formation of dense $GaAlO_3$ particles), which is however not enough to overcome the strong compressive stress (due to the existence of anti-site defects, as explained previously) generated during Stage I before reaching a steady state, thus the plateau is at a lower compressive stress.

Ga^+ in SiC

The slight decrease of the compressive stress (Figure 7.13, Figure 7.14) is mainly attributed to the thermal spike mechanism, while the densification mechanism is not as effective here as it was in Ga^+ implanted Al_2O_3. The TEM investigation in Chapter 4 indicates that the implanted Ga atoms are distributed uniformly in the damaged matrix rather than forming particles due to their low mobility in SiC. Therefore, there is no denser new compound formed during the implantation, which leads to the ineffectiveness of the densification mechanism in the present case.

The thermal spike mechanism itself is not strong enough to overcome the high compressive stress generated at Stage I. As a result, the residual stress remains compressive when a dynamic balance between the swelling mechanism and thermal spike mechanism was achieved.

Ga^+ in Si

The combination of thermal spike mechanism and densification mechanism overcomes the low compressive residual stress generated at Stage I, resulting in the transition from compressive to tensile stress (Figure 7.15). The formation of Ga particles (atom density = 50.9 atom/nm^3) in Ga^+ implanted Si (the atom density is 49.9 atom/nm^3 for pure crystalline Si and 49.1 atom/nm^3 for amorphous Si) is demonstrated by the TEM investigations from a wide range of literature[351, 390-392], which suggests that the densification mechanism is effective for the Ga implantation in Si.

Within the ion dose range applied in the present study, no steady state has been achieved. The relatively low tensile stress in the damaged layer compared to the yield strength of Si suggests that the overall deformation remains elastic.

Xe^+ in Al_2O_3

During Stage II implantation, the Xe^+ implanted Al_2O_3 cantilevers either exhibit brittle fracture (Figure 7.18, Figure 7.21) or extreme bending (Figure 7.24), with the thermal spike mechanism and bubble blistering mechanism contributing to the reduction of the compressive stress, and thermal spike mechanism alone dominating the generation of tensile residual stresses.

The calculated implantation stress in the cantilever No.6.2 based on the bending curvature goes up to 24 GPa, and to 22 GPa in the cantilever No.5.2 before it fractures. The possible explanations for such high apparent stresses are discussed below.

Option 1 – the entire cantilever deforms elastically. This means that the stress in the damaged layer has indeed reached ~24 GPa. However, this is unlikely to be true because the yield strength of crystalline α-alumina is about 6 GPa (i.e. yield strength is usually considered as 1/3 of the hardness which is ~18 GPa for alumina), or ~7.7 GPa for single crystal alumina according to the results from Chapter 7. Although the yield strength of the damaged layer might be higher than 7.7 GPa due to the size effect, it is unlikely to rise beyond 24 GPa. Taking a step back, even if the residual stress in the damaged layer is indeed ~24 GPa, the stress intensity factor at the tip of a crack throughout the

thickness of the damaged layer (~20 nm) is around 7 MPa·m$^{1/2}$, which is beyond the fracture toughness of sapphire. Therefore Option 1 is unlikely to be correct.

Option 2 – the undamaged part of the cantilever deforms plastically leading to an overestimate of the stress when calculated assuming elastic deformation. For the cantilever No.6.2, the maximum tensile stress in the substrate (at the bottom of the substrate) is $\sigma_{ts} = \frac{2\sigma_c t_c}{t_s} = 3.0\ GPa$ (where σ_c is the residual stress in the damaged layer, t_c is the thickness of the damaged layer, t_s is the thickness of the undamaged substrate). The maximum compressive stress in the substrate (at the top of the substrate, right beneath the damaged layer) is $\sigma_{cs} = -\frac{4\sigma_c t_c}{t_s} = -5.9\ GP$. Neither the maximum tensile nor compressive stress in the substrate is sufficiently high to yield plastically at room temperature.

The temperature distribution in FIBed cantilever simulated using COMSOL Multiphysics (Appendix C) suggests that the elevated temperature due to the thermal spike is highly localised without heating up the entire cantilever as most of the heat was lost by thermal conduction towards the bulk material. Therefore the potential reduction of yield strength due to elevated temperature is localised as well so that in the rest of the cantilever, the temperature is not high enough to reduce the local compressive yield strength to enable plastic deformation.

The curvature change in cantilevers No. 5.2 and 6.1 turned from stable to unstable without significant change in FIB conditions, which could be attributed to either (a) pre-existing critical flaw(s) in the cantilever or (b) the previous implantation steps created flaws in the cantilever, which disconnected the path for the heat to conduct towards the bulk material or reduce the thermal conductivity of the material, the implantation heat therefore accumulated and increased the temperature of the cantilever significantly (as demonstrated by COMSOL simulation in the Appendix C) to enable plastic deformation.

To confirm the proposed theory, the following investigation should be carried out.

(1) TEM characterisation on the bent cantilevers to find out if there are dislocations in the substrate, in order to check if the deformation was elastic or plastic.

(2) The top damaged layer can be removed using FIB lateral cutting or other techniques. If the undamaged substrate straightens completely, it means that the deformation of the undamaged substrate is elastic. If the curvature remains, then the deformation is plastic.

(3) Anneal cantilever No.6.2 to see if it bends back or not. Bending back indicates that the deformation was substantially elastic, otherwise the deformation of the substrate was plastic.

(4) Break cantilever No.6.2 using the nanoindenter to find out how weak the cantilever is.

(5) MD simulation can be employed to simulate the applied FIB conditions (i.e. high doses), in order to find out if anything irregular, or additional mechanisms that we have not been aware of, contribute to the observed phenomenon.

(6) FEM simulation could be employed to assist in the further investigation on the extremely bent and fractured sapphire cantilevers implanted with Xe ions.

Xe^+ in SiC

In Stage II, the compressive residual stress also decreases with increasing ion dose, followed by the transition to tensile stress, which is attributed mainly to the thermal spike mechanism. The tensile residual stress plateaus at an ion dose of ~3×10^4 ion/nm^2, indicating a dose threshold for achieving steady state. The possible plastic deformation that occurs in Xe^+ implanted Al_2O_3 does not happen here due to the high yield strength of SiC relative to Al_2O_3.

- **Proportionally increasing tensile stress**

Once the cantilevers bend upwards, the tensile residual stresses appeared to increase almost proportionally to ion dose, as shown in Figure 7.15, Figure 7.20, Figure 7.23 and Figure 7.25. It is proposed here that this may because the area above the neutral axis where the ions are implanted is under compression in a cantilever that exhibits upwards bending, coupled with the dynamic balance of removing the previously-formed damaged layer and creating the new damaged layer, as illustrated in Figure 7.31. The pre-existing compressive stress in the material enhances the tensile residual stress generated by the thermal spike mechanism – the pre-existing compressive strain 'squeezes' the

microscopic expanding heated core in the lateral direction more, which yields more plastic deformation in the lateral direction and also results in more 'adatoms' flowing on the surface in the vertical direction, therefore aiding the localised shrinking in the lateral direction after cooling down and yields a higher tensile residual stress in the damaged layer.

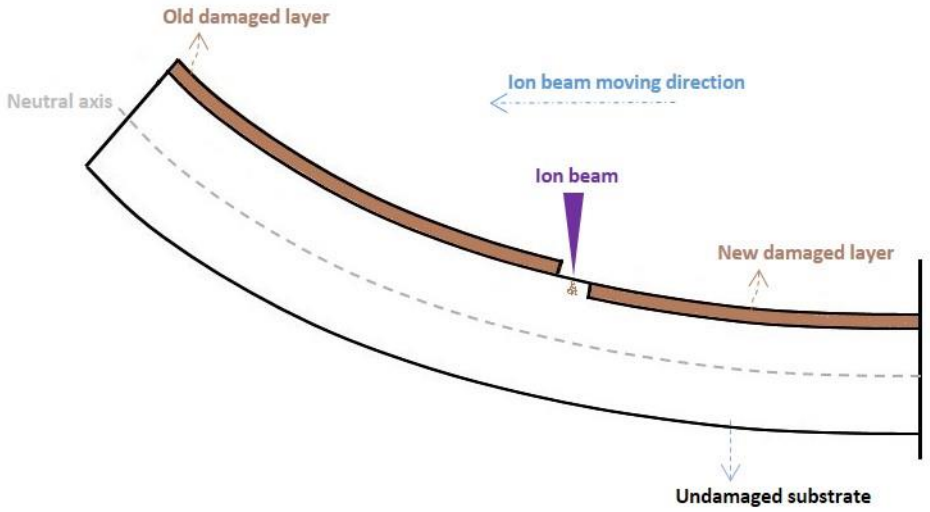


Figure 7.31. Schematic of ion implantation process on an already-damaged upwards-bending cantilever.

Noting the massive removal of material (i.e. hundreds of nm of thickness removed in each cantilever) during high dose implantation (Table 7.5, Table 7.6) which has exceeded the depth of implantation damage (i.e. tends of nm according to Table 7.2), a steady state must have been reached if the target was a solid block of material. The fact that the development of the implantation stresses did not reach a steady state therefore indicated that the continuously increasing residual stresses must have something to do with the continuous bending and the low thickness of the cantilever.

7.3.3 Comparison with literature

There exists very little literature for FIB ion damage residual stress in alumina. The only one known by the author is from the study conducted by Norton et al.[187] on single crystal ruby, which reported a much higher value of Ga^{+}-in-Al_2O_3 residual stress (−16 ± 6 GPa) than that from the present study (max. -2 GPa) although under similar FIB conditions. The possible reason for such a big difference is discussed via the two following points.

(a) In the experiment conducted by Norton et al.[187], the platinum coating layer on top of the Ga^+ implanted ruby TEM sample may have contributed to the apparent residual stress measured using the Fluorescence microscope.

Investigation on the residual stresses caused by Pt deposition is therefore conducted in the present study using the cantilever technique. A cantilever was manufactured on c-plane sapphire by following the same preparation procedure as stated in Section 7.1.2, followed by sputter coating of Pt to induce residual stress. The side view of the coated cantilever with increasing Pt layer thickness and the corresponding residual stress are presented in Figure 7.32 and Figure 7.33, respectively, showing significant compressive residual stress (≈ -8 GPa) in the deposited Pt layer. This suggests that the residual stress measured by Norton et al.[187] was overestimated by a significant amount due to the Pt coating layer.

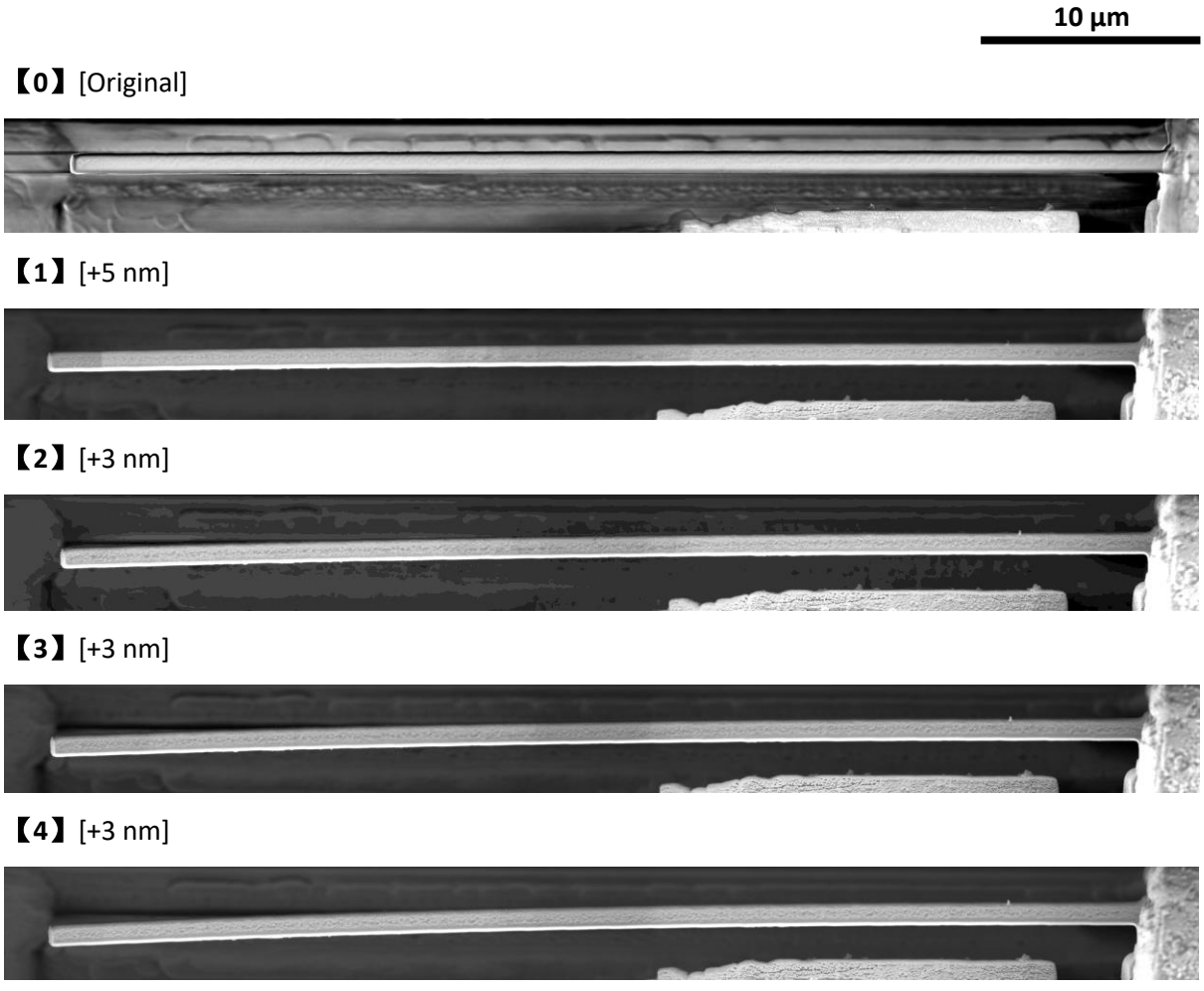


Figure 7.32. In-lens images showing the side view of the Pt coated sapphire cantilever

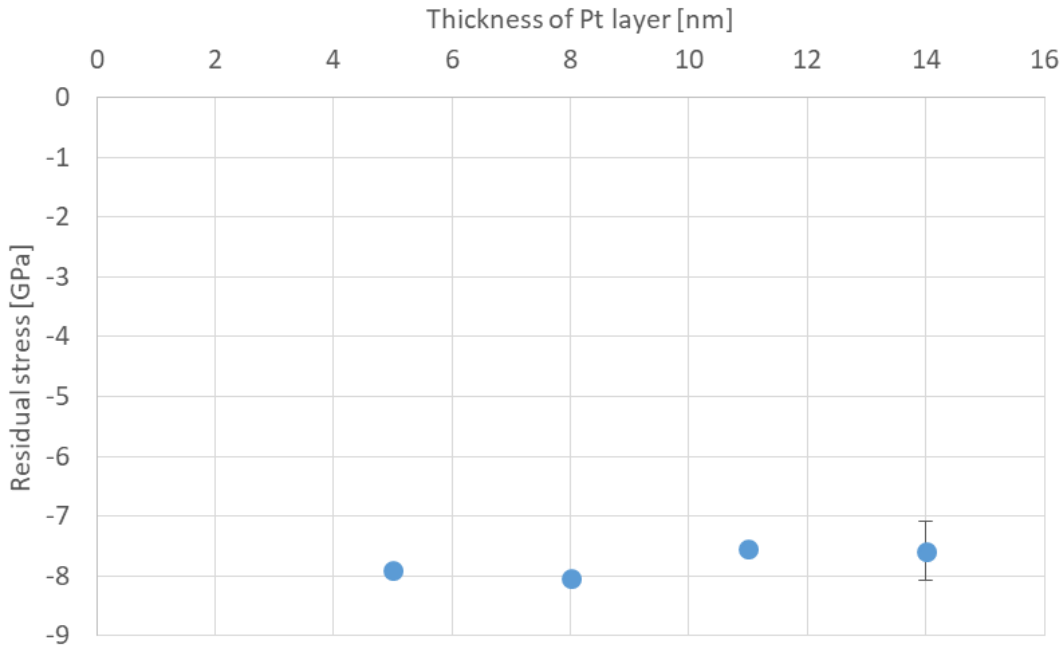


Figure 7.33. Residual stress induced by Pt deposition on sapphire

(b) As bending contributes to the relaxation of residual stresses in the damaged layer, it is suggested that the stress depends on thickness of substrate. The implantation conducted by Norton et al.[187], was performed on a bulk sample which has limited freedom to deform, while the cantilever used in the present study has much more freedom of deformation, suggesting that values measured in the present study might be underestimated. The most extreme case in the present study (i.e. cantilever No.6.2) was checked with the full elastic solution which takes into account the stress relaxation by cantilever deformation, rising the value of residual stress for our bent cantilever from 24.5 GPa (given by Equation 7.1) to 25.6 GPa for a thick substrate. The difference is small, so does not change any of the above conclusions, but the underestimation resulted still needs to be borne in mind.

The combination of the two above reasons may explain the significant gap between the residual stresses measured in the present study and by Norton et al.[187] for Ga^+ implantation in Al_2O_3.

For Ga^+ implantation residual stress in Si, Salvati et al.[393] employed a similar cantilever technique and FIB conditions to measure the eigenstrain in the FIB Ga^+ implanted Si cantilever, giving a tensile residual stress value of 0.07 GPa (calculated based on the dimensional data provided in the Appendix

of reference[393]), which is much lower than that measured in the present study (around 0.25 GPa). The discrepancy might be attributed to the pre-existing residual stress in the commercial Si AFM cantilever used in the literature[393] and the difference in the thicknesses of cantilevers employed. The FEM and MD simulation of Ga^+ implantation in Si [245] suggests that residual stress peaks at around 0.6 GPa, which makes more sense considering that the residual stress measured in the present study (Figure 7.15) had not yet reached a steady state value and a higher stress would likely be generated with further implantation.

7.3.4 Residual stresses at notch tips

Since the ultimate goal of the present study is to enable reliable fracture toughness measurement by quantifying the FIB damage residual stresses at FIBed notch tips, it needs to be pointed out that the residual stresses developed in the FIB-notched bulk materials are higher than that measured from the FIB ion implanted cantilevers as bulk substrate has almost no freedom of deformation. The stresses are therefore re-calculated using the stress-free strain from the cantilever results.

As shown in Table 7.8, the stress developed on a thick substrate (i.e. fully constrained development) is evaluated for each representative case, showing higher values than that developed on thin substrates. The larger the aspect ratio of t_f/d is, the larger the difference between the stresses evaluated in thin and thick substrates is, suggesting that the thickness of the substrate has a significant effect on apparent residual stress.

Table 7.8. Apparent residual stresses of representative specimens evaluated in thin and thick substrate

Ion	Target material	Cantilever Ref.	t_f/d	Stress on thin substrate [GPa]			Stress on thick substrate [GPa]	Difference[4]
				Standard Stoney[1]	Advanced Stoney[2]	Full solution[3]		
Ga	Al_2O_3	2.2.x	0.06	-0.92	-0.86	-0.87	-1.11	27.6%
	SiC	3.2.x	0.06	-1.08	-1.01	-1.02	-1.32	29.4%
	Si	4.1.x	0.17	0.30	0.25	0.29	0.53	82.8%
Xe	Al_2O_3	6.2	0.05	28.82	24.45	25.90	31.89	23.1%
	SiC	7.1.x	0.13	1.05	0.91	0.99	1.62	63.6%

[1] standard Stoney equation[330, 331] that assumes that the ratio t_f/d to be sufficiently small.

[2] advanced Stoney equation (Equation 7.1) that reduces the effect of large aspect ratio of t_f/d.

[3] full solution that evaluates the precise distribution of stresses via analytical solution.

[4] difference = $(\sigma_{\text{thick substrate}} - \sigma_{\text{thn substrate full solution}})/ \sigma_{\text{thn substrate full solution}}$

7.3.5 Effect on fracture toughness measurement

Referring to Eq.2.6, the difference in the measured stress intensity factor caused by the residual stress at the notch tip ΔK_{res} can be calculated using Eq.7.3.[187]

$$\Delta K_{res} = \sigma_{res} \psi \sqrt{\pi d\alpha} \tag{7.3}$$

where σ_{res} is the residual stress in the implanted region, assumed to be uniformly distributed. ψ is the geometrical factor and $d\alpha$ is the distance from the crack tip over which the residual stress is applied.

A compressive σ_{res} will inhibit crack initiation at the notch tip, and therefore results in an overestimation of the fracture toughness. Although a tensile σ_{res} will encourage the initiation of the crack within the damaged area, it is generally agreed that the crack still needs to propagate through the undamaged material so that the fracture properties of the target material will still be evaluated correctly. However, the undamaged substrate contains a compressive stress field right beneath the damaged layer, the effect of which on the fracture toughness measurement remains unknown due to the lack of relevant results and needs further investigation.

The effects of ion implantation stresses on the measurement of fracture toughness using the FIB-notched microcantilever technique will be separated by the target materials in the discussion below.

- Al_2O_3

The Ga^+ implantation stresses in Al_2O_3 remain compressive regardless of applied ion dose, indicating an overestimation of fracture toughness in alumina.

Taking a-plane sapphire as an example, with the dose required for making a reasonably deep notch (typically on the scale of 10^5 – 10^7 ion/nm^2), the compressive residual stress plateaus at around -1.1 GPa in a thick substrate (according to Table 7.8). Assuming that the incipient crack has an initial length of $d\alpha$ = 20 nm, equal to the thickness of the layer of residual stress, and a shape of a straight crack ψ = 1.12, the apparent fracture toughness is overestimated by about ΔK_{res} = 0.3 MPa·m$^{1/2}$ due to the ion implantation stress induced at 30 kV Ga-FIBed notch.

The higher compressive residual stress in a-plane sapphire compared to that in c-plane sapphire suggests that the effect of ion implantation on the fracture toughness measurement is anisotropic. A Ga-FIBed notch in a polycrystalline Al_2O_3 will therefore have compressive residual stress varying along the width of the crack.

The residual stress induced by Xe^+ implantation in Al_2O_3 is tensile within the ion dose range that is required to mill a reasonably deep notch (typically 10^5 – 10^7 ion/nm^2). However, the extreme implantation behaviour and the formation of bubbles in the damaged layer are likely to have additional effects on the crack initiation and propagation, which needs further investigation. Moreover, considering the fact that PFIB cannot mill sharp notches, which applied to all materials, it is recommended that PFIB cannot be used for finishing the notches but can only be used to make the first part of the notch, if necessary.

- SiC

The Ga^+ implantation stress also remains compressive in SiC regardless of ion dose, which means that the fracture toughness values of SiC measured using the Ga-FIB notched cantilever technique is overestimated. The stress plateaus at around -1.3 GPa, resulting in an overestimated ΔK_{res} of around 0.4 $MPa \cdot m^{1/2}$.

With the dose required for making a reasonably deep notch (typically on the scale of $10^5 - 10^7$ ion/nm^2), the residual stress at the PFIBed notch tip in SiC is tensile, the exact effect of which on the fracture toughness measurement remains unclear at the moment. But it is not relevant at present for this application because the PFIB cannot make sharp notches.

- Si

The measured Ga^+ implantation stresses in Si were small and tensile, so they should not affect K_c measurements so much. Literature measurements of K_c in Si do indeed give the same answer as macroscopic measurements[160, 167, 394], which is in agreement with this prediction.

Whether Xe^+ implantation would induce compressive or tensile stress in Si is not investigated in the present study. However, considering the bluntness of the notches produced using PFIB, the investigation is not necessary at present for this application.

Chapter 8. Conclusions

The present study has drawn the following conclusions.

8.1 Grain size distributions

The present study of grain size distributions exhibits a good integration of experimental and numerical research. The experimental method developed here not only enabled the precise measurement of 2D grain sizes in ceramics, but also allowed for the generation of representative models of 3D granular microstructures.

The empirically-measured distribution of 2D grain sizes was first used as input weights for the 3D Laguerre-Voronoi tessellation, and was then in turn used to validate the numerical model by a novel method – correlating the virtual cross sectioning outcome with the empirical data.

Laguerre-Voronoi tessellation provided significant improvement of the reproduction of realistic grain size distributions, compared to classic Voronoi tessellation. In particular, the ability to generate relatively large grains in the structure increases the representativeness of the numerical models, as proven by the validations presented.

The present work contributed to the development of a new routine in the simulation software LS-DYNA (Figure 8.1), which has now become available to use to the public.

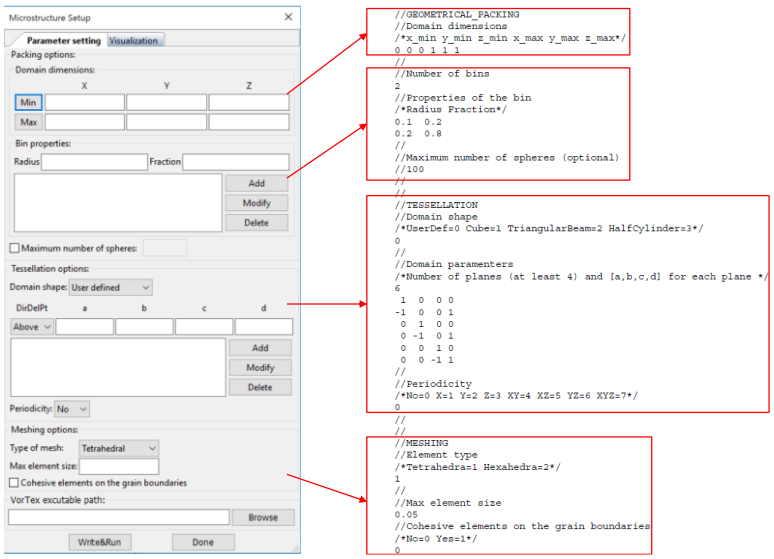


Figure 8.1. LS-PrePost graphic interface (left) and corresponding input file generated (right), developed by Dr Simone Falco.

8.2 Strength of grain boundaries

The effect of shear stresses on brittle failure of grain boundaries is mostly overlooked in understanding the failure mechanism of polycrystalline ceramics and is often neglected in microstructural numerical models. The present study, which is the first time that this effect has ever been investigated systematically through experiments, was therefore conducted to test the known assumptions usually adopted in micromechanical modelling.

The combination of experimental tests and numerical simulations on single grain boundaries inclined at three different angles provided clarification on the role of different stress components on the failure of grain boundaries. The results rule out the theory which considers only critical normal stresses for failure of grain boundaries, and suggest that the contribution of the shear component should not be neglected.

The present study also suggests that compressive stresses do not contribute to crack initiation on grain boundaries, and more importantly, hinder the effect of shear stresses.

The strength of grain boundaries is demonstrated to be lower than that of grains. Enhancing the grain boundary strength could therefore be effective to improve the bulk behaviour of ceramics.

8.3 Reliable fracture toughness measurement – stable crack growth

Stress intensity values for crack propagation K_p were measured in single crystal Al_2O_3 and SiC using chevron-notched microcantilevers. The stable crack growth enabled by using chevron notches allowed the K_p values to be measured reliably, free from the effects of FIB damage at notch tips and notch bluntness.

K_p measured in vacuum, where the moisture was excluded, represented fracture toughness K_c, giving values of 2.8 MPa·m$^{1/2}$ for a-plane sapphire. K_p measured in air was decreased substantially by moisture-assisted subcritical crack growth and was close to the threshold stress intensity for SCG, K_0. For sapphire, K_0 values for a- and m-planes were close to each other, both averaged at 1.8 MPa·m$^{1/2}$.

The crack velocities were on the scale of 10^{-8} m/s, corresponding to the lower end of Region I of the SCG curve which is supposed to be heavily affected by SCG. SiC exhibited a higher K_p measured in air than sapphire, giving a value of 2.2 MPa·$m^{1/2}$ for its $(\bar{1}100)$ plane.

Beyond its many consequences in measurement of intrinsic fracture toughness in laboratories, SCG plays an important role in many aspects of engineering design and materials performance in real life, because most engineering ceramics are challenged under stress corrosion conditions in their general use. This suggests that the measurement of K_0 is more important than K_C, from the practical point of view, for long term reliability of ceramics. The method investigated here provides an excellent method for the measurement of this property without the long timescales required in macroscopic tests. For the ceramics that are used in inert environment without moisture (such as for satellites, the international space station, etc.), K_C becomes more important and can be measured under inert conditions by the same method.

The cyclic loading test in vacuum demonstrated the reversibility of cracking upon withdrawal of loading, thus proving the self-healing capability of alumina at room temperature. The strength of the healed interfaces was found to be degraded due to an incomplete restoration of the lattice across the separation interface, reducing the fracture toughness of a-plane sapphire from around 2.6 MPa·$m^{1/2}$ to below 1.6 MPa·$m^{1/2}$. The more times the interface is healed, the more the strength is degraded.

8.4 Ion implantation damage – TEM investigation

The microstructural damage that the conventional Ga-FIB and the state-of-the-art PFIB induced in Al_2O_3 and SiC has been investigated using TEM-based techniques, with literature results on Si and diamond discussed in parallel for comparison.

Amorphous and crystalline damaged layers were observed in all the implantation cases. Ion species, target materials and FIB settings (i.e. voltage and dose) combined to determine the severity of crystallographic damage. SRIM simulation demonstrated reliable prediction of thicknesses of

amorphous layers, suggesting the importance of SRIM input parameters in understanding damage behaviour.

In the amorphous layer created by Ga^+ implantation in Al_2O_3, particles containing Ga-Al-O were found embedded in the Al_2O_3 matrix, and the sizes of these particles decreased with implanted ion concentration. No particle was, however, observed in Ga^+-implanted SiC, where the amorphous layers were separated into two sub layers. The upper sub layer exhibited darker contrast in TEM images than the lower sub layer due to the higher concentration of implanted ions. Further investigation is needed to find out the exact chemical composition of the Ga^+-amorphised SiC.

Xe bubbles with different sizes were formed in PFIBed Al_2O_3. Large bubbles were only observed with high energy (i.e. 30 keV) because the formation of large bubbles is dominated by the concentration of vacancies rather than ion doses. Low beam current was also found to encourage the formation of large bubbles by facilitating the bubble coalescence. These large Xe bubbles could be easily burst by the high energy electron beams that were used in TEM investigation.

The FIB damage listed above may alter the physical and mechanical properties of target materials as well as the stress field in the material, which can lead to inaccuracy of the micromechanical test based on FIB techniques, such as fracture toughness measurements using FIB notched microcantilevers, which was the main motivation for conducting the present investigation of FIB damage. The microstructural observation of FIB damage is therefore linked to the investigation of FIB-induced residual stresses in the following chapter.

8.5 Ion implantation damage – residual stresses

In the present study, the FIB implantation stresses in a variety of materials with different ion species have been quantified as a function of ion dose, beam acceleration voltage and beam current, using the cantilever-bending technique.

The formation of ion implantation residual stresses is complex, involving several competing and interacting mechanisms. The lattice swelling and bubble swelling mechanisms induce compressive

residual stresses, the thermal spike and densification mechanisms inducing tensile residual stresses, plasticity and bubble blistering relax the stresses. The dynamic interaction of these mechanisms results in different stress status at different implantation dose and beam current, with one or more mechanisms dominating at each stage.

The implantation stress development process can be separated into two stages. During Stage I (low dose), the residual stress is compressive regardless of ion species or target material due to the dominating role of the lattice-swelling mechanism. Stage I ends when the damaged layer becomes completely amorphised. At Stage II (high dose), the implantation behaviour differs from one ion species/target material to another. The Ga^+ implantation stress in Al_2O_3 and SiC remains compressive with increasing ion dose and plateaus at relatively low compressive stress values at steady state. The Ga^+ implantation stress in Si transits from compressive to tensile and increases proportionally with increasing ion dose before reaching a steady state. The Xe^+ implantation stresses in Al_2O_3 and SiC also transit from compressive to tensile with increasing ion dose, while dramatic bending was observed in Xe^+ implanted Al_2O_3, with the curvature depending on the stresses already present in the target substrates and therefore on the thickness of the substrates.

The implantation behaviour at Stage II is more important than Stage I for the main research purpose because the ion doses used for notching reasonably deep notches in the target materials of interests are typically within a range of $10^5 – 10^7$ ion/nm^2, which lies at Stage II. The fracture toughness of Al_2O_3 measured using Ga-FIB requires correction for the compressive residual stress at the notched tip, while PFIB is not recommended for notching Al_2O_3 due to the dramatic behaviour upon implantation and significant notch bluntness. Considering blunt notches produced using PFIB, Ga-FIB seem to be a better choice to notch SiC and Si as well.

Chapter 9. Future work

As future work, the following list can be considered to refine and extend the present study.

9.1 Grain size distribution

(i) The present method of the measurement of grain size distribution and development of representative numerical microstructure can be extended to other armour ceramics, e.g. SiC.

(ii) In order to increase the representability of the numerical microstructure and therefore further improve the predictive capability of numerical models, similar methods can be extended to include defects in the microstructure. Defect distribution and impact behaviour characterised near the beginning of the project (the relevant results are available but not included in the present thesis, as explained in Chapter 1) can be incorporated into the development and validation of the numerical models.

9.2 Strength of grain boundaries

(i) For each inclination angle, an increased number of tests needs to be performed to provide statistically representative results, thus allowing the refinement of the prediction of the effect of normal and shear stress on the failure of grain boundaries.

(ii) More inclination angles can be tested to refine the range of data points. It is recommended to polish specimens with all different angles at the same time to minimise the possibility of introducing a systematic bias.

(iii) Micro-compression tests can be done on bi-crystals with inclined grain boundaries to measure the compressive and shear stresses at grain boundary failure. Comparing the data with the results from the present study can help to further investigate how compression hinders the effect of shear stresses.

(iv) Tests on real grain boundaries to verify the present study on the artificial grain boundary would be beneficial.

(v) Once β^2 and α are determined, they can be implemented to enable the development of constitutive models that are more reliable to simulate the behaviour of grain boundaries in larger and more complex microstructures. Figure 9.1 shows polycrystalline cantilever numerical models that are generated in the present UNICAM II project (built by Dr Simone Falco) based on the Voronoi tessellation algorithm developed in Chapter 3. As future work, after inputting the grain strength data in this existing model, the numerical simulation of the deformation and failure of polycrystalline beams can be validated against the experimental measurements performed on polycrystalline alumina by Norton et al.[161].

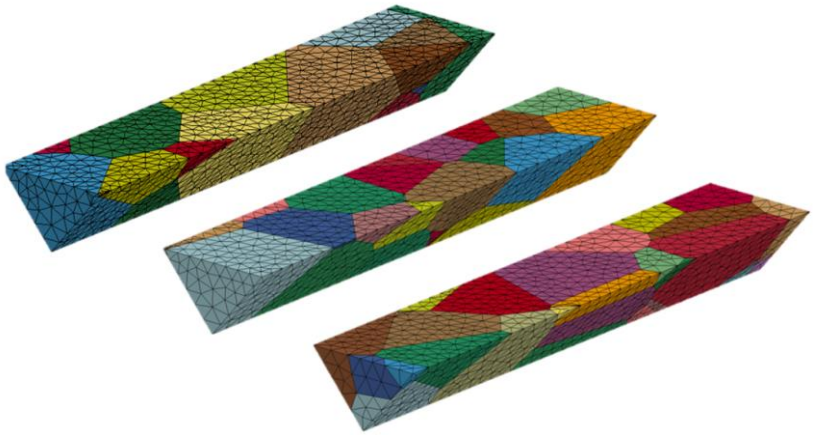


Figure 9.1. Finite element model of the polycrystalline cantilevers developed in the UNICAM II project

9.3 Reliable fracture toughness measurement – stable crack growth

(i) Complete the present set of investigations on SCG by testing chevron notched microcantilever under water. This could be achieved by building a specially-designed water container to fit into the ex-situ nanoindenter, or forming a moisturised testing environment by flowing gas (e.g. air, inert gas, etc.) through boiling water towards the testing chamber.

(ii) The cyclic loading test can also be conducted in air. In order to verify the existence of a threshold stress intensity value of SCG, K_0, the stress intensity at the crack tip can be held at a constant K after the crack initiates during the test in air, then find out if the load carries on decaying or whether if it reaches a limiting value.

(iii) In order to enable precise fracture toughness measurements of natural grain boundaries, alternative configurations need to be explored due to the difficulties of applying the configurations of chevron-notched specimens[175, 212] and double-cantilever beam[215] directly to individual grain boundaries in polycrystalline materials. This is because these configurations require the target grain boundary to be perfectly parallel with the central axis of the nanoindenter tip and therefore the test can only be performed on artificial grain boundaries that are oriented vertically in purpose during manufacturing process. The two-dimensional nature of the chevron notch and naturally random orientations of grain boundaries also make it difficult to have the planes of the notch and the grain boundary to completely coincide with each other.

Numerical simulation can be employed to evaluate the potential designs prior to experimental trials in order to minimise the waste of experimental resources.

9.4 Ion implantation damage – TEM investigation

(i) The TEM specimens that were not prepared successfully in the present study (i.e. Xe^+-implanted SiC, and Ga^+-implanted Al_2O_3 under 30 kV at 5 pA and 1000 pA) could be re-produced in the future work.

(ii) The effect of bubble bursting on fast removal rate of PFIB needs to be further confirmed.

9.5 Ion implantation damage – residual stresses

(i) The cantilever bending technique used for measuring ion implantation stress can be applied to other ceramics to extend existing knowledge.

(ii) Xe^+ implantation can be conducted on Si using the PFIB, as was done on Al_2O_3 and SiC, to complete the present study.

(iii) The effect of angle of incidence needs to be understood by varying the FIB ion beam incident angles during the implantation tests.

(iv) The dramatic behaviour of high dose Xe^+ implantation in Al_2O_3 can be further investigated by taking the actions listed in 7.3.2.

(v) Numerical modelling could be conducted to simulate the development of the implantation stresses and to understand what the stresses would be.

(vi) In-situ TEM investigation of Ga^+ or Xe^+ implantation in ceramics can be helpful in demonstrating visually the damage development process with increasing ion dose.

(vii) Implantation at constant low current for slowly increasing ion dose to rule out the effect of beam current and to refine the residual stress curve as a function of ion dose.

(viii) The implantation residual stress measured in the present study may not apply to FIBed notches due to different geometries and ion doses. Alternative methods can be explored to measure the residual stress around a FIBed notch directly, such as performing HR-EBSD on FIBed notches to obtain strain maps.

Reference

[1] F. S. Hannon and K. H. Abbott, "Ceramic armor stops bullets, lowers weight," *Materials Engineering,* vol. 68, pp. 42-43, 1968.

[2] R. F. Rolston, E. Bodine, and J. Dunleavy, "Breakthrough in armor," *Space Aeronautics,* vol. 50, pp. 55-63, 1968.

[3] D. Schmitz, "The History of Armor," *The Iowa Review,* vol. 10, pp. 105-105, 1979.

[4] S. R. Skaggs, "A brief history of ceramic armor development," in *27th International Cocoa Beach Conference on Advanced Ceramics Composites*, Cocoa Beach, Fl, pp. 337-349, 2003.

[5] P. J. Hazell, *Ceramic Armour: Design and Defeat Mechanisms*. Canberra, Australia: Argos Press, 2006.

[6] P. G. Karandikar, G. Evans, S. Wong, M. K. Aghajanian, and M. Sennett, "A review of ceramics for armor applications," in *32nd International Conference on Advanced Ceramics and Composites*, Daytona Beach, FL, pp. 163-175, 2008.

[7] R. Klement, S. Rolc, R. Mikulikova, and J. Krestan, "Transparent armour materials," *Journal of the European Ceramic Society,* vol. 28, pp. 1091-1095, 2008.

[8] H. Wu, S. Ghosh, C. E. J. Dancer, and R. I. Todd, "Ballistic Damage of Alumina Ceramics - Learning from Fragments," in *Advances in Ceramic Armor X: A Collection of Papers Presented at the 38th International Conference on Advanced Ceramics and Composites*, NJ, USA, p. 49, 2014.

[9] C. E. J. Dancer, H. M. Curtis, S. M. Bennett, N. Petrinic, and R. I. Todd, "High strain rate indentation-induced deformation in alumina ceramics measured by Cr3+ fluorescence mapping," *Journal of the European Ceramic Society,* vol. 31, pp. 2177-2187, 2011.

[10] C. E. J. Dancer, H. M. Curtis, S. M. Bennett, N. Petrinic, and R. I. Todd, "Measurement of Deformation in Alumina Samples Indented at High Strain Rates," *Advances in Ceramic Armor VII,* pp. 227-236, 2011.

[11] S. Falco, P. Siegkas, E. Barbieri, and N. Petrinic, "A new method for the generation of arbitrarily shaped 3D random polycrystalline domains," *Computational Mechanics,* vol. 54, pp. 1447-1460, 2014.

[12] S. Falco, "Numerical modelling and experimental characterisation of mechanical performance of ceramic materials at multiple scales," DPhil, University of Oxford, 2015.

[13] M. L. Wilkins, "Mechanics of penetration and perforation," *International Journal of Engineering Science,* vol. 16, pp. 793-807, 1978.

[14] S. M. Walley, "Historical review of high strain rate and shock properties of ceramics relevant to their application in armour," *Advances in Applied Ceramics,* vol. 109, pp. 446-466, 2010.

[15] CeramTec, "Ceramic materials for light-weight ceramic polymer armor systems," C. E. GmbH, Ed., ed, 2016.

[16] S. L. Rovner. (2009, July) 21st-Century Armor. *Chemical & Engineering News*. 51-53.

[17] E. K. Öberg, J. Dean, and T. W. Clyne, "Effect of inter- layer toughness in ballistic protection systems on absorption of projectile energy," *International Journal of Impact Engineering,* vol. 76, pp. 75-82, 2015.

[18] R. Zaera, S. Sánchez-Sáez, J. L. Pérez-Castellanos, and C. Navarro, "Modelling of the adhesive layer in mixed ceramic/ metal armours subjected to impact," *Composites Part A,* vol. 31, pp. 823-833, 2000.

[19] J. López-Puente, A. Arias, R. Zaera, and C. Navarro, "The effect of the thickness of the adhesive layer on the ballistic limit of ceramic/ metal armours. An experimental and numerical study," *International Journal of Impact Engineering,* vol. 32, pp. 321-336, 2005.

[20] "Ballistics," in *The World Book Encyclopedia*, ed New York: World Book, 1998.

[21] "Bullet," in *The World Book Encyclopedia*, ed New York: World Book, 1998.

[22] W. Walters, "Introduction to Shaped Charges," Army Research Laboratory, Aberdeen Proving Ground ARL-SR-150, 2007.

[23] C. Poole, "Penetration of a Shaped Charge," DPhil, Corpus Christi College, Department of Materials, University of Oxford, Oxford, UK, 2005.

[24] W. A. Gooch, "Overview of the development of ceramic armor technology: Past, present and the future," in *35th International Conference on Advanced Ceramics and Composites (ICACC)*, Daytona Beach, FL, pp. 195-213, 2011.

[25] M. J. Normandia and W. A. Gooch, "An overview of ballistic testing methods of ceramic materials," *Ceramic Armor Materials by Design,* vol. 134, pp. 113-138, 2002.

[26] W. A. Trzcinski and S. Cudzilo, "Investigation of the behaviour of steel and laminated fabric plates under blast load and fragment impact," *Journal De Physique IV,* vol. 134, pp. 1113-1118, 2006.

[27] B. James, "Practical issues in ceramic armour design," *Ceramic Armor Materials by Design,* vol. 134, pp. 33-44, 2002.

[28] J. C. LaSalvia, "Recent progress on the influence of microstructure and mechanical properties on ballistic performance," *Ceramic Armor Materials by Design,* vol. 134, pp. 557-570, 2002.

[29] G. E. Hauver, W. A. Gooch, P. H. Netherwood, R. F. Benck, W. J. Perciballi, and M. S. Burkins, "Variation of target resistance during long-rod penetration into ceramics," presented at the 13th International Symposium on Ballistics, Stockholm, Sweden, 1992.

[30] C. E. Anderson and J. D. Walker, "An analytical model for dwell and interface defeat," *International Journal of Impact Engineering,* vol. 31, pp. 1119-1132, 2005.

[31] C. E. Anderson, "Dwell and Post‐Dwell Penetration of Long Rods on Borosilicate Glass Targets," in *Shock Compression Of Condensed Matter 2009*, Nashville pp. 1447-1452, 2009.

[32] E. Strassburger, S. Bauer, S. Weber, and H. Gedon, "Flash X-ray cinematography analysis of dwell and penetration of small caliber projectiles with three types of SiC ceramics," *Defence Technology,* vol. 12, pp. 277-283, 2016.

[33] H. W. Lavendel, "Metalized ceramic/metal composites," *American Ceramic Society Bulletin,* vol. 52, pp. 424-424, 1973.

[34] P. Lundberg, B. Lundberg, and C. E. Anderson Jr, "Interface Defeat and Penetration: Two Modes of Interaction between Metallic Projectiles and Ceramic Targets," Uppsala: Acta Universitatis Upsaliensis, Uppsala, 2004.

[35] J. C. Li, X. W. Chen, F. Ning, and X. L. Li, "On the transition from interface defeat to penetration in the impact of long rod onto ceramic targets," *International Journal of Impact Engineering,* vol. 83, pp. 37-46, 2015.

[36] M. L. Wilkins, C. F. Cline, and C. A. Honodel, "Light armor," Lawrence Radiation Laboratory, University of California, Livermore, CA1969.

[37] G. E. Hauver, E. J. Rapacki, P. H. Netherwood, and R. F. Benck, "Interface Defeat of Long-Rod Projectiles by Ceramic Armor," U.S. Army Research Laboratory, Aberdeen Proving Ground, MD2005.

[38] P. Lundberg, R. Renstrom, and B. Lundberg, "Impact of metallic projectiles on ceramic targets: transition between interface defeat and penetration," *International Journal of Impact Engineering,* vol. 24, pp. 259-275, 2000.

[39] P. Lundberg, R. Renström, and B. Lundberg, "Impact of conical tungsten projectiles on flat silicon carbide targets: Transition from interface defeat to penetration," *International Journal of Impact Engineering,* vol. 32, pp. 1842-1856, 2006.

[40] C. Knight, M. Swain, and M. Chaudhri, "Impact of small steel spheres on glass surfaces," *J Mater Sci,* vol. 12, pp. 1573-1586, 1977.

[41] W. Janach, "The role of bulking in brittle failure of rocks under rapid compression," *International Journal of Rock Mechanics and Mining Sciences and Geomechanics Abstracts,* vol. 13, pp. 177-186, 1976.

[42] J. C. LaSalvia, J. Campbell, J. J. Swab, and J. W. McCauley, "Beyond Hardness: Ceramics and Ceramic-Based Composites for Protection," *Jom,* vol. 62, pp. 16-23, 2010.

[43] CoorsTek, "CeraShield and Cercom ceramic armor brochure," CoorsTek, Ed., ed, 2016.

[44] G. L. Harris, *Properties of silicon carbide*. London: INSPEC, 1995.

[45] V. Domnich, S. Reynaud, R. A. Haber, and M. Chhowalla, "Boron carbide: structure, properties, and stability under stress," *Journal of the American Ceramic Society,* vol. 94, pp. 3605-3628, 2011.

[46] O. P. Hugh, "Handbook of Refractory Carbides and Nitrides ", ed: William Andrew, 1996, p. 362.

[47] G. S. Rohrer, *Structure and bonding in crystalline materials*. Cambridge ; New York: Cambridge University Press, 2001.

[48] C. B. Carter and M. G. Norton, *Ceramic Materials*: Springer-Verlag New York, 2013.

[49] Y. Liao, *Practical Electron Microscopy and Database*, 2018.

[50] *Springer Materials*. Available: https://materials.springer.com/

[51] A. Erba, J. Maul, R. Demichelis, and R. Dovesi, "Assessing Thermochemical Properties of Materials through Ab initio Quantum-mechanical Methods: The Case of α-Al_2O_3," 2015.

[52] P. Auerkari, "Mechanical and physical properties of engineering alumina ceramics," Technical Research Centre of Finland1996.

[53] S. Burghartz and B. Schulz, "Thermophysical properties of sapphire, AlN and $MgAl_2O_4$ down to 70 K," *Journal of Nuclear Materials,* vol. 212-215, pp. 1065-1068, 1994.

[54] R. Castanet, *Selected Data on the Thermodynamic Properties of α-Alumina* vol. 16, 1984.

[55] J. B. Wachtman Jr, W. E. Tefft, D. G. Lam Jr, and R. P. Stinchfield, "Elastic Constants of Synthetic Single-Crystal Corundum at Room Temperature," *Journal of the American Ceramic Society,* vol. 43, pp. 334-334, 1960.

[56] D. B. Hovis, A. Reddy, and A. H. Heuer, "X-ray elastic constants for α-Al_2O_3," *Appl. Phys. Lett.,* vol. 88, 2006.

[57] J. Metson, "2 - Production of alumina," in *Fundamentals of Aluminium Metallurgy*, R. Lumley, Ed., ed: Woodhead Publishing, 2011, pp. 23-48.

[58] N. R. Council, *Opportunities in Protection Materials Science and Technology for Future Army Applications*. Washington, DC: The National Academies Press, 2011.

[59] M. N. Rahaman, *Sintering of Ceramics*. Boca Raton: CRC Press, 2007.

[60] N. K. Bourne, J. C. F. Millett, M. Chen, J. W. McCauley, and D. P. Dandekar, "On the Hugoniot elastic limit in polycrystalline alumina," *J. Appl. Phys.,* vol. 102, 2007.

[61] R. E. Tressler, "An assessment of low cost manufacturing technology for advanced structural ceramics and its impact on ceramic armor," in *Ceramic Armor Materials by Design*. vol. 134, ed, 2002, pp. 451-462.

[62] S. Huang, J. Binner, B. Vaidhyanathan, P. Brown, C. Hampson, and C. Spacie, "Development of Nano Zirconia Toughened Alumina for Ceramic Armor Applications," *Ceramic Engineering and Science Proceedings,* vol. 32, pp. 103-113, 2011.

[63] J. G. P. Binner and R. Stevens, "Improvement in the mechanical properties of polycrystalline beta-alumina via the use of zirconia particles containing stabilizing oxide additions," *Journal of Materials Science,* vol. 20, pp. 3119-3124, 1985.

[64] R. B. Heimann, *Classic and advanced ceramics : from fundamentals to applications*. Weinheim: Wiley-VCH, 2010.

[65] V. A. Izhevskyi, L. A. Genova, J. C. Bressiani, and A. H. A. Bressiani, "Review article: silicon carbide. Structure, properties and processing," *Cerâmica,* vol. 46, pp. 4-13, 2000.

[66] T. Ayalew, "SiC Semiconductor Devices Technology, Modeling, and Simulation," Addis Ababa, Äthiopien 1966.

[67] H. Föll. Available: http://www.tf.uni-kiel.de/matwis/amat/semi_en/kap_a/basics/ba_1_1.html

[68] "Silicon carbide (SiC), lattice parameters, thermal expansion," in *Group IV Elements, IV-IV and III-V Compounds. Part b - Electronic, Transport, Optical and Other Properties*, O. Madelung, U. Rössler, and M. Schulz, Eds., ed Berlin, Heidelberg: Springer Berlin Heidelberg, 2002, pp. 1-11.

[69] Z. Zolnai, "Irradiation-induced crystal defects in silicon carbide," PhD, Research Institute for Technical Physics and Materials Science, Hungarian Academy of Sciences, 2005.

[70] K. Kamitani, M. Grimsditch, J. C. Nipko, C. K. Loong, M. Okada, and I. Kimura, "The elastic constants of silicon carbide: A Brillouin-scattering study of 4H and 6H SiC single crystals," *Journal of Applied Physics,* vol. 82, pp. 3152-3154, 1997.

[71] M. Flinders, D. Ray, A. Anderson, and R. A. Cutler, "High-toughness silicon carbide as armor," *Journal of the American Ceramic Society,* vol. 88, pp. 2217-2226, 2005.

[72] J. A. Coppola, L. N. Hailey, and C. H. McMurtry, "Sintered alpha silicon carbide ceramic body having equiaxed microstructure," 1982.

[73] S. K. Lee and C. H. Kim, "Effects of alpha-SiC versus beta-SiC starting powders on microstructure and fracture-toughness of SiC sintred with Al_2O_3-Y_2O_3 additives," *Journal of the American Ceramic Society,* vol. 77, pp. 1655-1658, 1994.

[74] N. P. Padture, "In situ ‐ toughened silicon carbide," *Journal of the American Ceramic Society,* vol. 77, pp. 519-523, 1994.

[75] Y. w. Kim, M. Mitomo, and H. Hirotsuru, "Grain growth and fracture toughness of fine ‐ grained silicon carbide ceramics," *Journal of the American Ceramic Society,* vol. 78, pp. 3145-3148, 1995.

[76] N. L. Hecht, D. E. McCullum, and G. A. Graves, "Investigation of Selected Silicon Nitride and Silicon Carbide Ceramics," in *12th Annual Conference on Composites and Advanced Ceramic Materials: Ceramic Engineering and Science Proceedings*, pp. 1313-1332, 2008.

[77] D. E. McCullum, N. L. Hecht, L. Chuck, and S. M. Goodrich, "Summary of Results of the Effects of Environment on Mechanical Behavior of High-Performance Ceramics," in *Proceedings of the 15th Annual Conference on Composites and Advanced Ceramic Materials: Ceramic Engineering and Science Proceedings*, pp. 1886-1913, 2008.

[78] P. Chantikul, G. Anstis, B. R. Lawn, and D. Marshall, "A critical evaluation of indentation techniques for measuring fracture toughness: II, strength method," *Journal of the American Ceramic Society,* vol. 64, pp. 539-543, 1981.

[79] W. D. G. Boecker, R. S. Storm, and K. Y. Chia, "Silicon carbide bodies having high toughness and fracture resistance and method of making same," U. S. Patent, 1991.

[80] D. Kim, C. Jang, B. Park, and S. Baik, "Pressureless-sintering of silicon carbide with additions of yttria and alumina," *J. Korean Ceram. Soc,* vol. 26, pp. 228-234, 1989.

[81] S. Prochazka, "Hot pressed silicon carbide," 1974.

[82] A. Ezis, "Monolithic, fully dense silicon carbide material, method of manufacturing and end uses," 1994.

[83] M. K. Aghajanian, B. N. Morgan, J. R. Singh, J. Mears, and R. A. Wolffe, "A new family of reaction bonded ceramics for armor applications," *Ceramic Armor Materials by Design,* vol. 134, pp. 527-539, 2002.

[84] V. Domnich and Y. Gogotsi, "Phase transformations in silicon under contact loading," *Reviews on Advanced Materials Science,* vol. 3, pp. 1-36, 2002.

[85] D. B. Rahbek and B. B. Johnsen, "Dynamic behaviour of ceramic armour systems," Norwegian Defence Research Establishment (FFI)2015.

[86] M. Chheda, M. J. Normandia, and J. Shih, "Improving ceramic armor performance," *Ceramic Industry,* vol. 156, pp. 124-126, 2006.

[87] S. Elliott, "Silicon carbide ceramic armor," *Advanced Materials & Processes,* vol. 165, pp. 29-30, 2007.

[88] M. Flinders, D. Ray, and R. A. Cutler, "Toughness-hardness trade-off in advanced SiC armor," *Ceramic Armor and Armor Systems,* vol. 151, pp. 37-48, 2003.

[89] C. Roberson and P. J. Hazell, "Resistance of different ceramic materials to penetration by a tungsten carbide cored projectile," *Ceramic Armor and Armor Systems,* vol. 151, pp. 153-163, 2003.

[90] C. Roberson and P. J. Hazell, "Resistance of silicon carbide to penetration by a tungsten carbide cored projectile," *Ceramic Armor and Armor Systems,* vol. 151, pp. 165-174, 2003.

[91] N. J. Woolmore, P. J. Hazell, and T. P. Stuart, "An investigation into fragmenting the 14.5 mm BS41 armour piercing round by varying a confined ceramic target setup," *Ceramic Armor and Armor Systems,* vol. 151, pp. 175-186, 2003.

[92] T. M. Lillo, D. W. Bailey, D. A. Laughton, H. S. Chu, and W. M. Harrison, "Development of a pressureless sintered silicon carbide monolith and special-shaped silicon carbide whisker reinforced silicon carbide matrix composite for lightweight armor application," in *27th International Cocoa Beach Conference on Advanced Ceramics Composites*, Cocoa Beach, Fl, pp. 359-364, 2003.

[93] J. J. Hall, "Electronic Effects in the Elastic Constants of n-Type Silicon," *Physical Review,* vol. 161, pp. 756-761, 1967.

[94] M. V. Silva, D. Stainer, H. A. Al-Qureshi, O. R. K. Montedo, and D. Hotza, "Alumina- Based Ceramics for Armor Application: Mechanical Characterization and Ballistic Testing," *Journal of Ceramics,* vol. 2014, p. 6, 2014.

[95] J. J. Swab, "Recommendations for Determining the Hardness of Armor Ceramics," *International Journal of Applied Ceramic Technology,* vol. 1, pp. 219-225, 2004.

[96] I. ASTM, "Standard Test Method for Knoop Indentation Hardness of Advanced Ceramics," vol. ASTM C1326 - 13, ed, 2013.

[97] I. ASTM, "Standard Test Method for Vickers Indentation Hardness of Advanced Ceramics," vol. ASTM C1327 - 15, ed, 2015.

[98] I. G. Ritchie, "Improved resonant bar techniques for the measurement of dynamic elastic moduli and a test of the Timoshenko beam theory," *Journal of Sound and Vibration,* vol. 31, pp. 453-468, 1973.

[99] H. Ledbetter, "Dynamic vs. static Young's moduli: a case study," *Materials Science & Engineering A,* vol. 165, pp. L9-L10, 1993.

[100] D. Sirdeshmukh and K. Subhadra, "Consistency checks on elastic properties of crystals," *J Mater Sci,* vol. 40, pp. 1553-1570, 2005.

[101] I. ASTM, "Standard Test Method for Flexural Strength of Advanced Ceramics at Ambient Temperature," vol. ASTM C1161 - 13, ed, 2013.

[102] ASTM, "Standard Test Methods for Determination of Fracture Toughness of Advanced Ceramics at Ambient Temperature," vol. ASTM C1421-16, ed. West Conshohocken, PA: ASTM International, 2016.

[103] A. Krell and E. Strassburger, "Order of influences on the ballistic resistance of armor ceramics and single crystals," *Materials Science & Engineering A,* vol. 597, pp. 422-430, 2014.

[104] K. R. Kambale, A. Mahajan, and S. P. Butee, "Effect of grain size on the properties of ceramics," *Metal Powder Report,* vol. 74, pp. 130-136, 2019.

[105] R. W. Rice, C. C. Wu, and F. Borchelt, "Hardness grain-size relations in ceramics," *Journal of the American Ceramic Society,* vol. 77, pp. 2539-2553, 1994.

[106] J. Seidel, N. Claussen, and J. Rödel, "Reliability of alumina ceramics: Effect of grain size," *Journal of the European Ceramic Society,* vol. 15, pp. 395-404, 1995.

[107] E. O. Hall, "The Deformation and Ageing of Mild Steel: III Discussion of Results," *Proceedings of the Physical Society. Section B,* vol. 64, pp. 747-753, 1951.

[108] N. Hansen, "Hall–Petch relation and boundary strengthening," *Scripta Materialia,* vol. 51, pp. 801-806, 2004.

[109] A. Franco, S. G. Roberts, and P. D. Warren, "Fracture toughness, surface flaw sizes and flaw densities in Al_2O_3," *Acta Materialia,* vol. 45, pp. 1009-1015, 1997.

[110] A. Krell and S. Schadlich, "Nanoindentation hardness of submicrometer alumina ceramics," *Materials Science & Engineering A,* vol. 307, pp. 172-181, 2001.

[111] E. Straßburger, "Ballistic testing of transparent armour ceramics," *Journal of the European Ceramic Society,* vol. 29, pp. 267-273, 2009.

[112] A. Krell and E. Strassburger, "Discrimination of Basic Influences on the Ballistic Strength of Opaque and Transparent Ceramics," in *Advances in Ceramic Armor VIII*, ed: John Wiley & Sons, Inc., 2012, pp. 161-176.

[113] D. Viechnicki, W. Blumenthal, M. Slavin, C. Tracy, and H. Skeele, "Armor Ceramics - 1987," in *The third TACOM armor coordinating conference proceedings*, pp. 27-53, 1987.

[114] D. Ray, R. M. Flinders, A. Anderson, R. A. Cutler, and W. Rafaniello, "Effect of Room-Temperature Hardness and Toughness on the Ballistic Performance of SiC-Based Ceramics," in *Advances in Ceramic Armor*, ed: John Wiley & Sons, Inc., 2005, pp. 131-142.

[115] J. LaSalvia, J. Campbell, J. Swab, and J. McCauley, "Beyond hardness: Ceramics and ceramic-based composites for protection," *The Journal of The Minerals, Metals & Materials Society (TMS),* vol. 62, pp. 16-23, 2010.

[116] M. Wilkins, C. Honodel, and D. Sawle, "An approach to the study of light armor," Lawrence Livemore National Laboratory1967.

[117] M. L. Wilkins, C. F. Cline, and C. A. Honodel, "Fourth progress report of light armor program," Lawrence Livermore National Lab., CA , USA, Washington, D.C. :1969.

[118] M. L. Whittaker, R. A. Cutler, J. Campbell, and J. L. Salvia, "Microstructure, Mechanical Properties, and Performance of Magnesium Aluminum Boride ($MgAlB_{14}$)," in *Advances in Ceramics Armor VI*, ed: John Wiley & Sons, Inc., 2010, pp. 239-250.

[119] J. J. Swab, G. A. Gilde, P. J. Patel, A. A. Wereszczak, and J. W. McCauley, "Fracture analysis of transparent armor ceramics," in *Fractography of glasses and ceramics IV*. vol. 122, ed: The American Ceramic Society, 2001, pp. 489-508.

[120] A. Krell and E. Strassburger, "Ballistic strength of opaque and transparent armor," *American Ceramic Society Bulletin,* vol. 86, pp. 9201-9207, 2007.

[121] J.-K. Hyun, S. M. Sharma, and Y. M. Gupta, "Ruby R - line shifts for shock compression along $(1\bar{1}02)$," *Journal of Applied Physics,* vol. 84, pp. 1947-1952, 1998.

[122] G. J. Kleiser, L. C. Chhabildas, and W. D. Reinhart, "Comparison of dynamic compression behavior of single crystal sapphire to polycrystalline alumina," *International Journal of Impact Engineering,* vol. 38, pp. 473-479, 2011.

[123] J. Wackerle, "Shock‐Wave Compression of Quartz," *Journal of Applied Physics,* vol. 33, pp. 922-937, 1962.

[124] O. B. Tsiok, V. V. Brazhkin, A. G. Lyapin, and L. G. Khvostantsev, "Logarithmic kinetics of the amorphous-amorphous transformations in SiO_2 and GeO_2 glasses under high-pressure," *Physical Review Letters,* vol. 80, pp. 999-1002, 1998.

[125] A. Savinykh, G. Garkushin, S. Razorenov, and G. Kanel, "Longitudinal and bulk compressibility of soda- lime glass at pressures to 10 GPa," *Tech. Phys.,* vol. 52, pp. 328-332, 2007.

[126] E. Carton, G. Roebroeks, J. Weerheijm, A. Diederen, and M. Kwint, "Tno's Research on Ceramic Based Armor," in *Advances in Ceramic Armor XI*, ed: John Wiley & Sons, Inc., 2015, pp. 1-18.

[127] B. Lawn, *Fracture of brittle solides*, Second Edition ed.: Cambridege University Press, 1993.

[128] G. D. Quinn and R. Morrell, "Design data for engineering ceramics: a review of the flexure test," *Journal of the American Ceramic Society,* vol. 74, pp. 2037-2066, 1991.

[129] C. C. Holland and R. M. McMeeking, "The influence of mechanical and microstructural properties on the rate- dependent fracture strength of ceramics in uniaxial compression," *International Journal of Impact Engineering,* vol. 81, pp. 34-49, 2015.

[130] H. D. Espinosa and P. D. Zavattieri, "A grain level model for the study of failure initiation and evolution in polycrystalline brittle materials. Part I: Theory and numerical implementation," *Mechanics of Materials,* vol. 35, pp. 333-364, 2003.

[131] H. D. Espinosa and P. D. Zavattieri, "A grain level model for the study of failure initiation and evolution in polycrystalline brittle materials. Part II: Numerical examples," *Mechanics of Materials,* vol. 35, pp. 365-394, 2003.

[132] F. Aurenhammer, "Voronoi diagrams—a survey of a fundamental geometric data structure," *ACM Computing Surveys (CSUR),* vol. 23, pp. 345-405, 1991.

[133] R. Quey, P. R. Dawson, and F. Barbe, "Large-scale 3D random polycrystals for the finite element method: Generation, meshing and remeshing," *Computer Methods in Applied Mechanics and Engineering,* vol. 200, pp. 1729-1745, 2011.

[134] H. Leipold, E. A. Lazar, K. A. Brakke, and D. J. Srolovitz, "Erratum to 'Statistical topology of perturbed two-dimensional lattices (2016 J. Stat. Mech. P043103)," *Journal of Statistical Mechanics: Theory and Experiment,* vol. 2017, p. 079901, 2017.

[135] G. Johnson, R. Stryk, T. Holmquist, and S. Beissel, "Numerical algorithms in a lagrangian hydrocode," Wright Laboratory, Eglin Air Force Base1997.

[136] A. M. Rajendran and D. J. Grove, "Modeling the shock response of silicon carbide, boron carbide and titanium diboride," *International Journal of Impact Engineering,* vol. 18, pp. 611-631, 1996.

[137] T. J. Holmquist and G. R. Johnson, "Characterization and evaluation of silicon carbide for high-velocity impact," *J. Appl. Phys.,* vol. 97, 2005.

[138] P. H. Feenstra and R. De Borst, "A composite plasticity model for concrete," *International Journal of Solids and Structures,* vol. 33, pp. 707-730, 1996.

[139] S. R. Beissel, G. R. Johnson, and C. H. Popelar, "An element- failure algorithm for dynamic crack propagation in general directions," *Engineering Fracture Mechanics,* vol. 61, pp. 407-425, 1998.

[140] G. R. Johnson, S. R. Beissel, and R. A. Stryk, "A generalized particle algorithm for high velocity impact computations," *Computational Mechanics,* vol. 25, pp. 245-256, 2000.

[141] V. Deshpande and A. Evans, "Inelastic deformation and energy dissipation in ceramics: A mechanism-based constitutive model," *Journal of the Mechanics and Physics of Solids,* vol. 56, pp. 3077-3100, 2008.

[142] V. S. Deshpande, E. A. N. Gamble, B. G. Compton, R. M. McMeeking, A. G. Evans, and F. W. Zok, "A Constitutive Description of the Inelastic Response of Ceramics," *Journal of the American Ceramic Society,* vol. 94, pp. s204-s214, 2011.

[143] A. M. Rajendran, "Modeling the impact behavior of AD85 ceramic under multiaxial loading," *International Journal of Impact Engineering,* vol. 15, pp. 749-768, 1994.

[144] G. Johnson and T. Holmquist, "A computational constitutive model for brittle materials subjected to large strains, high strain rates and high pressures.," *Shock Wave and High-Strain-Rate Phenomena in Materials,* pp. 1075-1081, 1992.

[145] G. R. Johnson and T. J. Holmquist, "An improved computational constitutive model for brittle materials," *AIP Conference Proceedings,* vol. 309, pp. 981-984, 1994.

[146] G. R. Johnson, T. J. Holmquist, and S. R. Beissel, "Response of aluminum nitride (including a phase change) to large strains, high strain rates, and high pressures," *Journal of Applied Physics,* vol. 94, pp. 1639-1646, 2003.

[147] T. J. Holmquist and G. R. Johnson, "Response of silicon carbide to high velocity impact," *Journal of Applied Physics,* vol. 91, pp. 5858-5866, 2002.

[148] D. S. Cronin, K. Bui, C. Kaufmann, G. J. McIntosh, and T. Berstad, "Implementation and Validation of the Johnson-Holmquist Ceramic Material Model in LS-Dyna," in *4th European LS-dyna users conference*2003.

[149] C. H. M. Simha, S. J. Bless, and A. Bedford, "Computational modeling of the penetration response of a high-purity ceramic," *International Journal of Impact Engineering,* vol. 27, pp. 65-86, 2002.

[150] F. L. Addessio and J. N. Johnson, "A constitutive model for the dynamic response of brittle materials," *Journal of Applied Physics,* vol. 67, pp. 3275-3286, 1990.

[151] C. Denoual and F. Hild, "A Damage Model for the Dynamic Fragmentation of Brittle Solids," *Computer Methods in Applied Mechanics and Engineering,* vol. 183, pp. 247-258, 2000.

[152] H. D. Espinosa, "On the dynamic shear resistance of ceramic composites and its dependence on applied multiaxial deformation," *International Journal of Solids and Structures,* vol. 32, pp. 3105-3128, 1995.

[153] H. D. Espinosa, P. D. Zavattieri, and S. K. Dwivedi, "A finite deformation continuum\discrete model for the description of fragmentation and damage in brittle materials," *Journal of the Mechanics and Physics of Solids,* vol. 46, pp. 1909-1942, 1998.

[154] H. Horii and S. Nemat-Nasser, "Brittle failure in compression: splitting faulting and brittle-ductile transition," *Philosophical Transactions of the Royal Society of London. Series A, Mathematical and Physical Sciences,* vol. 319, pp. 337-374, 1986.

[155] P. Riou, C. E. Cottenot, and M. Boussuge, "Anisotropic damage model for impacted ceramic material: Application to silicon carbide," *International Journal of Impact Engineering,* vol. 21, pp. 683-693, 1998.

[156] D. E. J. Armstrong, A. J. Wilkinson, and S. G. Roberts, "Measuring anisotropy in Young's modulus of copper using microcantilever testing," *Journal of Materials Research,* vol. 24, pp. 3268-3276, 2009.

[157] K. Matoy, H. Schönherr, T. Detzel, T. Schöberl, R. Pippan, C. Motz*, et al.*, "A comparative micro-cantilever study of the mechanical behavior of silicon based passivation films," *Thin Solid Films,* vol. 518, pp. 247-256, 2009.

[158] J. Gong and A. Wilkinson, "Investigation of elastic properties of single-crystal α-Ti using microcantilever beams," *Philosophical Magazine Letters,* vol. 90, pp. 503-512, 2010.

[159] D. E. J. Armstrong and E. Tarleton, "Bend Testing of Silicon Microcantilevers from 21°C to 770°C," *JOM,* vol. 67, pp. 2914-2920, 2015.

[160] D. Di Maio and S. G. Roberts, "Measuring fracture toughness of coatings using focused-ion-beam-machined microbeams," *Journal of Materials Research,* vol. 20, pp. 299-302, 2005.

[161] A. D. Norton, "Measuring and understanding grain boundary properties of engineering ceramics," DPhil Department of Materials, University of Oxford, Oxford, UK, 2013.

[162] D. E. J. Armstrong, M. E. Rogers, and S. G. Roberts, "Micromechanical testing of stress corrosion cracking of individual grain boundaries," *Scripta Materialia,* vol. 61, pp. 741-743, 2009.

[163] S. Johansson, J. Å. Schweitz, L. Tenerz, and J. Tirén, "Fracture testing of silicon microelements in situ in a scanning electron microscope," *Journal of Applied Physics,* vol. 63, pp. 4799-4803, 1988.

[164] S. Sundararajan, B. Bhushan, T. Namazu, and Y. Isono, "Mechanical property measurements of nanoscale structures using an atomic force microscope," *Ultramicroscopy,* vol. 91, pp. 111-118, 2002.

[165] T. Namazu, Y. Isono, and T. Tanaka, "Evaluation of size effect on mechanical properties of single crystal silicon by nanoscale bending test using AFM," *Journal of Microelectromechanical Systems,* vol. 9, pp. 450-459, 2000.

[166] K. Komai, K. Minoshima, and S. Inoue, "Fracture and fatigue behavior of single crystal silicon microelements and nanoscopic AFM damage evaluation," *MEMS, Systems for Information Processing and Storage,* vol. 5, pp. 30-37, 1998.

[167] B. N. Jaya, C. Kirchlechner, and G. Dehm, "Can microscale fracture tests provide reliable fracture toughness values? A case study in silicon," *Journal of Materials Research,* vol. 30, pp. 686-698, 2015.

[168] J. Ast, M. Ghidelli, K. Durst, M. Göken, M. Sebastiani, and A. M. Korsunsky, "A review of experimental approaches to fracture toughness evaluation at the micro-scale," *Materials & Design,* vol. 173, p. 107762, 2019.

[169] B. N. Jaya and V. Jayaram, "Crack stability in edge-notched clamped beam specimens: modeling and experiments," *International Journal of Fracture,* vol. 188, pp. 213-228, 2014.

[170] S. Liu, J. Wheeler, P. Howie, X. Zeng, J. Michler, and W. Clegg, "Measuring the fracture resistance of hard coatings," *Applied Physics Letters,* vol. 102, p. 171907, 2013.

[171] M. Sebastiani, K. Johanns, E. G. Herbert, F. Carassiti, and G. M. Pharr, "A novel pillar indentation splitting test for measuring fracture toughness of thin ceramic coatings," *Philosophical Magazine,* vol. 95, pp. 1928-1944, 2015.

[172] D. E. J. Armstrong, A. J. Wilkinson, and S. G. Roberts, "Micro-mechanical measurements of fracture toughness of bismuth embrittled copper grain boundaries," *Philosophical Magazine Letters,* vol. 91, pp. 394-400, 2011.

[173] M. G. Mueller, V. Pejchal, G. Zagar, A. Singh, M. Cantoni, and A. Mortensen, "Fracture toughness testing of nanocrystalline alumina and fused quartz using chevron-notched microbeams," *Acta Materialia,* vol. 86, pp. 385-395, 2015.

[174] K. Yoshida, F. Wakai, N. Nishiyama, R. Sekine, Y. Shinoda, T. Akatsu*, et al.*, "Large increase in fracture resistance of stishovite with crack extension less than one micrometer," *Scientific Reports,* vol. 5, p. 10993, 2015.

[175] M. G. Mueller, V. Pejchal, G. Žagar, A. Singh, M. Cantoni, and A. Mortensen, "Fracture toughness testing of nanocrystalline alumina and fused quartz using chevron-notched microbeams," *Acta Materialia,* vol. 86, pp. 385-395, 2015.

[176] L. S. T. C. (LSTC), "LS-DYNA Keyword User's Manual, Volume 1, Version 971," in *7.18 (Contact)*, ed, 2007.

[177] L. S. T. C. (LSTC), "LS-DYNA Keyword User's Manual, Volume II, Version R7.1," in *MAT_185* ed, 2014.

[178] P. D. Zavattieri, P. V. Raghuram, and H. D. Espinosa, "A computational model of ceramic microstructures subjected to multi-axial dynamic loading," *Journal of the Mechanics and Physics of Solids,* vol. 49, pp. 27-68, 2001.

[179] I. Simonovski and L. Cizelj, "Cohesive zone modeling of intergranular cracking in polycrystalline aggregates," *Nuclear Engineering and Design,* vol. 283, pp. 139-147, 2015.

[180] A. C. Lewis, J. F. Bingert, D. J. Rowenhorst, A. Gupta, A. B. Geltmacher, and G. Spanos, "Two- and three-dimensional microstructural characterization of a super-austenitic stainless steel," *Materials Science and Engineering: A,* vol. 418, pp. 11-18, 2006.

[181] M. Nygårds and P. Gudmundson, "Three-dimensional periodic Voronoi grain models and micromechanical FE-simulations of a two-phase steel," *Computational Materials Science,* vol. 24, pp. 513-519, 2002.

[182] M. Ohata, M. Suzuki, A. Ui, and F. Minami, "3D-Simulation of ductile failure in two-phase structural steel with heterogeneous microstructure," *Engineering Fracture Mechanics,* vol. 77, pp. 277-284, 2010.

[183] Z. Wang and P. Li, "Voronoi cell finite element modelling of the intergranular fracture mechanism in polycrystalline alumina," *Ceramics International,* vol. 43, pp. 6967-6975, 2017.

[184] I. Simonovski and L. Cizelj, "Computational multiscale modeling of intergranular cracking," *Journal of Nuclear Materials,* vol. 414, pp. 243-250, 2011.

[185] M. Kamaya, Y. Kawamura, and T. Kitamura, "Three-dimensional local stress analysis on grain boundaries in polycrystalline material," *International Journal of Solids and Structures,* vol. 44, pp. 3267-3277, 2007.

[186] S. Rezaei, S. Wulfinghoff, and S. Reese, "Prediction of fracture and damage in micro/nano coating systems using cohesive zone elements," *International Journal of Solids and Structures,* vol. 121, pp. 62-74, 2017.

[187] A. D. Norton, S. Falco, N. Young, J. Severs, and R. I. Todd, "Microcantilever investigation of fracture toughness and subcritical crack growth on the scale of the microstructure in Al_2O_3," *Journal of the European Ceramic Society,* vol. 35, pp. 4521-4533, 2015.

[188] J. M. Liu and B.-W. Shen, "Grain boundary fracture in tungsten bi- crystals," *Acta Metallurgica,* vol. 30, pp. 1197-1202, 1982.

[189] S. Chikwembani and J. Weertman, "Fatigue crack-growth and fracture-behavior of bismuth-doped copper bicrystals," *Metallurgical Transactions a-Physical Metallurgy and Materials Science,* vol. 20, pp. 1221-1231, 1989.

[190] D. Armstrong, A. Wilkinson, and S. Roberts, "Measuring Local Mechanical Properties Using FIB Machined Microcantilevers," *Probing Mechanics at Nanoscale Dimensions,* vol. 1185, pp. 7-13, 2009.

[191] J. Tatami, M. Katayama, M. Ohnishi, T. Yahagi, T. Takahashi, T. Horiuchi*, et al.*, "Local Fracture Toughness of Si_3N_4 Ceramics Measured using Single-Edge Notched Microcantilever Beam Specimens," *Journal of the American Ceramic Society,* vol. 98, pp. 965-971, 2015.

[192] B. S. Li, T. J. Marrow, S. G. Roberts, and D. E. J. Armstrong, "Evaluation of Fracture Toughness Measurements Using Chevron-Notched Silicon and Tungsten Microcantilevers," *JOM,* vol. 71, pp. 3378-3389, 2019.

[193] T. Fett, D. Creek, S. Wagner, G. Rizzi, and C. A. Volkert, "Fracture Toughness Test with a Sharp Notch Introduced by Focussed Ion Beam," *International Journal of Fracture,* vol. 153, pp. 85-92, 2008.

[194] D. Picard, D. Leguillon, and C. Putot, "A method to estimate the influence of the notch-root radius on the fracture toughness measurement of ceramics," *Journal of the European Ceramic Society,* vol. 26, pp. 1421-1427, 2006.

[195] F. Iqbal, J. Ast, M. Göken, and K. Durst, "In situ micro-cantilever tests to study fracture properties of NiAl single crystals," *Acta Materialia,* vol. 60, pp. 1193-1200, 2012.

[196] S. Massl, W. Thomma, J. Keckes, and R. Pippan, "Investigation of fracture properties of magnetron-sputtered TiN films by means of a FIB-based cantilever bending technique," *Acta Materialia,* vol. 57, pp. 1768-1776, 2009.

[197] B. Merle and M. Göken, "Fracture toughness of silicon nitride thin films of different thicknesses as measured by bulge tests," *Acta Materialia,* vol. 59, pp. 1772-1779, 2011.

[198] T. Ando, X. Li, S. Nakao, T. Kasai, H. Tanaka, M. Shikida*, et al.*, "Fracture toughness measurement of thin-film silicon," *Fatigue & Fracture of Engineering Materials & Structures,* vol. 28, pp. 687-694, 2005.

[199] J. Bagdahn, W. N. Sharpe, and O. Jadaan, "Fracture strength of polysilicon at stress concentrations," *Journal of Microelectromechanical Systems,* vol. 12, pp. 302-312, 2003.

[200] H. D. Espinosa and P. Bei, "A new methodology to investigate fracture toughness of freestanding MEMS and advanced materials in thin film form," *Journal of Microelectromechanical Systems,* vol. 14, pp. 153-159, 2005.

[201] X. Li, T. Kasai, S. Nakao, T. Ando, M. Shikida, K. Sato*, et al.*, "Anisotropy in fracture of single crystal silicon film characterized under uniaxial tensile condition," *Sensors and Actuators A: Physical,* vol. 117, pp. 143-150, 2005.

[202] S. Wurster, C. Motz, and R. Pippan, "Characterization of the fracture toughness of micro-sized tungsten single crystal notched specimens," *Philosophical Magazine,* vol. 92, pp. 1803-1825, 2012.

[203] T. P. Halford, K. Takashima, Y. Higo, and P. Bowen, "Fracture tests of microsized TiAl specimens," *Fatigue & Fracture of Engineering Materials & Structures,* vol. 28, pp. 695-701, 2005.

[204] S. Nakao, T. Ando, M. Shikida, and K. Sato, "Effect of temperature on fracture toughness in a single-crystal-silicon film and transition in its fracture mode," *Effect of temperature on fracture toughness in a SCS film and transition in its fracture mode,* vol. 18, p. 015026, 2008.

[205] S. Massl, W. Thomma, J. Keckes, and R. Pippan, "Investigation of fracture properties of magnetron- sputtered TiN films by means of a FIB-based cantilever bending technique," *Acta Materialia,* vol. 57, pp. 1768-1776, 2009.

[206] S. M. Wiederhorn, "Moisture assisted crack growth in ceramics," *International Journal of Fracture Mechanics,* vol. 4, pp. 171-177, 1968.

[207] T. A. Michalske, B. C. Bunker, and S. W. Freiman, "Stress Corrosion of Ionic and Mixed Ionic/Covalent Solids," *Journal of the American Ceramic Society,* vol. 69, pp. 721-724, 1986.

[208] G. Žagar, A. Singh, V. Pejchal, M. G. Mueller, and A. Mortensen, "On measuring fracture toughness under load control in the presence of slow crack growth," *Journal of the European Ceramic Society,* vol. 35, pp. 3155-3166, 2015.

[209] ASTM, "Standard Test Methods for Determination of Fracture Toughness of Advanced Ceramics at Ambient Temperature," vol. ASTM C1421-18, ed. West Conshohocken, PA, 2018.

[210] ASTM, "Standard Test Method for Plane-Strain (Chevron-Notch) Fracture Toughness of Metallic Materials," vol. ASTM E1304 - 97(2014), ed, 2014.

[211] M. G. Mueller, G. Žagar, and A. Mortensen, "Stable room-temperature micron-scale crack growth in single-crystalline silicon," *Journal of Materials Research,* vol. 32, pp. 3617-3626, 2017.

[212] F. Y. Cui and R. P. Vinci, "A chevron-notched bowtie micro-beam bend test for fracture toughness measurement of brittle materials," *Scripta Materialia,* vol. 132, pp. 53-57, 2017.

[213] K. Minoshima, T. Terada, and K. Komai, "Influence of nanometre-sized notch and water on the fracture behaviour of single crystal silicon microelements," *Fatigue and Fracture of Engineering Materials and Structures,* vol. 23, pp. 1033-1040, 2000.

[214] G. D. Quinn, *Fractography of Ceramics and Glasses*: National Institute of Standards and Technology 2016.

[215] G. Sernicola, T. Giovannini, P. Patel, J. R. Kermode, D. S. Balint, T. B. Britton*, et al.*, "In situ stable crack growth at the micron scale," *Nature Communications,* vol. 8, p. 108, 2017.

[216] A. G. Evans, "Slow crack growth in brittle materials under dynamic loading conditions," *International Journal of Fracture,* vol. 10, pp. 251-259, 1974.

[217] B. R. Lawn, "An atomistic model of kinetic crack growth in brittle solids," *Journal of Materials Science,* vol. 10, pp. 469-480, 1975.

[218] A. Evans and H. Johnson, "The fracture stress and its dependence on slow crack growth," *Journal of Materials Science,* vol. 10, pp. 214-222, 1975.

[219] T. J. Chuang, L. Chuck, R. J. Fields, and E. R. Fuller, "Effects of crack growth on the load-displacement characteristics of precracked specimens under bending," *Engineering Fracture Mechanics,* vol. 18, pp. 1099-1109, 1983.

[220] D. Munz, G. Himsolt, and J. Eschweiler, "Comparison of High-Temperature Fracture Toughness of Hot-Pressed Si3N4 with Straight-Through and Chevron Notches," *Journal of the American Ceramic Society,* vol. 63, pp. 341-342, 1980.

[221] T. B. Troczynski and P. S. Nicholson, "Effect of Subcritical Crack Growth on Fracture Toughness and Work-of-Fracture Tests Using Chevron-Notched Specimens," *Journal of the American Ceramic Society,* vol. 70, pp. 78-85, 1987.

[222] J. Sung and P. S. Nicholson, "Valid K_{IC} Determination via In‐Test Subcritical Precracking of Chevron‐Notched Bend Bars," *Journal of the American Ceramic Society,* vol. 72, pp. 1033-1036, 1989.

[223] M. Ebrahimi, J. Chevalier, and G. Fantozzi, "Slow crack-growth behavior of alumina ceramics," *Journal of Materials Research,* vol. 15, pp. 142-147, 2000.

[224] C. Olagnon, J. Chevalier, and V. Pauchard, "Global description of crack propagation in ceramics," *Journal of the European Ceramic Society,* vol. 26, pp. 3051-3059, 2006.

[225] A. Krell, E. Pippel, J. Woltersdorf, and W. Burger, "Subcritical crack growth in Al2O3 with submicron grain size," *Journal of the European Ceramic Society,* vol. 23, pp. 81-89, 2003.

[226] V. M. Sglavo and D. J. Green, "Threshold stress intensity factor in soda-lime silicate glass by interrupted static fatigue test," *Journal of the European Ceramic Society,* vol. 16, pp. 645-651, 1996.

[227] S. M. Wiederhorn, "Fracture Surface Energy of Glass," *Journal of the American Ceramic Society,* vol. 52, pp. 99-105, 1969.

[228] J. A. Salem, "Slow Crack Growth and Fracture Toughness of Sapphire for the International Space Station Fluids and Combustion Facility," Glenn Research Center, NASA, Cleveland, Ohio, 2006.

[229] S. M. Wiederhorn, "Fracture of Sapphire," *Journal of the American Ceramic Society,* vol. 52, pp. 485-491, 1969.

[230] R. D. Kelley, K. Song, B. Van Leer, D. Wall, and L. Kwakman, "Xe+ FIB Milling and Measurement of Amorphous Silicon Damage," *Microscopy and Microanalysis,* vol. 19, pp. 862-863, 2013.

[231] R. P. Babu, S. Irukuvarghula, A. Harte, and M. Preuss, "Nature of gallium focused ion beam induced phase transformation in 316L austenitic stainless steel," *Acta Materialia,* vol. 120, pp. 391-402, 2016.

[232] T. L. Burnett, R. Kelley, B. Winiarski, L. Contreras, M. Daly, A. Gholinia*, et al.*, "Large volume serial section tomography by Xe Plasma FIB dual beam microscopy," *Ultramicroscopy,* vol. 161, pp. 119-129, 2016.

[233] J. Mayer, L. A. Giannuzzi, T. Kamino, and J. Michael, "TEM Sample Preparation and FIB-Induced Damage," *MRS Bulletin,* vol. 32, pp. 400-407, 2011.

[234] K. Thompson, D. Lawrence, D. J. Larson, J. D. Olson, T. F. Kelly, and B. Gorman, "In situ site-specific specimen preparation for atom probe tomography," *Ultramicroscopy,* vol. 107, pp. 131-139, 2007.

[235] N. Saowadee, K. Agersted, and J. R. Bowen, "Effects of focused ion beam milling on electron backscatter diffraction patterns in strontium titanate and stabilized zirconia," *Journal of Microscopy,* vol. 246, pp. 279-286, 2012.

[236] S. Shim, H. Bei, M. K. Miller, G. M. Pharr, and E. P. George, "Effects of focused ion beam milling on the compressive behavior of directionally solidified micropillars and the nanoindentation response of an electropolished surface," *Acta Materialia,* vol. 57, pp. 503-510, 2009.

[237] H. Bei, S. Shim, M. K. Miller, G. M. Pharr, and E. P. George, "Effects of focused ion beam milling on the nanomechanical behavior of a molybdenum-alloy single crystal," *Applied Physics Letters,* vol. 91, p. 111915, 2007.

[238] D. Kiener, C. Motz, M. Rester, M. Jenko, and G. Dehm, "FIB damage of Cu and possible consequences for miniaturized mechanical tests," *Materials Science and Engineering: A,* vol. 459, pp. 262-272, 2007.

[239] Z. Zhang, E. Hasenhuetl, K. Yabuuchi, and A. Kimura, "Evaluation of helium effect on ion-irradiation hardening in pure tungsten by nano-indentation method," *Nuclear Materials and Energy,* vol. 9, pp. 539-546, 2016.

[240] K. H. Park, S. Kondo, Y. Katoh, and A. Kohyama, "Mechanical Properties of β-SiC After Si- and Dual Si + He-Ion Irradiation at Various Temperatures," *Fusion Science and Technology,* vol. 44, pp. 455-459, 2003.

[241] T. Fett, D. Creek, S. Wagner, G. Rizzi, and C. Volkert, "Fracture Toughness Test with a Sharp Notch Introduced by Focussed Ion Beam," *Int J Fract,* vol. 153, pp. 85-92, 2008.

[242] T. Fett and D. Munz, *Stress intensity factors and weight functions*: Computational Mechanics Publications, 1997.

[243] F. Hofmann, E. Tarleton, R. J. Harder, N. W. Phillips, P.-W. Ma, J. N. Clark*, et al.*, "3D lattice distortions and defect structures in ion-implanted nano-crystals," *Scientific Reports,* vol. 7, p. 45993, 2017.

[244] E. Salvati, L. R. Brandt, C. Papadaki, H. Zhang, S. M. Mousavi, D. Wermeille*, et al.*, "Nanoscale structural damage due to focused ion beam milling of silicon with Ga ions," *Materials Letters,* vol. 213, pp. 346-349, 2018.

[245] A. M. Korsunsky, J. Guénolé, E. Salvati, T. Sui, M. Mousavi, A. Prakash*, et al.*, "Quantifying eigenstrain distributions induced by focused ion beam damage in silicon," *Materials Letters,* vol. 185, pp. 47-49, 2016.

[246] M. Nastasi, J. Mayer, and J. K. Hirvonen, *Ion-Solid Interactions: Fundamentals and Applications*. Cambridge: Cambridge University Press, 1996.

[247] G. Carter and W. A. Grant, *Ion implantation of semiconductors*. London: Edward Arnold, 1976.

[248] L. T. Chadderton, *Radiation damage in crystals*. London : New York: Methuen

John Wiley & Sons, 1965.

[249] P. Sigmund, "Theory of Sputtering. I. Sputtering Yield of Amorphous and Polycrystalline Targets," *Physical Review,* vol. 184, pp. 383-416, 1969.

[250] J. F. Ziegler, *The stopping and range of ions in solids*. New York: Pergamon, 1985.

[251] CAMECA, "Title," unpublished|.

[252] R. A. Spits, "Dynamical Behaviour of Implanted Ions in Diamond," Master Thesis, School of Physics, University of the Witwatersrand, 1990.

[253] B. I. Prenitzer, C. A. Urbanik-Shannon, L. A. Giannuzzi, S. R. Brown, R. B. Irwin, T. L. Shofner*, et al.*, "The Correlation between Ion Beam/Material Interactions and Practical FIB Specimen Preparation," *Microscopy and Microanalysis,* vol. 9, pp. 216-236, 2003.

[254] J. F. Gibbons, W. Johnson, and S. W. Mylroie, *Projected range statistics : semiconductors and related materials*. Stroudsburg: Dowden, Hutchinson & Ross, 1975.

[255] M. L. Swanson, J. R. Parsons, and C. W. Hoelke, "Damaged regions in neutron-irradiated and ion-bombarded Ge and Si," *Radiation Effects,* vol. 9, pp. 249-256, 1971.

[256] H. Föll, "Amorphization after Ion Implantation," in *Electronic Materials*, ed: University of Kiel.

[257] Z. Tong and X. Luo, "Investigation of focused ion beam induced damage in single crystal diamond tools," *Applied Surface Science,* vol. 347, pp. 727-735, 2015.

[258] A. G. Cullis, T. E. Seidel, and R. L. Meek, "Comparative study of annealed neon ‐ , argon ‐ , and krypton ‐ ion implantation damage in silicon," *Journal of Applied Physics,* vol. 49, pp. 5188-5198, 1978.

[259] L. Pelaz, L. A. Marqués, and J. Barbolla, "Ion-beam-induced amorphization and recrystallization in silicon," *Journal of Applied Physics,* vol. 96, pp. 5947-5976, 2004.

[260] N. G. Chew and A. G. Cullis, "The preparation of transmission electron microscope specimens from compound semiconductors by ion milling," *Ultramicroscopy,* vol. 23, pp. 175-198, 1987.

[261] R. J. Schreutelkamp, J. S. Custer, J. R. Liefting, W. X. Lu, and F. W. Saris, "Pre-amorphization damage in ion-implanted silicon," *Materials Science Reports,* vol. 6, pp. 275-366, 1991.

[262] H. Zhu, R. S. Averback, and M. Nastasi, "Molecular dynamics simulations of a 10keV cascade in β-NiAl," *Philosophical Magazine A,* vol. 71, pp. 735-758, 1995.

[263] B. I. Prenitzer, L. A. Giannuzzi, K. Newman, S. R. Brown, R. B. Irwin, F. A. Stevie*, et al.*, "Transmission electron microscope specimen preparation of Zn powders using the focused ion beam lift-out technique," *Metallurgical and Materials Transactions A,* vol. 29, pp. 2399-2406, 1998.

[264] L. A. Giannuzzi and F. A. Stevie, "A review of focused ion beam milling techniques for TEM specimen preparation," *Micron,* vol. 30, pp. 197-204, 1999.

[265] W. Möller and W. Eckstein, "Tridyn — A TRIM simulation code including dynamic composition changes," *Nuclear Instruments and Methods in Physics Research Section B: Beam Interactions with Materials and Atoms,* vol. 2, pp. 814-818, 1984.

[266] H. Hofsäss, K. Zhang, and A. Mutzke, "Simulation of ion beam sputtering with SDTrimSP, TRIDYN and SRIM," *Applied Surface Science,* vol. 310, pp. 134-141, 2014.

[267] J. Huang, M. Loeffler, W. Moeller, and E. Zschech, "Ga contamination in silicon by Focused Ion Beam milling: Dynamic model simulation and Atom Probe Tomography experiment," *Microelectronics Reliability,* vol. 64, pp. 390-392, 2016.

[268] A. Hössinger, "Simulation of Ion Implantation for ULSI Technology," PhD Thesis, Technische Universität Wien, Wien, Austria, 2000.

[269] G. Spoldi, S. Beuer, M. Rommel, V. Yanev, A. J. Bauer, and H. Ryssel, "Experimental observation of FIB induced lateral damage on silicon samples," *Microelectronic Engineering,* vol. 86, pp. 548-551, 2009.

[270] M. Presley, "The formation of amorphous and crystalline damage in metallic and semiconducting materials under gallium ion irradiation," PhD Thesis, The Ohio State University, 2016.

[271] S. Rubanov, P. Munroe, S. Prawer, and D. Jamieson, "Surface Damage In Silicon After 30 Kev Ga Fib Fabrication," *Microscopy and Microanalysis,* vol. 9, pp. 884-885, 2003.

[272] S. Rajsiri , B. Kempshall , S. Schwarz , and L. Giannuzzi, "FIB Damage in Silicon: Amorphization or Redeposition?," *Microscopy and Microanalysis,* vol. 99, pp. 50-51, 2002.

[273] S. Rubanov, "Damage Layers in Si vs. Ion Dose during 30 keV FIB Milling," *Microscopy and Microanalysis,* vol. 15, pp. 358-359, 2009.

[274] N. Bassim, K. Scott, and L. A. Giannuzzi, "Recent advances in focused ion beam technology and applications," *MRS Bulletin,* vol. 39, pp. 317-325, 2014.

[275] J. Jiruse, T. Hrncir, F. Lopour, M. Zadrazil, A. Delobe, and O. Salord, "Combined plasma FIB-SEM," *Microscopy and Microanalysis,* vol. 18, pp. 652-653, 2012.

[276] F. Altmann and R. J. Young, "Site-specific metrology, inspection, and failure analysis of three-dimensional interconnects using focused ion beam technology," *Journal of Micro/Nanolithography, MEMS, and MOEMS,* vol. 13, p. 12, 2014.

[277] S. Falco, J. Jiang, F. De Cola, and N. Petrinic, "Generation of 3D polycrystalline microstructures with a conditioned Laguerre-Voronoi tessellation technique," *Computational Materials Science,* vol. 136, pp. 20-28, 2017.

[278] J. C. Wurst and J. A. Nelson, "Lineal Intercept Technique for Measuring Grain Size in Two-Phase Polycrystalline Ceramics," *Journal of the American Ceramic Society,* vol. 55, pp. 109-109, 1972.

[279] M. I. Mendelson, "Average grain size in polycrystalline ceramics," *Journal of the American Ceramic Society,* vol. 52, pp. 443-446, 1969.

[280] Wikipedia. *Gamma Distribution*. Available: https://en.wikipedia.org/wiki/Gamma_distribution

[281] F. De Cola, S. Falco, E. Barbieri, and N. Petrinic, "New 3D geometrical deposition methods for efficient packing of spheres based on tangency," *International Journal for Numerical Methods in Engineering,* vol. 104, pp. 1085-1114, 2015.

[282] M. Broseghini, L. Gelisio, M. D'Incau, C. L. Azanza Ricardo, N. M. Pugno, and P. Scardi, "Modeling of the planetary ball-milling process: The case study of ceramic powders," *Journal of the European Ceramic Society,* vol. 36, pp. 2205-2212, 2016.

[283] C. Reid, J. Forrester, H. Goodshaw, E. Kisi, and G. Suaning, "A Study in the Mechanical Milling of Alumina Powder," *Ceramics International,* vol. 34, pp. 1551-1556, 2008.

[284] S. J. Bennison and M. P. Harmer, "Effect of MgO Solute on the Kinetics of Grain Growth in Al_2O_3," *Journal of the American Ceramic Society,* vol. 66, pp. C‐90-C‐92, 1983.

[285] W. Jo, D.-Y. Kim, and N.-M. Hwang, "Effect of Interface Structure on the Microstructural Evolution of Ceramics," *Journal of the American Ceramic Society,* vol. 89, pp. 2369-2380, 2006.

[286] O. Instruments. *Grain Size and Grain Boundary Characterisation in SEM*. Available: http://www.ebsd.com/solving-problems-with-ebsd/grain-size-and-grain-boundary-characterisation-in-sem

[287] G. D. Quinn, "NIST Recommended Practice Guide: Fractography of Ceramics and Glasses," *NIST Special Publication,* 2006.

[288] M. Iwasa and R. Bradt, *Fracture toughness of single-crystal alumina* vol. 10: American Ceramic Society, 1984.

[289] H. Jiang, F. Jiang, D. Hu, R. Wang, J. Lu, and B. Li, "Numerical modeling of compressive failure mechanisms in ceramic materials at high strain rates," *Computer Methods in Applied Mechanics and Engineering,* vol. 347, pp. 806-826, 2019.

[290] G. S. Rohrer, "Grain boundary energy anisotropy: a review," *Journal of Materials Science,* vol. 46, pp. 5881-5895, 2011.

[291] Z. P. Bažant, "Size effect on structural strength: a review," *Archive of Applied Mechanics,* vol. 69, pp. 703-725, 1999.

[292] F. Schmid and D. C. Harris, "Effects of Crystal Orientation and Temperature on the Strength of Sapphire," *Journal of the American Ceramic Society,* vol. 81, pp. 885-893, 1998.

[293] F. W. DelRio, R. F. Cook, and B. L. Boyce, "Fracture strength of micro- and nano-scale silicon components," *Applied Physics Reviews,* vol. 2, p. 021303, 2015.

[294] Y. Mitamura and Y. Wang, "Fracture toughness of single crystal alumina in air and a simulated body environment," *Journal of Biomedical Materials Research,* vol. 28, pp. 813-817, 1994.

[295] P. Chantikul, S. J. Bennison, and B. R. Lawn, "Role of Grain Size in the Strength and R-Curve Properties of Alumina," *Journal of the American Ceramic Society,* vol. 73, pp. 2419-2427, 1990.

[296] Y. Yang, A. Kushima, W. Han, H. Xin, and J. Li, "Liquid-Like, Self-Healing Aluminum Oxide during Deformation at Room Temperature," *Nano Letters,* vol. 18, pp. 2492-2497, 2018.

[297] B. R. Lawn, D. H. Roach, and R. M. Thomson, "Thresholds and reversibility in brittle cracks: An atomistic surface force model," *Journal of Materials Science,* vol. 22, pp. 4036-4050, 1987.

[298] B. J. Hockey and B. R. Lawn, "Electron microscopy of microcracking about indentations in aluminium oxide and silicon carbide," *Journal of Materials Science,* vol. 10, pp. 1275-1284, 1975.

[299] M. Swain, B. Lawn, and S. Burns, "Cleavage step deformation in brittle solids," *Journal of Materials Science,* vol. 9, pp. 175-183, 1974.

[300] J. Williams, B. Lawn, and M. Swain, "Cone crack closure in brittle solids," *physica status solidi (a),* vol. 2, pp. 7-29, 1970.

[301] H. Kitahara, Y. Noda, F. Yoshida, H. Nakashima, N. Shinohara, and H. Abe, "Mechanical Behavior of Single Crystalline and Polycrystalline Silicon Carbides Evaluated by Vickers Indentation," *Journal of the Ceramic Society of Japan,* vol. 109, pp. 602-606, 2001.

[302] H. T. Liu, L. W. Yang, S. Han, H. F. Cheng, W. G. Mao, and J. M. Molina-Aldareguía, "Interface controlled micro- and macro- mechanical properties of aluminosilicate fiber reinforced SiC matrix composites," *Journal of the European Ceramic Society,* vol. 37, pp. 883-890, 2017.

[303] D. Frazer, M. D. Abad, D. Krumwiede, C. A. Back, H. E. Khalifa, C. P. Deck*, et al.*, "Localized mechanical property assessment of SiC/SiC composite materials," *Composites Part A: Applied Science and Manufacturing,* vol. 70, pp. 93-101, 2015.

[304] W. Y. Kwong and W. Y. Zhang, "Electron-beam assisted platinum deposition as a protective layer for FIB and TEM applications," in *ISSM 2005, IEEE International Symposium on Semiconductor Manufacturing, 2005.*, pp. 469-471, 2005.

[305] T. Tao, J. Ro, J. Melngailis, Z. Xue, and H. D. Kaesz, "Focused ion beam induced deposition of platinum," *Journal of Vacuum Science & Technology B: Microelectronics Processing and Phenomena,* vol. 8, pp. 1826-1829, 1990.

[306] T. Malis, S. C. Cheng, and R. F. Egerton, "EELS log-ratio technique for specimen-thickness measurement in the TEM," *Journal of Electron Microscopy Technique,* vol. 8, pp. 193-200, 1988.

[307] Gatan, "EELS Atlas," ed: http://live-eels.pantheon.io/atlas/xenon.

[308] G. Lucas and L. Pizzagalli, "Ab initio molecular dynamics calculations of threshold displacement energies in silicon carbide," *Physical Review B,* vol. 72, p. 161202, 2005.

[309] M. Guthoff, W. de Boer, and S. Müller, "Simulation of beam induced lattice defects of diamond detectors using FLUKA," *Nuclear Instruments and Methods in Physics Research Section A: Accelerators, Spectrometers, Detectors and Associated Equipment,* vol. 735, pp. 223-228, 2014.

[310] M. Wilkens, M. L. Jenkins, and K.-H. Katerbau, "TEM diffraction contrast of lattice defects causing strain contrast and structure factor contrast simultaneously," *physica status solidi (a),* vol. 39, pp. 103-107, 1977.

[311] T. Gray. (2017). *Periodic Table*. Available: https://periodictable.com/

[312] G. Velişa, E. Wendler, L.-L. Wang, Y. Zhang, and W. J. Weber, "Ion mass dependence of irradiation-induced damage accumulation in KTaO3," *Journal of Materials Science,* vol. 54, pp. 149-158, 2019.

[313] S. O. Kucheyev, J. S. Williams, C. Jagadish, J. Zou, G. Li, and A. I. Titov, "Effect of ion species on the accumulation of ion-beam damage in GaN," *Physical Review B,* vol. 64, p. 035202, 2001.

[314] G. P. Tiwari and R. S. Mehrotra, "Diffusion and Melting," *Defect and Diffusion Forum,* vol. 279, pp. 23-37, 2008.

[315] Z. He, Z. Xu, M. Rommel, B. Yao, T. Liu, Y. Song*, et al.*, "Investigation of Ga ion implantation-induced damage in single-crystal 6H-SiC," *Journal of Micromanufacturing,* vol. 1, pp. 115-123, 2018.

[316] S. Rubanov and A. Suvorova, "Ion implantation in diamond using 30keV Ga+ focused ion beam," *Diamond and Related Materials,* vol. 20, pp. 1160-1164, 2011.

[317] V. G. Hill, R. Roy, and E. F. Osborn, "The System Alumina-Gallia-Water," *Journal of the American Ceramic Society,* vol. 35, pp. 135-142, 1952.

[318] A. Meldrum, L. A. Boatner, C. W. White, and R. C. Ewing, "Ion irradiation effects in nonmetals: formation of nanocrystals and novel microstructures," *Material Research Innovations,* vol. 3, pp. 190-204, 2000.

[319] S. J. Zinkle, "Effect of H and He irradiation on cavity formation and blistering in ceramics," *Nuclear Instruments and Methods in Physics Research Section B: Beam Interactions with Materials and Atoms,* vol. 286, pp. 4-19, 2012.

[320] R. W. Olesinski, N. Kanani, and G. J. Abbaschian, "The Ga−Si (Gallium-Silicon) system," *Bulletin of Alloy Phase Diagrams,* vol. 6, pp. 362-364, 1985.

[321] *Fundamental aspects of inert gases in solids*. New York, London: Springer US, 1991.

[322] G. S. Was, "Irradiation-Induced Voids and Bubbles," in *Fundamentals of Radiation Materials Science: Metals and Alloys*, G. S. Was, Ed., ed New York, NY: Springer New York, 2017, pp. 379-484.

[323] E. Gao and N. M. Ghoniem, "A coupled rate theory-Monte Carlo model of helium bubble evolution in plasma-facing micro-engineered tungsten," *Journal of Nuclear Materials,* vol. 509, pp. 577-590, 2018.

[324] M. Ojima and F. A. Podosek, *Noble gas geochemistry*, 2nd ed. Cambridge: Cambridge University Press, 2002.

[325] S. B. Fisher, "On the temperature rise in electron irradiated foils," *Radiation Effects,* vol. 5, pp. 239-243, 1970.

[326] Y. N. Osetsky and R. E. Stoller, "Atomic-scale mechanisms of helium bubble hardening in iron," *Journal of Nuclear Materials,* vol. 465, pp. 448-454, 2015.

[327] N. Yamamoto, T. Chuto, Y. Murase, and J. Nagakawa, "Correlation between embrittlement and bubble microstructure in helium-implanted materials," *Journal of Nuclear Materials,* vol. 329-333, pp. 993-997, 2004.

[328] K. Chockalingam, P. C. Millett, and M. R. Tonks, "Effects of intergranular gas bubbles on thermal conductivity," *Journal of Nuclear Materials,* vol. 430, pp. 166-170, 2012.

[329] L. Aprilia, R. Nuryadi, and D. Hartanto, "Calculation of stress and deflection in double layer microcantilever for biosensor application," in *International Journal of Computational Engineering Research*2013.

[330] G. G. Stoney, "The Tension of Metallic Films Deposited by Electrolysis," *Proceedings of the Royal Society of London. Series A, Containing Papers of a Mathematical and Physical Character (1905-1934),* vol. 82, pp. 172-175, 1909.

[331] G. C. A. M. Janssen, M. M. Abdalla, F. van Keulen, B. R. Pujada, and B. van Venrooy, "Celebrating the 100th anniversary of the Stoney equation for film stress: Developments from polycrystalline steel strips to single crystal silicon wafers," *Thin Solid Films,* vol. 517, pp. 1858-1867, 2009.

[332] N. Schwarzer and F. Richter, "On the determination of film stress from substrate bending: STONEY´s formula and its limits," 2006.

[333] J. M. Glasko, R. G. Elliman, J. Zou, D. J. H. Cockayne, and J. D. Fitz Gerald, "Strain and defect microstructure in ion-irradiated GeSi/Si strained layers as a function of annealing temperature," *Applied Physics Letters,* vol. 73, pp. 838-840, 1998.

[334] S. Decoster and A. Vantomme, "Implantation-induced damage in Ge: strain and disorder profiles during defect accumulation and recovery," *Journal of Physics D: Applied Physics,* vol. 42, p. 165404, 2009.

[335] L. Zhang, H. Shen, X. Jiang, B. Qian, Z. Han, and H. Hou, "Influence of annealing temperature on the properties of polycrystalline silicon films formed by rapid thermal annealing of a-Si:H films," *Journal of Materials Science: Materials in Electronics,* vol. 24, pp. 4209-4212, 2013.

[336] R. Mays, "Examination of the Stoney Equation and a Practical Determination of the Error in Residual Film Stress Measurements," University of Pennsylvania, Quattrone Nanofabrication Facility2017.

[337] S. G. Mayr and R. S. Averback, "Ion-irradiation-induced stresses and swelling in amorphous Ge thin films," *Physical Review B,* vol. 71, p. 134102, 2005.

[338] J. Li, L. Porter, and S. Yip, "Atomistic modeling of finite-temperature properties of crystalline β-SiC. II. Thermal conductivity and effects of point defects," *Journal of Nuclear Materials,* vol. 255, pp. 139-152, 1998.

[339] G. P. Pells and M. J. Murphy, "The effects of transmutation products on the radiation-induced swelling of Al2O3 and MgAl2O4," *Journal of Nuclear Materials,* vol. 183, pp. 137-144, 1991.

[340] S. J. Zinkle and G. P. Pells, "Microstructure of Al2O3 and MgAl2O4 irradiated at low temperatures," *Journal of Nuclear Materials,* vol. 253, pp. 120-132, 1998.

[341] I. Szlufarska, "Role of Defects in Swelling and Creep of Irradiated SiC," University of Wisconsin, Madison2016.

[342] X. Chen, W. Zhou, X. Zhang, Q. Feng, J. Zheng, X. Liu*, et al.*, "Mechanical properties of 6H-SiC irradiated by neutron and MeV heavy ions: A nanoindentation and finite element method study," *Journal of Applied Physics,* vol. 123, p. 025104, 2018.

[343] Y. R. Lin, L. G. Chen, C. Y. Hsieh, M. T. Chang, K. Y. Fung, A. Hu*, et al.*, "Atomic Configuration of Point Defect Clusters in Ion-Irradiated Silicon Carbide," *Scientific Reports,* vol. 7, p. 14635, 2017.

[344] M. Bertolus, F. Ribeiro, and M. Defranceschi, "Mechanisms of amorphization-induced swelling in silicon carbide: the molecular dynamics answer," *The European Physical Journal B,* vol. 60, pp. 423-433, 2007.

[345] L. L. Snead, Y. Katoh, and S. Connery, "Swelling of SiC at intermediate and high irradiation temperatures," *Journal of Nuclear Materials,* vol. 367-370, pp. 677-684, 2007.

[346] L. L. Snead, S. J. Zinkle, J. C. Hay, and M. C. Osborne, "Amorphization of SiC under ion and neutron irradiation," *Nuclear Instruments and Methods in Physics Research Section B: Beam Interactions with Materials and Atoms,* vol. 141, pp. 123-132, 1998.

[347] L. Gerward, "X-ray study of lateral strains in ion-implanted silicon," *Zeitschrift für Physik,* vol. 259, pp. 313-322, 1973.

[348] Y.-M. Chiang, D. P. Birnie, and W. D. Kingery, *Physical ceramics: principles for ceramic science and engineering*: John Wiley & Sons, 1996.

[349] N. Kalyanasundaram, M. C. Moore, J. B. Freund, and H. T. Johnson, "Stress evolution due to medium-energy ion bombardment of silicon," *Acta Materialia,* vol. 54, pp. 483-491, 2006.

[350] T. D. de la Rubia, R. S. Averback, R. Benedek, and W. E. King, "Role of thermal spikes in energetic displacement cascades," *Physical Review Letters,* vol. 59, pp. 1930-1933, 1987.

[351] V. Garg, B. Kamaliya, R. K. Singh, A. S. Panwar, J. Fu, and R. G. Mote, "Controlled Manipulation and Multiscale Modeling of Suspended Silicon Nanostructures under Site-Specific Ion Irradiation," *ACS Applied Materials & Interfaces,* vol. 12, pp. 6581-6589, 2020.

[352] L. Pastewka, R. Salzer, A. Graff, F. Altmann, and M. Moseler, "Surface amorphization, sputter rate, and intrinsic stresses of silicon during low energy Ga+ focused-ion beam milling," *Nuclear Instruments and Methods in Physics Research Section B: Beam Interactions with Materials and Atoms,* vol. 267, pp. 3072-3075, 2009.

[353] P. Dorogokupets, T. Sokolova, A. Dymshits, and K. Litasov, "Thermodynamic properties of rock-forming oxides, alpha-al2o3, cr2o3, alpha-fe2o3, and fe3o4 at high temperatures and pressures," *Geodynamics & Tectonophysics,* vol. 7, pp. 459-476, 2016.

[354] E. Sánchez-González, P. Miranda, J. J. Meléndez-Martínez, F. Guiberteau, and A. Pajares, "Temperature dependence of mechanical properties of alumina up to the onset of creep," *Journal of the European Ceramic Society,* vol. 27, pp. 3345-3349, 2007.

[355] S. G. Mayr and R. S. Averback, "Effect of ion bombardment on stress in thin metal films," *Physical Review B,* vol. 68, p. 214105, 2003.

[356] W.-L. Chan, K. Zhao, N. Vo, Y. Ashkenazy, D. G. Cahill, and R. S. Averback, "Stress evolution in platinum thin films during low-energy ion irradiation," *Physical Review B,* vol. 77, p. 205405, 2008.

[357] M. Ghaly, K. Nordlund, and R. S. Averback, "Molecular dynamics investigations of surface damage produced by kiloelectronvolt self-bombardment of solids," *Philosophical Magazine A,* vol. 79, pp. 795-820, 1999.

[358] M. Morgenstern, T. Michely, and G. Comsa, "Collective effects in the adatom production by 4.5 keV rare-gas impacts on Pt(111): A low-temperature scanning tunnelling microscopy analysis," *Philosophical Magazine A,* vol. 79, pp. 775-794, 1999.

[359] J. Macdonald, J. A. Gard, and F. P. Glasser, "Preparation and crystal chemistry of some mixed metal sesquioxides containing Fe, Al, Ga, Cr, Sc and In," *Journal of Inorganic and Nuclear Chemistry,* vol. 29, pp. 661-671, 1967.

[360] K. Nakata, S. Kasahara, S. Shimanuki, Y. Katano, H. Ohno, and J. Kuniya, "Damage structure obtained by cross-sectional observation in silicon carbide irradiated with helium ions," *Journal of Nuclear Materials,* vol. 179-181, pp. 403-406, 1991.

[361] P. Jung, H. Klein, and J. Chen, "A comparison of defects in helium implanted α- and β-SiC," *Journal of Nuclear Materials,* vol. 283-287, pp. 806-810, 2000.

[362] M.-F. Beaufort, M. Vallet, J. Nicolaï, E. Oliviero, and J.-F. Barbot, "In-situ evolution of helium bubbles in SiC under irradiation," *Journal of Applied Physics,* vol. 118, p. 205904, 2015.

[363] J. Chen, P. Jung, and H. Trinkaus, "Microstructural evolution of helium-implanted \ensuremath{\alpha}-SiC," *Physical Review B,* vol. 61, pp. 12923-12932, 2000.

[364] W. R. Allen and S. J. Zinkle, "Lattice location and clustering of helium in ceramic oxides," *Journal of Nuclear Materials,* vol. 191-194, pp. 625-629, 1992.

[365] Y. Katano, H. Ohno, and H. Katsuta, "Damage structure in Al2O3 single crystal irradiated with He-ions," *Journal of Nuclear Materials,* vol. 155-157, pp. 366-371, 1988.

[366] N. Sasajima, T. Matsui, S. Furuno, K. Hojou, and H. Otsu, "Damage accumulation in Al2O3 during H2+ or He+ ion irradiation," *Nuclear Instruments and Methods in Physics Research Section B: Beam Interactions with Materials and Atoms,* vol. 148, pp. 745-751, 1999.

[367] M. A. van Huis, A. van Veen, F. Labohm, A. V. Fedorov, H. Schut, B. J. Kooi*, et al.*, "Formation, growth and dissociation of He bubbles in Al2O3," *Nuclear Instruments and Methods in Physics Research Section B: Beam Interactions with Materials and Atoms,* vol. 216, pp. 149-155, 2004.

[368] J. Chen, Z. Y. He, and P. Jung, "Microstructure of helium-implanted α-Al2O3 after annealing," *Acta Materialia,* vol. 54, pp. 1607-1614, 2006.

[369] S. J. Zinkle and S. Kojima, "Helium-assisted cavity formation in ion-irradiated ceramics," *Journal of Nuclear Materials,* vol. 179-181, pp. 395-398, 1991.

[370] S. W. Bedell and W. A. Lanford, "Investigation of surface blistering of hydrogen implanted crystals," *Journal of Applied Physics,* vol. 90, pp. 1138-1146, 2001.

[371] K. J. Abrams, J. A. Hinks, C. J. Pawley, G. Greaves, J. A. v. d. Berg, D. Eyidi*, et al.*, "Helium irradiation effects in polycrystalline Si, silica, and single crystal Si," *Journal of Applied Physics,* vol. 111, p. 083527, 2012.

[372] T. Hojo, H. Yamamoto, J. Aihara, S. Furuno, K. Sawa, T. Sakuma*, et al.*, "Radiation effects on yttria-stabilized zirconia irradiated with He or Xe ions at high temperature," *Nuclear Instruments and Methods in Physics Research Section B: Beam Interactions with Materials and Atoms,* vol. 241, pp. 536-542, 2005.

[373] R. A. Langley, J. Bohdansky, W. Eckstein, P. Mioduszewski, J. Roth, E. Taglauer*, et al.*, "Data compendium for plasma-surface interactions," *Nuclear Fusion,* vol. 24, p. S9, 1984.

[374] S. K. Das, M. Kaminsky, and G. Fenske, "On the correlation of blister diameter and blister skin thickness in helium‐ion‐irradiated Nb," *Journal of Applied Physics,* vol. 50, pp. 3304-3311, 1979.

[375] T. Höchbauer, A. Misra, M. Nastasi, and J. W. Mayer, "Physical mechanisms behind the ion-cut in hydrogen implanted silicon," *Journal of Applied Physics,* vol. 92, pp. 2335-2342, 2002.

[376] E. P. EerNisse and S. T. Picraux, "Role of integrated lateral stress in surface deformation of He‐implanted surfaces," *Journal of Applied Physics,* vol. 48, pp. 9-17, 1977.

[377] E. Snoeks, A. Polman, and C. A. Volkert, "Densification, anisotropic deformation, and plastic flow of SiO2 during MeV heavy ion irradiation," *Applied Physics Letters,* vol. 65, pp. 2487-2489, 1994.

[378] C. A. Volkert and A. Polman, "Radiation-Enhanced Plastic Flow of Covalent Materials During Ion Irradiation," in *Mater. Res. Soc. Symp. Proceedings, Symposium A – Phase Formation and Modification by Beam-Solid Interactions*, p. 3, 1991.

[379] S. J. Zinkle, "Anisotropic dislocation loop nucleation in ion-irradiated MgAl2O4," *Journal of Nuclear Materials,* vol. 191-194, pp. 645-649, 1992.

[380] A. Hedler, S. L. Klaumünzer, and W. Wesch, "Amorphous silicon exhibits a glass transition," *Nature Materials,* vol. 3, pp. 804-809, 2004.

[381] C. Borschel, S. Spindler, D. Lerose, A. Bochmann, S. H. Christiansen, S. Nietzsche*, et al.*, "Permanent bending and alignment of ZnO nanowires," *Nanotechnology,* vol. 22, p. 185307, 2011.

[382] C. Ronning, C. Borschel, S. Geburt, and R. Niepelt, "Ion beam doping of semiconductor nanowires," *Materials Science and Engineering: R: Reports,* vol. 70, pp. 30-43, 2010.

[383] A. Debelle, A. Boulle, A. Chartier, F. Gao, and W. J. Weber, "Interplay between atomic disorder, lattice swelling, and defect energy in ion-irradiation-induced amorphization of SiC," *Physical Review B,* vol. 90, p. 174112, 2014.

[384] M. Caturla, T. Diaz de la Rubia, L. Marques, and G. Gilmer, "Ion-beam processing of silicon at keV energies: A molecular-dynamics study," *Physical review. B, Condensed matter,* vol. 54, pp. 16683-16695, 1997.

[385] C. J. McHargue, "Ion beam modification of ceramics," *Materials Science and Engineering: A,* vol. 253, pp. 94-105, 1998.

[386] H. Momida, T. Hamada, Y. Takagi, T. Yamamoto, T. Uda, and T. Ohno, "Theoretical study on dielectric response of amorphous alumina," *Physical Review B,* vol. 73, p. 054108, 2006.

[387] G. Gutiérrez and B. Johansson, "Molecular dynamics study of structural properties of amorphous Al_2O_3," *Physical Review B,* vol. 65, p. 104202, 2002.

[388] V. Heera, F. Prokert, N. Schell, H. Seifarth, W. Fukarek, M. Voelskow*, et al.*, "Density and structural changes in SiC after amorphization and annealing," *Applied Physics Letters,* vol. 70, pp. 3531-3533, 1997.

[389] J. S. Custer, M. O. Thompson, D. C. Jacobson, J. M. Poate, S. Roorda, W. C. Sinke*, et al.*, "Density of amorphous Si," *Applied Physics Letters,* vol. 64, pp. 437-439, 1994.

[390] J. Fiedler, V. Heera, R. Hübner, M. Voelskow, S. Germer, B. Schmidt*, et al.*, "High-fluence Ga-implanted silicon—The effect of annealing and cover layers," *Journal of Applied Physics,* vol. 116, p. 024502, 2014.

[391] Y. J. Xiao, F. Z. Fang, Z. W. Xu, W. Wu, and X. C. Shen, "The study of Ga+ FIB implanting crystal silicon and subsequent annealing," *Nuclear Instruments and Methods in Physics Research Section B: Beam Interactions with Materials and Atoms,* vol. 307, pp. 253-256, 2013.

[392] M. Tamura, S. Shukuri, M. Moniwa, and M. Default, "Focused ion beam gallium implantation into silicon," *Applied Physics A,* vol. 39, pp. 183-190, 1986.

[393] E. Salvati, T. Sui, A. J. G. Lunt, and A. M. Korsunsky, "The effect of eigenstrain induced by ion beam damage on the apparent strain relief in FIB-DIC residual stress evaluation," *Materials & Design,* vol. 92, pp. 649-658, 2016.

[394] K. Matoy, H. Schönherr, T. Detzel, and G. Dehm, "Micron-sized fracture experiments on amorphous SiOx films and SiOx/SiNx multi-layers," *Thin Solid Films,* vol. 518, pp. 5796-5801, 2010.

Appendix A Dimensionless compliance and geometrical function

Dimensionless compliance C' and geometrical function Y (α') as functions of normalised crack length α'.

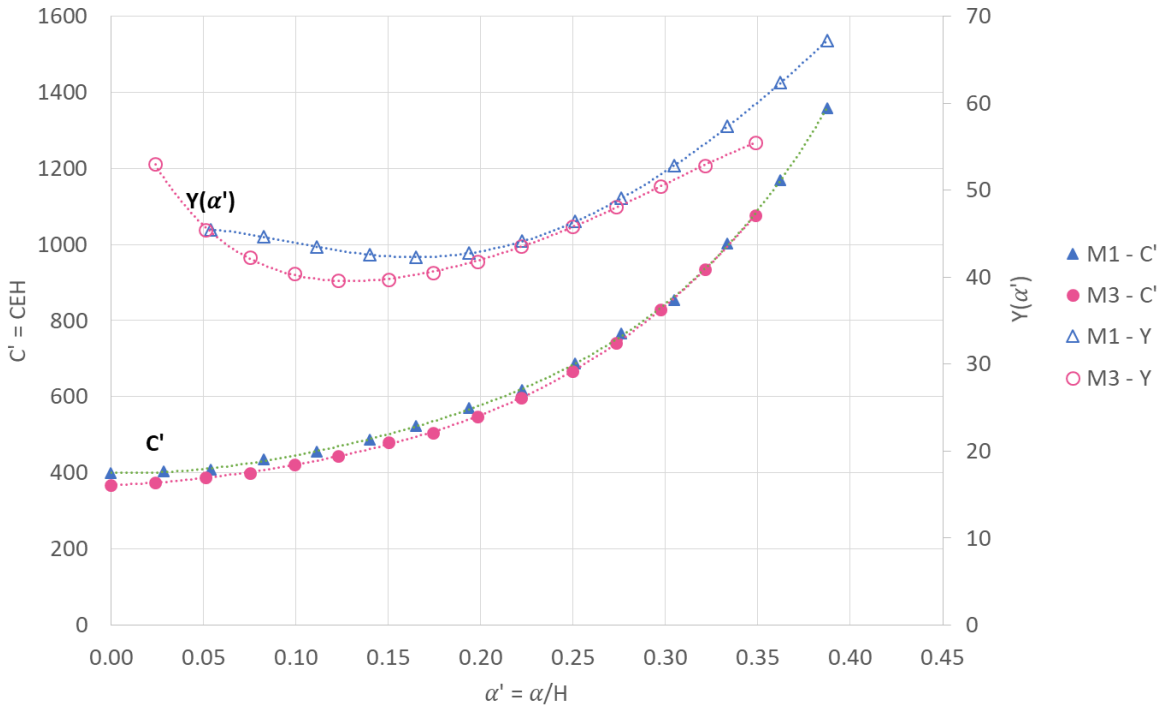


Figure A.1. Dimensionless compliance C' and Geometrical function Y (α') as a function of normalised crack length α' for m-axis chevron beams M1 and M3.

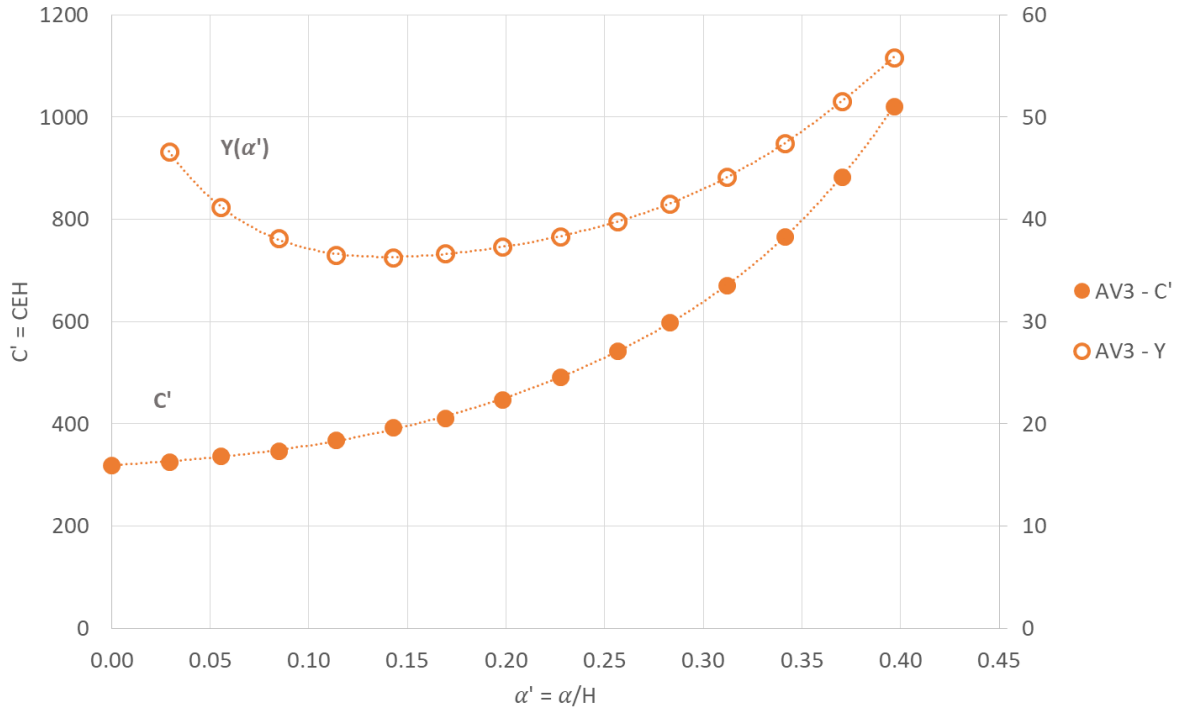


Figure A.2. Dimensionless compliance C' and Geometrical function Y(α') as a function of normalised crack length α' for a-axis chevron beam AV3.

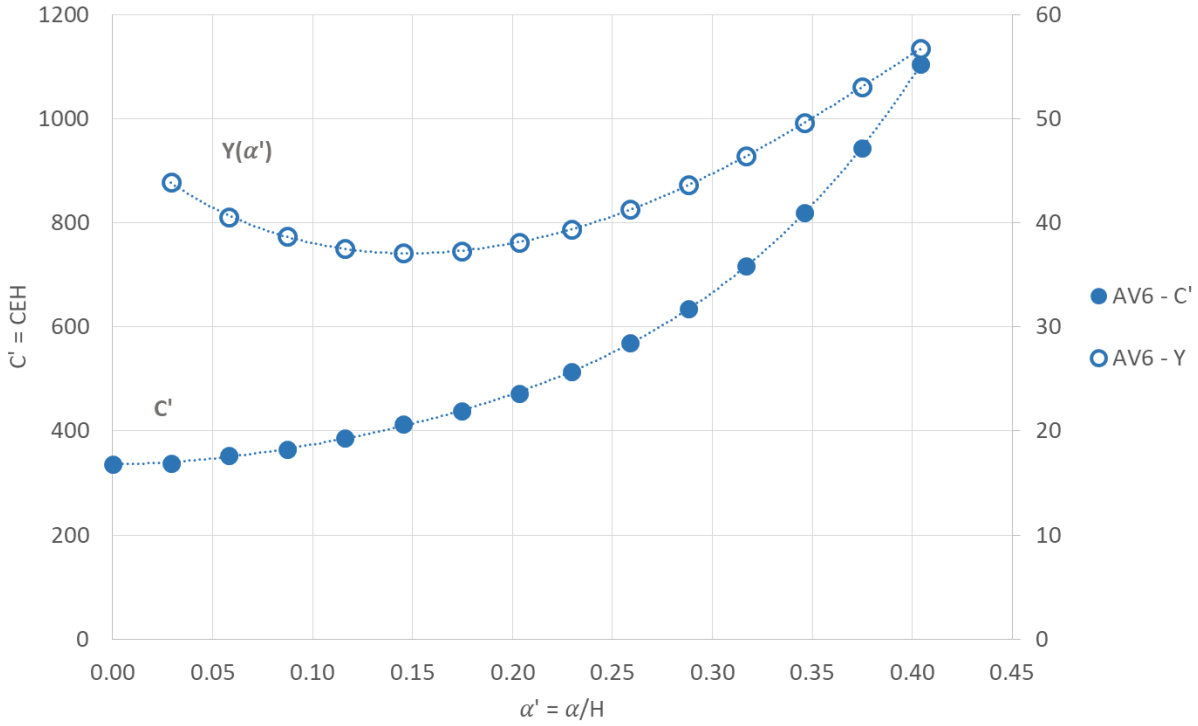


Figure A.3. Dimensionless compliance C' and Geometrical function Y(α') as a function of normalised crack length α' for a-axis sapphire beam AV6.

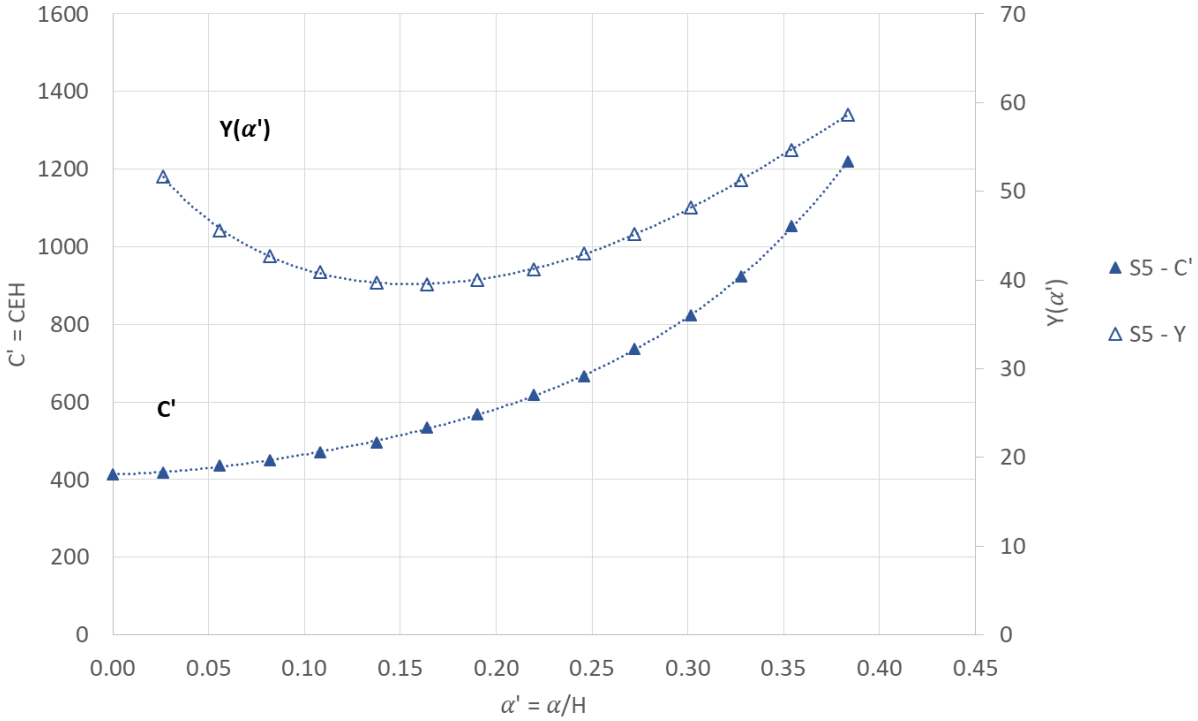


Figure A.4. Dimensionless compliance C' and geometrical function Y(α') as a function of normalised crack length α' for SiC beam S5.

Appendix B High resolution SEM images of ion implanted cantilevers

For some cantilevers, the implantation test was carried out by following one set of implantation procedures. For the others, the implantation on the same cantilever was seperated into multiple sets of procedures for different purposes of investigation. For example, Cantilever.2.2.Ga-a.Al_2O_3 was first tested under the Process #1 to study the effect of beam current, followed by Process #2 where the implantation ion dose was increased significantly to achieve massive removal of the target surface.

The side view of the ion implanted cantilevers are shown as follows.

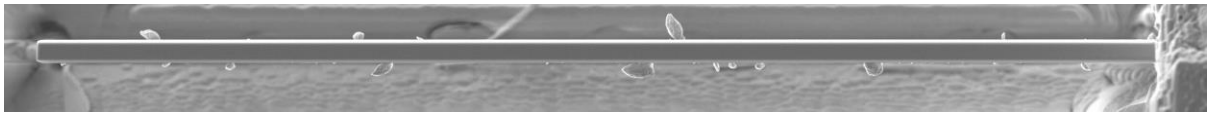
- **Cantilever. 1.2. Ga- c.Al_2O_3-IV** (Effect of beam current)

FIB condition: 30 keV, 4 ion/nm^2 at each current

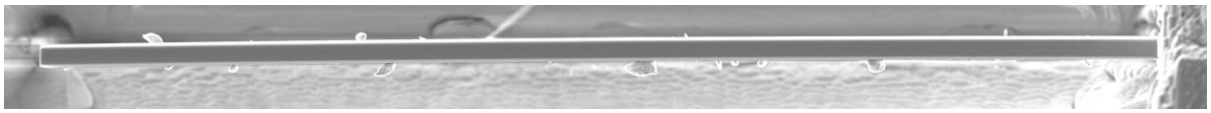
Process: 1 pA → 2 pA → 5 pA → 10 pA → 20 pA → 50 pA

10 µm

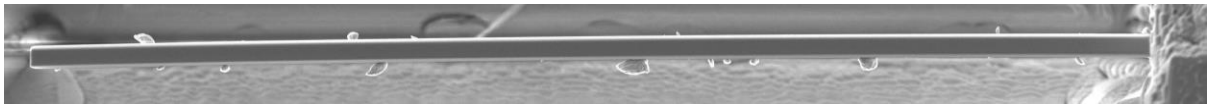
【0】[Original]



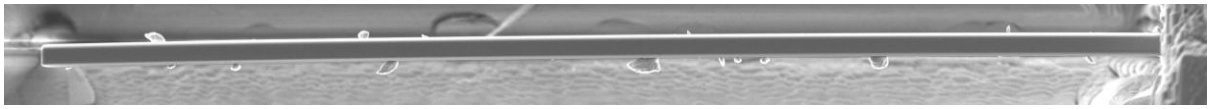
【1】[+ 1.0 ion/nm^2 @ 30 kV, 1 pA]



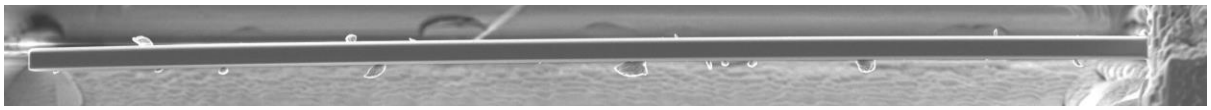
【2-4】[+ 3 × 1.0 ion/nm^2 @ 30 kV, 1 pA]



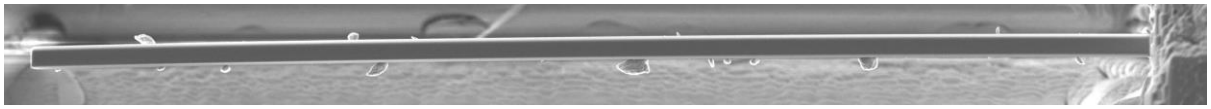
【5】[+ 1.0 ion/nm^2 @ 30 kV, 2 pA]



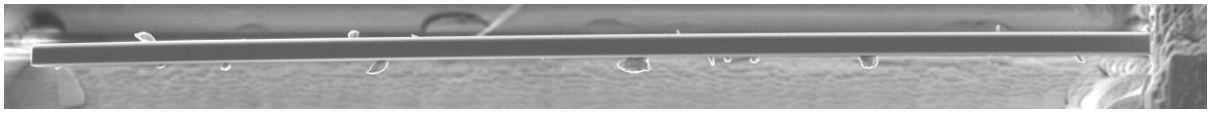
【6】[+ 3.0 ion/nm^2 @ 30 kV, 2 pA]



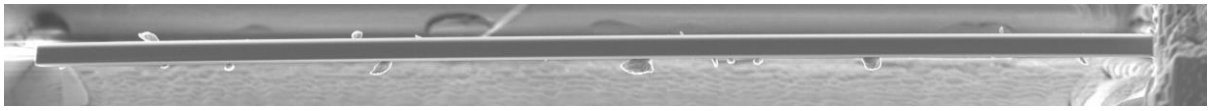
【7】[+ 4.0 ion/nm^2 @ 30 kV, 5 pA]



【8】[+ 4.0 ion/nm^2 @ 30 kV, 10 pA]



【9】[+ 4.0 ion/nm^2 @ 30 kV, 20 pA]



【10】[+ 4.0 ion/nm^2 @ 30 kV, 50 pA]

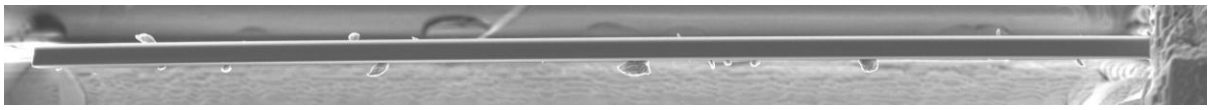


Figure B.1. SEM images of the Ga^+ implanted c-plane sapphire cantilever from the side view showing the curvatures. The beam current increased sequentially from 1 pA to 2, 5, 10, 20 and 50 pA, with the beam voltage remaining at 30 keV.

- **Cantilever. 1.3. Ga-c.Al_2O_3-IV** (Effect of beam voltage)

FIB condition: 1 pA, 4 ion/nm^2

Process: 2 keV→ 5 keV → 30 keV

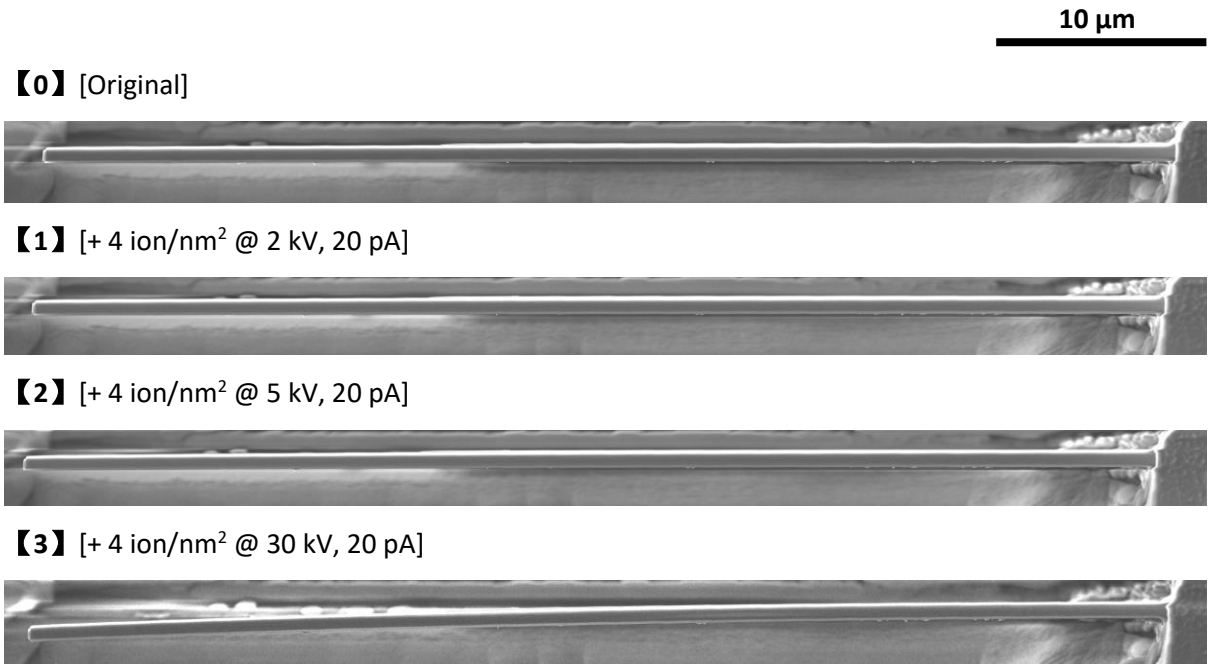


Figure B.2. SEM images of the c-plane sapphire cantilever from the side view showing the curvatures. The beam voltage increased sequentially from 2 keV to 5 and 30 keV, with the beam current remaining at 1 pA.

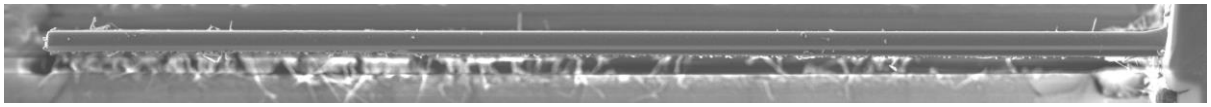
- **Cantilever. 2.1. Ga-a.Al_2O_3-IV** (Effect of ion dose)

FIB condition: 30 kV, 1pA

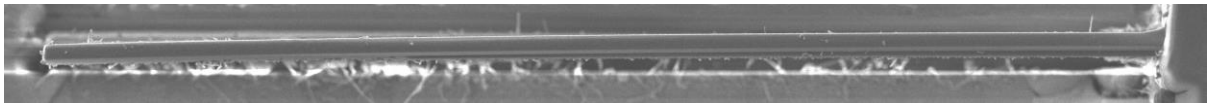
Process: 10 × 0.1 ion/nm^2 → +2 × 0.5 ion/nm^2 → +2 × 1.0 ion/nm^2

10 µm

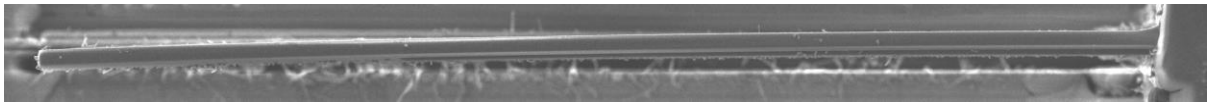
【0】[Original]



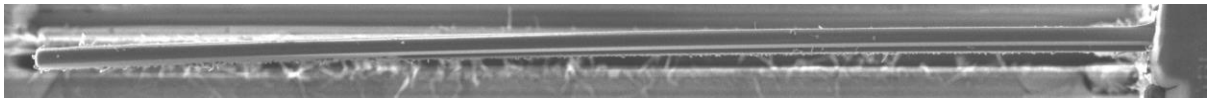
【1】[+ 0.1 ion/nm^2 @ 30 kV, 1 pA]



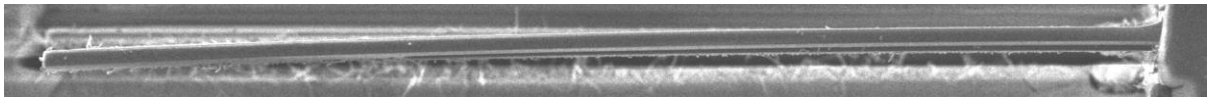
【2】[+ 0.1 ion/nm^2 @ 30 kV, 1 pA]



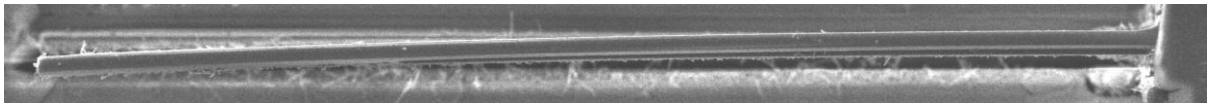
【3】[+ 0.1 ion/nm^2 @ 30 kV, 1 pA]



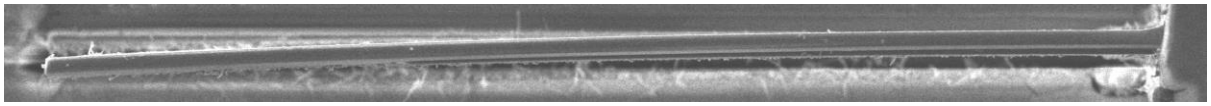
【4】[+ 0.1 ion/nm^2 @ 30 kV, 1 pA]



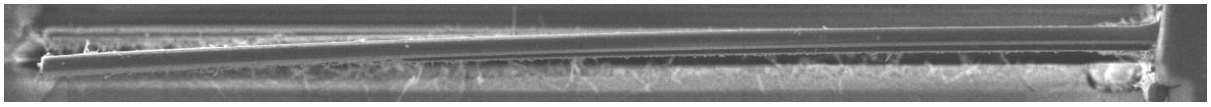
【5】[+ 0.1 ion/nm^2 @ 30 kV, 1 pA]



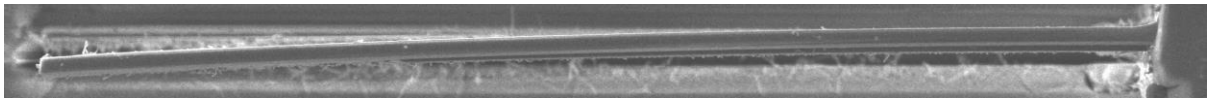
【6】[+ 0.1 ion/nm^2 @ 30 kV, 1 pA]



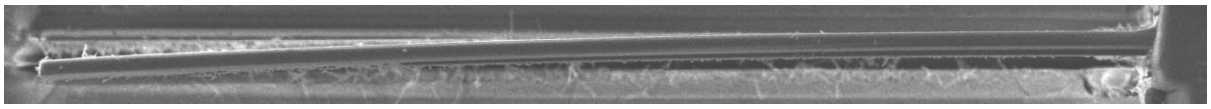
【7】[+ 0.1 ion/nm^2 @ 30 kV, 1 pA]



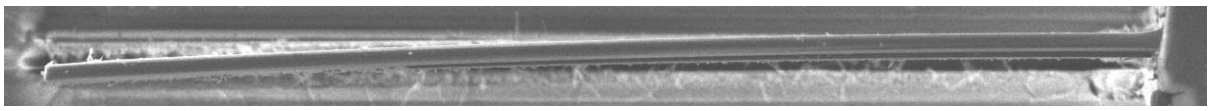
【8】[+ 0.1 ion/nm^2 @ 30 kV, 1 pA]



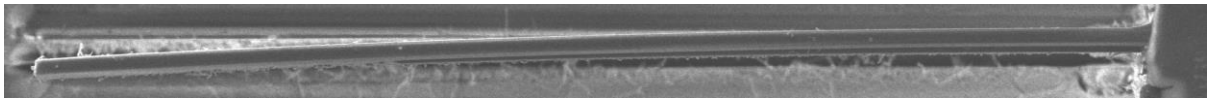
【**9**】[+ 0.1 ion/nm^2 @ 30 kV, 1 pA]



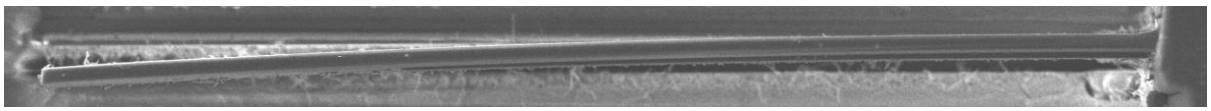
【**10**】[+ 0.1 ion/nm^2 @ 30 kV, 1 pA]



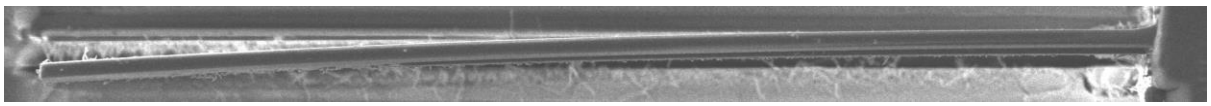
【**11**】[+ 0.5 ion/nm^2 @ 30 kV, 1 pA]



【**12**】[+ 0.5 ion/nm^2 @ 30 kV, 1 pA]



【**13**】[+ 1 ion/nm^2 @ 30 kV, 1 pA]



【**14**】[+ 1 ion/nm^2 @ 30 kV, 1 pA]

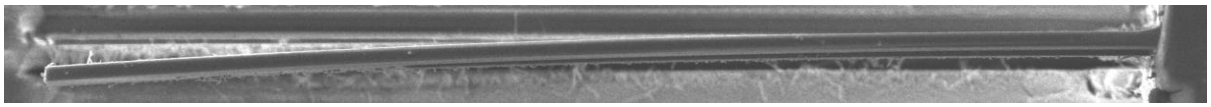


Figure B.3. SEM images of the Ga^+ implanted a-plane sapphire cantilever from the side view showing the curvatures. The ion dose was given at sequential steps under 30 keV, 1pA. Images are separated into two pages.

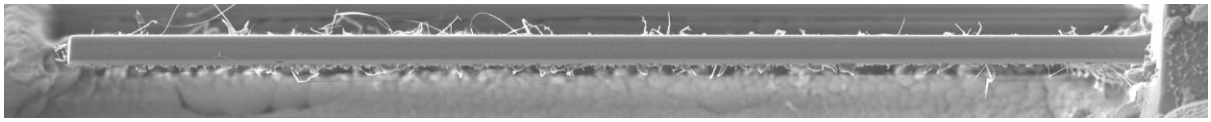
- **Cantilever. 2.2. Ga-a.Al_2O_3-II** (Effect of beam current)

FIB condition: 30 kV, 4 ion/nm^2

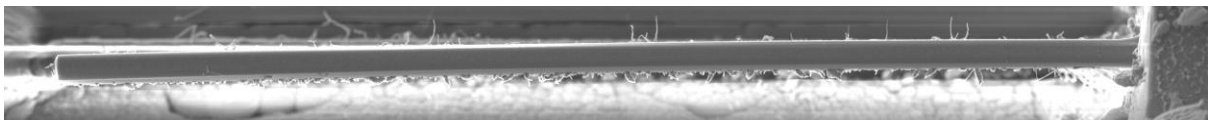
Process #1: 1 pA → 2 pA → 5 pA → 10 pA → 20 pA → 50 pA

10 µm

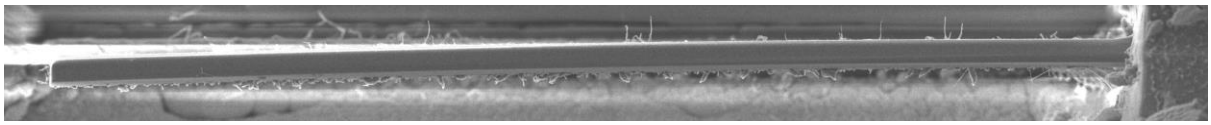
【0】[Original]



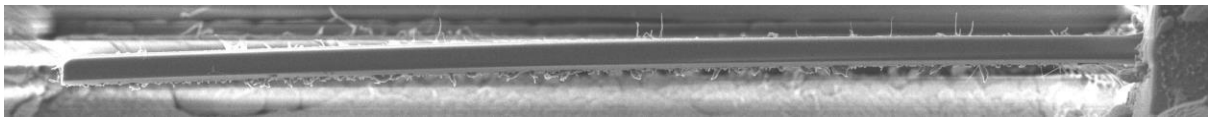
【1】[+ 4.0 ion/nm^2 @ 30 kV, 1 pA]



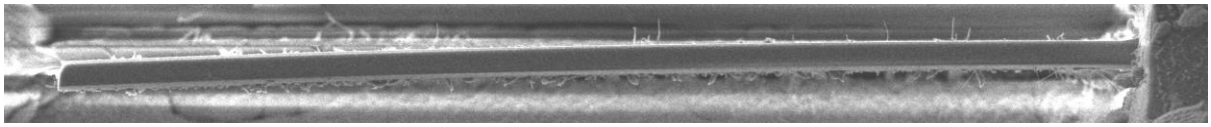
【2】[+ 4.0 ion/nm^2 @ 30 kV, 2 pA]



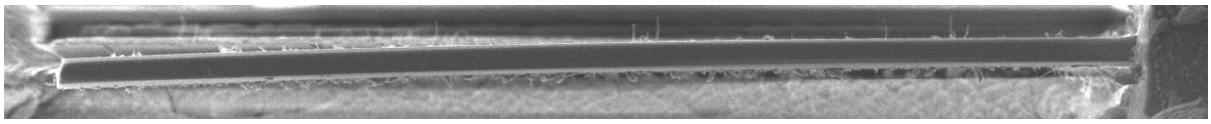
【3】[+ 4.0 ion/nm^2 @ 30 kV, 5 pA]



【4】[+ 4.0 ion/nm^2 @ 30 kV, 10 pA]



【5】[+ 4.0 ion/nm^2 @ 30 kV, 20 pA]



【6】[+ 4.0 ion/nm^2 @ 30 kV, 50 pA]

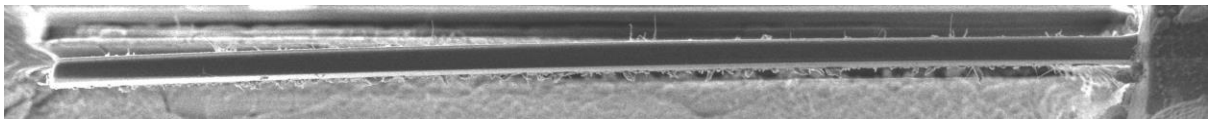


Figure B.4. SEM images of the Ga^+ implanted a-plane sapphire cantilever from the side view showing the curvatures. The beam current increased sequentially from 1 pA to 2, 5, 10, 20 and 50 pA, with the beam voltage remaining at 30 keV.

- **Cantilever. 2.3. Ga-a.Al_2O_3** (Effect of beam voltage)

FIB condition: 20 pA, 4 ion/nm^2

Process: 2 keV→ 5 keV → 30 keV

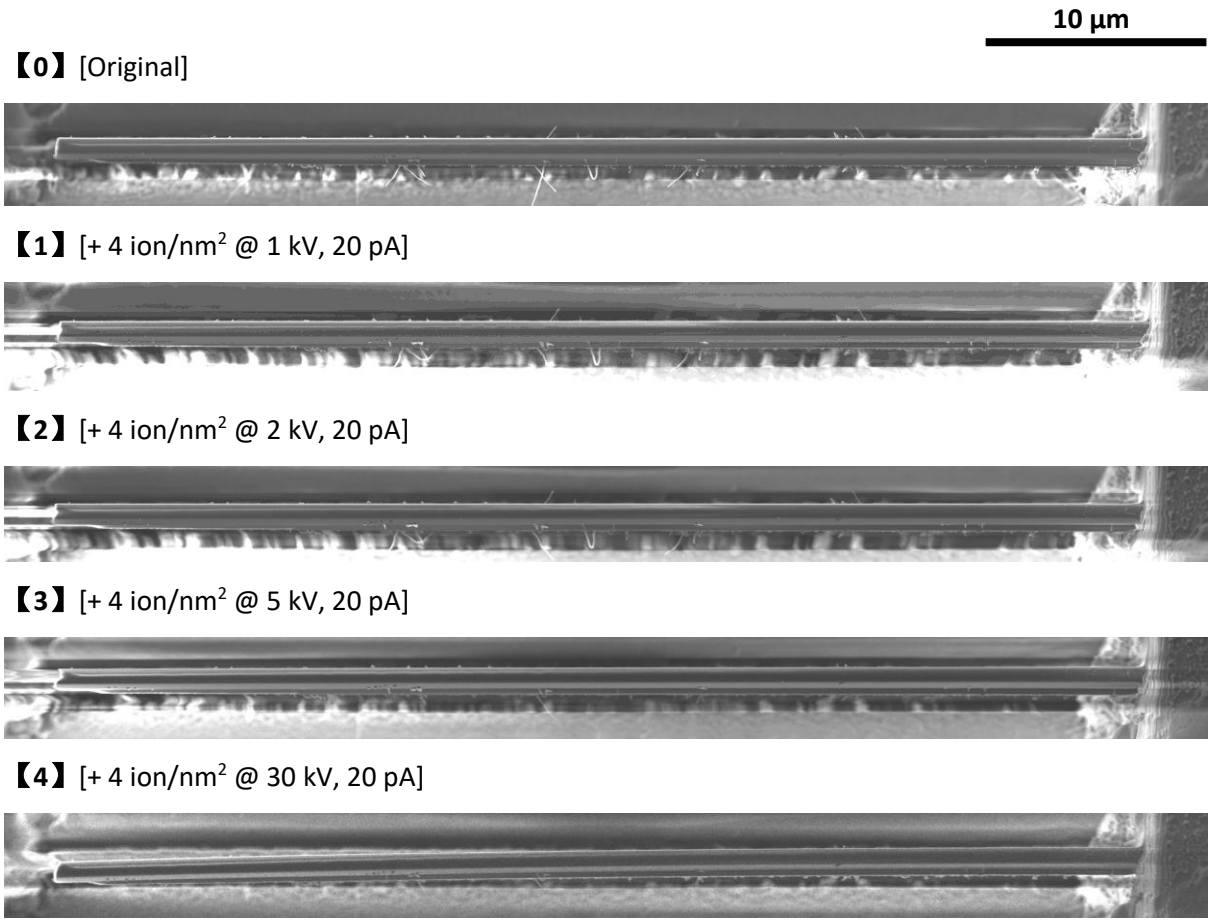


Figure B.5. SEM images of the a-plane sapphire cantilever from the side view showing the curvatures. The beam voltage increases sequentially from 2 keV to 5 and 30 keV, with the beam current remaining at 20 pA.

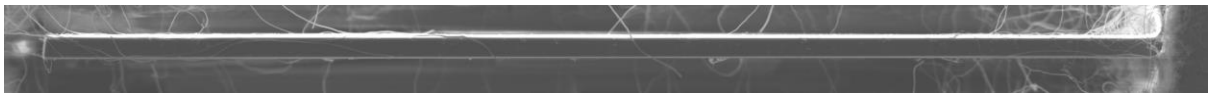
- **Cantilever. 3.1. Ga- SiC** (Effect of ion dose)

FIB condition #1: 30 keV, 1 pA

Process #1 **[1-13]**: 10 × 0.1 ion/nm^2 → +2 × 0.5 ion/nm^2 → +1.0 ion/nm^2

Whiskers were observed on the side walls of the trench after annealing, which is possibly due to the chemical changes happened in the re-deposited materials during the annealing process. No whisker was observed on the top surface of the cantilever, which means that the measurement of implantation stresses is not affected.

【**0**】[Original]



【**13**】[+10 × 0.1 + 2 × 0.5 +1 ion/nm^2 @ 30 keV, 1 pA]

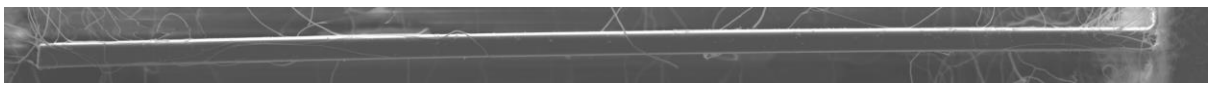


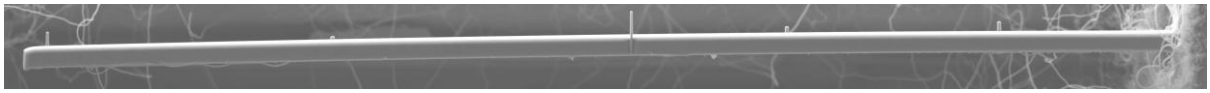
Figure B.6. SEM images of the Ga$^+$ implanted SiC cantilever from the side view showing the curvatures.

Process #2 **[14-18]**: +3000 ion/nm^2 @1000 pA → +5000 ion/nm^2 @1000 pA → +3 × 5000 ion/nm^2 @4000 pA

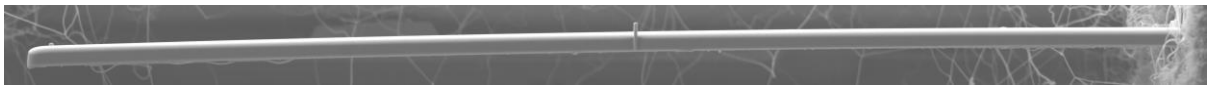
【**14**】[+ 3000 ion/nm^2 @ 30 keV, 1000 pA]



【**15**】[+ 5000 ion/nm^2 @ 30 keV, 1000 pA]



【**16**】[+ 5000 ion/nm^2 @ 30 keV, 4000 pA]



【**17**】[+ 5000 ion/nm^2 @ 30 keV, 4000 pA]



【**18**】[+ 5000 ion/nm^2 @ 30 keV, 4000 pA]

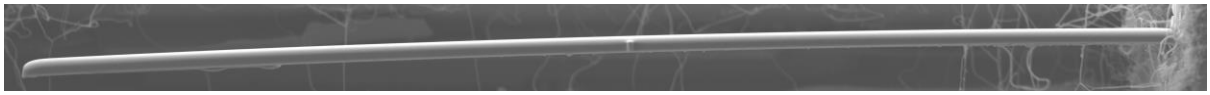


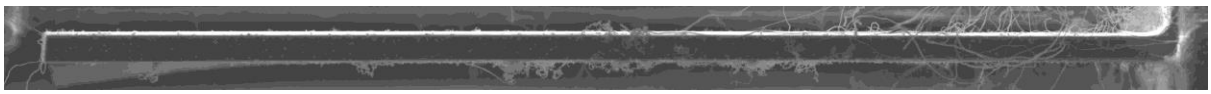
Figure B.7. SEM image of the SiC cantilever from the side view showing the curvature from the last step of Ga$^+$ implantation.

- **Cantilever. 3.2. Ga- SiC** (Effect of beam current)

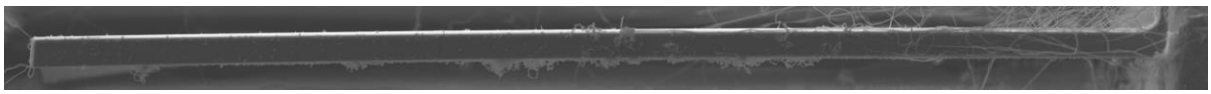
FIB condition #1: 30 keV, 4 ion/nm^2

Process #1**[1-6]**: 1 pA → 2 pA → 5 pA → 10 pA → 20 pA → 50 pA

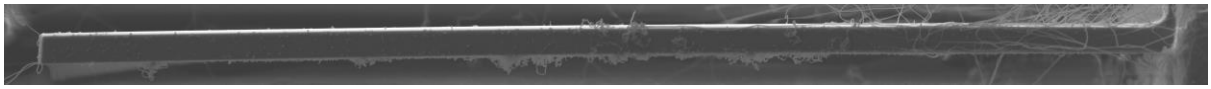
【0】[Original]



【1】[+ 4.0 ion/nm^2 @ 30 keV, 1 pA]



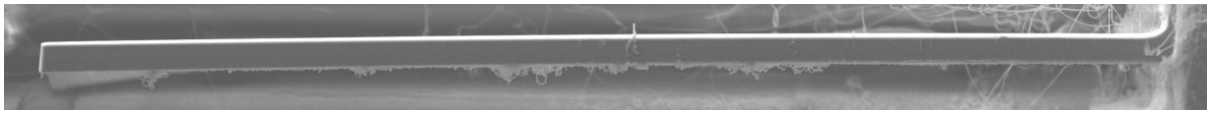
【6】[+ 4.0 ion/nm^2 @ 30 kV, 50 pA]



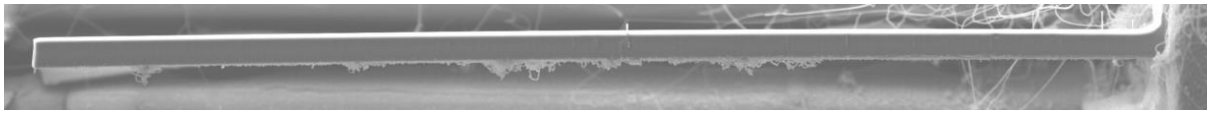
FIB condition #2: 30 keV

Process #2 **[7-16]**: +1000 ion/nm^2, @120 pA → +1000 ion/nm^2 @600 pA → +2000 ion/nm^2 @1000 pA → +2 × 3000 ion/nm^2 @2000 pA → +5 × 4000 ion/nm^2 @2000 pA

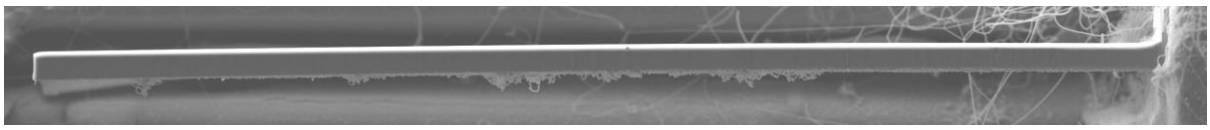
【7】[+ 1000 ion/nm^2 @ 30 kV, 120 pA]



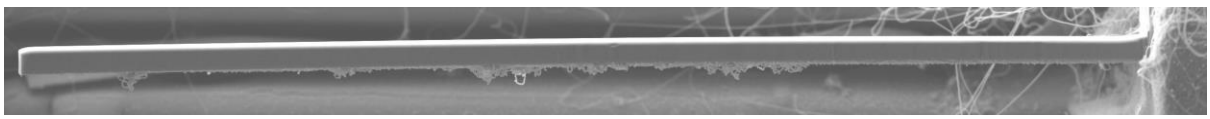
【8】[+ 1000 ion/nm^2 @ 30 kV, 600 pA]



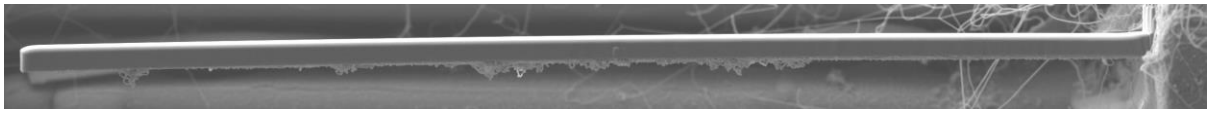
【9】[+ 2000 ion/nm^2 @ 30 kV, 1000 pA]



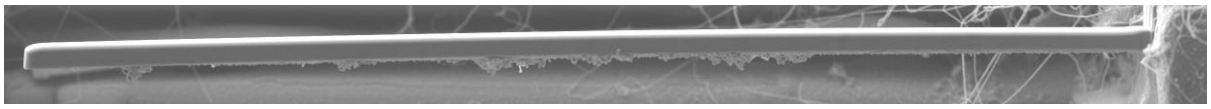
【10】[+ 3000 ion/nm^2 @ 30 kV, 2000 pA]



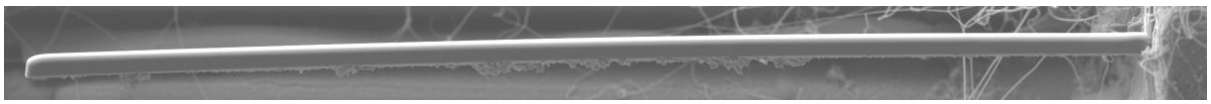
【11】[+ 3000 ion/nm^2 @ 30 kV, 2000 pA]



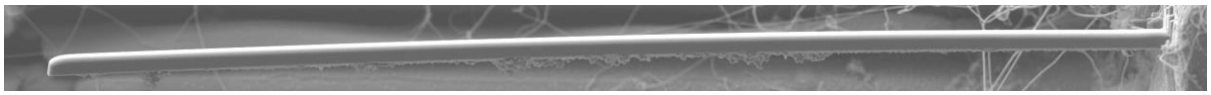
【**12**】[+ 4000 ion/nm^2 @ 30 kV, 2000 pA]



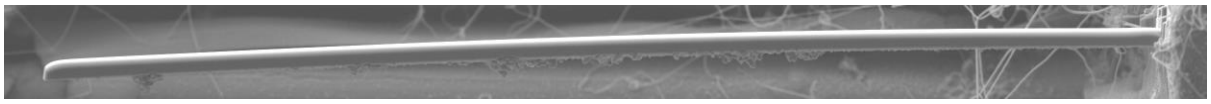
【**13**】[+ 4000 ion/nm^2 @ 30 kV, 2000 pA]



【**14**】[+ 4000 ion/nm^2 @ 30 kV, 2000 pA]



【**15**】[+ 4000 ion/nm^2 @ 30 kV, 2000 pA]



【**16**】[+ 4000 ion/nm^2 @ 30 kV, 2000 pA]

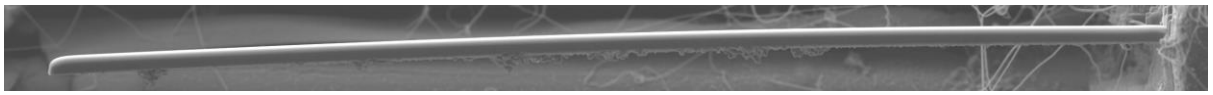


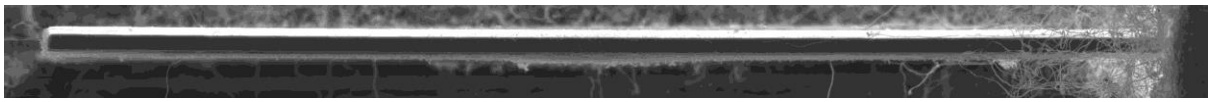
Figure B.8. SEM image of the SiC cantilever from the side view showing the curvature from the last step of Ga^+ implantation. Images are separated into two pages.

- **Cantilever. 3.3. Ga- SiC** (Effect of beam voltage)

FIB condition #1: 20 pA, 4 ion/nm^2

Process #1 **[1-3]**: 2 keV → 5 keV → 30 keV

【0】[Original]



【1-3】[+ 4 ion/nm^2 @ 2 kV + 4 ion/nm^2 @ 5 kV + 4 ion/nm^2 @ 30 kV, 20 pA]



Figure B.9. SEM images of the SiC cantilever from the side view showing the curvatures. The beam voltage increases sequentially from 2 keV to 5 keV and 30 keV.

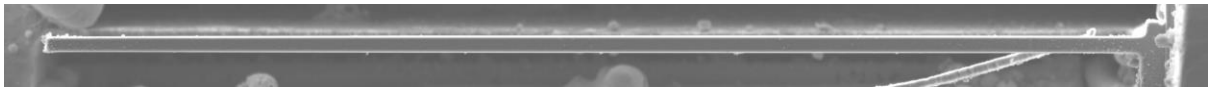
- **Cantilever. 4.1. Ga- Si** (Effect of dose & current)

FIB condition #1: 30 kV, 1 pA

Process #1 **[1-15]**: 10 × 0.1 ion/nm^2 → 2 × 0.5 ion/nm^2 → 3 × 1.0 ion/nm^2

10 µm

【0】[Original]



【1-15】[+10 × 0.1 ion/nm^2 +2 × 0.5 ion/nm^2 + 2 × 1.0 ion/nm^2, @ 30 kV, 1 pA]

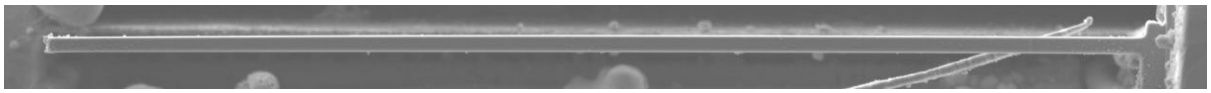
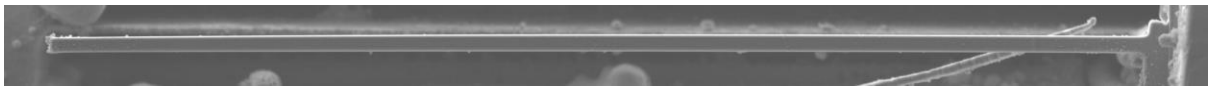


Figure B.10. SEM images of the Si cantilever from the side view showing the curvatures. The ion dose was given at sequential steps under 30 keV, 1pA.

FIB condition #2: 30 kV, 5.0 ion/nm^2

Process #2 **[16-21]**:(1 pA →) 2 pA → 5 pA → 10 pA → 20 pA → 50 pA → 120 pA

【16】[+5 ion/nm^2 @ 30 kV, 2 pA]



【17-21】[+ 5 ion/nm^2 at each current, @ 30 kV, 5 pA → 10 pA → 20 pA → 50 pA → 120 pA]

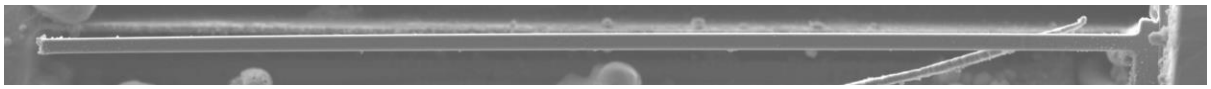
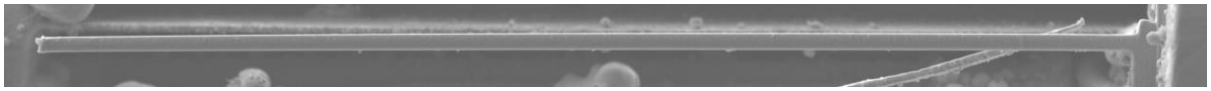


Figure B.11. SEM images of the Si cantilever from the side view. The beam current increases sequentially from 1 pA to 2, 5, 10, 20, 50 and 120 pA, with the beam voltage remaining at 30 keV and the ion dose implanted at each current being the same (5.0 ion/nm^2)

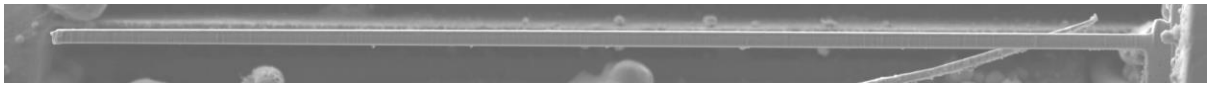
FIB condition #3: 30 kV

Process #3 **[22-29]**: +1000 ion/nm^2 @ 240 pA → +1000 ion/nm^2 @ 600 pA → 1000 ion/nm^2 @ 1000 pA → +4 × 2000 ion/nm^2 @ 2000 pA → +1000 ion/nm^2 @ 1000 pA

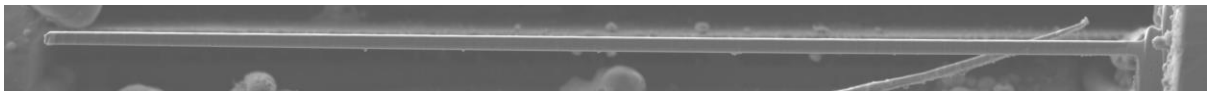
【22】[+ 1000 ion/nm^2 @ 30 kV, 240 pA]



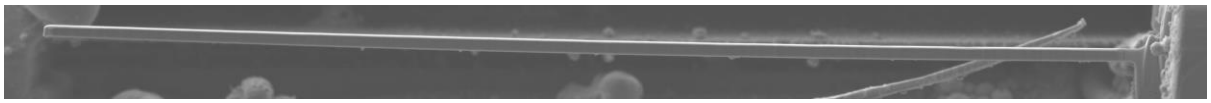
【23】[+ 1000 ion/nm^2 @ 30 kV, 600 pA]



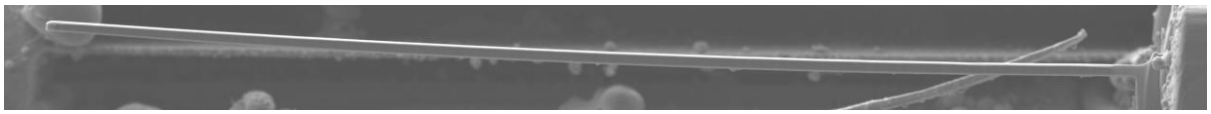
【**24**】[+ 1000 ion/nm^2 @ 30 kV, 1000 pA]



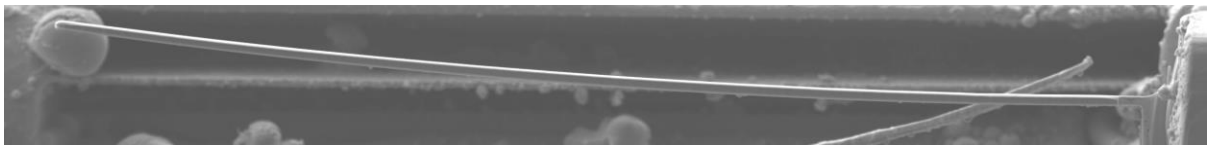
【**25**】[+ 2000 ion/nm^2 @ 30 kV, 1000 pA]



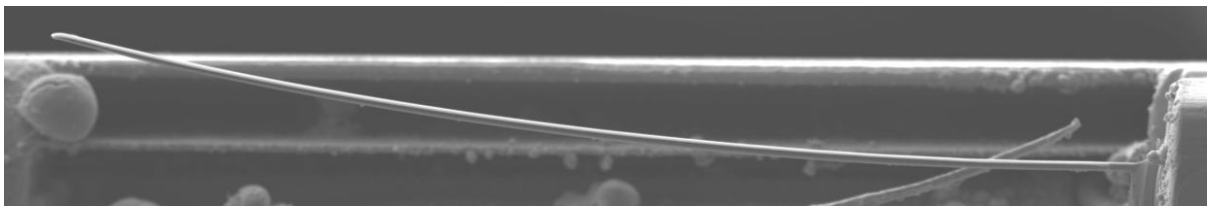
【**26**】[+ 2000 ion/nm^2 @ 30 kV, 1000 pA]



【**27**】[+ 2000 ion/nm^2 @ 30 kV, 1000 pA]



【**28**】[+ 2000 ion/nm^2 @ 30 kV, 1000 pA]



【**29**】[+ 1000 ion/nm^2 @ 30 kV, 1000 pA]

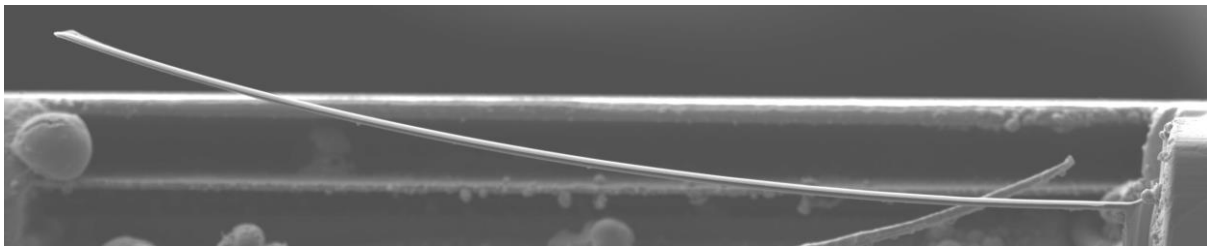


Figure B.12. SEM images of the Si cantilever from the side view. The ion dose increased by significant amount at each step. The cantilever bending transited from downwards to upwards.

- **Cantilever. 5.1. Xe-C.Al_2O_3** (Effect of ion dose)

FIB condition: 30 kV, 1.5pA

Process: 7 x 0.6 ion/nm^2 → +3 ion/nm^2

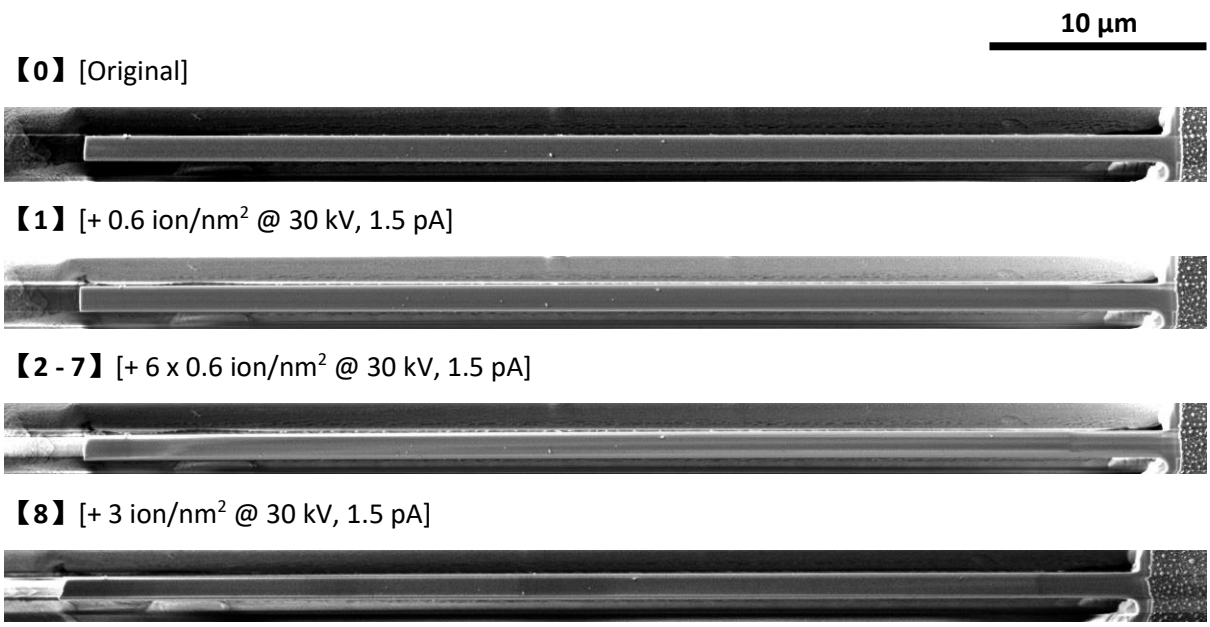


Figure B.13. SEM images of the side view of the c-plane Al_2O_3 cantilever implanted by Xe^+

- **Cantilever. 5.2. Xe-c.Al_2O_3** (Effect of beam voltage)

FIB condition #1: 4 ion/ nm^2, 3.8 - 5.2 pA

Process #1 **[1-4]**: 5 keV → 8 keV → 16 keV → 30 keV

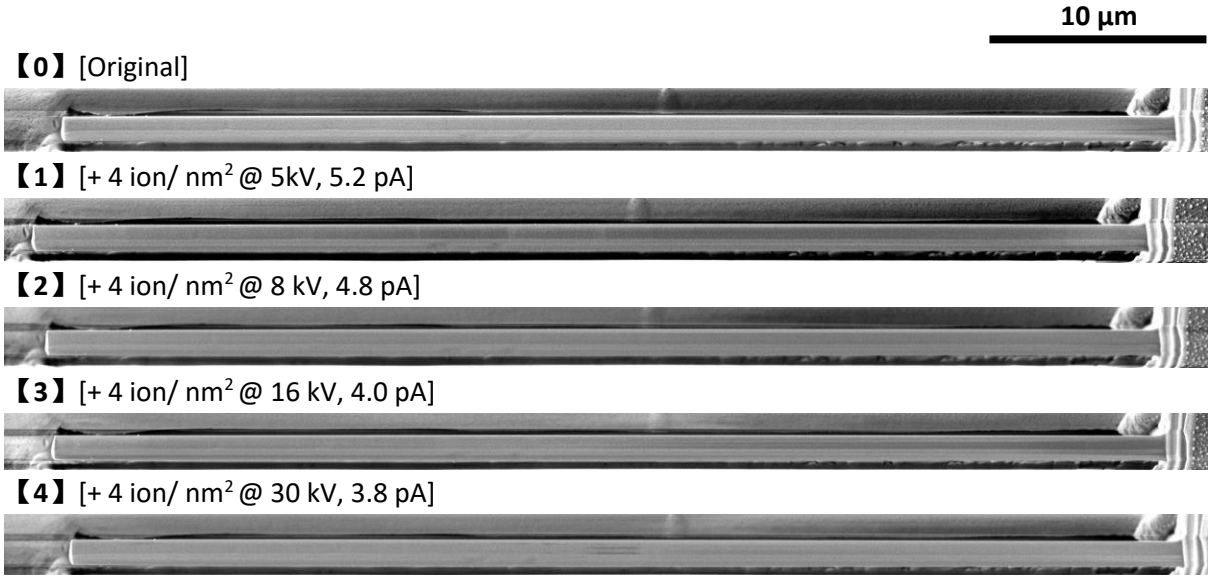


Figure B.14. SEM images of the side view of the c-plane Al_2O_3 cantilever implanted by Xe^+

FIB condition #2: 30 kV, 1800 pA

Process #2 **[5-6]**: +3000 ion/ nm^2 → +6000 ion/ nm^2

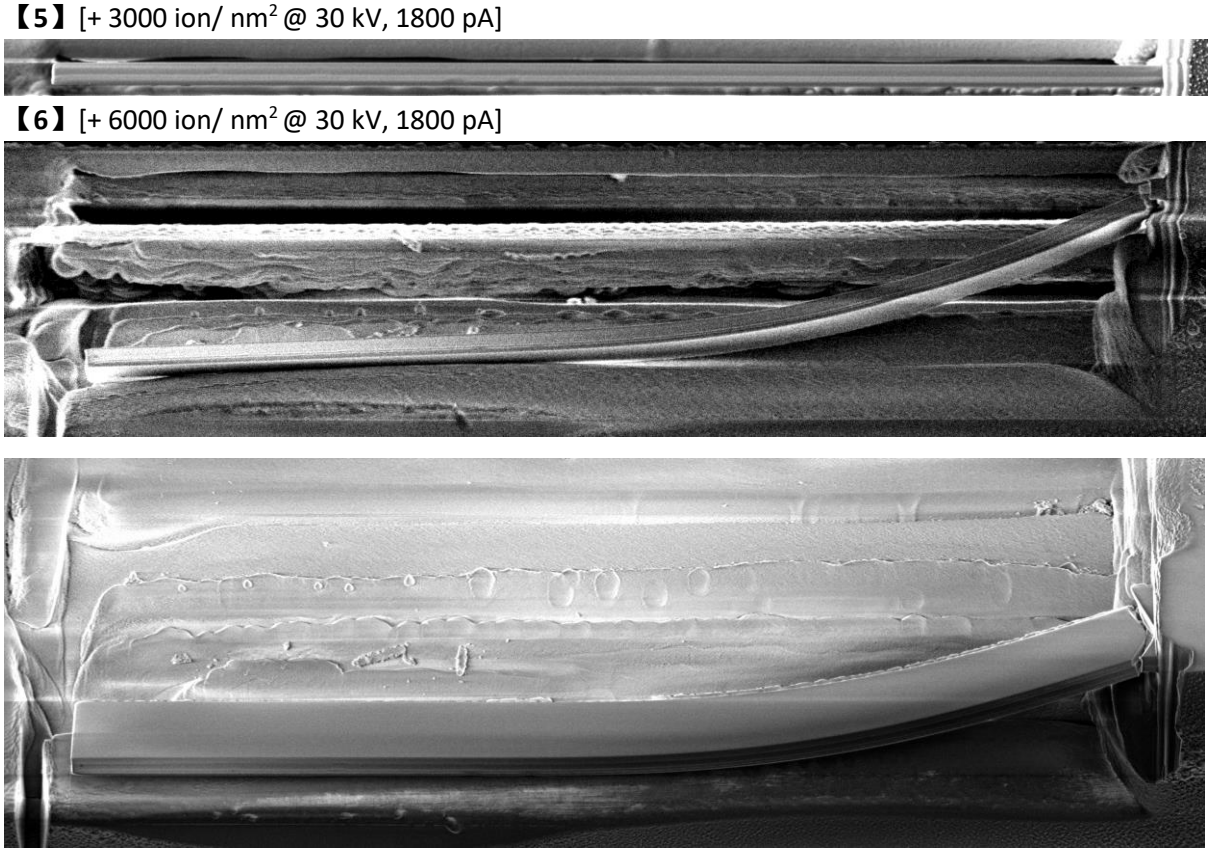


Figure B.15. SEM images of the c-plane Al_2O_3 cantilever implanted by Xe^+

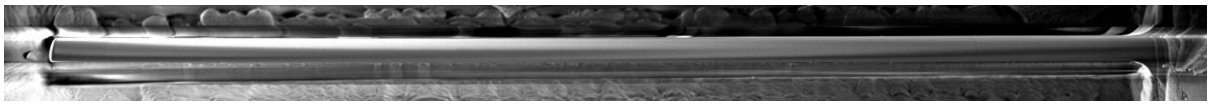
- **Cantilever. 6.1. Xe-a.Al_2O_3** (Effect of ion dose)

FIB condition #1: 30 kV, 1.5 pA

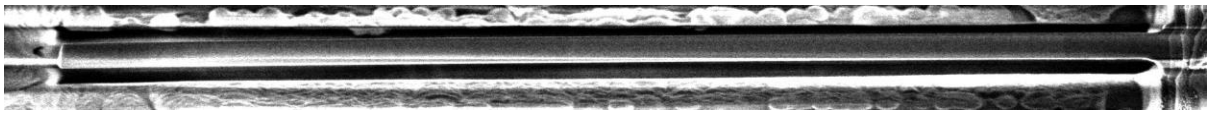
Process #1 **[1-9]**: 6 x 0.06 ion/ nm^2 → +2 x 0.6 ion/ nm^2 → +6 ion/nm^2

10 µm

【**0**】[Original]



【1 - 8】[+ 6 x 0.06 ion/ nm^2 + 2 x 0.6 ion/ nm^2]



【9】[+6 ion/nm^2]

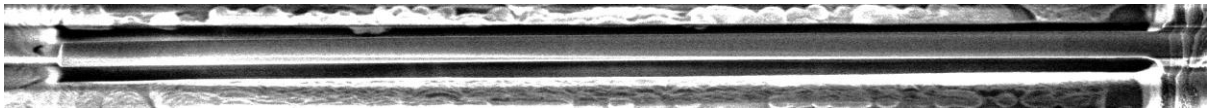
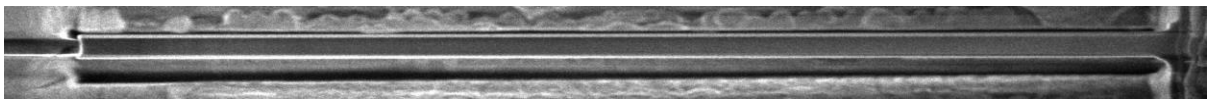


Figure B.16. SEM images of the a-plane Al_2O_3 cantilever implanted by Xe^+

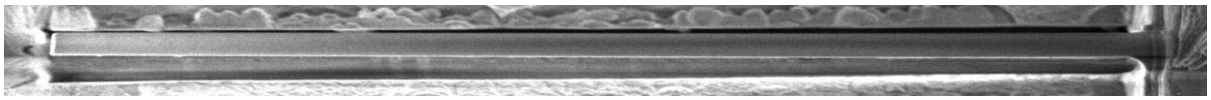
FIB condition #1: 30 kV

Process #2 **[10-14]**: +300 ion/ nm^2 @ 1.5 pA → +600 ion/ nm^2 @ 1800 pA → +3000 ion/ nm^2 @ 1800 pA → +6000 ion/ nm^2 @ 1800 pA → (+54 ion/ nm^2 @ 1800 pA)

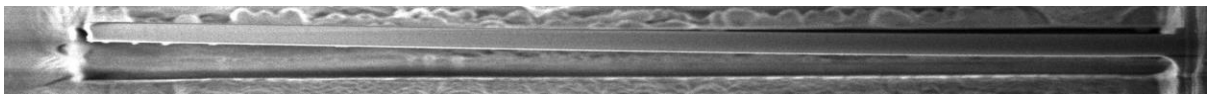
【11】[+600 ion/nm^2]



【12】[+3000 ion/nm^2]



【13】[+6000 ion/nm^2]



【14】[+54 ion/nm^2]

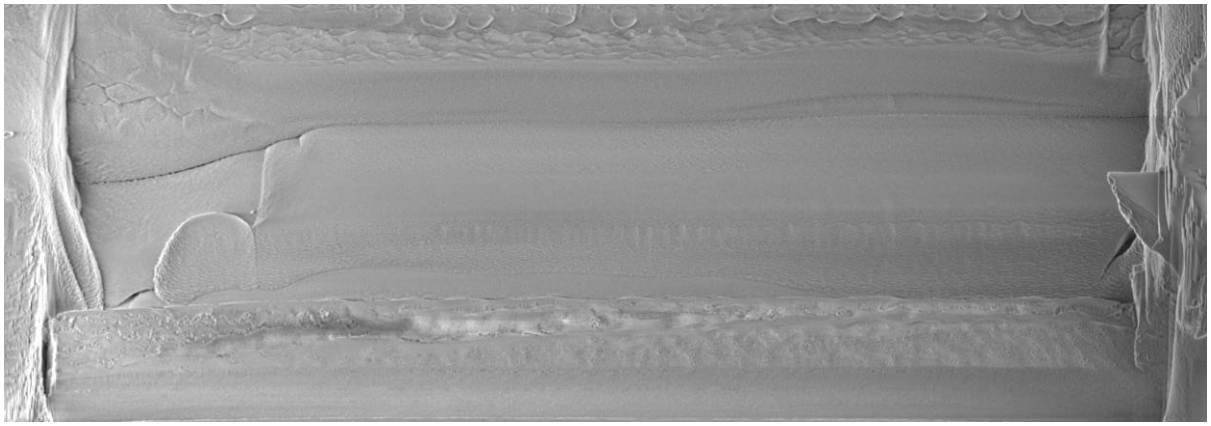


Figure B.17. SEM images of the side view of the a-plane Al_2O_3 cantilever implanted by Xe^+ with high doses at high currents

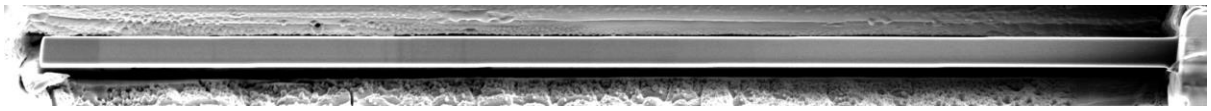
- **Cantilever.7.1. Xe-SiC** (Effect of ion dose)

FIB condition #1: 30 kV, 1.5 pA

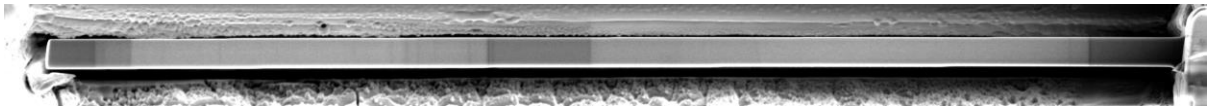
Process #1 **[1-8]**: 8 × 0.6 ion/nm^2

10 µm

【0】 [Original]



【1】 [+ 0.6 ion/nm^2 @ 30 kV, 1.5 pA]



【2 - 8】 [+ 7 × 0.6 ion/nm^2 @ 30 kV, 1.5 pA]

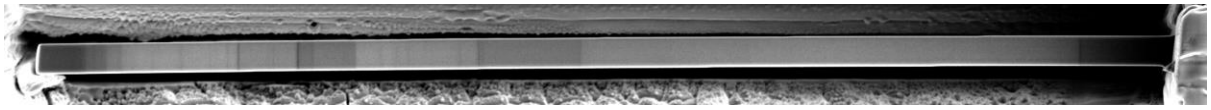
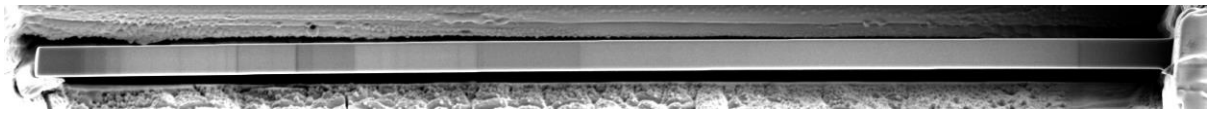


Figure B.18. SEM images of the side view of the Si cantilever implanted by Xe^+, showing the curvatures. The ions were implanted with a dose of 0.6 ion/nm^2 at each step under 30 keV, 1.5 pA.

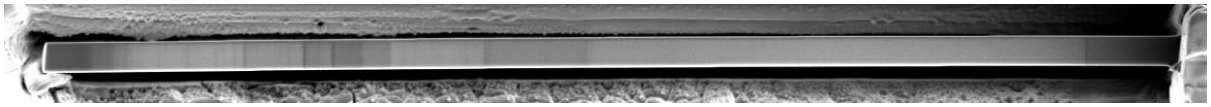
FIB condition #2: 30 kV

Process #2 **[9-11]**: +5 ion/nm^2 @2.8 pA → +5 ion/nm^2 @24 pA → +5 ion/nm^2 @230 pA

【9】 [+ 5 ion/nm^2 @ 30 kV, 2.8 pA]



【10】 [+ 0.5 ion/nm^2 @ 30 kV, 24 pA]



【11】 [+ 0.5 ion/nm^2 @ 30 kV, 230 pA]

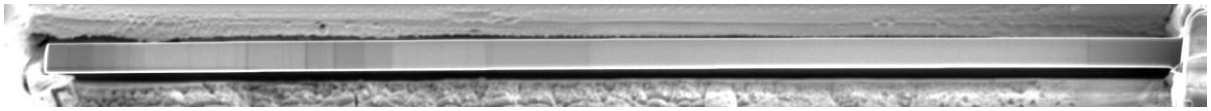


Figure B.19. SEM images of the side view of the SiC cantilever implanted by Xe^+. The beam current increased to 2.8 pA, 24 and 230 PA with higher dose given at each current.

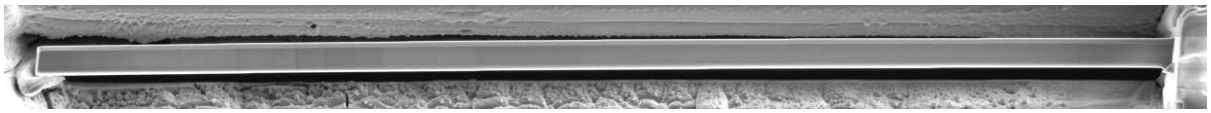
FIB condition #3: 30 kV

Process #3 **[12-19]**: +600 ion/nm^2+ 2400 ion/nm^2 @230 pA → +3000 ion/nm^2 @1800 pA → +6000 ion/nm^2 @2300 pA → +7800 ion/nm^2 + 3600 ion/nm^2+ 2 × 3000 ion/nm^2 @6700 pA

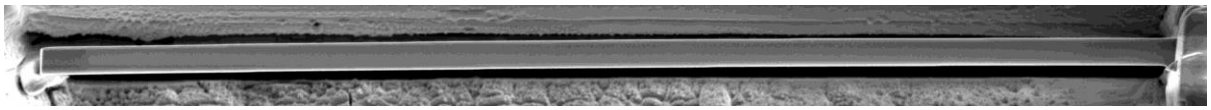
Following Process #2, the investigation continued with further implantation of high ion dose by following the procedure listed above, ending up with significant upwards bending (Figure 7.26). With

increasing ion dose, the apparent residual stress transited from compressive to tensile, and increased in an almost linear manner with the ion dose, ending up at +0.8 GPa.

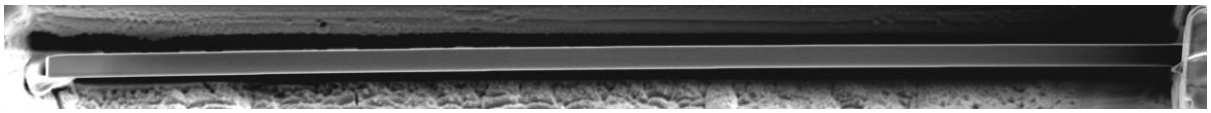
【12】[+ 600 ion/nm^2 @ 30 kV, 230 pA]



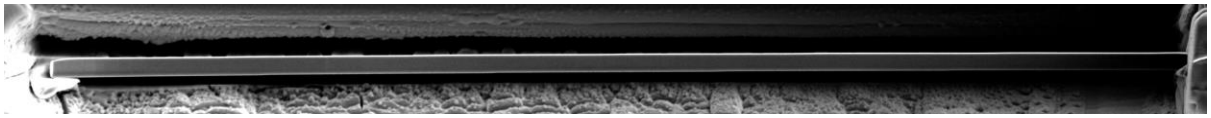
【13】[+ 2400 ion/nm^2 @ 30 kV, 230 pA]:



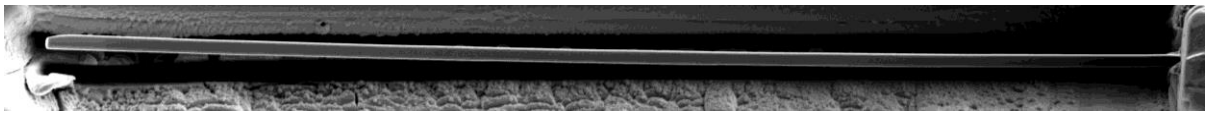
【14】[+ 3000 ion/nm^2 @ 30 kV, 1800 pA]:



【15】[+ 6000 ion/nm^2 @ 30 kV, 2300 pA]



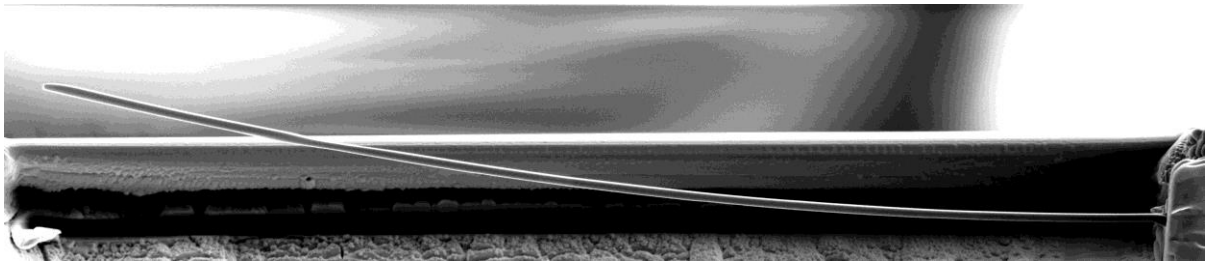
【16】[+ 7800 ion/nm^2@ 30 kV, 6700 pA]



【17】[+ 3600 ion/nm^2 @ 30 kV, 6700 pA]



【18】[+ 3000 ion/nm^2 @ 30 kV, 6700 pA]



【19】[+ 3000 ion/nm^2 @ 30 kV, 6700 pA]

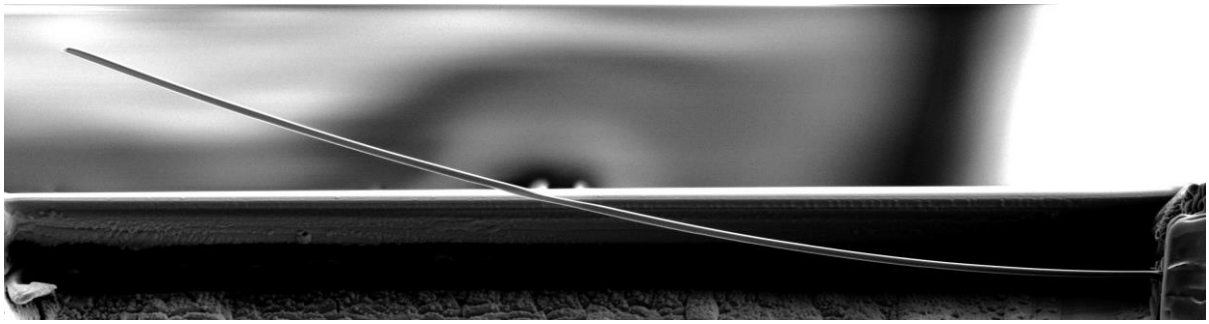


Figure B.20. SEM images of the side view of the SiC cantilever implanted by Xe^+ with high doses and high currents.

- **Cantilever. 7.2. Xe-SiC** (Effect of ion dose and beam current)

FIB condition: 30 kV

Process: 0.6 ion/nm^2@230 pA → +1 ion/nm^2 @230 pA → +3 ion/nm^2 @1800 pA → +6 ion/nm^2 @1800 pA → +60 ion/nm^2 @1800 pA → +2400 ion/nm^2 @1800 pA → +2400 ion/nm^2 @6700 pA → +2 × 12000 ion/nm^2 @6700 pA



Figure B.21. SEM images of the side view of the SiC cantilever implanted by Xe^+

Appendix C COMSOL simulation of temperature distribution in FIBed cantilever

The temperature distribution in a FIBed cantilever is simulated using COMSOL Multiphysics software by Robin Laurence. Using sapphire as the target material (thermal conductivity = 42 $W \cdot m^{-1} \cdot K^{-1}$, specific heat = 761 $J \cdot kg^{-1} \cdot K^{-1}$, emissivity = 0.48, density = 3980 $kg \cdot m^{-3}$, Stefan-Boltzmann constant = 5.67×10^{-8} $W \cdot m^{-2} \cdot K^{-4}$) with empirical dimensions (length = 50 µm, width = 4 µm, thickness = 1 µm), both the heat conduction to the bulk through the fixed end of the cantilever and heat radiation to the ambient environment (293.15 K) are taken into account. The original temperature of the cantilever and the bulk are both set to 293.15 K.

In the first model, a heat flux is applied constantly over the entire top surface of the cantilever. For the highest beam current employed in the present study, i.e. 6700 pA at 30 kV, equal to a heat flux of 1.0×10^{6} $W \cdot m^{-2}$, the maximum temperature in the cantilever at the steady state is only ~354 K (Figure C.1).

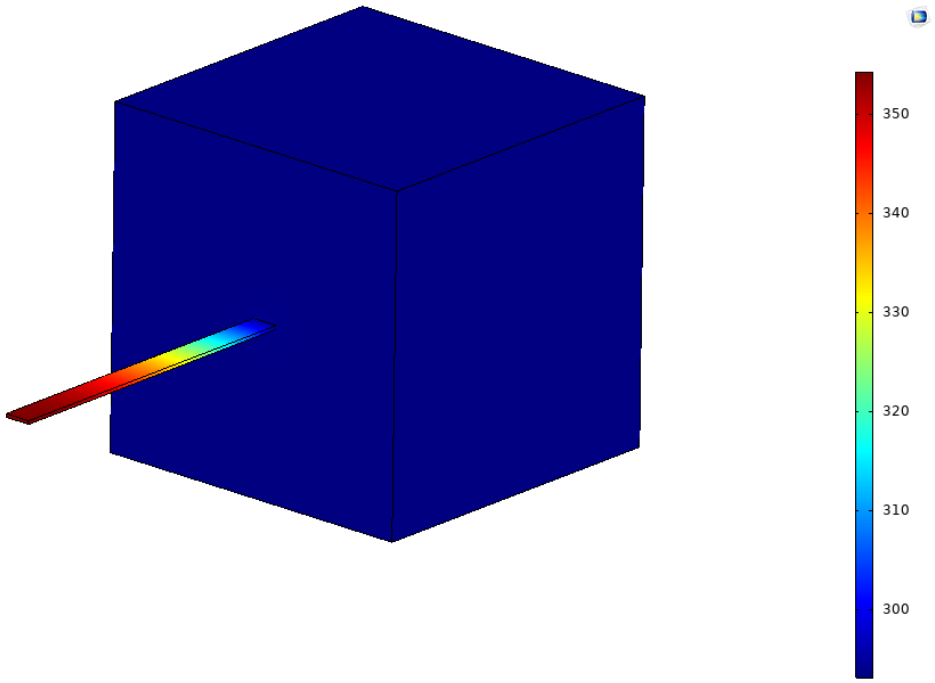


Figure C.1. COMSOL simulation of temperature distribution at steady state, with constant heat flux over the entire cantilever top surface, credit to Robin Laurence.

In the second model, the heat loading is applied in a different way – it is no longer uniformly distributed on the top surface but focuses on a single point, which heats constantly the local point temperature to 1500 K for 100 ps prior to cooling down (Figure C.2).

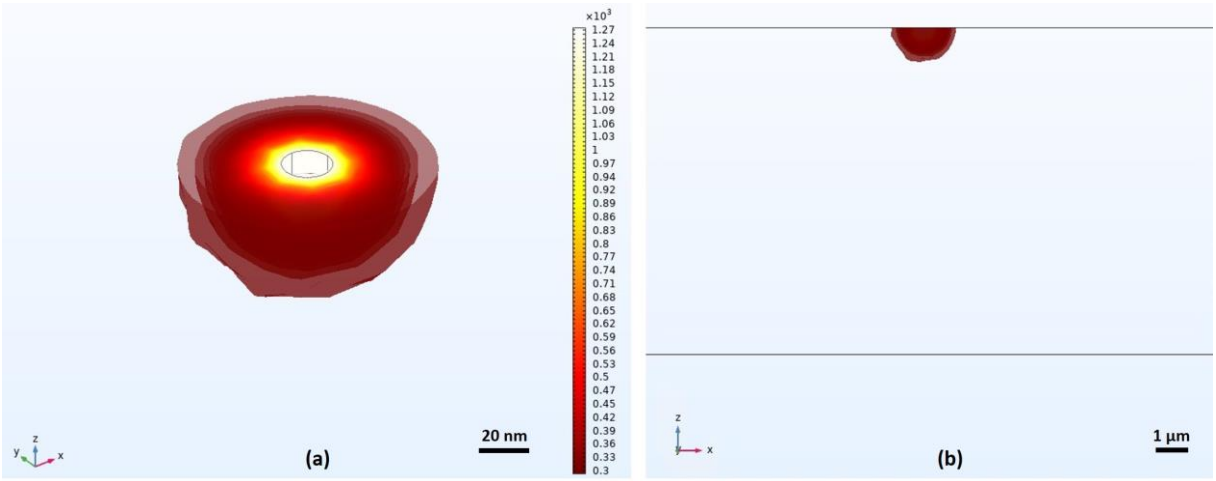


Figure C.2. COMSOL simulation of point heating on the top surface of the cantilever, by heating a 20 nm diameter x 20 nm height cylinder to 1500 K for 100 ps. (a) Heating point and the heated area around it. (b) Side view of the cantilever showing the heating point on the top surface. Credit to Robin Laurence.

The results (Figure C.3) shows that despite the high temperature at the heating point (i.e. 1500 K), the rest of the cantilever (more than 40 nm away from the heating point) is never heated to more than 400 K, suggesting that the thermal spike heating is highly localised.

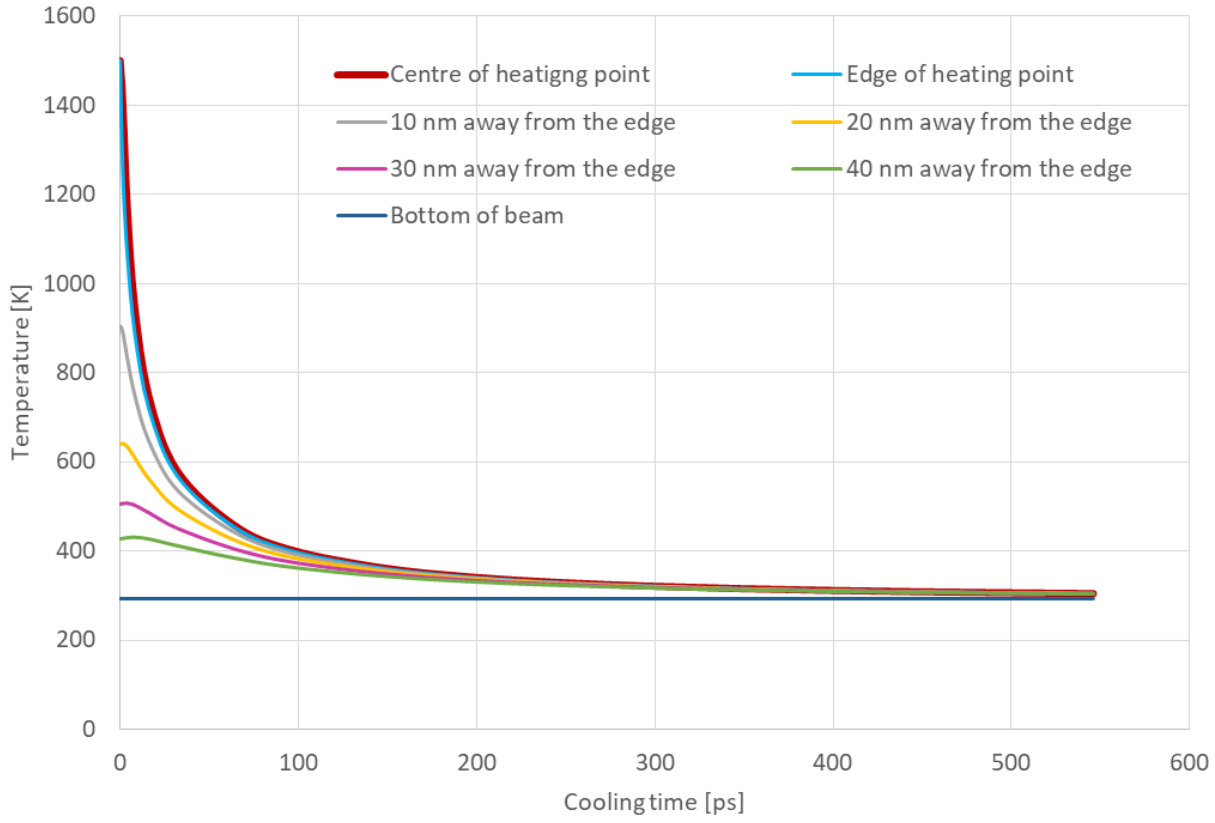


Figure C.3. Temperature gradient as function of cooling time for recording points at the centre and edge of the heating point, as well as 10, 20, 30 and 40 nm away from the edge of the heating point . Credit to Robin Laurence.

COMSOL was also used to simulate the case where cracks formed at the root of the cantilever disconnected the thermal conduction towards the bulk material or microcracks formed in the cantilever reduced the thermal conductivity of the entire beam. The result (Figure C.4a) indicated that the thermal conductivity of the cantilever needs to be reduced to 3 $W \cdot m^{-1} \cdot K^{-1}$ to have the cantilever heated to above 1100 K at the free end. Alternatively, the entire cantilever was heated to above 800 K if the local thermal conductivity at the root of the cantilever was reduced to 0.01 $W \cdot m^{-1} \cdot K^{-1}$ (Figure C.4b).

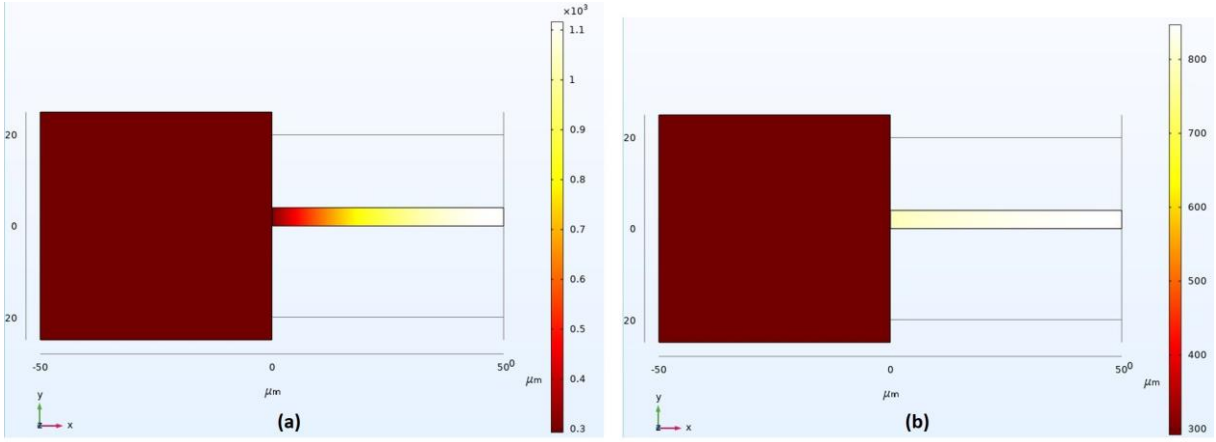


Figure C.4. COMSOL simulation of temperature distribution in the cantilever that received point heating to 1500 K, with all the parameters apart from thermal conductivity remaining the same as applied in Figure C.2. (a) The thermal conductivity of the entire cantilever was reduced to 3 $W \cdot m^{-1} \cdot K^{-1}$. (b) The thermal conductivity of the interface between the cantilever and the bulk material was reduced to 0.01 $W \cdot m^{-1} \cdot K^{-1}$, with the thermal conductivity of the rest of the cantilever remaining at 42 $W \cdot m^{-1} \cdot K^{-1}$. Credit to Robin Laurence.